Shankar Vallabhajosula

Molecular Imaging

Radiopharmaceuticals for PET and SPECT

Springer

Molecular Imaging

Shankar Vallabhajosula

Molecular Imaging

Radiopharmaceuticals for PET and SPECT

Springer

Shankar Vallabhajosula, Ph.D.
Professor of Radiochemistry and Radiopharmacy in Radiology
Weill Cornell Medical College of Cornell University
Citigroup Biomedical Imaging Center (CBIC)
New York, NY
USA

Cover design: eStudio Calamar, Figueres, Berlin.

Printed on acid-free paper

Springer is part of Springer Science+Business Media (www.springer.com)

*To my mother, Subbalakshmi,
and to the memory of my father,
Subbaraya Sastry, with respect
and gratitude, but most
of all with love.*

Foreword

Molecular imaging is a term that is now used frequently to describe much of what nuclear medicine has been involved in for almost 50 years. Since the early attempts to produce images representing the spatial distribution of specific tissue and organ functions such as the use of radioiodine to identify (and also to quantify) thyroid tissue function or the use radioiodine labeled human serum albumin (HSA) to identify the increased extracellular fluid in a brain tumor, nuclear medicine scientists and physicians have used the powerful tools, radioactive emission and decay and the tracer principle, for this purpose.

In the case of thyroid imaging with radioiodine, the radionuclide itself is the tracer that specifically recognizes (and is recognized by) the iodide transporter and the subsequent trapping and organification mechanism, results in thyroid hormone synthesis. In the early efforts to localize brain tumors, the radioiodine was chemically bound to HSA, and as a result of its molecular size, radioiodinated-HSA was useful to identify the increased extracellular fluid content of various brain tumors in contrast to normal cerebral cortex.

The number of applications of molecular imaging therefore depends upon the radionuclides available, their inherent biochemistry whereby the radionuclide itself might be a useful tracer [such as ^{131}I, ^{124}I or ^{123}I as an iodide for assessment of thyroid function and imaging or ^{18}F as the fluoride to measure bone kinetics and skeletal imaging]. In addition, depending upon the chemistry of a particular element, the radiotracer may be useful to evaluate and image other molecular and physiologic processes if the radionuclide can either be incorporated into the native molecular structure of a compound [such as ^{197}Hg in a mercurial diuretic for renal imaging in the pre-^{99m}Tc era or ^{57}Co within the cyanocobalamin molecule to evaluate the intestinal absorption of Vitamin B12] or bound to a messenger molecule without significantly interfering with recognition by the specific receptor [such as ^{111}In-DTPA-pentetreotide or ^{68}Ga-DOTATOC to Somatostatin receptor subtypes].

To fully utilize these various radiotracers and radiolabeled molecules, the medical scientist and physician needs also to appreciate issues related to production and availability, type of radioactive decay and dosimetry and the interaction of radiation and matter in order to efficiently detect the distributed signal or at least understand the inherent limitations and source of potential errors. Furthermore, by understanding existing instruments and radiotracers one may better design the next generation of strategies to help drive the field of molecular imaging.

"*Molecular Imaging: Radiopharmaceuticals for PET and SPECT*" is not a mere text on radiopharmaceuticals. In this volume, Shankar Vallabhajosula, Ph.D. has provided the reader with a single volume that describes and explains all of these

components of radionuclide based "molecular imaging". Dr. Vallabhajosula shares his insight that molecular imaging is based on an understanding of the continuum of science from atomic structure and relationships, through chemistry and physiology, the physics of instrumentation and the relationship of radiation and matter as well as the specific details of the radiopharmaceuticals themselves and the pharmaceutical principles including the practice of pharmacy. His description of his insight is further enriched by over 35 years of experience in nuclear medicine and all of its applications and his affection for the history and philosophy of science.

"Molecular Imaging: Radiopharmaceuticals for PET and SPECT" is a remarkable volume in that it comprehensively covers the entire scope of the basic sciences of nuclear medicine – and it does so in a highly readable style. It is further remarkable in that the entire text has been written by a single author, perhaps necessary to communicate, in addition to all of the scientific details, this over-riding view that all of the details are part of a continuum and that it is necessary to "see the forest as well as the trees" [to paraphrase an expression].

This is both a textbook on the subject and a history of the subject. It should be read by students and practitioners, medical doctors and scientists, radiochemists, physicists, radiopharmacists, technologists and research personnel. In addition, for those learning about molecular imaging using non-radionuclide (e.g., optical, MRI) based strategies, this book is an excellent introduction to important issues, lessons, and unifying principles for the entire field. The volume consists of 20 chapters and contains many excellent figures and tables. In addition to the science, it includes some brief history of the discoveries, the insights and developments that hopefully will sustain our memory of the science as well as of the scientists. Each Chapter begins with a quote from a senior scientist. These quotes set a tone; recognition of, and respect for, the complexity of the physical and biological world – and man's ability to understand it.

Dr. Vallabhajosula has performed a highly important service for nuclear medicine and the medical imaging community by creating this volume that brings together the scientific foundation of our field and by sharing his passion for the subject. Hopefully, the material and this stimulating presentation will motivate some of the readers to contribute to further evolution of this adventure.

Stanley J. Goldsmith, MD   Sanjiv Sam Gambhir MD, Ph.D.
New York Presbyterian Hospital   Stanford University Medical Center
and Weill Cornell Medical College
of Cornell University

Preface

Everything is determined, the beginning as well as the end, by forces over which we have no control. It is determined for the insect, as well as for the star. Human beings, vegetables, or cosmic dust, we all dance to a mysterious tune, intoned in the distance by an invisible piper.

Albert Einstein

In my life, the invisible piper has long been and will continue to be "science." Indeed, in 1967, during my second year in pharmacy school, while reading general books on science, I first learned that an unstable atom emits radiation, which might be used as a beacon or a signal for detecting the exact location of that atom. This initial introduction to atomic physics had a significant impact on my view of the universe and all that is within, and has shaped my academic and scientific career in a way I could not have foreseen, then.

The discipline of nuclear medicine has tremendously enriched my professional and personal life and several people have been instrumental in shaping my destiny. Professor Walter Wolf, who ignited my research interests in the development of radiopharmaceuticals, Professor Henry Wagner, Jr., the ambassador of nuclear medicine, Professor Michael Phelps, the pioneer and visionary of PET, in particular, have been my inspirational and intellectual gurus. Also, Professor Sanjiv Sam Gambhir, one of the founders of molecular imaging as a scientific discipline in diagnostic radiology has been a continuous source of inspiration not only to me but to a whole new generation of young investigators. Words cannot express my gratitude to Professor Stanley J. Goldsmith, who for almost three decades has instigated many challenging discussions, supported me in all my scientific endeavors, and is now a part of my family.

Molecular imaging is a fascinating and important technology in radiology that grows more diverse every day. Imaging based on radioisotopes is the major theme of this book and emphasizes both the basic and clinical science of nuclear medicine, based exclusively on radiopharmaceuticals for PET and SPECT. This book grew out of many lectures and my own struggles to more fully understand this subject. My goal in writing this book was not to discuss, in depth, the chemistry of radiopharmaceuticals. Instead it was my intention to provide a broad view of clinical applications in molecular imaging and, thereby, make the readers better understand and appreciate the importance of radiopharmaceutical design and development in the optimization of molecular imaging technology. Finally, although Chapter 2, which provides a history of the atom, is not necessarily relevant to the practical and clinical applications of molecular imaging, it is my way of paying tribute to those extraordinary scientists who have systematically studied "nature" and demonstrated the reality of atoms.

May 2009   Shankar Vallabhajosula

Contents

About the Author

Dr. Vallabhajosula attended high school in the small town of Bobbili, Andhra Pradesh, India. He graduated from Andhra University with a BS and MS in Pharmacy and subsequently obtained his Ph.D. from the University of Southern California, in 1980. After receiving the doctorate, he first worked at Mount Sinai Medical Center in New York and since 1997 has been a Professor of Radiochemistry and Radiopharmacy in Radiology at Weill Cornell Medical College of Cornell University and New York Presbyterian Hospital.

Molecular Imaging: Introduction

Chemistry is the language of health and disease and if the definition of the disease is molecular, diagnosis becomes molecular.

Henry N. Wagner, Jr.

1.1 Nuclear Medicine

Nuclear medicine can be defined quite simply as the use of radioactive materials for the diagnosis and treatment of patients, and perhaps the study of human disease (Wagner 1995a). Chemistry is the language of health and disease, since the entire body is a collection and vast network of millions of interacting molecules. If the definition of the disease is molecular, the diagnosis is also molecular. Because the treatment of many diseases is chemical, it becomes more and more appropriate that the chemistry be the basis of diagnosis and the planning and monitoring of a specific treatment. Nuclear medicine, therefore, is a medical specialty that is based on the examination of the regional chemistry of the living human body.

In the 1920s, George de Hevesy (Fig. 1.1) coined the term *radioindicator* or *radiotracer* and introduced the *tracer principle* in biomedical sciences. One of the most important characteristics of a true tracer is that it can facilitate the study of the components of a homeostatic system without disturbing their function. In the late 1920s, Hermann Blumgart and Soma Weiss, two physicians at the Massachusetts General Hospital, injected solutions of radium-C (^{214}Bi) into the veins of healthy persons and patients with heart disease to study the velocity of blood. Due to their pioneering work in nuclear medicine, Hevesy is regarded as the father of nuclear medicine, while Blumgart came to be known as the father of diagnostic nuclear medicine.

In the 1930s, the discovery of artificial radioactivity by Irene Curie and her husband Frederic Joliot, and the discovery of the cyclotron by Ernest Lawrence, opened the door for the production of radiotracers of practically every element, thus, enabling investigators to design radiotracers for the study of specific biochemical processes. Following the detection of radioactivity with the Geiger counter, it was discovered that thyroid accumulated ^{131}I as radioiodide. Consequently it was soon realized that ^{131}I can be used to study abnormal thyroid metabolism in patients with goiter and hyperthyroidism. More specifically, in patients with thyroid cancer, distant metastases were identified by scanning the whole body with the Geiger counter. The names *radioisotope scanning* and *atomic medicine* were introduced to describe the medical field's use of radioisotopes for the purpose of diagnosis and therapy. The era of nuclear medicine, as a diagnostic specialty began following the discovery of the *gamma camera* based on the principle of scintillation counting, first introduced by Hal Anger in 1958. Since then, nuclear medicine has dramatically changed our view of looking at disease by providing images of regional radiotracer distributions and biochemical functions. Over the last four decades, a number of radiopharmaceuticals have also been designed and developed to image the structure and function of many organs and tissues.

1.2 Molecular Medicine

At the present time, the precise definition of the *disease* is as difficult as defining what exactly *life* is. Defining disease at the cellular and molecular level, however, is much easier than defining disease at the level of an individual. Throughout the history of medicine, two main concepts of disease have been dominant (Wagner 1995b). The *ontological* concept views a disease as an

Fig. 1.1 George de Hevesy. The Nobel Prize in Chemistry, 1943

entity that is independent, self-sufficient, and runs a regular course with a natural history of its own. The *physiological* concept defines disease as a deviation from normal physiology or biochemistry; the disease is a statistically defined deviation of one or more functions from those of healthy people under circumstances that are as close as possible to that of a person of the same sex and age of the patient. The term *homeostasis* is used by physiologists to mean maintenance of static, or constant, conditions in the internal environment by means of positive and negative feedback of information. Approximately 56% of the adult human body is fluid. Most of the fluid is intracellular, however, one third is extra-cellular, which is, in constant motion throughout the body and contains the ions (sodium, chloride, and bicarbonate) and the nutrients (oxygen, glucose, fatty acids, and amino acids) needed by cells for the maintenance of life. Claude Bernard (1813–1878) described extracellular fluid as the internal environment of the body and hypothesized that the same biological processes that make life possible are also involved in disease. In other words, the laws of disease are the same as the laws of life. All the organs and tissues of the body perform functions that help maintain homeostasis. As long as the organs and tissues of the body perform functions that help maintain homeostasis, the cells of the body continue to live and function properly.

At birth, molecular blueprints collectively make up a person's *genome* or *genotype,* which is translated into cellular structure and function. A single *gene* defect can lead to biochemical abnormalities that produce many different clinical manifestations of disease (or *phenotypes*), a process referred to as *pleotropism*. Several gene abnormalities can result in the same clinical manifestations of disease; a process called *genetic heterogeneity*. Thus, diseases can be defined as abnormal processes as well as abnormalities in molecular concentrations of different biological markers, signaling molecules and receptors (Cotran 1999).

In 1839, Theodor Schwann discovered that all living organisms are made up of discrete cells. In 1858, Rudolph Virchow observed that a disease cannot be understood unless it is realized that the ultimate abnormality must lie in the cell (Virchow 1958). Virchow correlated disease with cellular abnormalities as revealed by chemical stains and, thus, founded the field of cellular pathology. He also aptly defined pathology as physiology with obstacles.

Most diseases begin with a cell injury that occurs if the cell is unable to maintain homeostasis. Since the time of Virchow, gross pathology and histopathology have been a foundation of the diagnostic process and the classification of diseases. Traditionally, the four aspects of a disease process that form the core of pathology are etiology, pathogenesis, morphologic changes, and clinical significance (McCance and Huether 1998). The altered cellular and tissue biology, and all forms of loss of function of tissues and organs, are, ultimately, the result of cell injury and cell death. Therefore, knowledge of the structural and functional reactions of cells and tissues to injurious agents, including genetic defects, is the key for understanding the disease process. Disease may be considered a genetic or environmental reprogramming of cells to gain or lose specific functions that are characteristic of disease. Currently, diseases are defined and interpreted in molecular terms and not just with general descriptions of altered structure.

Pathology is evolving into a bridging discipline that involves both basic science and clinical practice. More specifically, pathology is devoted to the study of the structural and functional changes in cells, tissues, and organs that underlie diseases (McCance and Huether 1998). Molecular, genetic, microbiologic, immunologic, and morphologic techniques are also helping us to understand both, the ontological and physiological causes of disease. In molecular medicine, normal and disease states are defined at the cellular and molecular levels (Wagner 2006). Therapeutic drugs are designed based on these definitions of disease are being used to treat diseases by correcting abnormal cellular or molecular processes.

1.3 Molecular Imaging

In the past, much of biological and medical imaging was driven by anatomy-based imaging or structural imaging, such as computed tomography (CT) and Magnetic resonance imaging (MRI). The field of nuclear medicine, by contrast, has focused on studying molecular events in living subjects, based on radiotracers, and is regarded as functional or physiologic imaging (Reba 1995, Massoud and Gambhir 2003). This traditional distinction between structural and functional imaging has increasingly become blurred by CT, MRI, and other techniques that provide both functional and structural information (Gabriel et al 2007).

Molecular imaging (MI) is an emerging field that aims to integrate patient-specific and disease-specific molecular information derived from diagnostic imaging studies (Jaffer and Weissleder 2005). The ultimate goal of MI is the noninvasive localization and quantification of certain molecular events in vivo, including endogenous or exogenous gene expression, signal transduction, protein–protein interaction, and transcriptional regulation. Among a variety of possible target applications, the use of MI will lead to further insights into the molecular pathology of animal models of human diseases, as well as to the development of new molecular-targeted drugs and to the design and implementation of improved patient-tailored therapies.

Most, but not all, of the functional imaging studies performed in traditional nuclear medicine can be regarded as MI. The use of ^{123}I sodium iodide to assess thyroid function and ^{111}In-DTPA-Octreotide (OctreoScan®) to image somatostatin receptor (SSTR) density of neuroendocrine tumors are clearly the best examples of MI. In contrast, ^{99m}Tc-DTPA and ^{99m}Tc-MAG3, which are used to study kidney function are not ideal examples of MI procedures.

Although, MI is not necessarily new, what is new is "molecular and anatomic correlation". Positron emission tomography (PET) is a highly sensitive, noninvasive technology that is ideally suited for imaging cancer biology based on [^{18}F]Fluorodeoxyglucose (FDG), a glucose analog and substrate for the enzyme *hexokinase*. With the introduction of "hybrid imaging" techniques which combine, for example, FDG-PET and CT, and thus providing anatomic and functional or molecular information in one image, a new era of MI has arrived. Clearly, this will have implications for the education of not only nuclear physicians, but also radiologists. More specifically, the former will need to learn cross-sectional anatomy and the latter the concepts of tracer techniques and functional imaging (Thakur 2006). MI is also likely to lead to a further blurring of the distinction between diagnosis and treatment and to a paradigm shift to early diagnosis that will lead to image-guided, individualized molecular therapy. Further, biomarkers will be able to be imaged and quantified to provide early evidence of the efficacy of a specific treatment.

1.3.1 Definitions

In 2005, the Radiological Society of North America (RSNA) and the Society of Nuclear Medicine (SNM) jointly convened a workshop on MI (Thakur 2006). At that time the group developed the following definition of MI, successfully testing it against the existing variety of imaging tools available in humans and in animal experimental contexts:

> MI techniques directly or indirectly monitor and record the spatiotemporal distribution of molecular or cellular processes for biochemical, biologic, diagnostic, or therapeutic applications.

The members of the Molecular Imaging Center of Excellence (MICoE) Standard Definitions Task Force recently developed the following four standard definitions and terms that will serve as the foundation of all communications, advocacy, and education activities for MICoE and the Society of Nuclear Medicine (SNM) (Mankoff 2007).

- MI is the visualization, characterization, and measurement of biological processes at the molecular and cellular levels in humans and other living systems. To elaborate; MI typically includes two- or three-dimensional imaging, as well as quantification over time. The techniques used include radiotracer imaging/nuclear medicine, MR imaging, MR spectroscopy, optical imaging (OI), and ultrasound.
- MI agents are "probes used to visualize, characterize, and measure biological processes in living systems. Both endogenous molecules and exogenous probes can be molecular imaging agents." MI instrumentation comprises tools that enable the visualization and quantification in space and over time of signals from MI agents.

- MI quantification is the determination of regional concentrations of MI agents and biological parameters. Further, MI quantification provides measurements of processes at the molecular and cellular levels. This quantification is a key element of MI data and image analysis, especially for inter- and intrasubject comparisons.
- MI has enormous relevance for patient care: it reveals the clinical biology of the disease process; it personalizes patient care by characterizing specific disease processes in different individuals; and it is useful in drug discovery and development, for example, for studying pharmacokinetics and pharmacodynamics.

MI is an emerging field that aims to integrate patient-specific and disease-specific molecular information with traditional anatomical imaging readouts. The information provided by this field may ultimately lead to noninvasive or minimally invasive molecular diagnostic capabilities, better clinical risk stratification, more optimal selection of disease therapy, and improved assessment of treatment efficacy. Development of an MI strategy for a particular disease requires addressing four key questions (Jaffer and Weissleder 2005):

- Is there a molecular target relevant to the disease of interest?
- Once a target is selected, is there a high affinity ligand (for example, a peptide, engineered antibody, or other small molecule) that will bind to the target?
- What is the appropriate MI system to provide the required spatial resolution, sensitivity, and depth penetration for the disease?
- For a given imaging system, can an agent be synthesized to detect the desired molecular target?

MI has the potential to improve the understanding of disease in a number of biological models and systems. MI targets should be able to define the disease status earlier than conventional imaging methods, identify the underlying molecular events in disease initiation and progression, distinguish between aggressive and indolent disease states, and represent downstream targets in a well-characterized molecular network or pathway.

1.3.2 Molecular Imaging Technologies

A wide range of technologies are available for noninvasive in vivo MI studies (Jaffer and Weissleder 2005, Levin 2005, Hoffman and Gambhir 2007, Judenhofer et al 2008). Various technical features of several MI technologies are summarized and compared in Table 1.1.

1.3.2.1 Magnetic Resonance Imaging

The primary advantage of MRI as an MI technique is its ability to provide soft tissue and functional information by exploiting proton density, perfusion, diffusion, and biochemical contrasts (Tempany and McNeil 2001). MRI offers two main advantages over nuclear imaging techniques: higher special resolution (<1 mm) and the ability to obtain anatomic, physiologic, and metabolic information in a single imaging session. In addition, MRI offers good depth penetration, similar to PET and CT (Jaffer and Weissleder 2005). Increasing MRI field strength (3 T magnets) is one of

Table 1.1 Noninvasive in vivo molecular imaging modalities

Imaging modality	Form of energy used	Spatial resolution (mm)		Acquisition time/ frame	Probe mass required	Sensitivity of detection	Depth of penetration
		Clinical	Animal	(s)	(ng)	Mol/l	(mm)
PET	Annihilation photons	3–8	1–3	1–300	1–100	10^{-11}–10^{-12}	>300
SPECT	γ-photons	5–12	1–4	60–2000	1–1,000	10^{-10}–10^{-11}	>300
CT	X-rays	0.5–1	0.03–0.4	1–300	–	–	>300
MRI	Radio frequency waves	0.2–0.1	0.025–0.1	50–3000	10^3–10^6	10^{-3}–10^{-5}	>300
Ultrasound	High frequency sound waves	0.1–1.0	0.05–0.1	0.1–100	10^3–10^6	–	1–200
BLI	Visible to infrared light	–	3–10	10–300	10^3–10^6	10^{-13}–10^{-16}	1–10
FLI	Visible to infrared light	–	2–10	10–2000	10^3–10^6	10^{-9}–10^{-11}	1–20

the recent advances designed to increase the signal-to-noise and contrast-to noise ratio, which permits reduction in overall scan length and improvement in spatial resolution. The magnetic field strength for small-animal imaging systems is also increasing, with 9.4 T magnets becoming standard. These systems produce microscopic resolution (tens of micrometers range) images in small-animal models and allow for the analysis of physiologic and molecular markers (Atri 2006). A number of paramagnetic- (e.g., gadolinium) and super paramagnetic- (e.g., iron oxide) based MI agents have been tested for preclinical and clinical MI applications. The primary disadvantage of MRI is its inherently low sensitivity for the detection of targeted agents compared with nuclear imaging techniques.

1.3.2.2 Optical Imaging

One of the most successful MI modes for preclinical studies is optical imaging, which is based on the detection of light photons after their interaction with the tissue. The two major OI methods are bioluminescence imaging (BLI) and fluorescence imaging (FLI).

BLI requires the cellular expression of an enzyme known as *luciferase* that is responsible for making some insects, jellyfish, and bacteria glow (Bhaumik and Gambhir 2002). The gene for this enzyme is incorporated into the DNA of cells in the animal models of disease. When an appropriate substrate (such as *D-luciferin*) interacts with the enzyme, a subtle glow of visible light (400–700 nm with energies of 1.5–3.0 eV) called *bioluminescence* (BL) is emitted. The detection of BL can be used to monitor the cellular and genetic activity of every cell that expresses the luciferase enzyme. The in vivo applications of BLI systems are most useful for small mouse models of disease since most of the organs of interest are found no more than 1–2 cm deep within the tissue. To obtain the best depth sensitivity, the camera system should be particularly sensitive to the red and near-infrared (NIR) portion of the BL emission spectrum (700–900 nm).

FLI is capable of imaging the surface distribution of FL signals. FL molecules may be genetically engineered into a mouse, for example by incorporating the gene for an FL protein as a reporter gene, or by using fluorophores or fluorescent particles known as *quantum dots* to label a biologically interesting molecule.

FLI can be performed in both live and fixed cells and no substrate is required. *Fluorochromes* can be coupled to peptides and antibodies and fluorescence signals may be activatable or switched on and off by the presence or absence of specific molecules or molecular events, which can help to further reduce the background signal (Sevick-Muraca et al 2002). In contrast, the generation of BL is specific to cells that contain the luciferase reporter gene, and is thus, of limited use for studying genetically manipulated cells, transgenic mice, or infectious agents, such as bacteria or viruses. FLT images molecular processes in 3D, by studying the distribution of molecular probes tagged with fluorescent proteins, preferably emitting in the NIR for better tissue transmission.

Although the penetration of light through the tissue is a limitation for all optical imaging methods, attenuation and autofluorescence, however, are minimized in the near-infrared window, permitting deep tissue imaging up to 10 cm. The advantages of FI methods include improved relative sensitivity, high resolution (which may be in the submillimeter range when imaged endoscopically), and the availability of a variety of imaging reporters and signal amplification strategies. In addition, OI offers a convenient way to co-register surface anatomical information with molecular information.

1.3.2.3 Ultrasound Imaging

Ultrasound offers high spatial resolution (<1 mm) and can provide excellent anatomical information for co-registration with molecular information. A number of targeted MI agents have been designed for ultrasound imaging (UI) using microbubbles, liposomes, or perfluorocarbon emulsions as scaffolds (Lanza and Wickline 2003, Lindner 2004) An important limitation of ultrasound for MI studies is the relatively large size of the imaging agent particles (<250 nm), which can restrict tissue penetration and, thus, limit application to vascular targets.

1.3.2.4 PET and SPECT

Nuclear imaging approaches, which include PET and SPECT, have the advantages of high intrinsic sensitivity and unlimited depth penetration. PET
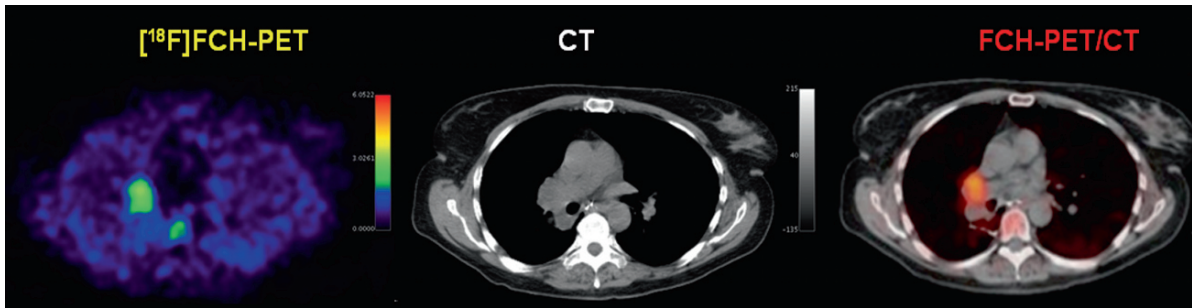
Fig. 1.2 FCH-PET/CT scan in a patient with lung cancer demonstrating the advantage of PET/CT fusion in image interpretation

has the additional advantages of being fully quanti-tative and providing higher spatial resolution than SPECT. In addition, hundreds of radiotracers based on a wide variety of radionuclides decaying due to β^+ or γ emission have been developed and tested in animal models and clinical studies documenting their potential utility as MI probes. With these tech-niques, the mass of the MI radiotracers is so small (ng or μg) that the toxicity of the administered dose is never an issue. In a typical FDG-PET study, the mass of FDG administered is <200 μg (approxi-mately one μmole). Similarly, with SSTR imaging, the mass of PET or SPECT radiotracer administered is <10 μg (<nmol), however, the spatial resolution of both these techniques is much less compared to that of CT and MRI. The fusion of molecular infor-mation of PET and SPECT with high resolution anatomical detail from CT or MRI techniques, how-ever, is playing an increasing role in routine clinical MI procedures.

The FDG-PET scans based on glucose metabolism of tumor tissue have demonstrated not only extensive clinical utility in the detection of several types of can-cers, but also in the monitoring and assessment of treat-ment responses (Fig. 1.2). [18F]Fluoride-PET scans are becoming increasingly useful in the detection of meta-static bone lesions compared to the standard 99mTc-MDP bone scans (Fig. 1.3). SSTR imaging of neuroendocrine tumors with PET and SPECT illus-trates the power and significance of MI studies, based on receptor binding radiotracers (Fig. 1.4). In brain tumors, an amino acid analog, [11C]methionine and thy-midine analog, and [18F]Fluorothymidine (FLT) provide
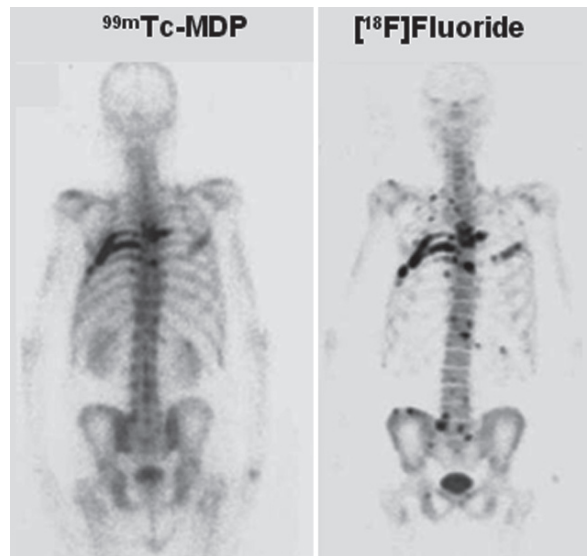
Fig. 1.3 Comparison of [18F]fluoride-PET (**b**) and 99mTc-MDP planar scintigraphy (**a**) results in a patient with bone metastases. Fluoride-PET shows more bone lesions with significantly greater spatial resolution compared to planar bone scan (Schwaiger 2003)

more specific tumor identification than glucose meta-bolic images with FDG (Fig. 1.5). In the area of neu-ropsychiatric diseases, neuroreceptor imaging with PET and SPECT has shown significant potential in clinical diagnosis and disease management. While FDG-PET is useful for the differential diagnosis of Alzheimer's disease (AD) from other dementias, sev-eral PET radiopharmaceuticals, designed to image the amyloid burden in patients with AD, are under aggressive

Fig. 1.4 Somatostatin receptor imaging in a patient with a diffusely metastasized carcinoid. [^{18}F]FP-Gluc-TOCA-PET (**a**) shows extensive metastases in more detail and with better contrast than the corresponding [^{111}In]octreotide (**b**), conventional gamma camera planar projection imaging (Wester 2003)
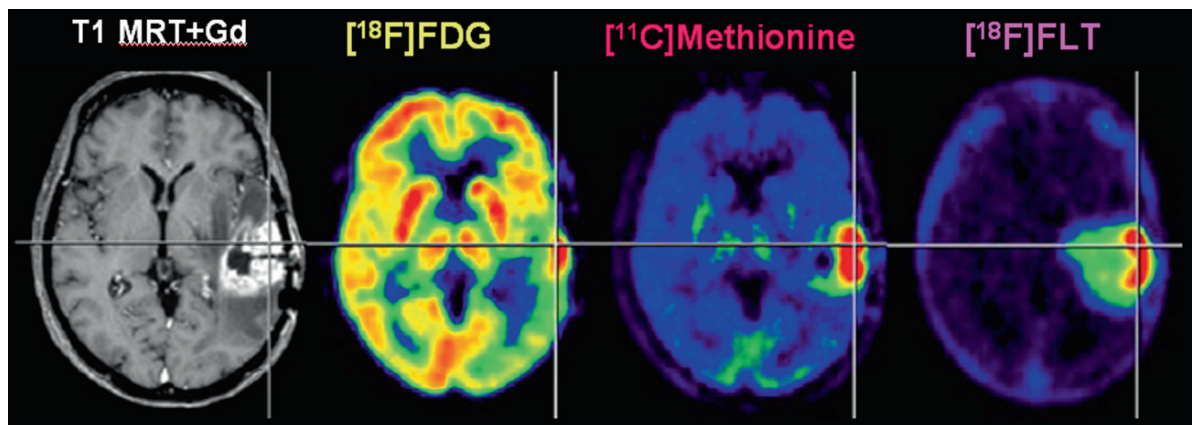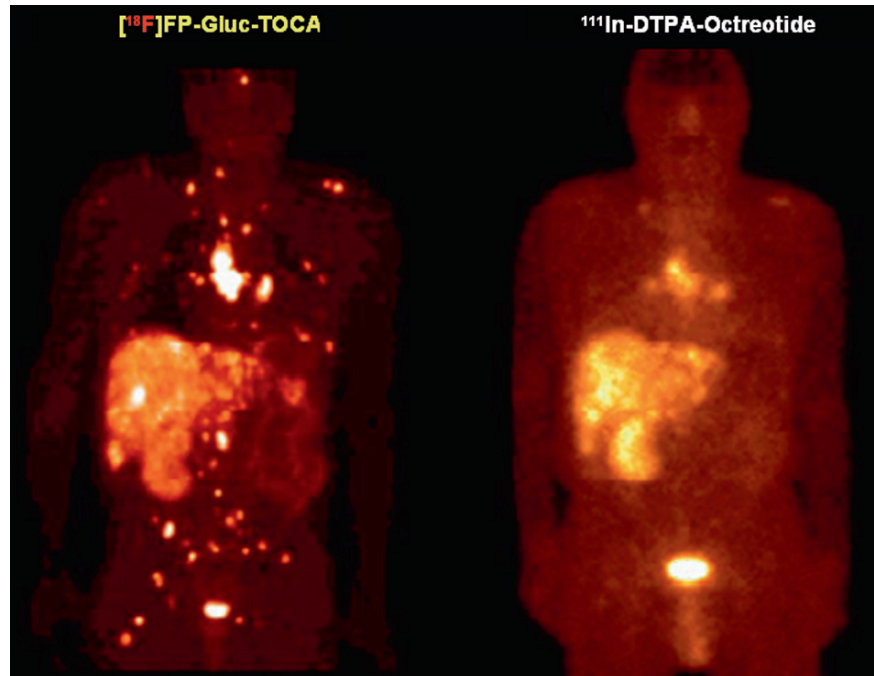
Fig. 1.5 Relative advantages of MR and PET imaging techniques to detect different biochemical processes in brain tumors (gliomas). MRI detects alterations of the blood–brain barrier and the extent of peritumoural edema, FDG-PET shows glucose metabolism, while increased cell proliferation can be imaged with specific tracers, such as [^{18}F]FLT and [^{11}C]MET (Jacobs 2005)

clinical development (Fig. 1.6). Also, dopamine transporter imaging with tropane analogs [^{18}F]FP-CIT and ^{99m}Tc-TRODAT has shown diagnostic potential for identifying patients with Parkinson's disease (PD).

At the NIH MI and contrast agent data base (Fig. 1.7), almost 600 MI radiotracers with potential clinical application have been listed. Over the next five to ten years, major clinical and basic research will be focused in assessing the diagnostic potential of some of these tracers.

1.3.2.5 Multimodality Molecular Imaging

Multimodality imaging has become an attractive strategy for in vivo imaging studies owing to its ability to provide accurate anatomical and functional information simultaneously (Catana et al 2008, Cherry 2006, Cherry et al 2008, Culver et al 2008, Insana and Wickline 2008, Townsend 2008). The combination of CT and PET was introduced commercially in 2001, followed by CT and SPECT in 2004 and PET and MRI in 2008.
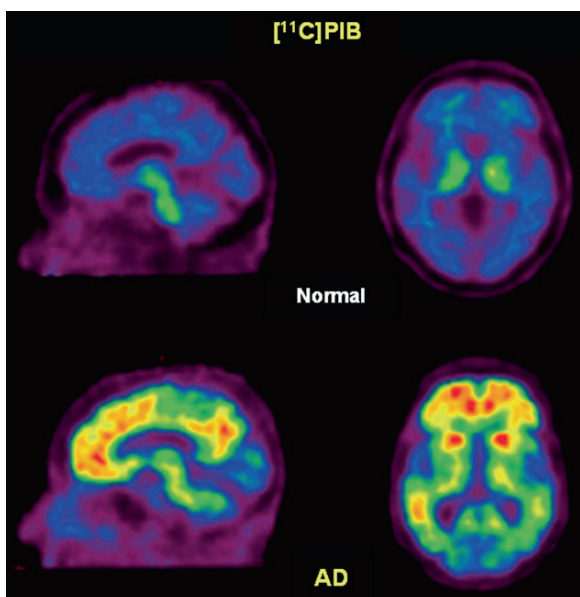
Fig. 1.6 [¹¹C]PIB-PET images show white matter uptake of PIB in an age-matched healthy control subject (Normal) and extensive cortical and subcortical uptake in a with AD (Ng et al 2007)

Fig. 1.7 Molecular imaging and contrast agent database (MICAD), which is a key component of the NIH Roadmap developed by the National Center for Biotechnology Information (NCBI), at the National Institutes of Health (NIH). Almost 650 agents are listed at this site providing full details on chemistry with preclinical and clinical data

Imaging probes that link two or three imaging labels at different sites of the same molecule are desirable for developing multimodality imaging techniques. PET and SPECT require an imaging probe while CT, MR, and optical tomography can be used with endogenous contrast. With the advent of multimodal imaging, the development of multimodal imaging probes has, thus, become important. The majority of dual-modality probes are based on nanoparticle or protein constructs. For instance, an iron oxide nanoparticle (MR) derivatized with a protein or peptide to target the probe and an NIR chromophore, simultaneously, as in the case of (a) antibodies functionalized with a PET isotope and an NIR dye (Xu et al 2007), and (b) fluorescent quantum dots derivatized with an RGD peptide for

tumor targeting and a ^{64}Cu-DOTA chelate for PET (Cai et al 2007). Another approach has been used to develop nanoparticles for sentinel node imaging based on amino terminated G6 PAMAM dendrimers as a scaffold for both Gd complexes (MR) and the NIR dye Cy5.5 (Koyama et al 2007).

1.4 Summary

There is no best modality for MI and one may have to use a combination of more than one imaging modality and molecular contrast strategy to answer the questions of interest. MRI and CT combine high-resolution morphological capabilities with physiological information, but require higher mass levels of contrast agents that may create toxicity problems. Further, MRI's morphological contrast resolution is high in soft tissue, while CT contrast resolution is best for bones and lungs. Ultrasound has the advantages of being widely available clinically, relatively inexpensive, and capable of acquiring real-time physiological information, however, the molecular probes needed for ultrasound are generally particles and, at this time, the technique is limited to only vascular targets.

The major advantage of PET and SPECT techniques is that the small probe mass and the radiolabeling strategies do not significantly perturb the biological processes under study. Further, PET has high molecular sensitivity and strong quantitative potential. SPECT can image multiple probes simultaneously provided they each emit distinct photon energies. BLI and FLI have high molecular sensitivity, but are not suitable for imaging large animal models or human subjects. In contrast, optical imaging techniques offer a low cost and quick alternative for real-time analysis of gene expression in small animal models, but are limited by the depth penetration and cannot be easily generalized to human applications.

References

Atri M (2006) New technologies and directed agents for applications of cancer imaging. J Clin Oncol 24:3299–3308

Bhaumik S, Gambhir S (2002) Optical imaging of renilla luciferase reporter gene expression in living mice. Proc Natl Acad Sci USA 99:377–382

Cai W, Chen K, Li Z-B, et al. (2007) Dual-function probe for PET and near-infrared fluorescence imaging of tumor vasculature. J Nucl Med 48:1862–1870

Catana C, Procissi D, Wu Y, et al. (2008) Simultaneous in vivo positron emission tomography and magnetic resonance imaging. Proc Natl Acad Sci USA 105:3705–3710

Cherry SR (2006) Multimodality in vivo imaging systems: Twice the power or double the trouble? Annu Rev Biomed Eng 8:35–62

Cherry SR, Louie AY, Jacobs RE (2008) The integration of positron emission tomography with magnetic resonance imaging. Proceedings of the IEEE 96:416–438

Cotran RS, Kumar V, Collins T (1999) Robbins pathologic basis of disease, 6th edn. WB Saunders, Philadelphia

Culver J, Akers W, Achilefu S (2008) Multimodality molecular imaging with combined optical and SPECT/PET modalities. J Nucl Med 49:169–172

Gabriel P, Miller KJC, Golding SJ, et al. (2007) Reinventing radiology in a digital and molecular age: Summary of proceedings of the sixth biannual symposium of the international society for strategic studies in radiology (IS^{3}R), August 25–27, 2005; Radiology 244:633–638

Hoffman JM, Gambhir SS (2007) Molecular imaging: the vision and opportunity for radiology in the future. Radiology 244:39–47

Insana MF, Wickline SA (2008) Multimodality biomolecular imaging. Proceedings of the IEEE 96:378–381

Jacobs AH, Winkler A, Castro MG, et al. (2005) Human gene therapy and imaging in neurological diseases Eur J Nucl Med Mol Imaging 32:S358–S383

Jaffer FA, Weissleder R (2005) Molecular imaging in the clinical arena. JAMA 293:855–862

Judenhofer MS, Wehrl HF, Newport DF, et al. (2008) Simultaneous PET-MRI: A new approach for functional and morphological imaging. Nat Med 14:459–465

Koyama Y, Talanov VS, Bernardo M, et al. (2007) A dendrimer-based nanosized contrast agent dual-labeled for magnetic resonance and optical fluorescence imaging to localize the sentinel lymph node in mice. J Magn Reson Imaging 25:866–871

Lanza GM, Wickline SA (2003) Targeted ultrasonic contrast agents for molecular imaging and therapy. Curr Probl Cardiol 28:625–653

Levin CS (2005) Primer on molecular imaging technology. Eur J Nucl Med Mol Imaging 32:S325–S345

Lindner JR (2004) Microbubbles in medical imaging: Current applications and future directions. Nat Rev Drug Discov 3:527–532

Mankoff DA (2007) A definition of molecular imaging. J Nucl Med 48:18N, 21N

Massoud TF, Gambhir SS (2003) Molecular imaging in living subjects: Seeing fundamental biological processes in a new light. Genes Dev 17:545–580

McCance KL, Huether SC (1998) Pathophisiology. The biological basis for disease in adults and children, 3rd edn. Mosby, St Louis

Ng S, Villemagne VL, Berlangieri S, et al. (2007) Visual assessment versus quantitative assessment of [^{11}C]PIB PET and [^{18}F]FDG PET for detection of Alzheimer's disease. J Nucl Med 48:547–552

Reba RC (1995) Molecular nuclear medicine. J Nucl Med 36(suppl):1S–30S

Schwaiger M (2003) Highlights of the 15th annual congress of the European association of nuclear medicine. Eur J Nucl Med 30:165–180

Sevick-Muraca EM, Houston JP, Gurfinkel M (2002) Fluorescenceenhanced, near infrared diagnostic imaging with contrast agents. Curr Opin Chem Biol 6:642–650

Tempany CM, McNeil BJ (2001) Advances in biomedical imaging. JAMA 285:562–567

Thakur M, Lentle BC (2006) Report of a summit on molecular imaging. AJR 186:297–299

Townsend DT (2008) Dual-modality imaging: Combining anatomy and function. J Nucl Med 49:938–955

Virchow R (1958) Disease, life and man. Stanford University Press, Stanford

Wagner HN Jr (1995a) Nuclear medicine: What it is and what it does. In: Wagner HN Jr, Szabo Z, Buchanan JW (eds) Principles of nuclear medicine. WB Saunders, Philadelphia

Wagner HN Jr (1995b) The diagnostic process. In: Wagner HN Jr, Szabo Z, Buchanan JW (eds) Principles of nuclear medicine. WB Saunders, Philadelphia

Wagner HN Jr (2006) From molecular imaging to molecular medicine. J Nucl Med 47(8):13N–39N

Wang DS, Dake MD, Park JM, Kuo MD (2006) Molecular imaging: a primer for interventionalists and imagers. J Vasc Interv Radiol 17:1405–1423

Weissleder R, Mahmood U (2001) Molecular imaging. Radiology 219:316–333

Wester HJ, Schottelius M, Scheidhauer K, et al (2003) PET imaging of somatostatin receptors: Design, synthesis and preclinical evaluation of a novel [^{18}F]-labeled, carbohydrated analogue of octreotide. Eur J Nucl Med Mol Imaging 30:117–122

Xu H, Baidoo K, Gunn AJ, et al. (2007) Design, synthesis, and characterization of a dual modality positron emission tomography and fluorescence imaging agent for monoclonal antibody tumor-targeted imaging. J Med Chem 50:4759–4765

Science of Atomism: A Brief History

<div style="text-align:right">**2**</div>

If, in some cataclysm, all scientific knowledge was to be destroyed, and only one sentence passed on to the next generations of creatures, what statement would contain the most information in the fewest words? I believe it is the atomic hypothesis (or the atomic fact, if you wish to call it that) that all things are made of atoms – little particles that move around in perpetual motion, attracting each other when they are a little distance apart, but repelling upon being squeezed into one another.

<div style="text-align:right">Richard P. Feynman</div>

2.1 Atomism

In natural philosophy, *atomism* is the theory that all the objects in the universe are composed of very small, indestructible elements – *atoms*. The notion of atomism first arose as a result of philosophic deduction. This idea of atomism is by no means self-evident. Since ancient times, philosophers in many cultures have been speculating on the nature of the fundamental substance or substances of which the universe is composed. These fundamental or basic substances are called *elements* in English, from a Latin word of unknown origin.

In India, during the sixth century BC, Kanada and Pakhuda Katyayana had propounded ideas about the atomic constitution (*Anu and Paramanu*) of the material world (Limouris 2006). Philosophy and science were not originally separate, but were born together as natural philosophy in Greece, at the beginning of the sixth century. In fact, the ancient Greeks were the first to propose that all matter in the universe was created from the following four elements: *water*, *earth*, *fire* and *air*. They also believed that matter is continuous; there is no *vacuum* (space with out any matter). The Greek philosopher Lucippus and his pupil Democritus (460–370 BC) (Fig. 2.1) conceived the idea of an *atom* as the smallest piece of a substance. The word atom comes from the Greek word *atomos* (ατομοσ) meaning "not cuttable" (unbreakable) and advocated that atoms are in continuous motion and are indestructible. The most famous Greek philosophers

Plato (427–347 BC) and Aristotle (384–322 BC), however, completely rejected the ideas of atomism. Nevertheless, the ideas of Democritus were further developed by the influential Greek Philosopher Epicurus almost a century later. One of the most important followers of the Epicurean philosophy was a Roman poet named Titus Lucretius carus (96–55 BC), who explained the philosophy of atomism in a long poem entitled, *De rerun Natura* (On Natural Things). One copy of this poem survived the Dark and Middle ages (it was discovered in 1417) and became a major source of the Greek theory of atomism. The French philosopher Pierre Gassendi (1592–1655) accepted atomism and spread this doctrine throughout Europe.

2.2 Chemical Elements

The British scientist Robert Boyle (1627–1691) was strongly influenced by Gassendi's writings and was probably the first person to perform experiments in connection with atomism. Boyle carefully measured and demonstrated an inverse relationship between the pressure and the volume of air (known as *Boyle's Law*), which clearly suggested that both atoms and vacuum are real. He, thus, revived the atomic hypothesis and called it the *Corpuscular Theory of Matter*. Newton also wrote in his *Opticks* that all matter is composed of solid and impenetrable particles – expressing a view similar to Democritus and Boyle.

Boyle was also the first chemist to recognize the significance of a *chemical element*. In his book, the *Skeptical Chemist*, published in 1661, he proposed that a substance was an element if it could not be broken into two or more simpler substances. In the early 1700, the quantitative sciences of physics and chemistry were born and 15 chemical elements came to be known. Following the discovery of important gases, such as carbon dioxide, nitrogen, hydrogen, and oxygen, the French chemist, Antoine Laurent de Lavoisier (1743–1794) in his remarkable book titled, *Traite elementaire de chemie*, published in 1789, listed 33 substances as chemical elements under four major categories; *gases*, *nonmetals*, *metals,* and *earths*.

2.2.1 Chemical Laws

Lavoisier advocated the importance of accurate measurements in quantitative experiments of chemical reactions and discovered the *law of conservation of mass* which states that: mass is neither created nor destroyed. The principle of the constant composition of compounds, known as the *law of definite proportions*, was discovered by the Frenchman, Joseph Proust who showed that a given compound always contains exactly the same proportion of elements by mass. Proust's discovery stimulated John Dalton (Fig. 2.1) an English school teacher, who noted that a series of compounds can be formed by the combination of two elements in different ratios and, thus, discovered the *law of multiple proportions*. These chemical laws supported the hypothesis that each element consists of a certain type of atom and that compounds are formed from specific combinations of these atoms.

2.2.2 Atomic Theory

In 1808, John Dalton converted the atomic hypothesis into a quantitative theory. In his publication, *A New System of chemical philosophy*, Dalton stated that each element is made up of identical atoms and presented a theory of atoms. He prepared the first table of *atomic weights* for different elements and suggested that atoms of each element had individual weights and that these could be calculated relative to one another. Dalton made the simple assumption that one atom of hydrogen combined with one atom of oxygen make a molecule of water. Many of the atomic masses proposed by Dalton were later proved be incorrect, but the construction of a table of atomic weights of different elements was a major step forward.

In 1808, Joseph Louis Gay-Lussac made the remarkable observation that although all elements combine in definite proportions of weight, gases combine in definite proportions by volume. For example, he observed that two volumes of hydrogen combined with one volume of oxygen make one volume of water vapor. The explanation of the *law of combining volumes* was provided in 1811 by Amadeo Avogadro, an Italian physicist, who hypothesized that equal volumes of any gas at a given temperature and pressure always contain equal number of the particles (atoms or molecules) of gas. Avogadro was the first to realize that certain gaseous elements, like hydrogen (H_2), nitrogen (N_2) and oxygen (O_2), under ordinary conditions contain two atoms each (also known as *diatomic molecule*). Avogadro's hypothesis was a brilliant guess and we now know, based on the *kinetic theory of gases*, that under normal conditions of temperature and pressure
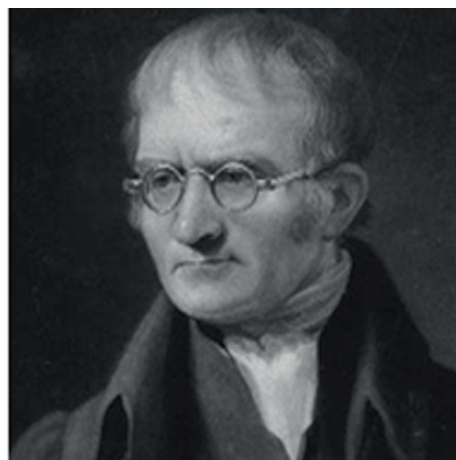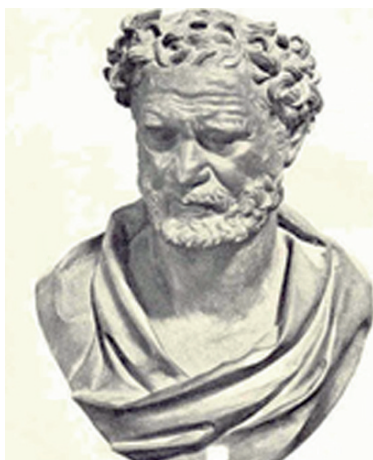
Fig. 2.1 Democritus, the Greek philosopher. John Dalton, an English chemist and physicist

(NTP), 22.4l of any gas contain exactly the same number of atoms or molecules. In chemistry, the concept of *mole* (as a unit of mass) is defined as gram atomic weight or molecular weight and one mole of any substance contains Avogadro's number (N_A) of atoms or molecules. Avogadro however, never knew the exact value of this universal constant. Almost 100 years later the value of N_A was determined to be 6.022×10^{23}.

Based on Avogadro's hypothesis, Jons Jakob Berzelius, a Swedish chemist published more accurate atomic weights of many elements between 1814 and 1826. He also invented a simple set of symbols for elements along with a system for writing the chemical formulas of compounds, in order to replace the awkward symbolic representations of alchemists. By the end of the nineteenth century, not all chemists and physicists believed in the reality of atoms however, they accepted that atomic weight is a very important property of an element.

In the late 1860s, two chemists, the Russian Dmitri Ivanovich Mendeleev and the German Julius Lothar Meyer, arranged the elements in the order of increasing atomic weight in a tabular form, called the *periodic system of elements*, since elements with similar chemical properties recurred at regular, periodic, intervals.

The discovery of electricity eventually provided important clues and the experimental evidence necessary to demonstrate the existence of atoms.

2.3 Electricity and Magnetism

The phenomena of magnetism and electricity have been known since ancient times. A certain piece of iron ore or loadstone, first found near the town of Magnesia on the eastern shore of the Aegean Sea was the basis for scientific investigation. The English physician William Gilbert (1544–1603), a contemporary of Galileo carefully studied the magnetic interactions and published the famous book, *De Magnete*, in which he concluded that the planet earth can be regarded as a giant magnet with geographical north and south poles; the magnetic south always pointing to the geographical north.

Since ancient times, people have also been aware that a piece of *amber*, when rubbed with fur will attract small bits of hair and other materials. Gilbert first introduced the term *electric* (*electrica* in Latin), after the Greek word *electron* for amber and found that other substances such as glass, sulfur, wax, and gems also exhibit similar attractive property as amber. He also proposed that electricity is some sort of fluid (an *effluvium*) that is produced or rubbed when bodies are rubbed together. Gilbert also recognized that despite their similarities, electricity and magnetism are different phenomena, but are deeply related.

The French chemist Charles-Francois de Cisternay Du Fay, eventually, realized that there are two types of electricity (*vitreous and resinous*), which are very different from each other; unlike types of electricity attract each other while like types repel each other. In contrast, the American inventor Benjamin Franklin (1706–1790), concluded that electricity consists of a single kind of fluid, and that this fluid consists of extremely subtle particles. He referred to the deficiency of electricity as *negative* electricity and to an excess as *positive* electricity. The amount of electricity (positive or negative) in any body is called the electric *charge* of the body. Franklin also observed that electricity is not created or destroyed and, thus, was the first one to introduce the fundamental hypothesis of the conservation of electric charge.

During the second half of the eighteenth century, physicists in many countries were trying to understand the quantitative aspects of both electric and magnetic forces. For example, French physicist Charles Augustine de Coulomb developed the so-called *torsion balance* for measuring very weak forces and published his results on electric and magnetic forces during 1785–1791. More specifically, Coulomb discovered that the forces of electrical attraction and repulsion are directly proportional to the product of two charges and inversely proportional to the square of the distance between them. Subsequently, this law, known as *Coulomb's law* helped to establish the unit for the electric charge. One *coulomb* of charge is defined as the amount of electric charge that passes a given point in one second in a wire that carries a one *ampere* current. Coulomb also found that the strength of the force of attraction or repulsion between the magnetic poles declines as the square of the distance between the poles increases. In 1687, Newton showed that the gravitational attraction between two bodies also followed the so called *inverse square law*.

In 1786 the Italian physiologist Luigi Galvani, accidentally discovered *electric current* while studying the phenomenon of muscular contraction in frog's legs. His friend, Alessandro Giusuppe Volta (1745–1827), a physicist soon proved that electric current is purely an inorganic phenomenon (also known as *galvanism*) by demonstrating that electricity could be produced when two different metals were both dipped into a salt

solution. Electricity, thus, was produced as a result of a chemical reaction. To produce a large electric current in the 1800's Volta constructed what is known as *Volta pile* using a number of alternating copper and iron or zinc disks, separated by layers of cloth soaked in a salt solution, in an attempt to produce a large electric current. Volta's invention of an electric battery had a significant impact on both chemistry and physics.

2.3.1 Electrolysis

While repeating Volta's experiments, William Nicholson and Anthony Carlisle in England, accidentally observed that when terminals of wires from a battery are immersed in a tube of water, hydrogen gas is produced at the wire attached to a negative terminal and oxygen gas at the positive wire. Soon Humphrey Davy (1778–1829), a professor of chemistry at the Royal Institution in London found that various salts could be decomposed by passing an electric current through molten salt solutions. He soon discovered a series of alkali and alkaline earth elements (Na, K, Ca, Mg, Sr and Ba) based on the decomposition of molten salts or salt solutions. This was the discovery of chemical decomposition by means of an electric current, or a *electrolysis*, as Michael Faraday, who had been Day's assistant and protégé called it in the 1830s.

The passage of an electric current through an electrolyte (salt solution) induces chemical changes and elements can appear at either electrode. If they are gases, they bubble off. Faraday introduced the term *ions* (Greek word meaning wanderer) to describe the chemical species passing through the solution. He also introduced the terms *anion* and *cation* for positive and negative ions and *anode* and *cathode* for positive and negative electrodes. Faraday carefully measured the mass of an element produced as a function of the amount of electricity and discovered two basic laws;

1. For a given solution, the amount of material deposited or liberated on the electrodes is proportional to the total amount of electricity.
2. The monovalent ions of different substances also carry equal amount of electricity while multivalent ions carry correspondingly larger charges.

The Faraday laws, for the first time, suggested the existence of a universal unit of electric charge, known at that time only to be attached to the chemical species.

He defined that one *Faraday* of electricity represents 96,500 C. A Faraday of electricity can be viewed as containing Avogadro's number of electrical units. This indivisible unit of electricity identified in electrolysis was given the name *electron* (ηλεκτρον), the Greek word for amber, by the Irish physicist and astronomer George Johnstone Stoney (1894). The Swedish chemist Savante August Arrhenius in his *theory of ionic dissociation* presented in 1887, proposed that Faraday's ions were actually atoms carrying positive and negative electric charge.

2.3.2 Electromagnetism

The credit for the discovery of *electromagnetism* belongs to Hans Christian Oersted, a professor of physics at the University of Copenhagen. In 1820, Oersted demonstrated that an electric current deflects a compass needle, thus, showing an intimate connection between electricity and magnetism. A current carrying wire exerts a force on a compass needle. If the compass is continuously moved in the direction it is pointed, it will trace out a circle around the wire. Oersted also observed that a magnet will exert a force on a coil of wire (*solenoid*) carrying an electric current – the solenoid would act like a bar magnet, one end acting like the north pole and the other end as the south pole. Thus the concept of electromagnetism as a unified force was realized. In 1820, Andre Marie Ampere, professor of mathematics at the Ecole Polytechnique in Paris, observed that parallel wires attract or repell each other if they carry electric currents flowing in the same or opposite directions, respectively. He concluded that all magnetism is electromagnetism and that the properties of a magnet (or loadstone) are due to tiny electric currents within the particles of the magnet.

In 1831, Faraday also observed that a magnet can induce an electric current in a wire and that the electric current in one coil can induce a current in another coil placed nearby. Before Faraday, the elctric and magnetic forces (like gravity) were considered as acting across empty space between the interacting objects. Faraday was the first to propose the idea of a field of forces (or simply *field*) to explain how forces act over large distances. In the 1860s, the field concept of Faraday was developed into a quantitative mathematical formulation by James Clerk Maxwell, a British

physicist. Maxwell showed that electric and magnetic fields do not exist independently, but only as a combined electromagnetic field with each of the components at right angles to each other. Using his equations Maxwell was also able to show that the electromagnetic field propagates through space as waves carrying away energy in the form of free electromagnetic radiation with a constant speed of 300,000 km s^{-1} or 3.0 × 10^{10} cm s^{-1}. In 1665, Newton showed that sunlight is not pure but consists of a band of colored light particles, which he called *spectrum* (from a Latin word meaning "ghost"). In contrast, the Dutch physicist, Huygens (1629–1695) revealed that light is composed of waves with different colors having different *wavelengths*. In 1801, Thomas Young, an English physicist, showed that the different colors of the spectrum have different wavelengths; red has longer wavelength (700 nm) than violet (400 nm). Since electromagnetic radiation travels with the same speed as light, in 1864, Maxwell was able to conclude that light is an electromagnetic radiation with certain wavelengths. His equations also suggested that there are many more varieties of electromagnetic radiations, differing only in their wavelengths. Maxwell theory predicted that radiations of different wave lengths, which our eyes can not see, can exist.

Even before Maxwell, the German–British astronomer, William Herschel in 1800 discovered *infra red rays* by showing that the temperature of the dark area beyond red end of the spectrum is almost one degree higher than that of visible light. In 1801, the German chemist, John William Ritter discovered *ultraviolet rays* when he observed that a paper soaked in silver nitrate solution darkens more rapidly when exposed to the dark area beyond the violet end of spectrum.

Almost 20 years after Maxwell's prediction of the existence of electromagnetic radiations of different wavelengths, in 1888 the German physicist, Heinrich Rudolph Hertz, while setting up an oscillating electric current in a rectangular wire, accidentally discovered a new kind of radiation. These rays called *radiowaves*, lay far beyond the infrared radiation and could have wavelengths of anywhere between a few centimeters to kilometers. Subsequently, electromagnetic radiations, such as *X-ra*ys and *gamma ray*s, far beyond the ultraviolet X-rays were discovered with wavelengths exceedingly smaller than that of visible light, thus, confirming Maxwells' electromagnetic theory.

2.4 Thermodynamics

The scientific study of heat started with the construction of the first thermometer in an attempt to express the amount of heat in quantitative terms. In 1592, Galileo first invented an instrument known as *thermoscope* to measure the temperature, however, he did not introduce temperature scale. The first thermometer using mercury was built in Italy around 1650 by the *Accademia del Cimento*. In 1714, the German physicist Daniel Gabriel Fahrenheit assumed that the temperature of a mixture of ice and salt is zero while the body temperature is set at 96. On this *Fahrenheit scale*, water has a freezing point of 32 and a boiling point of 212. In 1743, the Swedish astronomer Anders Celsius introduced a *Celsius* or *centigrade scale* and showed that the freezing point of water is 0°C and the boiling point is 100°C. Both these scales are based on the assumption that the expansion coefficient of mercury is relatively constant.

While working on the mechanical properties and the compressibility of air and other gases, Boyle discovered that the volume of a gas at a constant temperature is inversely proportional to its pressure. Almost a century later it was discovered that gases expand at higher temperature. In 1791, the expansion coefficient for air at constant pressure was measured by Volta and was found to be 1/273 on the Celcius scale. Around 1800, two French chemists Joseph Gay-Lussac and Jacques Charles observed that this expansion coefficient is the same for all gases regardless of the chemical nature of the gas. Similarly the pressure of any gas at a constant volume increases at a constant rate, 1/273 of its initial volume at 0°C for each degree of increase in temperature. Thus, at –273°C, the pressure and volume of any gas are expected to drop to zero value.

2.4.1 Heat, Energy and Temperature

Two different doctrines developed in the eighteenth century helped to explain the nature of heat and to establish units for the quantity of heat, separate from that of temperature. According to one, theory heat is a substance with or without mass (or weight) while the other theory suggests that heat is a type of motion or vibration. The Scotch physician Joseph Black regarded heat as a substance and called it *calor*. He defined the unit of heat as the amount necessary to raise the temperature of 1 lb of

water by 1°F. In the Metric system, 1 calorie is the amount of heat needed to raise 1 g of water by 1°C. In 1799, Benjamin Thompson (also known as Count Rumford) presented some data which suggested that heat is a type of motion and not a material substance. In 1842, the ideas of Count Rumford were further developed by the German physician Julius Robert Meyer who tried to establish a relationship between heat production and mechanical work and in the process discovered the *law of conservation of energy*. In the 1840s, the Englishman James Prescott Joule, performed many experiments to clearly measure the mechanical equivalent of heat and by 1875, he was able to show that one calorie is equal to 4.15 J.

The concept of energy is rather difficult to explain precisely; however, energy can be defined as the capacity to do work or to produce heat. In 1738, Daniel Bernoulli was one of the first scientists to show, mathematically, that the pressure of a gas depends on the mass, the number of molecules in a given volume of gas, and the average velocity of the gas molecules. However, he could not explain the relationship between the velocity of molecules and the temperature of gas. The Charles and Gay-Lussac law clearly demonstrated that the pressure of a gas is dependent on the temperature. Subsequently, based on Joule's work on the mechanical equivalent of heat, Maxwell discovered a statistical law which governs the velocity distribution in a monoatomic gas. More specifically, he found that the number of molecules in a given velocity interval is proportional to the density of gas and depends only on the temperature of the gas and the absolute mass of the gas molecules. His equations can be used to calculate the average kinetic energy of gas molecules at any temperature. The British scientist, William Thompson (also known as Baron or Lord Kelvin) suggested that the kinetic energy of gas molecules be used to establish a temperature scale. Maxwell's equation predicts that at −273.16°C, the average kinetic energy of gas molecules will have zero kinetic energy. Therefore, the temperature of −273.16°C can be regarded as *absolute zero* based on the *Kelvin scale* of temperature.

2.4.2 Emission of Light

In the beginning of the nineteenth century, the German physicist, Joseph von Fraunhofer (1787–1826) repeated Newton's experiments on the solar spectrum, using prisms of much better quality. He also invented a device,

known as *diffraction grating* (a plate of glass or metal on which fine and equally spaced scratches or grooves) light into its component colors and he observed that the spectrum of colors is intersected by a large number of very thin that can separate black lines. Von Frauenhofer recognized that these lines correspond to emission lines in sparks and flames. The significance of these lines (the signals coming from atoms and molecular species) was discovered in the 1860s by two German scientists Robert Wilhelm von Bunsen and Gustav Robert Kirchhoff.

It is well known that metals (such as iron, tungsten) become luminous or give off visible light when heated to sufficiently high temperatures. The color of light varies with the temperature of the metal, going from red to yellow to white as it becomes hotter and hotter, while other frequencies of electromagnetic radiation that are invisible are also emitted. At room temperature most of the radiation emitted is in the infrared range of the spectrum. Thus, at a high temperature, the emitted radiation has a high frequency and rapidly becomes more intense. In contrast, if we look through a prism at the light emitted by a hot gas, we see a continuous spectrum from red to violet. In a Bunsen burner however, the gas becomes very hot and emits very little of bluish light only. Bunsen discovered that when pure sodium or potassium is introduced into Bunsen flame, the corresponding spectra contains only yellow or red color. With the use of a spectroscope, Bunsen and Kirchhoff quickly realized that the dark lines in the solar spectrum correspond to the emission lines of specific hot gaseous elements. The law that all substances absorb the same light frequencies which they can emit was discovered by Kirchhoff, in 1860. The spectral analysis was soon utilized to discover new elements, such as Ce, Rb, Tl, In, and Ga.

2.5 Major Discoveries

2.5.1 Cathode Rays

Faraday's electrolysis experiments demonstrated the existence of ions, charged atoms, and molecules. In order to detect the particles of electricity, that are not associated with atoms or molecules, investigations were initiated to pass an electric current through a good vacuum. In 1838, Faraday was the first to actually force an electric current through a vacuum, however, since the vacuum was not good enough the observations lacked any significance.

In 1858, the German glassblower Johann Heinrich Wilhelm Geissler and the German physicist Julius Plucker developed a glass tube with two electrodes with very good vacuum (known as *Geissler tubes*). When the electrodes were connected to a source of electric current, a greenish luminescence appeared on the glass tube near the cathode. It was soon realized that the position of the glow does not depend on the anode, the nature of the gas molecules in the tube, or the kind of metal used to make the cathode. Instead, something from cathode appeared to be moving straight and hitting the glass before being collected by the anode. The German physicist Johann Wilhelm Hittorf suggested that objects placed in front of a cathode cast shadows. The German physicist Eugen Goldstein, however, maintained that the glow is associated with the current itself and in 1876 introduced a name for this mysterious phenomenon: *Cathodenstrahlen*, or *cathode rays*. In 1878 the British physicist William Crookes devised vacuum tubes that produced cathode rays which clearly moved in straight lines and which were better than the cathode rays produced in Geissler tubes. The investigations on the nature of cathode rays with the Hittorf and Crookes vacuum tubes ultimately led to the discovery of x-rays and electron.

2.5.2 X-Rays

In 1895, the German physicist Wilhelm Röntgen, while investigating the effects of cathode rays in a discharge tube, accidentally discovered a new form of penetrating radiation, which he called *x-rays*. He observed that when cathode rays (negatively charged particles) strike the atoms of a glass vacuum tube, they produce penetrating rays that cause salt (barium platinocyanide) to glow. Soon thereafter, it was realized that x-rays are (1) more penetrating than the cathode rays and (2) not prone to deflection by a magnetic field and physicists started to discuss what these mysterious x-rays might be.

The true nature of x-rays was discovered in 1912 when the German physicist Max von Laue, using crystals as a type of three-dimensional grating, discovered that x-rays do not behave like particles, but instead have the wave-like characteristics of an electromagnetic radiation. An accelerated electric charge will radiate electromagnetic waves. As the fast moving cathode rays approach the positive charge in the nucleus of glass atoms, electrons are brought to rest (accelerated) and the kinetic energy of the electrons is converted to electromagnetic waves. Radiation produced under these circumstances is been given the name *bremsstrahlung* (breaking radiation). It was also discovered, that when denser more massive atoms in a metal are used to stop the accelerated electrons, x-rays of higher energies can be generated. In 1911, the British physicist Charles Barkla noticed that each metal produced x-rays of a particular wavelength, called characteristic x-rays of a particular metal and called the more penetrating beam K x-rays and, the less penetrating beam L x-rays. Subsequently, it was discovered that these characteristic x-rays emitted by metals are due to the deexcitation of electrons in the atomic shells.

2.5.3 Electron

Following the discovery of cathode rays and radiowaves, the Dutch physicist Hendrick Antoon Lorentz, refined Maxwell's equations, and developed a new theory, called *electron theory*. More specifically, Lorentz proposed that microscopic particles, each of which carrying electric charge must be contained in all atoms and that these charged particles generate electric and magnetic fields. He also proposed that oscillations of these charged particles inside the atoms are the source of light.

In 1895, the French physicist Jean-Baptiste Perrin demonstrated that cathode rays, emitted from the cathode of a discharge tube, are negatively charged particles. In 1896, Lorentz deduced a value for the charge-to-mass ratio (e/m) for charged particles inside the atom. As a result of Lorentz's electron theory it was presumed that a magnetic field would affect the electron oscillations, and there by the frequencies of the light emitted. In 1896, Pieter Zeeman observed such a broadening of the spectral lines by the magnetic field. Based on the Zeeman effect, Lorentz and Zeeman were, subsequently, able to estimate the e/m ratio and predict that the charge of the particles within the atom is negative.

In 1897, the British physicist Joseph John Thompson confirmed Perrin's observations and obtained a precise value for the e/m ratio of cathode rays. The ratio turned out to be over a thousand times greater than that of a hydrogen ion. Thompson also demonstrated that the cathode rays could be deflected by both magnetic and

electric fields. He also discovered that cathode rays are negatively charged particles, which he initially called *corpuscles*. He later changed the name and called them electrons, the name first suggested by Johnstone G. Stoney in 1894. Thompson's measurement of an electron's mass and charge confirmed that cathode rays (electrons) are the same particles within the atom also responsible for the emission of light by the atom. In 1911, the American physicist Robert Andrews Milikan succeeded in measuring quite accurately, the minimum electric charge that could be carried by a particle and found that if this charge were carried by an electron, it would have to be only 1/1,837 as massive as a hydrogen atom.

In 1899, Philipp Lenard, while investigating the interaction of cathode rays with thin metal plates discovered that electrons are ejected when ultraviolet light strikes metal surfaces. He also discovered that the emission of electrons is dependent the frequency of light but not on the intensity of light. This phenomenon, known as the photoelectric effect, was later explained by Albert Einstein, and is based on the light quantum hypothesis proposed by Max Plank, in 1900.

2.5.4 Radioactivity

Henry Becquerel, professor of physics at the Ecole Polytechnique in Paris heard about the discovery of x-rays and immediately thought of a possible connection between x-rays and fluorescence. He quickly initiated a series of experiments testing whether fluorescent substances emitted x-rays. In February 1986, he was exploring the possibility that sunlight might cause crystals to emit penetrating rays like the x-rays. As luck would have it, he used uranium – potassium bisulfate (uranium salts were known to be phosphorescent). These crystals were placed next to a photographic plate wrapped in dark paper. If sunlight causes the crystals to emit penetrating rays, then these rays might penetrate the dark paper and darken the plate. Since the weather was cloudy, Becquerel placed the unwrapped plates in the drawer of a cabinet leaving the crystals on the cabinet. Much to his surprise, a couple of days later, when he developed the plates, he found intense darkening of the plate, due to exposure to some intense radiation. Becquerel quickly concluded that invisible rays from uranium had penetrated the cabinet and the dark paper covering the plate, and finally

exposed the photographic plate. For a few years, these rays were known as "Becquerel rays" or *rayons uranique*. In 1898, Maria Sklodowska Curie and Pierre Curie discovered that the element thorium also emitted such rays. That year, the Curies coined the name *radioactivity* to describe the phenomenon of penetrating radiation emitted by uranium and thorium.

In the following years, other new radioactive phenomena were discovered. For example, in 1900 the French chemist, Paul Villard discovered an extremely penetrating form of radiation coming from radioactive sources. However, it was Ernest Rutherford at the Cavendish Laboratory in England who played a major role in the study of radioactivity. Rutherford and his colleagues identified three different components in the radiations from radioactive elements based on their behavior in electric and magnetic fields. He called them, α-rays, β-rays, and γ-rays, these components were eventually identified as being helium nuclei, electrons, and high-energy photons, respectively. In 1903, Rutherford and Soddy sought to explain the cause and nature of radioactivity. They proposed a *disintegration theory*, which defined radioactivity as a change of one chemical element into another with the emission of alpha or beta particles. An unstable element reaches stability spontaneously by undergoing radioactive decay involving transmutation of elements and emission of energy; however, in the 1930s it was discovered that radioactive elements can also emit positively charged electrons or *positrons*.

2.5.5 Light Quantum

The classical theory of matter assumes that matter in general can absorb or emit any quantity of energy. It also predicts that the radiation profile of the emission spectrum has no maximum and goes to infinite intensity, at shorter wavelengths (or higher frequencies. This effect is called *ultraviolet catastrophae*. An ideal material body known as the *black body*, is one that can absorb all radiations incident on it. Therefore, since it can absorb all radiations, it should also emit radiations of all frequencies. The experimental evidence, however, indicated that when a piece of metal is heated to incandescence, the profile of radiation emitted shows that the maximum (peak) shifts to shorter wavelengths as the temperature is increased. The question is why does the intensity of radiation drop gradually as the

frequency of radiation increases? In 1901, the German physicist Max Planck's postulated that the energy of radiation can be absorbed or emitted by bodies only in specific packets or amounts and called of these small packets of energy a *quantum*. The energy (E) of each quantum is a product of the frequency of radiation (v) and a constant, h (known as Plank's constant). The value of h was determined to be 6.626×10^{-34} Js.

2.6 Reality of Atoms

2.6.1 Avogadro's Number

Avogadro's number is the calculated value of the number of atoms (or molecules) in a gram mole of any chemical substance. Although as early as the seventeenth century, Boyle had attempted to estimate the size of atoms, it was not until 1865 that the first successful attempt was made by the Austrian physicist and school teacher Josef Loschmidt. Based on Avogadro's hypothesis, the atomic weights of several gaseous elements were accurately determined in 1860 by the Italian chemist Stanislao Cannizzaro. Subsequently, in 1865, using the new *Kinetic Molecular Theory*, developed by Maxwell and Clausius, Loschmidt found the number of atoms in one cubic centimeter of gaseous substance, under ordinary conditions of temperature and pressure, to be somewhere around 2.6×10^{19} atoms cc^{-1} (this known as *Loschmidt's Constant*). Since one mole of any gas occupies 22.4 l at STP, the number of atoms in one mole is approximately equal to 5.8×10^{23} atoms.

2.6.2 Brownian Motion

In 1827, Robert Brown observed the random movement of pollen particles in a liquid. This phenomenon, known as *Brownian motion*, states that microscopic particles in a liquid are never at rest; they are in perpetual movement even under conditions of perfect external equilibrium or constant temperature. The only irrefutable explanation for this phenomenon ascribes the movements of the particles to the shocks produced by the atoms and molecules of the liquid themselves. A mathematical theory of this phenomenon was developed by Einstein, in 1905, and a theoretical estimate of Avogadro's number was given to

be 6.2×10^{23} particles. The first experimental proof of this theory was provided by Jean Baptiste Jean Perrin in France around 1908. More specifically, Perrin determined that the number of atoms in one mole is approximately 6.8×10^{23}. The work of Einstein and Perrin provided some of the first concrete evidence for the existence of atoms. The current experimental value of 6.022 1415 $\times 10^{23}$ atoms per mol is the average for measurements using the best methods.

2.7 Atomic Structure

2.7.1 Nuclear Atom

Since 1890, various discoveries have shown that the atom is not indivisible (as Dalton supposed), but is really composed of parts. The discovery of *radioactivity*, the interaction of electricity with matter, and the discovery of free *electrons* have all contributed to the discovery of the subatomic structure of atoms. In 1910 Rutherford (Fig. 2.2) presented a model of an atomic structure, known as *nuclear atom*. According to this nuclear model, atoms consist of a massive, compact, positively charged core, or *nucleus*, surrounded by a diffuse cloud of relatively light, negatively charged electrons. In 1913, Moseley formulated the property of *atomic number* (Z), which is the number of positive charges in the nucleus. Moseley showed that the sequence of elements in the periodic table is, in fact, is a sequence of elements that are arranged in order of their atomic numbers and not their atomic weight. In 1914, Rutherford named this positively charged particle in the nucleus, *proton* (from the Greek word first). A proton has an electrical charge exactly equal to that of an electron, but positive, and a mass 1836 times that of an electron. Incidentally, the nucleus of a hydrogen atom is known as the proton. In the electrically neutral atom, the number of orbiting electrons is sufficient to exactly balance the number of positive protons. In 1920s Rutherford speculated that a neutral particle (one that is the same size as a proton) within the nucleus accounts for the total mass of the atom. Such a neutral particle was discovered by James Chadwick, in 1932. Heisenberg soon proposed that nuclei of different elements consist of protons and neutrons which are held together by strong exchange

Fig. 2.2 Ernest Rutherford, an English physicist and the winner of the Nobel prize in chemistry. Niels Henrik David Bohr, a Danish Physicist and the winner of Nobel prize in physics
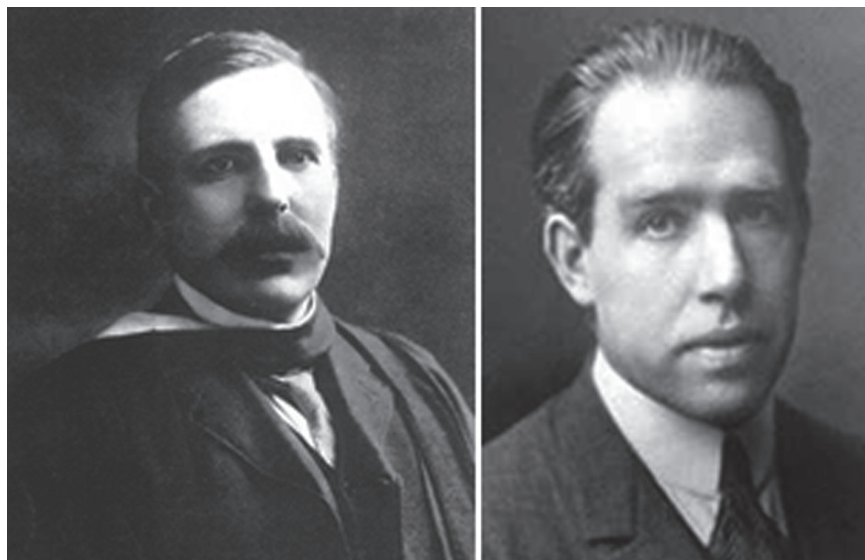
forces known as nuclear forces. The total number of protons and neutrons within the nucleus is called the *mass number* (*A*), which is very close to the atomic weight of an element. The mass number (*A*) of ^{12}C nuclide is 12 and its atomic mass is considered as 12 atomic mass units (AMU or u). The atomic weight of natural carbon is 12.011 since it is a mixture of ^{12}C (98.89%) and ^{13}C (1.11%) nuclides or isotopes.

2.7.2 Bohr's Model of Atom

The atom consists of an extremely dense, low positively charged nucleus surrounded by a cloud of electrons with small size and mass, each electron carrying a single negative charge equal but opposite to that of a proton in the nucleus. Because the number of electrons and protons, an atom are the same, the whole atom is electrically neutral. The *atomic volume* (10^{-8} cm diameter) with the cloud of electrons is significantly much larger compared to the volume of the nucleus (10^{-13} cm diameter). Based on Rutherford's discovery of atomic nucleus and Plank's discovery of energy quantum ($E = h\nu$), Neils Bohr (Fig. 2.2) developed the first quantum model of an atom (Fig. 3.4 in Chap. 3), in 1913. According to this model, an electron in a hydrogen atom rotates around the nucleus at high speeds in closed *circular orbits* associated with a characteristic *quantum number (n)*.

The electron in general exists in a low energy orbit (*ground state*). The gain or loss of a quantum of energy occurs only when an electron moves from one orbital to one of greater or lesser energy. As a result an atom can absorb or emit energy in discrete units or quanta.

In 1916, Arnold Sommerfeld suggested that the electron orbits can also be elliptical, and at different degrees. Subsequently, the orbital *quantum number (l)* was introduced, which assumes the circular and elliptical orbits are in a single plane. When atoms are in a magnetic field, however, the orbits may be tipped and can be best represented in a three dimensional spherical space around the nucleus. To account for this magnetic effect, a *magnetic quantum number (m)* was introduced. Subsequently, Wolfgang Pauli introduced the *spin quantum number* (s) to the represent the direction of the electron spin (clockwise or anti-clockwise). The arrangement of electrons around the nucleus in an atom can be described based on the four quantum numbers. A more detailed example of electron orbits based on quantum mechanics is provided in Chapter 7.

2.7.3 Isotopes

Dalton assumed that all the atoms of a given element have the same *atomic weight* or *atomic mass*. By 1914,

it was realized that atoms of the same element can vary in weight, but may have the same chemical properties. The word *isotope* was coined by Frederick Soddy to represent atoms of an element that have different weights but, still can be placed in the same place in the periodic table. An isotope can be stable or unstable (radioactive). Some of the elements in nature such as Na, F, Al, and Bi have no isotopes, while 81 of the elements listed in the periodic table have at least one stable isotope. Further, all elements heavier than Bi are unstable; no stable isotope exists for these elements. In 1947, the American chemist Truman Paul Kohman suggested that the word *nuclide* is a more appropriate term to represent both the stable and unstable atoms (or radionuclide), of an element.

For any given element, the percentage of each isotope found in nature is called the isotope's *isotopic abundance*. Natural carbon exists in two stable isotopic forms (^{12}C and ^{13}C); the isotopic abundance of ^{12}C is 98.9% while the abundance of ^{13}C is very small – only 1.1%. Since the atomic mass of an element is expressed as an average of all of the naturally occurring isotopes, the average atomic mass of carbon is 12.011. Similarly the average atomic mass of copper is 63.545, since it has two stable isotopes; ^{63}Cu (69.2%) and ^{65}Cu (30.8%).

2.7.4 Quantum Atom

At first Bohr's model appeared to be very promising but, by the mid 1920s, it became clear that Bohr's model needed refinement. The wave mechanics or quantum mechanics developed by Werner Heisenberg, Louis deBroglie, and Edwin Schrodinger finally provided a wave or quantum mechanical description of an atom. Quantum theory describes matter (electrons and electromagnetic radiation) as acting both as a particle and as a wave. This characteristic is called wave-particle duality. According to this model, the electron bound to the nucleus is similar to a standing or stationary wave, while the circumference of a particular orbit corresponds to a whole number of wavelengths. Schrodinger's famous wave equation ($H\psi = E\psi$) describes an electron in an atom, where ψ called the wave function, is a function of the coordinates (x, y, and z) of the electron's position in three dimensional space and H represents a set of mathematical instructions called an *operator*. When this equation is

analyzed, many solutions are found. Each solution consists of a wave function ψ that is characterized by a particular value of energy, *E*. A specific wave function for a given electron is often called an *orbital*. An orbital, however, is not a Bohr's orbit; the orbitals differ from each other in size, angular momentum, and magnetic properties. The wave function corresponding to the lowest energy of hydrogen atom is called 1*s* orbital. Quantum mechanics only provides the probability of an electron's position around the nucleus, but not the electron's motion around the nucleus. Also, each electron in an atom has a unique set of quantum numbers. *In a given atom, no two electrons can have the same set of four quantum numbers (n, l, m_e, m_s).* This is called *Pauli Exclusion Principle*, which can also be stated as follows: *An orbital can hold only two electrons, and they must have opposite spins*.

The atom's electron cloud- that is the arrangement of electrons around the nucleus in an atom – determines most of the atom's physical and chemical properties. The electrons in the outermost shell, in particular, determine the chemical properties of an atom. Atoms bond with other atoms by donating or sharing electrons in order to fill their shells. It requires less energy to exist in this bonded state; atoms always seek to exist in the lowest energy state possible.

2.7.5 Discovery of Antimatter

In particle physics, *antimatter* is an extension of the concept of antiparticle to matter, where antimatter is composed of antiparticles (such as antielectron and antiproton) in the same way that normal matter is composed of particles (electrons and protons). In 1928, Paul Adrien Maurice Dirac, a physicist at Cambridge, combined relativity and quantum mechanics in order to derive an equation that provides a complete description of the electron. Surprisingly, this theory not only described electrons but the particles we call *positrons* or antielectrons, as well. Dirac's theory predicted that when an electron encounters a positron, the two charges cancel and the pair annihilates, with the combined mass transforming into high-radiation (annihilation photons (511 KeV) in the most dramatic expression of Einstein's celebrated equation $E = mc^2$. The theory also predicted that high-energy photons can rematerialize as matter and antimatter in a process known as the *pair*

production. In 1932, positrons were first discovered by Carl D. Anderson, who gave the positron its name. More specifically, the positron was discovered by passing cosmic rays through a cloud chamber. In 1934, Irène Curie and Frédéric Joliot confirmed the existence of the positron by bombarding aluminum with alpha particles. This resulted in the artificial production of radionuclide ^{30}P, which quickly decayed to stable silicon by emitting positrons. Dirac, Anderson, Curie, and Joliot all received Nobel prizes for their pioneering discoveries. Subsequently in 1955, Emilio Segre and Owen Chamberlain discovered the antiproton using high energy protons (6.5 billion eV) generated in a Bevatron accelerator at the Lawrence Berkeley Radiation Laboratory, in California.

2.8 The Elementary Particles

In the 1930s, it seemed that protons, neutrons, and electrons were the smallest objects into which matter could be divided and these objects were termed *elementary particles* or fundamental particles. In particle physics, an *elementary particle* is a particle without a substructure; that is, it is not made up of smaller particles. All elementary particles are either *bosons* or *ferminons*; particles normally associated with matter are ferminons while particles associated with fundamental forces are bosons. Bosons are divided into *hadrons* and *leptons*; hadrons are composite objects and made from *quarks*, while leptons appear to be structureless.

Quarks are the fundamental constituents of protons and neutrons and interact via the strong nuclear forces.

The nobel laureates Murray Gell-Mann and George Zweig first proposed the quark model, in 1964. There are six *flavors* of quarks; the three positively charged quarks are called *up-type quarks* (Up, Charm and Top) and the three negatively charged quarks are called *down-type quarks (down, Strange and Bottom)*. Individuals quarks are the only known carriers of *fractional* charge, but because they combine in groups of three, only an *integer* charge is observed in nature. Individuals quarks are never found in nature; quarks always bind together to form composite particles – the hadrons. The up quark and the down quark are generally stable and are very common in the universe; they are found in protons and neutrons and are one of the primary building blocks of matter. The other more massive quarks produced in particle accelerators and cosmic rays are unstable and rapidly decay. For example, in the radioactive beta decay process, a neutron "splits" into a proton, an electron, and an antineutrino. This process occurs when one of the down quarks in the neutron (udd) decays into an up quark by emitting a W$^-$ boson, transforming the neutron into a proton (uud). The W$^-$ boson then decays into an electron (e^-) and an electron antineutrino (νe).

The notion that the atom is the ultimate building block of all matter in the universe is no longer valid. Because quarks cannot exist independently, the elementary particles in nature representing fermions are protons, neutrons, and electrons. It is the combination of the three subatomic particles that resulted in the formation of chemical elements, billions of years ago. Among the bosons, only the photon is the most realistic elementary energy particle (Table 2.1).

Table 2.1 Physical properties of elementary particles[a]

Particle	Charge	Mass (MeV/c^2)	Mass (Kg)	Charge radius (m)	Spin	Mean life-time
Photon (γ, $h\nu$)	0	0	0	–	1	Stable
Electron (e^-, β^-)	−1	0.511	9.109×10^{-31}	–	1/2	Stable
Positron (e^+, β^+)	1	0.511	9.109×10^{-31}	–	1/2	Stable by itself
Up Quark (u)	+2/3 e	1.5–3.3	–	10^{-18}	1/2	Stable
Down Quark (d)	−1/3 e	3.5–6.0	–	10^{-18}	1/2	Decays to u
Proton or uud (p$^+$ or H$^+$)	1	938.272	1.672×10^{-27}	$<10^{-15}$	1/2	$>2.1 \times 10^{29}$ year
Neutron or ddu (n, n^0)	0	939.565	1.674×10^{-27}	$<10^{-15}$	1/2	885.7 s

[a]The above values are from Wikipedia

Additional Reading

Asimov I (1992) Atom. Journey across the subatomic cosmos. Truman Tally Books, New York

Gamow G (1961) The great physicists from Galileo to Einstein. Dover, New York

Limouris GS (2006) From the atomism of Democritus to the therapeutic nuclear medicine today. Eur J Nucl Med Mol Imaging 33:s65–s68

Pais A (1982) Subtle is the Lord. The science and the life of Albert Einstein. Clarendon, Oxford

Pais A (1991) Niels Bohr's times, in physics, philosophy and polity. Clarendon, Oxford

Segrè E (1980) From x-rays to quarks. Modern physicists and their discoveries. Freeman, New York

Segrè E (1984) From falling bodies to radiowaves. Classical physicists and their discoveries. Freeman, New York

Atoms and Radiation

<div style="text-align:right">**3**</div>

Physics is mathematical not because we know so much about the physical world, but because we know so little; it is only its mathematical properties that we can discover.

<div style="text-align:right">Bertrand Russell</div>

3.1 Matter and Energy

Every thing in this Universe is made up of *matter* and *energy*. Matter is anything that has *mass* and occupies space. In contrast, light and heat are forms of energy. The concept of mass is central to the discussion of matter and energy. The mass of an object depends on the quantity of matter in the object, while the mass of a body (material object) is directly associated with its weight. On earth, the weight of a body is the pull of the earth on the body, which is proportional to its mass and depends on the distance of the body from the center of the earth. Energy is the ability to produce change or the capacity to do work. Energy occurs in many forms such as electrical energy, mechanical energy, chemical energy and nuclear energy. In addition, energy can also be *potential energy* (energy due to position) or *kinetic energy* (energy due to motion). The units for the quantities of mass and energy are shown in Table 3.1.

3.1.1 Mass–Energy Relationship

The most famous relationship Einstein derived from the postulates of special relativity – concerns mass (m) and energy or the rest energy (E_0).

$$E_0 = m_0 c^2 \qquad (3.1)$$

In nonrelativistic physics, kinetic energy (KE) of an object of rest mass m_0 and speed v is given by

$$KE = \frac{1}{2} m_0 v^2 \qquad (3.2)$$

In relativistic physics, if the mass is moving, the total energy (E) is

$$E = mc^2 = \frac{m_0 c^2}{\sqrt{1 - v^2 / c^2}} \qquad (3.3)$$

The mass of a body moving at the speed v relative to an observer is larger than its mass when at rest relative to the observer by the factor, $\sqrt{1 - v^2 / c^2}$ where "c" is the velocity of light. Relativistic mass increases are significant only at speeds approaching that of light. For particulate radiation, relativistic effects are significant. Since mass and energy are not independent entities, according to the principle of conservation of mass energy, mass can be created or destroyed. When this happens, an equivalent amount of energy simultaneously vanishes or comes into being, and vice versa. Mass and energy are different aspects of the same thing. This mass–energy relationship is key for the estimation of nuclear binding energies and for the explanation of the liberation of enormous amounts of energy during the radioactive transformation of nuclides.

3.2 Radiation

The term *radiation* simply refers to *energy in transit*. There are two specific forms of radiation:

Table 3.1 Primary and derived units of quantities based on Système Internationale (SI)

Quantity	Unit	Symbol	Equivalent
Mass	kilogram	kg	1 kg = 1,000 g
Amount	Mole	mol	1 mol = Avogadro's constant, 6.02×10^{23} particles (atoms or molecules)
length	Meter	m	Distance light travels in exactly 1/299,792,458 s. 1 m = 100 cm = 1.0×10^{10} Å
time	Second	s	Duration of 9,192,631,770 cycles of microwave radiation produced by Cs-133 atoms
Temperature	Kelvin	°K	°C + 273.16
Current	Ampere	A	1 coulomb s^{-1}
Energy	Joule	J	4.184 J = 1 cal
Electric potential	Volt	V	1 eV = 1.60269×10^{-19} J

Fig. 3.1 The electric and magnetic fields in an electromagnetic wave are perpendicular to each other and to the direction of the wave
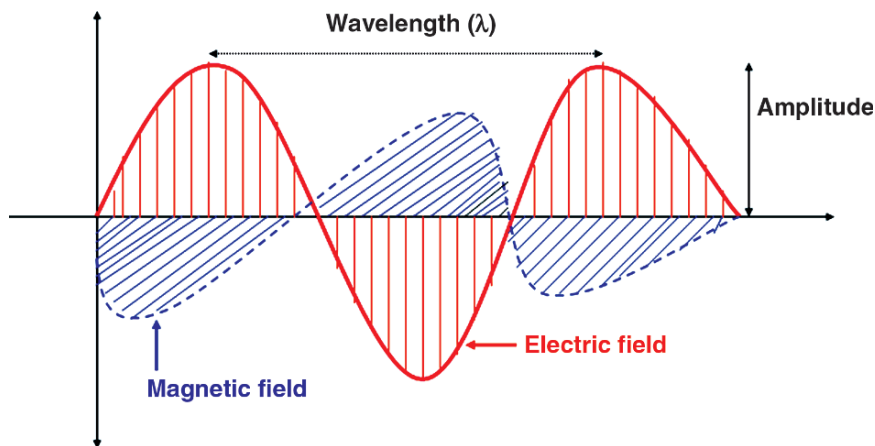
- Particulate radiation (nonpenetrating): mass (subatomic particles such as protons, neutrons, electrons) in motion carrying kinetic energy of particles
- Electromagnetic radiation: Oscillating electric and magnetic fields carrying energy and traveling through space with a constant velocity

3.2.1 Electromagnetic Radiation

Visible light is the most familiar form of electromagnetic radiation. Ultraviolet, infrared, microwave, radio waves, X-rays, γ rays, and annihilation radiation are all different types of electromagnetic radiation. All types of electromagnetic radiations exhibit "wave-like" behavior in their interactions with matter. The wavelength (λ) and frequency (ν) of the oscillating fields of electromagnetic radiation (Fig. 3.1) are related by

$$\lambda\nu = c \qquad (3.4)$$

where c is the velocity of light in free space (2.998×10^8 m/s).

Maxwell was able to show that that the speed "c" of electromagnetic waves in vacuum can be deduced mathematically by

$$c = \frac{1}{\sqrt{\varepsilon_0 \mu_0}} = 2.998 \times 10^8 \, \mathrm{m/s} \qquad (3.5)$$

where ε_0 is the electric permittivity of free space ($8.854 \times 10{-}12 \, c^2/N \, m^2$) and μ_0 is its magnetic permeability ($4\pi \times 10^{-7} \, T \, m/A$).

According to quantum theory, electromagnetic radiation, however, behaves as discrete packets of energy (with no mass or charge), called quanta or photons. The energy of the photon is related to the frequency of the electromagnetic radiation by

$$E = h\nu \qquad (3.6)$$

where h is known as Planck's constant whose value is 6.626×10^{-34} J s.
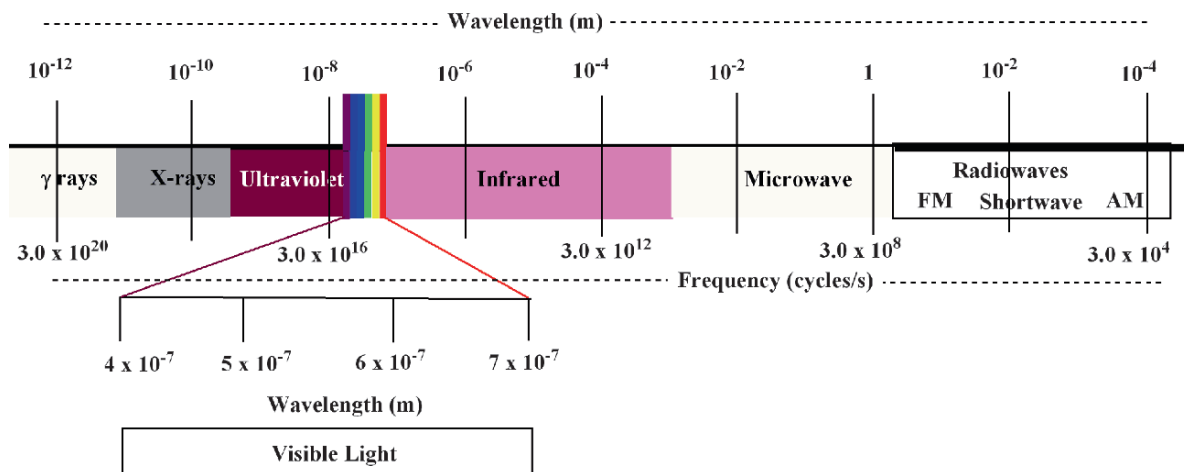
Fig. 3.2 The spectrum of electromagnetic radiation. The visible light (light waves) span only a brief frequency interval, from 4.3×10^{14} Hz for red light to about 7.4×10^{14} Hz for violet light

De Broglie suggested that a photon, an energy particle behaves in certain ways as though it has a wave nature. The wavelength of a photon is therefore specified by its momentum

$$\lambda = \frac{h}{\rho} \qquad (3.7)$$

where, the momentum

$$\rho = \frac{h\nu}{c} \qquad (3.8)$$

since

$$\lambda\nu = c \qquad (3.9)$$

Different types of electromagnetic radiation and their corresponding photon energies, wavelengths, and frequencies are shown in Fig. 3.2.

3.3 Classification of Matter

Based on the composition of matter as a basis for classification, matter may be regarded as a pure substance or as a mixture of substances. There are two kinds of substances: *elements* and *compounds*. An element or a chemical element is a substance that cannot be broken down to simpler substances by ordinary chemical means. Compounds are substances consisting of two or more elements (some times also called molecules) combined in definite proportions by mass, having properties different from that of any of its constituent elements. A mixture consists of two or more substances and there are two kinds of mixtures; homogenous mixtures (also called solutions) and heterogeneous mixtures.

3.3.1 Chemical Element

All matter in nature is made up of pure substances, known as chemical elements. In the periodic table (Fig. 3.3), 112 known chemical elements have been listed; 22 of these elements have been man made. Oxygen is the most abundant element in the earth's crust. Air is mostly a mixture of nitrogen (78%) and oxygen (21%). Since ancient times, the following ten elements have been known to be pure substances (carbon, sulfur, copper, silver, gold, iron, tin, mercury, tin and antimony) were known as pure substances. The rest of the elements were discovered by man. In 1869, based on the chemical properties and relative atomic weights of approximately 70 natural elements, Mendeleyev, a Russian chemist arranged the elements in a table of groups and periods, known as the periodic table. The long form of the modern periodic table with all the 112 elements is shown in Fig. 3.3.

Standard Periodic Table

Blocks

Groups ▼

1 **1A**																	**18** **8A**
1 H	**2** **2A**											**13** **3A**	**14** **4A**	**15** **5A**	**16** **6A**	**17** **7A**	2 He
3 Li	4 Be											5 B	6 C	7 N	8 O	9 F	10 Ne
11 Na	12 Mg	**2** **3B**	**4** **4B**	**5** **5B**	**6** **6B**	**7** **7B**	**8**	**9** **8B**	**10**	**11** **1B**	**12** **2B**	13 Al	14 Si	*15* *P*	16 S	17 Cl	18 Ar
19 K	20 Ca	21 Sc	22 Ti	23 V	24 Cr	25 Mn	26 Fe	27 Co	28 Ni	29 Cu	30 Zn	31 Ga	32 Ge	33 As	32 Se	35 Br	36 Kr
37 Rb	38 Sr	39 Y	40 Zr	41 Nb	42 Mo	43 Tc	44 Ru	45 Rh	46 Pd	47 Ag	48 Cd	49 In	50 Sn	51 Sb	52 Te	53 I	54 Xe
55 Cs	56 Ba	71 Lu	72 Hf	73 Ta	74 W	75 Re	76 Os	77 Ir	78 Pt	79 Au	80 Hg	81 Tl	82 Pb	83 Bi	84 Po	85 At	86 Rn
87 Fr	88 Ra	103 Lr	104 Rf	105 Db	106 Sg	107 Bh	108 Hs	109 Mt	110 Uun	111 Uun	112 Uub		114 Uuq		116 Uuh		118 Uuo

- ■ *s* block
- ■ *p* block
- ■ *d* block
- ■ *f* block

6	57 La	58 Ce	59 Pr	60 Nd	61 Pm	62 Sm	63 Eu	64 Gd	65 Tb	66 DY	67 Ho	68 Er	69 Tm	70 Yb
7	89 Ac	90 Th	91 Pa	92 U	93 Np	94 Pu	95 Am	96 Cm	97 BK	98 Cf	99 Es	100 Fm	101 Md	102 No

http://acswebcontent.acs.or g/periodic/tools/PT/html

Fig. 3.3 The modern standard periodic table showing 18 groups

3.4 Atoms

In 1804, John Dalton proposed the existence of atoms and attributed certain properties to the *atoms* based on experimental studies. Every chemical element is composed of individual particles, called atoms. An atom by definition is the smallest unit into which a chemical element can be broken down, without losing its chemical identity. Dalton assumed that all the atoms of a given element have the same *atomic weight* or *atomic mass*. By 1914, it was realized that atoms of the same element can vary in weight, but may have the same chemical properties. The word *isotope* was coined by Frederick Soddy to represent atoms of an element that have different weights, but which can still be placed in the same position in the periodic table. An isotope can be stable or unstable (radioactive).

Some of the elements in nature such as Na, F, Al, and Bi have no isotopes, while 81 of the elements listed in the periodic table have at least one stable isotope. Natural carbon exists in two stable isotopic forms (^{12}C and ^{13}C) while tin has ten stable isotopes. All elements heavier than Bi are unstable; no stable isotope exists for these elements. In 1947, the American chemist Truman Paul Kohman suggested that the word *nuclide* is a more

appropriate term to represent both, stable and unstable atoms (or radionuclide) of an element.

3.4.1 Atomic Structure

In 1910, Rutherford presented a model of an atomic structure known as *nuclear atom*. According to this nuclear model, atoms consist of a massive, compact, positively charged core, or *nucleus* surrounded by a diffuse cloud of relatively light, negatively charged electrons. In 1913, Moseley formulated the property of *atomic number* (Z), which is the number of positive charges in the nucleus. In 1914, Rutherford named this positively charged particle in the nucleus, *proton* (from the Greek word first). Proton has an electrical charge, equal to that of an electron; however; a proton is positive and has a mass 1836 times that of the electron. In the electrically neutral atom, the number of orbiting electrons is sufficient to balance the number of positive protons. In the 1920s, Rutherford sumrised that the existence of a neutral particle (the same size as a proton) within the nucleus accounts for the total mass of the atom. Such a neutral particle was discovered in 1932 by James Chadwick eventually discovered these

Table 3.2 Fundamental particles of matter

Particle	Mass[a]		Energy[b]	Charge	
	U	kg	MeV	Elementary	Coulombs (C)
Electron, e^-	0.0005486	9.11×10^{-31}	0.511	-1	-1.602×10^{-19}
Positron, e^+	0.0005486	9.11×10^{-31}	0.511	$+1$	$+1.602 \times 10^{-19}$
Proton, p/H^+	1.007825	1.673×10^{-27}	938.78	$+1$	$+1.602 \times 10^{-19}$
Neutron, n°	1.008665	1.675×10^{-27}	939.56	0	$-$

[a] Mass is expressed in international mass unit (u), which is equal to 1/12th the mass of carbon-12 atom (1.66054×10^{-24} g)

[b] The energy given here is the rest mass energy of the particle

neutral particles. Subsequently, Heisenberg proposed that the nuclei of different elements consist of protons and neutrons which are held together by strong exchange forces known as nuclear forces. The total number of protons and neutrons within the nucleus is called the *mass number* (A), which is very close to the atomic weight of an element. The mass number (A) of ^{12}C nuclide is 12 and its atomic mass is considered as 12 atomic mass units (AMU or u). The atomic weight of natural carbon, however, is 12.011 since it is a mixture of ^{12}C (98.89%) and ^{13}C (1.11%) nuclides or isotopes. The mass–energy relationships of the fundamental subatomic particles are summarized in Table 3.2.

3.4.2 The Bohr Model of an Atom

The atom consists of an extremely dense, small positively charged nucleus surrounded by a cloud of electrons with small size and mass, each carrying a single negative charge equal but opposite to that of a proton in the nucleus. Because the number of electrons and protons in an atom, is the same the whole atom is electrically neutral. The *atomic volume* (10^{-8} cm diameter) with the cloud of electrons is significantly larger than the volume of the nucleus (10^{-13} cm diameter). Based on Rutherford's discovery of the atomic nucleus and Plank's discovery of the energy quantum ($E = h\nu$), Neils Bohr developed the first quantum model of an atom in 1913 (Fig. 3.4). According to this model, an electron in a hydrogen atom rotates around the nucleus at high speeds in closed *circular orbits* associated with a characteristic *quantum number (n)*. The electron in general exists in a low energy orbit (*ground state*). Gain or loss of a quantum of energy occurs only when an electron moves from one orbit to one of greater or

Fig. 3.4 Schematic representation of the Bohr model of atom showing circular (*K* shell) and elliptical (*L* shell) orbits

lesser energy. As a result, an atom can absorb or emit energy in discrete units or quanta.

In 1916, Arnold Sommerfeld suggested that the electron orbits can be elliptical, and to different degrees. Consequently, the orbital *quantum number (l)* was introduced. The circular and elliptical orbits are assumed to be in a single plane. When atoms are in a magnetic field, however, the orbits may be tipped. These orbits can best be represented in a three dimensional spherical space around the nucleus. To account for this magnetic effect, a *magnetic quantum number (m)* was introduced. Subsequently, Wolfgang Pauli introduced the *spin quantum number* (*s*) to represent the direction of electron spin (clockwise or anticlockwise).

The arrangement of electrons around the nucleus (Fig. 3.4) in an atom can be described based on the four quantum numbers. A more detailed representation

of electron orbits based on quantum mechanics is described in the chemistry section Chap. 7.

3.4.2.1 Electron Binding Energy

When the atom is in a ground state, electrons in an atom occupy the innermost shells of an atom. In the most stable configuration, electrons are most tightly bound to the nucleus. Electrons can move to higher energy or higher shells or can even be completely removed from the atom by providing energy to the electrons. The amount of energy required to remove an electron from a given shell (and to overcome the force of attraction of the nucleus), is called the *binding energy* of the shell. The binding energy is greatest for the innermost shell (K shell, $n = 1$) and increases as the atomic number (Z) increases (Fig. 3.5). The energy required for an electron to jump from a lower shell (K shell) to a higher shell (L, M, N, etc) is exactly equal to the difference between the shells.

Calculations of the energy levels of electrons in an atom involve the following physical principles. Based on the electron rest mass (m), velocity (v) and radius of the orbit (r), the angular momentum (mvr) of the electron about the nucleus is given by

$$mvr = n\frac{h}{2\pi} \tag{3.10}$$

where n is the principal quantum number and h is Planck's constant (6.626×10^{-34} J s).

The force experienced by an electron (mv^2/r) in its orbit is supplied by the Coulomb attraction between the electron ($-e$) and the nuclear charge ($+Ze$), Therefore the equation for the motion of electron is given by

$$\frac{mv^2}{r} = \frac{Ze^2}{4\pi\varepsilon_0 r^2} \tag{3.11}$$

where ε_0 is the *permittivity of free space*, and $1/4\pi\varepsilon_0 = k_0 = 8.98755 \times 10^{-9}$ N m^2 C^{-2}.

The total energy of the electron in any orbit (nth orbit) is given by the sum of its kinetic and potential energy

$$KE = \frac{1}{2}mv^2 + PE = -\frac{e^2}{4\pi\varepsilon_0 r} \tag{3.12}$$

$$E_n = \frac{k_0^2 Z^2 e^4 m}{2n^2 \left(\dfrac{h}{2\pi}\right)^2} = -\frac{13.6 Z^2}{n^2} eV \tag{3.13}$$

The lowest energy occurs when $n = 1$. For a hydrogen atom, the ground state energy or the binding energy is -13.6 eV (Fig. 3.5). The energy required to remove an electron from its ground state is called the ionization
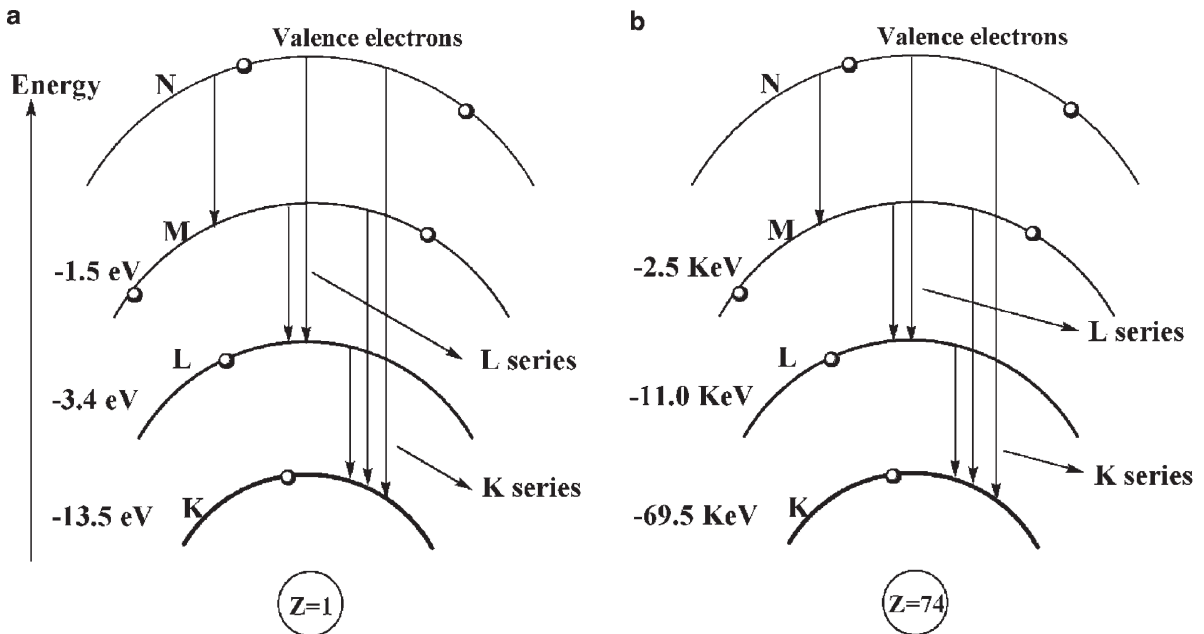
Fig. 3.5 The electron binding energy level diagram for hydrogen (**a**) and tungsten (**b**)

potential, which is 13.6 eV. In comparison, for lead, the electron binding energy of a K shell electron is 88,005 eV.

3.5 Nuclear Structure

3.5.1 Composition and Nuclear Families

The size or the diameter of the atomic nucleus is very small compared to the diameter of an atom (10^{-13} cm versus 101^{-8} cm). The nucleus is composed of protons and neutrons and, collectively, these elementary particles are known as *nucleons*. The mass of nucleons is almost 2,000 times that of electron mass. Therefore the density of the nucleus is very high compared to that of an atom.

For a given chemical element, the total number of protons (Z) and neutrons in the nucleus is known as the mass number (A), which is almost equal to the atomic weight (A_w). The difference between A and Z, is the neutron number (N).

A nuclide with a life span of greater than 10^{-12} s is generally characterized by an exact nuclear composition, given by A, Z, and the arrangement of nucleons within the nucleus. Even though 112 chemical elements are known, more than 3,000 nuclides have been discovered. The physical characteristics of the subatomic particles are summarized in Table 3.2.

Different combinations of protons and neutrons create different nuclear families. Atomic nuclei of the same element have the same number of protons (Z) but can have different numbers of neutrons (N) and different mass numbers (A). Such nuclides of an element are known as *isotopes* of that element. Nuclides with the same A, but different Z are called *isobars* while the nuclides with same N but different A and Z are called *isotones. Nuclear isomers* are nuclides with the same A and Z, but different nuclear energies. Examples of different nuclear families are shown below (Fig. 3.6).

3.5.2 Nuclear Binding Energy

The binding energy is the minimum amount of energy required to overcome the forces holding the nucleus together and to separate the nucleus completely into the individual components. Most of the binding energy,

Isotopes of Carbon	$^{11}_{6}C_5$	$^{12}_{6}C_6$	$^{13}_{6}C_7$	$^{14}_{6}C_8$
Isobars		$^{11}_{6}C_5$	$^{11}_{5}B_6$	
Isotones		$^{14}_{6}C_8$	$^{15}_{7}N_8$	
Isomers		$^{99m}_{43}Tc_{56}$	$^{99}_{43}Tc_{56}$	

Fig. 3.6 Various nuclides or nuclear species are grouped into four major families having certain common characteristics. For example, isotopes of an element have the same number of protons (Z), but different mass number (A)
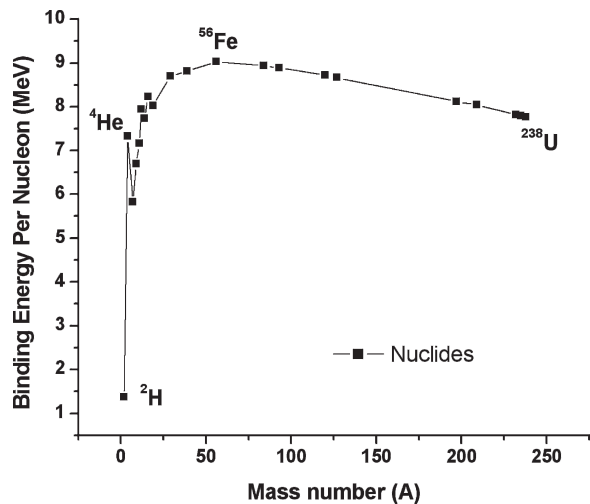
Fig. 3.7 Binding energy per nucleon versus mass number (A) for several stable nuclides. One of the isotopes of iron (^{56}Fe) has the highest nuclear binding energy

however, is nuclear binding energy, since energy required to remove electrons from an atom is relatively small. Mass defect or deficiency (Δm) is the difference between the mass of the atom and the sum of the masses of individual components. Binding energy (E_B) is the energy equivalent of Δm. For example, in the case of ^{12}C atom, the Δm is 0.09906 u, which is equal to 92.22 MeV. The binding energy per nucleon (E_B/A) for ^{12}C, is 7.685 MeV. The binding energies of several nuclides as a function of mass number are shown in Fig. 3.7.

3.5.3 Nuclear Stability

Protons and neutrons within the nucleus are subject to two kinds of forces. Since like charges repel, electrical

forces of repulsion exist between protons. In contrast, the strong exchange forces which can operate only at small distances (<3 fm), keep the protons and neutrons together in the nucleus. The shell model of the nucleus suggests that nucleons move in orbits about one another, while the liquid-drop model suggests that the nucleus is more like a drop of liquid.

Why are some combinations of protons and neutrons more stable than others? ^{12}C with six protons and six neutrons is stable forever, while ^{11}C with six protons and five neutrons is very unstable and decays with a half-life of only 20 min. In general, elements with a low atomic number ($Z < 10$) contain equal number of protons and neutrons and, therefore, are more stable. In contrast, as the atomic number Z increases, more and more neutrons are needed in the nucleus to keep the elements stable (Fig. 3.8). In general nuclides with even number of protons and neutrons are more stable than nuclides with an odd number of protons and neutrons. The nuclear stability, therefore depends on

- Neutron/proton ratio (n/p): Among the isotopes of every element, there is an optimal ratio favoring stability. The number of neutrons required to maintain stability is approximately 1.5 Z for heavy elements. All elements with $Z > 83$ and $A > 209$ are unstable and spontaneously decay or transform into more stable combinations of protons and neutrons.
- The binding energy/nucleon (E_B/A): The binding energy is greatest (>8 MeV) for nuclides with $A \approx 60$.
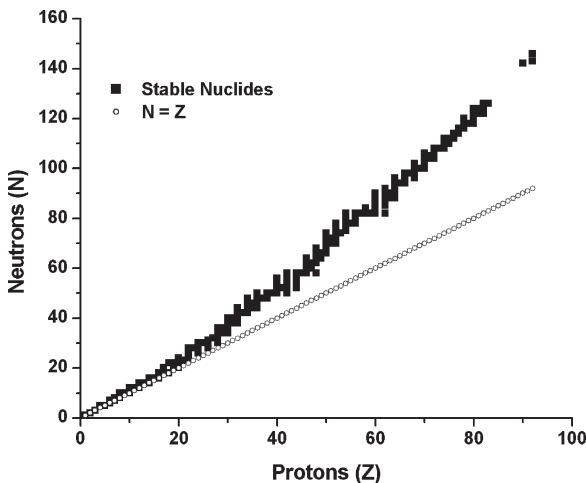
Fig. 3.8 Atomic number (Z) versus the neutron number (N) for the stable isotopes of elements. The neutron/proton ratio of unity represents a theoretical line of stability. The elements with higher Z, however, prefer $n/p > 1$ in order to achieve stability

It decreases slowly with increasing A, indicating the tendency toward instability for heavy elements.

The most stable arrangement of nucleons within the nuc-leus is called the ground state. *Excited states* are unstable and have higher energies. They also have a transient existence (10^{-12} s) and tend to transform into stable ground states. *Metastable states* exist longer (>10^{-12} s), but, eventually, also transform to ground states.

3.6 Atomic and Nuclear Emissions

3.6.1 Emissions from Electron Shells

When atoms are excited, electrons in the inner shells gain energy and jump to higher energy outer shells, but with lower electron binding energies. When these electrons jump back to more stable lower orbits, energy is emitted in the form of electromagnetic radiation. All types of electromagnetic radiations, visible, UV, infrared, radio waves, and X-rays are emitted from atomic shells (Fig. 3.2). Also, electrons (*photoelectrons* or *Auger electrons*) are emitted from atoms under certain circumstances. The emission of photoelectrons following interaction of energetic photons is discussed in Chap. 6.

3.6.1.1 X-rays

In the photoelectric effect, photons of light transfer energy to the electrons in an atom. In the inverse photoelectric effect, the kinetic energy of an electron is converted into a photon. In 1895, Röntgen discovered that when cathode rays (negatively charged particles, electrons) strike the atoms of a glass vacuum tube, they produce penetrating x-rays that cause a salt (barium platinocyanide) to glow. Soon it was realized that x-rays are high energy electromagnetic (em) radiation. An accelerated electric charge will radiate em waves. As the fast moving cathode rays approach the positive charge in the nuclei of atoms in the glass, electrons are brought to rest (accelerated), and the kinetic energy of electrons is converted to em waves. Radiation produced under these circumstances was given the name *bremsstrahlung* (breaking radiation). It was also realized that when denser, more massive atoms in a metal are used to stop accelerated electrons, x-rays of higher energies can be generated.

3.6.1.2 Characteristic X-rays

In 1911, the British physicist Charles Barkla noticed that each metal produces x-rays of a particular wavelength, depending on the metal (Fig. 3.9) and called the more penetrating beam *K* x-rays and the less penetrating beam *L* x-rays. The wavelength of x-rays decreases (energy increases) as the atomic number of elements increased. Emissions from transitions >100eV (0.1keV) are called *characteristic or fluorescent x-rays*. Emission of characteristic x-rays occurs when orbital electrons move from an outer shell to fill an inner shell vacancy (such as $L{\rightarrow}K$ or $M{\rightarrow}K$ shell). The energy of the characteristic x-rays is the difference in binding energies of these shells. For example, de-excitation (e.g., $M{\rightarrow}K$ transition $= K_\beta$) of a tungsten atom, results in the emission of characteristic x-rays of 67keV (Fig. 1.5 in Chap. 1); the difference in binding energy between *M* and *K* shells. The probability that the electron transition will result in the emission of characteristic x-rays is called *fluorescent yield* (ω), which is essentially zero for elements with low *Z* (<10) and increases as *Z* increases.

3.6.1.3 Auger Electrons

Just as in the production of characteristic x-rays, an electron from the outer shell drops down to fill the vacancy in a lower shell, and energy is released. As an alternative to the emission of x-rays, the energy is transferred to another orbital electron, which is ejected from the atom (Fig.3.9). The emission of the electron from the inner shell is known as the *Auger effect*, which in turn creates two vacancies in the shell. For example, the deexcitation (e.g., $M{\rightarrow}K$ transition $= K_\beta$) of a tungsten atom, results in the emission of an Auger electron with 64.5keV (Fig. 1.5 in Chap. 1): the difference in binding energy between *M* and *K* shells minus the binding energy of another electron in *M* shell, which is ejected. Again, this vacancy is filled by outer electrons resulting in characteristic x-rays or Auger electrons. Elements with lower *Z* are more likely to eject Auger electrons while elements with higher *Z* are more likely to emit characteristic x-rays.
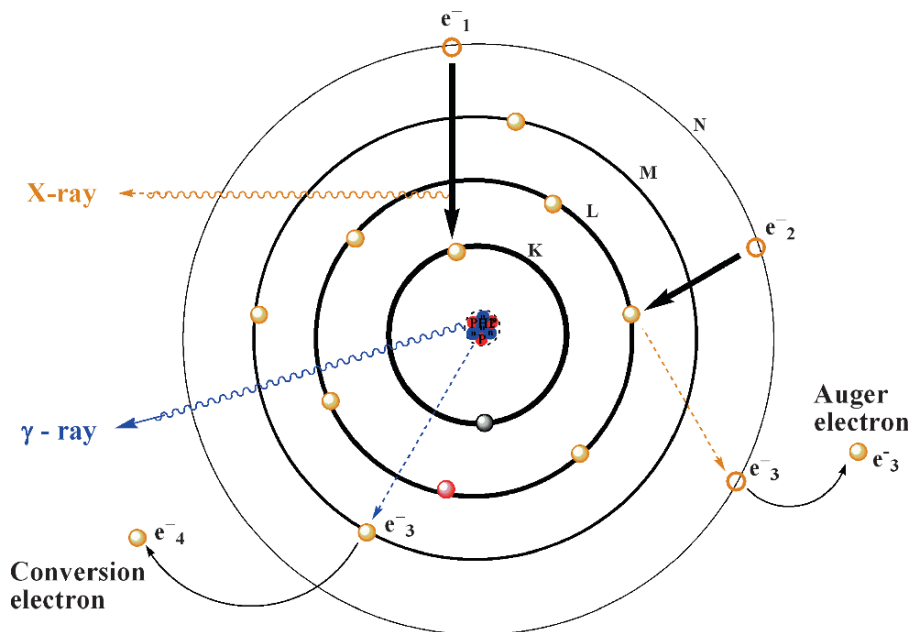
Fig. 3.9 Atomic emissions: When an electron from an outer higher energy shell moves in to fill a vacancy in a lower shell, the energy released may appear as electromagnetic radiations, such as x-rays or as an alternative, the atom may undergo Auger effect and may emit electrons, known as Auger electrons. In contrast, the energy from the nucleus may be emitted in the form of γ-rays or promote emission of conversion electrons

3.6.2 Nuclear Emissions

3.6.2.1 Gamma Rays

Like an excited atom, an excited nucleus can emit electromagnetic radiation in order to come to the ground state (Fig. 3.9). The photons emitted by the nuclei range in energy up to several MeV, and are traditionally called *γ rays*. The energy of a γ photon corresponds to the energy difference between the various initial and final states in the transitions involved. Deexcitation of the excited nuclei may emit only γ rays (as in the case of nuclear isomers) or emit γ rays in addition to nonpenetrating radiation such as β-rays, α-rays, protons and neutrons emitted during the radioactive decay process.

3.6.2.2 Internal Conversion

As an alternative to γ rays, an excited nucleus in some cases may return to its ground state by transferring the excitation energy to one of the orbital electrons, which is then ejected from the atom. This process of converting nuclear energy to eject an orbital electron (Fig. 3.9) is called *internal conversion*, which is analogous to the photoelectric effect. The *KE* of conversion electron is equal to the difference between the lost nuclear excitation energy and the binding energy of the electron from the ejected atomic shell.

Additional Reading

Beiser A (1995) Concepts of modern physics. 5th edn, McGraw-Hill, New York

Bushberg JT, Seibert JA, Leidholdt EM Jr (2002) The essential physics of medical imaging. 2nd edn, Lippincott, Philadelphia

Emsley J (1998) The elements. 3rd edn, Oxford University Press, Oxford

Saha G (2004) Fundamentals of nuclear pharmacy. 5th edn, Spriger, New York

Sorensom JA, Phelps ME (1987) Physics in nuclear medicine. Saunders, Philadelphia

Turner JE (1995) Atoms, radiation, and radiation protection. 2nd edn, Wiley, New York

Radioactivity

Scientific work must not be considered from the point of view of the direct usefulness of it. It must be done for itself, for the beauty of science, and then there is always the chance that a scientific discovery may become like the radium, a benefit.

Marie Curie

4.1 The Discovery

As previously discussed, in 1895 Röntgen discovered x-rays as a result of the fluorescence they caused on a screen coated with barium platinum cyanide noticed that x-rays became fluorescent in the area where the cathode rays (electrons) interacted with the glass.

Two months later, Henry Becquerel, Professor of Physics at the Ecole Polytechnique in Paris, heard about the discovery of x-rays and immediately thought of a possible connection between x-rays and fluorescence. He quickly initiated a series of experiments to test whether fluorescent substances emitted x-rays. In February 1986, he was exploring the possibility that sunlight might cause crystals to emit penetrating rays like the x-rays. As luck would have it, he used uranium–potassium bisulfate (uranium salts were known to be phosphorescent). These crystals were placed next to a photographic plate that was wrapped in dark paper. If sunlight causes the crystals to emit penetrating rays, then these rays might penetrate the paper, and darken the plate. Because the weather was cloudy, Becquerel placed the unwrapped plate in the drawer of a cabinet, but left the crystals on the cabinet. When he developed the plate a couple of days later, to his surprise he found an intense darkening on it, caused by exposure to radiation. He immediately concluded that some invisible rays from the uranium had penetrated the cabinet and the dark paper covering the plate, and finally exposed the photographic plate. For a few years, these rays were known as *Becquerel rays* or *rayons uranique*.

Becquerel soon discovered that the rays from the uranium also ionized gases, thus, making them conductors. A crude and simple gold leafed electroscope was used to measure the *activity* of this radiation.

In 1898, Maria Sklodowska Curie and Pierre Curie discovered that thorium also emitted such rays. That year, the phenomenon of penetrating radiation emitted by uranium and thorium was given the name radioactivity by the Curies. Marie observed that the uranium ore, pitchblende, was much more active and discovered that the increased activity was due to the presence of two new radioactive elements, *polonium* and *radium*.

In 1900, the French chemist Paul Villard discovered a form of radioactive emission that was extremely penetrating and was not deflected by a magnetic field analogous to x-rays. This radiation was later given the name, gamma rays.

4.2 Nuclear Disintegration

Ernest Rutherford and his coworkers at Cavendish Laboratory in England distinguished three components in the radiations from natural radioactive elements, which he called α-rays, β-rays, and γ-rays. These components were eventually identified as helium nuclei, electrons and high-energy photons, respectively (Fig. 4.1).

In 1903, Rutherford and Frederick Soddy explained the cause and nature of radioactivity. They discovered that when radioactive atoms emit α or β-rays, they are changed into other varieties of atoms. They also
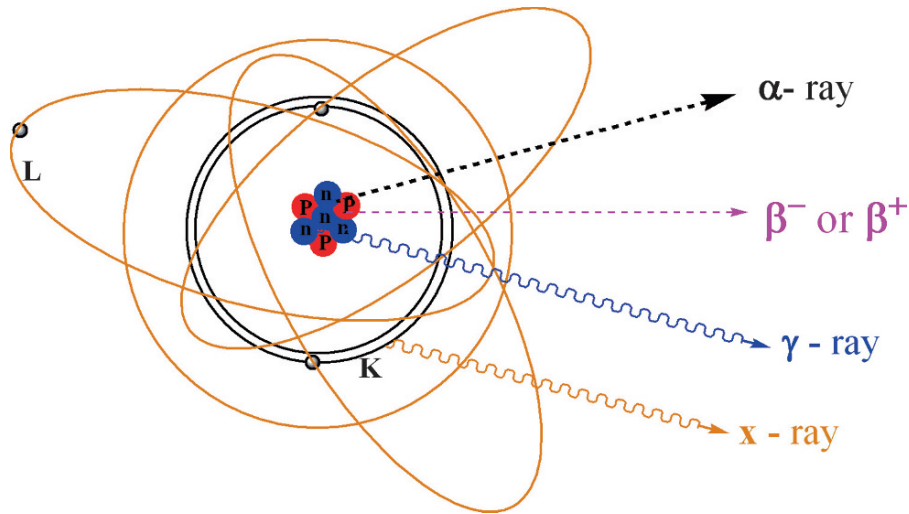
Fig. 4.1 The three components of radioactive emissions originating from the unstable nuclei of natural radionuclides of uranium and thorium: α, β⁻ and γ, as they were called by Rutherford.

Subsequently, two other decay modes, EC and positron emission were identified. In contrast, characteristic x-rays originate from the inner shells of electronic orbits

discovered the existence of atoms of the same element, having different atomic weights. In 1913, Soddy introduced the word *isotopes* to describe atoms of an element that have different atomic weights, but the same chemical properties. They proposed a *nuclear disintegration theory*, which states that radioactivity is actually the changing of one chemical element into another through the emission of α or β particles.

Nuclear transmutation is a phenomenon in which an unstable atomic nucleus disintegrates, in order to acquire a more stable state, by emitting subatomic particles and/or electromagnetic radiation. This phenomenon is called *radioactivity* or *radioactive decay*. One of the most important points to understand is that the energy liberated during the radioactive decay comes from within the individual nuclei of a radioactive element without any external excitation, unlike in the case of atomic radiation.

The emission of *positrons* (β^+) by radioactive isotopes was observed by Irene Curie and Frederick Joliot, in 1934 and they discovered that radioisotopes can be made artificially. With the discovery of nuclear fission, by Otto Hahn in 1939, scientists realized that some unstable nuclides with high atomic numbers may also undergo *spontaneous fission*.

Following the discovery of the proton by Rutherford in 1919, and the neutron by Chadwick in 1932, it became clear that the neutron/proton ratio of any nuclide, and the nuclear binding energy per nucleon

(Chap. 3) are the two most important characteristics of any nuclide that would determine the stability of an element, and the kind of radioactive decay it undergoes in order to attain stability.

4.2.1 Types of Radioactive Decay

The radioactive decay processes fall into two categories: one that involves a change in the mass number *A* of a radionuclide, and one in which both the parent and the daughter radionuclides have the same mass number (isobaric decay). The five major types of radioactive decay are shown in Table 4.1. The different radioactive decay modes are shown in the decay scheme diagram (Fig. 4.2).

4.2.1.1 Alpha (α) Decay

Alpha decay (Fig. 4.2) is generally seen in high atomic number elements such as ^{238}U, ^{230}Th and ^{226}Ra. The radionuclide ejects an α particle (two protons and two neutrons) and, because it loses two protons, it is converted into a nuclide with a lower atomic number. Alpha particles are *monoenergetic* and may have kinetic energies in the range of 4–9 MeV. Radionuclides emitting α particles may also emit γ photons. Nuclides with *A*

Table 4.1 Nuclear transmutations

Decaymode	Reason for instability of parent nucleus	Transformation	Example	n/p ratio change
Alpha decay	Too large	$_{Z}^{A}X \rightarrow {}_{Z-2}^{A-4}Y + {}_{2}^{4}\alpha$	$_{88}^{226}Ra \rightarrow {}_{86}^{222}Rn + {}_{2}^{4}\alpha$	Increases
Beta decay	Neutron rich	$_{Z}^{A}X \rightarrow {}_{Z+1}^{A}Y + e^{-}$	$_{6}^{14}C \rightarrow {}_{7}^{14}N + e^{-} + v$	Decreases
Positron emission	Neutron deficient	$_{Z}^{A}X \rightarrow {}_{Z-1}^{A}Y + e^{+}$	$_{6}^{11}C \rightarrow {}_{5}^{11}B + e^{+} + v$	Increases
Electron capture	Neutron deficient	$_{Z}^{A}X + e^{-} \rightarrow {}_{Z-1}^{A}Y$	$_{49}^{111}In + e^{-} \rightarrow {}_{49}^{111}Cd$	Increases
Isomeric transition	Excess energy	$_{Z}^{A}X* \rightarrow {}_{Z}^{A}Y + \gamma$	$_{43}^{99m}Tc* \rightarrow {}_{43}^{99}Tc + \gamma$	No change
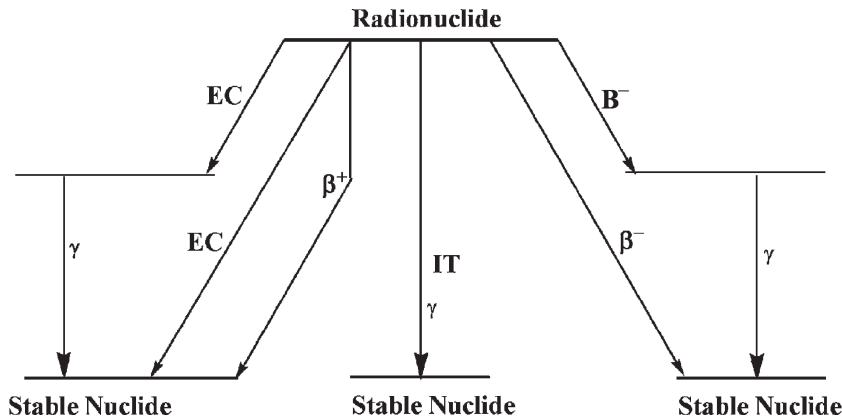
Fig. 4.2 The radioactive decay scheme diagram shows the major decay modes. The parent radionuclide is shown above while the lines to the left represent β⁻ decay and the lines to the right represent β⁺ decay or EC. Gamma emission is represented by the perpendicular lines. The lines at the bottom represent the ground state energy of the nuclide

>210 are so large, they need to eject α particles in order to reduce their size and become relatively more stable.

$$_{88}^{226}Ra \rightarrow {}_{86}^{222}Rn + {}_{2}^{4}\alpha \qquad (4.1)$$
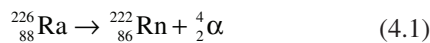
4.2.1.2 Beta (β⁻) Decay

In beta decay, neutron (*n*)- rich nuclides decay by emitting an electron or β⁻ rays. In an unstable nucleus, a neutron is converted into a proton (*p*), an electron, and an *antineutrino* (ν). Since only the electron and antineutrino are ejected, the daughter is the next element in the periodic table, with $Z +1$ protons, compared to the parent.

$$n \rightarrow p + e^{-} + \bar{v} \qquad (4.2)$$
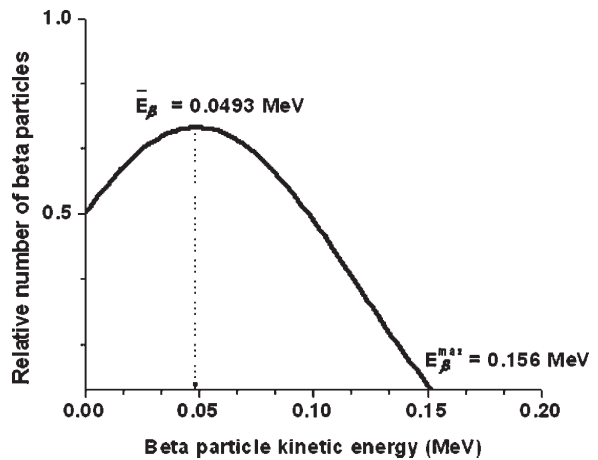
Fig. 4.3 The continuous β⁻ energy spectrum showing the distribution of β⁻ particles (relative number versus energy) emitted by ¹⁴C. The average energy is denoted by $\bar{E}_{\beta}$, while the maximum energy is denoted by E_{β}^{max}

The electron and proton do not exist in the neutron; they together with the neutrino, are created at the moment of decay. The kinetic energies of electrons ejected in the beta decay vary continuously from 0 to a maximum value of KE_{max} (E_β^{max}), characteristic of the radionuclide (Fig. 4.3). In an attempt to explain the continuous spectrum of β particle energies, Wolfgang Pauli, in 1930, proposed that a neutral particle with zero or a very small undetectable mass would carry off some of the energy equal to the difference between KE_{max} and the actual kinetic energy of the electron. This hypothetical particle was later called *neutrino* by Enrico Fermi, and was eventually detected in the 1950s by Reines and Cowan. Typically, the average kinetic energy of the β particle ($\bar{E}_\beta$), is about one third of E_β^{max}. With certain beta-emitting radionuclides, the daughter nuclide in an excited state, which promptly reaches ground state by the emission of γ rays. For example, in case of ^{131}I, 81% of the daughter [131]Xe atoms are in an excited state and emit γ photons (364 KeV). Since the emission of γ photons follows almost immediately after the beta emission, this sequential decay process is referred to as a β,γ decay.

4.2.1.3   Positron (β+) Decay

Nuclides that are deficient in neutrons are unstable, and decrease the number of positive charges in the nucleus (i.e., protons) by decaying either through positron emission or *electron capture* (EC). These two decay modes are regarded as *inverse beta decay*. They are alternatives to reach the ground state when an unstable nucleus is neutron-deficient. Positron emission may be more common in elements with a lower atomic number, while electron capture is seen mostly in elements with high atomic numbers.

A positron is an *antiparticle* of an ordinary electron (Fig. 4.2). In a proton-rich nuclide, a proton in the nucleus is transformed into a neutron, positron, and a neutrino (conversion of a proton into a neutron can only happen inside a nucleus).

$$p \rightarrow n + e^+ + v \qquad (4.3)$$

In 1928, Paul Adrien Maurice Dirac predicted the existence of an antielectron or positron. This prediction was unexpectedly confirmed in 1932 by the American physicist, Carl Anderson, who detected high energy positrons in cosmic radiation.

In 1934, Irene Curie and Frederick Joliot reported the discovery of artificial radioactivity. More specifically, when natural stable [27]Al was bombarded with alpha particles, [30]P ($T_{1/2}$ = 3 min) was produced, following which positron emission decayed to stable [30]Si, as shown below.

$$^{27}_{13}\text{Al} + ^4_2\alpha \rightarrow ^{30}_{15}\text{P} + n \qquad (4.4)$$

$$^{30}_{15}\text{P} \rightarrow ^{30}_{14}\text{Si} + e^+ + v \qquad (4.5)$$
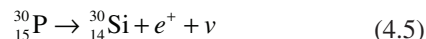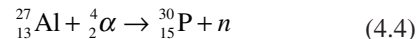
Positron emission leads to a daughter nucleus of a lower atomic number (Z−1), leaving the mass number unchanged. Just as in β− decay, the positron (β+) emission spectrum is continuous, (Fig. 4.2) with positron energies ranging from 0 to E_β^{max}. The average energy of the positron is 1/3rd of the maximum. The difference between the maximum energy and the actual energy of a positron is carried off by the neutrino. One of the consequences of positron emission is *annihilation radiation*, which is discussed in more detail in Chap. 6. Just as in β− decay, the daughter nuclide may be in an excited state and as a result, the sequential β+, γ decay process involves emission of gamma photons from the daughter nucleus. [11]C, ^{18}F, ^{64}Cu, ^{68}Ga and [124]I, used in developing molecular imaging radiopharmaceuticals for PET, are the most important radionuclides that decay by positron emission.

4.2.1.4   Electron Capture (Ec)

The unstable neutron-deficient nuclides may also reach the ground state by decreasing the positive charge in the nucleus by a process in which an orbital electron, usually from a *K*-shell, is captured by the parent nucleus, resulting in the conversion of one of the protons into a neutron. Since the energy of the parent nuclide is high, a neutrino is also produced, taking away some of the transition energy.

$$p + e^- \rightarrow n + v \qquad (4.6)$$

The electron capture (*K-capture*) decay process leads to a daughter nucleus of a lower atomic number (Z−1), leaving the mass number unchanged. As a vacancy is created in the *K*-shell of the daughter nuclide, characteristic x-rays and/or Auger electrons are ejected from the daughter nuclide. Sometimes, the daughter nuclide may also be in an excited state due to a change in the *n/p* ratio. As a result, gamma photons and conversion

electrons are emitted from the daughter nuclide in a process known as *EC, γ* decay mode. ^{67}Ga, ^{111}In, and ^{123}I are the most important radionuclides with EC decay mode that are useful for developing molecular imaging radiopharmaceuticals for SPECT.

4.2.1.5 Isomeric Transition (IT)

When an unstable decay occurs by any of the decay modes described above, the daughter nucleus may be in an unstable long-lived *metastable* state. Transitions or decays of such metastable nuclides (exist for >101^{-12} s) result in the emission of gamma photons (Fig. 4.2), but leave both *Z* and *A* unchanged. The two nuclides of an element that differ only in the energy content are called *isomers* (different from the concept of isomers in chemistry). The metastable states are called "isomeric states" (designated with letter *m* next to *A*), and the decay process is known as "isomeric transition." As an alternative, the nucleus of a metastable nucleus may transfer the energy to an orbital electron, also known as a conversion electron, and eject it from the atom. In contrast to beta decay, conversion electrons do not display a continuous energy spectrum, but show discrete energies. The most important radionuclide decaying by isomeric transition is ^{99m}Tc which is very

useful for developing molecular imaging agents for use with SPECT.

4.2.1.6 Multiple Decay Mode

Certain radionuclides decay by a single decay mode while some decay by multiple decay modes. As mentioned earlier, neutron deficient radionuclides may decay by EC or by positron emission. However, for a radionuclide to emit both β$^-$ and β$^+$ particles, the *n/p* ratio must be very close to that of the stable isotope of that element (Table 4.2). Every decay mode may also involve emission of γ photons.

4.2.2 Radioactive Decay Series

Often an unstable radionuclide, especially one with a high atomic number, cannot reach a stable ground state through a single decay process. In such a case a *decay series* occurs until a stable nuclide is formed. A well-known example of this is the decay series that starts with ^{238}U and ends with stable ^{206}Pb. During this process eight alpha particles and six beta particles are emitted before reaching the ground state, after losing ten protons and 22 neutrons.

Table 4.2 Radionuclides and decay modes

Element	Z	Isotope	n/p	Stability	% Decay abundance			
					β$^-$	β$^+$	EC	γ
Carbon	6	^{11}C	1.8333	Radioactive	–	99	1	*
		^{12}C	1.0	Stable (98.9%)	–	–	–	–
		^{13}C	1.1666	Stable (1.1%)	–	–	–	–
		^{14}C	1.3333	Radioactive	100	–	–	–
Fluorine	9	^{18}F	1.0	Radioactive	–	97	3	–
		^{19}F	1.1111	Stable (100%)	–	–	–	–
		^{20}F	1.2222	Radioactive	100	–	–	*
Copper	29	^{61}Cu	1.1035	Radioactive	–	100	–	*
		^{62}Cu	1.1379	Radioactive	–	98	2	–
		^{63}Cu	1.1724	Stable (69.17%)	–	–	–	–
		^{64}Cu	1.2069	Radioactive	39	19	41	*
		^{65}Cu	1.2414	Stable (30.83%)	–	–	–	–
		^{67}Cu	1.3103	Radioactive	100	–	–	*
Gallium	31	^{66}Ga	1.1290	Radioactive	–	56	43	*
		^{67}Ga	1.1613	Radioactive	–	–	100	*
		^{68}Ga	1.1935	Radioactive	–	90	10	*
		^{69}Ga	1.2258	Stable (60.1%)	–	–	–	–
		^{71}Ga	1.2903	Stable (39.9%)	–	–	–	–
		^{72}Ga	1.3226	Radioactive	100	–	–	*

With some radionuclides, the series may involve only two or three decays before reaching a stable ground state. For example, the unstable ^{99}Mo reaches stable ^{99}Ru as shown below. The intermediate ^{99}Tc has a long half-life (2.1×10^5 year).

$$^{99}_{42}\text{Mo}\xrightarrow{\beta^-}\,^{99m}_{43}\text{Tc}\xrightarrow{\text{IT}}\,^{99}_{43}\text{Tc}\xrightarrow{\beta^-}\,^{99}_{44}\text{Ru} \qquad (4.7)$$
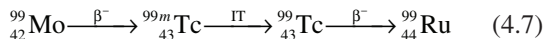
4.2.3 Nuclear Fission

Nuclear fission is the division or break-up of a heavy unstable nucleus into two lighter nuclei in order to reduce its size. Spontaneous fission may occur in heavy nuclides, but the probability is very low. For example, ^{235}U undergoes spontaneous fission with a very long half-life (2×10^{17} year).

In 1938, Otto Hahn, a German radiochemist, discovered that ^{235}U undergoes fission when struck by a slow neutron. It is not the impact of the neutron that induces fission. Instead, following absorption of the neutron, the ^{236}U nucleus is so unstable that almost at once it explodes into two lighter nuclei known as *fission fragments*. In addition, an enormous amount of energy ($\approx$200 MeV) and 2–3 high energy neutrons, per nuclear fission, are also released. Lise Meitner, a nuclear physicist, coined the name *fission* to describe the splitting of a uranium atom into two lighter elements.

$$^{235}_{92}\text{U}+n\rightarrow\,^{236}_{92}\text{U}*\xrightarrow{\text{fission}}\,^{140}_{54}\text{Xe}+^{94}_{38}\text{Sr}+2n+\text{Energy} \quad (4.8)$$

$$^{235}_{92}\text{U}+n\rightarrow\,^{236}_{92}\text{U}*\xrightarrow{\text{fission}}\,^{141}_{56}\text{Ba}+^{92}_{36}\text{Kr}+3n+\text{Energy} \quad (4.9)$$
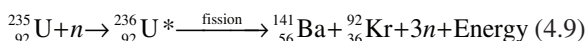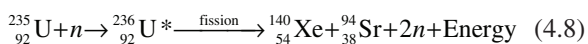
The above processes are only a couple of examples of the many fission fragments that ^{235}U can produce. In fact, over 200 different radio isotopes of 35 different elements have been observed among fission products. Most of these fragments are neutron rich and decay by beta decay.

4.3 Radioactive Decay Equations

4.3.1 Exponential Decay

Radioactive decay or transformation is a statistical process that obeys the laws of chance. No cause–effect relationship is involved in the decay of a radionuclide, only a certain probability per unit time.

The activity (A) of a sample of a radionuclide is the rate at which the nuclei of its constituent atoms (N) decay. Also the activity or the disintegration rate of a radionuclide at any time is proportional to the total number of radioactive atoms present at that time. Mathematically, the rate of decay (A) is given by

$$A = -\frac{dN}{dt} \propto N \qquad (4.10)$$

$$A = -\frac{dN}{dt} \lambda N \qquad (4.11)$$

Where N is the number of radioactive atoms and λ is the decay constant (or proportionality constant) which is defined as the probability of disintegration per unit time. The minus sign indicates that the number of atoms is decreasing with time. The above equation for the rate of decay is the rate law for a first order process. Upon integration, the formula for "radioactive decay" is given by

$$N = N_0 \text{e}^{-\lambda t} \qquad (4.12)$$

The formula for the time variation of activity or activity at any time t is given by

$$A_t = A_0 \text{e}^{-\lambda t} \qquad (4.13)$$

The above equations represent the *exponential decay* of any radionuclide in which λ, is the *decay constant* of the radionuclide and the factor $\text{e}^{-\lambda t}$ is known as the *decay factor*, which is the fraction of original activity A_0 remaining after time t.

The decay factor is an *exponential function* of time t. The exponential decay is characterized by the transformation of a constant fraction of the number of atoms or activity present per unit time interval. When the decay factor, number of atoms, or activity is plotted against time, it is a curve approaching zero on a linear plot, but is a straight line in a semilogarithmic plot (Fig. 4.4).

4.3.2 Units of Activity

The SI unit of radioactivity is named after Becquerel

$$1 \text{ Becquerel} = 1 \text{ Bq} = 1 \text{ decay}/s \qquad (4.14)$$
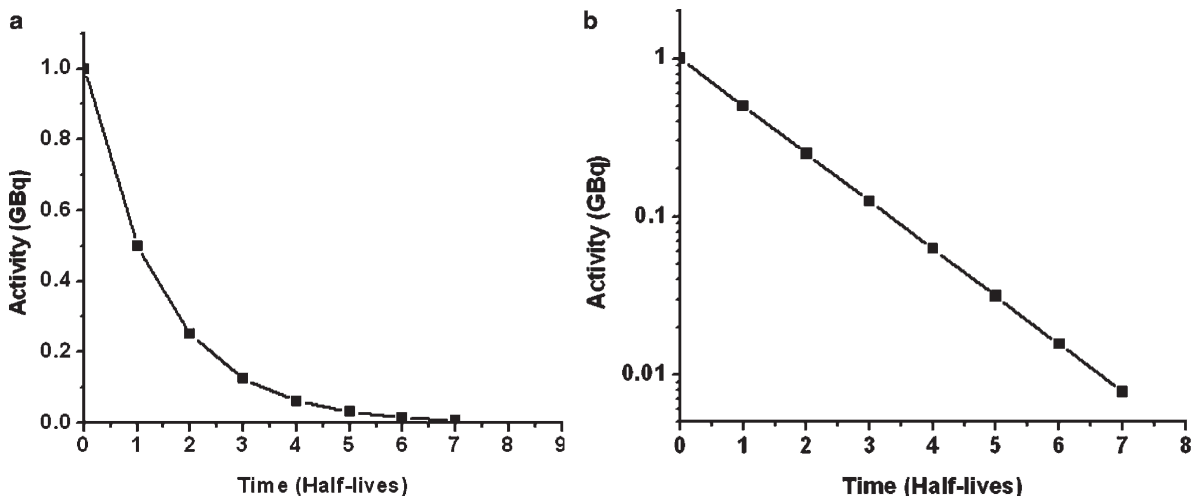
Fig. 4.4 The decay of radioactivity as a function of time (half-lives) plotted on a linear scale (**a**) and semilogarithmic scale (**b**)

The traditional unit of activity is the Curie (Ci), which was originally defined as the activity of one g radium, ^{226}Ra. Curie is now defined as

$$1\,Curie = 1\,Ci = 3.7 \times 10^{10}\,dps = 37\,GBq \qquad (4.15)$$

$$1\,milliCurie = 1\,mCi = 3.7 \times 10^{7}\,dps = 37\,MBq \quad (4.16)$$

$$1\,microCurie = 1\,\mu Ci = 3.7 \times 10^{4}\,dps = 37\,KBq \quad (4.17)$$

4.3.3 Half-Life and Average Life Time

Every radionuclide has a characteristic half-life ($T_{1/2}$), which is the time required for the activity to decay to 50% of its original value. That is, A_0 is reduced to $A_0/2$ in one half-life, $A_0/2^2$ in 2 half-lives, and $A_0/2^n$ in n half-lives. The activity A, of a radionuclide at any time t is given by

$$A_t = \frac{A_0}{2^n} = \frac{A_0}{2^{(t/T_{1/2})}} \qquad (4.18)$$

The half-life and the decay constant of a radionuclide are related

$$T_{1/2} = \frac{\ln(0.2)}{\lambda} = \frac{0.693}{\lambda} \qquad (4.19)$$

In a given sample of radionuclide, not all atoms decay with the same half-life; some atoms may have a shorter and some atoms may have a longer life span than one half-life. The average, or mean life (τ) of a radionuclide is, therefore, defined as the average of all individual life times of the atoms in a sample of radionuclide experience. The mean life is related to the decay constant and half-life

$$\tau = \frac{1}{\lambda} = \frac{T_{1/2}}{0.693} = 1.44\,T_{1/2} \qquad (4.20)$$

4.3.4 Specific Activity

The specific activity (SA) of a radioactive sample is defined as its activity per unit mass. The SA is the ratio of activity to the total mass of the element present. It has units of Ci g^{-1}, Ci mmole^{-1}, or GBq mmole^{-1}.

Many elements have several isotopes and some of the isotopes of an element can also be stable. The element carbon has four isotopes as shown below:

$$^{11}_{6}C,\ ^{12}_{6}C,\ ^{13}_{6}C,\ ^{14}_{6}C$$
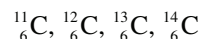
^{12}C and ^{13}C are stable and, in nature, most of the carbon is ^{12}C (99% abundance). ^{14}C ($T_{1/2} = 5{,}760$ year) decays by beta decay while ^{11}C ($T_{1/2} = 20$ min) decays by positron emission. When stable isotopes of an element are present along with the radioactive isotope, then the stable isotopes are called *carrier*. When the radioactivity of the sample is said to be with the carrier and the SA of such a radioisotope is low, because the total mass

of the element includes the mass of radioisotope and also that of the carrier. A radioactive sample that does not contain the carrier is called *carrier-free*. The highest possible SA of a radionuclide is its carrier-free SA (CFSA). It is also known as the theoretical SA, and may not necessarily be achieved practically by radionuclide production methods.

CFSA can be calculated since there is a well-defined Activity–Mass relationship based on the following mathematical relationships:

- Based on $T_{1/2}$, decay constant (λ) can be calculated as $\lambda = 0.693/T_{1/2}$
- Knowing the activity (Ci or GBq, etc.) and λ, the number of atoms (N) in a sample of radioactivity can be determined based on the activity law, $A = \lambda N$
- Based on N, the mass (g or moles) of a radioisotope can be determined because one mole (gram atomic weight) of any element contains 6.022×10^{23} atoms (Avogadro's number).

For a number of radioisotopes the carrier-free SA are shown in Table 4.3. The SA calculations for ^{11}C are shown below.

Carrier-free Specific Activity (CFSA) of ^{11}C

1 mole of ^{11}C (11 g) contains 6.022×10^{23} atoms (N)
Since $T_{1/2}$ of $^{11}C = 20\,min$,

$$\lambda = \frac{0.693}{20\,Mins \times 60s} = 5.775 \times 10^{-5}$$

Activity (Bq) in 1 mole:

$$B_q = 5.775 \times 10^{-5} \times 6.022 \times 10^{23} = 3.478 \times 10^{19}$$

since $1\,Ci = 3.7 \times 10^{10}\,Bq$,

$$\frac{3.478 \times 10^{19}}{3.7 \times 10^{10}} = 9.4 \times 10^{8}\,Ci\,mole^{-1}$$

since $1\,GBq = 10^9\,Bq$,

$$\frac{3.497 \times 10^{19}}{10^9} = 3.478 \times 10^{10}\,GBq\,mole^{-1}$$

CFSA of $^{11}C = 9,400\,Ci\ \mu mole^{-1}$ or 9.4×10^3 Ci $\mu mole^{-1}$
A similar calculation shows that CFSA of $^{14}C = 6.205 \times 10^{-5}$ Ci $\mu mole^{-1}$

4.3.5 Serial Radioactive Decay

When a sample of radioactivity consists of a pair of parent and daughter radionuclides, the parent activity (A_p) at any time t, is given by the equation 4.13. Because the daughter is continuously produced by the decay of the parent and at the same time the daughter activity is also decaying, estimating the daughter activity (A_d) at any time really depends on the decay constant or the $T_{1/2}$ of the daughter radionuclide. The *Bateman equa-*

Table 4.3 Radionuclides for PET and SPECT: Half-life and specific activity (SA)[a]

Radionuclides for PET			Radionuclides for SPECT		
Nuclide	$T_{1/2}$ (min)	SA (Ci μmol^{-1})	Nuclide	$T_{1/2}$ (min)	SA (Ci μmol^{-1})
^{82}Rb	1.20	150,400			
^{15}O	2.07	91,730			
^{122}I	3.62	51,912			
^{62}Cu	9.76	19,310			
^{13}N	10.0	18,900			
^{11}C	20.4	9,220			
^{94m}Tc	52.0	3,614	^{99m}Tc	360	522
^{68}Ga	68.3	2,766			
^{77}Br	96.0	1,960			
^{18}F	110	1,708			
^{66}Ga	567	331	^{67}Ga	4,320	40
^{64}Cu	768	245			
^{86}Y	884	213	^{111}In	4,020	47
^{89}Zr	4709	39.9			
^{124}I	6,048	31.0	^{123}I	780	237

[a]Maximum theoretical specific activity (SA)
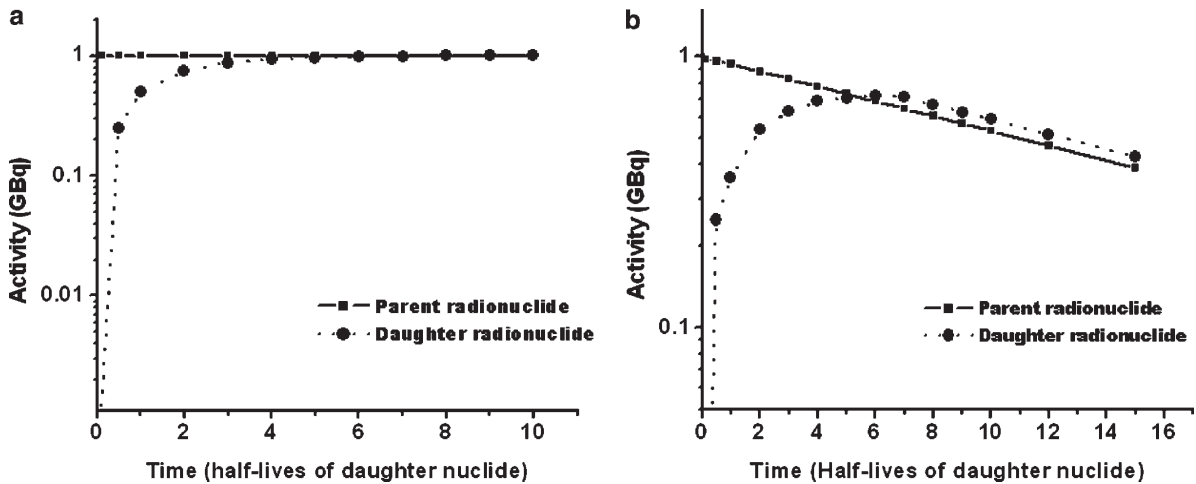
Fig. 4.5 In a parent–daughter decay, following the buildup of the daughter activity, the parent and daughter activities are said to be in secular equilibrium (**a**) or in transient equilibrium (**b**)

tion describes the parent–daughter relationship and provides an estimate of A_d.

$$A_{d(t)} = A_{p(t_0)} \frac{\lambda_d}{\lambda_d - \lambda_p} (e^{-\lambda_p t} - e^{-\lambda_d t}) + A_{d(t_0)} e^{-\lambda_d t} \quad (4.21)$$

At equilibrium, the parent and daughter activities appear to decay with the same rate, even if the two nuclides have different half-lives. Two different equilibrium conditions, however, may exit, depending on how short lived the daughter radionuclide is, compared to the parent. If the parent is short lived compared to the daughter, then there is no equilibrium at all.

4.3.5.1 Secular Equilibrium

When the daughter radionuclide is very short lived, compared to the parent ($T_{\frac{1}{2}d} << T_{\frac{1}{2}p}$), *secular equilibrium* is said to exist. The activity of the daughter builds up to that of the parent in about seven half-lives of the daughter. At equilibrium, $A_d = A_p$ (Fig. 4.5 (a)). The activity of the daughter at any time, however, is given by

$$A_{d(t)} = A_{p(t_0)} (1 - e^{-\lambda_d t}) \quad (4.22)$$

Two important examples are ^{68}Ge ($T_{\frac{1}{2}} = 270$ days)$\rightarrow^{68}$Ga ($T_{\frac{1}{2}} = 68$ min) generator and ^{82}Sr ($T_{\frac{1}{2}} = 25$ days)$\rightarrow^{82}$Rb ($T_{\frac{1}{2}} = 75$ s) generator.

4.3.5.2 Transient Equilibrium

When the parent half-life is longer than the daughter half-life ($T_{\frac{1}{2}p} > T_{\frac{1}{2}d}$), the daughter activity increases while the parent activity slowly decreases. The daughter activity reaches a maximum and is slightly greater than that of the parent. Once the *transient equilibrium* is reached (~7 $T_{\frac{1}{2}}$ of daughter), both radionuclides appear to decay with the same rate, the decay rate of the parent (Fig. 4.5(b)). The daughter activity (A_d) at any time t is given by

$$A_{d(t)} = A_{p(t)} \frac{\lambda_d}{\lambda_d - \lambda_p} \quad (4.23)$$

An example of transient equilibrium is ^{99}Mo ($T_{\frac{1}{2}} = 66$ h)$\rightarrow^{99m}$Tc ($T_{\frac{1}{2}} = 6$ h) generator.

Additional Reading

Beiser A (1995) Concepts of modern physics, 5th edn. McGraw-Hill, New York

Bushberg JT, Seibert JA, Leidholdt Jr EM (2002) The essential physics of medical imaging, 2nd edn. Lippincott, Philadelphia

Emsley J (1998) The elements, 3rd edn. Oxford University Press, Oxford

Saha G (2004) Fundamentals of nuclear pharmacy, 5th edn. Spriger, New York

Sorensom JA, Phelps ME (1987) Physics in nuclear medicine. Saunders, Philadelphia

Turner JE (1995) Atoms, radiation, and radiation protection, 2nd edn. Wiley, New York

Production of Radionuclides

Dr. Livingston has asked me to advise you that he has obtained 1,100,000 volt protons. He also suggested that I add "Whoopie"!

Telegram to Lawrence, 3 August 1931

5.1 Nuclear Transformation

When two nuclei come close together, a *nuclear reaction* can occur that results in a *nuclear transformation*, which is the conversion of one element to another. In 1919, Rutherford observed the first nuclear transformation following bombardment of natural nitrogen atoms (^{14}N) with α particles (He nuclei) from a radium–carbon source (Segrè 1980). More specifically, he observed that a nitrogen nucleus was converted into an isotope of oxygen, ^{17}O with the emission of a proton. The process that Rutherford discovered was the disintegration of the stable nucleus and the formation of a stable oxygen isotope. In 1925, using the cloud chamber, Blackett confirmed Rutherford's observation.

$$^{14}_{7}\text{N} + ^{4}_{2}\text{He} \rightarrow ^{17}_{8}\text{O} + ^{1}_{1}\text{H} \qquad (5.1)$$
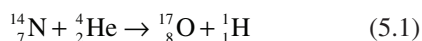
In 1932, when Chadwick bombarded a stable beryllium atom with α particles, the element beryllium was converted into a stable carbon isotope with the emission of a neutron (Segrè 1980).

$$^{9}_{4}\text{Be} + ^{4}_{2}\text{He} \rightarrow ^{12}_{6}\text{C} + ^{1}_{0}n \qquad (5.2)$$
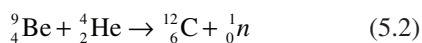
In the two nuclear reactions described above, the nuclear transformation involved conversion of a stable isotope of one element into a stable isotope of another element. In 1934, Irene Curie and her husband Frederic Joliot were the first to produce an unstable radioisotope that decayed by positron emission and the first to discover the artificial production of radioisotopes (Joliot and Curie 1934).

$$^{27}_{13}\text{Al} + ^{4}_{2}\text{He} \rightarrow ^{30}_{15}\text{P} \rightarrow ^{1}_{0}n \qquad (5.3)$$

$$^{30}_{15}\text{P} \rightarrow ^{30}_{14}\text{Si} + \beta^{+} \qquad (5.4)$$
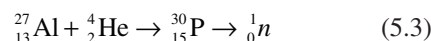
As shown above, the stable Al atom absorbs the helium nucleus and is converted into an unstable ^{30}P radionuclide ($T_{1/2} = 3$ min), which in turn is converted into a stable ^{30}Si atom following positron emission. Soon after the discovery of artificial radioactivity, physicists realized that charged protons with higher energies would be better projectiles for nuclear transformation reactions. During 1930s, charged-particle *accelerators* were developed to generate very high energy subatomic particles, such as protons, deuterons, and α particles.

For almost two decades following Rutherford's pioneering work, α particles from natural radioisotopes such as ^{238}U and ^{234}Th were used as projectiles to induce nuclear reactions. Following the discovery of neutrons by Chadwick in 1932, Fermi realized that a neutron beam could be used as a projectile to induce a nuclear reaction, because neutrons are neutral and not repelled by the stable target nucleus. He also realized that neutron rich atoms decay by beta emission and the daughter nuclide with an extra proton is normally an element with an atomic number, Z + 1. In 1934, Fermi bombarded ^{238}U with neutrons and reported the discovery

of element 93 (transuranic element not found in nature) (Segrè 1980), however, this turned out to be a false claim. In 1937, a colleague of Fermi, Emilio Segre bombarded the stable ^{98}Mo with neutrons (a reaction known as *neutron activation*) and produced the element 43, which he called technetium (meaning artificial).

$$^{98}_{42}\text{Mo} + {}^{1}_{0}n \rightarrow {}^{99}_{42}\text{Mo} \xrightarrow{\beta^-} {}^{99m}_{43}\text{Tc} \xrightarrow{IT} {}^{99}_{43}\text{Tc} \qquad (5.5)$$
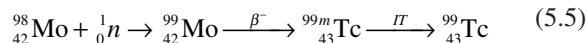
Otto Han and Lise Meitner continued the experimental strategy to produce transuranics by bombarding uranium with neutrons. However, in 1938 Han discovered that the nucleus of uranium isotope, ^{235}U undergoes fission, when struck by a neutron (Segrè 1980). More specifically, the ^{235}U nucleus absorbs the neutron to form a very highly unstable ^{236}U nucleus, which at once explodes to form two fission fragments (radionuclides) that are neutron rich and decay by beta emission.

Most of the naturally occurring radionuclides are either very long-lived isotopes of heavy elements. With the availability of neutrons and high energy charged particles, hundreds of nuclear reactions have been developed over the years to produce artificial radioisotopes that are either neutron rich or neutron deficient (proton rich). As discussed in the previous chapter, neutron rich radionuclides decay by β− or β−, γ emission, while neutron deficient radionuclides decay by β+ or electron capture. Both these decay modes may also involve emission of gamma photons. In addition, positron annihilation will also lead to the emission of high energy annihilation photons. Some of the early applications of radioisotopes in medicine involved naturally occurring radionuclides. It is the production of artificial radioisotopes, however, that eventually facilitated the development of nuclear medicine and molecular imaging technology.

5.1.1 Nuclear Reactions

In a nuclear reaction, when the atoms of a stable element (target) are bombarded by a subatomic particle (projectile), the nucleus of the stable atom absorbs the subatomic particle. The resultant *compound nucleus* is very unstable and excited. The compound nuclei have life times on the order of approximately 10^{-16} s. The compound nucleus may decay in one or more ways,

depending on its neutron/proton ratio and excitation energy. It may quickly decompose by emitting some radiation (subatomic particle and/or gamma radiation) to form an unstable product radionuclide.

The general equation for a nuclear reaction can be written as follows:

$$T(P, R)Y \qquad (5.6)$$

where T represents the target nuclide, P is the projectile, the incident or bombarding particle, R represents the radiation (subatomic particle or γ photons) emitted by the compound nucleus, and Y represents the unstable product radionuclide. The P and R in parenthesis, written as (P, R), represent the nuclear reaction. Reactions such as (p, n), (p, α), (d, α), (n, p), and (n, γ) are some of the common nuclear reactions used to produce artificial radioisotopes.

5.1.1.1 Excitation Energy and Q Value

The total amount of *excitation energy* (U) of the compound nucleus is given by the following equation (Finn and Schlyer 2002):

$$U = \frac{M_T}{M_T + M_P} T_P + S_P \qquad (5.7)$$

where,

   M_T = mass of the target nucleus
   M_P = mass of the incident particle or the projectile
   T_P = kinetic energy of the incident particle
   S_P = binding energy of the incident particle in the compound nucleus

In any nuclear reaction, the total kinetic energy of the products (radiation R and product nucleus Y) may be either greater or less than the total kinetic energy of the reactants (target T and projectile P). The *Q value* is the difference between the energy levels of the reactants and products. Q value can be calculated on the basis of the relationship $E = mc^2$ and by knowing the rest energies of all the particles involved.

$$Q = (M_T + M_P - M_R - M_Y)(c^2) \qquad (5.8)$$

If Q is a positive quantity, energy is given off in a nuclear reaction (*exoergic*). If Q is a negative quantity (*endoergic*), kinetic energy (KE) must be supplied to the reacting particles, so that the KE + $Q \geq 0$.

5.1.1.2 Activation Cross-Section

For any specific nuclear reaction, the probability that a bombarding particle will interact with, or activate the target nucleus employs the idea of *cross-section* (σ), which is expressed as an effective area (Beiser 1995). It is assumed that each target nucleus presents a certain area, called its cross section, to the incident particle. Therefore, the greater the cross section, the greater the likelihood of reaction. However, the activation cross section depends on the energy of the bombarding particle and the nature of the specific nuclear reaction. It is the effective "target area" presented by the target nucleus; the SI unit for nuclear cross section is m^2. The customary unit, however, is *barn*, where

$$1 \text{ barn} = 1\text{b} = 10^{-24} \text{ cm}^2 \text{ or } 10^{-28} \text{ m}^2 = 100 \text{ fm}^2 \quad (5.9)$$

$$1 \text{ millibarn (mb)} = 10^{-3} \text{ b or } 10^{-27} \text{ cm}^2 \text{ or } 10^{-31} \text{ m}^2 \quad (5.10)$$

The cross sections for most nuclear reactions depend on the energy of the incident particle. The nuclear cross sections for thermal neutrons (0.025 eV) with no charge are higher than those for charged particles. The positively charged bombarding particle must have kinetic energy sufficient to overcome the coulomb barrier and the negative Q value (kinetic energy of the products is less than that of the reactants). The higher the atomic number (Z) of the target atom, the higher the kinetic energy (E) of the charged particle needed for a higher nuclear cross section

(Schlyer 2003). A graphical relationship between σ and E for a specific nuclear reaction is known as *excitation function*. The excitation function for ^{18}F production is shown in Fig. 5.1 (Hess et al 2001), as an example.

5.1.1.3 Activity

The amount of radioactivity (dps) produced by irradiation of a target material with a charged particle beam can be described by the following equation (Finn and Schlyer 2002):

$$A(dps) = Inx\sigma(1 - e^{-\lambda t}) \quad (5.11)$$

In the above equation,

I is the beam current or the number of bombarding particles cm^{-2} s^{-1}

n is the number of target nuclei cm^{-3}

x is the thickness of a target in cm

σ is the nuclear cross section, expressed in cm^2 per nucleus

λ is the decay constant of the product radionuclide and

t is the time of irradiation in seconds

Saturation Yield

The amount of radioactivity (mCi) produced in a nuclear reaction is generally decay corrected to the end of bombardment (EOB). The saturation yield (mCi/μA)
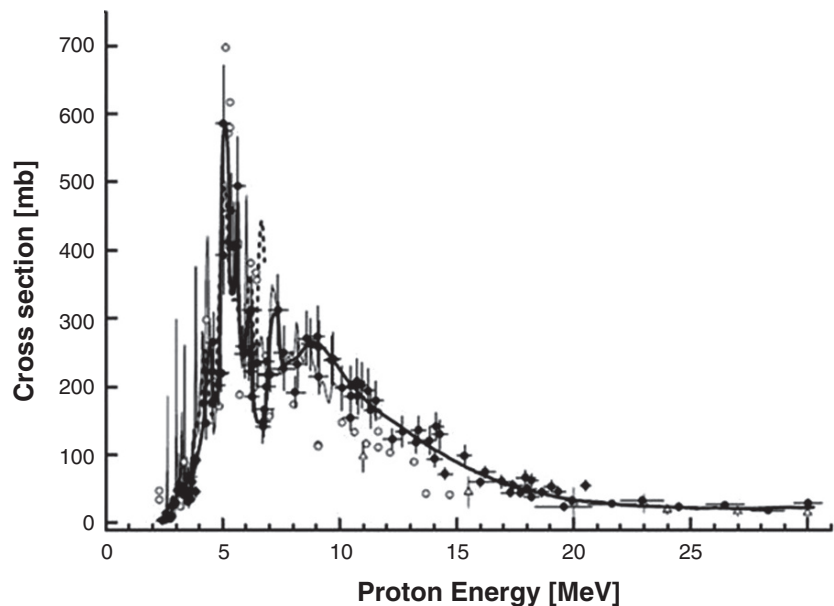
Fig. 5.1 Excitation function of the ^{18}O(p,n)^{18}F reaction. Results from several investigators were plotted with the *solid line* representing the data from the Julich group (Hess et al 2001)

is the theoretical maximum rate of production of a radioisotope for given beam energy conditions and can be calculated using the following equation:

$$\text{Saturation yield (mCi / } \mu A) = \frac{A_0}{I\,(1 - e^{\lambda t})} \qquad (5.12)$$

where, A_0 is the activity (mCi) at EOB, I is the beam current, and $1-e^{-\lambda t}$ is the saturation factor for the radioisotope.

The equation (5.11) is valid only for thin targets where the target beam is not attenuated. With thick targets (in which the energy of bombarding particle is completely absorbed), the particle beam is attenuated and the target nuclei are bombarded with particles of varying energies. Yields with thick targets, therefore, depend on the energy and stopping power (or specific energy loss) in MeV cm^2 g^{-1} of the bombarding particle.

Specific Activity (SA)

SA is generally, defined as the amount of radioactivity per unit mass of an element, molecule, or compound, which implies that the mass represents the combined mass of radioactive species and the nonradioactive (stable or cold) counterpart. The unit of SA can be expressed as mCi /mg^{-1}, Ci /mmol^{-1}, or GBq µmol^{-1}. When dealing with chemical or molecular reactions, the standard way to express SA is mCi µmol^{-1}. Because 1 mole represents 6.02×10^{23} atoms or molecules (Avogadro's number), one µmol consists of 6.02×10^{17} atoms or molecules.

For example, when ^{11}C radionuclide is produced in a cyclotron as $[^{11}C]CO_2$ gas, ^{11}C carbon atoms are always contaminated with natural carbon (^{12}C) and it is very difficult to obtain pure $[^{11}C]CO_2$ only. Therefore, if the SA of $[^{11}C]CO_2$ produced in a cyclotron target is 1.0 Ci µmol^{-1}, it implies that 1.0 Ci of radioactivity is present in a total mass of 1 µmole of carbon dioxide gas or a total of 6.02×10^{17} molecules (3.4×10^{14} molecules are present as $[^{11}C]CO_2$). That means, for every molecule of $[^{11}C]CO_2$, there are about 1,700 molecules of cold, nonradioactive CO_2. The theoretical maximum SA (Table 4.3) is never really achieved in routine production of positron-emitting radionuclides. However, the SA concept is very important in dealing with PET radiopharmaceuticals, especially in the preparation of radiolabeled receptor binding radiopharmaceuticals.

Carrier-Free

Carrier-free means that the radioactive species is not contaminated with nonradioactive counterpart, known as *carrier*. In the production of radionuclides in a cyclotron, the target element is converted into a different element (with a higher atomic number). As a result, cyclotron produced radionuclides are supposed to be *carrier-free* (CF). In reality, however, it is very difficult to eliminate the contamination of natural carbon, fluorine, or trace metals during the synthesis procedure. A more appropriate concept is *no carrier added* (NCA), because the carrier, a stable, nonradioactive species, is not intentionally added. To facilitate chemical and biochemical reactions, a carrier may be added intentionally during radioisotope production. Such preparations should specifically be reported as *carrier added* (CA).

5.2　Production of Radionuclides

5.2.1　Linear Accelerator

In 1928, two physicists, John Cockcroft and Ernest Walton, working at the Cavendish laboratory in Cambridge, developed an electrostatic *linear accelerator*, based on a voltage multiplying circuit, to accelerate protons along a linear path in order to achieve higher energies (Beiser 1995). The device (Fig. 5.2) consists of a series of tubes connected to a high voltage power supply, which can provide alternating polarities to the tubes. At first, the odd-numbered tubes in the accelerator (1, 3, 5,..) are negatively charged and the even-numbered tubes are positively charged to attract the protons from the H$^+$ ion source. As the protons enter and pass through tube 1, the polarities of the tubes are reversed. As tube 1 is now positive and tube 2 is negative, protons are attracted to tube 2. This process continues through many tubes, until the velocity and energy of the protons increase. The first disintegration of lithium into α particles by artificially accelerated protons was achieved by Cockcroft and Walton in 1932, using a proton beam with 0.77 MeV of energy (Segrè 1980). Following absorption of the proton, the element Li was converted into ^8Be nucleus, which quickly split into two He nuclei.
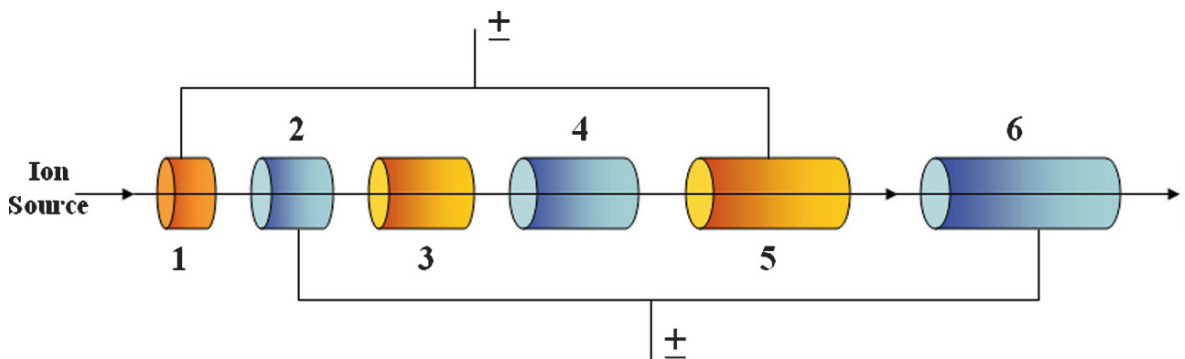
Fig. 5.2 An electrostatic linear accelerator based on a voltage multiplying circuit designed to accelerate protons along a linear path to achieve higher energies

$$\mathrm{^{7}_{3}Li + ^{1}_{1}H \rightarrow ^{8}_{4}Be \rightarrow 2\,^{4}_{2}He} \qquad (5.13)$$
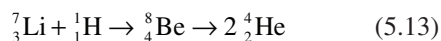
It soon became apparent that protons with higher energies were needed to penetrate the repulsive coulomb forces of the nucleus for the production of nuclear transformations involving higher Z elements. More specifically, based on the principle of linear acceleration, very high voltage (millions of volts) is necessary to increase the kinetic energy of charged particles.

5.2.2 Cyclotron

Ernest O. Lawrence, an American physicist and inventor, conceived the idea of a cyclic accelerator or *cyclotron*, in 1929. In the presence of a magnetic field, an ion of specific charge, when introduced at the center of a cyclotron, will accelerate in an expanding spiral path by use of an alternating electric field (Lawrence and Livingston 1931). The first cyclotron built by Lawrence had a diameter of a few inches and the glass vacuum chamber in which ions were supposed to circulate, could be held in one hand (Fig. 5.3). By 1932, the production of several radioisotopes using a 27-in.-diameter cyclotron was reported by Lawrence and his colleagues.

The most widely used particle accelerator is the *medical cyclotron*, which is capable of accelerating protons to low and medium energy levels (10–20 MeV) needed for the production of PET radionuclides (Ruth 2003). Certain cyclotrons have a deuteron beam capability also. The commercial cyclotrons with higher energy proton beams (>30 MeV) are needed to produce proton rich radionuclides that decay by electron capture.
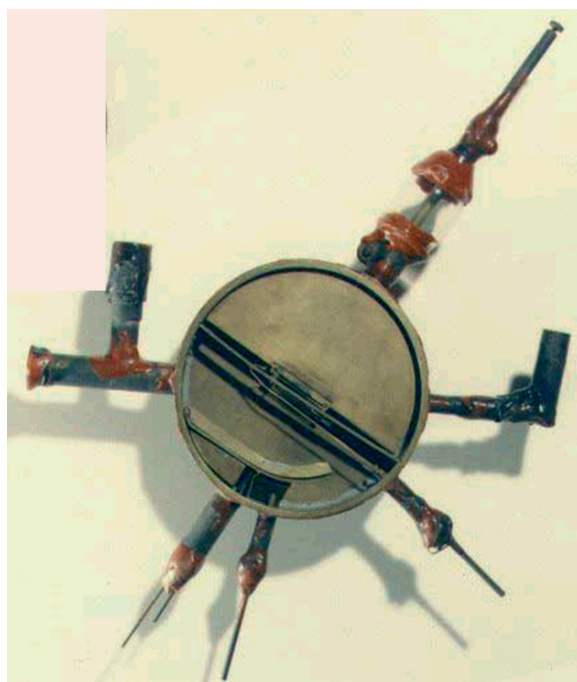
Fig. 5.3 The first working model of a 4.5 in. cyclotron, which accelerated protons to 80 KeV energy (Lawrence and Livingston 1931)

The technical features of several medical cyclotrons are summarized in Table 5.1.

5.2.2.1 Negative Ion cyclotron

Traditionally, cyclotrons were designed to accelerate positive ions (H^+ and $^2H^+$). The first cyclotron designed to accelerate negative ions, or hydrogen, or deuterium

Table 5.1 Cyclotrons for the production of positron-emitting radionuclides

		Particle beam			Number of targets
		Type	Energy MeV	Current μA	
CTI[a]	RDS-111	H^+	11	50	4
CTI[a]	RDS-112	H^+	11	50	2×8^b
IBA	Cyclone 10/5	$H^+/^2H^+$	10/5	60/35	8
IBA	Cyclone 18/9	$H^+/^2H^+$	18/9	80/35	8
GE[a]	MINItrace	H^+	9.6	50	4
GE	PETtrace	$H^+/^2H^+$	16.5/8.5	75/60	6
EBCO	TR 13/19	$H^+/^2H^+$	13, 19/9	150	2×4^c

[a]Self shielding for cyclotrons is standard
[b]Two beam ports, each with a eight target carousel
[c]Two beam ports, each with a four target carousel

atoms with two electrons in the *K*-shell (H^- and $^2H^-$), was built in 1966. Since the 1980s, all the commercial and medical cyclotrons are basically negative ion cyclotrons. One of most important advantages of the negative ion cyclotron is the elimination of a complex *beam extraction system*. As a result, negative ion cyclotrons provide the opportunity to extract beams with different energies thereby allowing for the simultaneous bombardment of two different targets (Satyamurthy 1999).

The cyclotron (Fig. 5.4) consists of three major components: an electromagnet with a field strength of 1.5–2.0 tesla, a pair of semicircular hollow copper electrodes, called *dees* located between the poles of the magnet, and an ion source (Penning ion gauge)
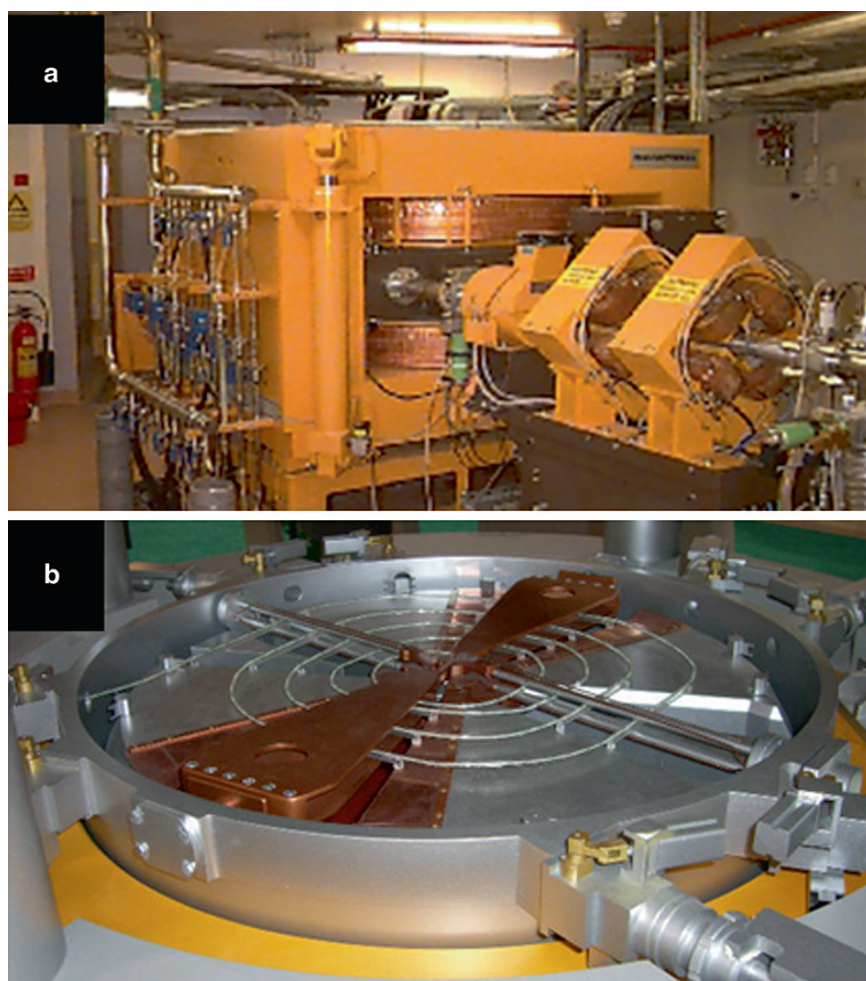
Fig. 5.4 A negative ion cyclotron (EBCO-TR19) with an external beam line (**a**). A model of the vacuum chamber (CTI systems) showing the copper electrodes (dees) in which a negatively charged proton beam making circular orbits (**b**)

capable of generating high intensity negative ions. The entire structure of the cyclotron is kept under high vacuum (up to 10^{-7} torr). Following ionization of the hydrogen gas in an ion source, the ions (protons or deuterons) are injected into the center of the gap between the dees. When a 20–30 MHz radiofrequency alternating potential of 30–100 kV, generated with an oscillator, is applied to the dees, the negative ions will accelerate towards a dee that is at a positive potential. Because the magnetic field is perpendicular to the plane of the dees and particle motion, the negative ions will trace a circular path. Further, because the electrical potential on the dees is alternatively positive and negative, the ions will gain energy at each crossing of the gap between the dees, as they move outward in a spiral path from the center. Lawrence (Lawrence and Livingston 1931) described the basic operational equations as follows:

The magnetic force operating on the ion is a centripetal force (Bev), which is exactly balanced by the centrifugal effect (mv^2/r).

$$Bev = \frac{mv^2}{r} \; and \; r = \frac{mv}{Be} \qquad (5.14)$$

In the above equations, B is the magnetic field strength while m, e, and v represent the mass, charge and velocity of the ion, respectively. Finally, r represents the radius of the ion's orbit. For a given cyclotron, the maximum kinetic energy that an ion can attain can be estimated if B and r are kept constant.

$$E = \frac{B^2 \, r^2}{2} \left(\frac{e^2}{m} \right) \qquad (5.15)$$

Beam Extraction

Once the desired kinetic energy of the accelerating particles is achieved, the positively charges ions (H^+ and $2H^+$) are extracted from the cyclotron by passing the negative ion beam through an ultra thin foil of carbon (graphite), which strips the electrons. The positively charged beam will rotate in an opposite direction, which can then be directed to bombard an appropriate target for the production of a positron-emitting radioisotope. The typical intensities (beam currents) and the energies of proton and deuteron beams generated in commercial cyclotrons are shown in Table 6. The beam current is generally expressed in units of microampere (μA). For example, a 1 μA proton beam current is equal to 6.25×10^{12} protons or deuterons/s.

5.2.3 Production of Positron-Emitters

The most important nuclear reactions used in the production of positron emitting radionuclides are summarized in Table 5.2 The target designed for the production of a positron-emitter consists of a target body suitable for the bombardment of a specific target material (gas, liquid, or solid) that undergoes nuclear transformation. Typical gas targets are made up of aluminum, while the liquid targets are made up of aluminum, silver, and titanium. A generic cyclotron target (Fig. 5.5) consists of a sealed metal tube with a window of thin metal foil at one end to allow the particle beam to pass through and irradiate the target material. In order to dissipate the excess heat generated during irradiation, the target

Table 5.2 Nuclear reactions for the production of positron emitting radionuclides

Radio isotope	Nuclear reaction	Target Body	Material	mL	Yield mCi/μA	Product chemical
^{18}F	^{18}O (p,n) ^{18}F	Ag, Ti	$[^{18}O]H_2O$	0.3–3.0	110	^{18}F$^-$
^{18}F	^{20}Ne $(d,\alpha)^{18}$F	Al, Ni	Ne gas + 0.1–0.2% F_2 gas		51	^{18}F$_2$
^{11}C	^{14}N (p,α) ^{11}C	Al	N_2 gas + <1% O_2 gas		40	^{11}CO$_2$
^{13}N	^{16}O (p,α) ^{13}N	Al	H_2O		7	^{13}NH$_4^+$
^{15}O	^{14}N $(d,n)^{15}$O	Al	N_2 gas		50	
^{15}O	^{15}N $(p,n)^{15}$O	Al	N_2 gas		47	
^{64}Cu	^{64}Ni $(p,n)^{64}$Cu		Ni metal		73	
^{124}I	^{124}Te$(d,2n)^{124}$I		AL oxide and Te oxide solid solution matrix		73	^{124}I as iodide
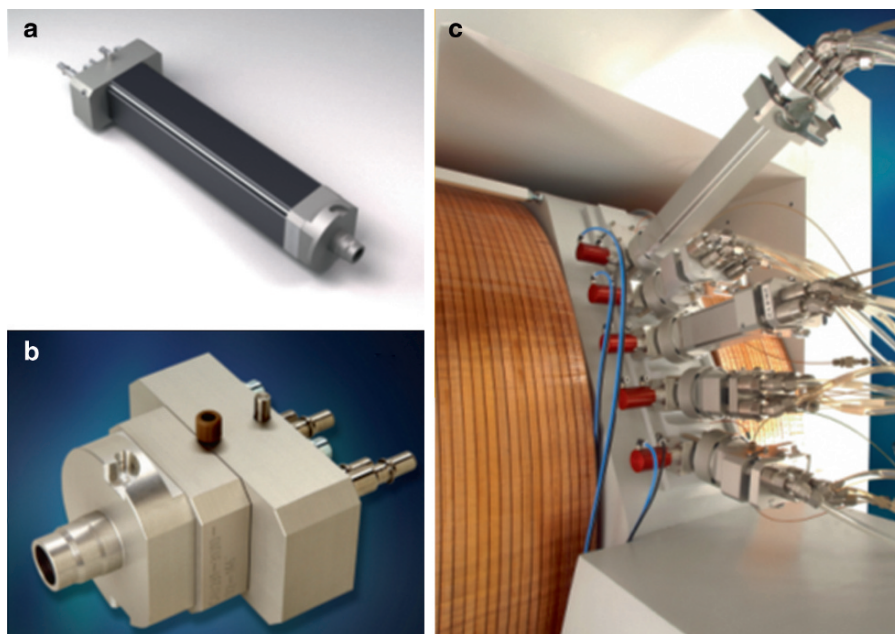
Fig. 5.5 ^{14}N gas target chamber (**a**) for the production of ^{11}C as carbon dioxide and an ^{18}O water target chamber (**b**) for the production of ^{18}F as fluoride. Placement of these targets in the PETtrace (GE) cyclotron (**c**)

body is generally surrounded by a cooling water jacket, while helium gas is circulated through the foils separating the target material and the vacuum isolation foil through which the beam enters the target.

5.2.3.1 Positron-Emitting Halogens

Among halogens, ^{18}F is the most important radionuclide for PET. The other halogens, ^{75}Br and ^{124}I may have potential clinical utility and can also be made using medical cyclotrons.

Production of ^{18}F

Basically, there are two kinds of targets used to produce two different chemical forms of fluorine. A liquid target for the production of ^{18}F as nucleophilic fluoride ion (^{18}F$^-$) and a gas target for the production of ^{18}F as electrophilic fluorine as [^{18}F]F$_2$ gas (Ruth and Wolf 1979; Casella et al 1980)

The most common nuclear reaction used to produce ^{18}F as fluoride ion is on the basis of proton bombardment of ^{18}O atoms using highly enriched [^{18}O] water as

the target material (Ruth and Wolf 1979; Schlyer 2003). A typical target body is made of aluminum to hold 0.3–3.0 mL of target water. Several curies of ^{18}F can easily be made in 1–2 h using 10–19 MeV protons with 20–35 µA beam current. While the theoretical SA of ^{18}F is 1,700 Ci/µmol^{-1}, the NCA ^{18}F is generally produced with a SA of <10 Ci/µmol^{-1}.

The most common nuclear reaction to produce [^{18}F] fluorine gas is on the basis of deuteron bombardment of ^{20}Ne atoms using natural neon gas (Schlyer 2003). A passivated nickel target (NiF) is loaded with neon gas containing 0.1% of natural fluorine gas. Following bombardment for 1–2 h with 8–9 MeV deuterons, <1.0 Ci of [^{18}F]F$_2$ is generated with a very low SA of (10–20 mCi/µmol^{-1}). A "double shoot" method was developed to produce [^{18}F]fluorine gas on the basis of proton bombardment of ^{18}O atoms using [^{18}O]oxygen gas loaded into a gas target (Nickels et al 1983). After irradiation, ^{18}F species stick to the walls of the target. The ^{18}O target gas is removed from the target, which is then loaded with argon gas mixed with 1% of cold fluorine gas. A second short irradiation for <10 min will generate [^{18}F]F$_2$ gas. This method is very useful to make electrophilic ^{18}F, using cyclotrons generating proton beams only. Since [^{18}F]F$_2$ is always diluted with

carrier (cold) fluorine gas, the SA of electrophilic [^{18}F] fluorine is very low and not optimal for synthesizing high SA ^{18}F labeled radiopharmaceuticals.

Production of ^{75}Br and ^{76}Br

Both these radionuclides are generally made by proton (17 MeV) bombardment of ^{76}Se atoms using [^{76}Se]selenium enriched (96%) Cu_2Se as the target material (Schlyer 2003). Subsequently, ^{76}Br is separated from the solid target by thermal diffusion. The longer half-life (16.2 h) of ^{76}Br is favorable for the synthesis of radiopharmaceuticals, and commercialization. However, ^{76}Br has a complex decay scheme and high energy positrons which may provide an unfavorable radiation dose to the patient.

^{75}Br with a shorter half-life (97 min) may be more optimal for developing PET radiopharmaceuticals. One of the common nuclear reactions is ^{76}Se(p,2n)^{75}Br, but the energy of proton needed for this reaction is between 18–28 MeV. ^{75}Br is separated from a solid target by dry distillation method and trapped using platinum wool.

Production of ^{124}I

A method using the proton bombardment of enriched ^{124}Te atoms using low energy protons (15 MeV), has been recently developed (Scholten et al 1995; Sheh et al 2000). The solid target material consists of a solid solution matrix containing aluminum oxide and enriched ^{124}Te oxide. [^{124}I]iodide is recovered from the target using dry distillation. The volatile radioiodine is trapped on a thin pyrex glass tube that is coated with a small amount of sodium hydroxide.

Because, radioiodination of proteins and peptides is relatively easy, ^{124}I has significant potential for the development of radiopharmaceuticals for PET. However, the longer half-life and complicated decay schemes with a number of high energy positrons may make this radionuclide suboptimal, as the radiation dose to the patient can be relatively high.

5.2.3.2 Organic Positron-Emitters

The greatest advantage of PET is the potential to image and study biochemical processes in vivo, without altering or affecting the homeostasis in any way. Low atomic number elements such as carbon, nitrogen, oxygen, and phosphorous are naturally stable. The development of cyclotrons in the 1930s created an opportunity to produce positron emitting radioisotopes of carbon (^{11}C), nitrogen (^{13}N), and oxygen (^{15}O). Since the 1950s, radioisotopes of organic interest have played a significant role in the development of biochemistry and pharmacology. Because, the half-lives of these radionuclides are relatively short, they have not been exploited to their full potential to develop radiopharmaceuticals for routine clinical PET imaging studies. However, with the availability of several hundred commercial medical cyclotrons, PET radiopharmaceuticals for routine clinical use have been developed by incorporating the organic positron-emitters.

Production of ^{11}C

The most common nuclear reaction used to produce ^{11}C is the proton bombardment of ^{14}N atoms by using natural nitrogen as the target gas (Casella et al 1978; Bida et al 1980; Schlyer 2003). Because nitrogen gas is relatively inert, it does not interfere with the carbon chemistry and can be easily eliminated. By mixing trace amounts (<1%) of oxygen or hydrogen with the target nitrogen gas, the chemical forms of ^{11}C produced in the target can be either [^{11}C]CO_2 or [^{11}C]CH_4 (methane). The gas target body is basically made up of an aluminum cylinder (or cone shape) that should be able to handle gas (10–100 cc) at pressures of 300–800 psi. Beam currents of 20–40 µA are typically used. It is very important to prepare or polish the inside of the aluminum target in order to significantly reduce the contamination of natural carbon. As the natural nitrogen gas is also contaminated with CO_2 gas, it is essential to use extremely high purity (99.99999%) target gases. [^{11}C] CO_2 can be produced in most cyclotron targets with a SA of 5–20 Ci/µmol^{-1} at EOB. Even higher SA can be achieved by producing [^{11}C]CH_4 directly in the target.

Production of ^{13}N

The first production of ^{13}N was based on bombarding boron atoms with α particles (Joliot and Curie 1934). The most common nuclear reaction for the production of ^{13}N is the proton (10–15 MeV) bombardment of

natural, stable ^{16}O atoms, using oxygen gas target or liquid (water) target (Tilbury and Dahl 1979; Berridge and Landmeier 1993; Schlyer 2003). When ^{13}N is produced in the target, it reacts with water forming nitrate and nitrite ions. The addition of a reducing agent, such as titanium chloride, to the target water will generate $[^{13}N]NH_3$. With a pressurized target, aqueous ethanol can be used in the target since ethanol acts as a hydroxyl free radical scavenger to improve the production of $[^{11}N]NH_3$.

Because the half-life of ^{13}N is very short (9.98 min), it is very difficult to synthesize ^{13}N labeled radiotracers for routine clinical PET studies. In the 1970s, $[^{13}N]$ Ammonia (NH_3 or NH_4^+ ion) has been shown to be clinically useful as a myocardial perfusion imaging agent. Therefore, the production of ^{13}N involves the generation of $[^{13}N]NH_3$ gas directly in the target itself.

Production of ^{15}O

^{15}O was one of the first artificial radioisotopes produced by low-energy deuterons using a cyclotron (Livingston and McMillian 1934). In order to use low energy protons (10–11 MeV), the target must be highly enriched ^{15}N gas (Vera-Ruiz and Wolf 1977; Schlyer 2003). However, the most common nuclear reaction used for the production of ^{15}O as $[^{15}O]O_2$ gas is deuteron bombardment of ^{14}N atoms using natural nitrogen containing 0.2–0.5% oxygen as the target gas. The target body is generally made of aluminum. To produce ^{15}O as $[^{15}O]$ CO_2, the target nitrogen gas is mixed with 2–2.5% carbon dioxide. To produce $[^{15}O]$water, outside the target, a stream of nitrogen gas continuously flows through the target to a hot cell containing a water synthesis module, in which ^{15}O combines with H_2 gas in the presence of palladium–aluminum catalyst at high temperatures (300–400°C) to produce water.

5.2.3.3   Positron-Emitting Metals (^{66}Ga, ^{86}Y and ^{64}Cu)

A number of positron emitting radionuclides, belonging to the Group III elements (Ga, In and Y), can be made in many of the medical cyclotrons. In addition, several radionuclide generator systems are available, yielding positron-emitting daughter radiometals of significant clinical interest.

For example, ^{66}Ga which is a medium half-life radionuclide, emitting very high energy (4.1 MeV) positrons and it can be produced via the $^{66}Zn(p,n)^{66}Ga$ nuclear reaction (Schlyer 2003). Subsequently, ^{66}Ga can be easily separated from zinc by cation exchange or solvent extraction techniques.

^{86}Y is also a medium half-life radionuclide emitting high energy (3.15 MeV) positrons. It can be produced via the $^{86}Sr(p,n)^{86}Y$ nuclear reaction using isotopically enriched ^{86}Sr foil or strontium carbonate pellet. Subsequently, ^{86}Y can be separated by dissolving the target in an acidic solution, followed by precipitation and purification by ion exchange chromatography.

Copper has several positron emitting radioisotopes, such as ^{61}Cu, ^{62}Cu, and ^{64}Cu. Because of its longer half-life of 12.7 h and low energy positrons, ^{64}Cu is more appropriate for developing commercial PET radiopharmaceuticals. It can be produced via the $^{64}Ni(p,n)^{64}Cu$ nuclear reaction using enriched nickel solid target foils (Schlyer 2003). Subsequently, ^{64}Cu is separated by dissolving the target in an acidic solution, followed by ion exchange chromatography. Using similar techniques, ^{61}Cu can also be produced via the $^{61}Ni(p,n)^{61}Cu$ nuclear reaction, using enriched nickel solid target foils.

5.2.3.4   SPECT Radionuclides (^{67}Ga, ^{111}In and ^{123}I)

^{67}Ga can be produced by several nuclear reactions using commercial cyclotrons. The most common reactions are $^{68}Zn(p,2n)^{67}Ga$ and $^{66}Zn(d,n)^{67}Ga$. Following irradiation, the zinc target is dissolved in concentrated HCl (7 N) and ^{67}Ga is extracted into an organic phase using isopropyl ether. Following evaporation of the organic phase, ^{67}Ga is formulated as chloride using dilute HCl (0.1 N). The typical SA of ^{67}Ga is around 1,000 mCi mg^{-1} (67 mCi µmol^{-1}) and radionuclidic purity is about 99.4%.

^{111}In can be produced by proton bombardment of cadmium using either $^{111}Cd(p,n)^{111}In$ reaction or $^{112}Cd(p, 2n)^{111}In$ reaction. Following irradiation, the cadmium target is dissolved in mineral acid and the acidity is kept at 1 N using HCl.

^{111}In is separated from the target using anion exchange resin and HCl (1 N). The high SA, no-carrier added ^{111}In has a radionuclidic purity of ≥99.9%.

^{123}I can be produced directly in a cyclotron using $^{124}Te(p,2n)$ reaction. The most common methods, however use indirect methods based on the following nuclear reactions:

$$^{127}\text{I}(p,5n)^{123}\text{Xe} \rightarrow ^{123}\text{I}$$

$$^{124}\text{Xe}(p,2n)^{123}\text{Cs} \rightarrow ^{123}\text{Xe} \rightarrow ^{123}\text{I}$$

$$^{124}\text{Xe}(p,pn)^{123}\text{Xe} \rightarrow ^{123}\text{I}$$
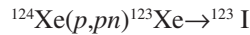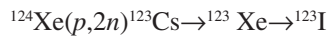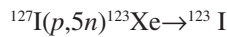
The high SA, NCA ^{123}I is supplied as sodium iodide in a 0.1 N NaOH solution with a radionuclidic purity >99.8%.

5.2.3.5   Nuclear Reactor

Shortly after the discovery of nuclear fission, scientists realized that, because fission leads to the release of additional neutrons, in a given mass of uranium fuel, known as the critical mass, a self-sustaining sequence of additional fissions can lead to a *chain reaction*, induced by at least one fission neutron. Such a reaction, in which the *multiplication factor* (MF) is ≥1, is called a *critical* reaction. However, if too few neutrons cause fissions, the reaction is *subcritical* (MF <1) and will stop. If the frequency of fissions increases at a faster rate (MF >1), the "runaway" reaction can be *supercritical* and may lead to a nuclear explosion. In 1942, Fermi was able to demonstrate that by carefully controlling the availability of neutrons, a sustained chain reaction (MF = 1) can be maintained. The *nuclear reactor* operates on the basis of this principle of controlled chain reaction.

Compared to ^{238}U, the cross section for induced fission reaction with slow or *thermal neutrons* (0.25 eV) is much higher for ^{235}U. Because the natural uranium contains only 0.7% of ^{235}U isotope, *enriched uranium* containing >3% of ^{235}U, is typically used as the fuel in a reactor core. In a nuclear reactor, the fuel cells containing enriched uranium (as UF_6 or UO_2) pellets are surrounded by a *moderator*, graphite or heavy water, to slow down the energetic fission neutrons. *Control rods* (cadmium and boron) capable of absorbing neutrons, but not undergoing any nuclear reaction, are used to sustain the chain reaction. In addition to ^{235}U, several other nuclides such as ^{232}Th, ^{233}U, ^{237}Np, and ^{239}Pu can all be used as fuel for nuclear reactors. Following the absorption of a neutron, the natural ^{238}U decays by emitting a beta particle to become ^{239}Np, which in turn emits a beta particle to become ^{239}Pu. These reactions are the basis of a *breeder reactor*, in which uranium produces more fuel in the form of ^{239}Pu.

5.2.3.6   Reactor Produced Radionuclides

When the reactor is in operation, the nuclear reaction *(n, f)* produces a number of neutron rich fission fragments (Z = 28–65), which decay by β⁻ or β⁻, γ emission. Radionuclides, such as ^{99}Mo, ^{131}I, and ^{137}Cs, accumulate in the fuel rods to produce enormous activity (thousands of GBq). All the fission fragments can be chemically separated and purified to yield no carrier added, high SA radionuclides.

Neutron Activation

A nuclear reaction in which a neutron is captured or absorbed by the nucleus of a stable atom, leading to a nuclear transformation, is called *neutron activation*. The most common nuclear reactions are *(n, γ) (n, p)*, *(n, 2n)*, and *(n, α)*, in which the atomic mass or atomic number of the target nucleus may change.

The neutrons released during the fission reaction have a wide range of energies, from a few KeV to 10 MeV. The average energy is approximately 2 MeV, which decreases substantially as a result of collisions with other atoms in the core and the moderator. The average energy of thermal neutrons at room temperature is about 0.038 eV. Neutrons between 0.01 and 0.1 MeV are known as slow or resonance neutrons, while neutrons with >0.1 MeV are known as fast neutrons. In general, the cross section (σ) for thermal neutrons in neutron activation reactions is very high, compared to that of higher energy neutrons.

In a $(n, γ)$ reaction, the target nucleus with a mass number A captures a neutron to become an unstable, excited radioisotope of the target nucleus, with a mass number A + 1. The excited nucleus immediately emits a gamma photon and the product radionuclide will eventually decay by beta emission to reach a ground state. Because the product nuclide is an isotope of the target element, the product can not be separated and purified to avoid the contamination of the carrier. As a result, radioisotopes produced using $(n, γ)$ reaction are generally very low in SA.

$$^{98}_{42}\text{Mo}\,(n, \gamma)\,^{99}_{42}\text{Mo}$$
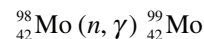
It is possible to produce carrier-free, high SA nuclides in a reactor. Certain $(n, \ \gamma)$ reactions produce a short-lived radioisotope of the target element, which decays

by beta emission to another unstable radioactive nuclide with longer half-life compared to that of the intermediate. ^{131}I can be produced by neutron activation of enriched ^{130}Te isotope.

$$^{130}_{52}Te\,(n,\,\gamma)\;^{131}_{52}Te\left(T_{1/2}=25\,\text{min}\right)\xrightarrow{\;\beta^-\;}$$
$$^{131}_{53}I\;\left(T_{1/2}=8.04\text{ days}\right)$$
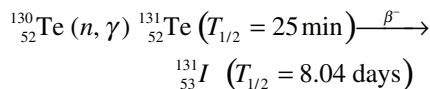
In a $(n,\,p)$ reaction, the target and the product are two different elements. As a result, it is very easy to separate the product from the target, chemically.

$$^{67}_{30}Zn\,(n,\,p)\;^{67}_{29}Cu$$
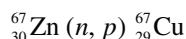
There are several examples of the reactor production of neutron deficient radionuclides that decay by β^+ emission or EC. However, these methods are not necessarily practical for routine production for clinical utility.

5.3 Radionuclide Generators

As discussed in Chap. 4, a parent–daughter radionuclide pair may exist either in a transient or in a secular equilibrium, when the parent is a longer lived radionuclide than the daughter. The parent radionuclide can be made in a reactor or in a cyclotron. If the parent and daughter nuclides are two different elements, they can be separated chemically, and the radioactivity of the daughter can be of high SA. Such a parent–daughter (mother–daughter) radionuclide pair is ideal to build a generator system to produce the daughter radionuclide, when needed (Qaim 1987; Welch and McCarthy 2000). The *radionuclide generator* is a device used to separate the daughter radionuclide from the parent radionuclide. Various types of physicochemical separation methods, such as distillation or liquid/liquid extraction may be used. A chromatographic method based on an inorganic or resin adsorbent material, however, is the most practical method for routine clinical utility. Four important generator systems (Table 5.3) are available to produce radionuclides of clinical interest.

5.3.1 ^{99m}Tc generator

The ^{99m}Tc generator was first developed in 1960s at the Brookhaven National Laboratories in New York (Richards 1965). As discussed earlier, ^{99}Mo is one of the fission products of ^{235}U fission and is known as "fission moly", and is produced in very high SA compared to ^{99}Mo which is produced by neutron activation. Most commercial generators are made with fission produced ^{99}Mo. The generator is made on the basis of a solid column method, in which 5–10 g of preheated alumina (Al_2O_3) is loaded in a plastic or glass column. The ^{99}Mo activity (2–32 Ci) in the form of molybdate ion MoO_H^2 is adsorbed on the column. The column is thoroughly washed to remove undesirable contaminants. The amount of ^{99}Mo activity on the column along with the date and time of calibration, for each generator, is provided. Commercial generators are sterilized and well shielded with lead or depleted uranium.

After the generator has been washed and calibrated, at time T_0, there is no ^{99m}Tc activity on the column. As $^{99}Mo(T_{1/2}=66\,h)$ decays, ^{99m}Tc activity ($T_{1/2}=6\,h$) is produced and builds up in the column as a function of time, as shown in Fig. 5.6. Unlike molybdenum, technetium does not bind to alumina, but is immediately converted into ^{99m}Tc-pertechnetate ion ($^{99m}TcO4^-$), which is the most stable chemical form of technetium with an oxidation state of +7. Typically, >75% of ^{99m}Tc-activity can be eluted with 3–10 mL of physiological saline solution. The equations to estimate the amount of ^{99m}Tc activity in a generator have been previously shown (equations (4.21) and (4.23)).

Small amounts of ^{99}Mo activity may occasionally *breakthrough* (leakage or partial elution) the column into the ^{99m}Tc-pertechnetate solution. The maximum ^{99}Mo contamination allowed is 0.15 µCi/mCi^{-1} or 0.15 KBq MBq^{-1} of ^{99m}Tc-pertechnetate solution at the time of elution. Each ^{99m}Tc dose to a patient, however, should not contain >5 µCi of ^{99}Mo activity. As a chemical impurity, Al ion concentration should be <10–20 µg mL^{-1} of eluant.

Table 5.3 Radionuclide generators

Parent				Daughter			Generator	
Nuclide	$T_{1/2}$	Decay	NR	Nuclide	$T_{1/2}$	Decay	Column	Eluent
^{99}Mo	66 h	β^-	^{235}U fission	^{99m}Tc	6 h	IT	Al_2O_3	0.9% Saline
^{82}Sr	2.5 days	EC	$^{85}Rb(p,\,4n)^{82}Sr$	^{82}Rb	75 s	β^+	SnO_2	0.9% Saline
^{68}Ge	271 days	EC	$^{69}Ga(p,\,2n)^{68}Ge$	^{68}Ga	68 min	β^+	TiO_2	1N HCl
^{62}Zn	9.3 h	EC, β^+	$^{63}Cu(p,\,2n)^{62}Zn$	^{62}Cu	9.7 min	β^+	Dowex	2N HCl
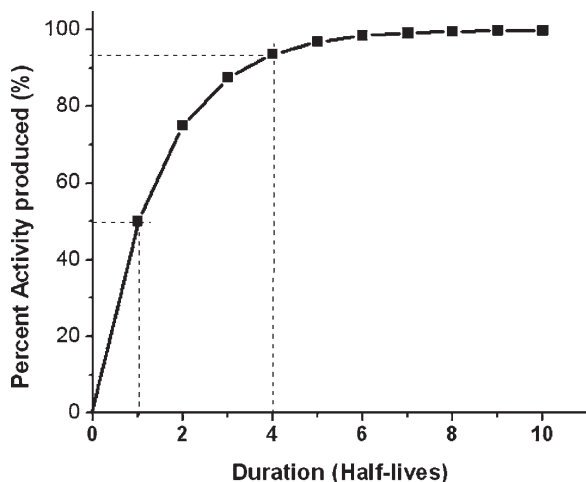
Fig. 5.6 The build-up of ^{99m}Tc activity in a generator as a function of time (half-life): 50% of the expected maximum yield can be produced following irradiation of the target for a minimum of one half-life of the radionuclide

Both, ^{99}Mo (13%) and ^{99m}Tc decay producing the long lived ^{99}Tc, which in turn decays slowly by beta emission, to the stable ^{99}Ru. Since ^{99m}Tc and ^{99}Tc are isomers and chemically the same element, ^{99}Tc may act as a carrier in the preparation of ^{99m}Tc radiotracers. If the generator is eluted once a day (every 24 h), the number of ^{99m}Tc atoms is 27% of the total Tc atoms. If the generator is eluted after 4 days, for example, the number of ^{99m}Tc atoms is only 5% of the total Tc atoms.

5.3.2 ^{82}Rb Generator (Cardiogen®)

^{82}Rb chloride was the first PET radiopharmaceutical approved by the FDA in 1989 for assessment of regional myocardial perfusion. Cardiogen® is manufactured and supplied by Bracco Diagnostics. The parent ^{82}Sr ($T_{1/2}$ = 25.6 days) is a neutron deficient radionuclide that decays by electron capture and is produced using a high energy cyclotron (Thomas 1987). ^{82}Sr (90–150 mCi) is loaded on a stannic oxide column and the daughter ^{82}Rb ($T_{1/2}$ = 75 s) is eluted from the column with a sterile saline solution using an infusion pump calibrated to administer a specific unit dose to a patient.

5.3.3 ^{62}Cu Generator

Several ^{62}Cu radiotracers are under development and clinical evaluation for assessing perfusion and hypoxia. ^{62}Zn ($T_{1/2}$ = 9.13 h) is a neutron deficient radionuclide produced by the proton irradiation of a copper disc or copper electroplated alloy on the basis of the nuclear reaction ^{63}Cu($p,2n$)^{62}Zn using 26-21 MeV protons (Finn and Schlyer 2002). ^{62}Zn is separated from the target copper using an anion-exchange column. Subsequently, an acidic solution of ^{62}Zn can be loaded onto an anion-exchange column and the daughter ^{62}Cu ($T_{1/2}$ = 9.76 min) can be eluted from the generator for the preparation of radiotracers (Robinson 1980; Haynes et al 2000; Fukumura 2006).

5.3.4 ^{68}Ga Generator

In many PET facilities, ^{68}Ga is routinely used for transmission scans (for attenuation correction of PET data) using a ^{68}Ge rod source (5–10 mCi). The parent, ^{68}Ge is a long lived ($T_{1/2}$ = 278 days) neutron deficient radionuclide, generally produced by a high energy cyclotron based on spallation reaction (Finn and Schlyer 2002). The ^{68}Ga generator was developed, in 1960s for brain imaging studies (Yano and Anger 1964) and, subsequently, improved (Schuhmacher et al 1981). Recent modifications involve loading ^{68}Ge onto a tin oxide column and the daughter, ^{68}Ga is eluted as chloride using dilute hydrochloric acid solution (Zhernosekov et al 2007).

References

Beiser A (1995) Concepts of modern physics. 5th edn, McGraw-Hill, New York

Berridge MS, Landmeier BJ (1993) In target production of [^{13}N] ammonia; target design, production and operating parameters. Appl Radiat Isot 44:1433–1441

Bida GT, Ruth TJ, Wolf AP (1980) Experimentally determined thick target yields for the ^{14}N(p,α)^{11}C reaction. Radiochim Acta 27:181–185

Casella VR, Christman DR, Ido T, et al (1978) Excitation function for the ^{14}N(p,α)^{11}C reaction up to 15 MeV. Radiochim Acta 25:17–20

Casella V, Ido T, Wolf AP, et al (1980) Anhydrous F-18 labeled elemental fluorine for radiopharmaceutical preparation. J Nucl Med 21:750–757

Finn RD, Schlyer DJ (2002) Production of radionuclides for PET. In: Wahl RL, Buchanan JW (eds) Principles and practice of positron emission tomography. Williams & Wilkins, Philadelphia

Fukumura T, Okada K, Suzuki H, et al (2006) An improved ^{62}Zn/^{62}Cu generator based on a cation exchanger and its fully remote-controlled preparation for clinical use. Nucl Med Biol 33:821–827

Haynes NG, Lacy JL, Nayak N, et al (2000) Performance of a ^{62}Zn/^{62}Cu generator in clinical trials of PET perfusion agent ^{62}Cu-PTSM. J Nucl Med 41:309–314

Hess E, Takacs S, Scholten B, et al (2001) Excitation function of the ^{18}O(p,n)^{18}F nuclear reaction from threshold up to 30 MeV. Radiochim Acta 89:357–362

Joliot F, Curie I (1934) Artificial production of a new kind of radio-element. Nature 133:201–202

Lawrence EO, Livingston MS (1931) The production of high speed protons with the use of high voltages. Phys Rev 38:834

Livingston MS, McMillian E (1934) The production of radioactive oxygen. Phys Rev 46:439–440

Nickels RJ, Hichwa RD, Daube ME, et al (1983) An ^{18}O target for the high yield production of ^{18}F fluoride. Int J Appl Radiat Isot 34:625–629

Nickels RJ, Daube ME, Ruth TJ (1984) An oxygen target for the production of [^{18}F]F$_2$. Appl Radiat Isot 35:117–112

Qaim SM (1987) Cyclotron production of generator radionuclides. Radiochim Acta 41:111–117

Richards P (1965) The Tc-99m generator. Report No BNL-9061. Brookhaven National Laboratory, Upton, New York

Robinson GD Jr, Zielinski FW, Lee AW (1980) The ^{62}Zn/^{62}Cu generator: A convenient source of 62Cu for radiopharmaceuticals. Int J Appl Radiat Isot 31:111–116

Ruth TJ (2003) Accelerators available for isotope production. In: Welch MJ, Redvanley CS (eds) Handbook of radiopharmaceuticals, radiochemistry and applications. Wiley, New York, pp 71–86

Ruth TJ, Wolf AP (1979) Absolute cross section for the production of ^{18}F via the ^{18}O(p,n)^{18}F reaction. Radiochim Acta 26:21–24

Saha GB (2004) Fundamentals of nuclear pharmacy. 5th edn, Springer, New York

Satyamurthy N, Phelps ME, Barrio JR (1999) Electronic generators for the production of positron emitter labeled radiopharmaceuticals: Where would PET be with out them? Clin Positron Imag 2:233–253

Schlyer DJ (2003) Production of radionuclides in accelerators. In: Welch MJ, Redvanley CS (eds) Handbook of radiopharmaceuticals, radiochemistry and applications. Wiley, New York, pp 1–70

Scholten B, Kovacs Z, Tarkanyi F, et al (1995) Excitation functions of ^{124}Te(p, xn)^{124}, ^{123}I reactions for 6–31 MeV with special reference to the production of ^{124}I at a small cyclotron. Appl Radiat Isot 46:255–259

Schuhmacher J, Maier-Borst W (1981) A new $_{68}$Ge/$_{68}$Ga radio-isotope generator system for production of ^{68}Ga in dilute HCl. Int J Appl Radiat Isot 32:31–36

Segrè E (1980) From x-rays to quarks. Modern physicists and their discoveries. Freeman, New York

Sheh Y, Koziorowski J, Balatoni J, et al (2000) Low energy cyclotron production and chemical separation of no-carrier added iodine-124 from a reusable enriched tellurium-124 dioxide/aluminum oxide solid solution target. Radiochim Acta 88:169–173

Thomas KE (1987) Strontium-82 production at Los Alamos National Laboratory. Appl Radiat Isot 38:175–180

Tilbury RS, Dahl JR (1979) ^{13}N species formed by the proton irradiation of water. Radiat Res 79:22–33

Vera-Ruiz H, Wolf AP (1977) Excitation function of ^{15}O production via the ^{14}N(d, n)^{15}O. Radiochim Acta 24:65–67

Welch MJ, McCarthy TJ (2000) The potential role of generator-produced radiopharmaceuticals in clinical PET. J Nucl Med 41:315–317

Yano Y, Anger HO (1964) A gallium-68 positron cow for medical use. J Nucl Med 5:485

Zhernosekov KP, Filosofov DV, Baum RP, et al (2007) Processing of generator-produced ^{68}Ga for medical application. J Nucl Med 48:1741–1748

PET and SPECT Scanners

6

What we observe as material bodies and forces are nothing but shapes and variations in the structure of space. Particles are just schaumkommen (appearances). The world is given to me only once, not one existing and one perceived. Subject as well as object is only one. The barrier between them cannot be said to have broken down as a result of recent experience in the physical sciences, for this barrier does not exist.

Erwin Schrodinger

6.1 Interaction of Radiation with Matter

Radiation emitted by radionuclides can be classified into electromagnetic (such as x-rays, γ-rays, annihilation photons) or particulate (such as β⁻, β⁺) radiation. When we speak of the interaction of radiation with matter, we mean its interaction with the electrons and nucleus of atoms. The interaction of radiation, in general, may be classified as *elastic* or *inelastic*. In an elastic interaction, the incident radiation is scattered in a different direction, but the total energy of the interacting particles is conserved. In contrast, in an inelastic interaction, a certain amount of energy is lost.

Ionization occurs when an electron is ejected from an atom, producing an ion pair, a free electron, and a positive atom. High-energy photons (X-rays, γ-rays, and annihilation photons) and charged particles (β⁻, β⁺, H⁺, and α or He²⁺) are regarded as ionizing radiation. If an electron is not ejected from the atom but merely raised to higher energy levels or outer shells, the process is termed *excitation*, and the atom is said to be *excited*. In certain materials, when the electrons in the excited state drop to a lower energy state, with the emission of visible light, then that material is said to exhibit *luminescence*. If the production of light ceases within 10^{-8} s of the end of irradiation (or interaction), then the process is one of *fluorescence*; if it continues beyond this point, then the process is called *phosphorescence* (also known as *afterglow*).

6.1.1 Interactions of Charged Articles

6.1.1.1 Ionization

Charged particles (such as electrons β⁻, β⁺, and H⁺) passing an absorbing medium transfer some of the energy to electrons of the medium and are then deflected. Therefore, they cause *ionization* and/or *excitation*. The probability of scattering increases with the atomic number Z of the absorbing medium, and decreases rapidly with the increasing kinetic energy of the incident electron. In a close encounter, an orbital electron may be separated from the atom, thus causing ionization. The ejected electron may have sufficient energy to cause secondary ionization and eject an orbital electron, known as delta (δ) rays. The *specific ionization* (SI), the number of primary and secondary ion pairs produced per centimeter in air, at standard temperature and pressure (STP), can be estimated on the basis of the velocity (v) of incident electron and the velocity of light (c) using the following equation:

$$SI = \frac{45}{(v/c)^2} \qquad (6.1)$$

A less close encounter of the incident charged particle with an atom or molecule may result in an orbital electron being raised to an excited state, thus causing atomic or molecular excitation. The energy absorbed by the atom is dissipated in the subsequent atomic emission of electromagnetic radiation (such as infrared, visible, or UV).

6.1.1.2 Bremsstrahlung Radiation

When an incident β⁻ particle penetrates the electron cloud of an atom, it may interact with the nucleus and may be deflected with a reduced velocity. The energy lost by the incident electron will appear as electromagnetic radiation, known as bremsstrahlung (breaking radiation) (Fig. 6.1). The probability of bremsstrahlung varies with Z^2 of the absorbing medium.

6.1.1.3 Annihilation Radiation

A positron (β⁺), after expending its kinetic energy in inelastic collisions, combines with an electron (β⁻) of the absorbing medium. Both the particles are annihilated, and their mass appears as electromagnetic radiation (usually two 511-keV photons), known as annihilation radiation (Fig. 6.1). This interaction of β⁻ and β⁺ particles (matter and antimatter) is called *pair annihilation*.

6.1.1.4 Cerenkov Radiation

Particles normally cannot exceed the velocity of light in a vacuum (3.0×10^{10} cm s⁻¹). Light, however, travels at slower speeds in different materials or media. It is possible for β⁻ rays to travel at speeds much higher than that of light in a specific medium. When this occurs,

visible light, known as *Cerenkov radiation*, is emitted. For example, the blue glow seen near the core of a swimming pool reactor is due to Cerenkov radiation.

6.1.2 Interaction of High-Energy Photons

The interaction of electromagnetic radiation with atoms, electrons, and nuclei of different materials is generally regarded as a collision involving transfer of their energy to matter without necessarily causing ionization directly. However, certain interactions do eject orbital electrons, produce ion pairs, and cause ionization effects. Therefore high-energy photons, similar to charged particles, are regarded as ionizing radiation. However, unlike charged particles, high-energy photons being massless can penetrate soft-tissue thickness of >10 cm in vivo and are considered to be highly penetrating radiation.

The high-energy photons of x-rays, γ-rays, and annihilation radiation associated with radiotracers in nuclear medicine undergo inelastic interactions by means of several mechanisms. The *photoelectric effect* and *Compton scattering* are important in radiation detection and measurement. Pair production and photodisintegration have a high energy threshold (>1 MeV) and are not relevant to the photon energies normally encountered in nuclear medicine.
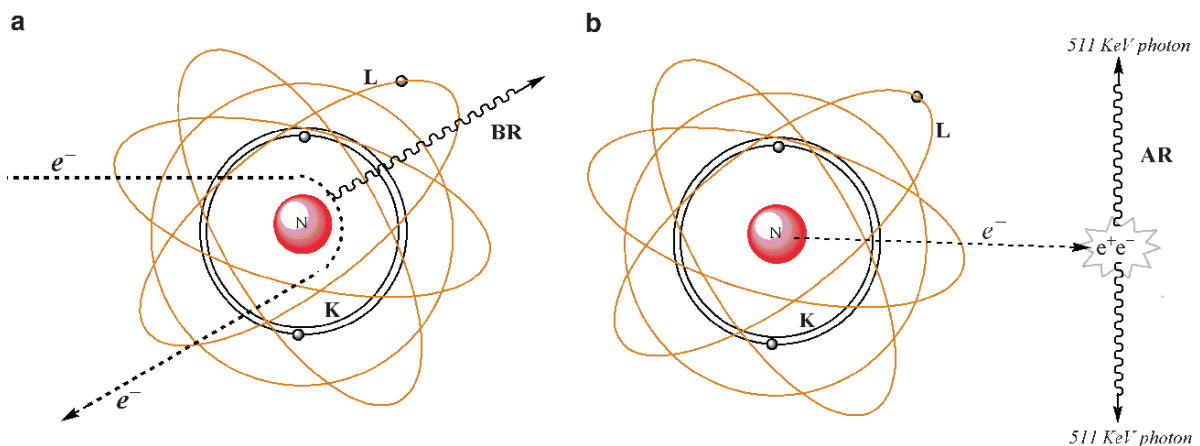
Fig. 6.1 Interaction of charged particles with matter. When high-energy electrons penetrate and approach the nucleus, they are decelerated and deflected (**a**). As a result, bremsstrahlung radiation (BR) is produced. The positron emitted from the

atomic nucleus finally interacts with an electron and annihilates it (**b**). As a result, annihilation radiation (AR) is produced in which two photons with a minimum of 511 keV energy travel in opposite directions

6.1.2.1 Photoelectric Effect

When a metal is exposed to electromagnetic radiation, electrons are ejected from the metal (Fig. 6.2). These electrons are called *photoelectrons*. Light with shorter wavelengths (such as UV) ejects electrons with greater speed. Thus the kinetic energy of photoelectrons is dependent on the frequency, however, the number of electrons ejected depends on the intensity of the electromagnetic radiation. Different metals have different threshold values for the frequency. Depending on the *Z* of the element, electrons may be held more loosely or tightly. Einstein was able to show that photons with higher energy eject electrons with greater kinetic energy. This phenomenon of the photoelectric effect is very important for the interaction of radiation with matter and for developing radiation detectors. The photoelectric effect should obey the following relationship:

$$h\nu = KE_{max} + \varphi \tag{6.2}$$

where

$$\varphi = h\nu_0 \tag{6.3}$$

Also, ν_0 is the critical frequency below which no photoelectric effect occurs and ϕ is the minimum energy (called the *work function* of the metal) needed for the electron to escape from a metal surface. The photoelectric effect is an atomic absorption process in which an atom totally absorbs the energy of the incident photon. It is an interaction of photons with orbital electrons in an atom, mostly the inner-shell electrons, in which the photon transfers all of its energy to the electron, which is then ejected. Some of the energy of the incident photon is used to overcome the binding energy of the electron, and the remaining energy is given to the photoelectron, as kinetic energy. Since the ejection of a photoelectron creates a vacancy in the inner shell, the photoelectric effect is usually accompanied by the emission of characteristic x-rays and/or Auger electrons.

The probability of a photoelectric interaction occurring at a particular shell depends on the energy of the incident photon and the binding energy of the shell (in other words, on *Z*). The probability is zero when the energy of photon is less than the binding energy of electron; it is greatest when the photon energy is equal to the binding energy of electron and thereafter decreases rapidly with increasing photon energy. Following the injection of radiotracers, the photoelectric effect plays a minor role with soft tissue. In radiation detectors, such as scintillation detectors, however, the photoelectric effect is the predominant mode of interaction of photons.
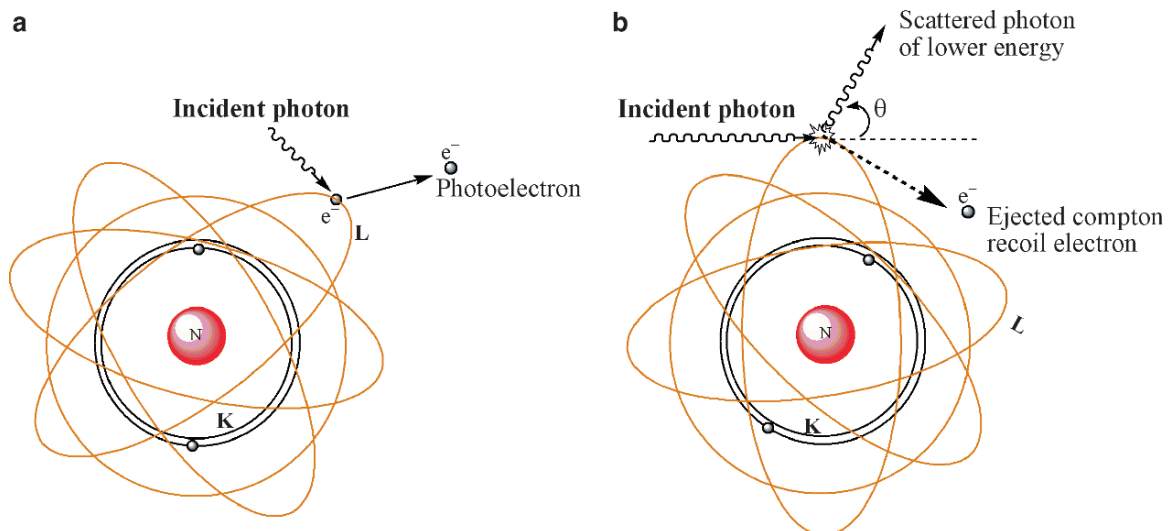
Fig. 6.2 Interaction of high-energy photons with matter. In the photoelectric effect (**a**), an incident photon transfers all its energy to an orbital electron, which leaves the atom and is known as a photoelectron. In Compton scattering (**b**), the incident photon transfers only part of its energy to an orbital electron, which is then ejected (recoil electron). The scattered photon is then deflected in a different angle (θ, the scattering angle)

6.1.2.2 Compton Scattering

Compton scattering is a collision between a photon and a loosely bound outer orbital electron. After the interaction, the *scattered photon* undergoes a change in direction and the recoil electron is ejected from the atom (Fig. 6.2). The scattered photon is deflected through an angle (θ_C) proportional to the amount of energy lost. The maximum energy loss occurs when the θ_C is 180° or when the photon is *backscattered*. For example, the annihilation photon (511 keV) after backscatter will have an energy of 170 keV. The energy lost by the scattered photon is divided between the small binding energy of the orbital electron and the kinetic energy of the recoil electron. The relative probability of Compton scattering increases slightly as the energy of the incident photon increases and as the effective atomic number (Z_{eff}) of the interacting medium decreases. Following administration of radiotracers, the most important and significant mode of interaction of photons with soft tissue is Compton scattering.

6.1.2.3 Pair Production

When a high-energy photon interacts with an electric field of a charged particle (atomic nucleus or even an electron), the incident photon may completely disappear and its energy is used to create a β^- and β^+ pair, known as *pair production*. Since the rest of the energy of the electron is 511 keV, the incident photon must have a minimum energy of 1.022 MeV. The difference between the incident photon energy and 1.022 MeV is imparted to the electron pair as kinetic energy.

6.1.3 Attenuation

If we measure the intensity of the radiation before (I_0) and after it interacts with a given medium (I_x) of particular thickness x, we find that the intensity of the radiation after passing through the medium has reduced; the beam of radiation is said to have been attenuated. By the processes of absorption and scattering in a medium, a beam of radiation undergoes attenuation. The atoms in the medium act as targets, which,

if hit, will attenuate a photon from the primary radiation beam. The probability of an interaction with a particular atom is low, but the very large number of atoms in a small volume of a solid increases the probability of attenuation, significantly. A parallel beam of monoenergetic electromagnetic radiation will undergo exponential attenuation as it passes through a uniform medium.

$$I_x = I_0 e^{-\mu x} \tag{6.4}$$

where μ is the total *linear attenuation coefficient*, which can be defined as the fraction of photons removed from a beam of radiation per unit thickness of the attenuating medium. The parameter μ is a property of both the photon energy and the nature of the medium. It increases (i.e., photons become less penetrating) for low photon energies and low mass density. In a given thickness of medium, the number of atoms (N) may be the same for different materials, but the density (ρ) may vary. Therefore, the total mass attenuation coefficient μ/ρ is the fraction of photons removed from a beam of radiation of unit cross-sectional area by unit mass of the medium. For photons with <1 MeV energy, the parameters μ and μ/ρ are largely made up of components due to photoelectric absorption (τ) and Compton scattering (σ).

Other important parameters derived from μ are half-value thickness (HVT) or half-value layer (HVL), tenth value layer (TVL), and the mean free path (MFP), which is the distance a photon (or a particle) travels before interacting. All these parameters are related mathematically as shown in the following equations:

$$\mu = 0.693 / HVL \tag{6.5}$$

$$MFP = 1.44 \, HVL \tag{6.6}$$

With radiation, the three most important media of interest are the tissue, radiation detector material (the crystal), and the type of shielding (lead, tungsten). For various materials, the linear attenuation coefficient and HVL values for photons of two different energies, 140 and 511 keV, are shown in Table 6.1. For 511-keV photons, the primary interaction is Compton scattering; therefore, correction for attenuation and scattering is essential for PET imaging studies.

Table 6.1 Linear attenuation coefficient and HVL values of photons for different materials

Material	Density (ρ) (g cm⁻³)	140-keV photon		511-keV photon	
		μ (cm⁻¹)	HVL	μ (cm⁻¹)	HVL
Water	1.0	0.15	4.62	0.095	7.29
Adipose tissue	0.95	0.142	4.88	0.090	7.70
Cortical bone	1.92	0.284	2.44	0.178	3.89
Pyrex glass	2.23	0.307	2.26	0.194	3.57
Lucite	1.19	0.173	4.01	0.112	6.19
NaI (Tl)	3.67	2.23	0.31	0.34	2.04
Bismuth germinate	7.13	~5.5		0.95	0.73
Lead	11.35	40.8	0.018	1.75	0.42
Tungsten				2.59	0.29

6.2 Radiation Detectors

Radiation detectors have been developed over the years on the basis of the two major consequences of interaction of radiation with matter; ionization and excitation. Radiation detectors are generally categorized as either ionization detectors or scintillation detectors.

6.2.1 Ionization Detectors

These detectors respond to radiation by means of ionization, which induces tiny electrical currents that can be detected and measured. The ionization detectors can be either gas-filled (also known as *ionization chambers*) or *semiconductor detectors*.

6.2.1.1 Gas-filled Detectors

Most gas-filled detectors are made up of a chamber, which contains a volume of gas (mostly air or an inert gas) between two electrodes with a voltage difference between them. Under normal circumstances, the gas is an insulator and no current flows between the electrodes. When the gas is ionized following an interaction with radiation, electrons are attracted to the anode and positive ionized atoms are attracted to the cathode, producing a small current. When gas-filled chambers operate at the saturation voltage (300–600 V), to ensure

complete collection of ions at the electrodes, they are called *ionization chambers*. If the detector is calibrated to express the measured current as an exposure rate (R h⁻¹, mR h⁻¹), it is called a survey meter; if it collects the total charge over a period of time, it is called a *pocket dosimeter*; and, finally, if the measured current is used to assay the activity (mCi, MBq, etc.), it is called a *dose calibrator*.

Ionization chambers are quite inefficient as detectors for X-rays and γ-rays. Their response to photons changes with photon energy, but the energy discrimination, especially in the case of dose calibrators, is achieved only by the use of precalibrated amplifiers, one for each radionuclide of interest.

If an ionization chamber is maintained between 900 and 1,200 V, the electrons generated by the interaction of radiation will accelerate and cause additional ionization. This process is known as *gas amplification* of the charge, and the factor by which the ionization is amplified is called the *gas amplification factor* (GAF). A Geiger–Muler (GM) counter is a gas-filled detector designed to have GAF as high as 10^{10}. In a GM counter, the size of the electrical signal output is relatively constant and independent of the energy of radiation. Because of their high sensitivity, GM counters are mainly used as survey meters to detect ambient radiation levels and radioactive contamination.

6.2.1.2 Semiconductor Detectors

Semiconductor detectors are essentially solid-state analogs of gas-filled detectors (Darambara and Todd-Pokropek 2002). Semiconductor materials, such as Si and Ge, when doped with Li, can function as solid ionization chambers, and are also called *solid-state detectors*. In order to create an ion pair in air, the energy needed is 34 eV per ionization. In contrast, the energy needed to create an ion pair is only 2.5 eV in Si(Li) and 3.0 eV in Ge(Li) detectors. When a small voltage is applied across a semiconductor detector, a high-energy photon will interact with the detector and liberate electrons leaving a positive hole in the lattice structure. Under an applied electric field, both the electron and the positive hole will move towards opposite electrodes

inducing an electric current. Since the size of the electrical signal is relatively large and proportional to the radiation energy absorbed, semiconductor detectors are useful for energy-selective radiation counting.

Both, Ge- and Si-based semiconductors conduct a significant amount of thermally induced electrical current at room temperature. Therefore, it is necessary to operate and maintain these detectors at relatively low temperatures. High-purity germanium (HPGe), however, needs to be cooled to low temperatures, while others such as cadmium telluride (CdTe) and cadmium zinc telluride (CZT) operate at room temperature. Ge(Li) and Si(Li) detectors are relatively inefficient for detecting high-energy gamma photons. Both, CdTe and CZT have stopping powers similar to NaI(Tl) scintillation detectors. Even denser semiconductors, such as lead iodide (PbI) and thallium bromide (TlBr), are currently under development and may be useful for detecting high-energy photons. CdTe and CZT are also available as pixelated detector arrays with a typical intrinsic spatial resolution of 2.4 mm.

6.2.2 Scintillation Detectors

When high-energy photons interact with the atoms of a scintillation crystal, the electrons are raised from a *valence band* or an orbital to a forbidden, unfilled *conduction band* of a higher energy state. The excited atoms quickly return to the ground state emitting a visible light in a process known as *luminescence*. The number of electrons raised to a higher energy level, and the consequent number of visible light photons emitted by the crystal, depends on the energy of the incident photon.

The photoelectric effect is the primary mode of interaction of photons with the atoms in the crystal. The visible light emitted by the crystal is usually in the ultraviolet range. For the crystal to emit light in the visible range (400–500 nm), an alkali halide crystal, with an impurity of (<1%), such as thallium iodide, must be *activated* (or *doped*). The scintillation photons produced by the luminescence are emitted *isotropically* (in all directions) from the point of interaction. The most important scintillators used in current PET and SPECT scanners are the following:

Sodium iodide doped with thallium iodide (NaI(Tl))
Bismuth germanate, $Bi_4Ge_3O_{12}$ (BGO)
Lutetium oxyorthosilicate doped with cerium, Lu_2SiO_5:Ce (LSO)
Yttrium oxyorthosilicate doped with cerium, Y_2SiO_5:Ce (YSO)
Gadolinium oxyorthosilicate doped with cerium, Gd_2SiO_5:Ce (GSO)
Barium fluoride (BaF_2)
Lutetium yttrium oxyorthosilicate (LYSO)

The physical properties of several scintillators are compared in Table 6.2. The most important properties of a detector are stopping power, light output, signal decay time, and the intrinsic energy resolution of the crystal. The following points may be noted: (1) The stopping power is characterized by the MFP or attenuation length, which depends on the density (ρ) and effective atomic number (Z_{eff}) of the crystal. A crystal with shorter attenuation length will have higher efficiency and sensitivity. (2) A crystal with high light output (photons keV^{-1} absorbed) will have good energy resolution. (3) A short decay time of the crystal can

Table 6.2 Physical properties of scintillators

	NaI (Tl)	YSO	BaF2	LYSO	GSO	BGO	LSO
Density (g cm^{-2})	3.67	4.53	4.89	5.31	6.71	7.13	7.4
Effective Z	50.6	34.2	52.2	54	58.6	74.2	65.5
Light output (photons/keV)	38	46	2		10	6	29
Relative light output (%)	100	118	5	76	25	15	75
Wavelength, λ (nm)	410	420	220	420	440	480	420
Decay time (ns)	230	70	0.6	53	60	300	40
Attenuation, μ (cm^{-1}) at 511 keV	0.3411	0.3875	0.4545	–	0.6978	0.9496	0.8586
Attenuation length (1/μ)	2.93	2.58	2.20	2.0	1.433	1.053	1.169
Photoelectric/Compton ratio	0.22	–	0.24	–	0.35	0.78	0.52

help process each pulse separately at higher counting rates with minimum dead time. (4) A crystal with better energy resolution can reject scattered photons more effectively. The overall scanner spatial resolution, however, depends on several other factors.

With NaI(Tl) crystal, the detection efficiency for 140-keV photons is >90%, but for 511-keV photons the efficiency drops to <10%. The intrinsic energy resolution of the crystal is more important for SPECT scanners, while the stopping power of the crystal is one of the main considerations in the choice of the crystal that can interact with 511-keV photons in PET scanners. With the current PET scanners, BGO and LSO are the preferred crystals, while NaI(Tl) is the only crystal that is used in all the major clinical SPECT scanners. A number of other scintillators such as CsI(Tl) and CsI(na) are also under evaluation. The technology of PET and SPECT scanners is continously evolving and is dependent on many other factors besides scintillators.

6.2.2.1 Photodetectors

One of the common characteristics of all scintillators is that following interaction with high-energy photons they all produce a very weak signal of visible light, or a scintillation photon. The purpose of a photodetector is to convert a scintillation photon with 3–4 eV energy into an electrical current. The probability of converting a photon into an electron is called *quantum efficiency*. The two categories of photodetectors used are photomultiplier tubes (PMTs) and semiconductor-based photodiodes.

A PMT is a vacuum tube that consists of an entrance window, *photocathode*, followed by a series of *dynodes* (electrodes), each of which is held at a greater voltage with a resistor chain. The scintillation photon strikes the photocathode and release photoelectrons, which are then accelerated to the first dynode and release even more electrons, which are then accelerated to the next dynode. After passing a series of dynodes, the number of electrons is amplified to >10^6, producing a sizeable current in the milliampere range at the anode. Despite of their bulkiness, almost all commercial PET and SPECT scanners use PMTs because of their high gain or amplification, ruggedness, and stability. The quantum efficiency of the photocathode in PMTs is about 15–25%. In order to improve this efficiency, more advanced PMTs, known as position-sensitive (PS) PMTs and multichannel (MC) PMTs, are under development and evaluation.

A photodiode consists of a thin piece of doped silicon wafer (a couple of hundred micrometers thick). The principle of operation is the same as that of a semiconductor. The quantum efficiency (60–80%) of photodiodes is much better than that of PMTs, but the signal of the electrical current is very weak because photodiodes do not have internal amplification or gain. In order to improve the signal-to-noise ratio (SNR), a new type of photodiode known as *avalanche photodiode* (APD) has been developed, which has an internal amplification, however it is still not as good as that of PMTs.

6.2.2.2 Radiation Detector Performance

Spectroscopy is the study of the energy distribution of a radiation field. Most spectrometers are operated in the pulse mode and the amplitude of each pulse is proportional to the energy deposited by the interaction of the photon with the crystal. The amplitude, however, may not be proportional to the total energy of the incident photon. A *pulse height spectrum* (Fig. 6.3) represents the number of interactions or counts per minute (cpm) as a function of the energy of the photon, but it is not the same as the actual energy spectrum of the incident radiation. The performance characteristics of radiation detectors can be expressed quantitatively using parameters, such as *sensitivity* and *energy resolution*.

Sensitivity (or *efficiency*) is the detected count rate per unit of radioactivity. *Geometric sensitivity* of a detector is the fraction of emitted photons that reach the detector, whereas the *intrinsic sensitivity* or the *quantum detection efficiency* (QDE) is the fraction of those photons that reach the detector which are actually detected. For example, 1 µCi of ^{99m}T has 2.2×10^6 disintegrations per minute (dpm), and each decaying atom produces one 140-keV photon. If the detector can detect 1.0×10^5 photons, then the sensitivity of the detector is 10%. As discussed previously, various physical characteristics of the crystal (Table 6.2) can affect the sensitivity of the scintillator.

Many radionuclides emit a number of photons (x-rays and γ-rays) of discrete energies. The electrical signal output from a detector–photodiode combination, however, appears as though it is coming from a range of energies
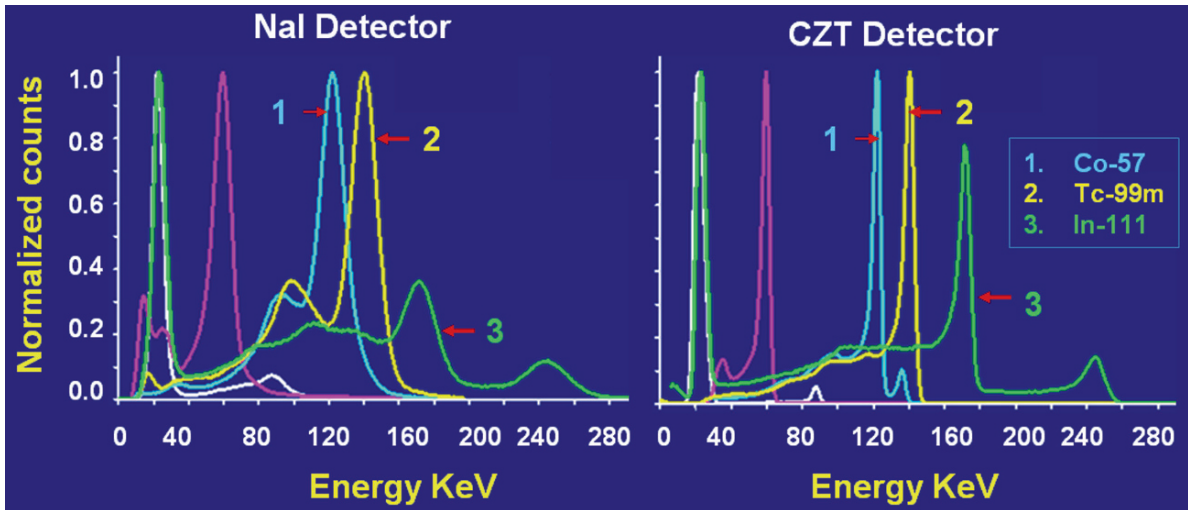
Fig. 6.3 Pulse height spectra of several radionuclides using NaI or CZT detector. The energy resolution with CZT detectors is much higher compared to that with NaI detector

due to the absorption and scattering of the incident photons. Energy resolution quantifies the ability of a specific crystal to differentiate or discriminate photons of different energies. It is expressed quanti-tatively as a percent of full width at half-maximum (FWHM = ΔE) of an energy spectrum (counts detected vs. energy (keV)) of a radionuclide with a specific photopeak energy (E_γ).

$$\text{FWHM}\,(\%) = \frac{\Delta E}{E_\gamma} \times 100 \qquad (6.7)$$

For energy-selective detection (as in Anger cameras), the FWHM determines the resolution of the detector. The sensitivity can be increased by increasing the value of ΔE, but that would degrade the resolution.

6.3 Radionuclide Imaging Systems

The purpose of radionuclide imaging is to obtain an image of the in vivo distribution of a radiotracer on the basis of the external detection of high-energy photons emitted by the radionuclide. In the 1940s, attempts were made to detect the distribution of radioactivity in vivo, but only in the 1950s, that in vivo radionuclide imaging became a practical clinical modality, due to the introduction of the rectilinear scanner, by Ben Cassen. In the 1950s, Hal Anger developed the first γ-ray camera using a single, large-area NaI(Tl) scintillation crystal coupled to PMTs. This camera, subsequently, called the *Anger*

scintillation camera, has become the predominant molecular imaging device in nuclear medicine. Since then, many refinements and modifications have been made to improve the image quality of this camera.

Conventional Anger camera images compress the three-dimensional (3D) distribution of the radiotracer into a two-dimensional (2D) image. As a result, the contrast between areas of interest and the surrounding territory is often significantly reduced. In *planar imaging* systems, the radiation from a source (patient) is collected and the data is presented as though all photons are coming from a single plane. In a patient, images of a specific area of interest at one depth are obscured by images of structures above and below the area of interest. *Tomography* simply means an image of a slice. Tomographic images are 2D representations of structures lying within a selected plane or depth in a 3D object. *Computed tomography* (CT) techniques are based on rigorous mathematical algorithms initially developed by Radon, in 1917. The introduction of CT, in the 1970s, helped to implement CT techniques to the radionuclide imaging methods. X-ray CT is a transmission CT since x-rays from an external source are transmitted through the patient to a detector. With radiotracers, high-energy photons are emitted from the patient; this technique is called *emission computed tomography* (ECT). Since radionuclides emitting γ-rays, are used for imaging, the technique is also called *single photon emission tomography* (SPECT). With positron-emitting radionuclides, the imaging technique is called *positron emission tomography* (PET).

6.3.1 Anger Camera

The Anger gamma camera consists of a single rectangular NaI(TL) crystal (~50–60 cm in area) optically coupled to a large number of PMTs (typically 37–91). While the thickness may vary from 0.25 in. (~6 mm) to 1 in. (~25 mm), most cameras are made up of a 3/8 in. (~10 mm) crystal for optimum performance of radionuclides with energies between 120- and 200-keV photons. Thinner crystals have better spatial resolution, but lower sensitivity.

A *collimator* (usually made of lead) with holes (round, square, rectangular, or hexagonal) allows high-energy photons coming from the patient in a specific direction to enter and interact with the crystal. The walls, called *septa*, around the holes in the collimator absorb photons that are traveling in an oblique angle to the axes of the holes. In other words, the collimator controls the direction of the photons entering the crystal. The thickness of the collimator and septa as well as the number of holes determines the overall sensitivity and resolution of the Anger camera. Most cameras have a wide choice of parallel hole collimators such as "low-energy high sensitivity," "low-energy all purpose (LEAP)," "low-energy high resolution," medium-energy, high-energy, and ultrahigh-energy collimators, each designed to optimize a specific imaging study. With all parallel-hole collimators, the spatial resolution degrades rapidly as the distance (space) between the patient and the collimator increases. A pinhole collimator, consists of a small hole (3–5 mm in diameter) in a piece of lead or tungsten, and is commonly used to produce magnified views of small objects. The magnification and sensitivity, however, decrease as an object is moved away from the pinhole.

Following interaction of photons with the crystal, the emitted light photons induce electrical signals in the PMTs. The PMTs closest to the scintillation even in the crystal receive more light than those that are most distant and as a result produce a larger electrical signal. The relative amplitude of these pulses determines the location of the interaction in the crystal and the exact location of the origin of the photons coming from the patient. The electrical pulses from PMTs pass through preamplifiers and ADCs (analog-to-digital converter). The digital X, Y, and Z signals are corrected using correction circuits, followed by energy discrimination using SCAs (single-channel analyzers). The signals are finally converted into digital images in a computer.

6.3.1.1 Anger Camera Performance

The measures of performance of a scintillation detector or camera alone are called *intrinsic* measurements, while the measures with the collimator are called *extrinsic* or system measurements; these measurements give the best indication or clinical performance.

Uniformity is a measure of the camera's response to uniform irradiation of the detector surface.

Spatial resolution is a measure of the camera's ability to accurately assess the spatial variations in radioactivity concentrations that are in close proximity, and to distinguish these areas as separate radioactive objects or source regions. A systems spatial resolution is normally determined by obtaining a *line spread function* (LSF) using a line source (capillary tube) of radioactivity. FWHM and *modular transfer function* (MTF) are derived from the LSF. On the basis of the system spatial resolution (R_s) and intrinsic resolution (R_i) of the detector, the collimator resolution (R_c) can be estimated using the following equation.

$$R_s = \sqrt{R_c + R_i} \tag{6.8}$$

Spatial linearity is the ability of a camera to, accurately, depict the true shape of the object. Any distortion of the shape is an indication of spatial nonlinearity.

The *system sensitivity* or *efficiency* (E_s) of a camera is the fraction of photons emitted by a source that produce counts in an image. It is the product of the intrinsic efficiency of the crystal (E_i), the collimator efficiency (E_c), and the fraction (f) of interacting photons accepted by the pulse height analyzers. The *photopeak efficiency* is defined as the fraction of photons reaching the crystal and produce counts, which represent the photopeak in the energy spectrum:

$$E_s = E_i \times E_c \times f \tag{6.9}$$

The *energy resolution* of an Anger camera is a measure of its ability to distinguish between the different energies of photons that are interacting with the crystal. A camera with good energy resolution can produce images with better *contrast* since it can reject scattered photons with lower energies. *Multiple energy (or window) spatial registration*, on other hand, is the ability of a camera to maintain the same magnification, regardless of the photopeak energy of the incident photons.

In a NaI(TL) crystal, approximately one visible photon is emitted for every 25 eV of energy deposited.

For example, when a 140-keV photon deposits all of its energy in the crystal, it will generate 5,600 visible light photons, of which only 20–25% may eject electrons from the photocathode and contribute to the signal from the PMT. The intrinsic efficiency (E_i) of the camera is determined by the thickness of the crystal and the energy of incident photons. With gamma cameras, there is a design compromise between the intrinsic efficiency (E_i) and the intrinsic resolution (E_s) since thinner crystals have better resolution, but lower sensitivity and, vice versa. The compromise between the collimator efficiency (E_c) and the collimator resolution (R_c) is the most important and significant an limitation of Anger camera performance. The systems spatial resolution (R_s) degrades (FWHM increases) as the collimator-to-object distance increases, without any significant impact on the system efficiency (E_s).

With many of the Anger scintillation cameras (with a 3/8 in. crystal), the intrinsic spatial resolution (R_i) for 140-keV photons of ^{99m}Tc is between 2.7 and 4.0 mm. With a parallel-hole collimator, however, the system resolution (R_s) could dramatically decrease to 8–12 mm at a distance of 10–20 cm from the collimator surface. The most important point is that the system resolution is not the same in the entire filed of view.

6.3.1.2 Planar Image Acquisition

Planar images with gamma cameras can be acquired either, in a *frame* mode, or a *list* mode. In a frame mode, an image is formed as the acquisition is in progress, whereas in a list mode, the images are created subsequently at the end of an acquisition.

The frame-mode acquisition is the most common method. Planar frame-mode acquisitions can be *static*, *dynamic*, or *gated*. In a static planar image acquisition, a single image (one frame) is obtained either for a preset time interval (such as 5 or 10 min) or for a total number of counts (such as 0.5 or 1 million counts). In a dynamic image acquisition, a series of images (many frames and each frame/specific time) is acquired one after another to follow the time–activity distribution of radioactivity in a specific organ or area of interest. In gated acquisition, each frame is acquired on the basis of a physiological trigger such as an electrocardiogram (ECG). Each image consists of many *pixels*, and each pixel stores the acquired counts. Common image formats are 56 × 56, 128 × 128, 256 × 256, or 256 × 1,028

(whole-body scans only). In the *byte mode* (8 *bits*), each pixel stores 255 counts, while in a *word mode* (2 bytes), each pixel can store 65,535 counts. As discussed earlier, the planar projection image depicts 2D projections of 3D distribution of radioactivity in a patient. In an ideal projection image, there is no attenuation of photons within the patient and also there is no degradation of the image resolution by the camera. Since planar images are not corrected for attenuation, and the resolution is not same at different depths, planar imaging studies are not ideal projection images.

6.3.1.3 SPECT Image Acquisition

The conventional tomography, also called *focal plane tomography*, is based on scintillation detectors with focused or converging collimators. Structures close to the focal plane are in focus and well resolved, while the structures out of plane are not removed from the images, but blurred by an amount proportional to their distance from the focal plane. In contrast, the SPECT technique is based mainly on parallel-hole collimators. The standard planar projection images acquired in many angles around the patient are processed or reconstructed mathematically to obtain an image of a slice, and the overlying structures are removed completely from the image of each of the contiguous slices. One of the most important assumptions in SPECT imaging studies is that the distribution of radioactivity in the body remains constant throughout the duration of the scan.

Most routine clinical SPECT imaging systems are based on dual-head fixed 180° or variable angle cameras and triple-head variable angle cameras. Standard projection images are acquired in a frame mode and 64^2 or 128^2 format, either in a "step and shoot mode" or while the heads are moving continuously. As mentioned earlier, since these projections images are not ideal, images are generally acquired over a complete revolution (360°). For cardiac studies, optimal imaging protocols require projection images acquired only over a 180° arc around the patient. While older SPECT systems followed circular orbits around the patient, current SPECT systems have been designed to provide both circular and noncircular (body contouring) orbits.

The projection images are first corrected for nonuniformities and axis-of-rotation misalignments.

GE Infinia Hawkeye   **Siemens Symbia**   **Philips Precedence**
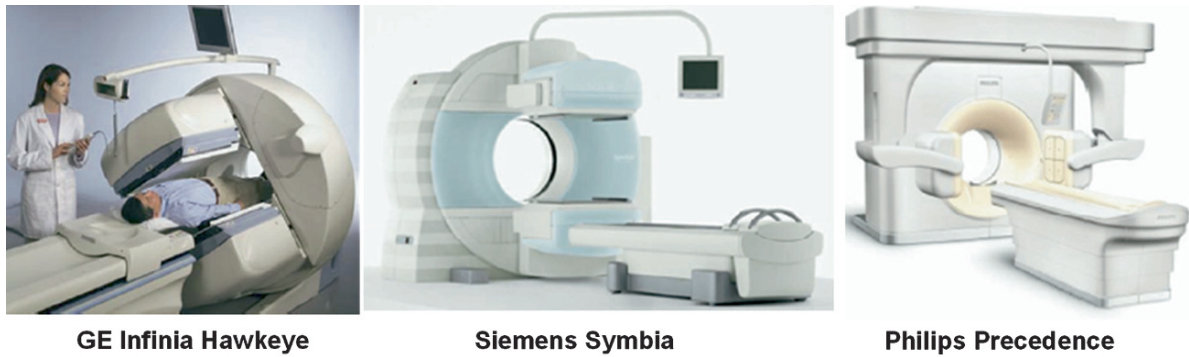
Fig. 6.4 SPECT/CT systems in routine clinical use

Table 6.3 Commercially available SPECT/CT systems

	Infinia Hawkeye	Precedence	True point
Manufacturer	GE Healthcare	Philips	Siemens
SPECT system	Infinia	Skylight	Symbia
CT system	Hawkeye	Brilliance	T, T2, T6
No. of CT slices	1 or 4	6 or 16	2 or 6
Slice thickness (mm)	10 or 5	0.6–12	0.6–10*
Tube rotation (s)	23	0.5	0.6–1.5*
Standard HC resolution (lp/cm) (2% MTF)	.3	13	15*
Room dimensions (cm)	470 × 711	442 × 640	358 × 419

*Values are for Symbia T6 (see text)

HC high contrast; *lp/cm* line pairs per centimeter; *MTF* modulation transfer function

Subsequently, the images are mathematically processed to reconstruct transverse images using either filtered backprojection, or iterative methods.

Since high-energy photons traverse long paths through the patient, attenuation effects are more severe in body SPECT than in brain SPECT. In addition, attenuation is not uniform throughout the patient. Therefore, standard methods of attenuation correction based on the assumption of uniform attenuation may not be applicable for SPECT studies. Several commercial SPECT systems use radioactive sources (such as ^{153}Gd) to generate transmission scans while acquiring the projection images. In the last 3–5 years, several SPECT/CT systems (Fig. 6.4 and Table 6.3) have been introduced primarily for coregistering anatomic and functional SPECT images. CT scans may also offer an opportunity for the development of attenuation–

correction methods. Attenuation–correction methods for clinical SPECT studies, however, are still under evaluation.

In SPECT studies, spatial resolution deteriorates as the radius of the camera orbit (body to collimator distance) increases. Brain SPECT produces images of better resolution than body SPECT. Also, noncircular body contouring orbits produce better resolution images than circular orbits. Compared to planar imaging, SPECT, in general, produces images with lower resolution for several reasons. In order to increase sensitivity, SPECT images are, generally, acquired with lower resolution parallel-hole collimators. Collimators are very inefficient, and allow only 1 in 5,000 photons that hit its surface to be transmitted through to the detector, and therefore, are the limiting component of count sensitivity and spatial resolution. Further, the distance between the body and the collimator is greater with SPECT. Since many projection images are obtained, counts/frame is much less with SPECT. SPECT images, however, do provide better contrast and reduced structural noise since the activity in the overlapping tissues is completely eliminated.

6.3.1.4 New Cardiac SPECT systems

Several clinical SPECT systems have been optimized for cardiac imaging. Some of these systems are still based on conventional dual-detector γ-camera systems, but the size of the systems were minimized to occupy less space. Three new systems have been introduced with certain new and novel technological advancements.

The Cardius system (Digirad) is available with up to three detector heads based on pixelated CsI(Tl) crystals. In this system, the detectors remain stationary and the projections are collected as the patient, sitting upright in a chair, is rotated. The other two clinical SPECT systems are based on semiconductor detector technology. The CardiArc has a 180° arc of pixelated CZT detectors with a series of lead plates (slats) to provide axial collimation for the detectors. A curved lead plate with a set of slits is located in front of the slats. The combination of the slits and slats, in addition to the motion of the slit plate, provides pinhole sampling with relatively high count sensitivity and better spatial resolution, compared to conventional SPECT systems. The D-SPECT system, on the other hand, consists of ten individual collimated pixelated CZT modules. Once the location of the heart has been determined, the CZT detector modules independently rock back and forth to acquire the data for the projection images. No gantry rotation is necessary. This system has both higher sensitivity and twofold improvement in spatial resolution compared to any conventional clinical SPECT system.

One of the major advantages of SPECT systems based on pixilated CZT modules is that it is now possible to image radiotracer distributions where the activity changes monotonically in a specific region of interest, during acquisitions. As a result, it is possible to derive additional information about the kinetics of the radiotracer distribution. With dynamic SPECT, it is possible to model the kinetics of distribution into the reconstruction algorithm to yield sequential time-sampled tomographic images. With its superior spatial resolution and high sensitivity, coupled with the ability to perform dynamic SPECT, the SPECT imaging technique provides new opportunities to perform molecular imaging studies with radiotracers based on ^{99m}Tc, ^{123}I, and ^{111}In.

In a recent review article, Mark Madsen (2007) concludes that "SPECT continues to progress with major improvements in instrumentation and reconstruction. The limits of spatial resolution and sensitivity have not yet been reached either for clinical devices or for small-animal imagers. Improvements in detector technology and image-forming apertures will yield intrinsically better projection information. At the same time, refinements in corrections for scattered radiation, attenuation, and spatial resolution losses will result in more accurate and quantitative reconstructed tomographic slices. The capability for combining this information with correlative imaging, both anatomic and functional, from other modalities is also expected to improve."

6.3.2 PET Scanners

PET scanners were designed to obtain in vivo images of the distribution and uptake of radiotracers on the basis of positron emitting radionuclides. A typical PET scanner consists of many rings of scintillation detectors which surround the subject. Following the interaction of the positron with the tissue, two annihilation photons (511 keV) are emitted, isotropically. The PET scanner uses the annihilation coincidence detection (ACD) method to obtain projection images of the radiotracer distribution. The images are first corrected for attenuation, scatter, etc. and then mathematically processed, as in the case of CT and SPECT, to obtain transverse images of several slices of the body in a given field of view (FOV). A number of reviews have been published, describing the historical development of the PET technology (Nutt 2002). The basic design, principles of operation, and performance characteristics of clinical PET, PET/CT, and MicroPET scanners are discussed in this section.

6.3.2.1 Positron Annihilation and Coincidence Detection

A positron ejected by a radionuclide travels a very short distance in a tissue, dissipating its kinetic energy in collisions with electrons, and finally combines with an electron to form a positronium, a state which lasts for a very short time (10^{-10} s). The subsequent positron–electron annihilation results in the emission of two 511-keV photons, 180° apart. A PET scanner is designed to detect this pair of annihilation photons almost simultaneously on the basis of a process known as *annihilation coincidence detection* (ACD), which establishes the trajectories of detected photons or lines of response (LOR). ACD only establishes the location of an annihilation event within the LOR; the exact location of a positron emitting radionuclide, however, is determined mostly using the CT techniques, based on mathematical processing of millions of LOR to generate a computed tomogram of the PET tracer distribution. In a different approach, known as *time of flight* method, measuring the difference in arrival time

of the two annihilation photons at the opposite detectors helps to determine the exact location *d* of the annihilation event along the LOR.

Positron Range and Noncolinearity

Determining the exact LOR along which a positron emitting radionuclide can be found is one of the major factors that determine the spatial resolution of a PET scanner. *Positron range* and *noncolinearity* are two effects that may lead to errors in determining the LOR.

Positron emitting radionuclides differ in the energy of emitted positrons. For example, the energy of positrons emitted by ^{18}F (E_{max} = 0.63 MeV) is almost one-fifth that of a positron emitted by ^{62}Cu (E_{max} = 2.93 MeV). The positron range is the direct distance traveled by the positron from the decaying atom to the exact location of the annihilation event. The positron range is a function of the energy of positron (Fig. 6.5). The mean positron range may vary from a fraction of a millimeter to 4–6 mm, depending on the radionuclide. The error due to the positron range may be significant and, therefore, this range limits the ultimate resolution attainable by PET. It is very important to appreciate the fact that the SPECT technique inherently offers no limitation in spatial resolution due to photon energy, while the PET technique has a theoretical limit in terms of spatial resolution.

In contrast to the positron range, noncolinearity is independent of the positron emitting radionuclide. The

positron and electron are not exactly at rest when the annihilation occurs. As a result, the two annihilation photons differ in their momentum, and are not emitted exactly at 180° apart (they may be emitted with a distribution of angles around 180° (typically ±0.25°)). For a given PET scanner with diameter *D*, this blurring effect, due to noncolinearity (Δ_{nc}), can be estimated as follows:

$$\Delta_{nc} = 0.0022 \times D \text{ (in mm)} \qquad (6.10)$$

With most clinical PET scanners that have a ring diameter of approximately 80 cm, the blurring due to a noncolinearity error may be 1.76 mm. However, in MicroPET, this effect is somewhat less significant.

Coincidence Event Types

A *true coincidence* is the simultaneous interaction of a pair of photons (511 keV) resulting from the annihilation of a positron-eletron pair (Fig. 6.8). A *random coincidence* occurs when two 511-keV photons from separate annihilation events, that occurred as a result of the decay of different atoms, strike the opposite detectors, simultaneously. In the tissue, the 511-keV photons undergo scatter and lose some energy. A *scatter coincidence* occurs when one or both of the 511-keV photons from a single annihilation event are scattered, but detected, simultaneously, by the opposite detectors. The total number of events (true, random, and scatter) detected by the coincidence circuit in a PET scanner is referred to as *prompt coincidences*. Also, when 511-keV photons or the scattered photons are detected, they are referred to as a "singles." Since photons travel at the speed of light (30 cm ns⁻¹), the detection times of a pair of photons by the coincidence circuit can be between 2 and 3 ns. Typically, a coincidence timing window (τ) of 6–12 ns is used to account for statistical fluctuations in timing the detection events.

6.3.2.2 Pet Scanner Design

Since the early 1970s, several different PET detector configurations have been developed. In most dedicated PET scanners, pixilated or multicrystal detectors are arranged in rings or polygonal arrays completely encircling the patient. In addition, two or three planar large-area detectors (as in Anger camera) are also used to configure the PET scanner. The majority of current
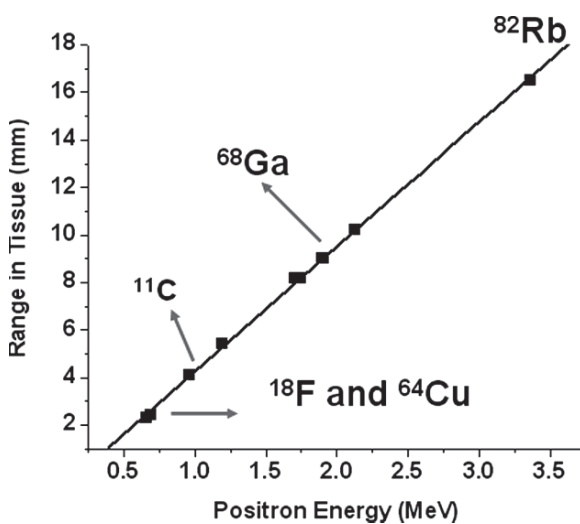

Fig. 6.5 The positron range in tissue as a function of positron energy

Fig. 6.6 The typical PET scanner with ring detector configuration

clinical PET and MicroPET scanners, however, are based on the full-ring configuration (Fig. 6.6). Scintillation crystals coupled to PMTs are used as detectors. Compared to full-ring detectors, the efficiency of other detector configurations for coincidence detection is significantly poor (<30%). A PET scanner typically consists of several components:

- Detector consisting of a scintillator coupled to PMTs
- Collimator
- Signal processing electronics
- Coincidence circuit
- Data-acquisition computer
- Reconstruction, display, and image analysis systems

The basic principles of a PET detector and collimation are discussed below. The electronics associated with the signal processing and the computer hardware needed for data acquisition, image processing, etc. are highly technical and are discussed in detail in many other publications (Nutt 2002; Townsend 2008; Seo et al. 2008).

Block Detector

The detectors in a PET scanner perform much more efficiently than those in a gamma camera. The relatively thin NaI(TL) crystal in the gamma camera detects many photons, simultaneously. In contrast, each of the pixilated scintillation crystal elements in the PET scanner detects one photon at a time and, hence, is more efficient. In order to detect the annihilation photons in PET, the scintillator needs be thick and should have a greater stopping power to interact with the 511-keV photons. In addition, the crystals should have relatively good light output and a short time constant to reduce random coincidences and dead time. Compared to the NaI(Tl) crystal, those of BGO or LSO detect significantly more (80%) of the incident 511-keV photons and, therefore, are the most common crystals used in PET scanners. GSO and BaF_2 also have suitable properties for use in PET scanners. The important properties of scintillators used in PET are given in Table 6.2.

In early PET scanners, each scintillation crystal was coupled to a single PMT, and the size of the crystal largely determined the spatial resolution of the PET scanner. Smaller crystals were needed to improve the resolution. Since the size of PMT is relatively large, it was difficult to couple one PMT for each of the small crystals. In the 1980s, a multicrystal, two-dimensional BGO *block detector* system was developed (Nutt 2002). The majority of dedicated clinical PET scanners in use today are based on the block detector design. A schematic of the block detector is shown in Fig. 6.7.

A block of scintillation detectors is made by segmenting (cutting or channeling) a relatively large block of crystal (typically, 4 × 4 in area and 3 cm deep) into an 8 × 8 or 6 × 6 array (Fig. 6.7). The channels are filled with a light-reflective material to prevent conduction of light from each crystal element to the next in the block. The scintillator block is then coupled to four PMTs and requires a high voltage (1,600–1,800 V) supply. Most PET scanners consist of 144–288 block detectors and contain 10,000–20,000 detector elements.

An alternative to the block detector design is the pixelated detector matrix, wherein individual small-area detector elements (typically 4 × 6 mm in area and 20 mm in depth) are fixed onto a continuous light guide, backed by a close-packed array of PMTs. In order to reduce the depth-of-interaction effect and improve the resolution, a combination of two crystals such as BGO and LSO, known as *phoswich*, has been developed, but not yet used, routinely, in PET scanners.
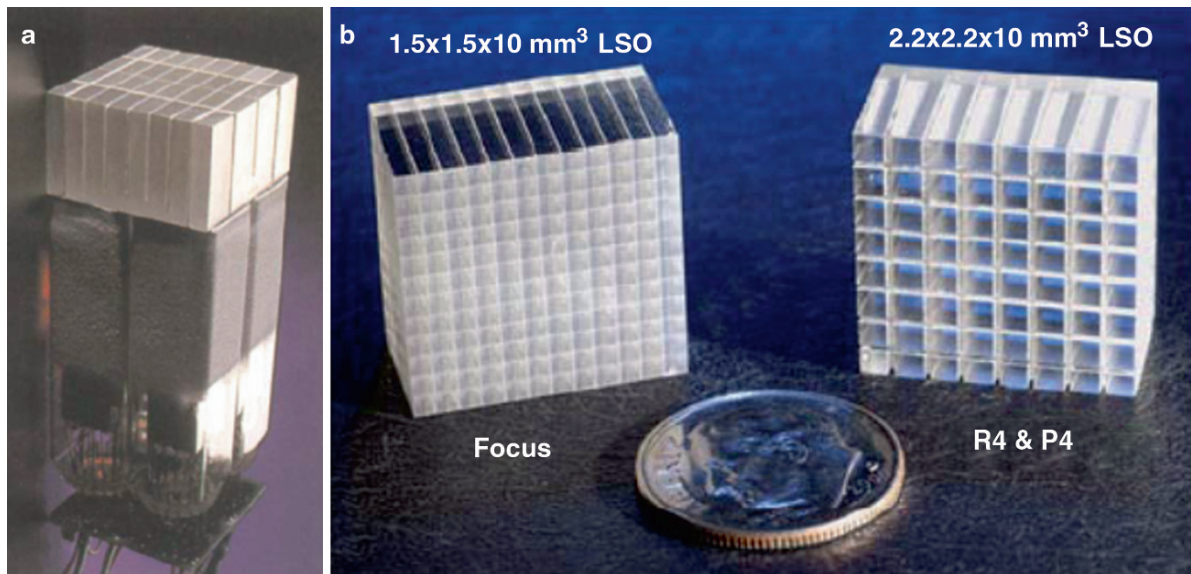
Fig. 6.7 The "block" detector (**a**), and Crystal arrays (**b**) used in the construction of microPET scanners (Levin 2005)

Collimation in PET

There are two kinds of collimation used in PET: one to direct the photons to the detector and the other to select the detected events. Thick lead rings are used to define the external axial FOV, while thin lead or tungsten rings (1–5 mm thick) (usually referred to as septa) are employed to define the individual imaging planes. These septa can be positioned to define the slices during 2D PET studies, but can be retracted during 3D PET acquisition, to increase sensitivity.

The electronic circuit of ACD provides the *electronic collimation* by selecting only those counts that are simultaneously detected by the opposite detectors, during the coincidence timing window. Typically, electronic collimation selects only 1% of the singles as prompt events for further processing, while the remaining 99% are rejected.

6.3.2.3   PET Data Acquisition

Most PET scanners have a data-acquisition computer system (DACS), which generally requires very large random access memory, approximately 500–1,000 mb. Reconstructing PET images is a very computation-intense task and, therefore, special purpose computers, called *array processors*, are used.

In order to obtain an in vivo PET image of a radiotracer distribution, the data acquisition involves obtaining two different scans; a transmission and emission scan, while the patient is in the scanner. In addition, two other scans, called *blank scan* and *normalization scan*, are necessary to process and reformat the PET projection data into a quantitative PET scan, with multiple slices.

Transmission Scan

In order to obtain a true quantitative PET image, the emission scan must be corrected for the attenuation of a pair of coincidence photons within the body. *A transmission scan*, in PET, is usually performed to correct for attenuation of the 511-keV photons in the body. With the object in the FOV, a transmission scan is performed using an external (transmission) rod source of activity or a CT scan. The probability of attenuation for each LOR can be determined by comparing the count rate from the transmission source, while the patient is in the FOV, with the unattenuated count rate from the same transmission source, when the patient is not in the FOV (referred to as *blank scan*).

With older PET scanners and several MicroPET devices, a transmission scan is first obtained by using external rod sources of radiation. The most common rod source is based on long-lived ^{68}Ge ($T_{1/2}$ = 270 days),

which decays by EC to ^{68}Ga that decays by emitting a positron. To improve counting statistics, some clinical PET scanners use ^{137}Cs ($T_{\frac{1}{2}}$ = 30.1 year), which emits a 662-keV gamma photon some MicroPET scanners use ^{57}Co ($T_{\frac{1}{2}}$ = 270 days), which emits a 120-keV gamma photon. In either case, the attenuation of 511-keV photons is estimated on the basis of the energy of photons used for the attenuation correction. Typically, transmission scans using rod sources ^{68}Ge or ^{137}Cs are performed prior to the administration of PET radiotracer. A good-quality transmission scan generally takes 20–30 min.

A blank scan (with no object in the FOV) must be completely noise free and is generally performed for 1 h or, at least 10 times the duration for which the emission scan is obtained. The blank scan is obtained using a rod source or CT scan depending on the technique used for the attenuation correction.

With the current PET/CT scanners (Fig. 6.8 and Table 6.4), the most common method for attenuation correction is based on the CT scan. A nondiagnostic CT scan can be used as a transmission scan. Since the CT scan is based on lower energy (~60-keV) X-ray photons, the CT scan can be performed either before or after the administration of a PET radiotracer. In addition, a CT scan for attenuation correction takes only 0.5–2 min.

Emission Scan

2D Vs. 3D PET

Many of the current PET or PET/CT scanners allow the scanner to perform both 2D and 3D imaging. PET scanners that do not have septa always work in the 3D mode only. In the 2D mode, the scanner is relatively insensitive to the scattered radiation and generally considered more quantitative than 3D imaging. In the 3D mode, the efficiency of detection increases by about 5 times, for unscattered photons and by about 20 times, for the scattered photons. Even though the scattered fraction is much higher in the 3D mode, with appropriate scatter correction algorithms there may not be any significant losses in spatial resolution. Three-dimensional imaging is recommended when the injected dose is suboptimal or delayed imaging is preferable to obtain improved contrast. With recent improvements in the 3D reconstruction and image data correcting, most commercial PET scanners are designed to optimize in the 3D acquisition.

PET Imaging Modes

Following the administration of a PET radiotracer into a subject, imaging can be performed in three different modes.

A *dynamic emission scan* is used to obtain PET images in order to study the time–activity distribution of a radiotracer in a specific tissue or organ of interest. Dynamic scans are performed using a series of imaging frames, which get longer as the study progresses. Measurement of blood flow and receptor imaging studies are often performed using dynamic scans. These studies, however, may require arterial or venous sampling to provide an *input function* to estimate quantitative parameters, based on pharmacokinetic modeling of radiotracer distribution.

A *static emission scan* is normally obtained only when the radiotracer distribution is fairly stable or reaches an equilibrium state. The static scan is acquired in a single frame, and it is assumed that the tracer concentration in a given tissue is constant, except for the

GE Medical Systems

Siemens/CTI

Philips

Fig. 6.8 PET/CT scanners

Table 6.4   Commercially available PET/CT systems[*]

	GE Healthcare	Siemens Healthcare	Philips Healthcare
Models	Discovery PET/CT 690	Biograph mCT	Gemini TF Big Bore (PET/CT)
	Discovery PET/CT 600	Biograph TruePoint	Gemini TF 64 (PET/CT)
	Discovery PET/CT STE16		Gemini TF 16 (PET/CT)
	Discovery PET/CT ST4		Gemini GXL 16 (PET/CT)
Number of detectors	24 rings	192	28 Pixelar Modules
Number of image planes	47	109	45 or 90
Plane spacing	3.27 mm	2 mm	2 or 4 mm
Number of crystals	12,288 – 13,440	32,448	28,366; 17,864 (GXL 16)
Number of PMTs	256 – 280		
Ring diameter	81 or 88.6 cm	84.2 cm	90 cm
Physical Axial FOW, cm	15.7 cm	21.6 cm	18. cm
Detector material	BGO	LSO	LYSO or Zr:GSO
Crystal size, mm	$4.7 \times 6.3 \times 30$	$4 \times 4 \times 20$	$4 \times 4 \times 22$
	$6.3 \times 6.3 \times 30$ (ST4)		$4 \times 6 \times 30$ (GXL 16)
PET Performance	**For Discovery PET/CT 690**	**For Biograph mCT**	**For Gemini TF Bigbore**
System sensitivity, 3D	76 kcps @ 15 KBq/mL	175 kcps ≤@ 28 KBq/cc (mCT)	94 kcps @14 KBq/mL
			And 220 kcps with TOF
Axial resolution at 10 cm, 3D	5.6 mm	5.5 mm	5.2 mm
Transverse resolution at 10 cm	5.6 mm	4.8 – 4.9 mm	5.1 – 5.2 mm or 6.0 mm (GXL 16)

[*] The data in this table was based on PET/CT systems comparison chart in Imaging Technology News, June 2009

Note: Two PET cameras (no CT) are also available for clinical use: Attrius™ (by Positron) and NeuroPET (by PhotoDetection Systems Inc)

physical decay. The routine FDG-PET scans are performed approximately 1 h post administration of the dose are designed to measure the glucose metabolism in the brain, the heart, and the tumor.

Whole-body emission scan represents a series of static scans performed at different segments or portions of the whole body. The studies are performed in several bed positions by acquiring a static scan for a specific time and then moving the patient (the bed) by a distance that is less than the axial FOV. Most clinical PET scanners have a FOV of 15–20 cm. Typically, five to seven bed positions, each requiring 3–5 min, will complete a whole-body emission scan from head to midthighs in 15–35 min. The data collected at each bed position are subsequently reconstructed into a whole-body volume and can be reoriented into *transaxial*, *coronal*, and *sagittal* views.

6.3.2.4   PET Image Data Correction

In order to produce a quantitative PET image of the radiotracer uptake and localization in various organs and/or tissues, a number of corrections need to be applied to the raw emission scan data, which usually are histogrammed into a 2D matrix and provided as a

sinogram. In general, the following steps are involved in the generation of a PET image. The sequence of steps 1–3, however, may vary depending on the data-processing software.

1. The emission scan (the emission sinogram) is corrected for random coincidences, scatter, and dead time.
2. An attenuation correction is then applied to the corrected emission sonogram, using the transmission scan (transmission sonogram) and the blank scan.
3. The detector normalization corrections are then applied to the attenuation-corrected PET scan.
4. Finally, the attenuation-corrected PET data is reconstructed to generate a quantitative PET image on the basis of the filtered back projection (FBP) technique or iterative reconstruction algorithms.

Random and Scatter Coincidence Correction

As discussed earlier, the prompt count rate or the measured count rate (N) includes, the true (T), random (R), and scattered (S) counts. Therefore, to obtain the true count rate associated with any LOR, the noise due to

random and scatter counts must be removed from the measured count rate to preserve the image contrast, improve quantitation, and prevent artifacts in the final PET image.

$$T = N - R - S \qquad (6.11)$$

In clinical brain PET studies, the ratio of the randoms to true count rate may only be <0.2, but this ratio may even be >1 for whole-body imaging. In general, the random count rate increases with increasing activities in the FOV and also with increases in the duration of the coincidence timing window (τ). If the counting rates for the two detectors in the coincidence circuit are C_{s1} and C_{s2}, then the random count rate R for these detectors is given by

$$R = 2\tau \, C_{sl} \, C_{s2} \qquad (6.12)$$

In general, the randoms can be decreased by using thick septa in the 2D mode. Also, by using faster scintillators, such as LSO, one can use a shorter timing window. To correct for randoms, the count rate is first estimated and then subtracted from each point in the sinogram. As shown in the above equation, on the basis of a single rate for each detector and the timing window, one can estimate the random count rate. Another approach is to use two timing windows, one for prompt counts and another that is delayed in time, such that the detector pair cannot measure any true coincidences.

In contrast to the randoms, the scatter coincidence count rate is independent of both the activity in the FOV and the coincidence timing window. Since the scattered photons can only be identified on the basis of the energy of scattered photon, correction for scatter is probably the most difficult to achieve, in PET. More specifically, because most PET scanners operate with a relatively large energy window between 350 and 650, it is difficult to separate scatter events from the primary, unscattered photons. Two-dimensional PET acquisition is the best way to reduce scatter since the thick septa absorb some of the scattered photons. The scattered fraction in 2D brain images may be <0.2, and this fraction may increase up to 0.4. Compared to lead, tungsten septa may help reduce scatter significantly. The 3D PET significantly increases the contribution of scatter events even in brain imaging studies. Since the

scatter increases with depth, scatter correction, however, may be of less importance in MicroPET studies of rodents.

Several scatter correction methods, based on analytical, dual-energy window, and simulation methods, have been developed. The discussion of these methods is given in detail in several other publications. Since scatter and attenuation are one and the same phenomenon, scatter can be estimated on the basis of emission data and the attenuation map. Scatter can then be simulated using analytical models or Monte Carlo simulation techniques.

Dead Time Correction

Each detector element in the PET scanner can record only one photon at a time. If another photon interacts with the crystal, while the crystal is still scintillating due to the prior interaction, both the energy and position of both photons will be incorrect. The minimum time needed to process each interaction is about one microsecond (1,000 ns) with BGO and 200 ns with LSO detectors. If the singles count rate is several hundred thousand counts per second, the detector's linear response will be compromised, significantly. Dead time represents the time during which the detector is unavailable to respond to the photon interaction. This parameter characterizes the counting behavior of the system at high count rates.

At low activity concentrations, the measured count rate (cps) follows the ideal linear response. However, as the activity concentration is increased, the observed count rate significantly decreases, depending on the dead time characteristics of the detector system. The most common way to characterize dead time is to fit the scanner response (measured count rate) using either a paralyzable or nonparalyzable dead time model. The paralyzable dead time model predicts that at higher concentrations, there is a gradual and significant decrease in the measured count rate, whereas the nonparalyzable dead time model predicts that at higher activities, the measured count rate gradually increases, but does not represent a linear response. Another problem associated with the dead time limitation is that, at higher activity concentrations, pulse pile-up can become a limiting factor and may contribute to degradation in resolution, and may even introduce artifacts.

Attenuation Correction

As discussed earlier, attenuation and scatter are manifestations of the same physical process. Correction for attenuation involves first removing the scattered events from LORs and then correcting each LOR for the fraction of events that were attenuated from that LOR. The problem of correcting for attenuation in the body is to determine the probability of attenuation for all sources lying along a particular LOR. The measurement of attenuation in PET is completely independent of the isotope distribution, and the location of the annihilation event along the LOR is given by

$$\text{Attenuation} = e^{-\mu d_1 + \mu d_2} = e^{-\mu D} \qquad (6.13)$$

For simple extension of the above equation can be made to a case of nonuniform attenuation. For example, μ changes along the LOR as the photon passes through different tissues, such as normal tissue, fat, or bone.

$$A = e^{-\int_0^D \mu(l)dt} \qquad (6.14)$$

For a patient, the above equation can be used to obtain a measure of the attenuation of 511-keV photons for a specific section or the whole body by obtaining a transmission scan.

The measured attenuation matrix as a ratio sinogram $R(r, \beta)$ is created by dividing the blank scan sinogram $B(r, \beta)$ by the transmission scan sinogram $T(r, \beta)$. The natural logarithm of this ratio sinogram will result in an attenuation sinogram $A(r, \beta)$ as shown by the following equations:

$$R(r, \beta) = \frac{B(r, \beta)}{T(r, \beta)} \qquad (6.15)$$

$$A(r, \beta) = \ln\left(\frac{B(r, \beta)}{T(r, \beta)}\right) \qquad (6.16)$$

The attenuation correction of the PET emission data is performed by multiplying the emission sinogram with the attenuation sinogram. This operation is performed on every element of the sinogram.

When a CT scan is used for the attenuation correction, the CT images are normally calibrated in Hounsfield units and must be converted to μ values. These μ values, based on low-energy X-ray photons, do not scale linearly with the 511-keV annihilation photons. In order to deal with these problems, the CT images are segmented into a discrete set of tissue types, which can be treated by applying an empirical scaling factor that scales the corresponding voxels to a μ value approximate for 511-keV photons.

As an alternative to measured attenuation correction methods, calculated attenuation methods have been developed, which assume a regular geometric body outline and constant density. While these methods may be applicable for brain PET studies, they introduce significant artifacts, when applied to whole-body PET imaging studies.

Normalization

The thousands of detectors in a PET scanner do not necessarily respond uniformly to a given number of incident photons, either because of the relative efficiencies of the individual detectors, or because of the geometric arrangement of these detectors. As a result, there are slight variations in the coincidence detection efficiency or the sensitivity between different LORs in the system, for the same activity. Therefore, the entire projection data needs to be corrected (or normalized) for the differences in the detectors, response. This normalization corrects each individual LOR with a multiplication factor that compensates for these nonuniformities.

The direct method of determining the normalization correction factors is based on a direct measurement, in which a low-activity source of a positron emitter (such as ^{68}Ge) is used to acquire a scan (similar to a blank scan) in the 2D mode. Alternatively, a uniform cylinder of a positron-emitting radionuclide can be scanned and the data, thus, acquired, analytically corrected for attenuation. It is important to acquire enough counts per LOR to provide a good estimate of the efficiencies with minimum statistical noise.

For example, in order to achieve 1% accuracy in normalization for 10^6 LORs, it is necessary to acquire 10^{10} counts. If the radioactive source generates 25,000 cps, it would take 111.2 h (4.63 days) to acquire a normalization scan. For a 3D PET acquisition, the requirements for normalization are much more complicated.

An alternative method of generating normalization correction factors uses a combination of measurement and mathematical techniques. With current PET scanners, normalization scans are usually performed once a month, or every alternate month.

6.3.2.5 PET Image Reconstruction

The raw projection data of a PET emission scan only defines the location of the positron-emitting atom to within a line across the object. PET scanners allow the data to be collected from many different angles around the object. The main goal of the image reconstruction process is to provide quantitatively accurate cross-sectional images of the radiotracer distribution, in vivo, with the highest signal-to-noise ratio, and spatial resolution, using the emission scan data, and the mathematical algorithms of the CT. Basically, the reconstruction algorithms used in PET are classified into two different approaches: image reconstruction by filtered backprojection (FBP) and iterative reconstruction.

FBP involves two principal steps: filtering the projection data and then backprojecting them to create the reconstructed image. A mathematical tool, known as *Fourier transform*, is used in the FBP method to express a function $f(x)$ in terms of its spatial frequencies, rather than in terms of its magnitude as a function of its position (providing a mathematical description of these methods is beyond the scope of this chapter). One of the major limitations of the standard FBP method, used in tomography, is statistical noise. To control the noise and preserve the spatial resolution, an appropriate postreconstruction smoothing filter (such as Ramp, Shepp-Logan, Hann, Butterworth) needs to be applied.

Iterative reconstruction methods are computationally more intense than FBP and especially useful in reconstructing images with relatively poor counts. This method basically involves making an initial guess or estimates of the image distribution $a^*(x, y)$, comparing the forward projection sinogram of these estimates to the measured projection data sonogram, and, on the basis of the difference between these sinograms, revising the estimates. The process or the iterations continue until there is a convergence between the estimated and the measured sinogram. The iterative reconstruction algorithms allow for the incorporation of realistic modeling of the data acquisition process (including effects of attenuation and scatter) and modeling of statistical noise. The maximum-likelihood expectation maximization (ML-EM) algorithm is the most extensively studied iterative algorithm that seeks to maximize the Poisson likelihood target function. When the projection data are organized into *ordered subsets* (OS), the OSEM algorithm is used to accelerate the iterative computational process. Currently, OSEM is the most widely used iterative reconstruction algorithm used in 2D PET. Especially in the reconstruction of lower-count whole-body imaging studies, OSEM is preferable to the standard FBP.

As discussed earlier, 3D PET acquisitions increase scanner sensitivity, significantly. As a result, the 3D brain PET image reconstruction may be quite satisfactory with FBP methods. A technique known as *Fourier rebinning* (FORE) algorithm has been developed, which is appropriate for large 3D data sets, such as dynamic PET studies involving many frames. The gold standard for the analytic 3D image reconstruction, however, is the *3D reprojection* algorithm (3DRP), which is based on the FBP method. Whole-body 3D PET imaging with ^{11}C, ^{64}Cu, and ^{124}I radionuclides may be optimal to reconstruct on the basis of iterative methods although, the computational complexity increases, dramatically. The row-action maximization-likelihood (RAMLA) algorithm, related to the OSEM algorithm, has been developed for direct reconstruction of 3D PET images. With this method, the reconstruction times are fairly long by clinical standards, but it does provide reliable results.

6.3.2.6 PET Scanner Performance

Since the commercial PET scanners may have significant variations in the overall design of the scanner, certain parameters that determine the performance of the scanner must be determined using standard testing procedures. The National Electrical Manufacturers Association (NEMA) performance protocols describe a series of explicitly defined testing methods to evaluate PET and SPECT scanner performance. In order to illustrate the differences in scanner performance of commercial PET scanners, three scanners are compared in Table 6.5 (Humm et al 2003).

The spatial resolution (SR) of a system is a parameter that indicates the system's ability to distinguish between two points of radioactivity in an image and is measured in the transverse slice in two directions, radial and tangential, and in the axial direction. Generally, SR is measured at two axial positions: at the center of the axial FOV and a position one-fourth of the axial FOV from the center. SR is usually expressed as the FWHM and is usually specified separately in transaxial and axial directions.

Table 6.5 Comparison of PET scanners and scanner performance

Performance characteristic	CTI ECAT Exact (922)	HR$^+$	GE discovery LS PET/CT
Crystal	BGO	BGO	BGO
Patient Port (cm)	56.2	56.2	59
Total no. of blocks	144	288	168
No. of crystal detectors/block	8 × 8	8 × 8	6 × 6
Crystal size, transaxial, (mm)	6.39	4.39	4.0
Axial	6.39	4.05	8.0
Radial	20	30.0	30.0
Transaxial FOW (cm)	58.5	58.5	55
Axial FOW	16.2	15.5	15.2
Slice thickness (mm)	3.375	2.46	4.25
No. of slices	47	63	35
Sensitivity 2D trues, NEMA 94 phantom (kcps μCi^{-1}cc^{-1})	180	200	146
Sensitivity 2D trues + Scatter	214	244	159
Sensitivity 3D trues	780	900	838
Sensitivity 3D trues + scatter	1,218	1,406	1,297
2D axial resolution (mm)			
FWHM at 0 cm	4.5	4.2	4.0
FWHM at 10 cm	5.9	5.0	5.4
FWHM at 20 cm	N/A	6.8	6.6
3D axial resolution (mm)			
FWHM at 0 cm	4.6	3.5	6.0
FWHM at 10 cm	6.5	5.3	6.3
FWHM at 20 cm	N/A	7.8	6.6
2D transaxial resolution (mm)			
FWHM at 0 cm	6.0	4.6	4.8
FWHM at 10 cm	6.7	5.4	5.4
FWHM at 20 cm	N/A	7.9	6.2
3D transaxial resolution (mm)			
FWHM at 0 cm	6.0	4.6	4.8
FWHM at 10 cm	6.7	5.4	5.4
FWHM at 20 cm	N/A	7.8	6.2

Table modified from Humm et al. 2003

Energy resolution is the precision with which the PET scanner can measure the energy of incident photons (511 keV). It may be defined on the basis of either *single events* or *coincidence events* determined in air or in a scattering medium.

Count rate (counts per second, cps) performance refers to the finite time the system takes to process the detected photons. Count rate curves, as a function of increasing amounts of activity concentration (kBq cc^{-1}), can be generated for true (unscattered plus scattered) coincidences, as well as random and multiple coincidences. For most scanners, the true coincidence count rate is linear for activity (for ^{18}F) concentrations of <100 kBq cc^{-1}).

The sensitivity performance parameter of a scanner represents its ability to detect annihilation radiation, and the system sensitivity is considered the most important parameter since it determines the image quality per unit scan time or, alternatively, the time required to perform a whole-body scan (Humm et al. 2003). The absolute sensitivity of a scanner is expressed as the rate of detected coincidence events in counts per second (cps) for a given source strength. For a clinical scanner, the sensitivity depends principally on three main factors: the detector material, the axial field of view of the camera, and the acquisition mode (2D or 3D). With 3D, there is a marked increase in scatter and random events. The scatter fraction, defined as the
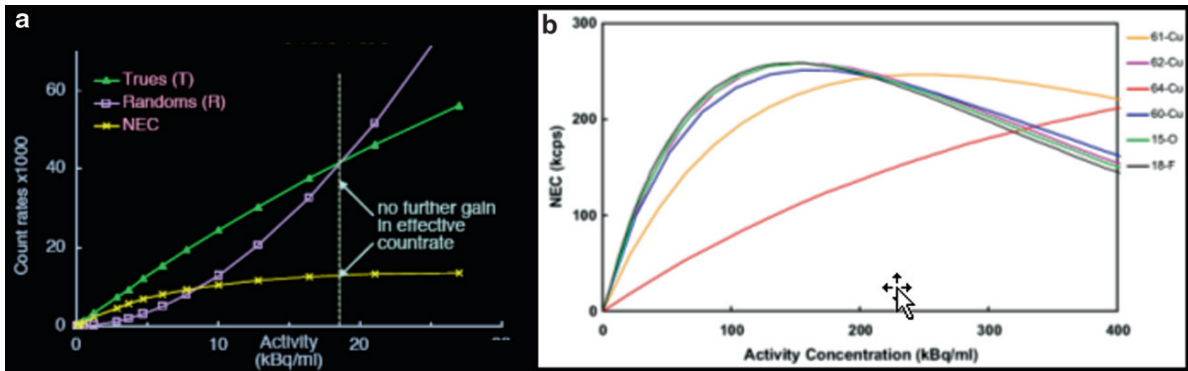
Fig. 6.9 Count rate with a PET scanner as a function of positron radionuclide concentration (**a**). Specifically, changes in NEC (**b**)

ratio of scattered events to total events, is independent of the activity within the patient, but is dependent on the patient's girth.

In order to provide a physical measure with which to assess PET camera performance, the concept of noise-equivalent count rate (NEC) was introduced. The NEC is defined as

$$NEC = T^2 / (T + R + 2S)$$

where T is the true coincidence rate, R is the random coincidence, rate, and S is the scatter coincidence rate. T, R, and NEC as a function of activity concentration and variations in NEC as a function of activity concentrations for different PET radionuclides are shown in Fig. 6.9. It is important to recognize that for a positron emitter such as ^{64}Cu with <20% positron emission, NEC reaches the maximum value at 4–5 times the activity concentration generally needed for ^{18}F or ^{68}Ga.

6.3.3 Small-Animal Imaging Systems

Clinical imaging systems have relatively coarse spatial resolution that is insufficient for imaging structures in small animals, which requires high spatial resolution (on the order of 1–2 mm or better). To achieve this, scanners must use higher resolution detectors and achieve finer spatial sampling (e.g., using smaller detector elements) while maintaining as high a sensitivity as possible (Rowland and Cherry 2008). In the late 1990s, several groups began making significant progress in the development of high-resolution small-animal PET and SPECT scanners for the study of molecular imaging techniques in several rodent disease models (Chatziioannou 2002; Cherry 2004; Meikle et al 2005; Beekman et al 2005; Rowland and Cherry 2008). For both clinical and animal scanners, for a given size of the detector and field of view (FOV), there is a tradeoff between the resolution and the sensitivity, as shown in Table 6.6. For example, microPET scanners typically have at least 10 times greater sensitivity, than the microSPECT scanners. Some of the commercial animal scanners are listed in Table 6.7.

The first animal PET tomographs designed for imaging nonhuman subjects were the SHR-2000 developed by Hamamatsu (Japan) and the ECAT-713 developed by CTI PET Systems Inc. (Knoxville, TN). The first PET system developed specifically for rodent imaging was the RATPET scanner developed by Hammersmith Hospital in collaboration with CTI PET Systems Inc. The measured spatial resolution of this scanner was found to be 2.4 mm transaxially by 4.6 mm axially, giving a volumetric resolution of 0.026 cc. The 3D data acquisition of that system and the high detector efficiency provided a relatively high absolute sensitivity of 4.3%. Based on the UCLA MicroPET system, Concorde

Table 6.6 General scanncer performance characteristics compared between clinical and preclinical cameras.

	Clinical PET	Preclinical PET	Clinical SPECT	Preclinical SPECT
Sensitivity (%)	1–3	~2–4	0.01–0.03	~0.3
Resolution (mm)	~5	1–2	~10	0.5–2
FOV (cm)	~50	~7	~50	~8

Adapted from Jansen and Vanderhevden (2007)

Table 6.7 MicroPET and MicroSPECT Commercial Scanners

Company	MicroPET	MicroSPECT/CT
GE Healthcare	**Explore Vista PET** PET is based on LSO and LYSO coupled to APD detectors	**Explore speCZT** Detector: pixilated Full Ring CZT with 8 slit collimator Resolution: 0.5 – 1.8 mm
	Options of 3 different axial fields of view, 3.75, 7.5, and 11.25 cm	Axial FOV: 34 mm
		Transaxial FOV: 37 mm
	Triumph, PET/SPECT/CT Multi-modality system	
Siemens	**Inveon MicroPET** based on LSO 1.59 × 1.59 × 10 cm pixel	**Inveon MicroSPECT/CT** NaI(Tl) detectors with Two Multi-pinhole providing 0.5 – 1.0 mm resolution
	12 cm Bore 12.7 cm Axial extent 64 Detector blocks	Four Single Pinhole providing 0.5 – 3.0 mm resolution
	Inveon, PET/SPECT/CT Multi-modality system	
BioScan	**NanoPET/CT** Bore size: 15 cm Transaxial FOV: 94 – 125 mm Axial FOV up to 30 cm Detector: LYSO (39,780 crystals) Resolution: <1.2 mm	**NanoSPECT/CT** Multi-pinhole SPECT NaI(Tl) detectors Axial FOV up to 27 cm Resolution: up to 0.4 mm
MILabs		**U-SPECT/CT** Micro-pinhole technology NaI(Tl) detectors Resolution: 0.35 mm in 3D

Microsystems Inc. introduced the commercial micro-PET systems for primates (P4) and rodents (R4) based on a new generation of electronics designed to take full advantage of the fast decay time of the LSO detector. Since then, several other scintillator/PMT-based animal PET systems have been introduced.

In the last five years, there has been a significant improvement in the design of microSPECT systems for small-animal imaging studies. Because in microSPECT devices the required FOV is very small it is possible to achieve a much higher resolution than with clinical SPECT scanners. A number of commercial systems (Table 6.7) are now available with a spatial resolution <2 mm. Some of these devices even report submillimeter resolution for specific organs and tissues that may accumulate significant amounts of radioactivity. For most of the animal SPECT scanners, the detection efficiency for high-energy photons (<200 keV) is <0.1%. As a result, it is necessary to inject radiotracers at dose levels that are hundreds of times more than the clinical doses. Many of these devices are based on a wide variety of detection instrumentation, including conventional scintillation cameras, pixelated detectors with PSPMTs or APDs, and semiconductor gamma cameras.

References

Beekman FJ, van der Have F, Vastenhouw B, et al. (2005) U-SPECT-I: a novel system for submillimeter-resolution tomography with radiolabelled molecules in mice. J Nucl Med 46:1194–1200

Chatziioannou AF (2002) PET scanners dedicated to molecular imaging of small animal models. Mol Imaging Biol 4(1):47–63

Cherry SR (2004) In vivo molecular and genomic imaging: new challenges for imaging physics. Phys Med Biol 49:R13–R48

Darambara DG, Todd-Pokropek A (2002) Solid state detectors in nuclear medicine. Q J Nucl Med 46:3–7

Daube-Witherspoon ME, Karp JS, Casey ME, et al. (2002) PET performance measurements using the NEMA NU 2–2001 Standard. J Nucl Med 43:1398–1409

Humm JL, Rosenfeld A, Del Guerra A (2003) From PET detectors to PET scanners. Eur J Nucl Med Mol Imaging 30:1574–1597

Jansen FP, Vanderheyden J-L (2007) The future of SPECT in a time of PET. Nucl Med Biol 34:733–735

Jaszczak RJ (2006) The early years of single photon emission computed tomography (SPECT): an anthology of selected reminiscences. Phys Med Biol 51:R99–R115

Karakatsanis N, Sakellios N, Tsantilas NX, et al. (2006) Comparative evaluation of two commercial PET scanners, ECAT EXACT HR+ and Biograph 2, using GATE

Levin CS (2005) Primer on molecular imaging technology. Eur J Nucl Med Mol Imaging 32(suppl 2):S325–S345

Madsen MT (2007) Recent advances in SPECT imaging. J Nucl Med 48:661–673

Meikle SR, Kench P, Kassiou M, et al. (2005) Small animal SPECT and its place in the matrix of molecular imaging technologies Phys Med Biol 50:R45–R61

National Electrical Manufacturers Association (2001) NEMA Standards Publication NU 2–2001: Performance measurements of positron emission tomographs. NEMA, Rosslyn, VA

Nutt R (2002) The history of positron emission tomography. Mol Imag Biol 4(1):11–26

Pichler BJ, Wehrl HF, Judenhofer MS (2008) Latest advances in molecular imaging instrumentation. J Nucl Med 49:5s–23s

Rowland DJ, Cherry S (2008) Small-animal preclinical nuclear medicine instrumentation and methodology. Semin Nucl Med 38:209–222

Seo Y, Mari C, Hasegawa B (2008) Technological development and advances in single-photon emission computed tomography/computed tomography. Semin Nucl Med 38:177–198

Townsend DW (2008) Positron emission tomography/computed tomography. Semin Nucl Med 38:152–166

Zaidi H (2006) Recent developments and future trends in nuclear medicine instrumentation. Z Med Phys 16:5–17

Zanzonico P (2004) Positron emission tomography: a review of basic principles, scanner design and performance, and current systems. Semin Nucl Med 34(2):87–111

Chemistry: Basic Principles

The underlying physical laws necessary for the mathematical theory of a large part of physics and the whole of chemistry are thus completely known, and the difficulty is only that the application of these laws leads to equations much too complicated to be soluble.

Paul Dirac

7.1 Chemical Elements

In general, chemistry is the study of matter and energy and the interaction between them. More specifically, chemistry is the study of matter, including its composition, properties, structure, the changes which matter undergoes, and the laws governing those changes. Chemical elements are the building blocks of all types of matter in the universe and, at present, 116 elements are known to exist. In nature, however, only 91 elements have been discovered. Some elements are only present in trace amounts while some are man made or artificially produced. From the point of view of chemistry, the smallest unit of an element is the atom, representing the chemical identity of that element. Among the elements that exist in nature, hydrogen is the lightest ($Z = 1$, $A = 1$) atom, while uranium is the heaviest atom ($Z = 92$, $A = 238$).

Chemical reactions take place between atoms of the same element or atoms of different elements to form molecules of compounds. Chemical interactions involve only the electrons in the outer orbits, while protons and neutrons of an atom do not participate in any chemical reactions. The chemical properties of an element are determined only by the number of electrons in an atom, which is equal to the number of protons in the nucleus (Z).

7.1.1 Chemistry and Radioactivity

Radioactivity is a process which primarily involves the decay of the unstable nucleus of an element, but all the chemical reactions of an element involve the outermost orbital electrons. Atoms of different isotopes of an element, both stable and radioactive, will have a similar chemistry, regardless of the radioactive emissions from an unstable nucleus. Similarly, the chemistry of an atom does not, in any way, affect the radioactive decay characteristics of an atom. In nuclear medicine, *tracer principle* is based on the fact that the chemistry and physiological behavior of radioisotopes of an element are identical to the corresponding naturally occurring stable isotopes of that element. Because, the mass of different isotopes of an element is slightly different, there may be some differences in the chemistry among the isotopes of an element. This effect known as *isotope effect* is only significant if the mass difference is substantial, as in the case of hydrogen isotopes, where the mass difference of the three isotopes is 200–300%. In contrast, the isotopes of iodine have only about 3% difference in their mass.

7.1.2 Periodic Table

The periodic table (Table 3.3) is a listing of the elements in the order of increasing atomic number (Z). More specifically, elements with similar chemical properties are aligned vertically in columns (called *groups* or *families*). It must be noted that in the modern periodic table, this order is based only on the atomic number and not the atomic weight. The horizontal series of elements are referred to as periods; the first two periods are short periods and consist of eight groups, while the remaining periods are called long periods, consisting of 18 groups. The position of an element in the periodic table explains the general chemical behavior of an element.

Most of the elements found in nature are metals and are shown in the periodic table as *alkali metals* (Group-1), *alkaline earth metals*, (Group-2), and *transition metals* including lanthanides and actinides (Groups 3–12). Elements in groups 13–16 are regarded as metals or *metalloids*; elements in Group 17 are known as *halogens*; and elements in Group 18 are known as inert or *noble gases*. Some of the important elements and their radioisotopes, useful for PET and SPECT, are listed in Table 7.1.

7.1.2.1 Electronic Structure of Atom

The atom consists of an extremely dense, small, positively charged nucleus surrounded by a cloud of electrons with small size and mass, each carrying a single negative charge equal but opposite to that of a proton in the nucleus. Because the number of electrons and protons in an atom are the same, the whole atom is electrically neutral. The atomic volume (10^{-8} cm diameter) with the cloud of electrons is significantly larger than the volume of the nucleus (10^{-13} cm diameter). According to Bohr's model of atom, an electron in a hydrogen atom rotates around the nucleus at high speeds in closed circular orbits associated with a characteristic quantum number. The electron, in general, exists in a low energy orbit (*ground state*). Gain or loss of a quantum of energy occurs only when an electron moves from one orbital to another of greater or lesser energy. As a result, an atom can absorb or emit energy in discrete units or quanta.

Table 7.1 Important elements and their useful radioisotopes for PET and SPECT

Element	Atomic number	Stable isotope	Natural abundance (%)	Useful radio-isotopes	Decay mode
Carbon	6	^{12}C	98.9	^{11}C	β$^+$
		^{13}C	1.10	^{14}C	β$^-$
Nitrogen	7	^{14}N	99.634	^{13}N	β$^+$
		^{15}N	0.366		
Oxygen	8	^{16}O	99.762	^{15}O	β$^+$
		^{17}O	0.038		
		^{18}O	0.200		
Fluorine	9	^{19}F	100	^{18}F	β$^+$
Copper	29	^{63}Cu	69.17	^{62}Cu	β$^+$
		^{63}Cu	30.83	^{64}Cu	β$^+$, β$^-$, EC
				^{67}Cu	β$^-$, γ
Gallium	31	^{69}Ga	60.1	^{66}Ga	β$^+$, EC, γ
		^{69}Ga	39.9	^{67}Ga	EC, γ
				^{68}Ga	β$^+$, EC, γ
				^{72}Ga	β$^-$, γ
Bromine	35	^{79}Br	50.69	^{75}Br	β$^+$, EC
		^{81}Br	40.31	^{77}Br	EC, γ
Rubidium	37	^{85}Rb	72.165	^{82}Rb	β$^+$
		^{87}Rb	27.845		
Yttrium	39	^{89}Y	100	^{86}Y	β$^+$, EC, γ
				^{87}Y	EC, γ
Zirconium Technetium	43	–	–	^{94}Tc	β$^+$
				^{99m}Tc	IT, γ
Indium	49	^{113}In	4.3	^{111}In	EC, γ
		^{115}In	95.7		
Iodine	53	^{127}I	100	^{123}I	EC, γ
				^{124}I	β$^+$, EC, γ
				^{131}I	β$^-$, γ

7.1.2.2 Quantum Model of Atom

At first Bohr's model appeared to be very promising. By the mid 1920s, however, it had become apparent that this model needed refinement. The wave mechanics or quantum mechanics developed by Werner Heisenberg, Louis deBroglie, and Edwin Schrodinger finally provided a wave or quantum mechanical description of an atom. According to this model, the electron bound to the nucleus is similar to a standing or stationary wave. The circumference of a particular orbit corresponds to a whole number of wavelengths. Schrodinger's famous wave equation ($H\psi = E\psi$)

describes an electron in an atom, where ψ, called the wave function, is a function of the coordinates (x, y, and z) of the electron's position, in three dimensional space, and H represents a set of mathematical instructions, called an *operator*. When this equation is analyzed, many solutions are found. Each solution consists of a wave function ψ, that is characterized by a particular value of energy, E. A specific wave function for a given electron is often called an *orbital* (an orbital is not a Bohr's orbit). The wave function corresponding to the lowest energy of hydrogen atom is called 1s orbital. The theory of quantum mechanics only provides the probable position of the electrons around the nucleus, but not the electrons motions around the nucleus.

Schrodingr's equation for the hydrogen atom or other multielectron atoms have many solutions with many wave functions or orbitals characterized by a set of quantum numbers (Table 7.2). In order to describe a given electron in atom a set of four quantum numbers are needed. The values and the physical meaning of these quantum numbers can be described as follows:

The *principal quantum number* (n), which can have integral values (such as 1,2,3,4,…,), is related to the size and energy of the orbital. As n increases, the orbital size and the energy increases. The value of n, or the shell number is represented by K, L, M, N,.., (old terminology)

The *angular momentum quantum number* (l), relates to the ellipticity of the orbital or the angular momentum of an electron in a given orbital. It can have integral values of 0 to $n-1$, for each value of n and the value of l determines the shape of the orbital (such as s, p, d, f,...). These orbitals are also called subshells

The *magnetic quantum number* (m_e), which can have integral values between l, and $-l$. including 0. The value of m_e, relates to the orientation in space of the angular momentum associated with the orbital

The *electron spin quantum number* (m_s), which has values of $+\frac{1}{2}$ and $-\frac{1}{2}$. The value of m_s represents the direction of the electron spin

Each electron in an atom has a unique set of quantum numbers. *In a given atom, no two electrons can have the same set of four quantum numbers (n, l, m_e, m_s). This is called Pauli Exclusion Principle*, which can also be stated as follows: *An orbital can hold only two electros, and they must have opposite spins*.

The electrons in atoms other than hydrogen and helium also occupy various energy levels or shells. The maximum number of electrons that can occupy a

Table 7.2 The electron configuration in different energy levels and the possible quantum numbers

Energy level	Principal shell	$2n^2$	Quantum numbers			Symbol	Electrons in each orbital	Explicit symbol
			n	l	m_e			
1	K	2	1	0	0	1s	2	1s
2	L	8	2	0	0	2s	2	
			2	1	0	2p	6	2px
			2	1	1			2py
			2	1	−1			2pz
3	M	18	3	0	0	3s	2	3s
			3	1	0	3p	6	3px
			3	1	1			3py
			3	1	−1			3pz
			3	2	0	3d	10	$3dz^2$
			3	2	1			3dxz
			3	2	−1			3dyz
			3	2	2			$3dx^2-y^2$
			3	2	−2			3dxy
4	N	32				4s	2	
						4d	6	
						4p	10	
						4f	14	
5	O	50				5s	2	
						5p	6	
						5d	10	
						5f	14	
						5g	18	

given energy level or shell (n) is $2n^2$. For example, if $n = 2$, then the total number of electrons in the 2nd shell (L) is eight. The number of orbitals (l) in 2nd shell is two since l can have values of 0 (called s) and 1 (called p). These two orbitals in the 2nd shell are called $2s$ and $2p$. Since the number of electrons in each orbital is $2(2l + 1)$, a $2s$ orbital can hold two electrons while a $2p$ orbital can have six electrons. Further, because m_e can have values between l, and $−l$. including 0, the $2p$ orbital has three orientations in space ($2px$, $2py$, $2pz$), and each one of them, in turn, can only hold a maximum of two electrons (since m_s has only two values $+\frac{1}{2}$ and $\frac{1}{2}$). The permitted values for quantum numbers for the electrons in the 2nd shell are shown in Table 7.3. The electron configuration in different energy levels and the possible quantum numbers are shown in Table 7.4.

Table 7.3 Permitted values of quantum numbers for the 2nd energy level ($n = 2$)[a]

N	2	2	2	2	2	2	2	2
l	0	0	1	1	1	1	1	1
m_e	0	0	−1	0	+1	−1	0	+1
m_s	−½	+½	−½	−½	−½	+½	+½	+½

[a]The second shell can have eight electrons and each vertical set of quantum numbers represents one electron

Table 7.4 Electron configuration of some of the elements

Element	K	L		M			N				O			
	1s	2s	2p	3s	3p	3d	4s	4p	4d	4f	5s	5p	5d	5f
H	1													
He	2													
Li	2	1												
C	2	2	2											
N	2	2	3											
O	2	2	4											
F	2	2	5											
Ne	2	2	6											
Na	2	2	6	1										
K	2	2	6	2	6		1							
Cu	2	2	6	2	6	10	1							
Ga	2	2	6	2	6		2	1						
Kr	2	2	6	2	6	10	2	6						
Rb	2	2	6	2	6	10	2	6			1			
Y	2	2	6	2	6	10	2	6	1		2			
Tc	2	2	6	2	6	10	2	6	5		2			
In	2	2	6	2	6	10	2	6	10		2	1		
I	2	2	6	2	6	10	2	6	10		2	5		
Xe	2	2	6	2	6	10	2	6	10		2	6		

7.1.2.3 Arrangement of Electrons in Orbitals

Since the chemical properties of an element are determined by the electrons, it is important to understand how these electrons are arranged in the orbitals (Fig. 7.1). According to the *Aufbau principle*, as protons are added one by one to the atomic orbitals to build elements, electrons are added one by one to the nucleus to build up the elements. In the ground state, the lowest-energy orbitals contain the electrons. The high-energy orbitals, however, are filled only after the lower-energy orbitals are filled. The various orbitals arranged in order of increasing energy are:

$1s$, $2s$, $2p$, $3s$, $3p$, $4s$, $4p$, $5p$, $6s$, $4f$, $5d$, $6p$, $7s$, $5f$, $6d$.

It is important to note that the $3d$ orbital is not filled until after the $4s$ is filled, the $4d$ until after the $5s$, the $4f$ until after the $6s$, and the $5d$ until the $4f$ orbital is filled. The series of elements in which the d orbital is being filled are called *transition metals*.

In a group of elements ($Z = 57–70$) known as *lanthanides* (elements that are also transition elements), each of the elements differs from the other element only in the number of electrons in the $4f$ orbital, while the $5s$, $5p$, and $6s$ orbital are completely filled. Similarly, in *actinides* ($Z = 89–102$), $5f$ electrons are being filled, while the $6s$, $6p$, and $7s$ orbitals are completely filled.

Pauli exclusion principle requires that only two electrons with opposite spin occupy any given subshell. The *Hund's rule* states that the lowest energy configuration for an atom is the one having the maximum number of unpaired electrons in a particular set of degenerate orbitals (orbitals with the same energy level), such as p, d, and f. The electron configuration of several elements, shown in Table 7.5, clearly illustrates the Hund's rule.

Valence Electrons and Stable Octet

The electrons in the outermost principle quantum level of an atom are known as *valence* electrons and the shell is frequently referred to as *valence shell*. These electrons are the most important elements in chemistry, because they are involved in the formation of *chemical bonds*. The inner electrons are known as *core electrons* and generally do not participate in forming chemical bonds. The elements listed in the same group of the
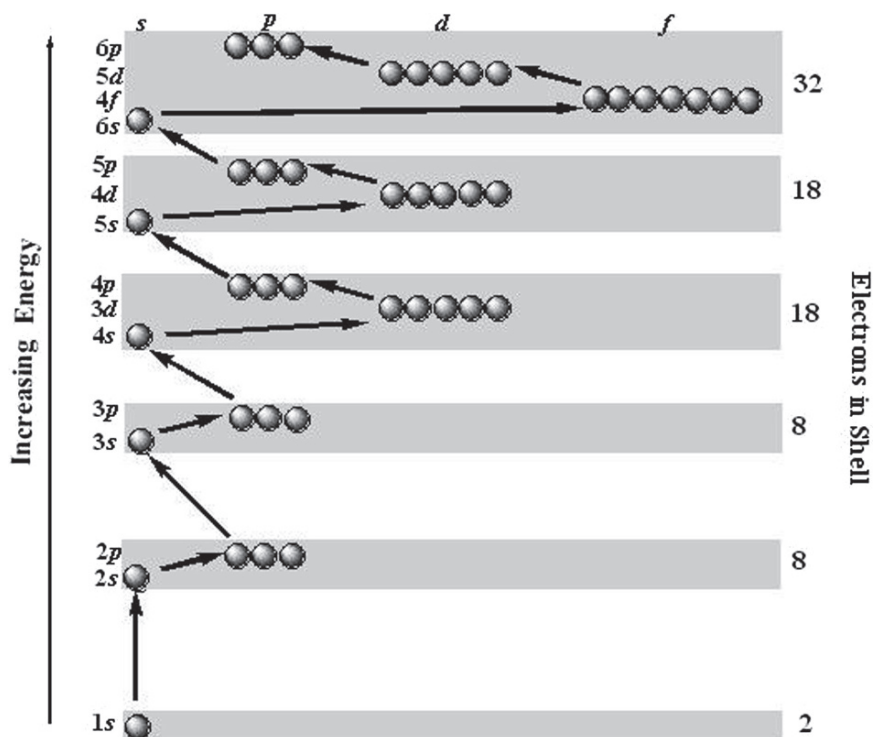
Fig. 7.1 Arrangement of electrons in orbitals. In the ground state, the lowest-energy orbitals contain the electrons. The high-energy orbitals, however, are filled only after the lower-energy orbitals are filled

Table 7.5 Valence electrons of elements in the eight groups of the periodic table

Element	K	L			
	$1s$	$2s$	$2px$	$2py$	$2pz$
H	↑				
He	↑↓				
Li	↑↓	↑			
Be	↑↓	↑↓			
B	↑↓	↑↓	↑		
C	↑↓	↑↓	↑	↑	
N	↑↓	↑↓	↑	↑	↑
O	↑↓	↑↓	↑↓	↑	↑
F	↑↓	↑↓	↑↓	↑↓	↑
Ne	↑↓	↑↓	↑↓	↑↓	↑↓

the *s* and *p* orbitals. Based on this observation, the theory of chemical compound formation postulates that the stable electron configuration for the outer electron shell is eight electrons. More specificall, the *stable octet rule* postulates that compounds are formed between atoms of the same or different elements as a result of the loss, gain or sharing of electrons so that each atom attains a stable octet electron configuration.

The valency of an element is determined by the number of electrons in the outermost shell (Table 7.5) that can participate in a chemical reaction. For example, the valency of hydrogen and fluorine is 1, while the valency for nitrogen is 3 or 5, and 4 for carbon.

periodic table (Table 3.3) have the same electron configuration and therefore, have similar chemical behavior.

The elements listed in Group-18 of the periodic table are known as noble or inert gases because they lack chemical reactivity, in general they form very few chemical compounds. The outer electron configuration for the inert gases (except for He) has eight electrons in

7.1.3 Chemical Bonding

John Dalton was probably the first to recognize that chemical compounds are a collection of atoms. Only in twentieth century, however, was it realized that electrons participate in the bonding of one atom to another atom. The forces that hold the atoms together in compounds

are called *chemical bonds*. The driving force behind the bond formation of any two atoms is the decreased overall energy state of the individual atoms.

7.1.3.1   Ionic or Electrovalent Bonds

Atoms are electrically neutral. An *ion* is an atom or a group of atoms that has a net positive (cation) or negative (anion) charge. The force of attraction between oppositely charged ions is called *ionic or electrovalent bond*. Ionic compounds are formed when a metal reacts with a nonmetal. Alkali and alkaline earth metals have one or two electrons in the outer shell. In order to reach a stable octet electron configuration, they can easily donate the valence electrons and become positively charged ions. Nonmetals such as halogens need only one electron to reach a stable octet configuration and so are willing to receive or gain an electron, and form a negatively charged ion. The *ionic bond* is formed when an atom that looses electrons easily interacts with an atom that has a high affinity for electrons. *The ion pair has lower energy than the separated ions*. For a mole of Na^+ and Cl^- ions, the energy of interaction is $-504\,kJ\,mole^{-1}$.

NaCl, NaF, NaI, CaO, and $CaCl_2$ are all known as ionic compounds or salts. When these compounds are dissolved in water, the ionic compound dissociates resulting in the regeneration of ions. Ionic compounds, however, are very sturdy materials; they have great thermal stability and high melting points. For example, NaCl crystal has a melting point of about 800°C. Ionic compounds conduct electricity in the solid state as well as in liquid state. Solutions of ionic compounds are known as *electrolytes*.

7.1.3.2   Covalent Bond

When atoms of the same element or different elements share a pair of electrons, a *covalent bond* is formed. The covalent bonding results from the mutual attraction of the two nuclei for the shared electron pair. The total energy of the molecule is less than that of the individual atoms. In the *diatomic* H_2 molecule both hydrogen atoms share a pair of electrons so that the $1s$ orbital has the maximum of two electrons needed for stability. Sometimes it is necessary for two atoms to share more than one pair of electrons to reach stable octet configuration. Based on the number of pairs of electrons shared,

covalent bonds may be called a *single bond*, *double bond* or *triple bond*. In the O_2 molecule, the two oxygen atoms share two pairs of electrons while in the N_2 molecule, the two nitrogen atoms share three pairs of electrons. Also, molecules such as H_2O, NH_3, and CH_4 contain covalent bonds. Covalent bonds are most common between carbon atoms in organic compounds. Molecules containing covalent bonds are nonionic and are poor conductors of electricity because the pair of electrons is normally shared equally by each atom participating in the bond formation. When the electron sharing by the two atoms is unequal, *polar covalent bonds* are formed. For example, in the HF molecule, the electron pair is drawn more towards fluorine nucleus. As a result, the H atom has a fractional positive charge (δ^+) and the F atom has a fractional negative charge (δ^-).

Coordinate Covalent Bond

In a covalent bond, the pair of electrons required for sharing is donated equally by the two atoms. In contrast, in a *coordinate covalent bond*, the pair of electrons required for bond formation is provided by an atom to another atom, which can accommodate the pair in octet formation. These bonds are also called *semipolar bonds* because the donor atom has a partial positive charge, while the acceptor atom has a partial negative charge, just like in polar covalent bonds. Some donor atoms, such as N, O and S, have a lone pair of electrons, and these atoms form coordinate covalent bonds with metal ions to form metal complexes that can be cationic, anionic or neutral and which are very stable.

7.1.3.3   Hydrogen Bond

Molecules that contain hydrogen atoms bonded covalently to very *electronegative* atoms, such as F, O, and N, also form another chemical bond called a *hydrogen bond*. The strong electronegative atom has greater attraction for the pair of electrons and, as a result, acquires a partial negative charge (δ^-). Therefore, a hydrogen atom has a partial positive charge (δ^+). Now there is an electrostatic attraction between the partial opposite charges of the hydrogen atom of one molecule and the electronegative atom of another molecule. Such bonds between the partial opposite charges of hydrogen and the electronegative atoms are known as *hydrogen*

bonds. Although, hydrogen bonds are weak chemical bonds, are important for the solvent properties of water and for the stability of the DNA structure.

7.1.3.4 Electronegativity

Different atoms have different affinities for the electrons that are being shared in a chemical bond. *Electronegativity* is a property, which describes the ability of an atom in a molecule to attract shared electrons. Linus Pauling developed a scale for electronegativity of different elements. In the periodic table of elements, electronegativity generally increases across a period and decreases down a group. For example, the value for Li is only 1.0 compared to a value of 4.0 for F (the most electronegative atom). In a chemical bond, the electronegativity difference between two identical atoms is zero and, therefore, no polarity occurs and covalent bonds are formed. When two atoms with widely differing electronegativities interact, ionic bonds are formed while unequal electron sharing results in polar covalent bonds.

7.1.3.5 Lewis Structures

In 1902, Lewis conceived the octet rule. The Lewis structure of a molecule represents the arrangement of valence electrons among the atoms in a molecule. In a covalent bond formation, the pair of electrons found in the space between atoms are called *bonding pairs* while those pairs of electrons localized on an atom are called *lone pairs*.

In ionic compounds, such as NaCl, the Lewis structure shows all eight electrons on the Cl^- ion while the Na^+ ion has no valence electrons.

$$Na^+ + Cl^- \rightarrow [Na]^+ [:\ddot{C}l:]^- \tag{7.1}$$
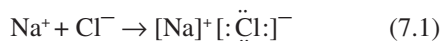
In molecules with covalent bonds, the Lewis structures show the bonding electron pairs in the place between the two sharing atoms.

$$H:H \quad :\ddot{F}::\ddot{F}: \tag{7.2}$$

Sometimes more than one valid structure is possible for a given molecule. *Resonance* occurs when more than one Lewis structure can be written for a molecule

and the electron structure represents an average of the resonance structures. For example, the nitrate ion is represented by a resonance structure. In reality, however, the electrons are delocalized or move around the entire molecule. Resonance is an exception to the general Lewis representation of electron configuration.

7.1.3.6 Formulas of Compounds

The formula of a compound indicates the numbers of atoms in the compound. An *empirical formula* represents the whole-number ratio of the various types of atoms in a compound. However, sometimes different compounds have the same ratio of moles of atoms of the same element. For example, the compounds acetylene (C_2H_2) and benzene (C_6H_6), each have 1:1 ratios of moles of carbon atoms to moles of hydrogen atoms. For both these compounds, the empirical formula is CH and it will not be able to establish the identity of a given molecule. The *molecular formula*, however, is a formula which gives all the information that the empirical formula does, plus information about the number of atoms present in each molecule. For an unknown compound, the molecular formula can be determined from the empirical formula, if the molar mass is known.

In organic chemistry, a *structural formula* is very important to establish the real identity of a specific molecule or substance. For example, the molecular formula $C_6H_{12}O_6$ may represent several different sugar molecules. The structural formula provides a detailed orientation of different atoms of a molecule in a 3-dimensional space.

7.1.3.7 Stoichiometry

All chemical reactions are dependent on the mass of the reactants. Therefore, it is essential to measure the absolute quantities of materials consumed and produced in chemical reactions. This area of study is called *chemical stoichiometry*.

The modern system of atomic masses, instituted in 1961, is based on ^{12}C as the standard and was assigned a mass of exactly 12 *atomic mass units* (amu). The masses of all other atoms are given relative to this standard. *Mass spec*trometer is used to determine the exact mass of atoms. The atomic mass of every element is shown in the periodic table as atomic weight.

It is important to note that the atomic weight of every element is the average mass of all stable isotopes of an element, present in nature. For example, the atomic weight of carbon is given as 12.01 amu since the natural carbon is a mixture of ^{12}C (98.89%) and ^{13}C (1.11%). Similarly, the atomic weight of copper is 63.55 since the natural copper is a mixture of 69.09% of ^{63}Cu (62.93 amu) and 30.91% of ^{65}Cu (64.93 amu).

The Mole

Mole (mol) is generally defined as the number equal to the number of carbon atoms in exactly 12 g of pure ^{12}C atoms. The number of atoms in one mol of ^{12}C was determined to be 6.022137×10^{23} (also known as *Avogadro's number*). Since the atomic mass of natural carbon is 12.011 amu, 12.011 g of a carbon element will have exactly 6.022137×10^{23} atoms. Thus m the mass of one mole of an element is equal to its atomic mass, expressed in grams.

Molar Mass (Molecular Weight)

A chemical molecule, compound, or substance is also a collection of atoms. For example, a molecule of methane (CH_4) contains 1 atom of carbon and 4 atoms of hydrogen. The mass of one mole of CH_4 contains one mole of carbon (12.011 g) and 4 moles of atomic hydrogen (4×1.008 g), or 2 moles of H_2 molecule (2.016 g). Therefore, the *molar mass* of CH_4 gas is 16.043 g. The term *molecular weight* was traditionally used to describe the molar mass of a substance. Thus, one mole of any substance is equal to the molecular weight or molar mass of that substance, expressed in grams. In case of salts and ionic compounds, such as NaCl or K_2CO_3, the term *formula weight* is used instead of the term molar mass or molecular weight.

It is often useful to know a compound's composition in terms of masses of its elements. For example the molar mass of glucose ($C_6H_{12}O_6$) is 181.122 g. In a glucose molecule, the mass percent (or weight percent) of carbon is 39.79%, of oxygen it is 53%, and of hydrogen it is 6.68%.

7.1.3.8 Solutions

Solutions are described in terms of the type of substance or *solute* that is dissolved in a medium known as the *solvent*. Both the solute and solvent may be solid, liquid or gas. The solvent, however, is mostly chosen based on the chemical properties of the solute, compatibility and physiologic conditions.

An *ionic solution* (also known as an *electrolyte*) is one that contains charged or ionic species, surrounded by solvent molecules. For example, in a NaCl solution Na^+ and Cl^- ions are solvated by the water molecules that are dipolar. In *molecular solutions*, such as a glucose solution, the individual glucose molecule with covalent bonds, retains its integrity and does not dissociate.

The amount or mass of a solute in a given solvent determines the strength or concentration of a solution.

Molarity and Normality

The term *molarity* (M) is defined as the number of moles of a substance (solute) per liter of a solvent and is a measure of the number of molecules per unit volume.

$$Molarity(M) = moles\ (m)/volume(v)$$

Different dilutions of a molar solution can also be expressed as millimolar (mM), micromolar (μM), etc. These concentration terms are very important in chemical equations and reactions, since these terms specify the number of atoms or molecules in a given volume. For example, 1 M glucose solution contains 6.022×10^{23} molecules of glucose in one liter, 6.022×10^{20} molecules in ml, and 6.022×10^{17} molecules in 1 μl.

In chemical reactions, it is, sometimes, very important to know the amount of reactive groups rather than the molecule itself. *Normality* (N) indicates the number of reactive groups (*equivalents*), such as proton (H^+), hydroxide (OH^-), or electron units per unit volume. For example, 1 M HCl is also equivalent to 1 N HCl since HCl has only one acidic hydrogen ion (H^+). In contrast, $1\,M\,H_2SO_4$ is equivalent to $2\,N\,H_2SO_4$ solution since it has two H^+ ions.

Volume Percent

Solutions can be prepared using certain mass, g (w) dissolved in 100 g of a solvent or in 100 ml (v) of a solvent. Generally, solutions are prepared on the w/v basis. For example, the 0.9% NaCl solution (physiological

saline) and the 5% dextrose solution are quite common in a clinic. It is important to recognize that in chemistry, solutions prepared on w/v basis are not useful for balancing chemical reactions and must be expressed in terms of molar concentrations. For example, a 0.9% NaCl solution represents a 0.15 molar solution of sodium chloride.

Radioactive Concentration

With radioactive solutions, it is quite common to express the concentration in units of activity/volume, such as mCi/ml or mBq/ml, etc. These radioactive concentration terms are mistakenly applied to SA, which really is an expression of activity per mass of the radionuclide or radiotracer.

7.2 Chemical Reactions

In a chemical reaction one or more substances, called *reactants* or *reagents*, are allowed to react to form one or more other substances, called *products*. A chemical change involves reorganization of the atoms in the reactants to form the product (bonds have been broken and new ones have been formed). This process is represented by a *chemical equation*. For example, methane gas reacts with oxygen to produce carbon dioxide and water.

$$CH_4 + O_2 \rightarrow CO_2 + H_2O \qquad (7.3)$$
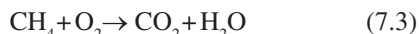
The law of conservation of mass dictates that in a chemical reaction atoms are neither created nor destroyed. All atoms in the reactants must be accounted for among the products. To show the quantitative relationships, the chemical equation must be balanced. *Coefficients* are, therefore, used before the molecular formula of each compound to represent the number of moles of the reactant or the product. The above equation is not balanced and is not correct. A *balanced chemical equation* of the above reaction is written as follows:

$$CH_4 + 2O_2 \rightarrow CO_2 + 2H_2O \qquad (7.4)$$
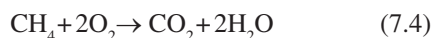
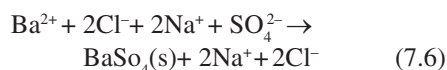In the above reaction, 2 moles of oxygen interact with 1 mole of methane to produce 1 mole of carbon dioxide and 2 moles of water. Stoichiometric calculations of chemical reactions are very important for determining the amount of reactants required to form a specific amount of a product.

7.2.1 Types of Chemical Reactions

In order to balance a chemical reaction, it is necessary to know the molecular and structural formulas of reactants and products. Also, one must be able to predict the products from the reactants. Simple chemical reactions are generally classified into five types. In a *Combination reaction*, two or more reactants combine to form one product. In a *decomposition reaction*, the reactant decomposes into its component elements or a simpler compound. Different elements have varying abilities to combine. In reactions involving several reactants, the possible product formation depends on the relative affinities, valency, and electronegativities of elements. *Substitution* (single or double) or *replacement reactions* involve the exchange of different elements based on their relative reactivities. In *combustion reactions*, compounds containing C, H, O, S and N atoms involve burning with the liberation of energy and heat.

There are millions of reactions described in chemistry (both inorganic and organic). Most of these reactions occur among substances dissolved in water. Certain organic compounds are relatively nonpolar and do not dissolve in water. As a result chemical reactions are performed in organic solvents. Both aqueous and nonaqueous chemical reactions can be categorized into three groups: *precipitation reactions*, *acid–base reactions*, and *oxidation–reduction reactions*.

(a) *Precipitation reactions*: When two solutions are mixed, an insoluble substance (a solid) sometimes forms and separates from the solution. Such a reaction is called a precipitation reaction and the solid that is formed is called a precipitate. For example, when a solution of barium chloride and a solution of sodium sulfate are mixed, a white, solid barium sulfate is formed, which can be separated from the sodium chloride solution simply by filtration. When ions combine to form a solid compound, the compound has to be neutral and not soluble in the solvent. The balanced equation can be written as a *molecular equation* or as a complete *ionic equation*.

$$BaCl_2 + Na_2SO_4 \rightarrow BaSO_4(s) + 2NaCl \qquad (7.5)$$

$$Ba^{2+} + 2Cl^- + 2Na^+ + SO_4^{2-} \rightarrow$$
$$BaSo_4(s) + 2Na^+ + 2Cl^- \qquad (7.6)$$

(b) *Acid–Base reactions*: Acids (from Latin word *acidus*) were first recognized as a class of substances that taste sour. In contrast, bases or *alkalis*, are characterized by their bitter taste and slippery feel. In the 1880s, Savante Arrhenius proposed that in a solution, an acid is a substance that produces a proton, H^+ ions, while bases produces hydroxide, OH^- ions. Since this concept applies only to aqueous solutions, Bronsted and Lowry, in 1923, defined an acid to be a proton donor, and a base to be a proton acceptor. In the 1920s, Lewis suggested a general definition for acid–base behavior in terms of electron pairs. An *acid is an electron pair acceptor* and a *base is an electron pair donor*.

(c) Acids react with bases (and vice versa) to produce salts. Such a reaction is called a neutralization reaction, resulting in the formation of a salt and water, as shown in the examples below. The hydrolysis of salts in turn can regenerate H^+ ions.

$$HCl + KOH \rightarrow KCl + H_2O \qquad (7.7)$$

$$H_2SO_4 + 2NaOH \rightarrow Na_2SO_4 + H_2O \qquad (7.8)$$
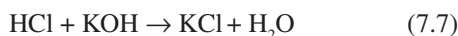
Strong acids, such as HCl, H_2SO_4 and $HClO_4$ (perchloric acid), dissociate completely in aqueous solution, forming hydronium, H_3O^+ ion. In solvents other than water, however, the dissociation can only be partial. For example, hydrogen cyanide molecule may dissociate to form.

$$HCN \leftrightarrow H^+ + CN^- \qquad (7.9)$$

$$NH_3 + H^+ \rightleftharpoons NH_4^+ \qquad (7.10)$$

Based on the Bronsted–Lowry definition, HCN is an acid since it can donate a proton and CN is a base since it can accept a proton. These two ions are called a *conjugate acid–base pair*. Similarly, ammonia is a base since it can accept a proton. A proton does not generally exist by itself, therefore, the Bronstead–Lowry equations usually show two sets of conjugate acid–base pairs and no protons, as shown in the example below.

$$HCN + NH_3 \rightarrow NH_4^+ + Cl^- \qquad (7.11)$$
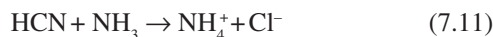
When HCl reacts with a CN^- ion, HCN is formed because a cyanide ion is a stronger base than a chloride ion and HCl is a stronger acid than HCN.

$$HCl + CN^- \rightarrow HCN + Cl^- \qquad (7.12)$$

Arhenius acids and bases deal with a H_3O^+ ion and a OH^- ion in aqueous solutions, while Bronstead–Lowry acids and bases deal with only protons or H+ ions in nonaqueous solvents. Lewis acids and bases deal with a pair of electrons in coordinate covalent bonds. A Lewis base can be an electron rich negative ion such as OH^- and HSO_4^-, or a molecule, such as NH_3, where the nitrogen atom has a lone pair of electrons to donate. Lewis acids include positive ions, such as H^+, Ag^+, and Al^{3+}, or a molecule, such as BF_3 and SO_3, with an atom that can accept a pair of electrons. The reaction between NH_3 and BF_3 forming NH_3BF_3 is a good example of an acid–base reaction, as shown below, there are covalent bonds between N and Hydrogen and coordinate covalent bond between N and B atoms.

$$NH_3 + BF_3 \rightarrow H_3N: BF_3 \qquad (7.13)$$

(d) *Oxidation–Reduction reactions*: Chemical reactions in which one or more electrons are transferred are called *oxidatio–reduction reactions* or *redox reactions*. Many important reactions, such as combustion and oxidation of sugars and fats, involve redox reactions. *Oxidation* is the loss of electron(s) from the electron configuration of an atom or ion, while *reduction* is the gain of electron(s) by the electron configuration of an atom or ion. In some of these reactions, the transfer of electrons occurs in a literal sense to form ions, as in the case of NaCl formation, while in the combustion of methane by oxygen transfer occurs in a formal sense by covalent bond breaking and new bond formation. In the oxidation of methane, none of the reactants and products are ionic (as one would expect when electrons are transferred), however, the reaction is still assumed to involve transfer of electrons from carbon to oxygen.

$$2Na(s) + Cl_2(g) \rightarrow 2NaCl(s) \qquad (7.14)$$

$$CH_4 + 2O_2 \rightarrow CO_2(g) + 2H_2O(g) \qquad (7.15)$$
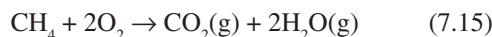
The concept of *oxidation states* or *oxidation numbers* provides a way to keep track of electrons in redox reactions. In the reaction of methane with oxygen,

the carbon undergoes a change in oxidation state from -4 in CH_4 to $+4$ in CO_2. Such a change can be accounted for by a loss of eight electrons. Because each of the oxygen atoms has gained two electrons in CO_2 and H_2O molecules, the oxidation rate of oxygen changes from 0 in O_2 to -2 in CO_2 and H_2O molecules. Based on this example, the oxidation number is defined as the number of valence electrons in the free atom minus the number "controlled" by the atom in the compound. In any molecule with a covalent bond, the nonmetals with the highest attraction for shared electrons are F, O, N and Cl. The relative electronegativity of these atoms is $F \gg O > N \approx Cl$.

$$CH_4 + 2O_2 \longrightarrow CO_2 + 2H_2O \qquad (7.16)$$
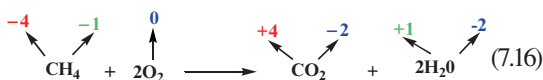
In the above reaction, carbon is *oxidized* as it loses electrons and the oxidation state is increased, while the oxygen is *reduced* because it gains electrons, and the oxidation state is decreased. In addition, because oxygen looses electrons, it is called the *reducing agent*, while methane is called the *oxidizing agent* since it gains electrons. It is important to remember that in a covalent bond electrons are shared between the atoms. However, in redox reactions, the shared electrons are drawn more towards the more electronegative atoms and, therefore, the atom has a net gain of the shared electrons.

7.2.2 Chemical Equilibrium

Many chemical reactions proceed to completion until one of the reactants is completely consumed and the product formation is finished. For example, sodium metal and chlorine gas combine to form NaCl salt, which can decompose only when it is electrolyzed. On the other hand, many other reactions stop far short of completion since such reactions can be *reversible*. The products formed react to give back the original reactants, even as the reactants are forming more products. In fact, the system (the chemical reaction) has reached *chemical equilibrium*, when the concentration of all reactants and products remain constant with time.

When nitrogen and hydrogen gases react with each other at 500°C and high pressure, ammonia is formed. Under the same conditions, ammonia is also decomposed. This situation, where two opposing reactions (forward and backward) occur at the same time and, leads to a state known as chemical equilibrium.

$$3H_2 + N_2 \rightleftharpoons 2NH_3 \qquad (7.17)$$

Some reactions proceed slowly, while other reactions can proceed very fast. The *rate of a reaction* is defined as the change in the concentration of any of its reactants or products per unit time. The nature and concentration of reactants, temperature, presence of a catalyst, pressure and the size of solid reactants, all contribute to the changes in the rate of a chemical reaction.

Le Chatelier's principle states that if a stress (such as change in concentration, temperature, pressure, or addition of a catalyst) is applied to the system at equilibrium, then the equilibrium will shift in order to reduce that stress. The reaction may shift to the right (product formation) or to the left (product decomposition). Soon, however, the system will reach a new equilibrium at the new set of conditions. Le Chatelier's principle, however, cannot predict how much an equilibrium will shift under different conditions of stress.

Based on empirical data, Guldberg and Waage, in 1864 proposed the *law of mass action* as a general description of equilibrium condition. For a chemical reaction in general,

$$aA + bB \underset{k_2}{\overset{k_1}{\rightleftharpoons}} cC + dD \qquad (7.18)$$
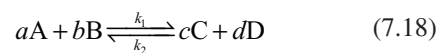
$$K_{eq} = \frac{[C]^c [D]^d}{[A]^a [B]^b} \qquad (7.19)$$

In the above equation, k_1 and k_2 are the forward and backward rate constants, while K_{eq}, is a constant called equilibrium constant. The square brackets indicate the concentration (in moles) of products and reactants at equilibrium and the coefficients represent the number of moles in the balanced chemical equation. The value of K_{eq} for a given reaction system can be calculated from the observed concentrations of reactants and products at equilibrium. For example, in the synthesis of ammonia, described above, under the conditions specified, $K_{eq} = 6.0 \times 10^{-2}$ L^2 mol^{-2}. The higher the value of K_{eq}, the more likely the reaction will shift to the right with a net increase in the product concentration or formation. There is only one value for K_{eq} for a particular system, and at a particular temperature, but there are an infinite number of equilibrium positions.

7.2.2.1 Ionic Equilibria

Various salts, acids and bases, and their dissociated ions in solution also exist in equilibrium. The equation for the equilibrium constant is the same for any of the chemical reactions discussed above. Certain salts, such as NaCl and KCl, ionize completely in a solution. For very slightly soluble salts, the equilibrium constant, is called *solubility product constant*, K_{sp}, because most of the salt concentration is relatively constant. For example, for very slightly soluble silver bromide (AgBr) salt,

$$K_{sp} = [Ag^+][Br^-] \tag{7.20}$$

The ionic equilibrium constant may be K_a (*acidity constant*) if it represents the dissociation of an acid or K_b if it represents the dissociation of a base. A strong acid (or base) is a strong electrolyte that dissociates completely into its ions in aqueous solution. A weak acid (or base) is a weak electrolyte that dissociates only partially in aqueous solution. The stronger the acid or base, the higher the K_a or K_b value.

7.2.2.2 Dissociation of Water

Water is said to be amphoteric because it can behave as either an acid or a base. Pure water behaves like a weak electrolyte. As a result of the autoionization of a very small extent of water, H_3O^+ and OH^- exist in water at 25°C. The concentration of each of these ions is 10^{-7}M.

$$H_2O \rightleftharpoons H_2O^+ + OH^- \tag{7.21}$$

$$K_i = \frac{\left[H_3O^+\right]\left[OH^-\right]}{H_2O} = \frac{\left[1\times10^{-7}M\right]\left[1\times10^{-7}M\right]}{55.6M} \tag{7.22}$$

Since the water concentration is relatively unchanged, K_i of water is the ion product of water, $K_w = 1 \times 10^{-14}M^2$. At neutrality, the concentration of H_3O^+ and OH^- ions is the same and is equal to 1×10^{-7}M.

The pH Scale

The acidity of a solution depends on the hydrogen (H^+) ion or hydronium (H_3O^+) ion concentration. Because the hydrogen ion concentration is typically very small,

the *pH scale* provides a convenient way to represent the acidity of an aqueous solution.

$$pH = -\log[H^+] \tag{7.23}$$

Thus for a solution in which

$$[H^+] = 1.0 \times 10^{-7}M \tag{7.24}$$

$$pH = -(-7.0) = 7.0 \tag{7.25}$$

The hydrogen ion concentration of an aqueous solution can be as high as 1.0M and as low as 1×10^{-14}M. Therefore, the pH scale (Fig. 7.2) ranges from 0 to 14.

Buffer Systems

A buffer solution is defined as solution that resists pH changes when acid or base equivalents are added to it. The components of a buffer solution are a weak acid and its anion. Similarly, a buffer solution can be made from a weak base and its salt. The addition of any acid or base to a buffer is neutralized by ions in the buffer keeping the pH relatively unchanged.

Acetate, citrate, and phosphate buffers are some of the most common buffer systems used. The pH of a buffer system can be calculated based on pK_a of the weak acid used (based on the *Henderson–Hasselbach equation*).

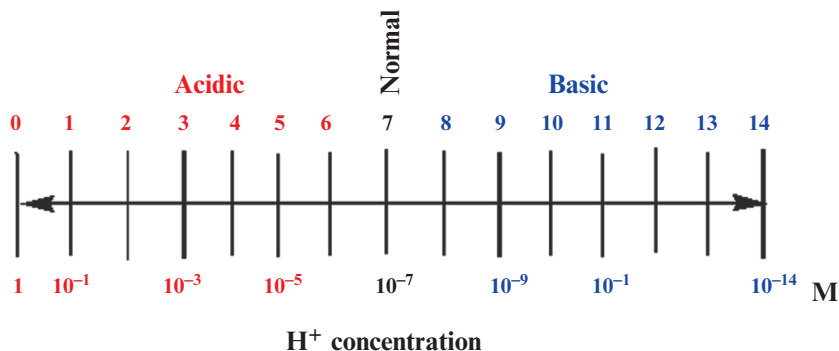$$pH = pK_a + \frac{\left[A^-\right]}{\left[HA\right]} \tag{7.26}$$

For example, in the preparation of an acetate buffer, the concentrations of the acetic acid and acetate ion is the same and is equal to 0.2M and K_a of the acetic acid is 1.8×10^{-5}M and the pH of the acetate buffer is 4.8.

$$CH_3COOH \rightleftharpoons CH_3COO^\blacklozenge + H^+ \tag{7.27}$$

$$pH = 1.8 \times 10^{-5}M + \frac{\left[0.2M\right]}{\left[0.2M\right]} = 4.8 \tag{7.28}$$

There are several things that must considered before selecting an appropriate buffer for a specific purpose. First, it is important to make sure that the buffer does not

Fig. 7.2 The pH is a log scale based on 10

Normal

Acidic   **Basic**

| 0 | 1 | 2 | 3 | 4 | 5 | 6 | 7 | 8 | 9 | 10 | 11 | 12 | 13 | 14 |

1   10^{-1} 10^{-3} 10^{-5} 10^{-7} 10^{-9} 10^{-1} 10^{-14} **M**

H^+ concentration

chemically interfere with the chemical reaction. Buffer systems are most effective at pH values near the pK_a values. Further, buffers should be used at relative concentrations (>0.1 M) to have a high capacity of buffering. Finally, buffers are very important physiologically. More specifically, because the pH of blood is maintained in a narrow range of 7.3–7.5. Also the enzyme activities within cells and in the plasma are pH dependent.

7.3 Organic Chemistry

Historically, the term organic chemistry has been associated with the study of compounds, obtained from plants and animals. In modern terms, the study of carbon containing compounds and their properties is called organic chemistry. In addition to carbon and hydrogen, the elements most likely to be present in organic compounds are nonmetals, such as oxygen, nitrogen, phosphorous, sulfur, and the halogens.

The element carbon is in group IV (or group 14) of the periodic table. The chemical bonds between atoms of carbon and between carbon and the other elements are essentially covalent. With a valence of 4 and an electronegativity of 2.5, carbon can be expected to form nonpolar covalent bonds with other carbon and hydrogen atoms, and increasingly polar covalent bonds with O, N, and halides. With an atomic number of 6, the orbital electron configuration is $1s^2 2s^2 2p^2$. The carbon adopts a set of orbitals for bonding other than its native 2s and 2p orbitals. This modification of the native atomic orbitals, to form special orbitals for bonding, is called *hybridization* (Fig. 7.3). The four new orbitals, called sp^3, are identical in shape, each having a larger lobe and a smaller lobe. The four orbitals are
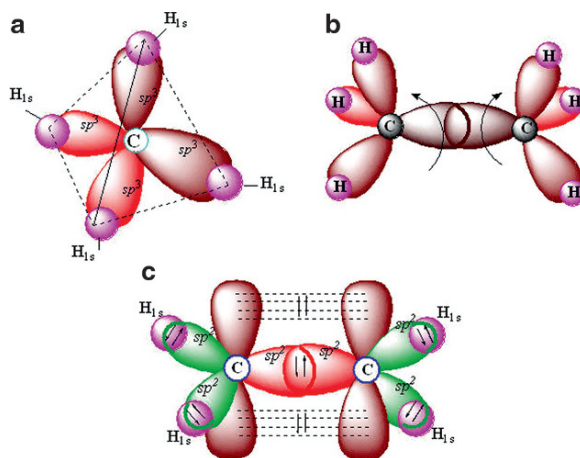

Fig. 7.3 The tetrahedral structure of methane (**a**) can be described in terms of carbon atom using an sp^3 hybrid set of orbitals to bond to the four hydrogen atoms. In case of acetylene, the carbon can be described as sp^2 hybridized (**c**), in which the C–C bond is formed by sharing an electron pair between sp^2 orbitals, while the π bond is formed by sharing a pair of electrons between p orbitals. As a result, the free rotation of the two CH$_2$ group is prevented. However, with ethane (**b**) the free rotation of two CH$_3$ groups is possible

oriented in space so that the larger lobes form a tetrahedral arrangement, as in the case of a methane (CH$_4$) molecule with bond angles of 109.5°. In a sp^2 hybridization, a set of three orbitals, arranged at 120-degree angles, can be obtained, as in the case of ethyle (CH$_2$CH$_2$) by combining one s orbital and 2p orbitals. For each bond, the shared electron pair occupies the region between the atoms. This type of covalent bond is called a *sigma (σ) bond*. The parallel p orbitals share an electron pair in the space above and below the sigma bond to form a *pi (π) bond*. In a sp hybridization, two hybrid orbitals form two sigma bonds, arranged at 180-degrees, oriented in opposite directions, as in the case of the

carbon dioxide molecule (CO_2). The p orbitals can also form two pi bonds, perpendicular to each other. A combination of sigma and pi bonds can also facilitate the formation of a triple bond between two carbon atoms, as in the case of acetylene (C_2H_2). It is important to realize that this hybridization of orbitals in a carbon atom determines the shape and the 3-dimensional organization of atoms in organic compounds.

7.3.1 Hydrocarbons

Compounds composed of only carbon and hydrogen are called *hydrocarbons*. Compounds, in which carbon–carbon bonds are all single bonds, are called *saturated hydrocarbons* and, if the carbon–carbon bonds involve multiple bonds, they are called *unsaturated hydrocarbons*. Hydrocarbons can be classified into four fundamental series; *alkanes*, *alkenes*, *alkynes* and *aromatic* hydrocarbons.

The simplest member of saturated hydrocarbons or alkanes, is *methane* (CH_4), followed by *ethane* (CH_3CH_3), and *propane* ($CH_3CH_2CH_3$). Alkanes in which the carbon atoms form long "strings" or chains are called *normal*, *straight-chain*, or *unbranched* hydrocarbons, which can be represented by the general formula, C_nH_{2n+2}. The four carbon butane and the subsequent members of alkanes exhibit *structural isomerism*. For example, butane can exist as a straight chain molecule (*n-butane*) or as a branched chain structure (*isobutane*). Besides forming chains, carbon atoms can also form rings, known as cyclic alkanes (C_nH_{2n}), *such as cyclopropane*, *cyclohexane*, etc.

Alkene series of unsaturated hydrocarbons are also known as *olefins* and have at least one double bond in the carbon chain (C_nH_{2n}) of each molecule. The simplest olefin is a *diene*, called *ethylene* (CH_2CH_2). Because of the restricted rotation of methylene ($-CH_2$) groups around double bonded carbon atoms, alkenes exhibit *cis–trans isomerism*. For example, there are two stereoisomers of 2-butene (Fig. 7.4). Idential substituents on the same side of the double bond are called *cis* and those on the opposite side are called *trans*. In a series of alkanes, if only one saturated carbon separates the double bond, then it is called *conjugated*, however, if more than one saturated carbon separates the double bond, then the alkene is said to be *unconjugated*.
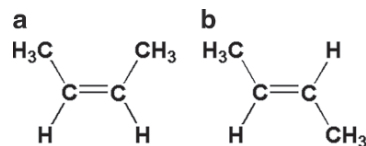

Fig. 7.4 The two stereoisomers of 2-butene: *cis*-2-butene (**a**) and *trans*-2-butene (**b**)

Alkynes are unsaturated hydrocarbons containing at least one triple carbon–carbon bond and have the general formula, C_nH_{2n-2}. The simplest alkyne is *ethyne* (C_2H_2), commonly called *acetylene*.

A special class of cyclic unsaturated hydrocarbons is known as the aromatic hydrocarbons. A six carbon conjugated olefin, cyclohexatriene, an aromatic hydrocarbon, also known as *benzene* (C_6H_6), has a planar ring structure. Benzene exhibits resonance, since all the three double bonds in benzene are equivalent. The delocalization of π electrons is usually indicated by a circle inside the ring. Benzene is the simplest aromatic molecule. More complex aromatic molecules, such as naphthalene, anthracene, phenanthrene, and 3,4-benzpyrene, consist of a number of "fused" benzene rings.

7.3.1.1 Reactions of Hydrocarbons

Combustion Reaction

Chemically, alkanes are relatively strong and fairly unreactive. Because of their limited reactivity, saturated hydrocarbons are called *paraffins* (meaning little affinity). At high temperatures, however, they react with oxygen, and these combustion reactions are the basis for their use as fuels.

Substitution Reaction

Alkanes can also undergo substitution reactions primarily where the more electronegative halogen atoms replace hydrogen atoms. For example, chlorine reacts with methane forming *chloromethane*, *dichloromethane*. Substituted methanes containing chlorine and fluorine are known as *freons* which are very unreactive and can be used as coolant fluids. Alkanes can also be converted

to alkenes by *dehydrogenation* reactions in which hydrogen atoms are removed.

Benzene being unsaturated is expected to be very reactive but, actually it is quite unreactive. The relative lack of reactivity of aromatic hydrocarbons is attributed to the delocalized double bonds. Because of its great stability, the benzene ring persists in most reactions. Substitution reactions are characteristic of alkanes. However, benzene also undergoes substitution reactions in which the hydrogen atoms are replaced by other atoms and functional groups, such as chlorine atom, nitro group ($-NO_2$), methyl group ($-CH_3$) and even a phenyl ($-C_6H_5$) group. These substitution reactions occur as a result of the attack of an *electrophilic* or electron-seeking ion on the π electrons of the benzene ring.

When the aromatic ring already contains a substituent, its reactivity will be greater or less than that of benzene itself. Electron releasing groups (such as $-OH$, $-OCH_3$, $-NH_2$) can be *activating* the benzene ring while electron withdrawing groups (such as $-F$, $-NO_2$, $-COOH$) can be *deactivating* the benzene ring. For example, both phenylalanine and tyrosine amino acids contain the benzene ring. However, iodination (or radioiodination) of tyrosine is chemically easier since the hydroxyl ($-OH$) group already present on the benzene ring activates the electrophilic attack of iodine (Fig. 7.5). A benzene ring can have more than one substitutent attached to the ring. If two identical substituents are attached to the ring, they are referred to as
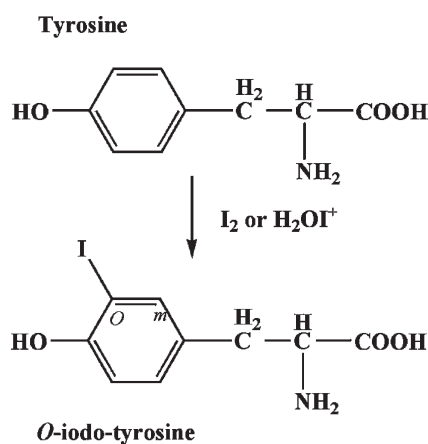

Fig. 7.5 Iodination of tyrosine is chemically easier since the hydroxyl ($-OH$) group already present on the benzene ring activates the electrophilic attack of iodine

ortho (*o*), *meta* (*m*), or *para* (*p*), depending on their relative position.

Addition Reactions

Because alkenes and alkynes are unsaturated, their most important reactions are addition reactions. In these reactions, π bonds, which are weaker than the σ bonds, are broken, and new σ bonds are formed with the atoms being added. For example, *hydrogenation reactions* involve addition of hydrogen atoms to carbon atoms with double bonds in the presence of catalysts such as platinum, palladium and nickel, which help break the strong covalent bonds of molecular hydrogen.

$$H_2C = CHCH_3 + H_2 \xrightarrow{\text{catalyst}} CH_3CH_2CH_3 \quad (7.29)$$
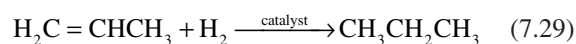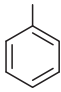
Halogenation of olefins involves the addition of halogen atoms to the carbon atoms with double bonds. Unlike the unsaturated hydrocarbons, benzene does not undergo rapid addition reactions.

7.3.1.2 Hydrocarbon Derivatives

The millions of organic compounds, other than hydrocarbons, can all be regarded as derivatives of hydrocarbons, where one or more of the hydrogen atoms on the parent molecule is replaced by another type of atom or groups of atoms, known as *radicals* and *functional groups*. A radical is a hydrocarbon with one hydrogen atom less and is reactive. For example, methyl ($-CH_3$) and ethyl ($-CH_2CH_3$) are often called radicals (Table 7.6) and usually denoted as "R" in formulas. If the radical is derived from an alkane, the radical is called *alkyl radical*; and if it is derived from an aromatic hydrocarbon, it is called *aryl radical* and if it is derived from benzene, it is called *phenyl radical*. Specific groups of atoms responsible for the characteristic properties of the organic compounds are called *functional groups*. The most common functional groups are listed in Table 7.7.

Alcohols are characterized by the presence of the hydroxyl ($-OH$) group. Alcohols are classified as primary, secondary and tertiary, depending on whether one, two, or three radical groups attached to the carbon atom

Table 7.6   The most common alkyl and phenyl substituents and their names

Structure	Name
$-CH_3$	Methyl
$-CH_2CH_3$	Ethyl
$-CH_2CH_2CH_3$	Propyl
$-CH_2CH_2CH_2CH_3$	Butyl
CH_3CHCH_3	Isopropyl
	Isobutyl
	tert-Butyl
	Phenyl

where the hydroxyl group is attached. Some common alcohols are methyl alcohol (methanol), ethyl alcohol (ethanol), glycerol, and phenol. Methanol is highly toxic while ethanol is the alcohol found in many beverages, such as beer, wine and whiskey. The fermentation of glucose by yeast generates ethanol from grains (barley, corn) and grapes. Some of the important polyhydroxyl alcohols are ethylene glycol and glycerol, which are 2 and 3 carbon alcohols. Alcohols are good solvents of organic compounds since the hydroxyl groups of alcohols contain polar C–O and O–H bonds, which help to form hydrogen bonds. As the number of carbon atoms in an alcohol increases, its water solubility decreases. A chemical reaction that removes a water molecule between two alcohol molecules results in the formation of an *ether*. Diethyl ether ($CH_3CH_2OCH_2CH_3$), or simply ether, is used as a solvent and as an anesthetic.

Aldehydes and *ketones* contain the carbonyl (−C=O) group. In an aldehyde, the *carbonyl* group is attached to at least one hydrogen atom while in ketones, the carbonyl group is attached to carbon atoms. Aldehydes have very strong odors. Formaldehyde (HCHO) or for-

Table 7.7   The common functional groups

Class	Functional group	General formula	Example
Halohydrocarbons	$-X$ (F, Cl, Br, I)	R–X	CH_3I Methyl iodide
Alcohols	$-OH$	R-OH	CH_3CH_2OH Ethanol
Ethers	$-O-$	R–O–R'	CH_3OCH_3 Dimethyl ether
Aldehydes	$\overset{\displaystyle O}{\overset{\displaystyle \|}{-C-H}}$	$\overset{\displaystyle O}{\overset{\displaystyle \|}{R-C-H}}$	HCHO Formaldehyde
Ketones	$\overset{\displaystyle O}{\overset{\displaystyle \|}{-C-}}$	$\overset{\displaystyle O}{\overset{\displaystyle \|}{R-C-R'}}$	CH_3COCH_3 Acetone
Carboxylic acids	$\overset{\displaystyle O}{\overset{\displaystyle \|}{-C-OH}}$	$\overset{\displaystyle O}{\overset{\displaystyle \|}{R-C-OH}}$	CH_3COOH Acetic acid
Esters	$\overset{\displaystyle O}{\overset{\displaystyle \|}{-C-O-}}$	$\overset{\displaystyle O}{\overset{\displaystyle \|}{R-C-O-R'}}$	$CH_3COOCH_2CH_3$ Ethyl acetate
Amines	$-NH_2$	$R-NH_2$	CH_3NH_2 Methylamine

malin is generally used in pathology to store tissue specimens. Vanillin is responsible for the pleasant odor in vanilla beans, while butyraldehyde is responsible for the unpleasant odor in rancid butter. The most common ketone is *acetone*, commonly used as a solvent for hydrophobic molecules and as a nail polish remover. Methylethylketone or MEK is a solvent used in the chromatography of ^{99m}Tc pertechnetate. Alcohols and aldehydes or ketones can be interconverted by oxidation and reduction reactions.

Caboxylic acids are characterized by the presence of the carboxyl (−COOH) group and are also known as the organic acids with a general formula of RCOOH. The simplest and most common acid is acetic acid (found in vinegar), while citric acid is found in all citrus fruits. Unlike inorganic acids, organic acids are weak acids in aqueous solution. Reaction with a strong base such as NaOH, converts them into caboxylate anion or sodium salt form, which increases water solubility. Carboxylic acids can be synthesized by oxidizing primary alcohols. For example, ethanol can be oxidized to acetic acid, using potassium permanganate

A carboxylic acid reacts with an alcohol to form an ester and a water molecule

$$CH_3COOH + HOCH_2CH_3 \rightarrow CH_3COOCH_2CH_3 + H_2O \quad (7.30)$$

The reaction of CO_2 gas with organic magnesium halides (*Grignard* reagent) also results in the formation of carboxylic acids (Fig. 7.6). This method is commonly used to prepare ^{11}C labeled organic acids, such as palmitic acid. Carboxylic acids can be converted to very reactive acid chlorides by the reaction of the acids with thionyl chloride ($SOCl_2$). The reaction
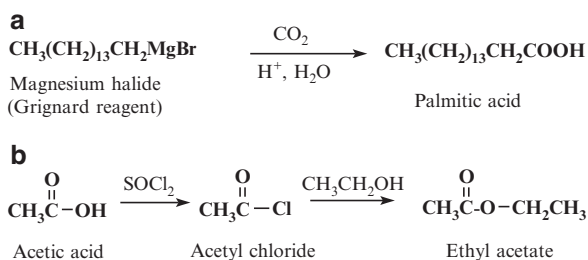
of acid chloride with an alcohol will result in the formation of an *ester* (Fig. 7.6).

Naturally occurring esters are fats and triglycerides and often have a sweet, fruity odor. For example, *n*-amyl acetate smells like bananas and *n*-octyl acetate smells like oranges. One of the very important *esters is acetylsalicylic acid* (aspirin) formed from the reaction of salicylic acid and acetic acid.

Amines can be considered derivatives of ammonia (NH_3), in which one or more hydrogen atoms have been replaced by organic radicals. Amines can be classified as the primary amines (RNH_2), secondary amines (R_2NH), and tertiary amines (R_3N). Many amines have unpleasant "fishlike" odors. *Putrescine* and cadaverin are responsible for the odor associated with decaying animal and human tissues. Also, amines are the bases of organic chemistry. Like ammonia, amines react as *Bronsted* bases by reacting with water and acids to form positively charged ammonium species (RNH_3^+), which are soluble in water. Amines react with acid chlorides to form amides that contain an amide group (−CONH), commonly found in peptides and proteins (Fig. 7.8). Amines also react with aldehydes and ketones to give *Schiff* bases.

7.4 Biochemistry

Biochemistry is the study of the chemistry of living systems. The *essential elements* for human life are known to include 30 elements. However, only six of these elements contribute to 99% of the body mass. The most abundant elements are oxygen 65%, carbon (18%) and hydrogen (10%). Certain transition elements, such as iron, zinc, copper, cobalt, and iodine, are present in *trace amounts*. Life is organized around the functions of the cell, the smallest unit of life, and the building block of all tissues and organs. The main thrust of biochemistry is to understand how cells operate at the molecular level. The *nucleus*, which contains the *chromosomes* and DNA, is separated from the *cytoplasm* (the cell fluid) by a membrane and the cell, in turn, is separated from the extracellular fluid by the cell membrane. A number of subcellular structures carry out various cell functions. For example, *mitochondria* process nutrients and produce the energy, the enzymes in *lysosomes* digest the proteins, and the *ribosomes* synthesize the proteins

a
$CH_3(CH_2)_{13}CH_2MgBr$ $\xrightarrow[H^+, H_2O]{CO_2}$ $CH_3(CH_2)_{13}CH_2COOH$

Magnesium halide
(Grignard reagent)

Palmitic acid

b
$CH_3\overset{\overset{O}{\|}}{C}-OH$ $\xrightarrow{SOCl_2}$ $CH_3\overset{\overset{O}{\|}}{C}-Cl$ $\xrightarrow{CH_3CH_2OH}$ $CH_3\overset{\overset{O}{\|}}{C}-O-CH_2CH_3$

Acetic acid   Acetyl chloride   Ethyl acetate

Fig. 7.6 The reaction of CO_2 gas with *Grignard* reagent to form carboxylc acid, which can then be converted to very reactive acid chloride by the reaction of the acid with thionyl chloride ($SOCl_2$). The reaction of acid chloride with an alcohol will result in the formation of an *ester*

based on mRNA. The four major categories of natural chemical compounds present in living systems are proteins, carbohydrates, lipids, and nucleic acids.

7.4.1 Proteins

Proteins make up about 15% of our body mass and perform many functions. *Fibrous proteins* provide structural integrity and strength to many tissues, such as muscle and cartilage, while *globular proteins* are the "worker molecules" in various processes, such as transport of oxygen and nutrients. Globular proteins also act as catalysts for thousands of chemical reactions and participate in the body's regulatory systems. Chemically, proteins are a class of natural polymers and the basic building blocks are α-*amino acids*, molecules containing both, a basic amino group and an acid carboxyl group.

7.4.1.1 Amino Acids

Amino acids are the basic structural units of proteins, peptide hormones, and peptide antibiotics. The 20 natural amino acids most commonly found in proteins are grouped as polar and nonpolar classes or as neutral, basic and acidic amino acids. The α-amino acids have the general formula (Fig. 7.7), where "R" represents a variable, organic polar (hydrophilic), or nonpolar (hydrophobic) side chain. They are called α- amino acids because the amino group is attached to the α-carbon, the one next to the carboxyl group. At the pH in biological fluids, the amino acids exist in a dipolar ionic form (known as *zwitterions*), where the proton from a carboxyl group is transferred to the amino group. Most of the amino acids are neutral. The basic amino acids (*lysine, arginine and histidine*) have two amino groups, while the acidic amino acids (*aspartic acid* and *glutamic acid*) have two carboxyl groups. The amino acids, *cysteine* and *methionine* contain organic sulfur atoms. The thiol group (−SH), similar to the hydroxyl group, can be oxidized in cysteine to a disulfide form, *cystine*. Methionine has a thioether linkage and serves as a biosynthetic intermediate in supplying the methyl group methylation reactions, in vivo. The amino acid, tyrosine, is important for radio-iodination reactions, while lysine and arginine are useful to attach bifunctional chelating agents for labeling peptides and proteins with radiometals.
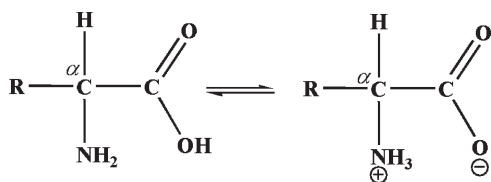
Stereochemistry of Amino Acids

When a carbon atom is attached to four different groups, it is called an *asymmetric* carbon atom. The compounds containing asymmetric carbon atoms, like mirror images, are said to be nonsuperimposable. The mirror image, *optical isomers* are called *enantiomers* (L and D forms). The amino acids in the solution can also rotate the plane-polarized light to the right (designated as *d* for dextrorotatory) or to the left (designated as *l* for levorotatory). Interestingly, L-amino acids are often dextrorotatory, while D-amino acids are levorotatory. The physical properties of L and D amino acids are identical. In biological systems, however, the reactivity of these two forms is quite different. For example, only the L-amino acids are mostly found in proteins. It is also important to recognize that the stereoche-mical requirements for biological activity are essential in the design of radiolabeled amino acids as molecular imaging agents.

Peptide Linkage

A condensation reaction between the amino group of one amino acid with the carboxy group of another amino acid will result in the formation of a dipeptide with reduced polarity. The structure, CONH is called a *peptide linkage* (also called an *amide*). Such peptide bonds (Fig. 7.8) between several amino acids lengthen the polymer chain to produce a polypeptide, and eventually a protein. A naturally occurring tripeptide, glutathione is derived from only three amino acids
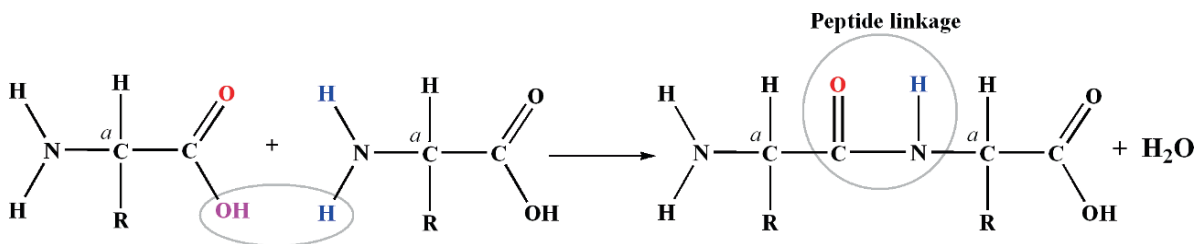

Fig. 7.7 The building blocks of all proteins are the α-amino acids, where R may represent H, CH_3, or a more complex substituent. At the physiological pH, there may be equilibrium between the neutral and charged species

Fig. 7.8 A condensation reaction between two amino acids results in the formation of a peptide bond and one water molecule

(glu–cys–gly), while insulin with a molecular weight of 5,700 is made up of 51 amino acids. Polypeptides with molecular weights of approximately 6,000 or higher are generally called proteins. The sequence and the number of amino acids in a polypeptide, determines the biological function of the molecule. With the 20 natural amino acids, which can be assembled in any order, there is essentially an infinite (10^{18}) variety of possible sequences of protein molecules.

7.4.1.2 Protein Structure and Function

The order, or sequence of amino acids in the protein chain, is called the *primary structure*, which determines the biological property. The arrangement of the chain of the long molecule is called the *secondary structure*, determined to a large extent by the hydrogen bonding within the chain coils, forming a spiral structure called an α-helix, which gives the protein elasticity. Proteins having nostructural functions are *globular*. The overall shape of the protein, long and narrow or globular is called its *tertiary structure*. The amino acid cysteine plays a special role in stabilizing the tertiary structure of proteins because of disulfide linkage. The process of breaking down the three dimensional structure of proteins is called *denaturation*. Proteins have a wide range of specific functions in the body such as structure, movement, transport, catalysis, energy transformation, control, and buffering. Receptor protein molecules on the cell membrane are highly specific and bind to hormones, neurotransmitters, and specific molecules to initiate specific functions within the cell. Nearly all chemical reactions in living systems are catalyzed by enzymes, which are almost always proteins. Expression of genetic information is also under the control of proteins.

7.4.2 Carbohydrates

Carbohydrates or sugars are characterized by structures in which each carbon atom has an oxygen atom attached to it. All the carbon atoms in the molecule, except one, have hydroxyl groups attached to them. The remaining one carbon atom has the oxygen in the form of an aldehyde (sugar is called *aldose*) or ketone (sugar is called *ketose*). For example, glucose is an aldose, while fructose is a ketose. Carbohydrates, such as starch and cellulose, are polymers composed of monomers called *monosaccharides* or *simple sugars*. Specific examples of pentoses (containing five carbon atoms), D-*ribose*, D-*arabinose*, and hexoses (containing six carbon atoms), and D-*glucose* and D-*fructose* (found in honey and fruit) are shown in Fig. 7.9.

7.4.2.1 Stereochemistry of Sugars

The number of optical isomers each sugar may have depends on the number of *chiral* centers or asymmetric carbon atoms. It turns out that there are 2^n possible different stereochemical forms, where *n* represents the number of chiral centers. For example, glyceraldehyde has one chiral center and two optical isomers; D and L forms (Fig. 7.10). On the other hand, glucose has four chiral centers and 16 optical isomers that differ in their ability to rotate plane-polarized light. The mirror-image forms of a pair of enantiomers will rotate the plane-polarized light in opposite directions to the same extent, but have identical properties. If we invert the stereochemistry of one of the chiral centers, the chemical properties also change. Compounds like glucose and mannose, that differ by the inversion of only one optical center are called *diastereomers*.
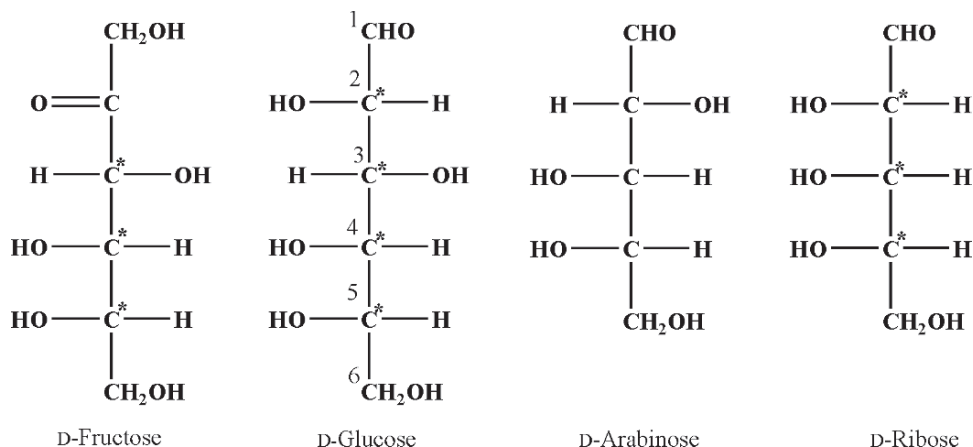
D-Fructose   D-Glucose   D-Arabinose   D-Ribose

Fig. 7.9 Most important carbohydrates, such as starch and cellulose, are polymers composed of monomers called *monosaccharides*, or simple sugars; *pentoses* (such as ara-

binose and ribose) contain five carbon atoms, while *hexoses* (such as fructose and glucose) contain six carbon atoms
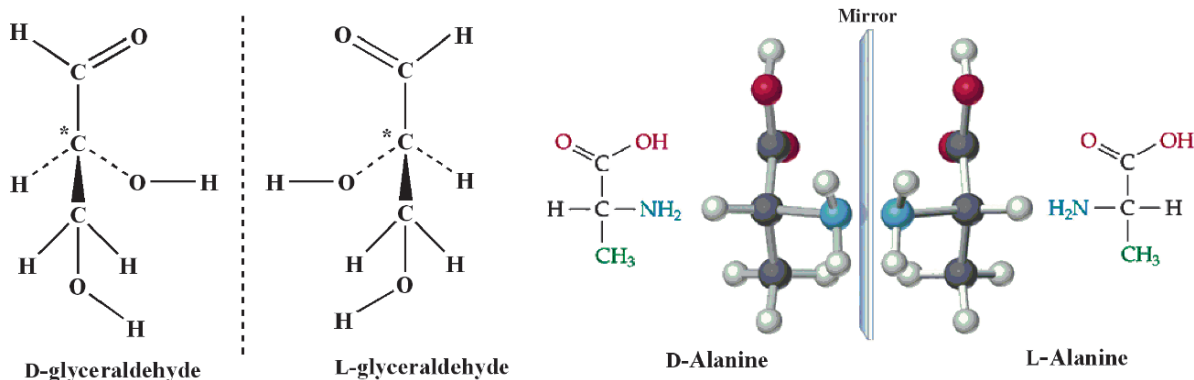

Fig. 7.10 A carbon atom with four different groups (also known as asymmetric carbon) bonded to it in a tetrahedral arrangement gives rise to a pair of *optical isomers*

that are *nonsuperimposable*. The D,L forms are based on glyceraldehydes. Similar optical isomers also exist with amino acids

The absolute configuration, designated by D- or L-, depends on the sugar's relationship to glyceraldehydes. In a sugar, if the terminus most remote from the carbonyl group has the D- configuration of glyceraldehyde, then that sugar is also called D- form. For example, the 5-carbon in D-glucose and D-fructose, has the same configuration as the D-glyceraldehyde. However, in terms of optical rotation, glucose D-glucose is dextrorotatory (*d* or (+)), while D-fructose is levorotatory (*l* or (−)).

Simple sugars in solution, usually *cyclize*, or form a ring structure due to the creation of a new bond between the oxygen atom of the terminal hydroxyl group and

the carbon of the aldehyde or ketone group. The cyclization of glucose resulting in the formation of a *hemiacetal*, will have two different rings, designated as α and β forms, which differ in the orientation of the hydroxy group and hydrogen atom on 1-carbon, as shown in the Fig. 7.11.

Polysaccharides

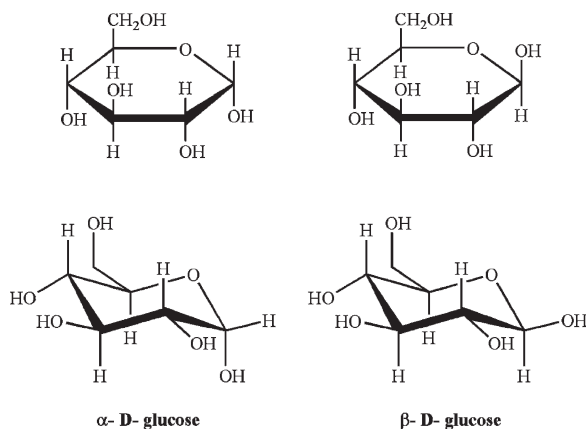More complex carbohydrates are formed by combining simple sugars. For example, sucrose, common

Fig. 7.11 The cyclization of glucose. Two different rings are possible; the two different forms designated as α and β, differ in the orientation of H and OH groups on C-1. The structural arrangement of atoms can be shown in the cyclohexane ring form (*top*) or the chair cyclohexane ring form (*bottom*)

table sugar, is a *disaccharide* formed from glucose and fructose by elimination of water to form a C–O–C bond between the rings, which is called a *glycoside linkage*. Another disachharide is lactose of milk sugar, which is a combination of glucose and galactose. Most of the carbohydrates in nature are polymers of repeating sugar units, called *polysaccharides* such as *starch*, *cellulose*, and *glycogen*. They are polymers of glucose (300–3,000 units) that yield only glucose upon hydrolysis. These polymers differ from each other in the nature of glycoside linkage, the amount of branching, and molecular weight.

Sugar derivatives

Carboxylic acid derivatives of glucose are quite common. If the C-1 aldehyde group is oxidized to a carboxyl group, the acid formed is called *gluconic acid*. On the other hand, if the C-6 hydroxy group is oxidized to a carboxyl group, *glucuronic acid* results. In vivo, the nonpolar drug metabolites are converted to polar metabolites by linking glucuronic acid, via a hydroxyl group. Such metabolites are called *glucuronides*. One of the most popular analogs of glucose, used in nuclear medicine, is glucoheptonic acid, which is a C-7 homologue of glucose.

7.4.3 Lipids

Lipids have widely variable chemical structures but a common nonpolar nature. They are defined as water-insoluble substances. The lipids found in the human body can be divided into four different classes according to their molecular structure: *fats*, *phospholipids*, *waxes*, and *steroids*. Fats and phospholipids are derived from trihydroxy alcohol, *glycerol* and *fatty aci*ds, while waxes are derived from monohydroxy alcohol and fatty acids. Steroids are derived from C_{30} compounds or *triterpenes*.

7.4.3.1 Fats

The most common fats in meats and the milk butterfat are esters made when glycerol reacts with long-chain carboxylic acids or *fatty acids*. Fats that are esters of glycerol are called triglycerides where the fatty acids may be saturated or unsaturated. Naturally occuring fatty acids (Table 7.8) are monocarboxylic acids that are unbranched and contain even number of carbon atoms.

In a process called *saponification*, fats are heated in the presence of an alkali (such as NaOH and KOH) to hydrolyze the ester and produce glycerol and salts of fatty acids (also known as *soaps*). The sparingly soluble salts of fatty acids, when dispersed in water, form *micelles* that are aggregates of fatty acid anions, which have nonpolar tails in the interior, while the polar anionic heads point outward to interact with the water molecules.
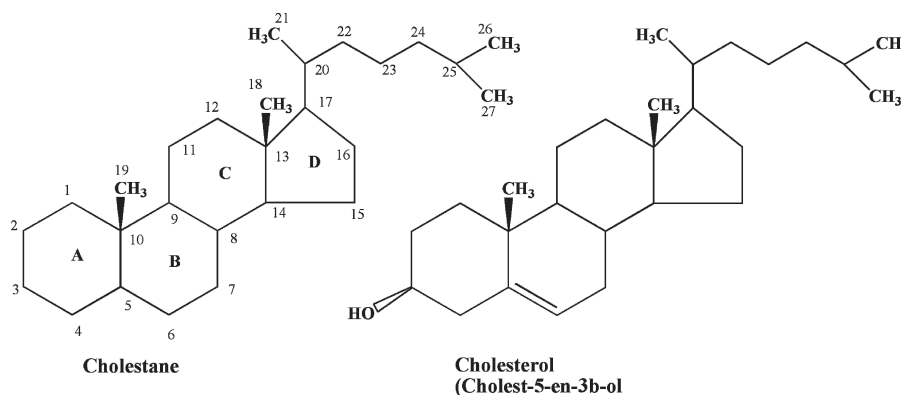
7.4.3.2 Phospholipids

Phopholipids are also esters of glycerol. However, unlike fats, phospholipids contain only two fatty acids, while the third ester linkage involves an phosphate group. The simplest form is phosphatidic acid, a major constituent of membranes. This molecule has a central asymmetric atom and can have a L or D configuration. It is the L-phosphatidic acid form which occurs naturally. Further, substitution on the phosphate group by molecules such as choline, ethanolamine and inositol, will produce phospholipids derivatives, which are con-

Table 7.8 Common fatty acids

Fatty acid	Molecular formula	Structural formula
Saturated fatty acids		
Butyric acid	$C_4H_8O_2$	$CH_3(CH_2)_2–COOH$
Caproic acid	$C_6H_{12}O_2$	$CH_3(CH_2)_4–COOH$
Lauric acid	$C_{12}H_{24}O_2$	$CH_3(CH_2)_{10}–COOH$
Palmitic acid	$C_{16}H_{32}O_2$	$CH_3(CH_2)_{14}–COOH$
Stearic acid	$C_{18}H_{36}O_2$	$CH_3(CH_2)_{16}– COOH$
Arachidic acid	$C_{20}H_{40}O_2$	$CH_3(CH_2)_{18}–COOH$
Unsaturated fatty acids		
Oleic acid	$C_{18}H_{34}O_2$	$CH_3(CH_2)_7CH=CH(CH_2)_7–COOH$
Linoleic acid	$C_{18}H_{32}O_2$	$CH_3(CH_2)_4CH=CH–CH_2–$ $CH=CH(CH_2)_7 – COOH$
Linolenic acid	$C_{18}H_{30}O_2$	$CH_3CH_2CH=CH–CH_2–CH=CH–$ $CH_2–CH=CH(CH_2)_7–COOH$
Arachidonic acid	$C_{20}H_{30}O_2$	$CH_3(CH_2)_4CH=CH–CH_2–CH=CH–$ $CH_2–CH=CH–CH_2–$ $CH=CH(CH_2)_3–COOH$

Fig. 7.12 The structure of steroids can be illustrated based on the completely saturated 27 carbon compound, cholestane while cholesterol is an unsaturated steroid alcohol, derived from cholestane

stituents of specialized membranes. One of the important phospholipids is L-*phosphatidylcholine* (*lecithin*).

The phospholipids have two distinct parts: the long nonpolar tail and the polar substituted phosphate head. Because of this dual nature, phospholipids tend to form bilayers in aqueous solution, similar to micelles described above. The bilayers of larger phospholipids can close to form *vesicles*. According to *the fluid mosaic model* of cell membranes, small uncharged molecules (such as H_2O, O_2, CO_2) can diffuse through the membrane, while other molecules pass through special *channels* and *transporters* provided by special proteins embedded in the cell membranes.

7.4.3.3 Steroids

Steroids are a class of lipids that have a characteristic ring structure consisting of four fused rings. Steroids include four major groups; cholesterol, adrenocorticoid hormones (such as cortisol and aldosterone), sex hormones (such as testosterone and estradiol), and bile acids. The simplest completely saturated compound is cholestane, which consists of 27 carbons, 17 of which constitute the ring system (Fig. 7.12), and three substituent groups; two methyl groups attached at C 10 and 13 and 8-carbon alkyl group at C 18 of the ring.

The biosynthesis of cholesterol starts with *lanosterol*, a 30 carbon steroid, first made from the triterpene, *squalene*. The liver synthesizes cholesterol and also disposes of it by transforming it into bile. In plasma, most of the cholesterol is conjugated to fatty acids by an ester linkage to the 3-hydroxyl group. Cholesterol also serves as a *precursor* for the formation of bile acids, steroid hormones and vitamin D. The 21 carbon adrenocorticoid hormones are synthesized in the adrenal gland. *Aldosterone* is involved in the regulation of water and the electrolyte balance in body fluids, while *cortisol* is

primarily involved in the regulation of protein and carbohydrate metabolism. The 19 carbon male sex hormone (*androgens*) *testosterone* is synthesized in the testes and adrenal cortex, but subsequently reduced to dihydrotetosterone in the prostate gland. There are two types of female sex hormones; 21 carbon progesterone, is produced by the corpus luteum and placenta, while the 18 carbon estrogens (17β-estradiol and estrone) are produced in the ovaries. Only in estrogens, is the A ring benzene-like or aromatic. Steroids are relatively nonpolar and in plasma they are solubilized by binding to transport proteins. The structures of steroid sex hormones are shown in Fig. 7.13.

7.4.4 Nucleic Acids

The ability of cells to maintain a high degree of order depends on the hereditary or genetic information that is stored in a polymer called *deoxyribonucleic acid* (DNA). Within the nucleus of all mammalian cells a full complement of genetic information is stored and the entire DNA is packaged into 23 pairs of *chromosomes*. A chromosome is formed from a single enormously long DNA molecule that consists of many small subsets called *genes* that represent a specific combination of DNA sequence, designed for a specific cellular function.

The chromosomes can undergo *self-replication* that permits DNA to make copies of itself. More specifically, as the cell divides and transfers the DNA (23 pairs of chromosomes) to daughter cells, which can thus inherit every property and characteristic of the original cell. There are approximately 30,000 genes per human genome, and the genes control every aspect of cellular function, primarily through protein synthesis. The sequence of amino acids in a particular protein or enzyme is encoded in a specific gene. The central dogma of molecular biology is that the overall process of information transfer in the cell involves the *transcription* of DNA into *ribonucleic acids* (RNA) molecules, which are much smaller than DNA and found in the cytoplasm. Subsequently, RNA is responsible for generating specific proteins on ribosomes by a process known as *translation*.

A major characteristic of DNA is its ability to encode an enormous quantity of biological information. Only a few picograms (10^{-12} g) of DNA are sufficient to direct synthesis of as many as 100,000 distinct proteins within a cell. This supreme coding effectiveness of DNA is due to its unique chemical structure.
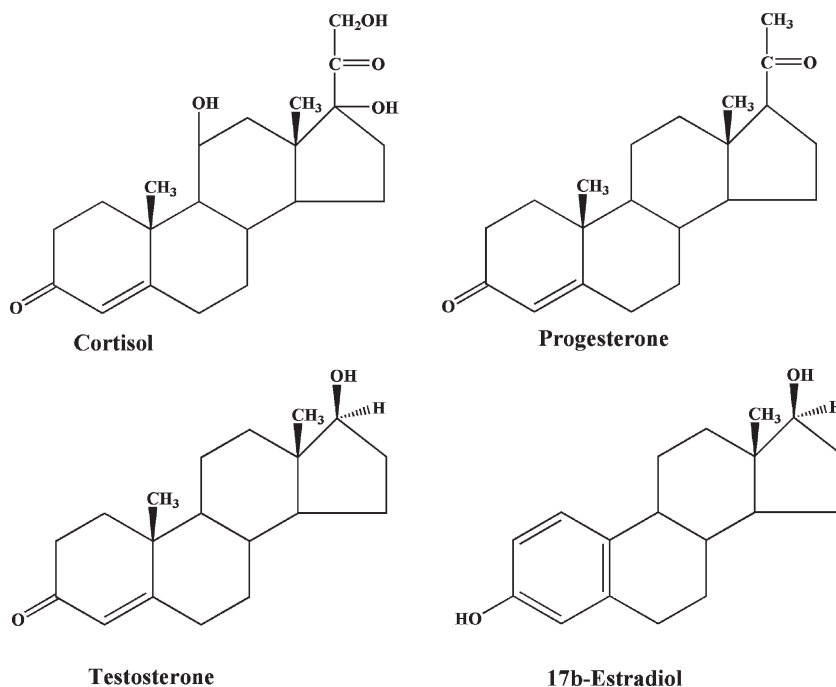

Fig. 7.13 The most common steroids hormones

7.4.4.1 DNA Structure

DNA was first discovered in 1869 by the chemist Friedrich Miescher who extracted a white substance from the cell nuclei of human pus and called it *nuclein*. Since nuclein is slightly acidic, it is known as nucleic acid. In the 1920s, the biochemist, P.A. Levine identified that there are two sorts of nucleic acids: DNA and RNA. Both DNA and RNA are *polynucleotide molecules* formed by the polymerization of nucleotides. Each nucleotide molecule is composed of three basic elements; a phosphate group, a five-carbon sugar, *deoxyribose* (in DNA) or *ribose* (in RNA), and one of the five types of nitrogen containing organic bases (Fig. 7.14). Three of the bases, *cytosine* (C), *thymine* (T) and *uracil* (U) are called *pyrimidines*, while the other two bases, *adenine* (A) and *guanine* (G) are called *purines*. Of the five bases, thymine is present only in DNA, while uracil is present only in RNA. The base and the sugar combine to form a unit called *nucleoside* by the elimination of one water molecule. The nucleoside in turn reacts with a phosphate group to form a unit called, nucleotide (Fig. 7.15), which is an ester. The nucleotides become connected through condensation reactions that eliminate water to give a polymer, which may contain billions of nucleotides in a single DNA molecule with a molecular weight as high as several billion grams per mole. In contrast, RNA molecules are small with molecular weights of 20,000–40,000.

The presence of 5′-phosphate and the 3′-hydroxyl groups in the deoxyribose molecule allows the DNA to form a long chain of polynucleotides by the joining of nucleotides by phosphodiester bonds (Fig. 7.16). Any
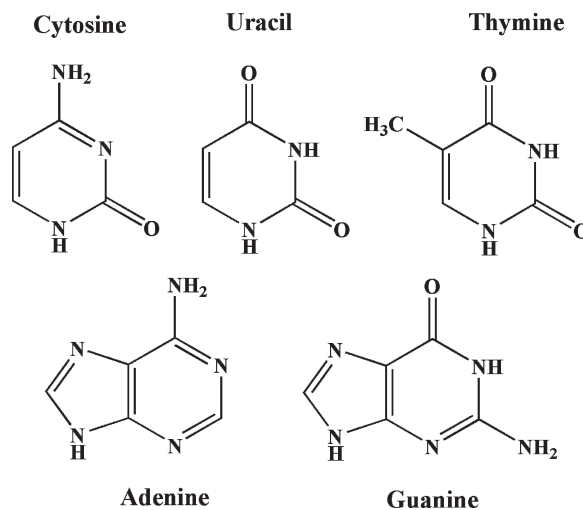

Fig. 7.14 The organic bases found in DNA and RNA. Thymidine is present only in DNA, while uracil is present only in RNA

linear strand of DNA will always have a free 5′-phosphate group at one end and a free 3′-hydroxyl group at the other end. Therefore, the DNA molecule has an intrinsic directionality (5′ to 3′ direction).

Although some forms of cellular DNA exist as single-stranded structures, the most widespread DNA structure, discovered by Watson and Crick in 1953, represents DNA as a double helix containing two polynucleotide strands that are complementary mirror images of each other. The "backbone" of the DNA molecule is composed of deoxyribose sugars joined by phosphodiester bonds to phosphate group, while the bases are linked in the middle of the molecule by hydrogen bonds. The relationship between bases in the double helix is
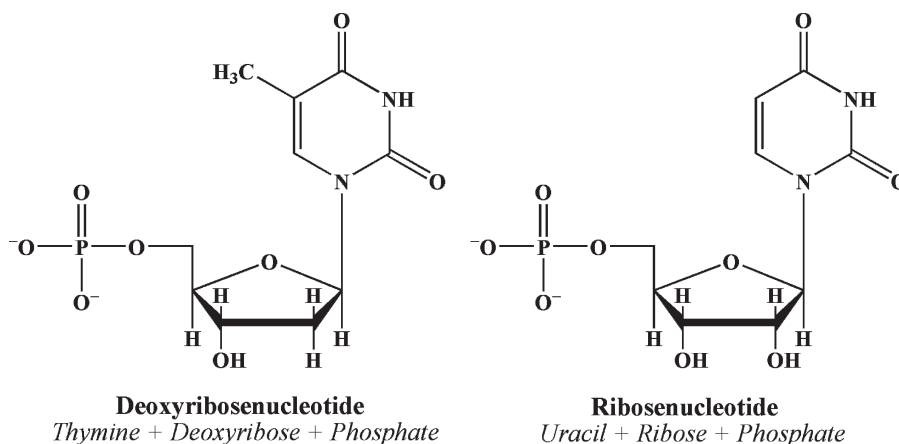

Fig. 7.15 The monomers of *nucleic acids* (DNA and RNA) are called *nucleotides*, which are composed of an organic base, a five-carbon sugar and a phosphoric acid molecule

Deoxyribosenucleotide
Thymine + Deoxyribose + Phosphate

Ribosenucleotide
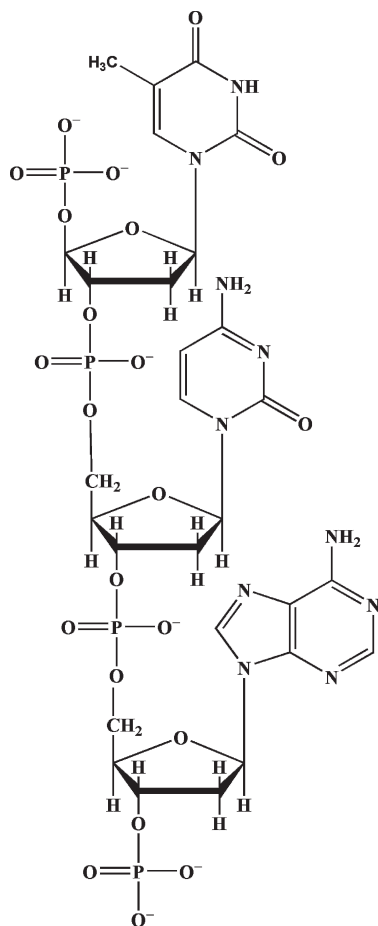*Uracil + Ribose + Phosphate*

Fig. 7.16 In a DNA molecule, the nucleotides become connected through condensation reactions to form a polymer, which may contain a billion units. DNA molecule, however, is a double-helical structure with complementary bases on the two strands that are connected by the bases, which form hydrogen bonds to each other

described as complementarity since adenine always bonds with thymine, and guanine always bonds with cytosine. As a consequence, the double-stranded DNA contains equal amounts of purines and pyrimidines. An important structural characteristic of the double-stranded DNA is that its strands are antiparallel meaning that the

two strands are aligned in opposite directions. During cell division, the two strands of DNA unwind and new complementary strands are generated.

7.4.4.2 Protein Synthesis

A given segment of DNA is called *gene*, which contains the code, the specific sequence of amino acids for a specific protein. The code is specific for each amino acid and consists of a set of three bases called a *codon* (Table 8.6). Gene expression involves the synthesis of a specific protein. This process is initiated by building a special RNA molecule, called *messenger RNA* (mRNA), in the nucleus from an appropriate gene. mRNA migrates into the cytoplasm where the protein is synthesized. Small RNA fragments, called *transfer RNA* (tRNA), containing only 75–80 nucleotides, decode the genetic message from the mRNA, using a complementary triplet of bases called an *anticodon*. mRNA builds the protein with the assistance of a ribosome. The tRNA molecule brings an appropriate amino acid to the mRNA. Soon after the codon and anticodon match, another tRNA, with its specific amino acid, moves to the second codon position. Once the two amino acids join together by peptide linkage, tRNA breaks away from its position. The process is repeated until the synthesis of protein is completed. The number of protein molecules synthesized by each cell, however, depends on the degree of gene expression that is warranted by the cell and the number of RNA molecules within the cytoplasm.

Additional Reading

Zumdahl SS (1998) Chemical principles, 3rd edn. Houghton Mifflin, Boston, MA, USA

Billinghurst MW, Fritzberg AR (1981) Chemistry for nuclear medicine. Year Book Medical, Chicago

Cell and Molecular Biology

<div style="text-align:right">**8**</div>

Almost all aspects of life are engineered at the molecular level, and without understanding molecules we can only have a very sketchy understanding of life itself.

<div style="text-align:right">Francis Harry Compton Crick</div>

8.1 Introduction

The cell is the basic unit of life in all forms of living organisms, from the smallest bacterium to the most complex animal. On the basis of microscopic and biochemical differences, living cells are divided into two major classes: *prokaryotes,* which include bacteria, blue–green algae, and rickettsiae, and *eukaryotes*, which include yeasts, and plant and animal cells. Eukaryotic cells are far more complex internally than their bacterial ancestors and the cells are organized into compartments or *organelles*, each delineated by a membrane. The DNA of the cell is packaged with protein into compact units called *chromosomes* that are located within a separate organelle, the *nucleus*. In addition, all eukaryotic cells have an internal skeleton, the *cytoskeleton* of protein filaments that gives the cell its shape, and its ability to arrange its organelles and provides the machinery for the movement.

The entire human body contains about 100 trillion cells, which are generated by repeated division from a single precursor cell. As proliferation continues, some of the cells become *differentiated* from others, adopting a different structure, chemistry, and function. In the human body, more than 200 distinct *cell types* are assembled into a variety of types of tissues, such as epithelia, connective tissue, muscle, and nervous tissue. Each organ in the body is an aggregate of many different cells held together by intercellular supporting structures. Although, the many cells of the body often differ markedly from one another, all of them have certain common basic characteristics. Each cell is a complex structure whose purpose is to maintain an intracellular environment favorable for complex metabolic reactions, to reproduce it when necessary, and to protect itself from the hazards of its surrounding environment.

8.2 Cell Structure and Function

The different substances that make up the cell are collectively called *protoplasm,* which is composed mainly of water, electrolytes, proteins, lipids, and carbohydrates. The two major parts of the cell (Fig. 8.1) are the *nucleus* and the *cytoplasm*. The nucleus is separated from the cytoplasm by a nuclear membrane, while the cytoplasm is separated from the extracellular fluid (ECF) by a cell membrane. The major organelles in the cell are of three general types: organelles derived from membranes, organelles involved in gene expression, and organelles involved in energy production. The important subcellular structures of the cell and their functions are summarized in Table 8.1.
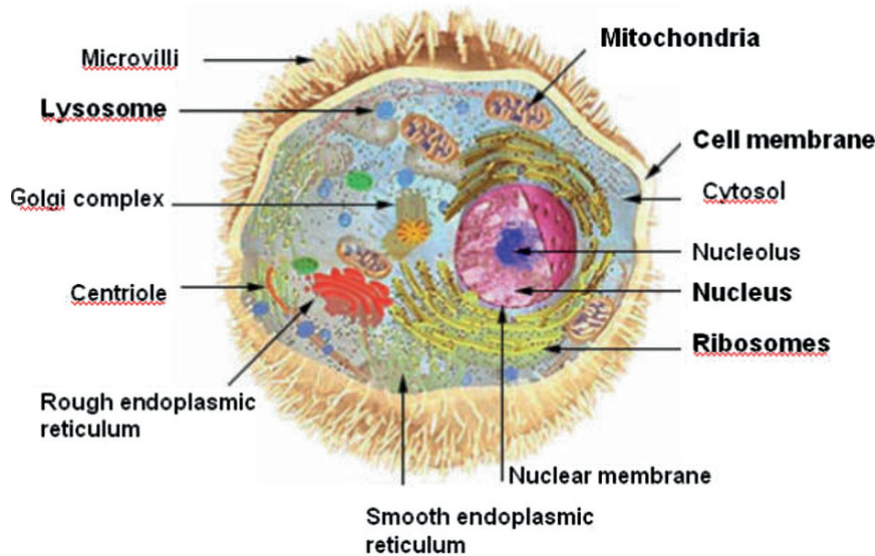
Fig. 8.1 A schematic drawing of an animal cell clearly depicting an intricate network of interconnecting, intracellular membrane structures such as the mitochondria, the nucleus, lysosomes, and the endoplasmic rough and smooth reticulum (facstaff.gpc. edu/~jaliff/anacell.htm)

Table 8.1 Cell structures (compartments) and their function

Cell structure	Major functions
Plasma membrane	Cell morphology and movement, transport of ions and molecules, cell-to-cell recognition, cell surface receptors
Endoplasmic reticulum	Formation of compartments and vesicles, membrane synthesis, synthesis of proteins and lipids, detoxification reactions
Lysosomes	Digestion of worn-out mitochondria and cell debris, hydrolysis of proteins, carbohydrates, lipids, and nucleic acids
Peroxisomes	Oxidative reactions involving molecular oxygen, utilization of hydrogen peroxide (H_2O_2)
Golgi complex	Modification and sorting of proteins for incorporation into organelles and for export, forms secretory vesicles
Microbodies	Isolation of particular chemical activities from the rest of the cell body
Mitochondria	Cellular respiration, oxidation of carbohydrates, proteins, and lipids, synthesis of urea and haeme
Nucleus	DNA synthesis and repair, RNA synthesis, control center of the cell, directs protein synthesis and reproduction
Chromosomes	Contain hereditary information in the form of genes
Nucleolus	RNA processing; assembling ribosomes
Ribosomes	Sites of protein synthesis in cytoplasm
Cytoplalasm	Metabolism of carbohydrates, lipids, amino acids, and nucleotides
Cytoskeleton	Structural support, cell movement, cell morphology

8.2.1 The Plasma Membrane

The plasma membrane encloses the cell, defines its boundaries, and maintains the essential difference between the cytosol and the extracellular environment. The cell membrane is an organized sea of lipid in a fluid state, a nonaqueous dynamic compartment of cells. The cell membranes are assembled from four major components: a lipid bilayer, membrane proteins, sugar residues, and a network of supporting fibers.

The basic structure of a cell membrane is a lipid bilayer of phospholipid molecules. The fatty acid portions of both the molecules are hydrophobic and occupy the center of the membrane, while the hydrophilic phosphate portions form the two surfaces in contact with intracellular fluid (ICF) and ECF. This lipid bilayer of 7–10 nm thickness is a major barrier impermeable to water-soluble molecules, such as ions, glucose, and urea. The three major classes of membrane lipid molecules are phospholipids (phosphatidylcholine, phosphatidylserine, phosphatidylethanolamine, sphingomyelin), cholesterol, and glycolipids. The lipid composition of different biological membranes varies depending on a specific function of the cell or cell membrane, as summarized in Table 8.2.

The cell surface often has a loose carbohydrate coat called *glycocalyx*. The sugar residues generally occur in combination with proteins (glycoproteins,

Table 8.2 The specific functions of the cell membrane components

Component	Composition	Function	How it works	Example
Lipid	Phospholipid bilayer	Permeability barrier	Polar molecules excluded	Glucose
Transmembrane protein	Channels	Passive transport	Creates a tunnel	Na^+, K^+ ions
	Carrier or transporters	Facilitated diffusion	Carrier "flip-flops"	Glucose transport
	Receptors	Transmits information into cell	Following receptor binding, induce activity in the cell	Peptide hormones, Neurotransmitters
Cell surface markers	Glycoprotein (GP)	"Self"-recognition	Shape of GP is characteristic of a cell or tissue	Major histo compatability complex recognized by immune system
	Glycolipid	Tissue recognition	Shape of carbohydrate chain is characteristic of tissue	A, B, O blood group markers
Interior Protein network	Clathrins	Anchor certain proteins to specific sites	Form network above the membrane to which proteins are anchored	Localization of LDL receptor within coated pits
	Spectrin	Determines cell shape	Forms supporting scaffold by binding to both membrane and cytoskeleton	Red blood cell

proteoglycans) or lipids (glycolipids). The oligosaccharide side chains are generally negatively charged and provide the cell with an overall negative surface charge. While some carbohydrates act as receptors for binding hormones, like insulin, others may be involved in immune reactions and cell–cell adhesion events.

The proteins of the membrane are responsible for most membrane functions, such as transport channels, pumps, carriers or transporters, specific receptors, enzymes, cell identity, and cell adhesion. The membrane proteins can be associated with the lipid bilayer in various ways, depending on the function of the protein. The polypeptide chain may extend across the lipid bilayer (transmembrane proteins) or simply be attached to one or the other side of the membrane.

8.2.2 *Cytoplasm and Its Organelles*

Cytoplasm or *cytosol* is an aqueous solution that fills the cytoplasmic matrix, the space between the nuclear envelope and the cell membrane. The cytosol contains many dissolved proteins, electrolytes, glucose, certain lipid compounds, and thousands of enzymes. In addition, glycogen granules, neutral fat globules, ribosomes, and secretory granules, are dispersed throughout the cytosol. Many chemical reactions of metabolism occur in the cytosol where substrates and cofactors interact

with various enzymes. The various organelles (Table 8.1) suspended in the cytosol are either surrounded by membranes (nucleus, mitochondria, and lysosomes) or derived from membranous structures (endoplasmic reticulum, Golgi apparatus). Within the cell, these membranes interact as an endomembrane system by being in contact, giving rise to one another, or passing tiny membrane-bound sacs called *vesicles* to one another. All biological membranes are phospholipid bilayers with embedded proteins. The chemical composition of lipids and proteins in membranes varies depending on a specific function of an organelle or a specific cell in a tissue or an organ.

8.2.2.1 The Endoplasmic Reticulum

The cytoplasm contains an interconnecting network of tubular and flat membranous vesicular structures called the *endoplasmic reticulum* (ER). Like the cell membrane, walls of the ER are composed of a lipid bilayer containing many proteins and enzymes. The regions of the ER rich in ribosomes are termed rough or granular ER, while the regions of the ER with relatively few ribosomes are called smooth or agranular ER. *Ribosomes* are large molecular aggregates of protein and ribonucleic acid (RNA) that are involved in the manufacture of various proteins by translating the messenger RNA (mRNA) copies of genes. Subsequently,

the newly synthesized proteins (hormones and enzymes) are incorporated into other organelles (Golgi complex, lysosomes) or transported or exported to other target areas outside the cell. Enzymes anchored within the smooth ER catalyze the synthesis of a variety of lipids and carbohydrates. Many of these enzyme systems are involved in the biosynthesis of steroid hormones and in the detoxification of a variety of substances.

8.2.2.2 The Golgi Complex

The *Golgi complex* or apparatus is a network of flattened, smooth membranes and vesicles. It is the delivery system of the cell. It collects, packages, modifies, and distributes molecules within the cell or secretes the molecules to the external environment. Within the Golgi bodies, the proteins and lipids synthesized by the ER are converted to glycoproteins and glycolipids, and collected in membranous folds or vesicles called cisternae, which subsequently move to various locations within the cell. In a highly secretory cell, the vesicles diffuse to the cell membrane and then fuse with it and empty their contents to the exterior by a mechanism called *exocytosis*. The Golgi apparatus is also involved in the formation of intracellular organelles, such as lysosomes and peroxisomes.

8.2.2.3 Lysosomes

Lysosomes are small vesicles (0.2–0.5 μm), formed by the Golgi complex and have a single limiting membrane. Lysosomes maintain an acidic matrix (pH 5 and below) and contain a group of glycoprotein digestive enzymes (hydrolases) that catalyze the rapid breakdown of proteins, nucleic acids, lipids, and carbohydrates into small basic building molecules. The enzyme content within lysosomes varies and depends on the specific needs of an individual tissue. Through a process of endocytosis, a number of cells either remove extracellular particles (phagocytosis), such as microorganisms, or engulf ECF with the unwanted substances (pinocytosis). Subsequently, the lysosomes fuse with the endocytotic vesicles and form secondary lysosomes or digestive vacuoles. Products of lysosomal digestion are either reutilized by the cell or removed from the cell by exocytosis. Throughout the lives of cells, lysosomes break down the organelles and recycle their component

proteins and other molecules at a fairly constant rate. However, in metabolically inactive cells, the hydrolases digest the lysosomal membrane and release the enzymes resulting in the digestion of the entire cell. By contrast, metabolically inactive bacteria do not die, since they do not possess lysosomes. Programmed cell death (apoptosis) or selective cell death is one of the principal mechanisms involved in the removal of unwanted cells and tissues in the body. In this process, lysosomes release the hydrolytic enzymes into the cytoplasm to digest the entire cell.

8.2.2.4 Peroxisomes

Peroxisomes are small membrane-bound vesicles or microbodies (0.2–0.5 μm), derived from the ER or Golgi apparatus. Many of the enzymes within the peroxisomes are oxidative enzymes that generate or utilize hydrogen peroxide (H_2O_2). Some enzymes produce hydrogen peroxide by oxidizing D-amino acids, uric acid, and various 2-hydroxy acids using molecular oxygen, while other enzymes, such as catalase, convert hydrogen peroxide to water and oxygen. Peroxisomes are also involved in the oxidative metabolism of long-chain fatty acids and different tissues contain different complements of enzymes depending on the cellular conditions.

8.2.2.5 Mitochondria

Mitochondria are tubular or sausage-shaped organelles (1–3 μm). They are composed mainly of two lipid bilayer-protein membranes. The outer membrane is smooth and derived from the ER. The inner membrane contains many infoldings or shelves called *cristae* which partition the mitochondrion into an inner matrix called *mitosol* and an outer compartment. The outer membrane is relatively permeable but the inner membrane is highly selective and contains different transporters. The inner membrane contains various proteins and enzymes necessary for oxidative metabolism, while the matrix contains dissolved enzymes necessary to extract energy from nutrients. Mitochondria contain a specific DNA. However, the genes that encode the enzymes for oxidative phosphorylation and mitochondrial division have been transferred to the chromosomes in the nucleus. The cell does not produce brand new

mitochondria each time the cell divides. Instead, mitochondria are self-replicative. Each mitochondrion divides into two and these are partitioned between the new cells. The mitochondrial reproduction, however, is not autonomous and is controlled by the cellular genome. The total number of mitochondria per cell depends on the specific energy requirements of the cell and may vary from less than one hundred to up to several thousand. Mitochondria are called the "power-houses" of the cell, where oxidative phosphorylation of various substrates derived from glucose and fatty acid enter the Krebs cycle to generate ATP molecules.

8.2.2.6 Ribosomes

Ribosomes are large complexes of RNA and protein molecules, and are normally attached to the outer surfaces of endoplasmic reticulum. The major function of ribosomes is to synthesize proteins. Each ribosome is composed of one large and one small subunit, with a mass of several million daltons.

8.2.3 Cytoskeleton

The cytoplasm contains a network of protein fibers called cytoskeleton that provides a shape to the cell and anchors various organelles suspended in cytosol. The fibers of the cytoskeleton are made up of different proteins of different sizes and shapes, such as actin (actin filaments), tubulin (microtubules), vimentin, and keratin (intermediate filaments). The exact composition of the cytoskeleton varies depending on the cell type and function. Centrioles are small organelles that occur in pairs within the cytoplasm, usually located near the nuclear envelope, and are involved in the organization of microtubules. Each centriole is composed of nine triplets of microtubules (long hollow cylinders of about 25 nm length) and plays a major role during cell division.

8.2.4 Nucleus

The nucleus is the largest membrane-bound organelle in the cell and occupies about 10% of the total cell volume. The nucleus is composed of a double membrane called *nuclear envelope* that encloses the fluid-filled interior called *nucleoplasm*. The outer membrane is contiguous with the ER. The nuclear envelope has numerous pores called nuclear pores which are about 90 Å in diameter and 50–80 nm apart, and permit certain molecules to pass into and out of the nucleus.

The primary functions of the nucleus are cell division and the control of the phenotypic expression of genetic information that directs all of the activities of a living cell. The cellular DNA is located in the nucleus as DNA-histone protein complex known as *chromatin* that is organized into *chromosomes*. The total genetic information stored in the chromosomes of an organism is said to constitute its *genome*. The human genome consists of 24 chromosomes (22 different chromosomes and two different sex chromosomes) and contains about 3×10^9 nucleotide pairs. The smallest unit of DNA that encodes a protein product is called a gene and consists of an ordered sequence of nucleotides located in a particular position on a particular chromosome. There are approximately 30,000 genes per human genome and only a small fraction (15%) of the genome is being actively expressed in any specific cell type. The genetic information is transcribed into RNA, which subsequently is translated into a specific protein on the ribosome. The nucleus contains a subcompartment called *nucleolus* that contains large amounts of RNA and protein. The main function of nucleolus is to form granular subunits of ribosomes, which are transported into the cytoplasm where they play an essential role in the formation of cellular proteins.

8.3 Cell Reproduction

All the cells in the human body are derived from a single cell, the fertilized egg, which undergoes trillions of cell divisions in order to become a new individual human being. Cells reproduce by duplicating their contents and then dividing into two equal halves. The reproduction of a somatic cell involves two sequential phases: *mitosis* (the process of nuclear division) and *cytokinesis* (cell division). In gametes, the nuclear division occurs through a process called *meiosis*. The life cycle of the cell is the period of time from one cell division to the next. The duration of the *cell cycle*, however, varies greatly from one cell type to another and is controlled by the DNA-genetic system.

8.3.1 The Cell Cycle

In all somatic cells, the cell cycle (Fig 8.2) is broadly divided into the *M phase* (or *mitosis*) and the *interphase* (growth phase). In most cells, the M phase takes only a small fraction of the total cycle, when the cell actually divides. The cell is in *interphase* during the rest of the time, which is subcategorized into three phases: G_1, S, and G_2. During the G_1 phase, most cells continue to grow, until they are committed to divide. If they are not ready to go into the S-phase, they may remain for a long time in a resting state known as G_0, before they are ready to resume proliferation. During the G_2 phase, cells synthesize RNA and proteins and continue to grow until they enter into the M-phase.

The reproduction of the cell really begins in the nucleus itself, where the synthesis and replication of the total cellular genome occurs during the S-phase. Every somatic cell is in a diploid phase, where the nucleus contains 23 pairs of chromosomes. Following replication, the nucleus has a total of 46 pairs of chromosomes. The chromosome pairs are attached at a point called *centromere*, and are called *chromatids*.

8.3.1.1 Mitosis and Cytokinesis

One of the first events of mitosis takes place in the cytoplasm. A pair of *centrioles* is duplicated just before DNA replication. Towards the end of interphase, the two pairs of centrioles move to the opposite poles of the cell.
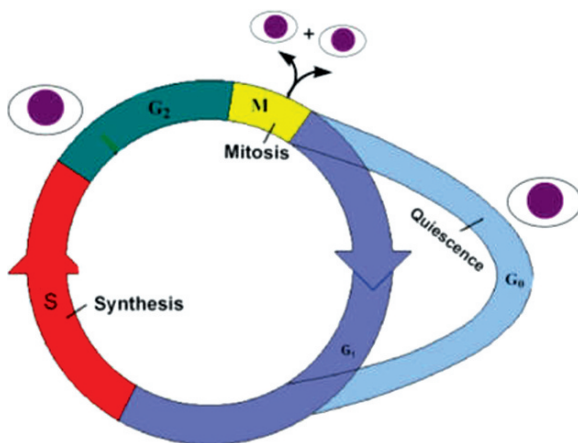
Fig. 8.2 The cell division cycle is generally represented by four successive phases

A complex of *microtubules* (spindle) pushes the centrioles farther apart creating the so-called mitotic apparatus. It is very important to note that mitochondria in the cytoplasm are also replicated before mitosis starts, as they have their own DNA. On the basis of specific events during nuclear division, mitosis is subcategorized into four phases. During the *prophase*, the nuclear envelope breaks down, chromosome condensation continues further, and the centromere of the chromatids is attached to opposite poles of the spindle. During the early *metaphase*, the spindle fibers pull the centromeres to the center forming an equitorial plate. At the end of the metaphase, the centromeres divide the chromatids into equal halves. During the *anaphase*, the sister chromatids are pulled apart, physically separated, and drawn to opposite poles, thus completing the accurate division of the replicated genome. By the end of the anaphase, 23 identical pairs of chromosomes are on the opposite sides of the cell. The *telophase*, the mitotic apparatus is disassembled, the nuclear envelope is reestablished around each group of 23 chromosomes, the nucleolus reappears, and finally the chromosomes begin to uncoil into a more extended form to permit expression of rRNA genes. Cytokinesis is the physical division of the cytoplasm and the cell into two daughter cells, which inherit the genome as well as the mitochondria.

8.3.2 Rates of Cell Division

For many mammalian cells, the standard cell cycle is generally quite long and may be 12–24 h for fast growing tissues. Many adult cells, such as nerve cells, lens of the eye, and muscle cells lose their ability to reproduce. Certain epithelial cells of the intestine, lungs, and skin divide continuously and rapidly in less than 10 h. The early embryonic cells do not grow, but divide very rapidly with a cell cycle time of less than an hour. In general, the mitosis requires less than an hour, while most of the cell cycle time is spent during the G_1 or G_0 phase. It is possible to estimate the duration of the S-phase by using tracers, such as ^{3}H-thymidine or bromodeoxyuridine (BrdU).

Control system regulating the cell division: The essential processes of cell reproduction such as the DNA replication and the sequence of cell cycle events are governed by a cell-cycle control system that is based on two key families of proteins: cyclin-dependent protein

kinases (Cdk), and activating proteins called *cyclins*. These two protein complexes regulate the normal cell cycle at the end of the G_1 and G_2 phases. The key component of the control system is a protein kinase known as *M-phase-promoting factor* (MPF), whose activation by phosphorylation drives the cell into mitosis. The mechanisms that the control cell division of mammalian cells in various tissues and organs depend on the social control genes and protein growth factors, as survival of the entire organism is the key, not the proliferation of individual cells. Growth factors, such as *platelet-derived growth factor* (PDGF), *fibroblast growth factor* (FGF), and *interlukin*-2, regulate cell proliferation through a complex network of intracellular signaling cascades, which ultimately regulate gene transcription and the activation of cell-cycle control system.

8.4 Cell Transformation and Differentiation

The zygote and blastomeres resulting from the first couple of cleavage divisions are *totipotent*, meaning that they are capable of forming any cell in the body. As the development progresses, certain decisions are made that narrow the developmental options of cells. At the decision point where cells become committed, a restriction event has occurred. The commitment of cells during cleavage to become either inner cell mass or *trophoblast* and the segregation of embryonic cells into the three germ layers are the early restriction events in the mammalian embryo. When a cell has passed its last decision point, its fate is fixed, and it is said to be *determined*. A cell is determined, if it has undergone a self-perpetuating change of internal character that distinguishes it and its progeny from other cells in the embryo and commits them to a specialized course of development. The determined cell may pass through many developmental stages, but can not move onto another developmental track. For example, a muscle cell can not become a nerve cell. Restriction and determination signify the progressive limitation of the development capacities in the embryo. Differentiation refers to the actual morphological or functional expression of the portion of genome that remains available to a determined cell or group of cells, and characterizes the phenotypic specialization of cells. Therefore, differentiation is the process of acquiring specific new characteristics

resulting in observable changes in cellular function. By contrast, cells within a developing embryo display the least amount of differentiation. In the adult, undifferentiated cells are known as *pluripotent cells,* which are precursor cells or *stem cells* that are not totally committed to a specific function.

The three germ layers *ectoderm*, *mesoderm* and *endoderm* have different fates. The endoderm forms a tube, the *primordium* of the digestive tract. It gives rise to the pharynx, esophagus, stomach, intestines, and several other associated organs such as liver, pancreas, and lungs. While the endoderm forms the epithelial components of these structures, the supporting muscular and fibrous elements arise from the mesoderm. In general, the mesoderm gives rise to the muscles and connective tissues of the body. The mesoderm first gives rise to *mesenchyme* and ultimately to cartilage, bone, fibrous tissue, and the dermis (the inner layer of the skin). In addition, the tubules of the urogenital system, vascular system, and the blood cells also develop from the mesoderm. The ectoderm forms the epidermis and the entire nervous system. In a process known as *neurulation*, a central portion of the ectoderm creates a neural tube that pinches off from the rest of the ectoderm and will form the brain and spinal cord. Some of the ectodermal cells develop into a *neural crest* and form all of the peripheral nervous system as well as the pigment cells of the skin.

Cells differentiate through several mechanisms. A cell and its progeny may contain sufficient intrinsic information to determine their phenotypic character. Cell differentiation generally depends on changes in gene expression rather than on gene loss, as the genome of a differentiated cell has the entire DNA content of the undifferentiated parent cell. In order to regulate the expression of genes, the most important point of control is the initiation of RNA transcription. These gene regulatory proteins can switch the transcription of individual genes on or off by recognizing short stretches of the DNA double helix of defined sequence and thereby determining which of the thousands of genes in a cell will be transcribed. Each cell may have a specific combination or different combinations of gene regulatory proteins. According to environmental models, cells respond to external signals and differentiate accordingly. For example, after exposure to 5-azacytidine, fibroblasts from a standard tissue culture line differentiate into skeletal muscle, cartilage, or adipose tissue.

8.5 Normal Growth

8.5.1 Cell Types

The human body is an ordered clone of cells, all containing the same genome but specialized in different ways. There are approximately 200 different cell types that represent, for the most part, discrete and distinctly different categories based on histological and morphological characteristics and cellular function. Recent subtler techniques involving immunohistology and mRNA expression are even revealing new subdivisions of cell types within the traditional classification. The different cell types, such as the neuron and lymphocyte, have the same genome, but the structural and functional differences are so extreme that it is difficult to imagine that they came from the same cell.

Different cell types synthesize different sets of proteins. However, many processes are common to all cells and have many proteins in common. However, some proteins are unique in the specialized cells, in which they function, and can not be detected anywhere else. The genome of a cell contains in its DNA sequence, the information to make many thousands of different proteins and RNA molecules. A cell typically expresses only a fraction of these genes and the different types of cells in a human body arise because different sets of genes are expressed. Moreover, cells can change the pattern of genes they express in response to signals from other cells or environment. Different cells perform different functions. The most important cellular functions are movement, conductivity, metabolic absorption, secretion, excretion, respiration, and reproduction.

8.5.2 Tissue Types

In the human body, specialized cells of one or more types are organized into cooperative assemblies called *tissues* that perform one or more unique functions. Different types of tissues combine to form organs, which in turn are integrated to perform complex functions.

The major types of tissues are epithelial, muscle, connective, nerve, blood, and lymphoid tissues that are further divided into many subtypes (Table 8.3). All cells are in contact with a network of extracellular

Table 8.3 Tissue types

Tissue	Tissue type	Location	Function
Epithelial	Simple squamous	Lines major organs	Absorption, filtration, and secretion
	Simple cuboidal	Lines tubules and ducts of glands	Absorption and secretion
	Simple columnar	Lines GI tract	Secretion and absorption
	Stratified Squamous	Lines interior of mouth, tongue, and vagina	Protection
	Transitional	Lines urinary bladder	Permits stretching
Connective	Loose connective	Deep layers of skin, blood vessels, and organs	Support, and elasticity
	Dense connective	Tendeons, and ligaments	Attaches structures together, and provides strength
	Elastic connective	Lungs, arteries, trachea, and vocal cords	Provides elasticity
	Reticular connenctive	Spleen, liver, and lymph nodes	Provides internal scaffold for soft organs
	Cartilage	Ends of long bones, trachea, and tip of nose	Provides flexibility and support
	Bone	Bones	Protection, support, and muscle attachment
	Vascular connective tissue	Within blood vessels	Transport of gases, and blood clotting
	Adipose tissue	Deep layers of skin, surrounds heart, and kidney	Support, protection, and heat conservation
Muscle	Smooth muscle	GI tract, uterus, blood vessels, and u.bladder	Propulsion of materials
	Cardiac muscle	Heart	Contraction
	Skeletal muscle	Attached to bones	Movement
Neural	Different types of Neurons	Brain and spinal cord	Conduction of electrical impulse, and neurotransmission

macromolecules, known as *extracellular matrix*, that holds cells and tissues together and provides an organized latticework within which cells can migrate and interact with one another.

8.6   Cell-to-Cell Communication

Cells in the human body are programmed to communicate with each other and to respond to a specific set of signals in order to regulate their growth, replication, development, and organization into tissues, and coordinate their overall biochemical behavior. Cells communicate with one another in three ways: (a) through physical contact with one another by forming cells junctions, (b) by secreting chemical signaling, molecules that help communication at a distance, and (c) by cellular receptors which bind to specific signaling molecules and respond by generating intracellular messengers.

8.6.1   Cell–Cell Interaction

Cells in tissues are in physical contact with neighboring cells and extracellular matrix at specialized contact sites, called cell junctions (communicating, occluding, and anchoring), which allow transport of molecules between cells or provide a barrier to passage of molecules between cells. Gap or communicating junctions are composed of clusters of channel proteins that create an intercellular gap (1.5 nm wide) to allow small molecules to pass directly from cell to cell. Cells connected by gap junctions are electrically and chemically coupled, since the cells share ions and small molecules. Occluding or tight junctions exist primarily in epithelial sheets. The tight junctions form a continuous, impermeable, or semipermeable barrier to diffusion and play an important part in maintaining the concentration differences of small hydrophilic molecules across epithelial sheets and restrict the diffusion of membrane transport proteins. Anchoring junctions such as *adherens*, *desmosomes*, and *hemidesmosomes* are most abundant in tissues that are subjected to severe mechanical stress and connect the cytoskeletal elements (actin or intermediate filaments) of a cell to those of another cell or to the extracellular matrix. To form an anchoring junction, cells must first adhere.

Such a selective cell adhesion or tissue-specific recognition process is mediated by two distinct classes of cell–cell adhesion molecules (CAMs). Cadherins, the transmembrane glycoproteins, mediate Ca^{2+}-dependent cell–cell adhesion, while the neural cell adhesion molecule (N-CAM) mediates the Ca^{2+}-independent cell–cell adhesion systems.

A substantial part of the tissue volume is the extracellular space that is filled by an extracellular matrix which is composed of proteins and polysaccharides that are secreted locally by the cells in the matrix. The extracellular matrix not only binds the cells together, but also influences their development, polarity, and behavior. The two main classes of macromolecules that make up the matrix are glycosaminoglycans (GAGs) and fibrous proteins.

8.6.2   Cell Signaling and Cellular Receptors

Cells communicate by means of hundreds of types of intercellular signaling molecules that include amino acids, peptides, proteins, steroids, nucleotides, fatty acid derivatives, and dissolved gases. The four primary modes of chemical signaling are *endocrine*, *paracrine*, *autocrine*, and *synaptic*. Endocrine signaling involves specialized endocrine cells that secrete the signaling molecules (hormones) into the blood stream, which are transported to distant target cells distributed throughout the body in order to produce a response in different cells and tissues. In paracrine signaling, the signal molecules that a cell secretes may act as local mediators, affecting only the neighboring cells. In autocrine signaling, the signal molecules secreted by a cell act on the same cell that generates them. In synaptic signaling, the signal molecules (neurotransmitters) secreted by a cell (neuron) bind to the receptors on a target cell at a specialized cell junction, called *synapse*.

The cellular receptors are very specific protein molecules on the plasma membrane, in the cytoplasm, or in the nucleus, that are capable of recognizing and binding the extracellular signaling molecules, also called *ligands*. As a consequence of ligand–receptor interaction, the cell may generate a cascade of intracellular signals that alter the pattern of gene expression and the behavior of the cell. One of the final steps in the signal transduction pathway is the phosphorylation of an effector protein by a protein kinase. Through cascades of

Table 8.4 Cell surface receptors

Receptor family	Enzyme	Second messenger	Signaling molecule
A. Ion-channel-linked			
G-protein-linked	Activate adenyl cyclase	Increase cyclic AMP	TSH, ACTH, LH, Adrenaline, glucagon, and vasopressin
	Inhibit adenyl cyclase	Decrease cyclic AMP	Cholera toxin, pertussis toxin
	Activate phosphoinositide-specific phospholipase C	Inositol triphosphate (IP3) increases Ca2+	Vasopressin, acetylcholine, and thrombin
	Activate or inactivate ion channels		Acetylcholine (nicotinic Ach receptors)
B. Enzyme-linked			
Receptor guanylyl cyclases	Activate guanylyl cyclase	Increase Cyclic GMP	Atrial natriuretic peptides (ANPs)
Receptor tyrosine kinases	Activate tyrosine kinase	Phosphorylate specific tyrosine residues	Growth factors (PDGF, FGF, VEGF, M-CSF), and insulin
Tyrosine-kinase-associated receptors	Receptor dimerization	same as above	Cytokines, interleukin-2, growth hormone, prolactin
Receptor tyrosine phosphatases	Activate tyrosine phosphatase	Remove phosphate groups from tyrosine residues	Extracellular antibodies
Receptor serine/threonine kinases		Phosphorylate serine and threonine residues	

highly regulated protein phophorylations, elaborate sets of interacting proteins relay most signals from the cell surface to the nucleus, thereby altering the cell's pattern of gene expression and, as a consequence, its behavior.

Small hydrophobic signal molecules, including the thyroid and steroid hormones, diffuse into the cell and activate receptor proteins that regulate gene expression. Some dissolved gases, such as nitric oxide and carbon monoxide, activate an intracellular enzyme (guanyl cyclase), which produces cyclic GMP in the target cell. Most of the extracellular signal molecules are hydrophilic and activate transmembrane receptor proteins on the surface of the cell membrane. The ligands that bind with membrane receptors include hormones, neurotransmitters, lipoproteins, antigens, infectious agents, drugs, and metabolites.

Generally, receptors are classified on the basis of their location and function. Three main families of cell-surface receptors (Table 8.4) have been identified. Following the binding of a specific signal, ion-channel-linked receptors open or close briefly to allow transport of molecules into the cell. G-protein-linked receptors activate or inactivate plasma membrane bound enzymes or ion channels via trimeric GTP-binding proteins (G proteins). Some G-protein linked receptors activate or inactivate adenyl cyclase and alter the intracellular concentration of cyclic AMP, while some others generate inositol triphosphate (IP_3), which increases intracellular Ca^{2+} levels. A rise in cyclic AMP

or Ca^{2+} levels stimulates a number of kinases and phosphorylates target proteins on serine or threonine residues. Enzyme-linked receptors, such as protein kinases, phosphorylate specific proteins in the target cell. There are five known classes of enzyme-linked receptors (Table 8.4). Among these, receptor tyrosine kinases and tyrosine-kinase-associated receptors are by far the most common. Most of the mutant genes (*Ras, Src, Raf, Fos, and Jun*) that encode the proteins in the intracellular signaling cascades that are activated by tyrosine kinases were identified as *oncogenes* in cancer cells, as their inappropriate activation causes a cell to proliferate excessively. By contrast, the normal genes are, therefore, referred to as *protooncogenes*.

8.7 Transport Through the Cell Membrane

About 56% of the adult human body is fluid. One third of the fluid is outside the cells and is called *ECF* while the remainder is called *ICF*. The ECF (the internal environment) is in constant motion throughout the body and contains the ions (sodium, chloride, and bicarbonate) and nutrients (oxygen, glucose, fatty acids, and amino acids) needed by cells for the maintenance of life. Cells secrete various intracellular signal molecules and expel metabolites and waste products into the ECF.

The cellular intake or output of different molecules occurs by different transport mechanisms of the plasma membrane, depending on the chemical and biochemical characteristics of the solute molecules.

The cell membrane consists of a lipid bilayer that is not miscible with either the ECF or the ICF and provides a barrier for the transport of water molecules and water-soluble substances across the cell membrane. Water and small molecules diffuse through the membrane via gaps or transitory spaces in the hydrophobic environment created by the random movement of fatty acyl chains of lipids.

The transport proteins within the lipid bilayer, however, provide different mechanisms for the transport of molecules across the membrane. Membranes of most cells contain pores or specific *channels* that permit the rapid movement of solute molecules across the plasma membrane. Examples of pores are plasma membrane gap junctions and nuclear membrane pores. Channels are selective for specific inorganic ions, whereas pores are not selective. Voltage-gated channels, such as the sodium channel, control the opening or closing of some channels by changes in the transmembrane potential. Chemically regulated channels, such as the nicotinic–acetylcholine channel, open or close on the basis of the binding of a chemical to the channel.

Plasma membranes contain transport systems (transporters) that involve intrinsic membrane proteins and actually translocate the molecule or ion across the membrane by binding and physically moving the substance. Transporters have an important role in the uptake of nutrients, maintenance of ion concentrations, and control of metabolism. Some carrier proteins transport a single solute or molecule across a membrane and these are called *uniporters*. With some other carrier proteins (coupled transporters), transfer of one solute depends on the simultaneous or sequential transfer of a second solute, either in the same direction (*symport*) or in the opposite direction (*antiport*). Transporters are classified on the basis of their mechanism of translocation of a substance and the energetics of the system. Transporters have specificity for the substance to be transported, have defined reaction kinetics, and can be inhibited by both, competitive and noncompetitive inhibitors. Membranes of all cells contain highly specific transporters for the movement of inorganic anions and cations (Na^+, K^+, Ca^{2+}, Cl^-, HCO_3^-), and uncharged and charged organic compounds (amino acids, sugars).

Transport through the lipid bilayer or through the transport proteins involves simple diffusion, passive transport (facilitated diffusion), or active transport mechanisms. Certain macromolecules may also be transported by vesicle formation involving either endocytosis or exocytosis mechanisms. The major transport systems in mammalian cells are summarized in Table 8.5.

8.7.1 Diffusion

Body fluids are composed of two types of solutes: electrolytes, which ionize in solution and exhibit polarity (cations and anions), and nonelectrolytes, such as glucose, creatinine and urea, that do not ionize in solution. The continous movement of solute molecules among one another in liquids or in gases is called *diffusion*. The solute molecules in the ECF or in the cytoplasm can spontaneously diffuse across the plasma membrane. However, the direction of movement of solutes by diffusion is always from a higher to a lower concentration and Fick's first law of diffusion describes the rate. The overall effect of diffusion is the passive movement of molecules down a concentration until the concentration on each side is at chemical equilibrium. Diffusion through the cell membrane is divided into two separate subtypes called simple diffusion and facilitated diffusion (Fig. 8.3).

8.7.1.1 Simple Diffusion

Simple Diffusion can occur through the cell membrane either through the intermolecular interstices of the lipid bilayer or through transport proteins (watery channels). The diffusion rate of a solute depends on its size (diffusion coefficient) and its lipid solubility. In addition, the diffusion rate is influenced by the differences in electrical potential across the membrane. Diffusion of small uncharged molecules (water, urea, glycerol) and hydrophobic molecules, such as gases (O_2, N_2, CO_2, NO), occurs rapidly and depends entirely on the concentration gradient. Uncharged lipophilic molecules (fatty acids, steroids) diffuse relatively rapidly, but hydrophilic substances (glucose, inorganic ions) diffuse very slowly. *Osmosis* is a special case of diffusion in which

Table 8.5 Transport mechanisms across plasma cell membrane

Mechanism	Transport process	Example
A. Nonspecific processes		
Simple diffusion	Direct through the membrane and is dependent on concentration gradient	Oxygen movement into cells
Osmosis	Direct diffusion of water molecules across a semipermeable membrane	Movement of water into cells, when placed in hypotonic solution
Endocytosis		
Phagocytosis	Particles are engulfed by membrane through vesicle formation	Ingestion of bacteria or particles by leukocytes
Pinocytosis	Fluid is engulfed by membrane through vesicle formation	Transport of nutrients by human egg cells
Exocytosis	Extrusion of material from a cell involves membrane vesicles	Secretion of proteins by cells via small membrane vesicles
B. Specific processes		
Facilitated diffusion	Transport of molecules into the cells involve protein channels or transporters and is dependent on concentration gradient	Movement of glucose into most cells
Primary active transport	Transport of molecules against concentration gradient involves carrier protein and requires energy derived by hydrolysis of ATP	Na^+, K^+, Ca^{2+}, H^+ and Cl^- ions
Secondary active transport	As a consequence of primary active transport, sodium ions can pull other solutes into the cell (cotransport)	Glucose and amino acids
Receptor-mediated endocytosis	Endocytosis is triggered by the binding of a molecule to a specific receptor on the cell surface followed by internalization of vesicles	Cholesterol (LDL) and transferrin uptake by cells

free passage of water molecules (but not that of solute molecules) across a cell membrane is permitted.

8.7.1.2   Facilitated Diffusion

Passive transport or facilitated diffusion (also known as carrier-mediated diffusion) involves the translocation of a solute through a cell membrane down its concentration gradient, as in simple diffusion, without expenditure of metabolic energy. However, facilitated diffusion requires the interaction of a carrier protein (transporter) with the solute molecules. Upon entering the protein channel, the solute chemically binds to the transporter and induces a conformational change in the carrier protein, so that the channel is open on the intracellular side and releases the molecule (Fig. 8.3). The rate of diffusion is dependent on the concentration gradient and approaches a maximum, called V_{max}, as
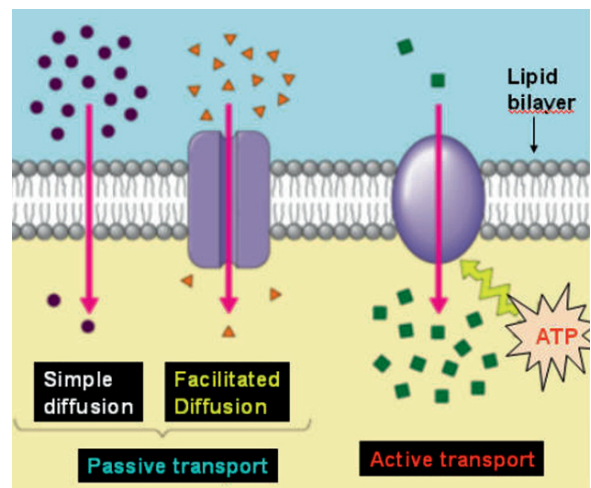
Fig. 8.3 Membrane transport mechanisms of small molecules; simple diffusion is simply dependent on the concentration gradient while facilitated diffusion involves specific membrane transporters, such as channel proteins or carrier proteins. Active transport requires expenditure of energy

the concentration of solute increases. It is very important to recognize that in facilitated diffusion, the transporters are very specific for a solute and exhibit saturation kinetics. Transport of D-glucose is facilitated and a family of transporters (glucose permeases or GLUT 1–6) has been identified. Similarly, an anion transporter (Cl^-–HCO_3^- exchanger) in erythrocytes involves antiport (two molecules in opposite directions) movement of Cl and HCO_3^- ions.

8.7.2 Active Transport

Active transport systems or pumps move the solute molecules through a cell membrane against their concentration gradient and require the expenditure of some form of energy (Fig. 8.3). As a result, the concentration of solute molecules on either side of plasma membrane is not equal. For example, the concentration of Na^+ ions in the ECF is 10 times more than the concentration of Na^+ ions in the cytoplasm, while the converse is true with K^+ ions. In active transport, the transporters are very specific for a solute and exhibit saturation kinetics. In addition, the carrier protein imparts energy to the solute to move against electrochemical or concentration gradient. If the energy source is removed or inhibited, the active transport mechanism is abolished. Most of the ions, amino acids, and certain sugars are actively transported across the plasma membrane.

In primary active transport, the energy is derived directly from the hydrolysis of ATP to ADP. The best known active transport system is the $Na^+ + K^+$-dependent ATPase pump (Fig. 8.3) found in virtually all mammalian cells. The transporter protein is an enzyme, ATPase. When three sodium ions bind on the inside and two potassium ions bind on the outside, the ATPase function of the transporter is activated. Following hydrolysis of one molecule of ATP, the liberated energy causes conformational change in the carrier protein, releasing sodium ions to the outside and potassium ions to the inside. The process leads to an electrical potential, with the inside of the cell being more negative than the outside. The excitable tissues (muscle and nerve), kidneys, and salivary glands have a high concentration of the $Na^+ + K^+$-dependent ATPase pump. The other important primary active transport pumps are for the transport of Ca^{2+} and H^+ ions.

The secondary active transport represents a phenomenon called cotransport, in which molecules are transported through the plasma membrane using the energy obtained not directly from the hydrolysis of ATP, but from the electrochemical gradient across the membrane. When sodium ions are transported out of the cells, an electrical potential develops which provides energy for the sodium ions to diffuse into the interior. This diffusion energy of sodium ions can pull other molecules into the cell. Glucose and many amino acids are transported into most cells via sodium cotransport system. Following the binding of sodium and glucose molecules to specific sites on the sodium–glucose transport protein, a conformational change is induced, and both the molecules are transported into the cell.

8.7.3 Transport by Vesicle Formation

Transport of macromolecules such as large proteins, polysaccharides, nucleotides, and even other cells across the plasma membrane, is accomplished by a unique process, and called *endocytosis* that involves special membrane bound vesicles. The material to be ingested is progressively enclosed by a small portion of the plasma membrane, which first invaginates and then pinches off to form an intracellular vesicle. Many of the endocytosed vesicles end up in lysosomes, where they are degraded. Endocytosis is subcategorized into two types: *pinocytosis* involves ingestion of fluid and solutes via small vesicles, while *phagocytosis* involves ingestion of large particles such as microorganisms via large vesicles called phagosomes.

Specialized cells that are professional phagocytes, such as macrophages and neutrophils, mainly carry out phagocytosis. For example, more than 10^{11} senescent red blood cells are phagocytosed by macrophages every day in a human body. In order to be phagocytosed, particles must bind to specialized receptors on the plasma membrane. Phagocytosis is a triggered process that requires the activated receptors to transmit signals to the interior of the cell to initiate the response. The Fc receptors on macrophages recognize and bind the Fc portion of antibodies that recognize and bind microorganisms.

Most cells continually ingest bits of their plasma membrane in the form of small pinocytic (endocytic) vesicles that are subsequently returned to the cell surface.

The plasma membrane has highly specialized regions, called clathrin-coated pits, that provide an efficient pathway for taking up macromolecules via a process called receptor-mediated endocytosis. Following binding of macromolecules to specific cell surface receptors in these clathrin-coated pits, the macromolecule-receptor complex is internalized. Most receptors are recycled via transport vesicles back to the cell surface for reuse. More than 25 different receptors are known to participate in receptor-mediated endocytosis of different types of molecules. The low density lipoprotein (LDL) and transferrin are the most common macromolecules that are transported into the cell via receptor mediated endocytosis.

The reverse of endocytosis is *exocytosis* that involves transport of macromolecules within vesicles from the interior of a cell to the cell surface or into the ECF. Proteins and certain neurotransmitters can be secreted from the cells by exocytosis in either a constitutive or a regulated process. For example, insulin molecules stored in intracellular vesicles are secreted into the ECF following fusion of these vesicles with the plasma membrane. By contrast, neurotransmitter molecules stored in synaptic vesicles of a presynaptic neuron are released into a synapse only in response to an extracellular signal.

8.7.4 Transmission of Electrical Impulses

Nerve and muscle cells are "excitable," which implies that they are capable of self-generation of electrochemical impulses at their cell membranes. These impulses can be employed to transmit signals, such as nerve signals, from the central nervous system to many tissues and organs throughout the body. There is a difference in the ionic composition of ECF and ICF. Whenever ion channels open or close, there is a change in the movement of ions across a cell membrane. Movement of electrical charges is called a *current*. The flow of the current reflects the charge separation across the membrane, i.e., its voltage or *membrane potential*, and is a measure of the electrical driving force that causes ions to move. When cells are excited, there is a change in current or voltage and information passes along the nerves as electrical currents and associated voltage changes (impulses).

All body cells are electrically polarized, with the inside of the cell being more negatively charged than the outside. The difference in electrical charge or voltage

is known as the *resting membrane potential* and is about −70 to −85 mV. The resting membrane potential is the result of the concentration gradient of ions and differences in the relative permeability of the membrane for different ions. The concentration of K^+ is higher inside the cell than outside, whereas the concentration of Na^+ is low inside cells and high outside. This difference in concentration is maintained by the Na^+–K^+-ATPase pump. In addition, the cell membrane is more permeable to K^+ than to other ions, such as Na^+ and Cl^-, and K^+ can diffuse easily from ICF to ECF. Within the cell, there is an excess of anions because of negatively charged proteins that are impermeable.

When a cell, such as a neuron, is stimulated through voltage-regulated channels in sensory receptors or at synapses, ion channels for sodium open and, as a result, there is a net movement of Na^+ into the cell, and the membrane potential decreases making the cell more positively charged. The decrease in resting membrane potential is known as *depolarization*. The point, at which the rapid change in the resting membrane potential reverses the polarity of the cell, is referred to as an *action potential* or simply a *nerve impulse*. Immediately following an action potential, the membrane potential returns to the resting membrane potential. The increase in membrane potential is known as *repolarization* that results in the negative polarity of the cell as the voltage-gated sodium channels close and potassium channels open. The Na^+–K^+-ATPase pump moves K^+ back into the cell and Na^+ out of the cell. The absolute refractory period is the period of time during which it is impossible to generate another action potential, while the relative refractory period is the period of time in which a second action potential can be initiated by stronger-than normal stimulus.

Depolarization, i.e., the opening of sodium ion channels, generates a nerve impulse and is propagated along the nerve, because the opening of sodium ion channels facilitates the opening of other adjacent channels, causing a wave of depolarization to travel down the membrane of nerve cell. When a nerve impulse reaches the far end of a nerve cell, the axon tip, the wave of depolarization causes the release of a neurotransmitter. At a neuromuscular junction, the release of acetylcholine depolarizes the muscle membrane and opens the calcium ion channels, permitting the entry of calcium ions into the cell, which triggers muscle contraction. In an excitatory neural synapse, the neurotrasmitter (acetylcholine) binds to the receptor in the

postsynaptic nerve fiber and opens sodium ion channels that lead to the depolarization and propagation of an impulse. By contrast, in an inhibitory synapse the neurotransmitter (γ-aminobutyric acid or GABA, glycine) binds to the receptor in the postsynaptic nerve fiber and opens the potassium ion channels or chloride ion channels, resulting in the repolarization and inhibition of the impulse.

8.8 Cellular Metabolism

8.8.1 Role of ATP

All of the chemical reactions involved in maintaining essential cellular functions are referred to as cellular metabolism. The life processes are driven by energy; anabolism requires energy, while catabolism releases energy. Atoms can store potential energy by means of electrons at higher energy levels. Energy is stored in chemical bonds when atoms combine to form molecules. Cells extract the chemical energy from nutrients and transfer it to a molecule known as adenosine triphosphate (ATP). Each molecule of ATP has two high-energy phosphate bonds and each of the phosphate bonds contains about 12,000 cal of energy per mole of ATP under physiological conditions. Oxidative cellular metabolism and oxidative phosphorylation reactions result in the formation of ATP that is used throughout the cell to energize all the intracellular metabolic reactions. The function of ATP is not only to store energy but also to transfer it from one molecule to another. The phosphate bond in ATP molecule is very labile and is broken down to form adenosine diphosphate (ADP) and a phosphoric acid radical with the release of energy. ATP is used to promote three major categories of cellular function: membrane transport of ions such as Na^+, K^+, Ca^{2+}, Mg^{2+}, and Cl^-, synthesis of biochemicals, such as proteins, enzymes, and nucleotides, and mechanical work, such as muscle contraction.

8.8.1.1 Production of ATP

The catabolism of nutrients can be divided into three different phases. Phase 1 represents the process of digestion that happens outside the cells where proteins, polysaccharides, and fats are broken down into their corresponding smaller subunits: amino acids, glucose and fatty acid. In phase 2, the small molecules are transported into the cell where the major catabolic processes take place with the formation of acetyl CoA and limited amounts of ATP and NADH. Finally, in phase 3, the Acetyl-CoA molecules are degraded in mitochondria to CO_2 and H_2O with the generation of ATP.

Cellular oxidation–reduction reactions play a key role in energy flow within a cell and electrons transfer the energy from one atom to another, either by oxidation (loss of electrons) or by reduction (gain of electrons). In a biological system, oxidation refers to the removal of a hydrogen atom (proton plus electron) from a molecule, while reduction involves the gain of a hydrogen atom by another molecule. In many of these enzyme-catalyzed oxidation–reduction reactions, involving the formation of ATP, cells employ coenzymes (cofactors) that shuttle energy as hydrogen atoms are transferred from one reaction to another. One of the most important coenzymes is nicotinamide adenine dinucleotide (NAD+) that can accept an electron and a hydrogen atom, and gets reduced to form NADH.

8.8.1.2 Glycolysis

The most important process in phase 2 of the catabolism is the degradation of glucose in a sequence of ten biochemical reactions, known as glycolysis or oxidative cellular metabolism. Glycolysis can produce ATP in the absence of oxygen. Each glucose molecule is converted into two pyruvate molecules with a net generation of 6 ATP molecules. If oxygen is absent, or significantly reduced within the cell, the pyruvate is converted to lactic acid, which then diffuses into ECF. In many of the normal cells, ATP generation by glycolysis accounts for less than 5% of the overall ATP generation within the cell.

8.8.1.3 Oxidative Phosphorylation

Phase 3 begins in the mitochondria with a series of reactions, called citric acid cycle (also called the tricarboxylic acid cycle or the Krebs cycle), and ends with oxidative phosphorylation. Following glycolysis, in the presence of oxygen, pyruvate molecules enter the mitochondria and are converted to acetyl groups of acetyl coenzyme A (Acetyl-CoA). The amino acid and fatty acid molecules are also converted to Acetyl-CoA.

The citric acid cycle begins with the interaction of Acetyl-CoA and oxaloacetate to form the tricarboxylic acid molecule called citric acid, which, subsequently, is oxidized to generate two molecules of CO_2 and oxaloacetate. The energy liberated from the oxidation reactions is utilized to produce three molecules of NADH and one molecule of reduced flavin adenine nucleotide ($FADH_2$). Oxidative phosphorylation is the last step in the catabolism, in which NADH and $FADH_2$ transfer the electrons to a series of carrier molecules, such as cytochromes (the electron-transport chain), on the inner surfaces of the mitochondria with the release of hydrogen ions. Subsequently, the molecular oxygen picks up electrons from the electron-transport chain to form water, releasing a great deal of chemical energy that is used to make the major portion of the cellular ATP. The energy released in the electron-transfer steps causes the protons to be pumped outward. The resulting electrochemical proton gradient across the inner mitochondrial membrane induces the formation of ATP from ADP and phosphoric acid radical. The aerobic oxidation of glucose results in a maximal net production of 36 ATP molecules, all but four of them produced by oxidative phosphorylation.

8.9 DNA and Gene Expression

8.9.1 DNA: The Genetic Material

The ability of cells to maintain a high degree of order depends on the hereditary or genetic information that is stored in the genetic material, the DNA. Within the nucleus of all mammalian cells a full complement of genetic information is stored and the entire DNA is packaged into 23 pairs of chromosomes. A chromosome is formed from a single enormously long DNA molecule that consists of many small subsets called genes each of which represents a specific combination of DNA sequence designed for a specific cellular function. The three most important events in the existence of a DNA molecule are replication, repair, and expression.

The chromosomes can undergo self-replication that permits DNA to make copies of itself, as the cell divides and transfers the DNA (23 pairs of chromosomes) to daughter cells, which can thus inherit every property and characteristic of the original cell. There

are approximately 30,000 genes per human genome which control every aspect of cellular function, primarily through protein synthesis. The sequence of amino acids in a particular protein or enzyme is encoded in a specific gene. Most of the chromosomal DNA, however, does not code for proteins or RNAs. The central dogma of molecular biology is that the overall process of information transfer in the cell involves transcription of the DNA into RNA molecules, which subsequently generate specific proteins on ribosomes by a process known as translation.

A major characteristic of DNA is its ability to encode an enormous quantity of biological information. Only a few picograms (10^{-12} g) of DNA are sufficient to direct the synthesis of as many as 100,000 distinct proteins within a cell. This supreme coding effectiveness of DNA is because of its unique chemical structure.

8.9.1.1 DNA Structure

As described previously, DNA was first discovered in 1869 by the chemist, Friedrich Miescher who extracted a white substance from the cell nuclei of human pus and called it "nuclein." Because nuclein is slightly acidic, it is known as nucleic acid. In the 1920s, the biochemist, Levine identified two types of nucleic acids: DNA and RNA. Levine also concluded that the DNA molecule is a polynucleotide (Fig. 7.16) formed by the polymerization of nucleotides. Each nucleotide subunit of a DNA molecule is composed of three basic elements: a phosphate group, a five-carbon sugar (deoxyribose), and one of the four types of nitrogen containing organic bases. Two of the bases, thymine and cytosine, are called pyrimidines, while the other two bases, adenine and guanine are called purines. Their first letters commonly represent the four bases: T, C, and A, G.

The presence of the 5′-phosphate and the 3′-hydroxyl groups in the deoxyribose molecule allows the DNA to form a long chain of polynucleotides by joining nucleotides through phosphodiester bonds. Any linear strand of DNA will always have a free 5′-phosphate group at one end and a free 3′-hydroxyl group at the other; therefore, the DNA molecule has an intrinsic directionality (5′→3′ direction). Although some forms of cellular DNA exist as single-stranded structures, the most widespread DNA structure discovered by Watson and Crick in 1953 represents the DNA as a double helix containing

two polynucleotide strands that are complementary mirror images of each other (Fig. 8.4). The "backbone" of DNA molecule is composed of deoxyribose sugars joined by phosphodiester bonds to phosphate groups, while the bases are linked in the middle of the molecule through hydrogen bonds. The relationship between bases in the double helix is described as complementary, because adenine always bonds with thymine and guanine always bonds with cytosine. As a consequence, the double-stranded DNA contains equal amounts of purines and pyrimidines. An important structural characteristic of the double-stranded DNA is that its strands are antiparallel meaning that the two strands are aligned in opposite directions.

8.9.1.2   DNA Replication

In order to serve as the basic genetic material, all the chromosomes in the nucleus duplicate their DNA before every cell division. When a DNA molecule replicates, the double-stranded DNA separates or unzips at one end, forming a replication fork (Fig. 8.5). The principle of complementary base pairing dictates that the process of replication proceeds by a mechanism in which a new DNA strand that matches each of the original strands that serve as a template, is synthesized. If the sequence of the template is ATTGCAT, the sequence of the new strand in the duplicate must be TAACGTA. Replication is semiconservative in the sense that at the end of each round of replication, one of the parental strands is maintained intact, and combines with one newly synthesized complementary strand.

DNA replication requires the cooperation of many proteins and enzymes. While DNA helicases and single-strand binding proteins help unzip the double helix and hold the strands apart, a self-correcting DNA polymerase moves along in a $5'{\rightarrow}3'$ direction on a single strand (leading strand) and catalyzes nucleotide polymerization or base pairing. Because the two strands are antiparallel, this $5'{\rightarrow}3'$ DNA synthesis can take place continuously on the leading strand only, while the base

Fig. 8.4 DNA double helix (from Wikipedia)
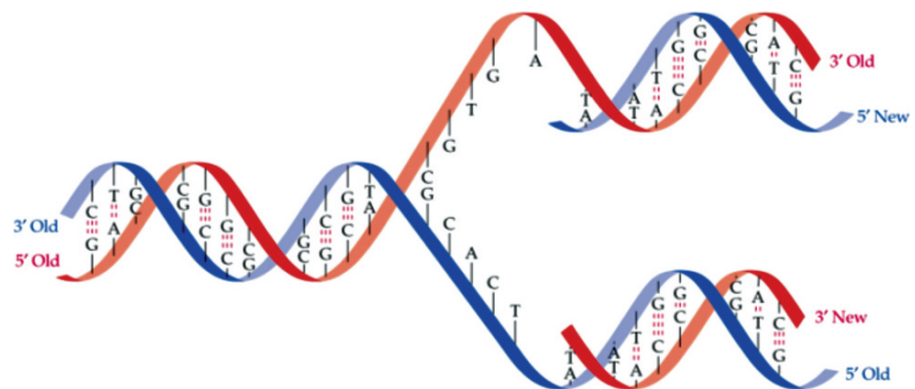
Fig. 8.5 DNA replication

pairing on the lagging strand is discontinuous, and involves synthesis of a series of short DNA molecules that are subsequently sealed together by the enzyme DNA ligase. In mammals, DNA replication occurs at a polymerization rate of about 50 nucleotides per second. At the end of the replication, a repair process known as DNA proof reading is catalyzed by DNA ligase and DNA polymerase enzymes, which cut out the inappropriate or mismatched nucleotides from the new strand and replace these with the appropriate complementary nucleotides. The replication process occurs with few mistakes being made, thus, the DNA sequences are maintained with very high fidelity. For example, a mammalian germ-line cell with a genome of 3×10^9 base pairs is subjected on average to only about 10–20 base pair changes per year. However, genetic change has great implications for evolution and human health, and is the product of mutation and recombination.

8.9.1.3 Gene Mutation

A mutation is any inherited change in the genetic material involving irreversible alterations in the sequence of DNA nucleotides. These mutations may be phenotypically silent (hidden) or expressed (visible). Mutations may be classified into two categories: base substitutions and frame-shift mutations. Point mutations are base substitutions involving one or a few nucleotides in the coding sequence and may include replacement of a purine–pyrimidine base pair by another base pair (transitions) or a pyrimidine–purine base pair (transversions). Point mutations cause changes in the hereditary message of an organism and may result from physical or chemical damage to the DNA or from spontaneous errors made during replication. Frameshift mutation involves spontaneous mispairing and may result from the insertion or deletion of a base pair. Mutational damage to the DNA is generally caused by three sources: (a) ionizing radiation causes breaks in the DNA double strand as a result of the action of free radicals on phosphodiester bonds, (b) ultraviolet radiation creates DNA cross links because of the absorption of UV energy by pyrimidines, and (c) chemical mutagens modify the DNA bases and alter the base-pairing behavior. Mutations in germline tissue are of enormous biological significance, while somatic mutations may cause cancer.

8.9.1.4 DNA Recombination

DNA can undergo important and elegant exchange events through recombination. These change event refer to a number of distinct processes of rearranging the genetic material. Recombination is defined as the creation of new gene combinations and may include the exchange of an entire chromosome or rearrangment of the position of a gene or a segment of a gene on a chromosome. Homologous or general recombination produces an exchange between a pair of distinct DNA molecules, usually located on two copies of the same chromosome. Sections of DNA may be moved back and forth between chromosomes, but the arrangement of genes on a chromosome is not altered. An important example is the exchange of sections of homologous chromosomes in the course of meiosis that is characteristic of gametes. As a result, homologous recombination generates new combinations of genes that can lead to genetic diversity. In a site-specific recombination, DNA homology is not required; it involves the alteration of the relative positions of short and specific nucleotide sequences in either one or both of the two participating DNA molecules. Transpositional recombination involves the insertion of viruses, plasmids, and transposable elements or transposons into the chromosomal DNA. Gene transfer in general, represents a unidirectional transfer of genes from one chromosome to another. The acquisition of an AIDS-bearing virus by a human chromosome is an example of a gene transfer.

8.9.2 Gene Expression and Protein Synthesis

8.9.2.1 DNA Transcription

Proteins are the tools of heredity. The essence of heredity is the ability of the cell to use the information in its DNA to control and direct the synthesis of all proteins in the body. The production of RNA is called transcription and it is the first stage of gene expression (Fig. 8.6). The result is the formation of messenger RNA (mRNA) from the base sequence specified by the DNA template. All types of RNA molecules are transcribed from the DNA. An enzyme called RNA polymerase first binds to a promoter site (beginning of a gene), unwinds the two strands of the DNA double helix, moves along the DNA
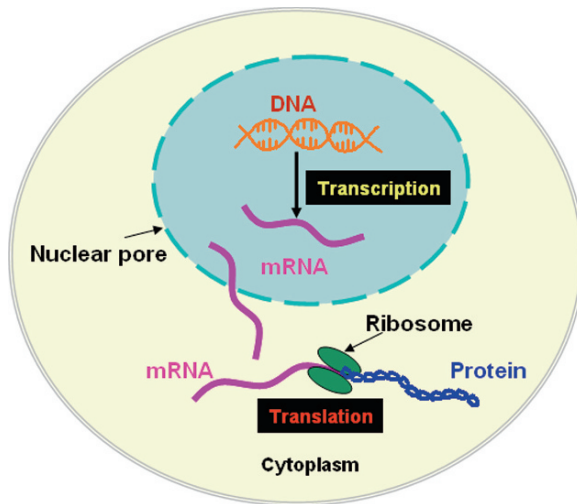
Fig. 8.6 Transcription and translation. http://fajerpc.magnet. fsu.edu/Education/2010/Lectures/26_DNA_Transcription_files/ image006.jpg

strand, and synthesizes the RNA molecule by binding complementary RNA nucleotides with the DNA strand. Upon reaching the termination sequence, the enzyme breaks away from the DNA strand and at the same time a RNA molecule is released into the nucleoplasm. It is important to note that only one strand (the sense strand) of the DNA helix contains the appropriate sequence of bases to be copied into an RNA sense strand. This is accomplished by maintaining the 5′→3′ direction in producing the RNA molecule. As a result, the RNA chain is complementary to the DNA strand, and is called the primary RNA transcript of the gene. This primary RNA transcript consists of long stretches of noncoding nucleotide sequences called introns that intervene between the protein coding nucleotide sequences called exons. In order to generate mRNA molecules, all the introns are cut out and the exons are spliced together. Further modifications to stabilize the transcript include, 5-methylguanine capping at the 5′ end and polyadenylation at the 3′ end. The spliced, stabilized mRNA molecules are finally transported to the endoplasmic reticulum in the cytoplasm where proteins are synthesized.

8.9.2.2 RNA Structure

Both transcription and translation are mediated by a RNA molecule, which is an unbranched linear poly-

mer of ribonucleoside 5′-monophophates. RNA is chemically similar to DNA. The main difference between RNA and DNA is that the RNA molecule contains ribose sugar and another pyrimidine, uracil, in place of thymine. RNAs are classified according to the different roles they play in the course of the protein synthesis. The length of the molecules varies from approximately 65 to 200,000 nucleotides depending on the role they play. There are many types of RNA molecules within a cell and some RNAs contain modified nucleotides which provide greater metabolic stability. mRNA molecules carry the genetic code to the ribosomes where they serve as templates for the synthesis of proteins. A transfer RNA (tRNA) molecule, also generated in the nucleus, transfers specific amino acids from the soluble amino acid pool to the ribosomes and ensures the alignment of these amino acids in a proper sequence. Ribosomal RNA (rRNA) forms the structural framework of ribosomes where most proteins are synthesized. All RNA molecules are synthesized in the nucleus. While the enzyme, RNA polymerize II, is mainly responsible for the synthesis of mRNA, RNA polymerase I and III mediate the synthesis of rRNA and tRNA.

8.9.2.3 Genetic Code

The genetic code in a DNA sense strand consists of a specific nucleotide sequence that is coded in successive "triplets" that will eventually control the sequence of amino acids in a protein molecule. A complementary code of triplets in mRNA molecules, called codons, is synthesized during the transcription. For example, the successive triplets in a DNA sense strand are represented by bases, GGC, AGA, and CTT. The corresponding complementary mRNA codons, CCG, UCU, and GAA, represent the three amino acids proline, serine, and glutamic acid, respectively. Each amino acid is represented by a specific mRNA codon. The various mRNA codons for the 20 amino acids and the codons for starting and stopping of protein synthesis are summarized in Table 8.6. The genetic code is regarded because degenerate, because most of the amino acids are represented by more than one codon. An important feature of the genetic code is that it is universal; all living organisms use precisely the same DNA code to specify proteins.

Table 8.6 Amino acids and the genetic code

Amino acid	Abbreviation	Lettercode	RNA codons					
Neutral amino acids								
Glycine	gly	G	GGU	GGC	GGA	GGG		
Alanine	ala	A	GCU	GCC	GCA	GCG		
Valine	val	V	GAU	GUC	GUA	GUG		
Leucine	leu	L	CUU	CUC	CUA	CUG	UUA	UUG
Isoleucine	ile	I	AUU	AUC	AUA			
Praline	pro	P	CCU	CCC	CCA	CCG		
Phynylalanine	phe	F	UUU	UUC				
Tyrosine	tyr	Y	UAU	UAC				
Tryptophan	try	W	UGG					
Serine	ser	S	UCU	UCC	UCA	UCG	AGC	AGU
Threonine	thr	T	ACU	ACC	ACA	ACG		
Cysteine	cys	C	UGU	UGC				
Methionine	met	M	AUG					
Asparagine	asn	D	AAU	AAC				
Glutamine	gin	Q	CAA	CAG				
Acidic amino acids								
Aspartic acid	asp	N	GAU	GAC				
Glutamic acid	glu	E	GAA	GAG				
Basic amino acids								
Lysine	lys	K	AAA	AAG				
Arginine	arg	R	CGC	CGA	CGG	AGA	AGG	
Histidine	his	H	CAU	CAC				

8.9.2.4 DNA Translation: Protein Synthesis

More than half of the total dry mass of a cell is made up of proteins. The second stage of gene expression is the synthesis of proteins, which requires complex catalytic machinery. The process of mRNA-directed protein synthesis by ribosomes is called translation and is dependent on two other RNA molecules, rRNA and tRNA. Ribosomes are the physical structures in which proteins are actually synthesized and are composed of two subunits: a small subunit with one rRNA molecule and 33 proteins, and a large subunit with 4 rRNAs and 40 proteins. Proteins that are transported out of the cell are synthesized on ribosomes that are attached to the ER, while most of the intracellular proteins are made on free ribosomes in the cytoplasm. A tRNA molecule contains about 80 nucleotides and has a site for attachment of an amino acid. Because tRNA needs to bind to mRNA to deliver a specific amino acid, tRNA molecules consists of a complementary triplet of nucleotide bases, called anticodon. Each tRNA acts as a carrier to transport a specific amino acid to the ribosomes and for each of the 20 amino acids, there are 20 different tRNA molecules.

Protein biosynthesis is a complex process and involves bringing together mRNA, ribosomal sub units, and the tRNAs. Such an ordered process requires a complex group of proteins, known as initiation factors, that help initiate the synthesis of the protein. The first step in the translation is the recognition of mRNA by ribosomes and its binding to mRNA molecule at the 5′ end. Immediately, the appropriate tRNA that carries a particular amino acid (methionine) to the 3′ end of mRNA is attached to the ribosome and binds mRNA at the start codon (AUG). The process of translation then begins by bringing in tRNAs that are specified by the codon–anticodon interaction. The ribosome exposes the codon, immediately adjacent to the AUG, on the mRNA to allow a specific anticodon to bind to the codon. At the same time the amino acids (methionine and the incoming amino acid) are linked together by a peptide bond and the tRNA carrying methionine is released. Next, the ribosome moves along the mRNA molecule to the next codon, when the next tRNA binds to the complementary codon, placing the amino acid adjacent to the growing polypeptide chain. The process is continued until the ribosome reaches a chain-terminating nonsense stop codon (UAA, UAG, UGA). In other words, the process stops when a release factor binds to the nonsense codon, stops the synthesis of protein, and releases the protein from the ribosome. Some proteins emerging from the

ribosome are ready to function, while others undergo a variety of posttranslational modifications to convert the proteins to functional forms, or to facilitate the transport to intracellular or extracellular targets.

8.10   Disease and Pathophysiology

8.10.1   Homeostasis

The term *homeostasis* is used by physiologists to describe the maintenance of static, or constant conditions in the internal environment by means of positive and negative feedback of information. About 56% of the adult human body is fluid. Most of the fluid is ICF and about one third is ECF that is in constant motion throughout the body and contains the ions (sodium, chloride, and bicarbonate) and nutrients (oxygen, glucose, fatty acids, and amino acids) needed by the cells for the maintenance of life. Claude Bernard (1813–1878) defined ECF as the internal environment of the body and hypothesized that the same biological processes that make life possible are also involved in disease (Wagner 1995b). The laws of disease are the same as the laws of life. All the organs and tissues of the body perform functions that help maintain homeostasis. As long as the organs and tissues of the body perform functions that help maintain homeostasis, the cells of the body continue to live and function properly.

8.10.2   Disease Definition

At the present time, precisely defining what disease is, is as complex as defining what exactly life is. It may be relatively easier to define disease at a cellar and molecular level than at the level of an individual. Throughout the history of medicine, two main concepts of disease have been dominant. The *ontological* concept views a disease as an entity that is independent, self-sufficient, and running a regular course with a natural history of its own. The physiological concept defines disease as a deviation from the normal physiology or biochemistry; the disease is a statistically defined deviation of one or more functions in a patient from those of healthy people of the same age and sex under very similar circumstances.

At birth, molecular blueprints collectively make up a person's genome or genotype that will be translated into cellular structures and functions. A single gene defect can lead to biochemical abnormalities that produce many different clinical manifestations of disease, or phenotypes, a process called *pleotropism*. Many different gene abnormalities can result in the same clinical manifestations of disease; this process is called genetic heterogeneity. Thus, diseases can be defined as abnormal processes as well as abnormalities in the molecular concentrations of different biological markers, signaling molecules, and receptors.

8.10.3   Pathophysiology

In the 1839, Theodor Schwann discovered that all the living organisms are made up of discrete cells. In 1858, Rudolph Virchow observed that a disease could not be understood unless it is realized that the ultimate abnormality must lie in the cell. He correlated disease with cellular abnormalities as revealed by chemical stains, thereby founding the field of cellular pathology. Consequently, he defined pathology as physiology with obstacles.

Most diseases begin with a cell injury that occurs if the cell is unable to maintain homeostasis. Since the time of Virchow, gross pathology and histopathology have been a foundation of the diagnostic process and the classification of disease. Traditionally, the four aspects of a disease process that form the core of pathology are etiology, pathogenesis, morphologic changes, and clinical significance. The altered cellular and tissue biology, and all forms of loss of function of tissues, and organs are, ultimately, the result of cell injury and cell death. Therefore, knowledge of the structural and functional reactions of cells and tissues to injurious agents, including genetic defects, is the key for understanding the disease process.

Currently diseases are defined and interpreted in molecular terms and not just with general descriptions of altered structures. Pathology is evolving into a bridging discipline that involves both basic science and clinical practice, and is devoted to the study of the structural and, functional changes in cells, tissues, and organs that underlie disease. The molecular, genetic, microbiologic, immunologic, and morphologic techniques help to understand both, the ontological and the physiological causes of disease.

8.10.3.1   Altered Cellular and Tissue Biology

The normal cell is able to handle normal physiologic and functional demands, so-called normal homeostasis. However, physiologic and morphologic cellular adaptations, normally occur in response to excessive physiologic conditions or some adverse, or pathologic stimuli. The cells adapt in order to escape and protect themselves from injury. An adapted cell is neither normal nor injured, but has an altered steady state and preserves the viability of the cell. If a cell can not adapt to severe stress or pathologic stimuli, the consequence may be *cellular injury* that disrupts cell structures or deprives the cell of oxygen and nutrients. Cell injury is reversible up to a certain point, but irreversible (lethal) cell injury ultimately leads to cell death, generally known as *necrosis*. By contrast, an internally controlled suicide program, resulting in cell death, is called *apoptosis*.

Cellular Adaptations

Some of the most significant physiologic and pathologic adaptations of cells involve changes in cellular size, growth, or differentiation. These include: (a) *atrophy*, a decrease in size and function of the cell, (b) *hypertrophy*, an increase in cell size, (c) *hyperplasia*, an increase in cell number, and (d) *metaplasia*, an alteration of cell differentiation. The adaptive response may also include the intracellular accumulation of normal and abnormal endogenous substances (lipids, protein, glycogen, bilirubin, and pigments), or abnormal exogenous products. Cellular adaptations are a common and central part of many disease states. The molecular mechanisms leading to cellular adaptations may involve a wide variety of stimuli and various steps in the cellular metabolism. Increased production of cell signaling molecules, alterations in the expression of cell surface receptors, and overexpression of intracellular proteins are typical examples.

8.10.3.2   Cellular Injury

Cellular injury occurs if the cell is unable to maintain homeostasis. The causes of cellular injury may be *hypoxia* (oxygen deprivation), infection, or exposure to toxic chemicals. In addition, immunologic reactions, genetic derangements, and nutritional imbalances may also cause cellular injury. In hypoxia (oxygen deprivation), glycolytic energy production may continue, but *ischemia* (loss of blood supply) compromises the availability of metabolic substrates and may injure tissues faster than hypoxia. Various types of cellular injuries and their responses are summarized in Table 8.7.

Biochemical Mechanisms

Regardless of the nature of the injurious agents, there are a number of common biochemical themes or mechanisms responsible for cell injury.

1. ATP depletion: It is one of the most common consequences of ischemic and toxic injury. ATP depletion induces cell swelling, decreases protein synthesis, decreases membrane transport, and increases membrane permeability.
2. Oxygen and oxygen derived free radicals: Ischemia causes cell injury by reducing blood supply and cellular oxygen. Radiation, chemicals, and inflammation generate oxygen free radicals that cause

Table 8.7   Progressive types of cell injury and responses

Type	Responses
Adaptation	Atrophy, hypertrophy, hyperplasia, and metaplasia
Active cell injury	Immediate response of "entire cell"
Reversible	Loss of ATP, cellular swelling, detachment of ribosomes, and autophagy of lysosomes
Irreversible	"Point of no return" structurally when vacuolization occurs of the mitochondria and calcium moves into the cell.
Necrosis	Common type of cell death with severe cell swelling and breakdown of organelles
Apoptosis	Cellular self-destruction for elimination of unwanted cell population
Chronic cell injury (subcellular alterations)	Persistent stimuli response may involve only specific organelles or cytoskeleton, e.g., phagocytosis of bacteria
Accumulations or Infiltrations	Water, pigments, lipids, glycogen, and proteins
Pathologic calcification	Dystrophic and metastatic calcification

The above table modified from reference (McCance and Huether 1998)

the destruction of the cell membrane and cell structure.

3. Intracellular Ca^{2+} and loss of calcium homeostasis: Most of the intracellular calcium is in the mitochondria and endoplasmic reticulum. Ischemia and certain toxins increase the concentration of Ca^{2+} in the cytoplasm resulting in the activation of a number of enzymes, causes intracellular damage, and increases the membrane permeability.

4. Mitochondrial dysfunction: A variety of stimuli (free Ca^{2+} levels in cytosol, oxidative stress) cause mitochondrial permeability transition (MPT) in the inner mitochondrial membrane, resulting in the leakage of cytochrome c into the cytoplasm.

5. Defects in membrane permeability: All forms of cell injury, as well as many bacterial toxins and viral proteins, damage the plasma membrane. As a result, there is an early loss of selective membrane permeability.

Intracellular Accumulations

Normal cells generally accumulate certain substances such as electrolytes, lipids, glycogen, proteins, calcium, uric acid, and bilirubin that are involved in normal metabolic processes. As a manifestation of injury and metabolic derangements in cells, abnormal amounts of various substances, either normal cellular constituents or exogenous substances, may accumulate in the cytoplasm or nucleus, either transiently or permanently. One of the major consequences of the failure of the transport mechanisms is cell swelling due to excess intracellular water. Abnormal accumulations of organic substances, such as triglycerides, cholesterol and cholesterol esters, glycogen, proteins, pigments, and melanin, may be caused by disorders in which the cellular capacity exceeds the synthesis or catabolism of these substances. Dystrophic calcification occurs mainly in the injured or dead cells, while metastatic calcification may occur in the normal tissues. Hypercalcemia may be a consequence of increased parathyroid hormone, destruction of bone tissue, renal failure, and vitamin D related disorders. All of these accumulations harm cells by "crowding" the organelles and by causing excessive and harmful metabolites that may be retained within the cell or expelled into the ECF and circulation.

8.10.3.3 Necrosis

Cellular death resulting from the progressive degradative action of enzymes on the lethally injured cells, ultimately leading to the processes of cellular swelling, dissolution, and rupture, is called necrosis. The morphologic appearance of necrosis is the result of denaturation of proteins and enzymatic digestion (autolysis or heterolysis) of the cell. Different types of necrosis occur in different organs or tissues. The most common type, *coagulative necrosis*, resulting from hypoxia and ischemia, is characterized by the denaturation of cytoplasmic proteins, breakdown of organelles, and cell swelling. It occurs primarily in the kidneys, heart, and adrenal glands. *Liquefactive necrosis* may result from ischemia or bacterial infections. The cells are digested by *hydrolases,* and the tissue becomes soft and liquefies. As a result of ischemia, the brain tissue liquefies and forms cysts, In an infected tissue, hydrolases are released from the lysosomes of neutrophils; they kill bacterial cells and the surrounding tissue cells resulting in the accumulation of pus. *Caseous necrosis* present in the foci of tuberculous infections is a combination of coagulative and liquefactive necrosis. In *fat necrosis*, the *lipase* enzymes break down triglycerides and form opaque chalky necrotic tissue as a result of saponification of free fatty acids with alkali metal ions. In a patient, the necrotic tissue and the debris usually disappear by a combined process of enzymatic digestion and fragmentation, or become calcified.

8.10.3.4 Apoptosis

Apoptosis, a type of cell death implicated in both normal and pathologic tissue, is designed to eliminate unwanted host cells in an active process of cellular self-destruction effected by a dedicated set of gene products. Apoptosis occurs during normal embryonic development and is a homeostatic mechanism to maintain cell populations in tissues. It also occurs as a defense mechanism in immune reactions and during cell damage by disease or noxious agents. Various kinds of stimuli may activate apoptosis. These include injurious agents (radiation, toxins, free radicals), specific death signals (TNF and *Fas* ligands), and withdrawal of growth factors and hormones. Within the cytoplasm a number of protein regulators (Bcl-2 family of proteins) either promote or inhibit cell death. In the final phase, the execution *caspases* activate the

proteolytic cascade that eventually leads to the intracellular degradation, fragmentation of nuclear chromatin, and breakdown of the cytoskeleton. The most important morphologic characteristics are cell shrinkage, chromatin condensation, and formation of cytoplasmic blebs, and apoptotic bodies that are, subsequently, phagocytosed by adjacent healthy cells and macrophages. Unlike necrosis, apoptosis involves nuclear and cytoplasmic shrinkage and affects scattered single cells.

Additional Reading

Alberts B, Bray D, Lewis J, et al (1994) Molecular Biology of the Cell, 3rd edn. Garland, New York

Cotran RS, Kumar V, Collins T (1999) Robbins Pathologic Basis of Disease, 6th edn. Saunders, Philadelphia

Devin TM (1997) Text Book of Biochemistry with Clinical Correlates, 4th edn. Wiley, New York

Guyton AC, Hall JE (1997) Human Physiology and Mechanisms of Disease, 6th edn. Saunders, Philadelphia

McCance KL, Huether SE (1998) Pathophysiology. The Biologic basis for disease in adults and children, 3rd edn. Mosby Year Book, St. Louis

Raven PH, Johnson GB (1992) Biology, 3rd edn. Mosby Year Book, St. Louis

Virchow R (1958) Disease, Life and Man. (translated by Rather LJ). Stanford University Press, CA, USA

Wagner HN Jr (1995a) Nuclear Medicine: What it is and What it Does. In: Wagner HN Jr, Szabo Z, Buchanan JW (eds) Principles of Nuclear Medicine. Saunders, Oxford, pp 1–8

Wagner HN Jr (1995b) The Diagnostic Process. In: Wagner HN Jr, Szabo Z, Buchanan JW (eds) Principles of Nuclear Medicine. Saunders, Philadelphia

Radiopharmaceuticals

An experiment is a question which science poses to Nature, and a measurement is the recording of Nature's answer

Max Planck

9.1 Radiotracer Vs. Radiopharmaceutical

In the 1920s, George de Hevesy, coined the term *radioindicator* or *radiotracer* and introduced the *tracer principle* in biomedical sciences. Initially, β⁻-emitting radioisotopes were used as therapeutic agents. For example, ^{32}P was used for the treatment of *polycythemia vera* and *leukemia*, and ^{131}I was used for the treatment of thyroid disease (toxic and nontoxic goiter) and thyroid cancer.

Following the discovery of the scintillation scanner by Benedict Casen, ^{131}I was introduced as a radiotracer for diagnostic imaging purpose. In 1956, Merrill Bender introduced ^{131}I-labeled serum albumin as a radiotracer to image brain tumors. The introduction of the Anger camera and the ^{99m}Tc generator, in the 1960s, stimulated the development of a number of radiolabeled compounds as radiotracers for diagnostic studies in nuclear medicine.

A radiotracer can be defined as a specific radiolabeled molecule (or probe) that resembles or traces the in vivo behavior of a natural molecule and can be used to provide information about a specific biological process. The degree of similarity between the radiotracer and the natural substance, however, may vary depending on the particular radiotracer. For example, $[^{11}C]$glucose and $[^{14}C]$glucose are true tracers of glucose because they are chemically identical to natural glucose, while $[^{18}F]$fluorodeoxyglucose (FDG), an analog of glucose, also traces glucose, but does not behave identically to glucose since it is chemically different.

One of the most important characteristics of a true radiotracer is the ability to study the components of a homeostatic system without disturbing their function. Occasionally, the term *radioligand* is also used in the context of imaging studies. A radioligand can be defined as any radiolabeled molecule that can bind with another molecule or substance (binder) in a predictable way under controlled conditions. For example, $[^{11}C]$raclopride is a radioligand that binds, specifically, to dopamine D_2 receptors, while $[^{18}F]$FDOPA is a radiotracer used to image dopamine metabolism.

9.1.1 Radiopharmaceutical Vs. Radiochemical

All radiolabeled compounds or substances used for the purpose of diagnosis or therapy have been defined as *radioactive drugs* or *radiopharmaceuticals* by the U.S. Food and Drug Administration (FDA). Diagnostic radiopharmaceuticals are administered in trace amounts (<100 μg) and, typically, do not induce any physiological response or pharmacological effect in patients. The term radioindicator, however, may be more appropriate to describe radiolabeled compounds or substances used for the purpose of diagnosis.

In 1954, the U.S. Atomic Energy Commission (AEC) and, subsequently, the U.S. Nuclear Regulatory Commission (NRC) were given the responsibility for directing the medical use of reactor-produced by-products. Since the 1960s, the stated mission of the FDA has been to "assure safety and efficacy in marketed medicinal agents and medicinal devices." In 1972, the FDA took over the responsibility to regulate the medical usage of reactor-produced radiolabeled compounds, from the NCR. Subsequently, in 1975, the FDA decided to also assume the responsibility for the cyclotron-produced radiolabeled compounds. In addition, the FDA adopted the same regulations for radiolabeled compounds (or nuclear medicine imaging probes) as those in existence for traditional drugs (pharmaceuticals). As a result, the term radiopharmaceutical has become the official FDA categorization for all radioindicators and radiotracers used for diagnosis and therapy. Although the field of nuclear medicine evolved into a more sophisticated molecular imaging technology, the FDA continues to extend the usage of the term "radiopharmaceuticals" to include the novel radiolabeled molecular imaging probes (RMIPs).

The term *radiochemical* is sometimes used for any radiolabeled compound or radiotracer. From the standpoint of chemistry and radiochemical purity, there is no difference between the terms radiochemical and radiopharmaceutical. From a regulatory point of view, however, a radiopharmaceutical must also be sterile, pyrogen free, safe for human use, and efficacious for a specific indication. In contrast, a radiochemical is not an FDA-approved agent for routine human use.

9.2   Radiolabeled Molecular Imaging Probe

The terms, radiotracer, radioligand, and RMIP, have specific meaning depending on their specific use and application. However, from a regulatory point of view, the term radiopharmaceutical represents any radiolabeled molecule intended for human use.

The members of the molecular imaging center of excellence (MICoE) standard definitions task force recently developed the following standard definitions and terms (Mankoff 2007).

- Molecular imaging is the visualization, characterization, and measurement of biological processes at the molecular and cellular levels in humans and other living systems.
- Molecular imaging agents as "probes used to visualize, characterize, and measure biological processes in living systems. Both, endogenous molecules and exogenous probes can be molecular imaging agents."

Because the emphasis of this text book is on molecular imaging, it is important to understand the subtle difference between the conventional nuclear imaging technology and the molecular imaging technology. Many of the radiopharmaceuticals used in nuclear medicine are *nonspecific*, while all the RMIPs, by definition, are highly *specific* for the measurement of a specific biological process.

Keeping *specificity* as the only requirement, the current FDA-approved radiopharmaceuticals, in general, can be divided into "specific" and nonspecific agents (Table 9.1). Several examples would clearly illustrate the difference between specific and nonspecific agents. Radioiodide is a very good example of a molecular imaging probe; just like the natural iodide, it is actively transported into the thyroid gland and incorporated into the thyroid hormones. In contrast, ^{99m}Tc pertechnetate, while useful for thyroid imaging, is not a specific radiotracer to assess thyroid function. ^{67}Ga citrate is a nonspecific diagnostic imaging agent to identify tumor tissues and abscesses, while ^{111}In-cotreotide is a highly specific agent to image neuroendocrine tumors expressing somatostatin type 2 (SSTR 2) receptors.

The metabolic and molecular information provided by [^{18}F]FDG-PET can be considered as the first validated "clinically useful" molecular imaging technique. FDG is a substrate for the enzyme *hexokinase* and highly specific in assessing the glucose metabolism of any tissue. FDG, however, is not a non-specific molecular imaging probe to image malignant tissue, since it is also taken up by inflammatory tissue macrophages, and many other normal cells that have augmented glucose utilization.

9.2.1   Molecular Imaging Probe

As previously discussed, the term *homeostasis* is used by physiologists to describe maintenance of static, or constant, conditions in the internal environment by means of positive and negative feedback of information. Diseases can be defined as abnormal processes as

Table 9.1 FDA-approved radiopharmaceuticals in nuclear medicine

Radiopharmaceuticals		
Nonspecific	Specific[a]	Biological process or targeted molecular target
^{99m}Tc-HMPAO (Ceretec®)	[^{15}O]Water	Cerebral blood flow and perfusion
^{99m}Tc-HexaMIBI (cardiolyte®)	[^{15}O]Water	Myocardial perfusion
^{99m}Tc-Tetrophosmin (Myoview)	[^{13}N]Ammonia	
^{201}Tl-Thallous chloride	^{82}Rb-chloride	
^{67}Ga-citrate	^{111}In-Octreotide (OctreoScan®)	Tumor (malignant tissue)
	^{111}In-ProstaScint	
	[^{18}]FDG	
^{67}Ga-citrate	^{111}In-Leukocytes	Infection
[^{18}F]FDG		
^{99m}Tc-pertechnetate	^{123}I, ^{124}I or ^{131}I as iodide	Thyroid
^{99m}Tc-DTPA		Kidney function (glomerular filtration)
^{99m}Tc-MAG3	^{123}I-Hippuran	Kidney function (tubular secretion)
^{99m}Tc-DISIDA (Disofenin®)	^{131}I-Bilirubin	Hepatibiliary function
	^{123}I and ^{131}I-MIBG	Pheochromocytoma and transported by adrenergic presynaptic transporter
[^{18}F]Fluoride, ^{99m}Tc-MDP or HDP		Bone (hydroxyapatite)
	[^{18}F]FDG	Glucose metabolism
^{201}Tl-Thallous chloride	[^{18}F]FDG	Myocardial Viability
^{99m}Tc-MAA		Lung perfusion
^{99m}Tc-sulfur colloid		Liver

[a]Radiopharmaceuticals that are specific can be categorized as radiolabeled molecular imaging probes (RMIPs)

well as abnormalities in molecular concentrations of different biological markers, signaling molecules and receptors. In the last two decades, there has been a revolution in our basic understanding of the biology and biochemistry of disease. With the elucidation of the human genome and the description of the genetic abnormalities, responsible for numerous diseases, we now have a better understanding of the basic molecular pathways, proteins, and signal transduction processes that are present in the normal cell.

The basis of molecular medicine is that chemical disturbances will precede anatomical abnormalities in disease. The new generation of molecular therapeutics is based on the rationale drug design to reverse or control chemical imbalances by targeting key specific receptors, enzymes, membrane transporters, and antigens. The ultimate goal of molecular medicine is to treat the disease in its early stages with an appropriate patient-specific "targeted molecular therapy." In order to achieve this goal, it is essential to develop highly specific RMIPs. In the design and development of an ideal RMIP, it is important to identify first a molecular imaging probe (MIP), which may be a biochemical or a synthetic molecule, specific for a biological process

(such as metabolism, angiogenesis, and apoptosis) or a molecular target (such as *hexokinase*, *thymidine kinase*, and neuroreceptor) in an organ, or tissue of interest. Subsequently, an appropriate radionuclide can be used to synthesize a RMIP suitable for imaging based on either PET or SPECT techniques.

The development of MIPs will greatly benefit from the science of molecular medicine and from the chemical insights of molecular therapeutics. MIPs and drugs (therapeutics) share common concepts of structural design and mechanisms of localization and/or action because they target the same enzyme, receptor or antigen. Drugs block or inhibit their targets and restore the chemical imbalance associated with a disease, while MIPs, at tracer levels, can provide noninvasive quantitative assessment of the functional status of the molecular target in a specific disease. Drugs lead to the development of MIPs, and MIPs in turn may also lead to the development of new drugs. Thus, drugs (therapeutics) and MIPs typically share structural requirements, being the same molecule or structural analogs of each other (Barrio 2004).

Chemically, the MIPs (Table 9.2) with biochemical target specificity are organic molecules or drugs that are

- Relatively low in molecular size or mass (<1,000 Da).
- Classified as simple sugars, fatty acids, or amino acids.
- Either peptide hormones or hormone analogs, such as octreotide.
- Relatively large protein molecules (25–150 KDa), such as monoclonal antibodies and antibody fragments.

9.2.2 RMIPs: Categories and Types

A number of biological processes and biochemical targets (Table 9.2) have been identified in order to develop RMIPs for PET and SPECT. On the basis of these molecular targets, imaging probes can be divided into nine different categories.

Table 9.2 Molecular imaging probes (MIP)

Biochemical process	Specific target for MIP	RMIP
Blood flow	Simple diffusion	[¹⁵O]Water
Metabolism:		
Glucose	*Hexokinase*	[¹⁸F]FDG
Fatty acid	*Thiokinase*	[¹⁸F]FTHA
Choline	*Choline kinase*	[¹⁸F]Fluorocholine
DNA synthesis	*Thymidine kinase*	[¹¹C]Thymidine, [¹⁸F]FLT
Receptor binding	Estrogen receptor	[¹⁸F]Fluoroestradiol
	Somatostatin receptor	⁶⁸ Ga-DOTATOC
Macrophage (microglia)	Peripheral benzodiazepine receptor	[¹¹C]PK11195
Tumor antigen	Prostate Specific Membrane Antigen (PSMA)	⁶⁴Cu-J591 MAb
Amyloid binding	*β-Amyloid*	[¹¹C]PIB
Apoptosis	*Phosphatidylserine*	¹²⁴I-Annexin V
Angiogenesis	*Integrin receptors, $\alpha_v\beta_3$*	¹⁸F-FB–E[c(RGDyK)]2
Hypoxia	*Acidic pH in cells*	[¹⁸F]FMISO
Gene imaging	*HSV1-TK, mRNA*	[¹⁸F]FHBG
Amino acid transport	Protein synthesis	[¹¹C]L-Methionine, [¹⁸F]Fluoro-*m*-tyrosine
Neuroreceptors Dopamine metabolism	*Aromatic amino acid decarboxylase (AAADC*	[¹⁸F]FDOPA
Dopamine receptor	Dopamine D2 receptor	[¹¹C]Raclopride, ¹²³I-IBZM
Dopamine reuptake	Dopamine presynaptic transporter	[¹⁸F]FP-CIT, ¹²³I-β-CIT

1. Probes for the determination of perfusion and membrane transport
2. Probes based on specific substrates for metabolism
3. Probes based on enzyme-mediated transformation
4. Probes based on receptor-mediated interactions
5. Probes based on antigen–antibody interactions
6. Probes based on abnormal protein expression or protein deposits
7. Probes based on nucleic acids (DNA and RNA)
8. Probes based on nanoparticles
9. Probes based on cellular migration or trafficking

RMIPs may also be classified based on their clinical utility and the nature of application for which they are designed as tools in the drug development program (Maclean et al. 2003). Four classes of RMIPs have been identified:

1. A *radiolabeled drug substance* in which the cold stable atom is replaced by a radioisotope of the same element, which can be used for assessing the pharmacokinetics and biodistribution of the parent drug.
2. A *radioligand* with good binding affinity for a biologic target, which can be used to evaluate the effect of other unlabeled compounds at that target.
3. A *pathway marker* interacting with one component of a set of related biologic molecules, which may be used to probe the overall status of that system.
4. A *biomarker*, or surrogate marker, which provides a more general readout at the level of cell or organ for a specific biological process.

9.2.3 RMIP: Choice of Radionuclide

A number of radionuclides that emit either a positron or a γ photon are available (Table 9.3) for developing RMIPs for PET or SPECT. These radionuclides, basically, belong to four groups of chemical elements: elements of organic substances (C, N, and O), halogens (F, Br, and I), metals (Ga and In), and transition metals (such as Cu, Y, and Tc). Only certain elements (I, Ga, Cu, In) are useful for the development of RMIPs for both PET and SPECT using a radioisotope of the same chemical element.

The organic radionuclides that decay by positron emission are ¹¹C, ¹³N and ¹⁵O. These three radionuclides are isotopes of natural elements that are part of the majority of biochemicals and drugs. Interestingly, for

Table 9.3 Radionuclides useful for developing RMIPs for PET and SPECT

	For PET			For SPECT		
Elements	Radionuclide	$T_{1/2}$	β^+ (MeV)	Radionuclide	$T_{1/2}$	γ (MeV)
Organic compound elements	^{11}C	20.4 months	0.959			
	^{13}N	9.96 months	1.197			
	^{15}O	2.03	1.738			
Halogens	^{18}F	109.8 months	0.635			
	^{75}Br	98 months	1.74			
	^{76}Br	16.1 h	3.98			
	^{124}I	4.2 days	2.13	^{123}I	13.2 h	0.159
				^{131}I	8.04 days	0.364
Metals	^{66}Ga	9.45 h	4.153	^{67}Ga	78.2 h	0.093, 0.184, 0.300
	^{68}Ga	68.3 months	1.898			
	^{83}Sr	32.4	1.150			
	^{110}In	66 months	2.250	^{111}In	67.2 h	0.173, 0.247
Transition metals	^{44}Sc	3.92 h	1.470			
	^{45}Ti	3.09 h	1.040			
	^{51}Mn	46.2 months	2.170			
	^{52}Mn	5.6 days	0.575			
	^{52}Fe	8.2 h	0.800			
	^{55}Co	17. h	1.500			
	^{61}Cu	3.32 h	1.220	^{67}Cu	2.6 days	0.185, 0.92
	^{62}Cu	9.76 months	2.910			
	^{64}Cu	12.8 h	0.656			
	^{86}Y	14.74 h	3.150			
	^{89}Zr	78.4 h	0.900			
	^{94m}Tc	52 months	2.440	^{99m}Tc	6.0 h	0.140

these three elements there Tre no corresponding radio-isotopes that decay by γ emission. RMIPs developed with the organic positron emitters are true MIPs since these probes, biochemically, are indistinguishable from their natural counterparts. For example, [^{11}C]thymidine and [^{15}O]water are chemically and biochemically the same as natural [^{12}C]thymidine and [^{16}O]water.

The group of elements known as halogens (F, Cl, Br and I) are very unique in nature. While chloride and iodide ions are quite common in the human body, fluorine and bromine atoms, generally, are not part of the natural molecules. Among all the halogens, however, the fluorine atom is the only one that closely mimics the hydrogen atom in size (Table 9.4) (Park et al. 2001). The van der Wall's radii of fluorine and hydrogen are very similar, 1.35 and 1.2 Å, respectively. As a result, one can expect that, in any given organic molecule, the C–F bond closely mimics the biological behavior of the C–H bond. In addition, the fluorine atom is also the

Table 9.4 Comparison of physico-chemical parameters

	Hydrogen	Fluorine	Oxygen (OH)	Iodine
Electronegativity	2.2	3.98	3.44	2.66
[a]Bond length, Å	1.09	1.39	1.43	2.14
Van Der Wal's radius, Å	1.20	1.35	1.40	2.15
Bond energy, KCal/mol^{-1}	99	116	85	51

[a]Bond length for –CH2X reported here where X = H, F, or OH
Table modified from Park et al. (2001)

most electronegative of all halogens. As a result, the fluorine atom introduces a polarity more akin to a hydroxyl substituent in a molecule. The other halogens are bigger in size and are less electronegative compared to fluorine. Consequently, labeling a biochemical with bromine or iodine radioisotopes would alter the biological behavior of the molecule. However, halogen

Table 9.5 Specific activity (SA) of radionuclides

| Nuclide | Maximum SA | | Practical SA |
	$mCi\ \mu g^{-1}$	$Ci\ \mu mole^{-1}$	$Ci\ \mu mole^{-1}$
^{11}C	838,000	9,220	<100
^{18}F	95,000	1,170	10–20 as F^- < 0.03 as F_2
^{68}Ga	40,600	2,766	
^{67}Ga	597	47	<3.35
^{111}In	423	40	<5.55
^{123}I	1,926	237	
^{124}I	250	31	

atoms in drug molecules are quite common, and sometimes, the halogen-containing drug molecules may have even greater affinity for a receptor or an enzyme, in vivo, than the nonhalogenated molecules (Park et al. 2001). In the last two decades, a number RMIPs were developed based on ^{123}I for SPECT imaging studies. Compared to the positron emitter, ^{124}I, the theoretical specific activity (Table 9.5) of ^{123}I is even higher (because of shorter half-life). Organic molecules containing aromatic rings can be easily labeled with radionuclides. Therefore, ^{123}I and ^{124}I will play a major role in the development of RMIPs.

Among the metals (Table 9.3), Ga, In and Y are trivalent and have similar chemistries. The transition metals such as copper, scandium, and zirconium have complex coordination chemistries. The radionuclides of all these metals can be used to label peptides and proteins using bifunctional chelating agents. ^{111}In- and ^{68}Ga-labeled octreotide analogs have already demonstrated significant potential as molecular imaging probes for SPECT and PET imaging studies of neuroendocrine tumors, expressing somatostatin receptors. Among the transition metals, radioisotopes of copper have useful physical characteristics to develop RMIPs. Several other positron-emitting metals, such as ^{89}Zr and ^{94m}Tc (Table 9.3), may also be useful for developing RMIPs.

9.2.4 General Criteria for the Design of RMIPs

For any RMIP to be successful as an imaging agent for PET or SPECT, the RMIP must have the following ideal characteristics:

- Rapid plasma clearance to reduce blood pool background in the target tissue
- Rapid washout or clearance from nonspecific areas
- Low nonspecific binding
- Preferably no peripheral metabolism of RMIP
- High membrane permeability and intracellular trapping
- Target specificity and high affinity for molecular targets
- Specific activity must be high to prevent saturation of specific binding sites
- Tissue distribution, localization, and target binding should be favorable for developing simple kinetic modeling to estimate quantitative data
- Radiation dosimetry of RMIP must be favorable for multiple diagnostic imaging studies (if necessary)
- Synthesis of RMIP must be rapid and suitable for automation using automated synthesis modules

Developing a specific RMIP involves careful design of the structural requirements in a molecule in order to optimize target specificity and at the same time optimize the pharmacokinetic and pharmacodynamic behavior of the probe to meet the demand of the imaging technique. The physicochemical properties of the RMIP, such as size, charge, solubility, lipophilicity, and SA are very important criteria and must be addressed in designing the structural features of the molecule. Factors, such as rapid metabolism and plasma protein binding (PPB), and nonspecific binding in nontarget tissues, are not desirable for optimal in vivo behavior. It is important to identify the most appropriate structural analog that meets most of the criteria for an ideal RMIP. Some of these criteria will be discussed in greater detail with specific examples, later, in order to emphasize the importance of a careful design of structural features in order to develop a clinically useful MIP.

9.2.4.1 The size of MIP

The molecular size or molecular mass of the MIP is one of the major properties of a molecule that determines the rate of clearance from circulation. Small organic molecules, natural or synthetic, clear from circulation rapidly and provide much higher target/background ratios. With small organic molecules, however, it may not be possible to put more than one radiolabel per molecule. Also, with small molecules it may be difficult to optimize high SA and high target affinity, and to achieve appropriate pharmacokinetic and metabolic behavior. Therefore, with large proteins, such as antibody molecules (150,000 Da), it may be possible to label with

more than one radiolabel per molecule. Liposomes and nanoparticles, because of their size, shape, structural flexibility, multivalency/multifunctionality characteristics, may offer greater potential for developing high specific activity imaging agents.

9.2.4.2   The Position of Radiolabel in the RMIP

The position of the radiolabel in the RMIP must be carefully selected so that the presence of a radionuclide at that position preserves the overall chemical and pharmacological properties of the parent unlabeled molecule. In addition, the position of the radiolabel must also preserve the metabolic stability of the RMIP during the time course of the imaging study. The importance of the position of the radiolabel in the imaging probe is illustrated using FDG and FLT molecules.

Design of FDG Molecule

2-[^{18}F]Fluoro-2-deoxy-D-glucose (FDG) is regarded as the most important, clinically useful, and successful RMIP in nuclear medicine. The design of FDG (Pacák and Černý 2002; Fowler and Ido 2003) is a perfect example to illustrate the significance of the position of the ^{18}F atom in the FDG molecule (Fig. 9.1).

In the 1940s, 6-deoxy-6-[^{19}F]fluoro-6-deoxy-D-glucose ([6-^{19}F]FDG) was first reported (Pacák and Černý

Fig. 9.1 Analogs of D-glucose: Substitution of hydrogen or fluorine atom for the hydroxyl group on C-2 position of glucose would produce DG and FDG, which can be transported into the cell by glucose transporters similar to that of D-glucose

2002). In 1954, it was suggested that the hydroxyl group on carbon 2, was not essential for (1) the carrier-mediated membrane transport into the cell, and (2) the substrate specificity of D-glucose for *hexokinase*-mediated phosphorylation reaction (Sols and Crane 1954). It also became apparent that the hydroxyl group on C-2 was essential for further metabolism of the glucose-6-phosphate. Subsequently, 2-fluoro-[^{19}F]-2-deoxy glucose ([2-^{19}F] FDG) was developed as an anticancer agent (Pacák and Černý 2002). However, due to the very high toxicity of FDG, further clinical studies with FDG were abandoned. Later, 2-[^{14}C]-2-deoxy glucose (CDG) was developed as a tracer to measure cerebral glucose metabolism in animals based on autoradiography (Sokoloff 1979).

On the basis of Sokoloff's work, [^{11}C]CDG would be an appropriate tracer for PET imaging studies (MacGregor et al. 1981). However, the attachment of the ^{18}F atom to the carbon 2 atom in the D-glucose molecule is justified since FDG is a good substrate for *hexokinase*. The kinetic constant (K_m) of the reaction with hexokinase for FDG (0.19 ± 0.03) is very similar to that of D-glucose (0.17). Attaching the ^{18}F atom to carbon 3 or 4 alters the substrate specificity, significantly ($K_m > 70$) (Barrio 2004). Also, the ^{18}F atom in the C-2 position prevents further metabolism of the molecule. As a result, FDG-6-phosphate accumulates in the cell.

Another interesting difference between FDG and CDG concerns the renal excretion of the molecule. The hydroxyl group on C-2 is essential for the active transport across the renal tubules for reabsorption of D-glucose. In contrast to CDG, FDG is not reabsorbed, but excreted. As a result, the body background of the ^{18}F activity is less and the radiation dosimetry with FDG is much more favorable.

Design of FLT Molecule

The DNA synthesis is a measure of cell proliferation. The four nucleotides required for DNA synthesis are cytosine, guanine, adenine, and thymidine. Thymidine is the only one incorporated exclusively into the DNA, and not into the RNA (Cleaver 1967). Intracellularly, thymidine is first phosphorylated in the cytoplasm by the enzyme *thymidine kinase-1* (*TK-1*) to thymidine monophosphate (TMP), prior to incorporation into the DNA. [^{3}H]Thymidine was introduced to measure thymidine incorporation into DNA (thymidine labeling

index) in tumor tissue (Cronkite et al. 1959; Livingston et al. 1974). The nonradioactive 3-[^{19}F]fluoro-3-deoxy-thymidine (FLT) (Fig. 9.2) was first developed in 1969 as an anticancer agent (Langen et al. 1969). Subsequently, [^{11}C]thymidine was introduced as a PET tracer (Christman et al. 1972). Almost two decades later, 3-[^{18}F]fluoro-3-deoxythymidine (FLT), the metabolically stable thymidine analog, was introduced for PET imaging studies (Shields et al. 1996).

FLT is transported into the cell similar to thymidine and then phosphorylated to [^{18}F]FLT-5'-monophosphate by the enzyme, *TK-1*. FLT-MP is further phosphorylated to FLT-TP by the enzyme *thymidilate kinase* (Seitz et al. 2002). FLT phosphates, however, are (1) impermeable to the cell membrane, (2) resistant to degradation and, (3) metabolically trapped inside the cells. The incorporation of FLT into the DNA, however is relatively insignificant (<1%).

The pyrimidine analogs, 2'-fluoro-5-[^{11}C]methyl-1-β-D-arabinofuranosyluracil (FMAU) and 2'-[^{18}F]fluoro-5-methyl-1-β-D-arabinofuranosyluracil (FMAU) have been shown to be useful for imaging tumor cell proliferation (Conti et al. 1995; Sun et al. 2005). FMAU can be taken up by cells and phosphorylated by TK-1 and TK-2 and subsequently incorporated into DNA by *DNA polymerase*. FMAU employs the same DNA synthetic pathway as thymidine and, therefore, has the potential to image DNA synthesis. It is important to recognize that FMAU is incorporated into DNA synthesis, but not into FLT (Seitz et al. 2002; Shields 2003). This observation suggests that the hydroxyl group on the C-3 atom (Fig. 9.2) is essential for the incorporation of thymidine analogs into DNA, but not for substrate specificity of the enzyme TK-1. Despite the fact that FLT lacks the hydroxyl group on C-3, necessary for its incorporation into DNA, it appears to outperform both FMAU and FIAU in terms of uptake, and retention based on in vitro studies (Grierson et al. 2004).

9.2.4.3 Stereospecificity

As discussed in Chap. 7, *stereoisomers* have the same bonds, but exhibit different spatial arrangements of their atoms. One type, known as optical isomerism, is exhibited by molecules with asymmetric carbon atoms (chiral centers) that have nonsuperimposable mirror images. The optical isomers, called *enantiomers* rotate plane-polarized light in opposite *directions; dextroro-*
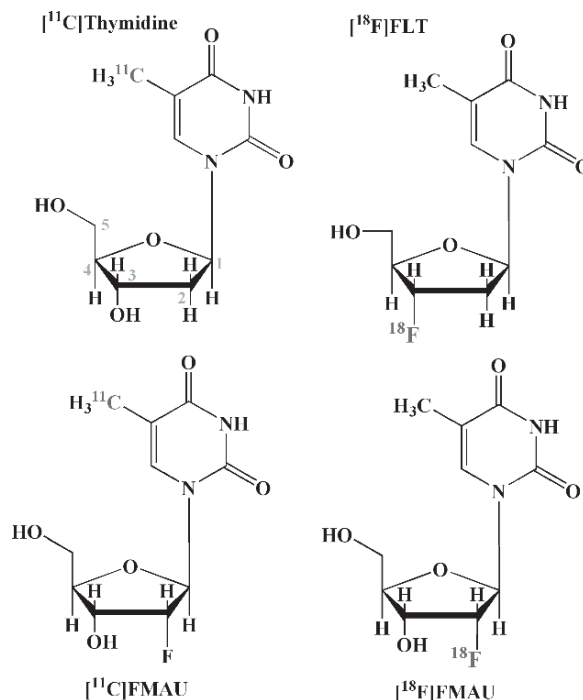
Fig. 9.2 Radiolabeled analogs of thymidine for imaging DNA synthesis: The hydroxyl group on C-3 in the organic base is essential for incorporation into DNA synthesis

tatory (D or (+)) and *levorotatory* (L or (−)). These designations only refer to the experimental values of rotation, while the letters D and L relate asymmetric centers to glyceraldehydes (as in sugars), for which an absolute stereochemistry has been defined. On the basis of this designation, in the case of amino acids, L-amino acids are often dextrorotatory. Only L-amino acids are found in nature.

A molecule is said to be *chiral* if it exists as an *enantiomer*. Molecular targets such as receptors and enzymes often exhibit stereoselectivity or binding selectivity for one enantiomer over the other. The stereochemical requirements of biological activity have consequence for the radiolabeled amino acids and sugars (Fowler and Ido 2003). For example, only the radiolabeled L-amino acid and D-glucose analogs are biologically active. Further, it is important to recognize that radiolabeled drug molecules also exhibit stereoselective binding to neuroreceptors. For example, only the [^{11}C]-(+)McN-5652 binds to the serotonin transporter (Szabo et al. 1995) and [^{11}C]dexetimide binds to the muscarinic cholinergic receptor (Dannals et al. 1988).

9.2.4.4 Lipophilicity

Lipophilicity is the affinity of a molecule or moiety for a lipophilic environment. Molecular size, mass (weight), and hydrogen-bonding capacity also contribute to the overall lipophilicity of the molecule (Riant and Tillement 1999). Lipophilicity is a fundamental physicochemical property of a compound and plays a pivotal role in the absorption, distribution, metabolism, and elimination of drug molecules. The most common experimental lipophilicity measurement involves partitioning of a compound between an octanol and a buffer, where the log of the ratios of the compound concentration in the octanol layer is divided by that in the buffer layer, often called the Log P. Lipophilicity is also expressed in several different ways, including terms such as Log P, clogP, delta Log P, and Log D, depending on the method of estimation (Waterhouse 2003).

Very polar compounds, normally, exhibit high water solubility, fast clearance through the kidneys, and often contain ionizable functional groups that limit blood–brain barrier (BBB) penetration. In general, only the neutral, lipophilic molecules can pass through the BBB and enter into the brain tissue. The brain penetration, and specific to nonspecific binding ratios, exhibited in vivo by radiotracers, involves a complex interplay between many critical factors, including lipophilicity, receptor affinity, metabolism, molecular size, and shape, etc. Based on an extensive literature search, Waterhouse recently noted that for most neutral radiotracers, the relationship between lipophilicity and molecular weight shows the expected parabolic relationship (Waterhouse 2003) (Fig. 9.3). The general criteria for adequate brain penetration and optimum target to nontarget ratios of high SA radiotracers are as follows:

- Log P or Log D < 3.5
- Molecular weight < 450 g mol^{-1}
- An absence of functional groups that will strongly ionize at physiological pH
- No appreciable affinity for efflux pumps (such as PGP)
- No appreciable affinity for specific binding sites for high-capacity peripheral sites, including albumin or other plasma proteins
- Not a substrate for enzymes at the BBB

9.2.4.5 Plasma Protein Binding

It is well documented that both, specific and nonspecific binding (NSB) of drugs can occur with plasma proteins, cell membranes, and other components present in the blood (Kosa et al. 1997). NSB may be saturable, when drugs are administered at high-enough mass, and bioavailability may not be an issue. The NSB of radiotracers, however, may significantly reduce the bioavailability (Kosa et al. 1997). NSB to albumin and other plasma proteins is known to correlate positively and linearly with increasing lipophilicity (Kratochwil et al. 2002). Some radiotracers exhibit high NSB (>90%) and may enter the brain nearly as well as those that exhibit much lower plasma protein binding (Riant and Tillement 1999). In addition, increasing lipophilicity has been correlated with increased lung deposition, liver and spleen uptake, and higher affinity to many metabolic enzymes such as cytochrome P450. Such processes serve to decrease the percentage of the administered dose that may enter the brain and other target organs, and tissues.

Fig. 9.3 Liopophilicity (log P) vs. brain uptake for simple low-mass radiolabeled compounds, such as [^{11}C]ethanol and [^{11}C] butanol. The results indicate that the brain uptake of these radiotracers does indeed correlate with lipophilicity and that the relationship is parabolic in nature. Also, the uptake is dependent on the blood flow (Waterhouse 2003)

9.2.4.6 Metabolism

In the design of a RMIP, it is very important that the label (radionuclide) is ideally in a metabolically stable position. When a radiotracer is injected into a human subject, the signal from the radionuclide is detected, regardless of whether it is coming from the intact radiotracer or from a radiolabeled metabolic fragment. The fate of the radionuclide, as a result of metabolism, must be considered in selecting the position of the label in a molecule. Peripheral metabolism, especially in the blood, may dramatically decrease the delivery of the probe to the target site. Metabolism the RMIP at or near the target site may decrease the specific binding to the molecular target. In addition, the quantitative estimation of molecular target concentration based on kinetic modeling may get complicated if the metabolic products are also trapped at the target site. Whatever the case may be, it is essential that all the metabolic products and their relative concentrations are known so that a meaningful interpretation of the imaging data can be made. Several examples will be discussed to emphasize the importance of metabolism in molecular imaging studies.

[18F]FDOPA Metabolism

In the presynaptic dopaminergic neuron, the amino acid tyrosine is converted to dihydroxyphenylalanine (L-DOPA). Subsequently, *DOPA decarboxylase* or *aromatic amino acid decarboxylase* (*AAAD*) converts L-DOPA to dopamine. The position of the ^{11}C or ^{18}F label in the L-DOPA molecule clearly illustrates the importance of metabolism and its role in drug design (Fig. 9.4). A ^{11}C label can be introduced in the carboxyl group (COOH) as in the case of [^{11}C-carboxyl]L-DOPA. Since AAAD eliminates the carboxyl group, the ^{11}C label is quickly lost. However, if the β-carbon atom is labeled with ^{11}C, as in the case of [β-^{11}C]L-DOPA, the ^{11}C activity is still retained with the dopamine molecule (Bergstrom et al. 1996).

[18F]6-Fluoro-L-DOPA (FDOPA) was also developed as a tracer to examine the transport of dopamine precursor from plasma and its decarboxylation by AAAD to fluorodopamine (Firnau et al. 1987). FDOPA, however, undergoes extensive metabolism in vivo (Luxen et al. 1992) as shown in Fig. 9.5. FDOPA is decarboxylated by *AAAD* to produce [18F] Fluorodopamine (FDA). FDOPA can be *O*-methylated by catechol-*O*-
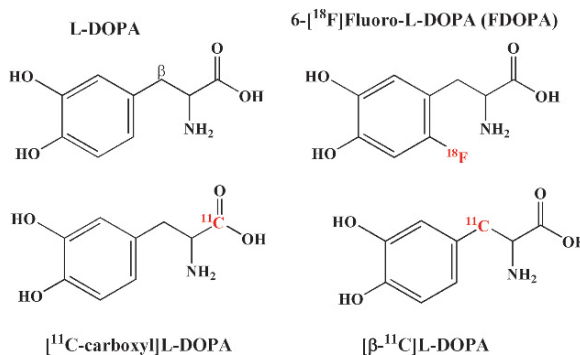
Fig. 9.4 Radiolabeled analogs of L-DOPA: The position of ^{11}C or ^{18}F label is very important to prevent metabolic degradation and elimination in vivo

methyltransferase (COMT) to 3-*O*-methyl-6-[18F] fluoro-L-dopa (3-OMFDOPA), which is uniformly distributed throughout the brain. FDA can be oxidized by *monoamine oxidase (MAO)* to L-3,4-dihydroxy-6-[18F]fluorophenylacetic acid ([18F]FDOPAC), which is subsequently *O*-methylated by COMT to 6-[18F] fluorohomovanillic acid ([18F]FHVA). *AAAD* and *COMT* are also present in peripheral tissues, such as liver, kidneys, and lung. Both, the decarboxylation of the compound and the release of radiometabolites into the blood, however, can be reduced with carbidopa, a decarboxylase inhibitor.

While FDOPA has already demonstrated its value as a diagnostic probe in Parkinson's disease and in neuroendocrine tumors, the metabolic profile of this probe, however, complicates the estimation of quantitative parameters by kinetic modeling.

Thymidine Metabolism

[^{11}C]Thymidine was developed as a PET tracer to image tumors and measure proliferation rate. Analysis of thymidine PET images, however, is complicated by the fact that the tracer is rapidly metabolized (Fig. 9.6). As a result, much of the ^{11}C activity imaged in thymidine studies is in the form of labeled metabolites, which are no longer available to be incorporated into the DNA.

The large pools of *thymidine phosphorylase* (*TP*) present in the blood, liver and spleen rapidly degrade thymidine in vivo. Thymidine can be degraded by *TP* to thymine and then be reduced to dihydrothymine (DHT), β-ureidoisobutyric acid (BUIB), and β-amino isobutyric

Fig. 9.5 In vivo metabolism of FDOPA

6-[^{18}F]Fluoro-L-DOPA (FDOPA)

6-[^{18}F]Fluorodopamine (FDA)

AAAD

COMT

[^{18}F]3-OMFDOPA

MAO

COMT

6-[^{18}F]FDOPAC

6-[^{18}F]FHVA
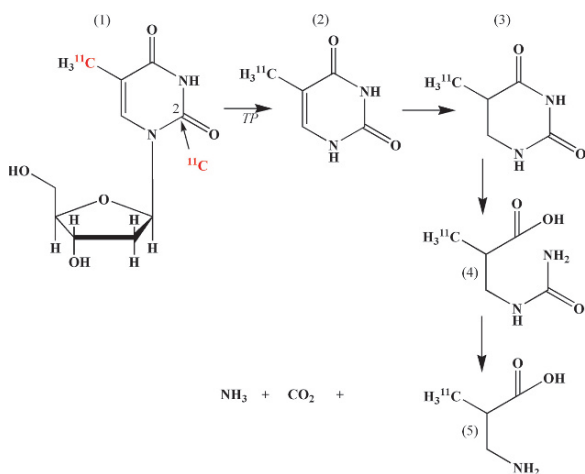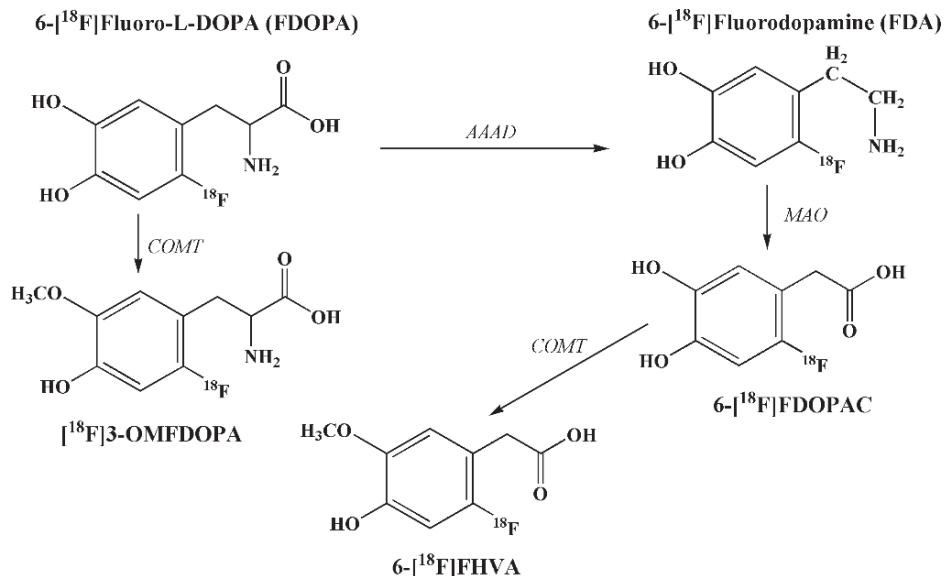
Fig. 9.6 In vivo metabolism of [^{11}C]thymidine: Labeling C-2 in the carbonyl group will result in the elimination of 11C activity as CO_2. Labeling the methyl group with ^{11}C provides relatively more stable tracer for imaging DNA synthesis

can accumulate in cells in a number of pathways and limit the ability to develop a comprehensive, validated kinetic model to measure the DNA synthesis using methyl-labeled thymidine. On other hand, The C-2 label is lost as [^{11}C]CO_2, which rapidly enters the large bicarbonate pool in the body.

To overcome the practical limitations of [^{11}C]thymidine imaging, metabolically stable ^{18}F-labeled thymidine analogs, FLT and FMAU (Fig. 9.2) have been developed (Shields et al. 1996; Grierson and Shields 2000). FLT does not generate significant metabolites during the imaging procedure as does [^{11}C]thymidine. FLT is not a substrate for *TP*, the enzyme that breaks the bond between the pyrimidine and deoxyribose. However, FLT is glucoronidated in the liver and then delivered to the blood. FLT-glucuronide is restricted to the vascular space and is cleared by the kidneys.

acid (BAIB). For thymidine, labeled at the C-2 position, degradation products beyond BUIB do not contain the label, which leaves the pathway as [^{11}C]CO_2. Degradation takes place rapidly in the liver and blood, and labeled metabolites appear in significant quantities in the blood within minutes after injection (Mankoff et al. 2005).

Thymidine can be labeled with ^{11}C in the methyl (^{11}CH$_3$) or in the C-2 (^{11}CO) position of the pyrimidine ring. The former gives rise to acidic metabolites, which

Metabolism of WAY-100,635

WAY-100,635 is a 5HT$_{1A}$ receptor antagonist (Fig. 9.7). Initially, the ^{11}C label was introduced in the methoxy group (OCH$_3$). Subsequently, ^{11}C was introduced in the carbonyl (CO) position to reduce the contribution of labeled metabolites (Pike et al. 1996). The molecule was finally modified resulting in a ^{18}F-labeled analog with improved metabolic stability and greater potential for commercial distribution.
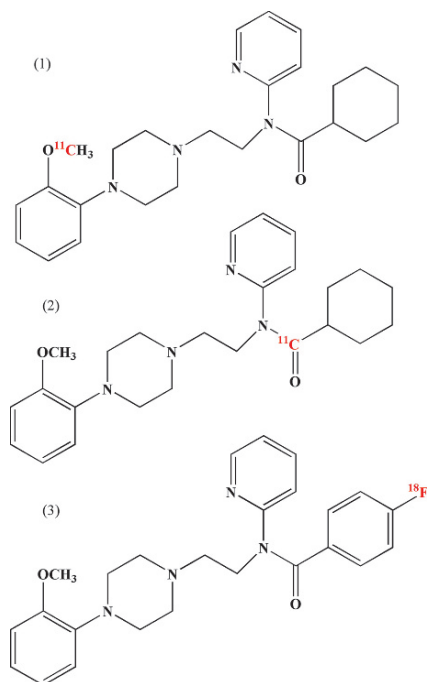
Fig. 9.7 Radiolabeled WAY-100,635, a 5HT$_{1A}$ receptor antagonist: ^{11}C in the carbonyl position (2) provides a more stable radiotracer when compared to ^{11}C labeling in the methoxy group (1). The ^{18}F-labeled analog provides even greater in vivo stability and is the preferred radiotracer (3)

A key step in the development of a new RMIP is to characterize its binding specificity in vivo by imaging studies. It is important to compare the biodistribution and pharmacokinetics of RMIP with and without a pharmacological dose of the MIP to assess the specificity and saturation ability. In order to address the significance of the metabolism on a specific binding at the target site, MIP should be labeled at different positions in the molecule and then the in vivo distribution and kinetics of these analogs should be compared.

Table 9.6 Specific activity requirements for molecular imaging probes

Imaging study based on	SA (Ci µmole^{-1}) of RMIP for	
	PET	SPECT
Enzyme-mediated cellular trapping	0.01–0.1	0.1–0.5
Antigen–antibody binding	0.1–1.0	1–5
Neuroreceptor binding	2–10	2–10
Gene expression	2–10	>10

9.2.4.7 Specific Activity

As previously discussed, SA (Ci/µmole^{-1}) of the RMIP is very important for molecular imaging studies based on PET and SPECT since it is a measure of the number of probe molecules that can give a radioactive signal in a given mass of RMIP. The SA needed for a given radiotracer depends on the concentration of the target molecules (receptors, enzymes of antigens) present in a given cell or tissue (Table 9.6). Typically, the concentration of high affinity molecular targets is between 10^{-12}–10^{-9} moles L^{-1}. For neuroreceptor and gene imaging studies very high SA (2–10 Ci µmole^{-1}) is absolutely necessary. For enzyme-mediated molecular imaging studies, 100–1,000 times lower SA may be adequate. For animal (rodent) studies, based on MicroPET and MicroSPECT, it is important to recognize that the SA requirements may be even higher than what is needed for clinical studies (Kung and Kung 2008). The relative size of the brain in different species (humans, rats and mice) and dopamine receptor levels in striatum are compared in Table 9.7. With the typical dose of [^{11}C]raclopride (SA = 1.0 Ci µmol^{-1}) injected for imaging studies, the receptor occupancy in mice is almost 70% compared to relatively insignificant levels of occupancy in humans (Table 9.6). These results suggest that for MicroPET imaging studies, the SA of

Table 9.7 Brain dopamine D$_2$ receptor occupancy of [^{11}C]Raclopride in different species[a]

Species	Body wt (g)	Brain wt (g)	Stratum wt (g)	D$_2$/D$_3$ receptor mol kg^{-1}	Dose(mCi)	[^{11}C]Raclopride (mCi µmol^{-1})	Occupancy(%)
Humans	70,000	1,500	40	13.6	10–15	1,000	<1.0
Rats	250	1.5	0.05	19.8	1.0	1,000	19.0
Mice	25	0.4	0.03	20.0	1.0	1,000	70.0

[a]The above table was modified from reference (Kung and Kung 2008)

radiotracers must be at least 10 times more than what is needed for human studies.

9.2.4.8 RMIP: Mechanism of Localization

RMIP can be generally classified based on their ability to image a specific biochemical process or based on their unique mechanism of localization in a specific organ/tissue of interest (Table 9.2). The localization of RMIP in a specific target organ or tissue of interest depends on three important phenomena:

- Rapid blood clearance and transport of RMIP to the target organ or tissue of interest.
- Transport of RMIP from capillaries into the extracellular fluid and subsequent transport into the cells through the cell membrane. Transport processes such as simple diffusion, facilitated diffusion, active transport and receptor-mediated endocytosis (Chap. 8, Sect. 8.7) play a very important role in the localization of the radiotracer at the target site.
- Localization at the target site and intracellular trapping may be due to any one of these following biochemical processes:
  - Specific binding to receptors on the cell membrane or within the cell
  - Specific binding to extracellular or intracellular antigens
  - Specific enzyme-mediated intracellular metabolism, followed by trapping of metabolites
  - Incorporation into the biochemical synthesis of intracellular proteins or DNA.

9.2.5 General Methods of Radiolabeling

Depending on the type of radioisotope chosen and the method used to radiolabel a MIP, three different types of RMIPs can be synthesized, as shown below:

1. *Isotope exchange*: PMIP prepared by direct exchange (isotopic substitution) of one or more stable atoms of an element in a molecule with one or more nuclides of a radioisotope of the same element. The radiolabeled molecule and the unlabeled molecule are chemically identical and behave in vivo in a similar manner. This method of radiolabeling is generally used to prepare radioiodinated radiopharmaceuticals in which the stable ^{127}I atom is replaced with a ^{123}I or ^{124}I a tom (Chap. 10). Also, in the preparation of ^{11}C compounds the stable ^{12}C atom is replaced with a ^{11}C radionuclide, but the preparation of ^{11}C compounds may involve multistep alkylation reactions (Chap. 11).

2. *Introduction of a foreign element*: RMIP can be prepared by the introduction of a foreign element or radionuclide in a parent MIP. Most of the radiopharmaceuticals are prepared based on this method. The RMIP and MIP are not chemically identical and may have different in vivo behavior. For example, preparation of [^{18}F]FDG involves the introduction of a ^{18}F atom in the deoxyglucose molecule (Chap. 10). Also, in the preparation of radioiodinated peptides and hormones, ^{123}I or ^{124}I is added to the parent molecule that do not contain a natural stable iodine atom.

3. *Metal chelation*: This method also introduces a foreign element (radiometal such as ^{99m}Tc, ^{62}Cu and ^{111}In) into an organic compound, known as chelating agent. One or more atoms (such as O, N and S) in the chelating agent donate a pair of electrons to the foreign metal atom to form coordinate covalent bonds (Chap. 11). As a result, the chemical and biological properties of the radiometal-chelate complex are different than that of the chelating agent.

4. Certain peptides and macromolecules such as monoclonal antibodies can be labeled with radiometals based on the metal chelation method, described above. This technique, however, requires conjugation of a bifunctional chelate (BFC) to the peptide or protein first, and then subsequent chelation of the radiometal by the BFC molecule. The radiometal is not directly incorporated into the peptide or protein molecule.

9.2.5.1 Important Factors of Radiolabeling

In developing an appropriate radiolabeling technique, suitable for a specific RMIP, several important factors need to be considered in order to optimize the synthesis procedure.

Efficiency of Radiolabeling: During the synthesis of RMIP, the percent of radioactivity incorporated in the desired chemical form of RMIP compared to the

total radioactivity in the reaction mixture is given by the labeling yield or labeling efficiency (LE), which may be expressed as a percent at the end of the synthesis (%LE @EOS) or at the end of bombardment (% LE @EOB), as in the case of cyclotron-produced PET radiopharmaceuticals. It is always desirable to have very high labeling LE, but some times 2–5% LE is acceptable, provided the radiolabeled product is pure and acceptable for human studies.

Purification of the final product: Most radiopharmaceutical preparations require a purification step to separate or isolate the desired RMIP from the unlabeled radiochemical contaminants and/or undesirable chemical species present in the reaction mixture. High-pressure liquid chromatography (HPLC) is one of the most common techniques used to obtain the purified RMIP. A number of solid-phase purification techniques, using mini cartridges based on alumina and ion exchange resins, are becoming increasingly popular. The *radiochemical purity* (RCP) of the final RMIP must be very high (>95%) for human studies, while the contamination of the final RMIP formulation with the undesirable radiochemical impurities must be very low (<5–10%). For every radiopharmaceutical acceptable quality control criteria, especially regarding the purity of the final radiolabeled drug product, must be carefully established.

Radiolysis: Radiolabeled compounds may be degraded or decomposed by the high-energy radiations involving both γ photons and electrons (both β⁻ and β⁺). When radiations from a radionuclide in a radiotracer molecule break the chemical bonds, within the same molecule, then such a process is known as *autoradiolysis*. The high-energy radiation may generate free radicals in water, such as hydrogen peroxide and perhydroxyl free radicals, which in turn may damage the radiotracer molecules. Radiolysis is very much dependent on the concentration of the final radiolabeled drug product formulation (activity/mL); the higher the concentration, the greater the radiolysis effect. Peptides and protein molecules may be more susceptible for radiation damage than small organic molecules.

Stability of the RMIP: The in vitro chemical stability of radiotracer is very important for optimal shelf life. In addition, the in vivo stability of the RMIP is critical for optimal targeting of the imaging probe. Radiopharmaceuticals prepared, based on metal chelation, may be unstable in vivo because of the presence of competing metallic ions and binding agents.

9.2.6 Automated Synthesis Modules

Computer-controlled automation of the synthesis of PET radiopharmaceuticals is desirable for routine commercial production and to reduce the radiation exposure to the personnel involved in the production of these PET drugs. A number of automated synthesis modules (ASM) for routine production of radiolabeled precursors (such as $^{11}CH_3I$) or radiopharmaceuticals ready for clinical studies (such as FDG, FDOPA, Raclopride) are commercially available (Table 9.8 and Fig. 9.8). The main purpose of the ASMs is to

Table 9.8 Automated synthesis modules for the production of PET radiopharmaceuticals

Radiotracer /Precursor	Synthesis module	Manufacturer	Comments
[^{18}F]FDG	TRACERlab MX$_{FDG}$	GE	Disposable cartridge
	TRACERlab FX$_{FDG}$	GE	Multiple use
	Metatrace FDG®	CTIPETNET	Infinite run capability
	FDG-Plus Synthesizer	Bioscan	Disposable module
	Synthera®	IBA Molecular	
[^{18}F]FDOPA	TRACERLab FX$_{FDOPA}$	GE	FDOPA from [^{18}F]F$_2$
[^{11}C]CH$_3$I (MeI)	TRACERlab FX$_c$	GE	Gas-phase MeI + methylation
	Microlab	GE	Gas-phase MeI
	MeI-Plus	Bioscan	Liquid-phase MeI
^{18}F-Tracers	TRACERlab FX$_{F^-\ E}$	GE	Electrophilic fluorination by the use of [^{18}F]F$_2$
^{18}F-Tracers	TRACERlab FX$_{F^-\ N}$	GE	Nucleophilic fluorination by the use of [^{18}F] F$^-$ (fluoride)
^{18}F-Tracers	Synthera®	IBA Molecular	Modular multipurpose synthesizer
^{11}C and ^{18}F-Tracers	AutoLoop	Bioscan	General purpose unit for the synthesis of radiotracers
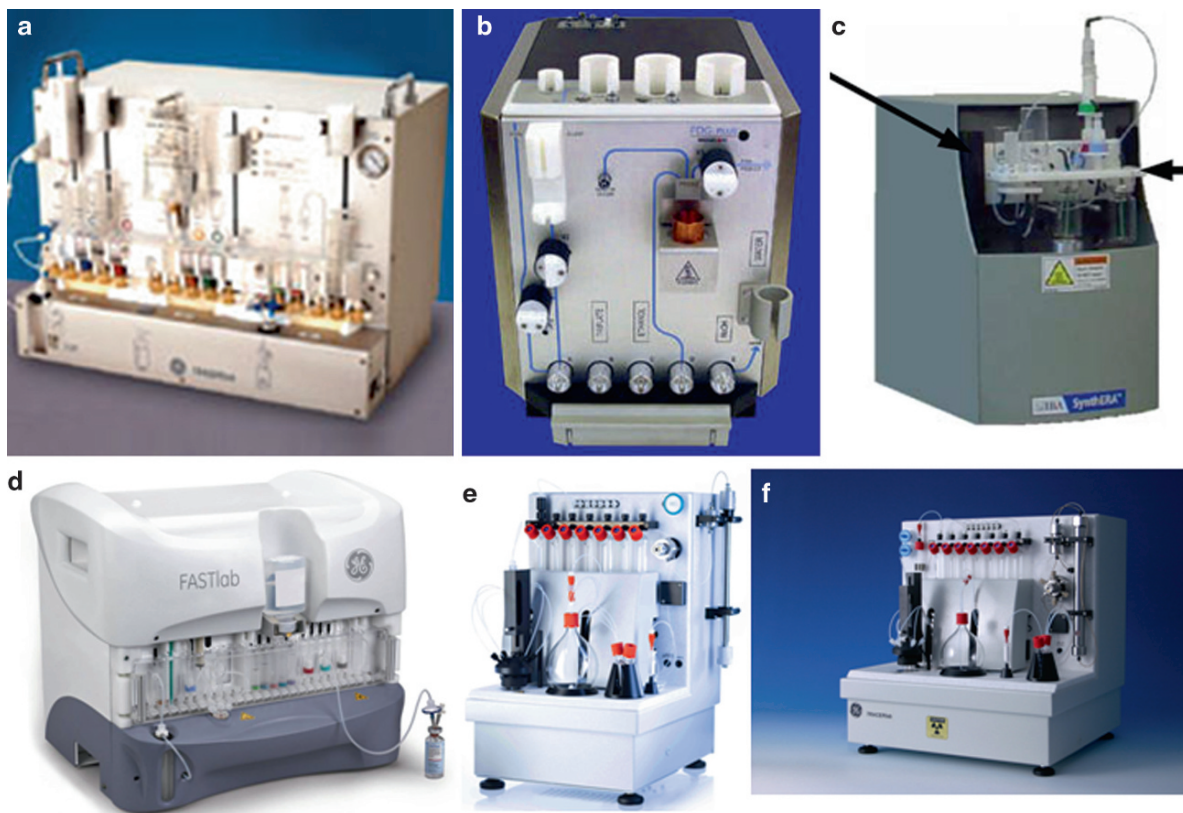
Fig. 9.8 Automated synthesis modules for the production of PET radiopharmaceuticals. (**a**) TRACERLab MX$_{FDG}$; (**b**) Bioscan FDG; (**c**) Synthera (IBA); (**d**) GE FastLab; (**e**) GE TRACERLab FX$_M$; (**f**) GE TRACERLab FXc pro

- Reduce exposure to high levels of harmful radiation
- Reduce the need for manual steps to accelerate the overall radiolabeling synthesis procedure
- Use the time of personnel efficiently and minimize operator errors due to the operator
- Obtain better reproducibility of RMIP synthesis from batch-to-batch
- Facilitate compliance with FDA regulations

ASMs are based on the principle of unit operations, in which a complex synthetic procedure is reduced to a series of simple operations (or reactions), such as evaporation, fluorination, chromatography, hydrolysis, purification, and sterilization. These operations are controlled by PCs with software programs that are user friendly and flexible enough to change various reactions conditions. Some of these ASMs, such as the TracerLab FX are based on the use of sterile disposable kits with ready-to-use reagent vials for each batch

production. At this time, several commercial ASMs are used routinely for the synthesis of radiochemically pure, sterile and pyrogen-free FDG used in clinical studies. In the future, such ASMs may also be available for the production of FLT, FCH and other PET radiopharmaceuticals.

For the development of ^{11}C PET radiopharmaceuticals, ASMs capable of generating [^{11}C]Methyl iodide or triflate are critical for the reliable synthesis of radiotracers. Several commercial modules are under extensive testing and evaluation.

9.2.7 Microfluidic Systems

The development of miniaturized radiosynthesis devices (also known as microfluidic systems) is an emerging area of PET radiochemistry that has the potential to offer several advantages compared to the ASMs, discussed

above. The current ASMs for the production of FDG use many of solenoid activated isolation valves and are typically about 2-3 feet in width without the shielding, and the purification equipment. Also, the reagent and solvent volumes are typically 1–5 mL and need reaction vessels that are typically over 10 mL in volume. Most of the current ASMs are designed to produce multicurie amounts of FDG (in 10–15 mL) by using 15–25 mg of precursor (mannose triflate) and 2–5 mL of target water containing 1–10 Ci of ^{18}F activity.

Miniaturization of synthesis modules based on microfluidic technology may dramatically (a) improve reaction efficiency, (b) increase efficient use of hot-cell space for radiotracer productions, (c) decrease the utilization of precursor mass, (d) facilitate easier separation and purification steps, and finally, (e) may provide highly controlled, reproducible, and reliable radiotracer production through the use of inexpensive, interchangeable, disposable radiochemistry modules.

In order to synthesize FDG, microfluidic reactors were first developed in 2005 (Lee et al. 2005; Gillies et al. 2006). The device built by Lee et al, incorporates five sequential processes; [^{18}F]fluoride concentration, evaporation of water and solvent, radiofluorination, solvent exchange, and hydrolytic deprotection. All of these five steps, involved in the synthesis of FDG, proceed with high radiochemical yield and purity, and with shorter synthesis time relative to conventional automated synthesis. Unfortunately, however, these systems are not yet available for routine clinical use.

References

Barrio JR (2004) The molecular basis of disease. In: Phelps ME (ed) PET: Molecular imaging and its biological applications. Springer, New York

Bergstrom MJ, Eriksson B, Oberg K, et al (1996) In vivo demonstration of enzyme activity in endocrine pancreatic tumors. Decarboxylation of C-11 DOPA to Carbon-11 dopamine. J Nucl Med 37:32–37

Christman D, Crawford EJ, Friedkin M, et al (1972) Detection of DNA synthesis in intact organisms with positron-emitting methyl-[C-11]-thymidine. Proc Natl Acad Sci U S A 69:988–992

Cleaver JE (1967) Thymidine metabolism and cell kinetics. Front Biol 6:43–100

Conti PS, Alauddin MM, Fissekis JR, et al (1995) Synthesis of 2′fluoro-5-[11C]-methyl-1-beta-D-arabinofuranosyluracil ([^{11}C]-FMAU): a potential nucleoside analog for in vivo study of cellular proliferation with PET. Nucl Med Biol 22:783–789

Cronkite EP, Fliedner TM, Bond VP, et al (1959) Dynamics of hemopoietic proliferation in man and mice studied by 3H-thymidine incorporation into DNA. Ann N Y Acad Sci 77:803

Dannals RF, Langstrom B, Ravert HT, et al (1988) Synthesis of radiotracers for studying muscarinic cholinergic receptors in the living human brain using positron emission tomography [^{11}C]dexetemide and [^{11}C]levetimide. Int J Radiat Appl Instrum A 39:291–295

Firnau G, Sood S, Chirakal R, et al (1987) Cerebral metabolism of 6-[^{18}F]fluoro-L-3,4-dihydroxy-phenylalanine in the primate. J Neurochem 48:1077–1082

Fowler JS, Ding Y-S (2002) Chemistry. In: Wahl, Buchanan JW (eds) Principles and practice of positron emission tomography. Lippincott, Philadelphia, USA

Fowler JS, Ido T (2003) Design and synthesis of 2-deoxy-2-[^{18}F]fluoro-D-glucose (^{18}FDG). In: Welch MJ, Redvanley CS (eds) Handbook of Radiopharmaceuticals. Wiley, New York

Gillies JM, Prenant C, Chimon GN, et al (2006) Microfluidic reactor for the radiosynthesis of PET radiotracers. Appl Radiat Isot 64:325–332

Grierson JR, Shields A (2000) Radiosynthesis of 3′-Deoxy-3′-[^{18}F]fluorothymidine:[^{18}F]FLT for imaging of cellular proliferation in vivo. Nucl Med Biol 27:143–156

Grierson JR, Schwartz JL, Muzi M, et al (2004) Metabolism of 3′-deoxy-3′-[^{18}F]fluorothymidine in proliferating A549 cells: validations for positron emission tomography. Nucl Med Biol 31:829–837

Hanahan D, Weinberg RA (2000) The hallmarks of cancer. Cell 100:57–70

Kosa T, Maruyama T, Otagiri M (1997) Species differences of serum albumins: I. Drug binding sites. Pharm Res 14: 1607–1612

Kung M-P, Kung H-F (2008) Mass effect of injected dose in small rodent imaging by SPECT and PET. Nucl Med Biol 32:673–678

Kratochwil NA, Huber W, Muller F, et al (2002) Predicting plasma protein binding of drugs: a new approach. Biochem Pharmacol 64:1355–1374

Langen P, Etzold Z, Hintsche R, et al (19693′deoxy-3′fluorothymidine, a new selective inhibitor of DNA synthesis. Acta Biol Med Ger 23:759–766

Lee C-C, Sui G, Elizarov A, et al (2005) Multistep synthesis of a radiolabeled imaging probe using integrated microfluidics. Science 310:1793–1796

Livingston RB, Ambus U, George SL, et al (1974) In vitro determination of thymidine-[H-3] labeling index in human solid tumors. Cancer Res 34:1376–1380

Lu S-Y, Watts P, Chin FT, et al (2004) Syntheses of ^{11}C- and ^{18}F labeled carboxylic esters within a hydrodynamically-driven micro-reactor. Lab on a Chip 4(6):523–525

Luxen A, Guillaume M, Melega WP, et al (1992) Production of 6-[^{18}F]fluoro-L-dopa and its metabolism in vivo- a critical review. Int J Rad Appl Instrum B 19:149–158

MacGregor RR, Fowler JS, Wolf AP, et al (1981) A synthesis of ^{11}C-2-deoxy-D-glucose for regional metabolic studies. J Nucl Med 22:800–803

Maclean D, Northrop JP, Padgett HC, et al (2003) Drugs and probes: the symbiotic relationship between pharmaceutical discovery and imaging science. Mol Imaging Biol 5:304–311

Mankoff DA (2007) A definition of molecular imaging. J Nucl Med 48:18N and 21N

Mankoff DA, Shields AF, Krohn KA (2005) PET imaging of cellular proliferation. Radiol Clin N Am 43:153–167

Pacák J, Černý M, PhD (2002) History of the first synthesis of 2-deoxy-2-fluoro-D-glucose the unlabeled forerunner of 2-deoxy-2-[18F]fluoro-D-glucose. Mol Imaging Biol 4: 352–354

Park KB, Kitteringham NR, O'Neill PM (2001) Metabolism of Fluorine-containing drugs. Annu Rev Pharmacol Toxicol 41:443–470

Pike VW, McCarron JA, Lammertsma AA, et al (1996) Exquisite delineation of 5HT1A receptors in human brain with PET and [carbonyl-11C]WAY-100,635. Eur J Pharmacol 301:R5–R7

Riant JP, Tillement JP (1999) Drug transfer across the blood-brain barrier and improvement of brain delivery. Fundam Clin Pharmacol 13:16–26

Seitz U, Wagner M, Neumaier B, et al (2002) Evaluation of pyrimidine metabolising enzymes and in vitro uptake of 3′-[18F] fluoro-3′-deoxythymidine ([18F]FLT) in pancreatic cancer cell lines. Eur J Nucl Med Mol Imaging 29:1174–1181

Shields AF (2003) PET imaging with 18F-FLT and thymidine analogs: promise and pitfalls. J Nucl Med 44:1432–1434

Shields AF, Grierson JR, Kozawa SM, et al (1996) Development of labeled thymidine analogs for imaging tumor proliferation. Nucl Med Biol 23:17–22

Silverman M (1970) Specificity of monosaccharide transport in the dog kidney. Am J Physiol 218:743–750

Sols A, Crane RA (1954) Substrate specificity of brain *hexokinase*. J Biol Chem 210:581–595

Sokoloff L (1979) Mapping of local cerebral functional activity by measurement of local cerebral glucose utilization with [14C]deoxyglucose. Brain 102:653–668

Sun H, Sloan A, Mangner TJ, et al (2005) Imaging DNA synthesis with [18F]FMAU and positron emission tomography in patients with cancer. Eur J Nucl Med Mol Imaging 32:15–22

Szabo Z, Kao PF, Scheffel U, et al (1995) Positron emission tomography imaging of serotonin transporters in the human brain using [11C](+)McN5652. Synapse 20:37–43

Waterhouse RN (2003) Determination of lipophilicity and its use as a predictor of blood–brain barrier penetration of molecular imaging agents. Mol Imaging Biol 5: 376–389

If your experiment needs statistics, you ought to have done a better experiment.

Ernest Rutherford

10.1 Halogens

The family of Group 7A elements – fluorine, chlorine, bromine, iodine, and astatine, known as *halogens*, are nonmetals and generally not found in nature as free elements. Instead, they are found as halide ions (X^-) in various minerals and sea water. Radioisotopes of chlorine and astatine are not useful for imaging and are not discussed further in this chapter. Some of the important physical properties of fluorine, bromine, and iodine are compared to that of hydrogen in Table 10.1. Various radionuclides of halogens useful for developing molecular imaging agents are listed in Table 10.2.

All halogens are characterized by the presence of two *s* electrons and five *p* electrons in the outer most valence shell (ns^2, np^5). The electronegativity values reveal that among halogens, fluorine has the greatest attraction for electrons and iodine has the least. This means that a F^- ion is more stable than a I^- ion. Since fluorine is the most electronegative element, it has only one oxidation state (-1). In contrast, bromine and iodine may attain positive oxidation states when interacting with the more electronegative element – oxygen. The higher ionization potentials of halogens suggest that it is difficult to remove an electron from halogen atoms. Also, among halogens, fluorine is the most powerful oxidizing agent, while iodine is the most powerful reducing agent.

The chemistry of bromine and iodine however, is, in many aspects, similar more similar in many aspects compared to the chemistry of fluorine. In general, halogens can react as *electrophiles*, electron-deficient positively charged species; or *nucleophiles*, electron rich negatively charged species. Electrophiles (X^+) seek electron-rich reactants such as carbon atoms with high local electron densities, while nucleophiles (X^-) seek electron-deficient reactants.

10.2 Synthesis of ^{18}F labeled Radiopharmaceuticals

For the development of PET radiopharmaceuticals, ^{18}F appears to be an ideal radionuclide due to the following reasons:

- Low positron energy (0.64 MeV) with a short range in tissue (Max. 2.4 mm) and provides high resolution images
- Can be produced in high specific activity (20–50 Ci µmole^{-1})
- Can be produced in large amounts (>10 Ci) in a cyclotron
- Fluorine is the most electronegative of all elements and can react with many organic and inorganic chemicals.
- It can react as an electrophile or a neucleophile chemical specie.
- Relatively high labeling yields (20–70%) in the synthesis of ^{18}F-PET tracers
- Acceptable radiation dosimetry for multiple studies in a patient
- The physical $T_{1/2}$ (110 min) allows for the transport from the production site to the PET centers

The fact that fluorine atom is only slightly larger than a hydrogen atom (Table 10.1) is important to appreciate. The replacement of a hydrogen atom or hydroxyl

Table 10.1 Physical properties of hydrogen and halogens

	Element			
Physical property	H	F	Br	I
Atomic number	1	9	35	53
Atomic radius (pm)	78	71	114	133
Ionic radius (pm)	154	133	196	216
Electron structure	$1s^1$	$[He]2s^2, 2p^5$	$[Ar]3d^{10}, 4s^2, 4p^5$	$[Kr]4d^{10}5s^2, 5p^5$
Electronegativity	2.20	3.98	2.96	2.66
Oxidation state	?	−1	−1, +1, +3, +5	−1, +1, +5, +7
First ionization Potential (ev)	?	17.42	11.84	10.44

Table 10.2 Radioisotopes of halogens

	Stable isotopes		Radioactive isotopes				
Halogen	Nuclide	%	Nuclide	$T_{1/2}$ (h)	Decay	%	Max. Energy of β^+ (MeV)
Fluorine	^{19}F	100	^{18}F	1.83	β^+	97	0.635
					EC	3	
Bromine	^{79}Br	50.69	^{75}Br	1.62	β^+	76	1.74
	^{81}Br	49.31			EC	24	
			^{76}Br	16.1	β^+	57	3.98
					EC	43	
Iodine	^{127}I	100	^{123}I	13.2	EC		
					γ	84	0.159 γ
			^{124}I	100.8	$\beta+$	25	2.13
					EC, γ	75	γ
			^{131}I	192.8	β^-	87	0.6 MeV β^-
					γ	82	0.364 γ

Table 10.3 Physicochemical properties of carbon–fluorine bond

Element	Electro negativity	Bond length CH$_2$X, Å	Van der Walls radius (Å)	Bond Energy (kcal mol^{-1})
H	2.1	1.09	1.20	99
F	4.0	1.39	1.35	116
O (OH)	3.5	1.43	1.40	85

group by a fluorine atom is a strategy, widely used in drug development, to alter the biological function. The introduction of a fluorine atom as a substitute to a hydrogen atom, or a hydroxyl group (F for H or OH) in a drug or metabolic substrate, however, does not cause any sterical changes (Table 10.3), but may induce changes in the in vivo behavior of the fluorinated molecule (Park et al. 2001). For example, as a substituent, fluorine can alter the metabolic properties of the parent molecule and prolong drug action by preventing hydroxylation. Also, the higher electro negativity of the fluorine atom may alter the lipophilicity of the compound. A large number of pharmaceuticals contain

fluorine atom and in the last few decades, hundreds of ^{18}F labeled radiotracers have been developed (Kirk and Filler 1996).

The design and synthesis of ^{18}F labeled radiopharmaceuticals of clinical interest (Table 10.4) have been extensively reviewed previously in several publications (Kilbourn 1990; Fowler and Ding 2002; Snyder and Kilbourn 2003; Mason and Mathis 2005; Vallabhajosula 2007). Some of the basic principles of the ^{18}F chemistry are briefly described below.

10.2.1 Production of ^{18}F

Basically there are two kinds of targets used to produce two different chemical forms of fluorine; the water and the gas target. The water target for the production of ^{18}F as nucleophilic fluoride ion (^{18}F$^-$) is based on the nuclear reaction ^{18}O$(p,n)^{18}$F. Several curies of ^{18}F can easily be made in 1–2 h using 10–19 MeV protons using 20–35 µA. Recently, cyclotron targets have been developed to produce 5–10 Ci of

Table 10.4 ^{18}F labeled PET radiopharmaceuticals of clinical interest

Biochemical process	Radiotracer	Mechanism of uptake or localization
Glucose metabolism	[^{18}F]FDG	Substrate for *hexokinase* in glucose metabolism
Bone metabolism	^{18}F-fluoride	Incorporation in the hydroxyapatite crystals in bone
Membrane synthesis	[^{18}F]Fluorocholine	Substrates for *choline kinase* in choline mtabolism
Lipid synthesis	[^{18}F]Fluoroacetate	Substrate for *acetyl-CoA synthetase*
DNA synthesis	[^{18}F]Fluorothymidine (FLT)	Substrates for *thymidine kinase* in DNA synthesis
	[^{18}F]FMAU	
Hypoxia	[^{18}F]FMISO	Intracellular reduction and binding
	[^{18}F]FAZA	
Receptor Binding	[^{18}F]FES	Specific binding to estrogen receptors
Somatostatin Receptors	[^{18}F]Gluco-TOC	Specific binding to somatostatin receptor (SSTR-II)
Dopamine receptors	[^{18}F]Fallypride	Specific binding to D2/D3 receptors
Dopamine transporters	[^{18}F]FP-CIT	Binding to presynaptic dopamine transporters
Benzodizzepine receptors	[^{18}F]Flumazenil	Specific binding to central benzodiazepine receptors to assess neuronal integrity
Amino Acid transport and protein synthesis	[^{18}F]FDOPA	Precursor for the synthesis of dopamine
	[^{18}F]Fluoroethyltyrosine	
	[^{18}F]Fluoro-α-methyltyrosine	Brain amino acid transport
	[^{18}F]FCCA	
Apoptosis	^{18}F-Annexin V,	Specific binding to Phosphatidylserine (PS)
Angiogenesis	^{18}F-FB-E[c(RGDyK)]2	Integrin receptors ($\alpha_V \beta_3$) on endothelial cells
Gene expression	[^{18}F]Oligonucleotide	In vivo hybridization with mRNA
	[^{18}F]FHBG	Substrate to herpes virus *thymidine kinase*

^{18}F as fluoride. While the theoretical SA of ^{18}F is 1,700 Ci/μmole^{-1}, the NCA ^{18}F produced is generally <10 Ci/μmole^{-1}.

The most common nuclear reaction to produce ^{18}F as electrophilic fluorine gas ([^{18}F]F$_2$) is based on the reaction ^{20}Ne(d,α)^{18}F. Following bombardment for 1–2 h, with 8–9 MeV deuterons, <1.0 Ci of [^{18}F]F$_2$ is generated with very low SA (10–20 mCi/μmole^{-1}). A "double shoot" method was developed to produce [^{18}F] fluorine gas based on the reaction ^{18}O(p,n)^{18}F using [^{18}O]O$_2$ gas. Since [^{18}F]F$_2$ is always diluted with carrier (cold) fluorine gas, the SA of electrophilic [^{18}F]fluorine is very low and not optimal for synthesizing high specific activity ^{18}F labeled radiopharmaceuticals.

10.2.1.1 ^{18}F Labeled Precursors

In addition, to the two primary ^{18}F precursors (fluoride and fluorine gas), several secondary precursors have been developed to radiolabel a number of organic molecules (Fig. 10.1). Fluoride ion has to be activated (discussed below) prior to fluorination reactions. Metal fluorides (such as K^{18}F, Cs^{18}F), and tetra-*n*-butyl ammonium fluoride (*n*Bu$_4$N^{18}F) are the most widely
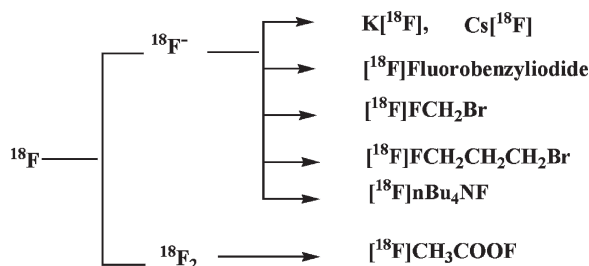
Fig. 10.1 ^{18}F primary and secondary precursors used in nucleophilic and electrophilic fluorination reactions

used ^{18}F precursors in nucleophilic fluorination reactions (Kilbourn 1990), while [^{18}F]CH$_3$COOF (acetyl hypofluorite) is the most common precursor in the electrophilic reactions.

10.2.2 Nucleophilic Fluorination Reactions

The most successful approach to preparing high SA ^{18}F radiotracers is based on nucleophilic fluorination reactions. Synthesis of ^{18}F radiopharmaceuticals using fluoride

ion utilizes two general categories or types of chemical reactions (Kilbourn 1990); (1) aliphatic nucleophilic substitution, also known as substitution nucleophilic bimolecular (S_N2) and (2) aromatic nucleophilic substitution (S_NAr).

In aliphatic S_N2 reactions, the fluoride ion attacks and binds to the carbon atom of the substrate at 180° opposite to a leaving group (Fig. 10.2) which is a weak base such as iodide, bromide, triflate, tosylate, nosylate, mesylate, etc.

S_NAr nucleophilic reactions were designed to incorporate ^{18}F atom directly into the aromatic ring as well as into prosthetic groups containing aromatic ring of a molecule. In these reactions, the leaving group is activated by the electron-withdrawing groups *ortho* and or

para to the leaving group (Fig. 10.2), such as halide, NO_2, and R_3N^+.

The fluoride ion in aqueous solution is very unreactive and has to be activated to increase its solubility and lipophilicity. The [^{18}F]fluoride ion is generally activated by complexing it with a metal or a positively charged ion. When alkali metal halides ($K^{18}F$, $Cs^{18}F$, $Rb^{18}F$) are used, it is essential to have the metal to be coordinated by cryptands and polyaminoethers (such as Kryptofix 2.2.2) so that the relatively free fluoride can show very good reactivity. Instead of alkali metal halides, a variety of tetraalkylammonium [^{18}F]fluorides have also been used. These reactions generally take place in basic or neutral conditions in the presence of an appropriate dipolar aprotic solvent (such as acetonitrile, dimethyl-

1.   Aliphatic Nucleophilic Substitution (S_N2)
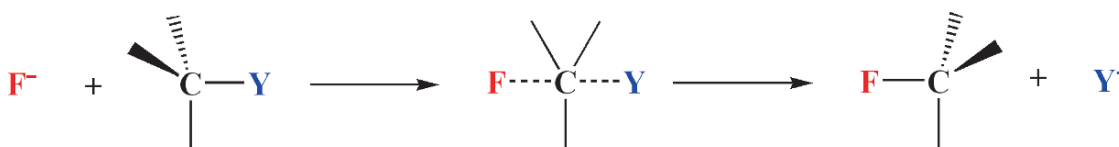
Y = Leaving group such as halide, triflate, tosylate, etc

2.   Aromatic Nucleophilic Substitution (S_NAr)

Y = Leaving group such as halide, NO_2, R_3N

A = Electron withdrawing group such as CHO, COR, COOR, CN, NO_2

3.   Electrophilic fluorination
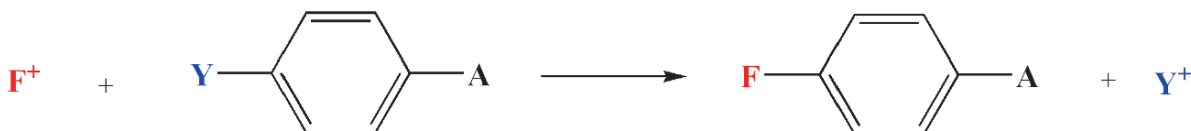
Y = Leaving group such as H, SnR_3, HgR, SiR_3

A = Electrondonating group such as OH, OCH_3, NH_2, SR

Fig. 10.2   Nucleophilic and electrophilic fluorination reactions

sulfoxide (DMSO), and dimethylformamide (DMF)) in which the reactants show good solubility.

Sometimes, the [^{18}F]fluoride ion is first converted to another reactive species, such as alkyl halides (Fig. 10.1), ([^{18}F]fluorobromoethane, [^{18}F]fluorobromo-propane) and benzylic halides (Kilbourn 1990).

10.2.3   Electrophilic Fluorination Reactions

The [^{18}F]F$_2$ precursor has only one of the atoms as ^{18}F while the other atom is stable ^{19}F atom. Therefore the labeling yields are always <50%. Since fluorine is a non-selective electrophile and acts as an oxidizing agent, it is frequently converted to [^{18}F]acetyl hypofluorite, a milder fluorinating agent, much less reactive and with greater solubility than the elemental fluorine. With these precursors, direct electrophilic fluorinations are not necessarily regioselective and the ^{18}F atom can attack any of the C–C double bonds in the molecule. Therefore, these precursors are used only in rare situations where nucleophilic reactions are not appropriate. However, regioselective electrophilic fluorodemetallation reactions were developed to take advantage of the reactive electrophiles in the preparation of ^{18}F PET tracers. Electrophilic fluorination reactions (Fig. 10.2) are facilitated by the presence of electron donating groups (such as OH, OCH$_3$, NH$_2$, etc) and appropriate leaving groups (such as H, SnR$_3$, SiR$_3$ and HgR) in the precursor molecule.

In order to synthesize relatively high SA ^{18}F radiotracers based on electrophilic reactions, a multi-step method was also developed to generate high SA [^{18}F]F$_2$ by using [^{18}F]fluoride ion (Nickels et al. 1984). The reactive ^{18}F$^-$ is first converted to [^{18}F]methyl fluoride and purified by gas chromatography. Subsequently, when methyl fluoride is passed through a discharge chamber (operating at 20–30 kV and 280 μA), small amounts of high SA [^{18}F]F$_2$ can be generated and collected using very small amounts of carrier (<0.2 μmole) fluorine gas.

10.2.4   Organic Precursors for ^{18}F Labeling

The synthesis of ^{18}F labeled PET tracer is a multistep process and it is ideal to introduce ^{18}F in the last step to reduce synthesis time. In the design and development of a PET tracer, the most important step is the synthe-sis of an appropriate precursor of the desired radiotracer, which will facilitate ^{18}F labeling. As discussed above, the ^{18}F reactions require an appropriate leaving group (halide, triflate, triflate, tosylate, H, SnR$_3$, etc), in the precursor molecule.

In addition, the molecules to be labeled may have a number of functional groups (such as OH, COOH, NH$_2$), which may react and interfere with the labeling of radioisotope in a specific position in a molecule. Therefore, in order to facilitate the regioselective labeling of substrates, organic precursors have to be synthesized first with protective groups attached to functional groups. It is very important that the protective groups are very stable during the labeling procedure and can be removed (functional groups deprotected) rapidly and easily under conditions favorable to maintain the stability of the radiolabeled molecule. A number of precursors for ^{18}F labeling have been developed over the years and are now commercially available.

Several examples of precursors with appropriate leaving and protective groups, developed for the synthesis of [^{18}F]FDG, [^{18}F]Fallypride, and [^{18}F]FDOPA are shown in Fig. 10.3. In the case of FDG, the precursor mannose triflate was developed, in which the four hydroxyl groups of deoxyglucose are protected by adding acetate (Ac) groups. Also, in order to facilitate ^{18}F labeling, a leaving group, trifluoromethane sulfonate (TFMS) is added to the carbon in the second position. S$_N$Ar nucleophilic reactions were designed to incorporate the ^{18}F atom directly into the aromatic ring as well as into the prosthetic groups containing the aromatic ring of a molecule. In these reactions, the leaving group is activated by the electron-withdrawing groups ortho and or para to the leaving group. The precursors for the synthesis of ^{18}F-altanserin (Tan et al. 1999) and [^{18}F]MPPF (Le Bars et al. 1998) have been designed to have a leaving nitro group (NO$_2$) situated para to a carbonyl group, which activates the leaving group to be substituted by the reactive [^{18}F]fluoride ion.

In the preparation of certain radiotracers, the ^{18}F labeled alkyl halides are prepared first using aliphatic nucleophilic reaction and the [^{18}F]alkyl halide (also known as "synthon") is subsequently used to prepare the radiotracer of interest (Block et al. 1987). For example, [^{18}F]fluorobromomethane is reacted with *N,N*-dimethylamino-ethanol (precursor) to synthesize [^{18}F]fluoromethylcholine (FCH) (DeGrado et al. 2001; Iwata et al. 2002). Similarly, 1-[^{18}]fluoro-3-bromopropane is used to synthesize [^{18}F]β-CFT-FP (Kamarainen et al. 2000).
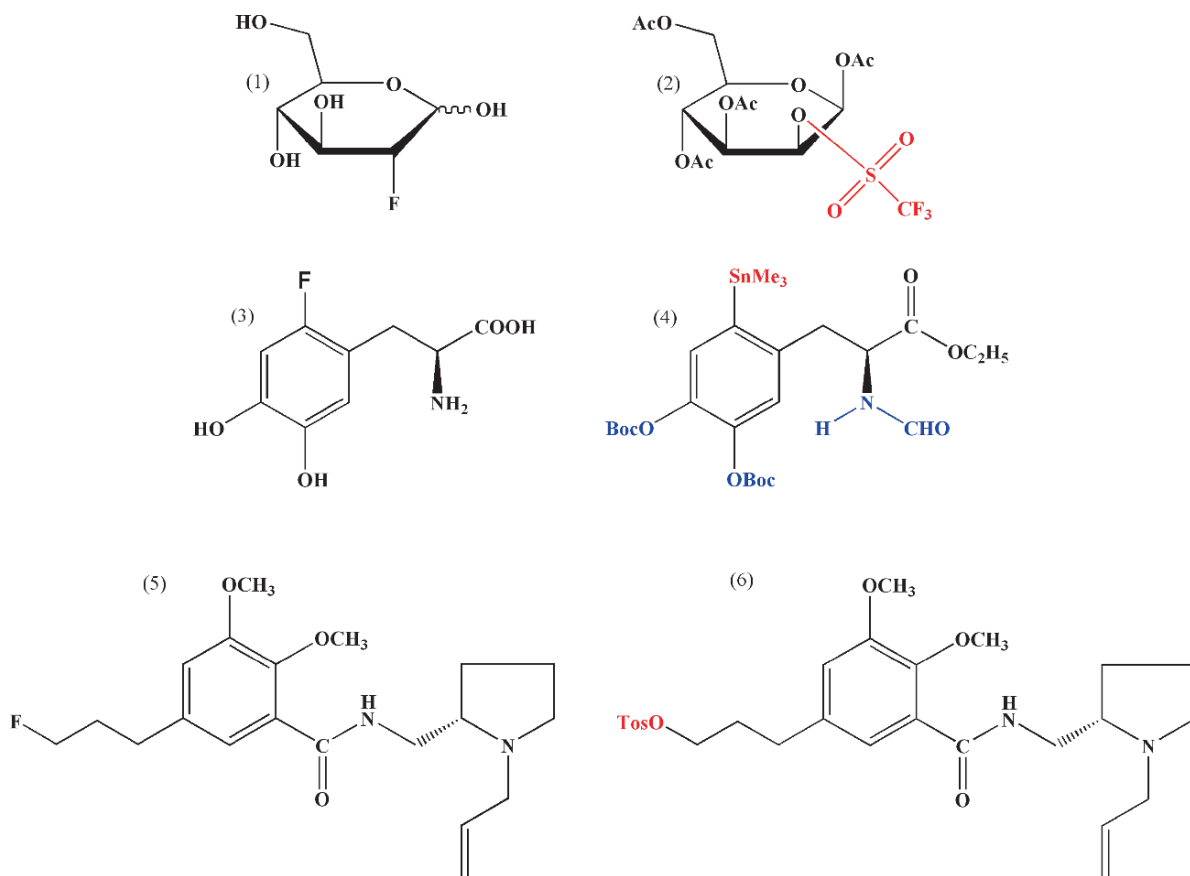
Fig. 10.3 Organic precursors for the synthesis of 18F labeled radiopharmaceuticals: For FDG synthesis, glucose (1) is converted to mannose triflate (2). For FDOPA synthesis, L-DOPA (3) is converted to trimethylstannyl L-DOPA (4). For these two precursors, the functional groups (OH, COOH and NH$_2$) are protected to prevent fluorination. For the synthesis of fallypride (5), the precursor is simply a tosyl-fallipride analog (6)

10.2.5 Radiotracers Based on Nucleophilic Reactions

A number of radiotracers of clinical interest (Table 10.4) such as 2-deoxy-2-[^{18}F]fluoro-D-glucose (FDG), [^{18}F]3′-deoxy-3′-fluorothymidne (FLT), 9-(4-[^{18}F]fluoro-3-hydroxymethylbutyl)-guanine (FHBG), 1-amino-3-[^{18}F] fluorocyclo-butane-1-carboxylic acid (FCBCA), [^{18}F] Fallypride, and 16α-[^{18}F]Fluoroestradiol can all be prepared using commercially available precursors (Stocklin 1998; Varagnolo et al. 2000; Shiue and Welch 2004; Couturier et al. 2004; Vallabhajosula 2007).

10.2.5.1 Synthesis of [^{18}F]FDG

The original synthesis developed by the Brookhaven group in 1976 was based on electrophilic reaction (Ido

et al. 1978). Most of the current synthesis procedures use a modification of a nucleophilic procedure developed in 1986 (Hamacher et al. 1986). The synthesis of FDG is the most established procedure, to date, and PET centers all over the world use automated synthesis modules for the production and distribution of FDG. The synthesis of FDG (Fig. 10.4) involves the following basic steps:

• Following production of ^{18}F in the cyclotron, the target water ([^{18}O]H$_2$O), containing several curies of [^{18}F]fluoride ion, is trapped on a small column of anion exchange resin (Waters Accel plus QMA cartridge) and then collected in a vial for future use.

• The [^{18}F]fluoride ion is eluted into a reaction vial using a solution of aqueous base, potassium carbonate (K$_2$CO$_3$), and Kryptofix 222 in acetonitrile. Some procedures substitute Kryptofix with either
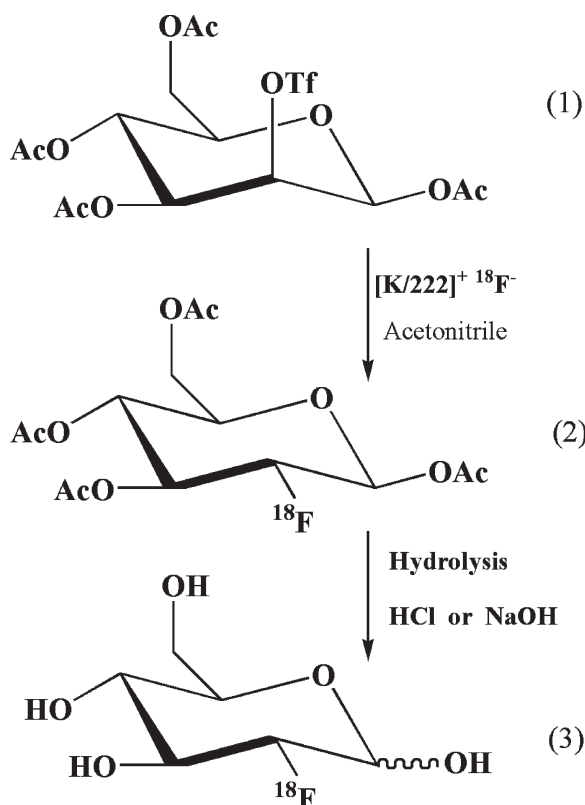
Fig. 10.4 Synthesis of [¹⁸F]fluoro-2-deoxy-ᴅ-glucose or FDG (3). Following evaporation and drying, the K[¹⁸F] and kryptofix complex, are incubated at 80°C with the precursor mannose triflate (1) in acetonitrile. Subsequently, FDG (3) is obtained following acid or base hydrolysis of the fluorinated intermediate (2)

tetramethyl ammonium carbonate or tetrabutyl ammonium bi-carbonate or hydroxide.

- The residual water is removed by repeated azeotropic distillations using anhydrous acetonitrile and a stream of nitrogen.
- The organic precursor, mannose triflate (10–25 mg) in acetonitrile, is added to the dried fluoride ion and the mixture is heated at 80–90°C for 5 min.
- In order to generate FDG from [¹⁸F]acetyl protected FDG (intermediate complex), hydrolysis of acetyl groups (deprotection) is performed using an acidic (HCl) solution by heating the mixture at 130°C for 10–15 min. In recent techniques, the acetylated FDG intermediate is loaded on a solid support (C₁₈ Sep-Pak® cartridge) and hydrolysis is performed under basic conditions at room temperature using KOH or NaOH solution.

- The purification procedures involve passing the intermediate mixtures or the final FDG solution through the C₁₈ Sep-Pak and alumina cartridges and washing them with water to eliminate Kryptofix and organic solvent contamination.
- The purified FDG is finally obtained from the cartridge by eluting it with physiological saline, sterilized it by passing it through a 0.2 μ membrane filter and collecting it in a sterile vial.
- Almost all of the automated FDG synthesis modules provide FDG with a radiochemical yield of 40–70% and a radiochemical purity of >90% in 30–45 min of total synthesis time.

10.2.5.2   FLT Synthesis

The synthesis of FLT was first reported in 1991, but the low radiochemical yield prevented routine clinical use of the compound. Subsequent improvements in synthesis and radiochemical yields helped start clinical evaluations of FLT (Grierson and Shields 2000). Since then a number of precursors and different labeling protocols have been evaluated to improve labeling yields and radiochemical purity (Martin et al. 2002; Oh et al. 2003, 2004; Suehiro et al. 2007). The most reliable radiosynthesis of [¹⁸F]FLT involves a simple three step procedure based on a protected nosylate precursor known as 3-*N*-Boc-5′-*O*-dimethoxytrityl-3′-*O*-nosyl-thymidine (Fig. 10.5). Fluorination reactions involve displacement of a 3-*O*-nosyl group with [¹⁸F]fluoride and yield an ¹⁸F labeled protected intermediate, which generates [¹⁸F]FLT following hydrolysis. The final radiochemical yields of FLT vary (10–40%) and depend on the amount of mass, precursor, and kryptofix used. Increased amounts of precursor may result in higher labeling yields, but may also increase the chemical impurities in the final product. It has also been shown that the kryptofix plays a very important role and that by carefully adjusting the precursor/kryptofix molar ratio, higher labeling yields with minimal chemical impurities can be obtained (Suehiro et al. 2007). HPLC purification is essential to reduce chemical impurities (Fig. 10.6). A fully automated method for the synthesis of FLT with a 50% radioche-mical yield, by modifying a commercial FDG synthesizer and its disposable fluid pathway has also been reported (Oh et al. 2004).
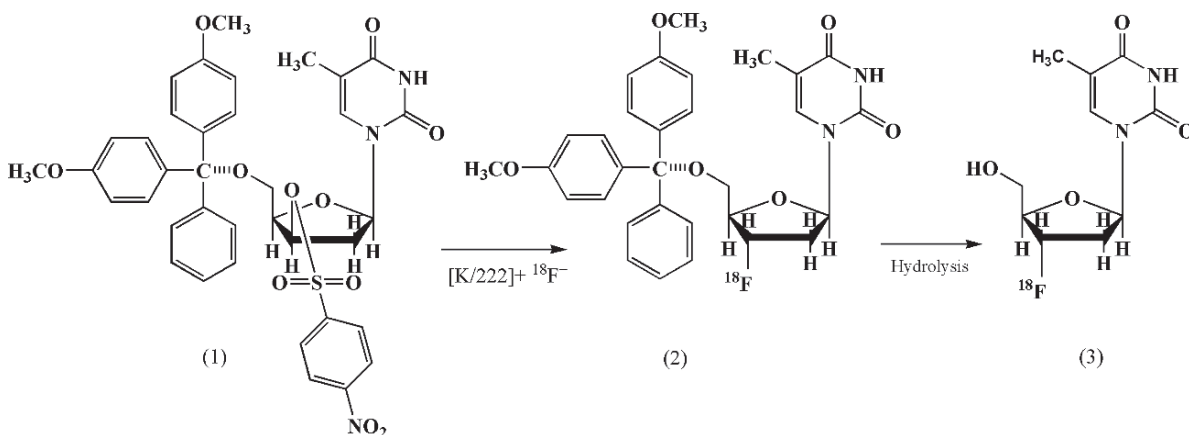
Fig. 10.5 Synthesis of 3′-deoxy-[¹⁸F]fluorothymidine or FLT (3). The protected nosylate precursor, 3-*N*-Boc-5′-*O*-dimethoxytrityl-3′-*O*-nosyl-thymidine (1). The fluorinated intermediate (2) upon hydrolysis will produce FLT, which subsequently is purified using HPLC
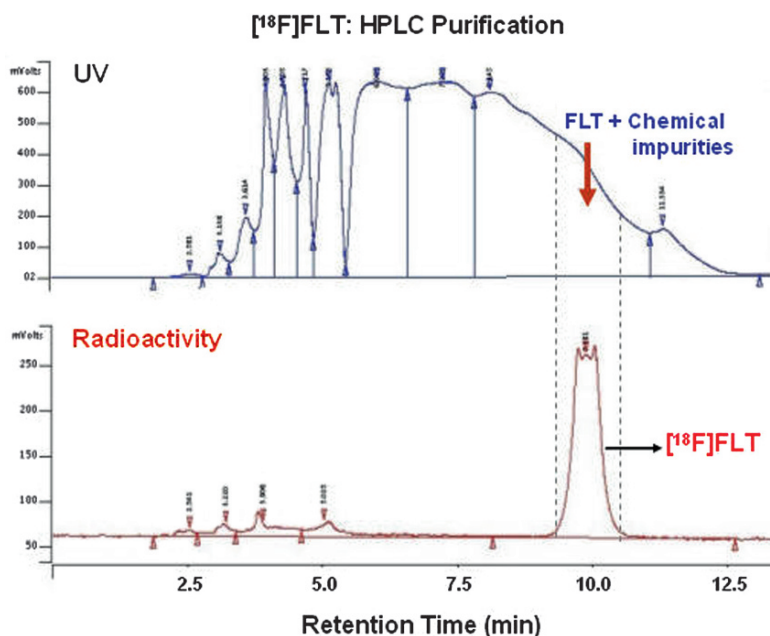
Fig. 10.6 Purification of FLT using HPLC: Following fluorination and hydrolysis, several radiochemical and chemical impurities are generated as seen by UV absorbance (*top*). The fraction of eluent representing FLT radioactive peak (*bottom*) is collected

10.2.5.3 FMISO Synthesis

The first synthesis of fluoronitroimidazoles was reported in 1986 (Jerabeck et al. 1986). Subsequently, a two-step synthesis of FMISO was developed with a high yield (40% at EOB) and purity with a SA of 37 TBq mmol⁻¹ (Grierson et al. 1989). The first step involves the synthesis of fluoroalkylating agent [¹⁸F]epifluorohydrin, which subsequently reacts with 2-nitroimidazole to yield FMISO. HPLC purification is needed to obtain high radiochemical purity. Further modifications have been reported with increasing labeling yields (Patt et al. 1999; Kamarainen et al. 2004). The most practical method is based on the nucleophilic substitution of the tolysate leaving group by [¹⁸F]fluoride on the tetrahydropyranyl-protected precursor 1-(2′-nitro-1′-imidazolyl)-2-*O*-tetrahydropyranyl-3-*O*-toluenesulfonylpropanediol (NITTP), followed by the hydrolysis of the protecting

group (Fig. 10.7). An automated synthesis of [^{18}F] FMISO by this method using either HPLC or Sep-Paks for the purification of the radiotracer was also recently reported (Tang et al. 2005). The radiochemical yield obtained when using NITTP was found to be ≤40% and reproducible, with a radiochemical purity ≥97%, and a SA of about 34 TBq mmol^{-1}. Further, the whole synthesis time was <50 min.

10.2.5.4 FES Synthesis

The first synthesis of FES (Kiesewetter et al. 1984) was based on the nucleophilic displacement of the aliphatic triflate of 3,16β-bis (trifluoromethene-sulfonyloxy)-

estrone using tetrabutylammonium [^{18}F]fluoride, followed by hydrolysis and ketone reduction. HPLC purification provided a 30% radiochemical yield of FES in about 90 min. Subsequently a new procedure was developed in which the nucleophilic substitution of [^{19}F]fluoride led directly to [^{19}F]FES using 3-O-Methoxy-methyl-16, 17-O-sulfuryl-16-epiestriol (MMSE) as a precursor (Tewson 1983). This procedure worked well with non-radioactive fluoride, with carrier added [^{18}F] fluoride. The first successful preparation with [^{18}F]fluoride with further modifications, however, was published, subsequently (Lim et al. 1996). A one-pot synthesis of FES (Fig. 10.8) based on the MMSE precursor was also developed to provide radiochemical yields of 30–45% with a SA of about 37 GBq μmol^{-1}
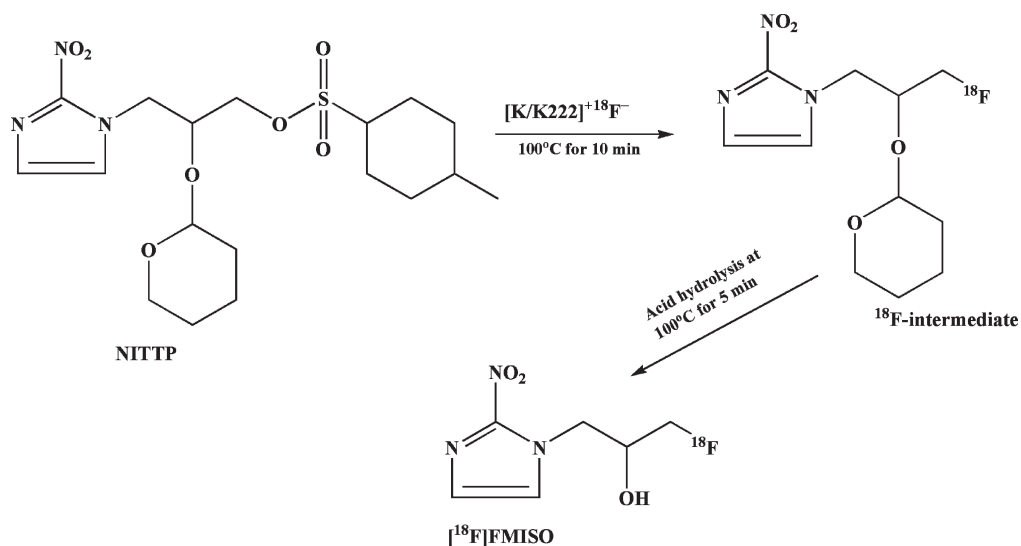
Fig. 10.7 Synthesis of [^{18}F]Fluoromisonidazole (FMISO) (3): Following fluorination reaction with the precursor, NITTP (1), the intermediate (2) is hydrolyzed to yield the final drug product
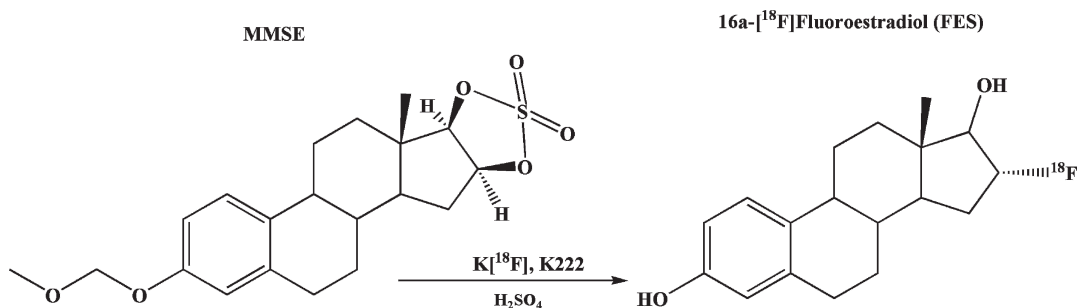
Fig. 10.8 Synthesis of 16α-[^{18}F]Fluoroestradiol (FES) (3): The precursor is 3-O-Methoxymethyl-16, 17-O-sulfuryl-16-epiestriol (MMSE) (1). The fluorinated intermediate (2) after hydrolysis will produce FES

(1.0 Ci μmol⁻¹) in 60–120 min. Subsequently, an automated module for the synthesis of FES was developed using the same method to give about 50% radiochemical yields in 50 min (Romer et al. 1999).

10.2.5.5 FCH Synthesis

In the1990s, Hara and his colleagues developed the synthesis of both [11C[choline (CH) and the ^{18}F labeled choline analog, 2-[^{18}F]fluoroethylcholine (FEC) (Hara et al. 2002). Subsequently, on the basis of structural similarity, it was speculated that [^{18}F]fluoromethylated choline (FCH) would mimic choline transport and metabolism more closely than FEC (DeGrado et al. 2001) and the first synthesis of FCH based on nucleophilic fluorination method was reported. The ^{18}F precursor, [^{18}F]fluorobromomethane (FBM) was first prepared using [^{18}F]fluoride and dibromomethane (DBM). Subsequently, FBM was reacted with dimethylethanolamine to yield FCH with radiochemical purity greater than 98% and an uncorrected radiochemical yield of 20–40%. This method was modified to automate the synthesis using a commercial FDG synthesis module (Tadino et al. 2004). An automated method of FCH synthesis was also achieved by the reaction of [^{18}F]fluoromethyl triflate (FMT) with dimethylethanolamine on a Sep-Pak column (Iwata et al. 2002). The total time required for obtaining the finished chemical was 30 min, while the radiochemical yield (decay corrected) was 80% with a radiochemical and chemical purity of >98%. The synthesis procedure using both FBM and FMT is shown in Fig. 10.9.

10.2.6 Radiotracers Based on Electrophilic Reaction

10.2.6.1 Synthesis of 6-[^{18}F]fluoro-L-DOPA (FDOPA)

The first ^{18}F labeled analog of L-DOPA was 5-[^{18}F] Fluoro-DOPA (Firnau et al. 1973). The metabolism of this tracer, however, was accelerated because the fluorine atom was close to the hydroxyl groups of FDOPA. Consequently, 6-[^{18}F]Fluoro-L-DOPA was developed and the first FDOPA-PET brain imaging was performed to visualize the dopaminergic neurons in basal ganglia (Firnau et al. 1984). A number of methods have been developed to synthesize FDOPA (Adam et al. 1986; Luxen et al. 1990; Namavari et al. 1992; Dolle et al. 1998). The organic precursor is an aryl substituted trialkyl tin derivative in which the trimethylstannyl group (Sn(CH$_3$)$_3$) is replaced by the ^{18}F atom. The FDOPA precursor, also known as TriBoc-L-Dopa ethyl ester was designed to have alkyl (tertiary butyl and ethyl) groups attached to the carboxyl groups for protection during the fluorination reaction. The electrophilic radiofluorination by destannylation of FDOPA precursor, has emerged as the preparation method of choice and has been used by many groups, employing a custom-built apparatus or a commercial PC-controlled automated synthesis module. Fluorination of the precursor (Fig. 10.10) in freon solvent can be performed using [^{18}F]F$_2$ gas directly or acetylhypofluorite reagent, [^{18}F]CH$_3$COOF. Finally, following acidic removal (deprotection) of the protective groups using hydrogen
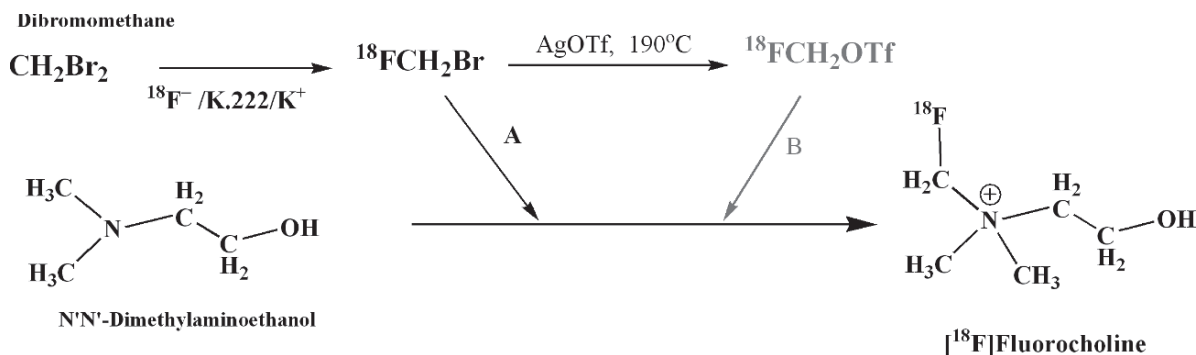
Fig. 10.9 Synthesis of [^{18}F]fluorocholine (FCH) (3): Dibromomethane (1) is first fluorinated to generate fluorobromomethane (FBR) (2) which reacts with the precursor, dimethylethanolamine (4) to produce FCH. In a second method, FBR can also be converted to fluoromethyltriflate (3) which would react more efficiently with the precursor (4) to produce FCH
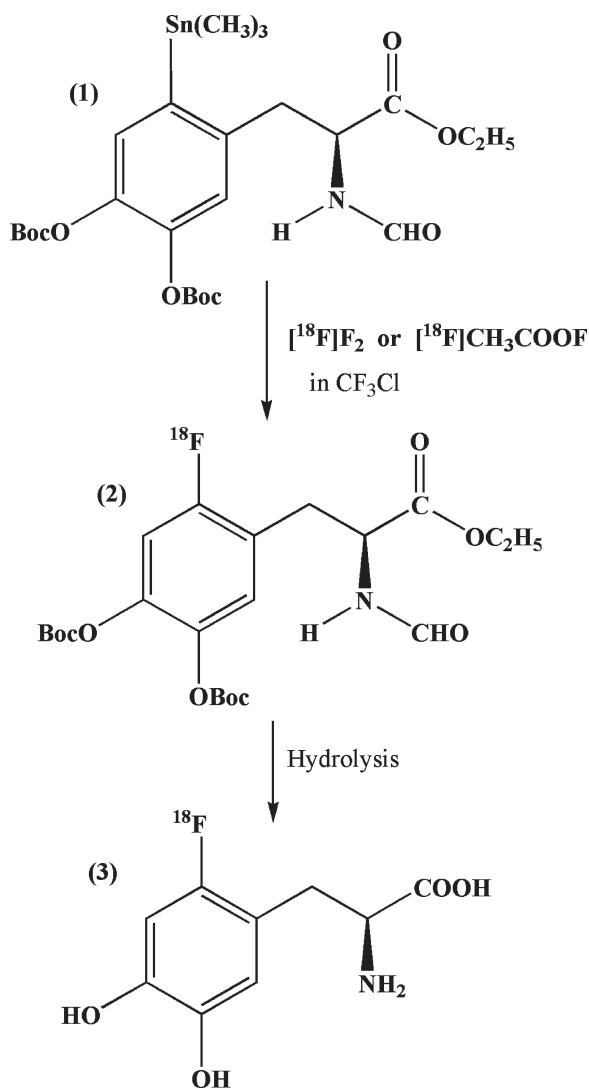
Fig. 10.10 Synthesis of 6-[^{18}F]fluoro-L-FDOPA (FDOPA) (3): The precursor, an aryl substituted trialkyl tin derivative, known as Triboc-L-Dopa ehtyl ester (1). The fluorinated intermediate (2) upon hydrolysis will produce FDOPA

bromide (HBr), [^{18}F]FDOPA can be generated. HPLC purification is required to achieve high chemical and radiochemical purity. The final decay corrected yields are typically 20–30% and the SA is about 37 GBq μmol^{-1} (1.0 Ci μmol^{-1}) at the EOS. Nucleophilic methods using the [^{18}F]fluoride ion have been developed and may have the potential to provide a higher yield and a higher SA.

Similarly, the synthesis of [^{18}F]fluoro-meta-tyrosine (FMT) (VanBrocklin et al. 2004) and [^{18}F]β-CFT (Happaranta et al. 1996) have been developed using

fluorodemetallation reactions. In general, electrophilic fluorination reactions produce low SA (<30 mCi μmole^{-1}) PET radiopharmaceuticals.

10.3 Synthesis of Radioiodinated Radiopharmaceuticals

Among the radioisotopes of iodine, ^{123}I, ^{124}I and ^{131}I have physical characteristics suitable for developing molecular imaging radiopharmaceuticals for both PET and SPECT (Table 10.2). In the last two decades, ^{123}I has been the most widely used radioiodine for developing receptor binding radiopharmaceuticals for SPECT. Since ^{131}I decays by β$^-$ emission, it is predominantly useful for radionuclide therapy. However, the abundant 364 KeV γ emissions and relatively longer half-life (8.04 days) of ^{131}I do offer certain advantages in developing certain radiotracers with relatively longer biological clearance, such as monoclonal antibodies. However, the β$^+$ emitter ^{124}I with a moderate half-life (4.2 days) may be more appropriate for developing radioiodinated antibodies as imaging probes based on PET. Several important and clinically useful radioiodinated molecular imaging agents are summarized in Table 10.5.

10.3.1 Production of ^{123}I and ^{124}I

Depending on the target material and the proton energy used in the cyclotron, several nuclear reactions can be utilized to produce ^{123}I, as shown below.

Currently the best source of ^{123}I, having the least contamination with other radioiodides, is the proton bombardment of highly enriched ^{124}Xe. Based on this method, high purity, no-carrier added (nca) ^{123}I can be

$$^{124}\text{Te}(p,2n)^{123}\text{I}$$
$$^{124}\text{Xe}(p,2p)^{123}\text{I}$$
$$^{124}\text{Xe}(p,pn)^{123}\text{Xe}_{(T\frac{1}{2}=2.08\,\text{h})} \rightarrow ^{123}\text{I}$$
$$^{124}\text{Xe}(p,2n)^{123}\text{Cs}_{(T\frac{1}{2}=5.9\,\text{min})} \rightarrow ^{123}\text{Xe}_{(T\frac{1}{2}=2.08\,\text{h})} \rightarrow ^{123}\text{I}$$
$$^{127}\text{I}(p,5n)^{123}\text{Xe}_{(T\frac{1}{2}=2.08\,\text{h})} \rightarrow ^{123}\text{I}$$
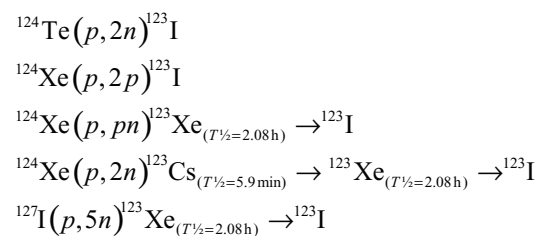
Table 10.5 ^{123}I labeled PET Radiopharmaceuticals of Clinical Interest

Radioiodinated compound	Biological process
[123]I-*ortho*-iodohippurate (OIH)	Renal function
^{123}I-IBZM	Dopamine D_2 receptors
[123]I-Iomezenil	Central benzodiazepine receptors
[123]I-β-CIT	Dopamine transporters
^{123}I-BMIPP	Myocardial free fatty acid metabolism
[123]I-Iodo-α-methyltyrosine	Brain amino acid transport
[123]I or [124]I-MIBG	Adrenergic neuroreceptors
[124]I-FIAU	Thymidine synthesis

produced with high SA (8,695 GBq mmol^{-1}), suitable for preparing receptor binding radiopharmaceuticals (Eersels et al. 2005). The reaction, (p,5n) using natural iodine target also produces high SA ^{123}I, but requires 69–70 MeV protons.

The most common method used for [124]I production is based on the reaction [124]Te(p,n)[124]I using enriched [124]Te and low energy <15 MeV protons. (Sheh et al. 2000). The solid target material consists of a solid solution matrix containing aluminum oxide and enriched [124]Te oxide. [[124]I]iodide is recovered from the target using dry distillation. The volatile radioiodine is trapped on a thin pyrex glass tube coated with a small amount of sodium hydroxide. The SA of [124]I is typically around 150 mCi/μg^{-1}.

10.3.2   *Chemistry of Iodine*

Iodine (I$_2$) sublimes at atmospheric pressure and temperature resulting in a blue–violet gas with an irritating odor. It occurs in nature mostly in the form of salts or iodides of sodium and potassium. Unlike fluorine, iodine can exist in several oxidation states (Table 10.1). Several iodine oxides (such as I_2O_4, I_4O_9, I_2O_7, I_2O_5) do exist in nature but readily decompose to iodine and oxygen at high temperatures. Iodine dissolves readily in nonpolarsolvents, such as chloroform and carbon tetrachloride, but is only slightly soluble in water.

The free molecular iodine (I$_2$) has the structure of I$^+$–I$^-$ in aqueous solution. The electrophilic species (I$^+$), however, does not exist as a free species, but forms complexes with nucleophilic entities, such as water or pyridine. The reactions with water can be written as follows:

$$I_2 + H_2O = H_2OI^+ + I^- \qquad (10.1)$$

$$I_2 + OH^- = HOI^- + I^- \qquad (10.2)$$

$$3I_2 + 6OH^- = 5I^- + IO_3^- + 3H_2O \qquad (10.3)$$
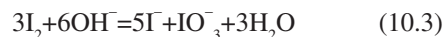
The hydrated iodonium ion H_2OI^+ and the hypoiodous acid HOI, are believed to be highly reactive electrophilic species. In an iodination reaction, iodination occurs by (a) electrophilic substitution of a hydrogen ion by an iodonium ion in a molecule of interest or (b) nucleophilic substitution (isotope exchange) where a radioactive iodine atom is exchanged with a stable iodine atom that is already present in the molecule. Other cationic species, such as I_2Cl^+, ICl_2^+, $I_2B_r^+$, may exist under special conditions and may also behave like powerful electrophiles.

10.3.2.1   Radioiodination

The advantages and disadvantages of different radioiodination techniques were recently reviewed (Kabalka and Mereddy 2004; Eersels et al. 2005). In general, the aliphatic carbon–iodine bond is relatively weak and, as a result, in vivo deiodination occurs either by nucleophilic substitution or β-elimination. In the preparation of radioiodinated compounds, the radioiodine is preferentially attached to a carbon atom, in a vinylic or aromatic moiety in which the carbon–iodine bond strength is high. Therefore, the radioiodination is often implemented by electrophilic or nucleophilic aromatic substitution.

Electrophilic labeling reactions can often be performed fast and under mild reaction conditions. The electrophilic species (HO*I, H$_2$O*I) generated from radioiodide and the oxidant react directly with the aromatic moiety of the compound to be labeled (Fig. 10.11). The most frequently used oxidizing agents are peracetic acid and the *N*-chloro compounds, such as chloramine-T, iodogen, and succinimides. The *N*-chloro compounds are by far the most popular oxidants; however, their relatively strong oxidizing properties often induce by-products. In order to limit these oxidative side reactions, chloramine-T is immobilized on spherical polystyrene particles (iodobeads1) while iodogen, which contains four functional chlorine atoms, is coated as a thin layer on the walls of a reaction vessel. Of the two immobilized oxidants,

Electrophilic Radioiodination

$$*I^+$$
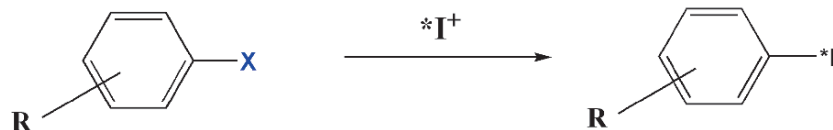
where X = H, HgCl, Tl(OCOCF$_3$)$_2$, Sn(CH$_3$)$_3$, Si(CH$_3$)$_3$

Nucleophilic Radioiodination

$$+ \quad Cu^+ \quad \xrightarrow{\ *I^-\ } \quad \cdots \quad *I \quad + \quad X^-$$
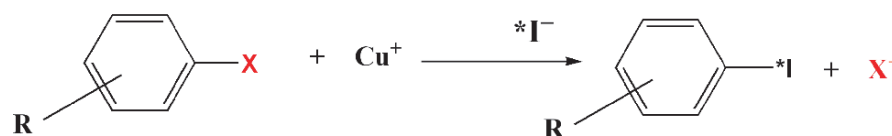
where X = I, Br

which are mostly used for protein-labeling, iodogen is the best to prevent loss of immunoreactivity (Richardson et al. 1986). For the labeling of small organic molecules, peracetic acid is often preferred due to its mild oxidizing properties. Protein molecules labeled with radioiodine have long been used in nuclear medicine and basic biomedical research. The aromatic amino acids tyrosine and histidine are the sites of iodination in protein molecules (Greenwood et al. 1963; Bolton and Hunter 1973). With tyrosine, substitution of a hydrogen ion with the reactive iodonium ion occurs *ortho-* to the phenolic hydroxyl group. With histidine, substitution occurs at the second position of the imidazole ring. Electrophilic substitutions can often be carried out on a nonderivatized substrate. However, in case of low reactivity or lack of regioselectivity, radioiodo destannylation is the method of choice.

The method of choice in nucleophilic radioiodination is the well-established Cu(I)-catalysed halogen–halogen exchange reaction in an acidic, aqueous medium (Fig. 10.11). The exchange reaction can be either isotopic (*I/I) or nonisotopic (*I/Br), which specifically enables the synthesis of a high SA radiopharmaceuticals (Mertens and Gysemans 1991). A nucleophilic exchange can be successfully applied on activated (presence of electron-deficient substituents, e.g., carbonyl group) or nonactivated (e.g., alkyl group) aromatic compounds. However, in organic media,

electron-donating substituents are also well-tolerated. The purity, labeling yield, and SA can be controlled by carefully optimizing the concentration of copper and the precursor.

Several examples of radioiodination techniques commonly used in the preparation of radiopharmaceuticals are briefly discussed below.

Preparation of ^{123}I-Annexin V

Annexin V (AnxV) is one of the numerous members of the calcium- and phospholipids-binding superfamily of annexin proteins. The mature AnxV molecule consists of 319 amino acids with a total molecular weight of 35.8 kDa. The recombinant human annexin V (rh-AnxV) can be labeled with ^{123}I by the direct radioiodination method using 1,3,4,6-tetrachloro-3,6-diphenylglycoluril (Iodo-Gen) (Lahorte et al. 2001). Clinical grade ^{123}I-rh-AnxV is labeled using a modified iodogen method (Lahorte et al. 2001) in which 250 µg ml^{-1} of freshly prepared iodogen in 2 ml was evaporated under a gentle stream of nitrogen in a 10-ml reaction vial. The vial washed twice with 2 ml 0.05 M phosphate-buffered saline (PBS) before use. Then, 1 mg of rh-AnxV in 0.05 M PBS (pH 7.4) was mixed with 370 MBq (10 mCi) of ^{123}I in 0.5 M PBS (volume twice that of ^{123}I) and incubated with gentle stirring at room temperature for 20 min. The reaction was
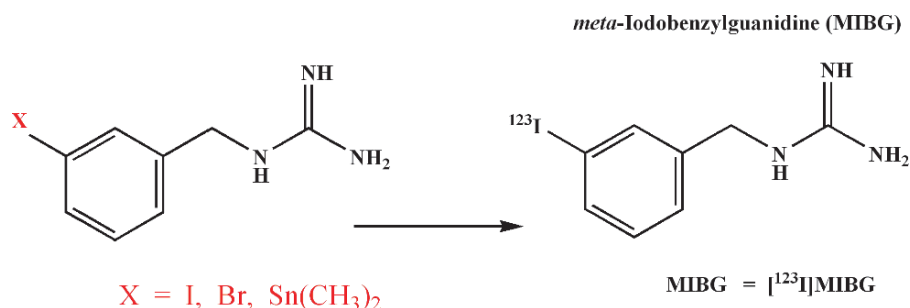
Fig. 10.12   Synthesis of [^{123}I]meta-iodobenzylguanidine (MIBG): Radioiodination can be performed based on isotopic exchange using cold MIBG precursor, or based on nonisotopic Cu(I) assisted iododebromination and iododestannylation methods

stopped by purification on a PD10(G25) Sephadex column using 0.25% human serum albumin PBS as eluent. The final product filtered through a 0.22-μm sterile filter. The radiochemical yield was 87.0 ± 6.5% with >98% radiochemical purity and a final SA of 13,400 MBq μmol^{-1} (362 mCi/μmol^{-1}).

$^{123/124}$I-MIBG

Meta-iodobenzylguanidine (MIBG) is a norepinephrine (NE) analog that contains a benzyl and a guanidine group and structurally resembles NE. The synthesis of [^{131}I]MIBG was first developed based on the radioiodide exchange reaction (Weiland et al. 1986). The SA of ^{131}I-MIBG based on this method is typically <400 MBq/μmole^{-1}. MIBG can also be labeled with ^{123}I and ^{124}I using the same procedure, but an improved method of preparing no-carrier added ^{123}I-MIBG was subsequently developed based on non-isotopic Cu(I) assisted iododebromination and iododestannylation methods (Fig. 10.12) (Samnick et al. 1999).

A mixture of ^{123}I sodium iodide (10–15 mCi in 10–20 μL in 0.01N NaOH) solution and 5 μL of Na$_2$S$_2$O$_5$ (4 mg/ml^{-1}) is evaporated to dryness by passing a stream of N$_2$ through a reaction vessel at 100°C. Subsequently, 50 μL of precursor, *meta*-bromobenzyl-guanidine (MBBG) (2.5 mg/ml^{-1} acetic acid) and 5 μL of aqueous Cu(I) sulfate (0.1 M) is added to dry ^{123}I and the mixture is heated for 10 min at 180°C in a heating module. At the end, the mixture is cooled, and the residue dissolved in 150 μL of ethyl alcohol and ^{123}I-MIBG is finally purified by isocratic reverse phase HPLC.

Alternatively, ^{123}I-MIBG can be prepared by using the tributyltin precursor (MTBBG). A mixture of ^{123}I sodium iodide (10–15 mCi in 10–20 μL in 0.01N NaOH) solution, 20 μL of HCl (0.2 M), and 50 μL H$_2$O$_2$ solution (5% w/v) or 20 μL of chloramine-T solution (1 mg ml^{-1}) are added to a septum sealed vial containing MTBBG (50 μg 50 μL^{-1} ethanol). After 15 min incubation at RT, 5 μL aqueous Na$_2$S$_2$O$_5$ (4 mg ml^{-1}) is added and then neutralized with sodium bicarbonate. ^{123}I-MIBG is finally purified by reverse phase HPLC. The SA is typically >6 TBq μmole^{-1}.

References

Adam MJ, Ruth TJ, Grierson JR, et al (1986) Routine synthesis of L-[^{18}F]6-fluorodopa with fluorine-18 acetyl hypofluorite. J Nucl Med 27:1462–1466

Ahmed N, Langlois R, Rodrigue S, et al (2007) Automated synthesis of 11β-methoxy-4–16α-[16α-^{18}F]difluoroestradiol (4F-M[^{18}F]FES) for estrogen receptor imaging by positron emission tomography. Nucl Med Biol 34:459–464

Block D, Coenen HH, Stocklin G, et al (1987) The NCA nucleophilic ^{18}F-fluorination of I,N-disubstituted alkanes as fluoralkylation agents. J Label Compd Radiopharm 24:1029–1042

Bolton AE, Hunter WM (1973) The labeling of proteins to high specific radioactivities by conjugation to a ^{125}I containing acylating agent. Biochem J 133:529–538

Coenen HH, Dutschka K, Muller SP, et al (1995) NCA radiosynthesis of of [^{123}I, ^{124}I]beta-CIT, plasma analysis, and pharmacokinetic studies with SPECT and PET. Nucl Med Biol 22:977–984

Couturier O, Luxen A, Chatal J-F, et al (2004) Fluorinated tracers for imaging cancer with positron emission tomography. Eur J Nucl Med Mol Imaging 31:1182–1206

DeGrado TR, Baldwin SW, Wang S, et al (2001) Synthesis and evaluation of [^{18}F]-labeled choline analogs as oncologic PET tracers. J Nucl Med 42:1805–1814

Dolle F, Demphel S, Hinnen F, et al (1998) 6-[18F]Fluoro-L-DOPA by radiofluoro-destannylation: A short and simple synthesis of a new labeling precursor. J Label Compd Radiopharm 41:105–114

Eersels JLH, Travis MJ, Herscheid JDM (2005) Manufacturing I-123-labeled radiopharmaceuticals: Pitfalls and solutions. J Label Compd Radiopharm 48:241–257

Firnau G, Nahmias C, Garnett ES (1973) The preparation of [18F]5-fluoro-DOPA with reactor produced fluorine-18. Int J Appl Radiat Isot 24:182–184

Firnau G, Chiakal R, Garnett ES (1984) Aromatic radiofluorination with 18F fluorine gas: 6-[18F]fluoro-L-dopa. J Nucl Med 25:1228–1233

Fowler JS, Ding Y-S (2002) Chemistry. In: Wahl RL, Buchanan JW (eds) Principles and practice of positron emission tomography. Lippincott Williams & Wilkins, Philadelphia

Glaser M, Brown DJ, Law MP, et al (2001) Preparation of no carrier added [124I]-A14-iodoinsulin as a radiotracer for positron emission tomography. J Label Compd Radiopharm 44:465–480

Goodman MM, Kung M-P, Kabalka GW, et al (1994) Synthesis and characterization of radioiodinated N-(3-iodopropen-1-yl)-213-carbomethoxy-313-(4-chlorophenyl)tropanes: potential dopamine reuptake site imaging agents. J Med Chem 37:1535–1542

Greenwood FC, Hunter WM, Glover JS (1963) The preparation of 131I-labeled human growth hormone of high specific radioactivity. Biochem J 89:114–123

Grierson JR, Shields AF (2000) Radiosynthesis of 3′-Deoxy-3′-[18F]fluoro thymidine: [18F]FLT for imaging of cellular proliferation in vivo. Nucl Med Biol 27:143–156

Grierson JR, Link JM, Mathis CA, et al (1989) A radiosynthesis of fluorine-18 fluoromisonidazole. J Nucl Med 30:343–350

Hamacher K et al (1986) Efficient stereospecific synthesis of no-carrieradded 2-[18F]fluoro-2-deoxy-D-glucose using amino-polyether supported nucleophilic substitution. J Nucl Med 27:235–238

Happaranta M, Bergman J, Laakso A, et al (1996) [18F]CFT ([18F]WIN,35428), a new radioligand to study the dopamine transporter with PET. Biodistribution in rats. Synapse 23:321–327

Hara T, Kosaka N, Kishi H (2002) Development of [18F]-Fluoroethylcholine for cancer imaging with PET: Synthesis, biochemistry, and prostate cancer imaging. J Nucl Med 43:187–199

Ido T, Wan CN, Casella JS, et al (1978) Labeled 2-deoxy-D-glucose analogs: 18F labeled 2-deoxy-2-fluoro-D-glucose, 2-deoxy-2-fluoro-D-mannose and 14C-2-deoxy-2-fluoro-D-glucose. J Label Compd Radiopharmacol 14:175–183

Iwata R, Pascali C, Bogni A, et al (2002) [18F]Fluoromethyl triflate, a novel and reactive [18F]fluoromethylating agent: Preparation and application to the on-column preparation of [18F]fluorocholine. Appl Radiat Isot 57:347–352

Jerabeck PA, Patrick TB, Kilbourn MR, et al (1986) Synthesis and biodistribution of 18F labeled fluoronitroimidazoles: Potential in vivo markers of hypoxic tissue. Int J Radiat Appl Instrum 37:599–605

Kabalka GW, Mereddy AR (2004) A facile no-carrier-added radioiodination procedure suitable for radiolabeling kits. Nucl Med Biol 31:935–938

Kabalka GW, Varma RS (1989) The synthesis of radiolabeled compounds via organometallic intermediates. Tetrahedron 45(21):6601–6621

Kamaraninen E-L, Kyllonen T, Airaksinen A, et al (2000) Preparation of [18F]CFT-FP and [11C]CFT-FP, selective radioligands for visualization of the dopamine transporter using positron emission tomography (PET). J Label Compd Radiopharm 43:1235–1244

Kamaraninen EL, Kyllonen T, Nihtila O, et al (2004) Preparation of fluorine-18-labeled fluoromisonidazole using different synthesis methods. J Label Compd Radiopharm 47:37–45

Kiesewetter DO, Kilbourn MR, Landvatter SW, et al (1984) Preparation of four fluorine-18 labeled estrogens and their selective uptakes in target tissues of immature rats. J Nucl Med 25:1212–1221

Kilbourn MR (1990) Fluorine-I8 labeling of radiopharmaceuticals. National Academy of Sciences, National Academy Press, Nuclear Science Series no. NAS-NS-3203

Kirk KL, Filler R (1996) Recent advances in the biomedicinal chemistry of fluorine containing compounds. In: Biomedical frontiers of fluorine chemistry. ACS Symposium Series, vol. 639. American Chemical Society, Washington, DC, pp 1–24

Kung HF, Kasliwal R, Pan S, et al (1988) Dopamine D 2 receptor imaging radiopharmaceuticals: Synthesis, radiolabeling and in vitro binding of R(+)- and S(−)-3-iodo-2-hydroxy-6-methoxy-N-[(1-ethyl-2-pyrrolidinyl)-methyl] -benzamide. J Med Chem 31:1039–1043

Kung MP, Hou C, Oya S, et al (1999) Characterization of [123I] IDAM as a novel single-photon emission tomography tracer for serotonin transporters. Eur J Nucl Med 26:844–853

Kung HK, Kung M-P, Choi SR (2003) Radiopharmaceuticals for single-photon emission computed tomography brain imaging. Semin Nucl Med 33(1):2–13

Lahorte C, Slegers G, Philippe J, et al (2001) Synthesis and in vitro evaluation of 123I-labeled human recombinant annexin V. Biomol Eng 17(2):51–53

Le Bars D et al (1998) High-yield radiosynthesis and preliminary in vivo evaluation of p-[18F]MPPF, a fluoro analog of WAY-100635. J Nucl Med Biol 25(4):343–350

Lim JL, Zheng L, Berridge MS, et al (1996) The use of 3-methoxymethyl-l6β, 17β-Epiestriol-O-Cyclic sulfone as the precursor in the synthesis of F-l 8–16α- Fluoroestradiol. Nucl Med Biol 23:911–915

Luxen A, Perlmutter M, Bida GT, et al (1990) Remote, semiautomated production of 6-[18F]fluoro-L-dopa for human studies with PET. Int J Rad Appl Instrum A 41:275–281

Madras BK, Meltzer PC, Liang AY, et al (1998) Altropane, a SPECT or PET imaging probe for dopamine neurons: I. Dopamine transporter binding in primate brain. Synapse 29:93–104

Mangner TJ, Wu J-I, Wieland DM (1982) Solid-phase exchange radioiodination of aryl iodides: Facilitation by ammonium sulfate. J Org Chem 47:1484–1488

Martin SJ, Eisenbarth U, Wagner-Utermann U, et al (2002) A new precursor for the radiosynthesis of [18F]FLT. Nucl Med Biol 29:263–273

Mason NS, Mathis CA (2005) Radiohalogens for PET imaging. In: Bailey DL, et al (eds) Positron emission tomography. Basic Sciences, Springer, London

Mertens J, Gysemans M (1991) Cu(1+) assisted nucleophilic exchange; application and mechanistic approach. In: Emram

AM (ed) New trends in radiopharmaceutical synthesis, quality assurance, and regulatory control. Plenum, New York

Mock BH, Weiner RE (1988) Simplified solid-state labeling of [^{123}I]-*m*-iodobenzulguanidine. Appl Radiat Isot 39(9): 939–942

Namavari M, Bishop A, Satyamurthy N, et al (1992) Regioselective radiofluorodestannylation with [^{18}F]F$_2$ and [^{18}F]CH$_3$COOF. A high yield synthesis of 6-[^{18}F]Fluoro-L-DOPA. Int J Rad Appl Instrum 43:989–996

Nickels RJ, Daube ME, Ruth TJ (1984) An oxygen target for the production of [^{18}F]F$_2$. Appl Radiat Isot 35:117

Oh SJ et al (2003) High radiochemical yield synthesis of 3′-deoxy-3′-[^{18}F]Fluorothymidine using (5′-*O*-dimethoxytirtyl-2′-deoxy-3′-*O*nosyl-β-D-*threo*-pentofuranosyl)thymine and its 3-N-BOCprotected analogue as a labeling precursor. Nucl Med Biol 30:151–157

Oh SJ, Mosdzianowski C, Chi DY, et al (2004) Fully automated synthesis system of 3′-deoxy-3′-[^{18}F]fluorothymidine. Nucl Med Biol 31:803–809

Park BK, Kitteringham NR, O'Neill PM (2001) Metabolism of fluorine-containing drugs. Annu Rev Pharmacol Toxicol 41:443–470

Patt M, Kuntzsch M, Machulla HJ (1999) Preparation of [^{18}F] fluoromisonidazole by nucleophilic substitution on THP-protected precursor: yield dependence on reaction parameters. J Radioanal Nucl Chem 240:925–927

Richardson AP, Mountford PJ, Baird AC, et al (1986) An improved iodogen method of labeling antibodies with ^{123}I. Nucl Med Commun 7:355–362

Romer J, Fuchtner F, Steinbach J, et al (1999) Automated production of 16α-[^{18}F]fluoroestradiol for breast cancer imaging. Nucl Med Biol 26:473–479

Samnick S, Bader JB, Muller M, et al (1999) Improved labeling of no-carrier-added ^{123}I-MIBG and preliminary clinical evaluation in patients with ventricular arrhythmias. Nucl Med Commun 20(6):537–545

Sheh Y, Koziorowski J, Balatoni J, et al (2000) Low energy cyclotron production and chemical separation of no-carrier added iodine-124 from a reusable enriched tellurium-124 dioxide/aluminum oxide solid solution target. Radiochim Acta 88:169–173

Shiue CY, Welch MJ (2004) Update on PET radiopharmaceuticals: Life beyond fluorodeoxyglucose. Radiol Clin N Am 42:1033–1053

Snyder SE, Kilbourn MR (2003) Chemistry of fluorine-18 radiopharmaceuticals. In: Welch MJ, Redvanly CS (eds) Handbook of radiopharmaceuticals. Wiley, West Sussex, England

Stocklin GL (1998) Is there a future for clinical fluorine-18 radiopharmaceuticals (excluding FDG)? Eur J Nucl Med 25:1612–1616

Suehiro M, Vallabhajosula S, Goldsmith SJ, et al (2007) Investigation of the role of the base in the synthesis of [^{18}F] FLT. Appl Radiat Isot 65:1350–1358

Tadino V, Kothari PJ, Vallabhajosula S, et al (2004) [^{18}F]-Fluoroalkylation using the "Loop" System. J Nucl Med 45:P445

Tan PZ, Baldwin RM, Tao FU, et al (1999) Rapid synthesis of F-18 and H-2 dual-labeled altanserin. A metabolically resistant PET ligand for 5-HT1A receptors. J Label Compd Radiopharm 42:457–467

Tang G, Wang M, Tang X, et al (2005) Fully automated one-pot synthesis of [^{18}F]fluoromisonidazole. Nucl Med Biol 32:553–558

Tewson TJ (1983) Synthesis of 16α-fluoroestradiol using fluoride ion as a source of fluorine. J Nucl Med 24:P52

Vallabhajosula S (2007) ^{18}F-labeled PET radiopharmaceuticals in oncology: an overview of radiochemistry and mechanisms of tumor localization. Semin Nucl Med 37:400–419

VanBrocklin HF, Henry F, Blagoev, et al (2004) A new precursor for the preparation of 6-[^{18}F]Fluoro-L-m-tyrosine (FMT): Efficient synthesis and comparison of radiolabeling. Appl Radiat Isot 61(6):1289–1294

Varagnolo L, Stokkel MPM, Mazzi U, et al (2000) ^{18}F-labeled radiopharmaceuticals for PET in oncology, excluding FDG. Nucl Med Biol 27:103–112

Weiland DM, Brown LE, Beierwaltes WH, Wu JL (1986) Imaging agent and method of use. United States Patent number 4584187

Yun M, Oh SJ, Ha H-J, et al (2003) High radiochemical yield synthesis of 3′-deoxy-3′-[^{18}F]Fluorothymidine using (5′-O-dimethoxytirtyl-2′-deoxy-3′-Onosyl-D-threopentofuranosyl)thymine and its 3-N-BOC protected analogue as a labeling precursor. Nucl Med Biol 30:151–157

Chemistry of Organic Radionuclides (C, N, and O)

<div style="text-align:right">

11

</div>

Science is built up of facts, as a house is built of stones; but an accumulation of facts is no more a science than a heap of stones is a house.

<div style="text-align:right">

Henri Poincaré

</div>

11.1 Advantages of Organic Radionuclides

All natural organic molecules or biochemicals in the human body and many drug molecules are made up of carbon, hydrogen, nitrogen and oxygen. The organic radionuclides useful for developing radiotracers for PET are ^{11}C, ^{13}N, and [15]O (Table 11.1). These three elements, however, do not have any radionuclides suitable for developing radiotracers for SPECT.

Among the three organic radionuclides, ^{11}C offers the greatest potential to develop radiotracers for routine clinical applications because ^{11}C, as a label, can be easily substituted for a stable carbon in an organic compound without changing the biochemical and pharmacological properties of the molecule. Furthermore, the short half-life of ^{11}C provides favorable radiation dosimetry to perform multiple studies in the same subject under different conditions. The short half-life of ^{11}C may be disadvantageous for commercial production of radiotracers, but has significant potential for developing

- Radiotracers with high SA to study drug interactions associated with very small concentrations of neuroreceptors and
- Radiolabeled drugs for monitoring the response to treatment

In addition, the relatively short physical half-life of [11]C (20 min) allows for multiple imaging studies to be obtained in the same subject within a short period of time (3–4 h) with the same tracer (at base line followed by experimental intervention) or with multiple tracers to assess the specificity of the receptor interaction.

Compared to ^{11}C, the potential clinical utility of ^{13}N and [15]O radiotracers is very limited. In the last three decades, [^{13}N]ammonia and [^{15}O]water are the only tracers that have shown clinical utility in the assessment of regional blood flow and perfusion. The radiochemistry of ^{13}N and [15]O is described briefly at the end of this chapter.

11.2 [11]C Labeled Radiopharmaceuticals

[11]C was first produced in 1934 (Crane and Lauritsen 1934) and the first biological application was based on the use of [^{11}C]CO$_2$ to investigate the photosynthesis in plants (Ruben et al. 1939). [^{11}C]CO was the first radiotracer used in human subjects to investigate the fixation of CO by red blood cells (Tobias et al. 1945). Several reviews have extensively discussed the chemistry and potential application of ^{11}C labeled radiotracers (Långström et al. 1999; Fowler and Ding 2002; Antoni et al. 2003). In the last three decades, a number of ^{11}C labeled radiotracers have been developed for clinical studies (Table 11.2).

11.2.1 Production of [11]C

The most commonly used method of ^{11}C production is based on the nuclear reaction, $^{14}N(p,\alpha)^{11}C$, in which the natural nitrogen gas is used as the target.

Table 11.1 Organic elements: stable and radioactive isotopes

Element	Radionuclide	Decay mode	Half-life	β^+ Energy (MeV)
Carbon	^{10}C	β^+ and γ	19.3 s	3.65
	^{11}C	β^+ and EC	20.3 m	1.982
	^{12}C	Stable (98.9%)		
	^{13}C	Stable (1.1%)		
	^{14}C	β^-	5715 y	0.156 (β^-)
Nitrogen	^{13}N	β^+ decay	9.97 m	2.2205
	^{14}N	Stable (99.634%)		
	^{15}N	Stable (0.366%)		
Oxygen	^{14}O	β^+ and γ	70.6 s	5.143
	^{15}O	β^+ decay	122.2 s	2.754
	^{16}O	Stable (99.762%)		
	^{17}O	Stable (0.038%)		
	^{18}O	Stable (0.20%)		

One of the competing nuclear reactions is $^{14}N(p,pn)^{13}N$, but the relative amount of ^{13}N activity produced is dose-dependent, and short irradiation times may lead to relatively large amounts of ^{13}N (Qaim et al. 1993). With trace amounts of oxygen in the target (<1%), $[^{11}C]CO_2$ and $[^{11}C]CO$ are formed (Bida et al. 1978). With relatively higher proton energies (>13 MeV), longer irradiation times (>30 min), and higher beam currents (>30 μA), the most predominant ^{11}C precursor generated is $[^{11}C]CO_2$ gas. In the presence of hydrogen (5%) in the target, $[^{11}C]$methane (CH_4) and $[^{11}C]$hydrogen cyanide (HCN) can be produced by a recoil synthesis, however, due to radiolysis, $[^{11}C]CH_4$ is the main precursor available for processing (Lamb et al. 1971; Christman et al. 1975).

^{11}C radioactivity from the cyclotron target can be recovered in the form of two major precursors;

Table 11.2 PET radiotracers for neurotransmitter systems

Biological process/neurotransmitter	Radiotracer	Mechanism of uptake and localization
Membrane synthesis	$[^{11}C]$Choline	Substrates for *choline kinase* in choline mtabolism
DNA synthesis	$[^{11}C]$Thymidine	Substrates for *thymidine kinase (TK)* in DNA synthesis
Amino acid (AA) transport	$[^{11}C]$L-methionine	Transport into the cells involves AA carrier protein
	$[^{11}C]$5-Hydroxy-tryptophan (5HTP)	Precursor for the synthesis of serotonin
Oxygen metabolism	$[^{11}C]$Acetate	Substrate for oxidative phosphorylation
β-Amyloid plaques	$[^{11}C]$PIB	Binding to β-Amyloid plaques
Dopamine	$[^{11}C]$-L-DOPA	Analog of L-DOPA, substrate for AAAD
	$[^{11}C]$Cocaine	Bind selectively to dopamine transporters
	$[^{11}C]$WIN35,428	
	α-(+)-$[^{11}C]$dihydro-tetrabenazine	Binds to vesicular amine transporters (VMAT) in presynaptic terminals
	$[^{11}C]$NMSP	High affinity D_2 receptor binding
	$[^{11}C]$Raclopride	Moderate affinity D_2 receptor binding
	$[^{11}C]$Chlorgyline	Suicide inactivators of *MAO*
	$[^{11}C]$-L-Deprenyl	
	$[^{11}C]$SCH23390	D_1 receptor antagonist
	(+)-$[^{11}C]$NNC-112	High affinity D_1 receptor antagonist
Serotonin	$[^{11}C]$5-HTP	Precursor for serotonin synthesis
	$[^{11}C]$WAY 100635	$5HT_{1A}$ receptor antagonist
	$[^{11}C]$MDL-100907	$5HT_{2A}$ receptor antagonist
	(+)-$[^{11}C]$McN-5652	Binds to serotonin transporter
	$[^{11}C]$DSAB	
	$[^{11}C]$Citalopram	
Opiate system	$[^{11}C]$Carfentanil	High affinity μ opiate receptor agonist
	$[^{11}C]$Diprenorphine	Nonsubtype (mixed) opiate receptor agonist
Benzodiazepine (BDZ) system	$[^{11}C]$Flumazenil	Central BDZ receptor (GABA$_A$) antagonist
	$[^{11}C]$Iomezanil	
	$[^{11}C]$PK11195	Peripheral BDZ receptor antagonist. Binds to activated microglia and macrophages
Cholinergic system	$[^{11}C]$Dexetimide	Muscarinic cholinergic receptor antagonist
Adrenergic system	$[^{11}C]$Hydroxyephedrine	Transported into sympathetic presynaptic terminals in myocardium

Fig. 11.1 [11C] labeled precursors prepared from [11C]carbon dioxide and [11C] methane

$$^{11}CO_2 \longrightarrow \begin{cases} ^{11}CH_3OH \longrightarrow {}^{11}CH_3I \longrightarrow \begin{cases} ^{11}CH_3Li \\ ^{11}CH_3OSO_2CF_3 \\ ^{11}CH_3NO_2 \\ ^{11}CH_3MgBr \end{cases} \\ ^{11}CH_4 \longrightarrow H^{11}CN \longrightarrow {}^{11}CNBr \\ ^{11}CO \longrightarrow {}^{11}COCl_2 \end{cases}$$
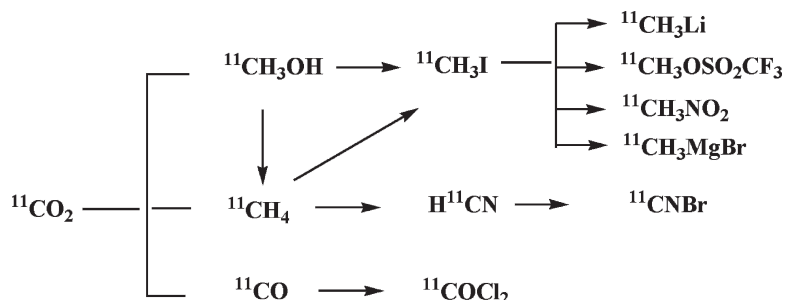
Table 11.3 Specific activity (SA) of [11C] and [18F]

Radio-nuclide	Half-life min	Theoretical SA		Practical SA	
		Ci nmol^{-1}	nmol Ci^{-1}	Ci nmol^{-1}	nmol Ci^{-1}
[11C]	20.4	9.22	0.108	0.01–0.1	10–100
[18F]	110	1.71	0.585	0.001–0.02	50–1000

[11C]carbon dioxide or [11C]methane. Subsequently, these gases can be converted into several secondary precursors (Fig. 11.1), such as methyl iodide, methyl triflate, HCN, nitromethane, and phosgene.

11.2.1.1   Specific Activity (SA) of [11C]

The theoretical SA of [11C] is 9,220 Ci μmol^{-1} or 9.22 Ci nmol^{-1} (Table 11.3). Since the contamination of the target and the gas lines with stable [12C] is unavoidable, [11C] is always contaminated with [12C] atoms. Also, both CO_2 and CH_4 gases are present in the atmosphere and provide a ubiquitous source of carrier as a contaminant that decreases the SA. As a consequence, the practical SA of [11C] precursors achieved from the typical production in a cyclotron target varies from 0.01 to 0.1 Ci nmol^{-1} depending on a number of factors. In other words, every [11C] atom is contaminated with 100 or 1,000 atoms of stable carbon atoms, which implies that the majority of the mass is mostly due to stable [12C] and very little of the carbon is from the [11C] activity. There is a significant potential and also a need to improve the SA of [11C] production with the current cyclotron targets and generate [11C] precursors with ultrahigh SA.

11.2.2   [11C] Precursors

[11C]Methyl iodide is the precursor of choice for introducing [11C] into organic molecules. However, a number of other precursors (Fig. 11.1) have been developed in

the last few decades in order to meet the demands of synthetic strategies used for the development of [11C] labeled radiotracers. [11C]Methyl iodide can also be used to prepare a number of secondary [11C] precursors, such as methyl triflate ($CH_3OSO_2CF_3$), methyl lithium, nitromethane, and methyl magnesium iodide or bromide. Starting with [11C]methane, precursors, such as hydrogen cyanide, cupric cyanide, carbon tetrachloride, and phosgene can be prepared (Ferrieri 2003; Antoni and Långström 2005). Synthesis of several [11C] precursors is shown in Fig. 11.2.

Methyl triflate, introduced in 1991 as an alkylating agent, is more advantageous than methyl iodide for alkylation reactions under mild conditions (Jewett 1991). More specifically, it can be easily prepared by passing [11C]methyl iodide through a small soda-glass column containing sliver triflate-impregnated graphitized carbon and the conversion to [11C]methyl triflate is very efficient, and fast. The other precursor for methylations under mild conditions is methyl lithium [11C] CH_3Li, which can be prepared by an equilibrium reaction between n-butyl lithium (n-BuLi) and [11C] methyl iodide (Reiffers et al. 1980).

The Grignard reagent, methyl magnesium iodide, [11C]CH_3MgI, is useful to add a methyl group to a carbonyl (CO) group in a molecule. This precursor can be prepared by the interaction of [11C]methyl iodide with magnesium turnings mixed with iodobenzene in ether (Elsinga et al. 1995).

Nitroalkanes, such as nitromethane [11C]CH_3NO_2 can easily be converted into carbon nucleophile in the presence of a base. Also, an aldehyde group in a molecule can easily be substituted with a nitromethane. Subsequently, the nitrogroup can be reduced to an amine (Schoeps et al. 1993). [11C]CH_3NO_2 can also be easily prepared by the reaction of methyl iodide with silver nitrate at 80°C (Schoeps et al. 1989). Other nitroalkanes such as nitroethane and nitropropane can also be prepared similarly.

Fig. 11.2 Methods for the synthesis of ^{11}C labeled precursors

$$[^{11}C]CH_3I \xrightarrow[150\ ^oC]{AgOSO_2CF_3} [^{11}C]CH_3OSO_2CF_3$$

$$[^{11}C]CH_3I\ +\ n\text{-}BuLi \longrightarrow [^{11}C]CH_3Li\ +\ BuI$$

$$[^{11}C]CH_3I\ +\ Mg \xrightarrow[Iodobenzene]{Diethyl\ ether,\ Iodine} [^{11}C]CH_3MgI$$

$$[^{11}C]CH_3I \xrightarrow[80\ ^oC]{AgNO_2} [^{11}C]CH_3NO_2$$

$$[^{11}C]CH_4\ +\ NH_3 \xrightarrow[1000\ ^oC]{Pt} H[^{11}C]CN \xrightarrow[Na_2S_2O_3]{CuSO_4} Cu[^{11}C]CN$$

$$[^{11}C]CH_4\ +\ Cl_2 \xrightarrow[390\ ^oC]{} [^{11}C]CCl_4 \xrightarrow[300\ ^oC]{Fe/O_2} [^{11}C]COCl_2$$

$$[^{11}C]CO_2 \xrightarrow[450\ ^oC]{Zn\ asbestos} [^{11}C]CO \xrightarrow[280\ ^oC]{PtCl_4} [^{11}C]COCl_2$$
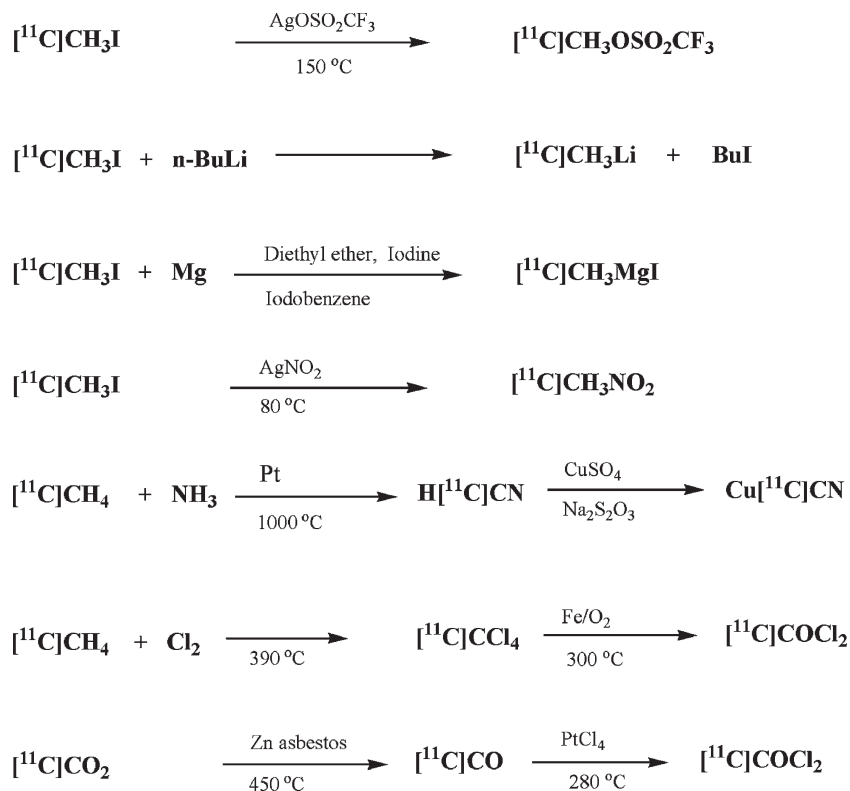
Cyanide (HCN) can be an extremely useful precursor for replacing halogen atoms, through nucleophilic substitution, with the cyano group. $[^{11}C]HCN$ can be used to label amines, amino acids, aldehydes and acids, and can be easily prepared by the reaction of $[^{11}C]$methane with ammonia over a platinum catalyst, at a very high temperature (Christman et al. 1975). Since copper salts mediate certain aromatic nucleophilic substitutions, $[^{11}C]HCN$ can easily be converted to $Cu[^{11}C]CN$ (Ponchant et al. 1997).

Phosgene, $[^{11}C]COCl_2$) is a useful precursor that can be prepared easily by the catalytic chlorination of $[^{11}C]CO$, which typically is produced through the reduction of $[^{11}C]CO_2$ over hot zinc (Roeda et al. 1978). Phosgene can also be prepared by converting $[^{11}C]$methane to carbon tetrachloride, $[^{11}C]CCl_4$ through reaction with hot Cl_2 gas. Carbon tetrachloride is then mixed in a stream of oxygen gas and passed through a second furnace at 300°C containing iron granules (Steel et al. 1999). $[^{11}C]$Phosgene has been used to prepare $[^{11}C]$ urea, a precursor for the synthesis of 2-$[^{11}C]$thymidine.

11.2.2.1 [¹¹C]Methyl Iodide

$[^{11}C]CH_3I$ is the most common precursor used to make ^{11}C radiotracers. It was first prepared in 1976 to synthesize $[^{11}C]$methionine (Långström and Lundqvist 1976). Two methods are used for the synthesis of $[^{11}C]CH_3I$ (Fig. 11.3). In a "liquid-phase" synthesis, $[^{11}C]CO_2$ is first reduced to methanol $[^{11}C]CH_3OH$, using lithium aluminum hydroxide ($LiAlH_4$) which then reacts with hydroiodic acid (HI) to generate methyliodide. In a "gas-phase" synthesis, $[^{11}CH_4]$ gas (either from the target directly or produced from $[^{11}CO_2]$) reacts with iodine vapors generating methyl iodide (Larsen et al. 1997; Link et al. 1997). Commercial automated synthesis modules (Fig. 11.4) are available to synthesize $[^{11}C]$methyl iodide.

The *GE MicroLab* and *GE TracerLab FXc Pro* modules were designed to generate methyl iodide based on the gas phase method, while *Bioscan MeI-Plus* was designed based on the liquid phase method.

Fig. 11.3 Synthesis of [^{11}C]methyl iodide: Liquid phase method (**a**) and gas phase method (**b**)

a   Liquid Phase

$$[^{11}C]CO_2 \xrightarrow{\text{LiAlH}_4} [^{11}C]CH_3O^- \xrightarrow[130^0 \text{ C}]{\text{HI}} [^{11}C]CH_3I$$

b   Gas Phase

$$[^{11}C]CO_2 \xrightarrow[\substack{\text{2. Shimalite-Ni} \\ \text{Catalyst, H}_2\text{, }350^0\text{C}}]{\text{1. Molecular Sieve}} [^{11}C]CH_4 \xrightarrow[720^0\text{C}]{I_2 \text{ Vapours}} [^{11}C]CH_3I$$
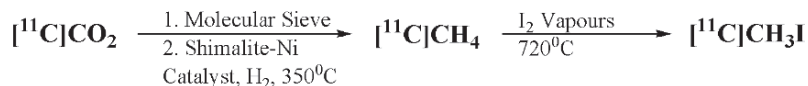
Fig. 11.4 Commercial automated synthesis modules for the production of [^{11}C] Methyl iodide: TracerLab$_{FXC}$ pro based on gas phase method and MeI-plus based on liquid phase method

Tracerlab FXc Pro consists of the following major components:

- Molecular sieve and Ni catalyst column to trap [^{11}C] CO_2 from the cyclotron and convert it to $^{11}CH_4$
- [^{11}C]CH_4 trap (CO_2 passes through it)
- I_2 oven to generate I_2 vapor
- MeI oven, where [^{11}C]CH_4 is converted to [^{11}C]CH_3I
- MeI trap, to trap [^{11}C]CH_3I; 5) glass reaction vessel where [^{11}C]CH_3I is collected in a solvent (DMF)
- [^{11}C]CH_3I is finally delivered into the reaction vessel approximately 15 min after EOB

MeI-Plus consists of the following major components:

- Molecular sieve column to trap [^{11}C]CO_2
- LAH dispenser (10 mL vial)
- HI dispenser (10 mL vial)
- One mL conical glass vial, where [^{11}C]CO_2 is reduced with LAH and converted to [^{11}C]CH_3I
- One mL glass vial containing 0.2 mL solvent (DMF) to trap [^{11}C]CH_3I

- [^{11}C]CH_3I is delivered into the reaction vial in <10 min after EOB. After each run, the system cleans itself with ethanol, acetone, and ether

Generally, the radiochemical purity, and SA of [^{11}C] CH_3I depend on the synthesis procedure and the automated module employed (Makiko et al. 2005; Kothari et al. 2005). The specific activity of [^{11}C]CH_3I (collected in DMF or acetone) can be determined by analytical HPLC using a Novapak C_{18} column (Waters, 4.6 × 150 mm) and a mobile phase, consisting of acetonitrile/water (40/60) containing 0.1 M ammonium formate at a flow rate of 2 mL min^{-1}. The retention time of [^{11}C]CH_3I is 2.7 min (Fig. 11.5). The gas-phase method generates higher SA of [^{11}C]CH_3I and may be appropriate for receptor binding radiotracers.

11.2.3 Synthesis of ^{11}C Labeled MIPs

A number of ^{11}C labeled molecular imaging probes of significant clinical interest have been developed, in

mon synthetic approach used in the routine production of ^{11}C labeled radiopharmaceuticals. Several examples are discussed below.

11.2.3.1   L-[S-methyl-^{11}C]Methionine

The amino acid L-Methionine, labeled with ^{11}C in the methyl position, has been used for brain imaging of brain tumors. The routine production involves an alkylation on a sulfur nucleophile by the reaction of [^{11}C] methyl iodide with S-benzyl-L-homocysteine in the presence of liquid ammonia and sodium, as shown in Fig. 11.6 (Långström and Lundqvist 1976; Schmitz et al. 1995). Following reverse phase HPLC of the reaction mixture, the final drug product, L-[S-methyl-^{11}C]methionine, is eluted using a phosphate buffer.

11.2.3.2   Synthesis of [O-methyl-^{11}C]Raclopride

Raclopride is a dopamine D$_2$ receptor antagonist and is one of the most extensively used neuroreceptor imaging probes. Raclopride is labeled with ^{11}C by O-methylation using [^{11}C]methyl iodide, as shown in Fig. 11.7. The enantiomerically pure S-precursor (O-desmthylraclopride) in DMSO is reacted with [^{11}C] CH$_3$I in the presence of sodium hydroxide. The purified drug product, [^{11}C]raclopride, is obtained following reverse phase HPLC of the reaction mixture using a C-18 column, a 10 mM phosphoric acid, and acetonitrile (70:30 v/v) as an eluent. The fraction containing [^{11}C]raclopride is subsequently evaporated to remove acetonitrile, reformulated in physiological saline, and sterilized by membrane filtration.

the last few decades (Table 11.2). Historically, several different approaches have been used for the production of ^{11}C labeled radiotracers, but the most practical approaches have been based on either (a) organic synthetic methods, or (b) enzyme catalysis (Antoni et al. 2003; Antoni and Långström 2005).

The methods based on organic synthesis typically involve alkylations of C, N, O, and S nucleophiles with [^{11}C]methyl iodide or methyl triflate. The alkylation reactions require an organic precursor, also known as *nor* compound (a molecule of interest without a methyl group on a specific C, N, O, or S atom). If a molecule of interest has several reactive groups, the organic precursors must have protective groups that can be easily deprotected by hydrolysis following methylation to generate the final drug product. This is the most com-

Fig. 11.6 Synthesis of L-[S-methyl-^{11}C]methionine

Fig. 11.7 Synthesis of [¹¹C]Raclopride

Desmethyl Raclopride

[¹¹C]Raclopride
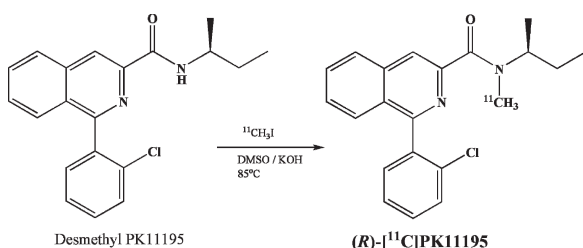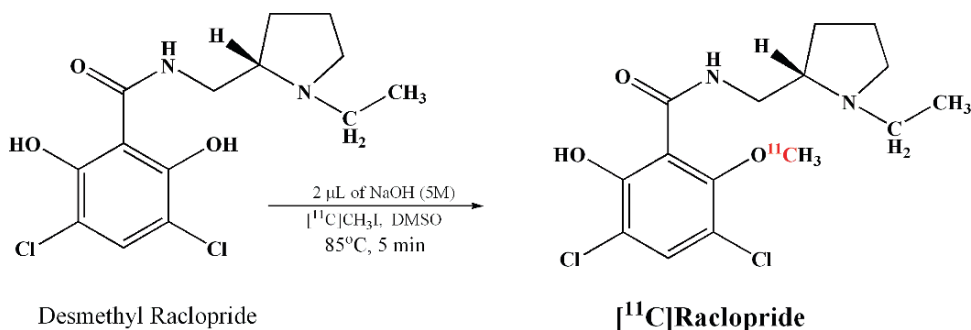
Fig. 11.8 Synthesis of [¹¹C]PK11195

11.2.3.3 Synthesis of R-[N-methyl-¹¹C]PK11195

PK11195, a peripheral benzodiazepine receptor ligand, labeled with ¹¹C, was originally developed as a tracer to image activated microglia in the brain (Banati et al. 1999; Hashimoto et al. 1989). PK11195 can be labeled with ¹¹C by *N*-methylation using [¹¹C]methyl iodide, as shown in Fig. 11.8. The precursor, *R*-desmethyl PK11195 (1.0 mg), is mixed with KOH (20 mg) in DMSO (0.4 mL) for 5 min. Subsequently, the mixture is reacted with [¹¹C]CH₃I for 3 min at 80°C. The mixture is diluted with 2–3 mL of mobile phase (70% methanol and 30% water) and purified using reverse phase HPLC column. The eluent fraction containing the drug product is passed through a C18 sep-pack cartridge to remove methanol. The final drug product is reformulated in 10% ethanol and physiological saline, and sterilized by membrane filtration.

11.2.3.4 [¹¹C]PIB

Based on an amyloid dye thioflavin-T, a ¹¹C tracer, *N*-Methyl-¹¹C-2-(4′-methylaminophenyl)-6-hydroxy-benzothiazole (¹¹C-6-OH-BTA-1, also known as

MOMO-BTA-0
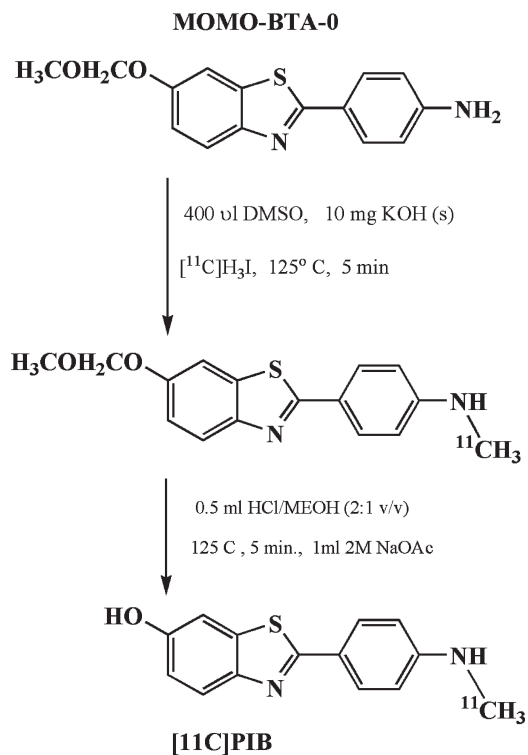
[11C]PIB

Fig. 11.9 Synthesis of [¹¹C]PIB

"Pittsburgh Compound-B" or [¹¹C]-PIB), was developed to image brain amyloid plaques in patients with Alzheimer's disease (Mathis et al. 2002, 2003). PIB can be labeled with ¹¹C by *N*-methylation using [¹¹C] methyl iodide as shown in Fig. 11.9. The precursor, desmethyl PIB with a protective group known as MOMO-BTA-0 (1.5 mg) is mixed with KOH (10 mg) in DMSO (0.4 mL) for 5 min. Subsequently, the mixture is reacted with [¹¹C]CH₃I for 5 min at 125°C. At the end, the protective group is removed by hydrolysis

at 80°C for 5 min using 0.5 mL of methanolic HCl (2:1). The mixture is diluted with mobile phase (35%) acetonitrile and 65% triethyl ammonium phosphate, pH 7.2) and purified using reverse phase HPLC. The eluent fraction containing [^{11}C]PIB is passed through the C18 sep-pak cartridge to remove the organic solvent. The final drug product can be reformulated in physiological saline with 10% ethanol and sterilized by membrane filtration.

11.2.3.5 Synthesis of [^{11}C]5-Hydroxy-L-tryptophan (HTP)

Preparation of certain ^{11}C radiopharmaceuticals can be very complicated and may involve many steps in the synthesis followed by purification procedures. ^{11}C labeled amino acids can be prepared using enzyme catalyzed reactions (especially to prepare the desired enantiomer with biological activity rather than a racemic mixture). For example, in the synthesis of [^{11}C]5-HTP (Bjurling et al. 1989), [^{11}C]-L-alanine is synthesized first, by reacting [^{11}C]CH$_3$I with N-(Diphenyl methylene)glycine tertiary butyl ester. Subsequently, [^{11}C]-L-alanine is converted to pyruvic acid using enzymes GPT, DAO and GPT. The interaction of labeled alanine with 5-hydroxyindole, in the presence of *tryptophanase*, will finally produce [^{11}C]5-HTP (Fig. 11.10). The final drug product is purified by HPLC and sterilized by membrane filtration.

11.3 ^{13}N Labeled Radiopharmaceuticals

^{13}N was first produced by the bombardment of boron with α particles using the ^{10}B(α,n)^{13}N reaction (Joliot and Curie 1934). The first ^{13}N radiotracer of biological interest was [^{13}N]ammonia (NH$_3$) and, based on cyclotrons, a number of nuclear reactions were used over the years to produce ^{13}N (Schlyer 2003). However, the most popular method of producing ^{13}N is based on the proton (8–15 MeV) bombardment of natural oxygen gas, using the ^{16}O(p,α)^{13}N reaction (Tibury et al. 1977). ^{13}N can also be produced by the proton (4–9 MeV) bombardment of isotopically enriched ^{13}C using the ^{13}C(p,n)^{13}N reaction (Ferrieri et al. 1983).

11.3.1 [^{13}N]Ammonia (NH$_3$)

The most predominant chemical species of ^{13}N produced in the water target is [^{13}N]nitrate (NO$_3^-$), while the other two species, [^{13}N]nitrite (NO$_2^-$) and [^{13}N] ammonia may represent only a small fraction of the total ^{13}N radioactivity (Table 11.4). [^{13}N]ammonia is formed as the primary product by the abstraction of hydrogen atoms from the water, as shown in the Fig. 11.11. As the irradiation dose to target is increased, radiolytic oxidation occurs producing oxoanions of nitrogen, consisting of mainly nitrates and nitrites (Clark and Aigbirhio 2003). The most common method
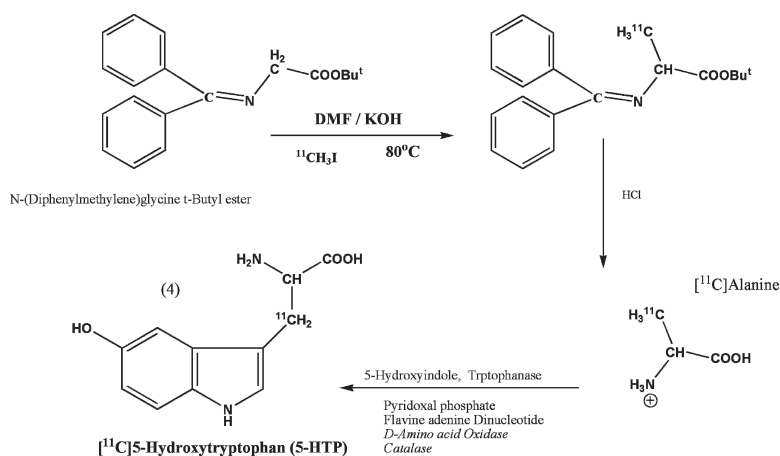
Fig. 11.10 Synthesis of [^{11}C]5-Hydroxytryptophan (5HTP)

Table 11.4   Methods for the production of ^{13}N and ^{15}O radiotracers

Target material	Nuclear reaction	In-target product(s)	Post irradiation treatment	Final product
H_2O	$^{16}O(p,\alpha)^{13}N$	NO_3^-, BO_2^-, NH_2^+	Reduction of anions using DeVarda's alloy and NaOH	$[^{13}N]NH_3$
H_2O/Ethanol (1 mM)	$^{16}O(p,\alpha)^{13}N$	NH_4^+	Radiochemical purification using cation exchange cartridge	$[^{13}N]NH_3$
N_2/O_2 (0.1–4.0%)	$^{14}N(d,n)^{15}O$ $^{15}N(d,n)^{15}O$	$[^{15}O]O_2$	Remove traces of NO_2 and O_3	$[^{15}O]O_2$
N_2/CO_2 (0.1–2.0%)	$^{14}N(d,n)^{15}O$	$[^{15}O]CO_2$	Remove traces of $[^{15}O]O_2$	$[^{15}O]CO_2$ with trace ^{13}N levels
N_2/H_2 (5.0%)	$^{14}N(d,n)^{15}O$	$[^{15}O]CO_2$	Remove traces of $[^{15}O]O_2$	$[^{15}O]CO_2$ with trace ^{13}N levels

$$^{13}N + H\text{-}OH \longrightarrow {}^{13}NH_3$$

$$^{13}NH_3 + HOH \longrightarrow {}^{13}NH_4^+ + OH^-$$

$$^{13}NH_4^+ \dashrightarrow {}^{13}NO_3^- + {}^{13}NO_2^-$$
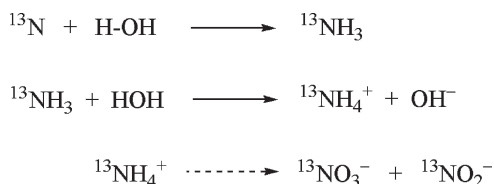
Fig. 11.11   Reactions of ^{13}N with water in the cyclotron target

of increasing the radiochemical yield of [^{13}N]ammonia is by the addition of free radical scavengers, such as ethanol and acetic acid to the target water (Weiland et al. 1991). Subsequently, the [^{13}N]NH$_4^+$ ion can be trapped on a small cation exchange cartridge, from which it can be eluted using physiological saline.

[^{13}N]Ammonia can be used to prepare a number of ^{13}N labeled amino acids for the determination of protein synthesis rates in tumors. [^{13}N]Ammonia has also been used to prepare ^{13}N labeled anticancer drugs, such as CCNU, BCNU, and cisplatin (Clark and Aigbirhio 2003).

11.3.2 Synthesis of [^{13}N]Gemcitabine

Gemcitabine (Gemzar®, Eli Lilly) is a chemotherapy drug most commonly used to treat nonsmall cell lung, pancreatic, bladder, and breast cancer. [^{13}N]Gemcitabine (GT) can be prepared using [^{13}N]ammonia, as shown in Fig. 11.12. Following production of [^{13}N]ammonia based on $^{16}O(p,\alpha)^{13}N$ reaction, the target water is passed through an ion exchange CM cartridge to trap [^{13}N] ammonia. Subsequently, it is eluted into a vial containing a DeTet, (a gemcitabine precursor containing a tetrazol group) using 0.6 mL of sodium acetate buffer (1 M, pH 8.5). The mixture is then heated at 150–160°C for 5 min. Finally, at the end of the reaction, the mixture

is filtered and the filtrate is purified by HPLC to isolate the pure [^{13}N]GT, which is then sterilized using membrane filtration (Vallabhajosula et al. 2008).

11.4 ^{15}O labeled Radiotracers

The potential utility of [^{15}O]oxygen to study regional tracer biology was first demonstrated in murine experimental neoplasms at the Washington University in St Louis (Ter-Pogossian and Powers 1958). Since that time, different chemical forms of ^{15}O, such as carbon dioxide (CO_2), carbon monoxide (CO), water (H_2O), and n-butanol ($CH_3(CH_2)_3OH$) have been used to study oxygen metabolism, blood volume, and blood flow in humans with PET.

^{15}O can be produced in a cyclotron using a variety of nuclear reactions (Clark and Aigbirhio 2003), but the most commonly used reactions are $^{14}N(d,i)^{15}O$ and $^{15}N(p,n)^{15}O$. The chemical forms of ^{15}O generated in the target vessel, depend on the nuclear reaction, energy of the bombarding particle, and the mixture of target gases (such as N_2/O_2, N_2/CO_2, and N_2/H_2) (Table 11.4).

11.4.1 ^{15}O Labeled Gases

When N_2 gas is bombarded with deuterons, the presence of oxygen (0.1–4.0%) leads to the generation of [^{15}O]O$_2$ with higher radiochemical purity. Subsequently, [^{15}O]O$_2$ can be used to synthesize labeled CO and CO_2 gases.

[^{15}O]CO can be synthesized, when [^{15}O]O$_2$ is reacted with carbon (activated charcoal) at 900–950°C. However, when [^{15}O]O$_2$ reacts with carbon at 400–450°C, the predominant species formed is [^{15}O]CO$_2$.

Fig. 11.12 Synthesis of [^{13}N]Gemcitabine

DeTet
Tetrazole precursor

NH$_3$

150° C, 5 min

[^{13}N]Gemcitabine
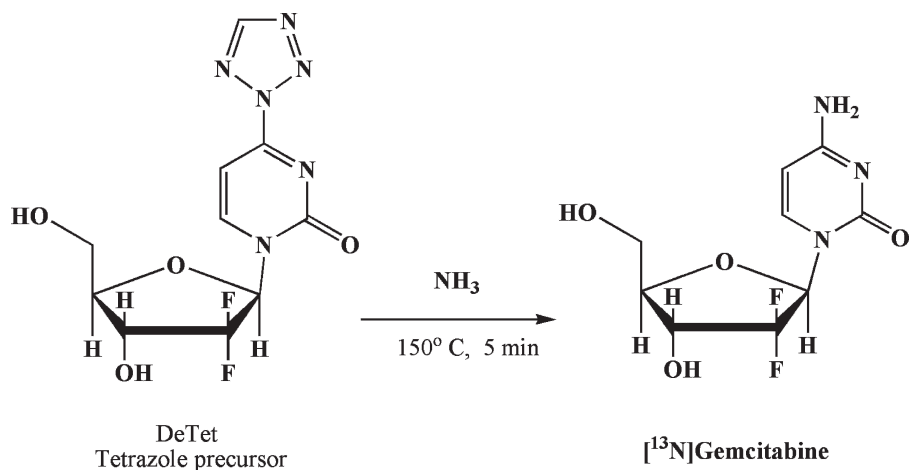
Methods for the in-target production of ^{15}O labeled CO and CO$_2$ gases have also been developed. When the target N$_2$ gas is mixed with minimal O$_2$ levels (0.25%), [^{15}O]CO is produced. Also, the presence of a source of hot carbon within the target volume has been shown to be optimal for the in-target production of [^{15}O]CO (Votaw et al. 1986; Berridge et al. 1990). When N$_2$/CO$_2$ gas mixture is used as the target gas, the product ^{15}O$_2$ is converted to [^{15}O]CO$_2$ in the target. Due to secondary nuclear reaction, ^{12}C(d,n)^{13}N, the major radionuclidic impurity in [^{15}O]CO$_2$ preparations is [^{13}N]N$_2$ gas.

11.4.2 Synthesis of [^{15}O]Water

When a N$_2$/H$_2$ mixture is bombarded with deuterons, the predominant ^{15}O labeled product in the target vessel is [^{15}O]H$_2$O (Vera Ruiz and Wolf 1978). Also, [^{15}O]H$_2$O is readily synthesized outside the target by the palladium-catalyzed reaction of [^{15}O]O$_2$ with H$_2$ gas (Clark et al. 1987). A flow of purified [^{15}O]O$_2$ in nitrogen is mixed with hydrogen and passed over a few pellets of palladium–alumina catalyst, and the resulting [^{15}O]H$_2$O vapor is trapped by bubbling the nitrogen carrier through sterile saline solution. Based on this principle, an advanced automated system for the administration of [^{15}O]water at the bedside was developed by the investigators at the Hammersmith Hospital in London.

References

Antoni G, Kihlberg T, Langstrom B (2003) Aspects on the synthesis of ^{11}C-labeled compounds. In: Welch MJ, Redvanley CS (eds) Handbook of radiopharmaceuticals. Wiley, West Sussex, UK

Antoni G, Långström B (2005) Progress in ^{11}C radiochemistry. In Bailey DL, Townsend DW, Valk PE, Maisey MN (eds) Positron emission tomography- Basic sciences. Springer, London, pp 223–236

Banati RB, Goerres GW, Myers R, et al (1999) [^{11}C](R)-PK11195 positron emission tomography imaging of activated microglia in vivo in Rasmussen's encephalitis. Neurology 53:2199–2203

Berridge MS, Terris AH, Cassidy EH (1990) Low carrier production of water and carbon monoxide. Appl Radiat Isot 41:1173–1175

Bida GT, Ruth TJ, Wolf AP (1978) Experimentally determined thick target yields for the 14N(p,α) reaction. Radiochim Acta 27:181–185

Bjurling P, Watanabe Y, Tokushige M, et al (1989) Synthesis of β-^{11}C-labeled L-tryptophan and 5-hydroxy-L-tryptophan using a multi-enzymatic reaction route. J Chem Soc Perkin Trans 1 1331–1334

Christman DR, Finn RD, Kalstrom KI, et al (1975) The production of ultra high specific activity ^{11}C labeled hydrogen cyanide, carbon dioxide, carbon monoxide, and methane via the 14N(p, α)11C reaction. Int J Appl Radiat Isot 26:435–441

Clark JC, Aigbirhio FI (2003) Chemistry of nitrogen-13 and oxygen-15. In: Welch MJ, Redvanley CS (eds) Handbook of radiopharmaceuticals. Wiley, West Sussex, UK

Clark JC, Crouzel V, Meyer CJ (1987) Current methodology for oxygen-15 production for clinical use. Appl Radiat Isot 38:597–600

Conti PS, Alauddin MM, Fissekiss JR, et al (1995) Synthesis of 2′-fluoro-5-^{11}C-methyl-1-β-D-arabinofuranosyluracil ([^{11}C]FMAU): a potential nucleoside analog for in vivo study of cellular proliferation with PET. Nucl Med Biol 22:783–789

Crane HR, Lauritsen CC (1934) Further experiments with artificially produced radioactive substances. Phys Rev 45:497

Dannals RF, Ravert HT, Frost JJ, et al (1985) Radiosynthesis of an opiate receptor binding radiotracer: [11C]carfentanil. Int J Appl Radiat Isot 36:303–306

Elsinga PH, Keller E, De Groot TJ, et al (1995). Synthesis of [11C]methyl magnesium iodide and its application to the introduction of [11C]-*N*-ter-butyl groups and [11C]-sec-alcohols. Appl Radiat Isot 46:227–231

Farde L, Ehrin E, Eriksson L, et al (1985) Substituted benz-amides as ligands for visualization of dopamine receptor binding in the human brain by positron emission tomography. Proc Natl Acad Sci U S A 82:3863–3867

Ferrieri RA (2003) Production and application of synthetic precursors labeled with carbon-11 and fluorine-18. In: Welch MJ, Redvanley CS (eds) Handbook of radiopharmaceuticals. Wiley, West Sussex, UK

Ferrieri RA, Schlyer DJ, Wieland BW, et al (1983) On-line production of [N-13]-nitrogen from solid enriched [C-13] targets and its application to [N-13]ammonia using microwave radiation. Int J Appl Radiat Isot 34:897–900

Fowler JS, Ding Y-S (2002) Chemistry. In: Wahl RL, Buchanan JW (eds) Principles and practice of positron emission tomography. Lippincott Williams and Wilkins, Philadelphia

Jewett DM (1991) A simple synthesis of [11C]methyl triflate. Appl Radiat Isot 43:1383–1385

Joliot F, Curie I (1934) Artificial production of a new kind of radio-element. Nature 133:201–202

Hashimoto KI, Inoue O, Suzuki K, et al (1989) Synthesis and evaluation of 11C-PK11195 for in vivo study of peripheral-type benzodiazepine receptors using positron emission tomography. Ann Nucl Med 3:63–71

Kamarainen E-L, Kyllonen T, Airaksinen A, et al (2000) Preparation of [18F]CFT-FP and [11C]CFT-FP, selective radio-oligands for visualization of the dopamine transporter using positron emission tomography (PET). J Label Compd Radiopharm 43:1235–1244

Kothari PJ, Suehiro S, Vallabhajosula S (2005) Evaluation of commercial automated [11C]methyl iodide (MeI-Plus) synthesis module. J Label Compd Radiopharm 48:S226

Kothari PJ, Vallabhajosula S, Lampiri E, Goldsmith SJ (2007) An improved gas phase module (GE TracerLab FXc) for the production of [11C]methyl iodide. J Nucl Med 48:181p

Lamb JF, James RW, Winchell HS (1971) Recoil synthesis of high specific activity 11C-cyanide. Int J Appl Radiat isot 22:475–479

Langer O, Dolle F, Halldin C, et al (1999) A general method for the synthesis of Raclopride, FLB 457 and Epidepride and corresponding Desmethyl-precursors. J Label Compd Radiopharm 42:5366–5368

Långström B, Lundqvist H (1976) The preparation of [11C] methyl iodide and its use in the synthesis of [methyl-11C]-L-methionine. Int J Appl Radiat Isot 27:357–363

Långström B, Kihlberg T, et al (1999) Compounds labeled with short-lived β+ emitting radionuclides and some applications in life sciences. The importance of time as a parameter. Acta Chem Scand 53:651–669

Larsen P, Ulin J, Dahlstrom K, et al (1997) Synthesis of [11C] iodomethane by iodination of [11C]methane. Appl Radiat Isot 48:153–157

Link JM, Krohn KA, Clark JC (1997) Production of [11C]CH3I by single pass reaction of [11C]CH4 with I2. Nucl Med Biol 24:93–97

Makiko S, Kothari PJ, Vallabhajosula S (2005) Quality control studies of [11C]methyl iodide produced in liquid and gas phase synthesis modules. J Label Compd Radiopharm 48:S213

Mathis CA, Bacskai BJ, Kajdasz ST, et al (2002) A lipophilic thioflavin-T derivative for positron emission tomography (PET) imaging of amyloid in brain. Bioorg Med Chem Lett 12:295–298

Mathis CA, Wang Y, Holt DP, et al (2003) Synthesis and evaluation of 11C-labeled 6-substituted 2-aryl benzothiazoles as amyloid imaging agents. J Med Chem 46:2740–2754

Nagren K, Halldin C (1998) Methylation of amide and thiol functions with [11C]methyl triflate, as exemplified by [11C] NMSP, [11C]flumazenil and [11C]methionine. J Label Compd Radiopharm 41:831–841

Ponchant M, Hinnen F, Demphel S, et al (1997) [11C]Copper(I) cyanide: a new radioactive precursor for 11C-cyanation and functionalization of haloarenes. Appl Radiat Isot 48:755–762

Qaim SM, Clark JC, Crouzel C, et al (1993) PET radionuclide production. In: Stöcklin, Pike (eds) Radiopharmaceuticals for positron emission tomography. Kluwer, Dordrecht, The Netherlands.

Reiffers S, Vallburg W, Wiegman T, et al (1980) Carbon-11 labeled methyl lithium as a methyl donating agent: the addition to 17-keto steroids. Int J Appl Radiat Isot 31:535–539

Roeda D, Crouzel C, Van Zanten (1978) Synthesis of 11C-urea for medical use. Radiochem Radioanaltical Lett 33:175–176

Ruben S, Hassid WZ, Kamen MD (1939) Reactive carbon in the study of photosynthesis. J Am Chem Soc 61:661

Schlyer DJ (2003) Production of radionuclides in accelerators. In: Welch MJ, REdvanley CS (eds) Handbook of radiopharmaceuticals, radiochemistry and applications. Wiley, New York

Schmitz F, Plenevaux A, Del-Fiore G, et al (1995) Fast routine production of L-[11C-Methyl]-methionine with Al2O3/KF. Appl Radiat Isot 46:893–897

Schoeps K-O, Stone-Elander S, Halldin C (1989) On line synthesis of [11C]nitroalkanes. Appl Radiat Isot 40:261–262

Schoeps K-O, Halldin C, Nagren K, et al (1993) Preparation of [1-11C]dopamine, [1-11C]*p*-tyramine, and [1–11C]*m*-tyramine. Nucl Med Biol 20:669–678

Steel CJ, Brady F, Luthra S, et al (1999) An automated radiosynthesis of 2-[11C]thymidine using anhydrous [11C]urea derived from [11]phosgene. Appl Radiat Isot 51:377–388

Ter-Pogossian MM, Powers WE (1958) The use of radioactive oxygen-15 in the determination of oxygencontent in malignant neoplasms. In: Exterman RC (ed) Radioisotopes in Scientific Research, III, Pergamon Press, Oxford.

Tilbury RS, Dahl JR, Marano SJ (1977) N-13 species formed by proton irradiation of water. J Label Compd Radiopharm 13:208

Tobias CA, Lawrence JH, Roughton FJW (1945) The elimination of carbon monoxide from human body with reference to possible conversion of CO to CO2. Am J Physiol 145:253

Vallabhajosula S, Zatorski A, Kothari PJ, et al (2008) [13N] Gemcitabine: a new PET tracer to assess gemcitabine (GT) tumor uptake. J Nucl Med 49(s1):98p

Vera Ruiz H, Wolf AP (1978) Direct synthesis of 15O-labeled water at high specific activities. J Label Compd Radiopharm 15:185–189

Votaw JR, Satter MR, Sunderland JJ, et al (1986) The Edison lamp: [15O]carbon monoxide production in the target. J Label compd Radiopharm 23:1211–1213

Wieland BW, Bida G, Padgett H, et al (1991) In-target production of 13N-ammonia via proton irradiation of dilute aqueous ethanol and acetic acid mixtures. Appl Radiat isot 42:1095–1098

Chemistry of Metal Radionuclides (Rb, Ga, In, Y, Cu and Tc)

12

The doubter is a true man of science; he doubts only himself and his interpretations, but he believes in science.

Claude Bernard

12.1 Introduction

Clearly, and extensive knowledge, experience, and understanding of the metal chemistry at the tracer level, would enable us to develop a number of new molecular imaging radiotracers based on β+ emitting radiometals. In nuclear medicine, ^{99m}Tc continues to be the most widely used diagnostic radionuclide because of its ideal nuclear properties ($T_{1/2}$ = 6 h and 140 keV γ photon) and its ready availability as a generator produced radionuclide. In the last three decades, a number of ^{67}Ga and ^{111}In labeled radiopharmaceuticals (based on chelates, peptides, antibodies) have been developed for both planar and SPECT imaging studies. In addition, a number of therapeutic radiopharmaceuticals have been developed based on beta emitting radiometals (^{90}Y, ^{177}Lu and ^{67}Cu), however, many of these agents are still under active clinical evaluation. The extensive knowledge, experience, and understanding of the metal chemistry at the tracer level, would enable us to develop a number of new molecular imaging radiotracers based on β^{+} emitting radiometals. The advantages of metal labeled molecular imaging radiotracers can be summarized as follows:

- Easy availability: ^{66}Cu and ^{68}Ga generators are available for easy in house preparation based on kit production. Cyclotron production of metallic nuclides has been optimized using medical cyclotrons using primarily (*p,n*) nuclear reactions
- 40 year experience with metal-labeled SPECT tracers
- Ability to label target specific biomolecules (peptides and proteins)

- Availability of radionuclide pairs for imaging and therapy (^{68}Ga/^{67}Ga ^{62}Cu/^{64}Cu/^{67}Cu, ^{110}In/^{111}In, ^{86}Y/^{90}Y)
- High SA of radiometal
- High SA of metal-labeled peptide or protein
- High in vivo stability of metal-labeled tracers
- Favorable radiation dosimetry

12.1.1 Physical and Chemical Characteristics of Metals

Some of the important physical properties and the electron configuration of various metals useful in developing molecular imaging probes are summarized in Table 12.1. Among these metals, gallium, and indium belong to group IIIB, while yttrium belongs to group IIIA of the periodic table (Fig. 3.3). All other metals, useful for developing radiopharmaceuticals, are transition metals with complex coordination chemistries.

Radioisotopes of various metals useful for PET and SPECT imaging studies are listed in Tables 12.2 and 12.3. The selection of a radiometal for labeling a specific peptide or protein is dependent on several factors, such as physical half-life, SA, type(s) of decay and emission(s), energy of the emission(s), and cost and availability. In addition, pharmacokinetics, drug delivery of the radio-metal-complex to the target site, and clearance of the radiometal complex from both the target and nontarget tissues, are all important factors that determine the selection of an appropriate radiometal in tracer development.

Among the β^{+} emitting metallic nuclides, ^{64}Cu ($T_{1/2}$ = 12.6 h), ^{66}Ga ($T_{1/2}$ = 9.45 h), ^{86}Y ($T_{1/2}$ = 14.74 h), and

Table 12.1 Physical properties and electron configuration of metals

Physical property	Element					
	Cu	Ga	Y	Zr	In	Tc
Atomic number	29	31	39	40	49	43
Atomic radius (pm)	128	122	181	160	163	136
Ionic radius (pm)	2^+, 72	3^+, 62	3^+, 106	2^+, 109	3^+, 92	7^+, 56
Electron structure	[Ar] $3d^{10}$ $4s^1$	[Ar] $3d^{10}$ $4s^2$ $4p^1$	[Kr] $4d^1$ $5s^2$	[Kr] $4d^1$ $5s^2$	[Kr] $4d^{10}$ $5s^2$ $5p^1$	[Kr] $4d^5$ $5s^2$
Electronegativity	1.90	1.81	1.22	1.65	1.78	1.9
Oxidation state	+1, +2	+3	+3	+4, +2	+3	−1 to +7

Table 12.2 Important radioisotopes of metals useful for PET and SPECT

Metal	Stable isotopes		Radioactive isotopes				
	Nuclide	%	Nuclide	$T_{1/2}$ (h)	Decay	β (% emission)	SA (Ci µmole^{-1})
Copper	^{63}Cu	69.17	^{60}Cu	0.39	EC, β$^+$	β$^+$ (93)	
	^{65}Cu	30.83	^{61}Cu	3.32	EC, β$^+$	β$^+$ (62)	
			^{62}Cu	0.163	EC β$^+$	β$^+$ (98)	19,310
			^{64}Cu	12.80	EC, β$^+$, β$^-$	β$^+$ (19), β$^-$ (40)	245
			^{67}Cu	61.92	β$^-$, γ	β$^-$ (100)	
Gallium	^{69}Ga	60.10	^{66}Ga	9.45	EC, β$^+$	β$^+$ (62)	331
	^{71}Ga	30.90	^{67}Ga	78.24	EC, γ		40
			^{68}Ga	1.14	EC, β$^+$	β$^+$ (90)	2,766
Rubidium	^{85}Rb	72.16	^{82}Rb	75 s	EC, β$^+$	β$^+$ (96)	
	^{87}Rb	27.84					
Yttrium	^{89}Y	100	^{86}Y	14.74	EC, β$^+$	β$^+$ (34)	213
			^{90}Y	64.08	β$^-$	β$^-$ (100)	
Zirconium	^{90}Zr	51.45	^{89}Zr	78.48	EC, β$^+$	β$^+$ (23)	39.9
	^{91}Zr	11.22	^{97}Zr	16.80	β$^-$, γ	β$^-$ (100)	
	^{92}Zr	17.15					
	^{94}Zr	17.38					
	^{96}Zr	2.80					
Indium	^{113}In	4.3	^{110}In	1.1	EC, β$^+$, γ	β$^+$ (71)	
	^{115}In	95.7	^{111}In	67.2	EC, γ		47
Technetium			^{94m}Tc	0.88	EC, β$^+$	β$^+$ (72)	
			^{99m}Tc	6.01	IT		522

Table 12.3 Positron emitting radiometals with potential clinical utility

Metal	Stable isotopes		Radioactive isotopes			
	Nuclide	%	Nuclide	$T_{1/2}$ (h)	β$^+$ Decay (%)	β$^+$ E_{max} (MeV)
Scandium	^{45}Sc	100	^{44}Sc	3.92	β$^+$ (95)	1.47
Titanium	^{48}T1	73.8	^{45}Ti	3.09	β$^+$ (86)	1.04
Cobalt	^{59}Co	100	^{55}Co	17.5	β$^+$ (77)	1.50
Strontium	^{88}Sr	87.9	^{83}Sr	32.4	β$^+$ (24)	1.15
Iron	^{56}Fe	91.72	^{52}Fe	8.275	β$^+$ (55.5)	0.80

^{89}Zr ($T_{1/2}$ = 3.27 days) are more appropriate for development of commercial PET radiopharmaceuticals that can be transported across the country. For most of these metallic radionuclides, cyclotron production methods have been optimized, using medical cyclotrons using primarily (p,n) nuclear reactions (Table 12.4). Also, the ^{82}Sr($T_{1/2}$ = 25 days)→^{82}Rb ($T_{1/2}$ = 1.25 months) generator (cardioGen-82®) has been FDA

Table 12.4 The most common nuclear reactions for the production of positron emitting radiometals

Radiometal	Nuclear reaction	Target abundance (%)	Useful energy range (MeV)
^{44}Sc	^{44}Ca (p,n) ^{44}Sc	2.086	≈ 11
^{60}Cu	^{60}Ni (p,n) ^{60}Cu	26.16	
^{61}Cu	^{61}Ni (p,n) ^{61}Cu	1.25	9–12
^{64}Cu	^{64}Ni (p,n) ^{64}Cu	0.91	8–15
^{66}Ga	^{66}Zn (p,n) ^{66}Ga	27.8	8–15
^{67}Ga	^{68}Zn $(p,2n)$ ^{67}Ga	19.0	12–22
^{86}Y	^{86}Sr (p,n) ^{86}Y	9.86	10–15
^{89}Zr	^{89}Y (p,n) ^{89}Zr	100	≈ 14
^{94m}Tc	^{94}Mo (p,n) ^{94m}Tc	9.12	10–15
^{110}In	^{110}Cd (p,n) ^{110}In	12.5	10–20
^{111}In	^{112}Cd $(p,2n)$ ^{111}In	24.0	12–22

approved for myocardial perfusion studies. The two nuclides with short half-lives, ^{68}Ga ($T_{1/2} = 68.3$ min) and ^{62}Cu ($T_{1/2} = 9.76$ min), can be produced on demand from generator systems without the need for an on-site cyclotron. Interestingly, the short half-life positron emitting nuclides ^{110}In and ^{94m}Tc may also have potential utility in developing specific targeted molecular imaging probes with relatively faster blood clearance, similar to ^{68}Ga labeled agents.

12.1.1.1 Specific Activity of Radiometals

The SA of the radiometal is an indicator of potency; the higher the SA of the radiometal, the higher is the SA of the radiometal-labeled biomolcule. The theoretical SA of carrier-free radiometals, useful for developing PET and SPECT radiotracers is shown in Table 12.2. The practical SA that can be achieved by cyclotron production or by generator, however, depends on many other factors. In general, SA of all β^+ emitting radiometals is much higher than the corresponding SPECT nuclides, except for ^{89}Zr. Also, the SA of ^{68}Ga (2.766 Ci nmol^{-1}) is even much higher than that of ^{18}F (1.71 Ci nmol^{-1}).

The maximum theoretical SA of ^{64}Cu is ~4,000 mCi μg^{-1}, but the cyclotron production of ^{64}Cu achieves a maximum SA of ~200 mCi μg^{-1} at EOB (McCarthy et al. 1997). In practice, purity control difficulties in solid target production often cause much lower SA to be delivered due to cold Cu contamination. In comparison, the SA of generator-produced ^{62}Cu is >70,000 mCi μg^{-1}, and levels approaching this maximum can be routinely achieved.

12.1.1.2 Decay Characterisitics

The intensity of β^+ emission from a radionuclide, or branching ratio directly affects the rate of true coincidences, because lower β^+ decay fraction results in fewer annihilation events per MBq (Williams et al. 2005). Also, the β^+ must slow down and rest before it can annihilate with an electron. Thus, annihilation takes place in a spherical volume whose radius depends on the energy. Consequently with PET, positrons with lower energy will have shorter range in tissue and higher expected spatial resolution.

Another important consideration is the emission of γ photons associated with certain positron emitters. The number of photons, amount of energy, and the abundance (%) for several radiometals useful for PET are shown in Table 12.5. Except for ^{62}Cu, ^{64}Cu and ^{68}Ga, all other radiometals have significant gamma emissions. Radionuclides, such as ^{66}Ga, ^{86}Y, ^{89}Zr and ^{124}I, have a very high proportion of γ emission compared to the intensity of β^+ emission. Detection of gamma photons or scattered photons, along with annihilation photons, may reduce the coincidence count rate performance (true counts) in several different ways (Robinson et al. 2004; Haddad et al. 2008). Also, the associated gamma emission will have a significant impact on the radiation dose to the patient, radiation exposure, and burden to the technical staff (Williams et al. 2005).

Table 12.5 β^+ Emitting radionuclides and associated γ emissions

Nuclide	β^+ decay (%)	E_{mean} (MeV)	Major γ energy (KeV) and abundance (%) 1	2	3
^{18}F	96.73	0.2498			
^{62}Cu	97.2	1.316			
^{64}Cu	17.4 and 39 (β^-)	0.2782 0.1902	1346 (0.47)		
^{66}Ga	50.0 3.8	1.9 0.397	1039 (37)	2751 (23)	4.295 (4)
^{68}Ga	88.0	0.836	1077 (3)		
^{86}Y	11.9 5.6 3.6	0.535 0.681 0.883	443 (17)	627 (33)	1.076 (83)
^{89}Zr	22.74	0.3955	908 (100)		
^{94m}Tc	67.0	1.0942	871 (94.2)	1522 (4.5)	1869 (5.7)
^{82}Rb	83.3 11.7	1.535 1.638	777 (13.4%)		

On the basis of a model incorporating radionuclide decay properties of copper radioisotopes and scanner parameters for GE Advance scanner, it has been shown that spatial resolution, sensitivity, scatter fraction, and noise-equivalent count rate (NEC) depend very much on the branching ratio and β^+ range (or spatial resolution) of the radionuclide (Table 12.6). Compared to ^{18}F, the sensitivity of the PET scanner (cpm Bq^{-1} mL^{-1}) for ^{64}Cu is significantly decreased (5.44 vs 0.98). In addition, predicted variation of NEC depends on the activity concentration (KBq mL^{-1}) (Williams et al. 2005). As a result, it is essential to administer approximately 5 times more ^{64}Cu activity in order to achieve similar NEC to that of ^{18}F. Since β^+ energy is similar for both these radionuclides, spatial resolution with ^{64}Cu is close to that of ^{18}F. On the basis of the data in Table 12.7, one can expect that for ^{68}Ga, sensitivity would be similar to that of ^{18}F.

12.2 Chelation Chemistry of Radiometals

12.2.1 Chelating Agents

In 1970s, ligands known as *bifunctional chelating agents* (BFC) were introduced to complex radiometals such as ^{111}In and ^{67}Ga. Various BFCs (Table 12.7) have been designed and synthesized over the years to develop a wide variety of radiopharmaceuticals based on radiometals.

A *ligand* is a neutral molecule or an ion having a lone pair of electrons that can be donated to form a bond with a metal ion. A chelating agent (or a chelate) is a molecule containing more than one ligand or an atom (such as N, O, and S) that can donate a lone pair of electrons. The chelating agents listed in Table 12.7 all contain N and O atoms that can form coordinate covalent bonds with central metal ions.

Chelates, such as EDTA and DTPA, are open chain polyaminopolycarboxylic acids, while NOTA, DOTA and TETA are cyclic polyaminoploycarboxylates (or macrocyclics) consisting of triaza or tetraaza macrocycle ranging from a 9 to 14 membered ring size. BFCs based on bis(thiosemicarbozone) or BTS containing N and S atoms have been developed specifically to bind Cu metal. Similarly, BFCs such as PnAOs, DADTs and MAG3 containing N and S atoms were designed to develop ^{99m}Tc radiopharmaceuticals. A wide variety of derivatives of the BFCs have been designed to improve the in vivo stability and optimize the kinetics of a specific metal–chelate complex. The structures of various BFCs are shown in Figs. 12.1 and 12.2

In coordination compounds, the metal ions have two types of valence; *primary valence* (also known as oxidation state) refers to the ability of metal ion to form ionic bonds with oppositely charged ions, while *secondary valence* (also known as coordination number) refers to the ability of a metal ion to bind to Lewis bases (ligands) to form complex ions. Therefore, the

Table 12.6 PET scanner sensitivity as a function of β^+ decay fraction and spatial resolution

Nuclide	β^+ Decay fraction	β^+ Energy E_{max} (KeV)	Spatial resolution (mm) Tangential	Radial	Sensitivity Cps Bq^{-1} mL^{-1}
^{15}O	1.0	1,723	5.8	6.0	5.62
^{18}F	0.97	635	4.7	5.0	5.44
^{62}Cu	0.97	2,925	7.2	7.4	5.5
^{60}Cu	0.92	2,194	6.3	6.6	5.23
^{61}Cu	0.62	1,159	5.1	5.4	3.43
^{64}Cu	0.17	657	4.7	5.0	0.98
^{68}Ga	0.90	1,900	–	–	$\approx 5.0^a$

The table modified from Williams et al. 2005
^{a}Sensitivity for ^{68}Ga is approximated based on the data for other radionuclides

Table 12.7 Bifunctional chelating agents

	Diethylenetriamene-pentaacetic acid	DTPA
Polyaminocaboxylic acids	Ethylenediaminetetraacetic acid	EDTA
Macrocyclics	1,4,7,10-tetraazacyclododecane-N,N″″,N‴,N″″-tetraacetic acid	DOTA
	1,4,8,11-tetraazacyclotetradodecane N,N″,N‴,N″″-tetraacetic acid	TETA
	1,4,7,-triazacyclododecane-N,N″,N‴,N″″-tetraacetic acid	NOTA
	SAR ????	SAR
Others	Bis(thiosemicarbazone)	BTS
	Propyleneamine oxime	PnAO
	Diaminedthiol	DADT
	Mercaptoacetylglycyl-glycylglycine	MAG$_3$

coordination number is the number of bonds formed by the metal ion with the atoms (that can donate a pair of electrons) in a chelating agent. This number varies from 2 to 8, depending on the size, charge and electron configuration of the metal ion. The ligand geometric arrangements of coordination compounds can be linear, square planar, tetrahedral or octahedral depending on the coordination number. Transition metals (Cu, Y, Tc) usually form coordination compounds.

The BFCs contain a side chain for conjugation to a peptide or protein. The side chain can be attached to the carbon backbone of the chelate (C-functionalized chelate), or by substitution to one of the nitrogen atoms in the molecule. C-functionalized chelating agents are preferable and provide greater stability to the metal–chelate complex, since all the nitrogen and oxygen atoms will be available for coordination with the metal ion. It is also preferable to conjugate the chelating agent to the peptide or protein of interest first, before complexation with the radiometal.

12.2.2 Stability of Metal–Ligand Complex

As shown in Table 12.1, except for Ga and In, all other metals are transition metals. The elctronegativity and oxidation state play a major role in the formation of metal–ligand complexes. Since metal ions form insoluble hydroxides in water at physiological pH, direct labeling of peptides and proteins with metallic radionuclides is relatively very difficult. Chelating agents can complex and stabilize the metal. Therefore, it is necessary to first attach a chelating agent, by covalent bonds, to a peptide or protein in order to develop radiometal labeled peptides and proteins as imaging agents.

The metal ions dissolved in water are complexed to form aqua ions. However, in the presence of a chelating agent or the ligand (L) with greater affinity for the metal

Diethylenetriamenepentaacetic acid (DTPA)

Ethylenediaminetetraacetic acid (EDTA)
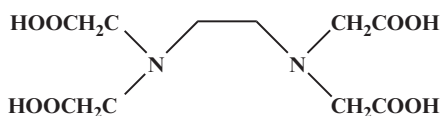
Fig. 12.1 Bifunctional open chelating agents (DTPA and EDTA)
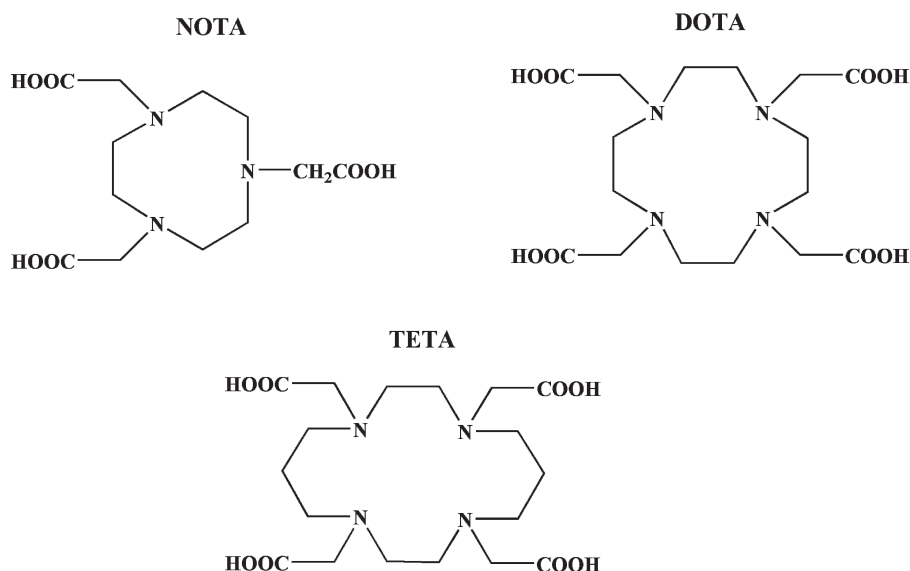
NOTA

DOTA

TETA

Fig. 12.2 Bifunctional macrocyclics (NOTA, DOTA and TETA)

than the affinity of OH⁻ ion for the metal, the formation of metal–chelate complex is preferred, as shown below.

$$M+L \leftrightarrow ML \qquad (12.1)$$

$$K_S = \frac{[ML]}{[M][L]} \qquad (12.2)$$

In the above equation, [ML] represents the concentration of the metal–ligand complex, while [M] and [L] represent the concentrations of the free metal and the free ligand. The stability of the metal–ligand complex is defined by the stability constant (K_s) when the system reaches an equilibrium between interacting chemical species (Brunner et al. 1995). The higher the value of K_s, the greater the thermodynamic stability of the metal–ligand complex (Table 12.8). The values of K_s (such as 10^4 or 10^{30}) are normally represented as log K_s values (such as 4 and 30).

It is important to appreciate that the stability constant can only reveal the direction of the reaction (formation or dissociation), but not the rate of the reaction. For example, when a purified metal–ligand complex is injected into the circulation, the rate of dissociation of the complex may be significantly increased due to extreme dilution of the complex. Therefore, the *kinetic stability* of the metal–ligand complex is very important under in vivo conditions where competing ions and ligands may augment the transchelation of the radiometal (Brunner et al. 1995).

The K_s values are usually determined for reaction in ideal conditions of buffer, pH and temperature, and do not necessarily reflect the stability of metal–ligand complex in vivo. A quantity known as *conditional stability constant* can be measured or estimated as a function of pH and in the presence of different amounts of other competing ligands.

Table 12.8 Stability constants of metal–ligand complex

	Ga	In	Y	Cu	Fe
DTPA	25.5	29.0	22.1	21.4	
EDTA	21.7	21.7		18.8	
DOTA	21.3	23.9	24.9	22.2	
NOTA	30.98				
TETA				21.6	
Citrate	10.02	6.18			
OH–	39.4	36.9			
HSA			16.2		
Transferrin	19.75	18.3			21.44

as Ga(OH)$_4^-$ or In (OH)$_4^-$

12.3   Chemistry of Gallium, Indium and Yttrium

Both gallium and indium have a filled *d* shell and three electrons in the outermost shell (Table 12.1). In contrast, yttrium has an incomplete *d* shell with one electron and two electrons in the outermost shell. However, for these three metals (M), the most important oxidation state is M^{III}. Their coordination chemistry is somewhat similar however, due to small differences in their ionic radii and electronegativities, minor, but significant differences do exist in their chemistries. These three metals also share chemical characteristics with ferric ion (Fe^{3+}). This similarity with ferric ion is important in the development of radiopharmaceuticals with Ga, In, and Y since iron is an essential element in the human body and a number of iron binding proteins, such as transferrin (in blood), exist to transport and store iron in vivo. As a result, the atoms of iron always compete with these radiometals for specific binding with proteins, such as transferrin, lactoferrin and ferritin, in vivo (Weiner and Thakur 2003).

The aqueous chemistry of Ga, In and Y is dominated by their ability to form strong complexes (both soluble and insoluble) with the hydroxyl ion. The fully hydrated (hexaaquo) M^{3+} ions are only stable under acidic conditions. As the pH is raised above 3, these three metals form insoluble hydroxides (M(OH)$_3$). A variety of OH intermediates are formed as a function of pH and the mass of the metal. Among these three metals, gallium is more amphoteric than indium and yttrium. As a result, at physiological pH, gallium exists predominantly as a soluble species, [Ga(OH)$_4$]⁻ (gallate) (Green and Welch 1989). With indium, soluble [In(OH)$_4$]⁻ starts forming only at pH values higher than 7.0. Similar to Ga and In, with Y only the trivalent ion is stable in aqueous solution at acidic pH; the ionic radius of Y is larger than Ga and In, Y binds larger number of water molecules.

The total solubility of these three metals at the physiological pH is very limited; very high SAs of radiometals are needed to keep them soluble in water. However, it is a common practice to add weak chelating agents (such as citrate, acetate or tartrate ion) to complex the metal and prevent precipitation at the neutral pH. For example, ^{67}Ga is used in the clinic as ^{67}Ga-citrate. Following intravenous administration, ^{67}Ga binds to transferrin in plasma and transported to

tumors and infectious foci as "Ga-transferrin complex" (Vallabhajosula et al. 1980).

The coordination chemistry of the metallic radionuclide will determine the geometry and stability of the "metal–chelate complex." Different metallic radionuclides have different coordination chemistries and require BFC with different donor atoms, and chelator frameworks. Both, Ga and In are classified as hard acids and prefer hard bases (Weiner and Thakur 2003). It has been shown that in +3 oxidation state, both Ga and In form thermodynamically stable complexes with either 4, 5, or 6 coordinate ligands, with 6-coordinte being the most stable, while Y prefers octadentate coordinating ligands. The advantage of using the acyclic chelators (DTPA and EDTA) is their extremely fast and high radiolabeling efficiency under mild conditions and greater thermodynamic stability; however, their kinetic lability often results in the dissociation of the radiometal. The macrocyclic chelates (NOTA, DOTA, and TETA), however, provide greater thermodynamic stability as well as kinetic stability. While Ga and In form greater thermodynamically stable complexes with NOTA, DTPA and EDTA, Y prefers DOTA. The labeling kinetics of DOTA-based BFCs is usually slow, and much more dependent on the radiolabeling conditions, including the DOTA-conjugate concentration, pH, reaction temperature, heating time, buffer agent and concentration, and presence of other metallic impurities such as Fe^{3+} and Zn^{2+} (Kukis et al. 1998).

12.3.1 ^{68}Ga-Labeled Radiopharmaceuticals

The recent development of ^{68}Ga-PET is a true landmark in molecular imaging that will allow for the use of diverse molecules and receptor analogues in clinical practice. The inherent superiority of PET imaging is a clear advantage compared to SPECT. Also the feasibility of using the ^{68}Ge/^{68}Ga generator, a round the clock for more than a year, is extremely cost-effective negating the need for on-site cyclotron (AL-Nahhas et al. 2007; Dijkgraaf et al. 2007; Maecke and Andre 2007)

12.3.1.1 ^{68}Ga Generator

The ^{68}Ga generator was first developed in the 1960s for brain imaging studies (Yano and Anger 1964). Subsequent generators (Fig. 12.3) utilized ^{68}Ge germanate adsorbed on tin dioxide and ^{68}Ga was eluted with HCl (Loc'h et al. 1980; Schuhmacher and Maier-Borst 1981). The use of a relatively high concentrations

Fig. 12.3 Gallium-68 generators: Obninsk (**a**) generator (10–100 mCi ^{68}Ge) and AGG100 (**b**) generator (10–50 mCi) supplied by The Eckert and Ziegler Isotope Products (EZIP)

of HCl (1.0 N) presents a problem due to the volatility of $GeCl_4$ and the subsequent spread of airborne, long-lived [68]Ge contamination. In addition, ^{68}Ga is eluted in a large volume of acid (>5 mL), containing metal impurities that are known to bind with high affinity to DOTA. A commercial generator (Fig. 12.3) is available based on the use of TiO_2 as an inorganic matrix to immobilize [68]Ge in the oxidation state IV+. Consequently, [68]Ga (III) can be easily separated by eluting it with dilute HCl. It has also been reported that the SA of the generator eluted ^{68}Ga can be as high as 27 Ci µmol^{-1} (Breeman and Verbruggen 2007). These generators, however, are not necessarily optimized for the synthesis of ^{68}Ga-labeled radiopharmaceuticals. The eluates have rather large volumes with a pH of 1, a breakthrough of [68]Ge, increasing with time or frequency of use, and impurities such as stable Zn(II), Ti(IV), Fe(III). In order to avoid these impurities, additional concentration and purification can be performed using a miniaturized column with organic cation-exchanger resin and hydrochloric acid/acetone eluent (Zhernosekov et al. 2007). The processed ^{68}Ga fraction can be directly transferred to solutions containing labeling precursors such as DOTATOC. Labeling yields of >95% and specific activities of (50–500 MBq nmol^{-1}) can be obtained under optimized conditions. Further, fully automated synthesis modules have been developed to prepare ^{68}Ga radiopharmaceuticals for clinical use (Azhdarinia et al. 2007; Decristoforo et al. 2007; Velikyan et al. 2008).

[68]Ga Labeled Biomolecules

Somatostatin receptor binding peptide octreotide and its analogs (Chap. 15), DOTATOC (Fig. 12.4), DOTATATE and DOTANOC have all been labeled with ^{68}Ga and evaluated to determine the diagnostic potential in patients with neuroendocrine tumors (Antunes et al. 2007; Lucignani 2008). Preclinical studies have demonstrated that [67/68]Ga-DOTA-octapeptides show distinctly better preclinical pharmacological performance than the ^{111}In-labeled peptides, especially on SST2-expressing cells and the corresponding animal models (Antunes et al. 2007). ^{68}Ga-octreotide analogs may be excellent candidates for further development for use in clinical studies.

Bombesin (BBN), an amphibian analog of the mammalian gastrin-releasing peptide, is a tetradecapeptide neurohormone that binds to gastrin-releasing peptide receptors (GRPr) that are expressed in a variety of

DOTA-Octreotide (DOTATOC) labled with [111]**In,** [68]**Ga or** [64]**Cu**
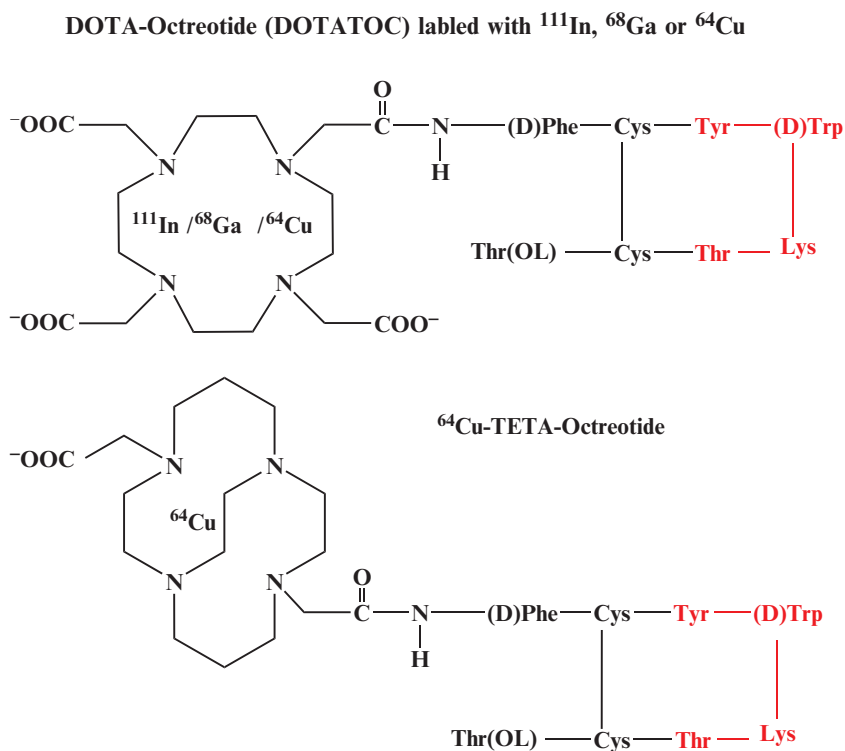
Fig. 12.4 Radiolabeled octreotide analogs for imaging neuroendocrine tumors expressing somatostatin receptors

cancers, including breast, lung, pancreatic, and prostate cancer. Recently, a novel bombesin analog, DOTA-PEG(4)-BN(7–14) (DOTAPESIN), has been developed to synthesize radiolabeled analogs for diagnosis and radionuclide therapy of prostate and other human cancers, which overexpress bombesin receptors (Zhang et al. 2007). In preclinical studies, ^{68}Ga-DOTAPEPSIN has demonstrated significant tumor targeting and potential for noninvasive imaging studies of prostate cancer.

12.4 Transition Metals

In the last few decades, several radioisotopes of transition metals such as [99]Mo, ^{99m}Tc, ^{59}Fe, and ^{90}Y have been used extensively in nuclear medicine. A number of positron emitting radiometals such as [44]Sc, [45]Ti, [52]Fe, [55]Co, ^{64}Cu, [86]Y, [89]Zr, and [94m]Tc have also been found to have suitable radioactive decay and emission characteristics for PET imaging studies.

Since the tracer chemistry of [86]Y is similar to that of ^{67}Ga and ^{111}In, [86]Y labeled peptides and antibodies have also been evaluated as potential diagnostic PET imaging agents. While the potential utility of [86]Y-labeled peptides for PET imaging studies in patients has been documented (Lövqvist et al. 2001), the physical half-life of [86]Y is suboptimal (not long enough) to follow the in vivo kinetics of labeled mAbs. It is more appropriate to use long-lived positron emitters (half-lives of days) for developing immuno-PET to allow optimal target/background ratios with radiolabeled mAbs. [89]Zr may be more appropriate since it has the ideal physical half-life ($T_{1/2}$ = 3.27 days), which is compatible with the time needed for intact mAbs to achieve optimal tumor/background ratios (Verel et al. 2003, 2005). The use of shorter-lived positron emitters, such as [86]Y and ^{64}Cu, however, does provide an attractive opportunity for the development of radiolabeled mAb fragments for use with immuno-PET.

The radioisotopes of copper, such as [62]Cu, ^{64}Cu and [67]Cu, have attracted considerable attention because the emission properties of these radionuclides offer the potential to develop both diagnostic and therapeutic radiopharmaceuticals (Blower et al. 1996). [64]Cu labeled porphyrin and [67]Cu-citrate were introduced almost 40 years ago as tumor imaging agents (Bases et al. 1963; Raynaud et al. 1973). Also, [67]Cu labeled antibodies have been extensively evaluated for radioimmunotherapy (DeNardo et al. 1991). Following the development of the high SA (>10 Ci

µmol[−1]) production of ^{64}Cu, based on enriched [64]Ni target and proton bombardment, using a biomedical cyclotron, there has been renewed interest in the development of molecular imaging probes based on [64]Cu (McCarthy et al. 1997). In addition, the production of large quantities of [60]Cu and [61]Cu, have also been optimized, based on enriched Ni targets (McCarthy et al. 1999).

12.4.1 Chemistry of Copper

The chemistry of copper is dominated by two oxidation states, I and II (Anderson et al. 2003). Copper salts form the aqua ion $[Cu(OH)_6]^{2+}$. The compounds of Cu (I) oxidation state are unstable in aqueous solution and readily oxidize to Cu(II), which can form 4, 5, or 6 coordination bonds with ligands. In the Cu (II) oxidation state, the metal binds strongly with N- and S-containing molecules forming coordination complexes. Complex formation with chelating agents occurs at pH < 7 because formation of insoluble $Cu(OH)_2$ is not a major concern.

The ability to fully exploit Cu radionuclides for PET tracer development is limited, at least in part, by the high lability of the Cu(II) complexes (i.e., high k_d). As a result, the stability of the Cu complexes is not very high and there is a significant loss of Cu from the BFC, especially in vivo (Anderson et al. 2003). There are several mechanisms by which Cu can be removed from a ligand, in vivo. These include reduction to Cu(I) with subsequent demetallation and metabolic degradation of the ligand itself. In circulation, Cu binds to the human serum albumin (HSA), which typically exists at a concentration of 5×10^{-4} M. Since the concentration of HSA is relatively high compared to the mass of Cu, the amount of Cu that is transferred from the chelator to the endogenous proteins is of major concern. Therefore, the choice of the BFC used for labeling copper radionuclides to peptides and proteins is very important. The choice of BFC really depends on the blood clearance kinetics of the target specific molecule (peptide, protein or nanoparticle) to be labeled with the copper radionuclide.

In order to bind radionuclides of copper to peptides and antibody molecules, macrocyclic chelators, such as TETA have been developed (Blower et al. 1996; Anderson et al. 2001). However, Cu (II)-TETA complexes are not optimal as imaging agents since they are not stable in vivo (Bass et al. 2000). Recently, a new class of bicyclic tetraazamacrocycles (Fig. 12.5), the
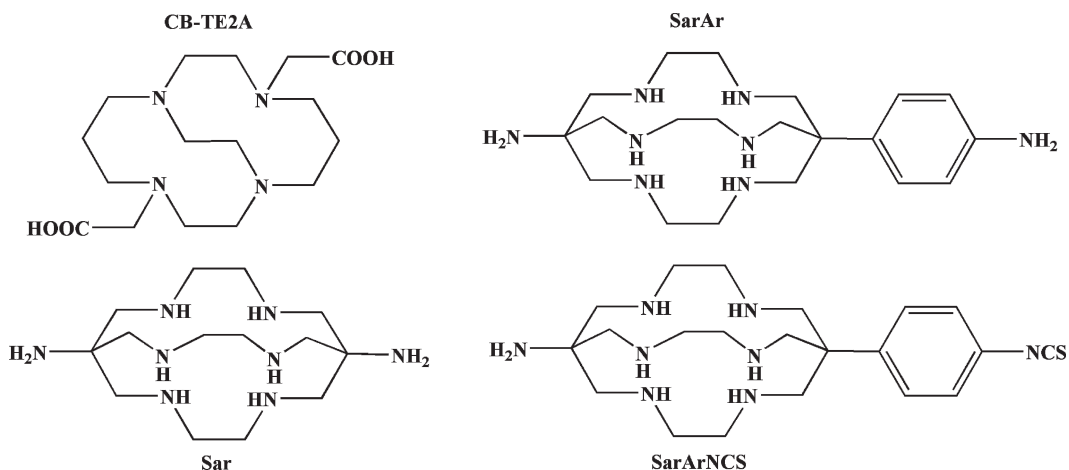
Fig. 12.5 Bifunctional aacrocyclics for complexing copper radionuclides. The ethylene "crossbridged" cyclam (CB-cyclam) derivative (CB-TE2A) and hexa-aza cages (Sar, SarAr, and SarArNCS)

ethylene "crossbridged" cyclam derivatives (CB-2ETA), were developed which form highly kinetically stable complexes with Cu(II) and are less susceptible to transchelation in vivo (Boswell et al. 2004; Wadas et al. 2007). Similarly, another series of TETA analogs known as hexa-aza-cryptand ligands SarAr and SarArNCS were also reported to form strong and stable Cu (II) complexes by wrapping the Cu atom more tightly (Di Bartolo et al. 2001; Smith 2007). This approach does not, however, take into account other factors that may affect complex stability in vivo, such as the chelate ring size, chelate flexibility, and ring substitution.

12.4.1.1 ^{62}Cu-BTS Complexes

^{62}Cu is a decay product of the parent ^{62}Zn ($T_{1/2}$ = 9.13 h). In a ^{62}Cu generator, an acidic solution of ^{62}Zn is loaded onto a Dowex anion-exchange column and the daughter ^{62}Cu ($T_{1/2}$ = 9.76 min) can be eluted from the generator with 0.1 N HCl containing NaCl (100 mg mL^{-1}) and with or without carrier CuCl$_2$ (1 μg mL^{-1}) (Robinson et al. 1980). A commercial generator has been used to develop radiopharmaceuticals for clinical evaluation (Haynes et al. 2000). An improved and fully remote-controlled ^{62}Zn/^{62}Cu generator based on a cation exchanger for clinical use was recently discussed (Fukumura et al. 2006).

On the basis of the Cu (II)-bis(thiosemicarbazone) or Cu-BTS complex, several PET radiopharmaceuticals (Fig. 12.6) have been developed (Anderson et al.
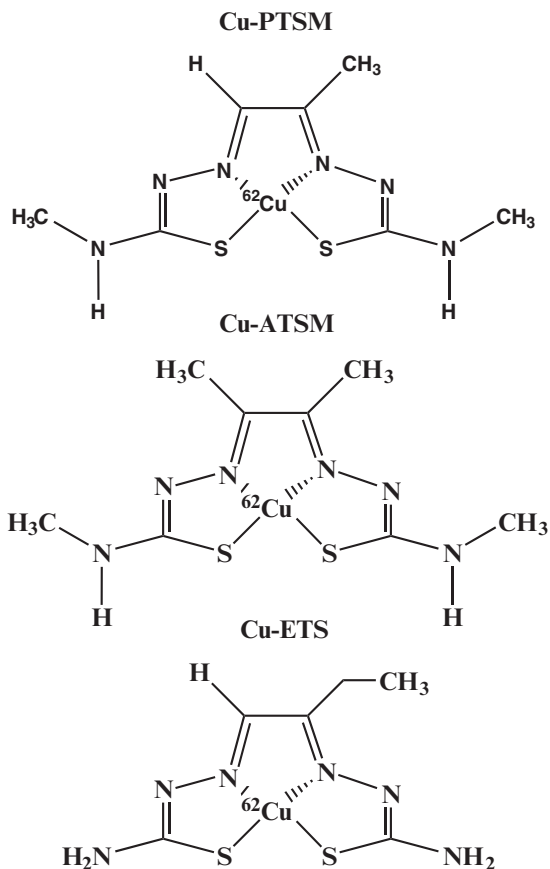
Fig. 12.6 Cu (II)-bis(thiosemicarbazone) or Cu-BTS complexes: ^{62}Cu-PTSM and ^{62}Cu-ETS for designed to measure myocardial blood flow while ^{62}Cu-ATSM has preferential uptake in hypoxic tissue

2003). Among these tracers, ^{62}Cu-pyruvaldehyde-bis(N^4-methylthiosemicarbazone (Cu-PTSM) and ^{62}Cu-diacetyl-bis(N^4-methylthiosemicarbazone) (Cu-ATSM) (Mathias et al. 1990; Lewis and Welch 2001) have been extensively evaluated in patients. Cu-PTSM was designed as a tracer to measure blood flow, while Cu-ATSM has preferential uptake in hypoxic tissue. These agents are neutral, lipophilic, and rapidly diffuse into the cells. Subsequently, the intracellular enzymes, which will bind to macromolecules within the cell reduce the complex to the Cu(I) oxidation state. While Cu-PTSM has demonstrated significant potential for imaging myocardial blood flow, its very high binding to albumin in the circulation impairs its ability for quantitative determination of myocardial perfusion (Basken et al. 2008). A second generation of Cu-BTS complex, known as ^{62}Cu-ETS, with minimal plasma protein binding is currently under clinical evaluation.

12.4.1.2 ^{64}Cu Labeled Peptides and Proteins

A second class of radiopharmaceuticals, based on biomolecules such as peptides and proteins, are being developed using ^{64}Cu and ^{67}Cu. Attachment of Cu radionuclides to molecular probes requires the use of a BFC, which is used to connect a radionuclide and a biological molecule. The two most common chelators studied thus far have been the macrocyclic ligands TETA and DOTA. Since the 1980s, mAbs labeled with ^{67}Cu have been evaluated extensively as therapeutic agents, however, ^{64}Cu labeled peptides have attracted much attention recently as radiopharmaceuticals due to their relatively low immunogenicity, good pharmacokinetic properties, and binding affinities (Fichna and Janecka 2003).

^{64}Cu Labeled Peptides and Proteins

The somatostatin receptor binding peptide, octreotide, was, recently, conjugated with TETA and labeled with ^{64}Cu (Anderson et al. 2001). Preliminary preclinical studies have demonstrated that the ^{64}Cu-TETA-octreotide detects more tumor lesions than the clinically approved ^{111}In-DTPA-octreotide. In addition, ^{64}Cu-TETA-octreotide significantly inhibits the growth of somatostatin receptor positive tumors in animal models. Similar results have been documented with a number of other ^{64}Cu labeled octreotide analogs.

The cyclic peptide Arg–Gly–Asp (RGD) binds to cancer cells and/or neoplastic vascular endothelial cells via the $\alpha_v\beta_3$ integrin receptor. RGD has been labeled with ^{64}Cu as ^{64}Cu-DOTA-RGD and ^{64}Cu-DOTA-pegylated RGD peptide for PET imaging studies (Li et al. 2008). The introduction of a bifunctional polyethylene glycol moiety between DOTA and RGD led to some improved in vivo kinetics of the resulting radiotracer, compared to that of ^{64}Cu-DOTA-RGD, but the insertion of a long PEG also reduced the receptor binding affinity to some extent.

Bombesin analogs radiolabeled with ^{64}Cu, which contain various aliphatic linkers placed between the BBN peptide and the DOTA-chelator, have previously been evaluated for tumor imaging studies. Since new chelation systems, such as CB-TE2A (Fig. 12.5) have been reported to significantly stabilize the ^{64}Cu labeled complexes in vivo, BBN analogs of ^{64}Cu-CB-TE2A chelate complex, such as ^{64}Cu-CB-TE2A-8-AOC-BBN(714)NH$_2$ has been recently prepared and evaluated in preclinical studies (Garrison et al. 2007; Prasanphanich et al. 2007). These studies have demonstrated very high selectivity and affinity for the GRPr.

The EphA2 receptor tyrosine kinase is significantly overexpressed in a wide variety of cancer types. High EphA2 expression has been correlated with increased metastatic potential and poor patient survival. Further, a humanized mAb (IC1) specific for both human and murine EphA2, has been labeled with ^{64}Cu using DOTA and evaluated for tumor imaging studies in animal models with different EphA2 expression levels. Quantitative radioimmuno-microPET imaging studies have demonstrated excellent correlation between tumor uptake and receptor expression (Cai et al. 2007a). ^{64}Cu-DOTA-cetuximab, a chimeric mAb specific for epidermal growth factor receptors (EGFR) has also been prepared and evaluated in preclinical studies (Cai et al. 2007b). The success of EGFR-positive tumor imaging using ^{64}Cu-DOTA-cetuximab can be used in the clinic to characterize the pharmacokinetics, select the right population of patients for EGFR-targeted therapy, monitor the therapeutic efficacy of antiEGFR treatment, and to optimize the dosage of either cetuximab alone or cetuximab in combination with other therapeutic agents (Lucignani 2008).

12.4.2 ^{89}Zr-Labeled mAbs

Preclinical and clinical studies have also previously demonstrated the diagnostic potential of immuno-PET

based on ^{86}Y- or ^{124}I-labeled mAbs. While ^{86}Y is an ideal radiometal for developing antibody-based radiopharmaceuticals, the physical characteristics (short half-life, positron energy, and gamma emission) are not ideal for PET radioimmuno imaging studies. Because iodine-labeled proteins are dehalogenated in vivo, ^{124}I is, therefore, not ideal for preparing radioiodinated mAbs.

Further, since the intact antibodies need 2–3 days to penetrate a solid tumor, the selection of the radionuclide with suitable half-life is essential. ^{89}Zr, a transition metal has an ideal physical half-life (78.4 h) and appropriate β^+ energy (E_{mean} = 0.39 MeV) for PET imaging studies (DeJesus et al. 1990). The most preferred method of production is based on the reaction ^{89}Y(p,n)^{89}Zr using ^{89}Y (natural abundance 100%) foil as the target material. Subsequently, ^{89}Zr is purified by anion-exchange chromatography. Zr complexes with hydroxamates in acidic solutions (>1N HCl), compare to other metallic impurities (Fe, Al, Y), which do not interact. The most common and convenient chemical form is ^{89}Zr in oxalic acid (0.5 M) with a purity >99.99% (Verel et al. 2003).

It has been shown that the methanesulfonate salt of desferrioxamine or desferal (DF) is an ideal BFC to complex ^{89}Zr since it forms stable bonds with the three hydroxamate groups (Meijs et al. 1992). For the coupling of DF to mAbs, a modified form of DF, N-(S-acetyl)mercaptoacetyldesferrioxamine B (SATA-Df) can be used. Conjugation to mAb can be performed following modification of lysine groups of mAb into maleimide groups (Meijs et al. 1992). Also, a conjugation method based on the reaction of an active 2,3,5,6-tetrafluorophenol-chelate ester (TFP-chelate ester) with the lysine moieties of mAb, results in a stable amide bond as the linker unit. This method provides optimal control over the number of groups conjugated to the mAb and has been used for the production of radioimmuno-PET (Verel et al. 2003). Since direct conjugation of mAbs with TFP-chelate ester is not possible, first blocking it with iron is an essential step for developing a postconjugation labeling method. Following removal of the iron with EDTA, the radiolabeling of mAb involves the transchelation of ^{89}Zr from oxalate to DF coupled mAb at a physiological pH (Fig. 12.7). Further, because the ^{89}Zr labeling procedure uses lysine residues of the mAb for the stable coupling of the chelate moiety, the method is applicable to any mAb, as well as to mAb fragments or peptides that contain a lysine group.
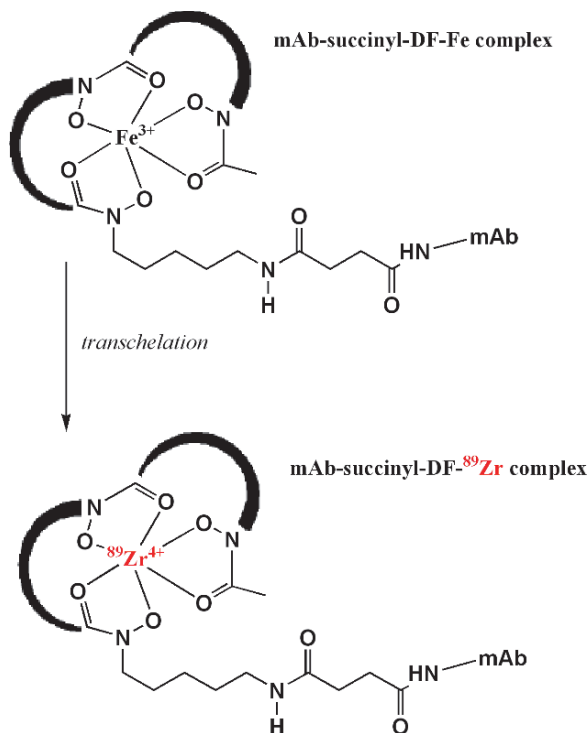
Fig. 12.7 Labeling monoclonal antibodies (mAb) with ^{89}Zr using desferal (DF) with its three hydroxamate groups. First step involves conjugation of mAb to DF and subsequent labeling with Fe to prepare mAb-succinyl-DF-Fe complex. Final step involves transchelation and labeling to obtain mAb-succinyl-DF-^{89}Zr complex

12.4.3 Technetium Chemistry

Technetium (Tc) was first discovered in 1937 by Emilio Segre and Carlo Perrier. Because it was artificially produced by bombarding molybdenum with deuterons, the name technetium for this new element was derived from the Greek word *technetos*, meaning artificial. Trace amounts of ^{99}Tc, however, were isolated from a uranium-rich ore in 1961 and totay more than 20 isotopes of technetium are known, all of which are radioactive. The most useful isotope, the metastable ^{99m}Tc ($T_{1/2}$ = 6.01 h), decays by isomeric transition to the relatively long-lived ^{99}Tc ($T_{1/2}$ = 2.1 × 10^5 year) following emission of a 140 KeV gamma photon. As previously noted, in 1958 scientists at the Brookhaven National Laboratory (BNL) reported the development of the first ^{99m}Tc generator based on the parent radioisotope ^{99}Mo. Since the 1970s, ^{99m}Tc radiopharmaceuticals have played a major role in the advancement of nuclear

medicine as a diagnostic specialty. Also, since the SA ^{99m}Tc can be very high (599 Ci μmol^{-1}), it is an excellent nuclide for developing molecular imaging radiopharmaceuticals for SPECT. ^{94m}Tc, a positron emitting radionuclide ($T_{\frac{1}{2}}$ = 53 min) with even higher theoretical SA, may also have significant potential for developing radiopharmaceuticals for use with PET.

Tc is a second row group VII transition metal that is capable of multiple oxidation sates (−1 to +7). In aqueous solution, the pertechnetate anion, ^{99m}TcO$_4^-$, is the most stable chemical species with a +7 oxidation state. Because of the similar size and charge as that of iodide (I$^-$), the in vivo distribution of pertechnetate is similar to that of an iodide ion (Deutsch et al. 1983). However, because pertechnetate is chemically stable and inert, it can not bind directly to any organic molecule or chelate. Following reduction by appropriate reducing agents, pertechnetate can be transformed into lower oxidation states that are chemically more reactive. Several reducing agents have been investigated with stannous chloride (SnCl$_2$) being the most widely used agent for preparing complexes of Tc(V) and Tc(I), while boronhydrides are used to prepare organometallic Tc(I) complexes. During reduction by the stannous ion (Sn^{2+}), in an appropriate buffer and pH, the presence of a ligand stabilizes Tc in its lower oxidation state. In a specific Tc-complex, the oxidation state of Tc, however, depends on the chelate and pH (Deutsch et al. 1983). As a transition metal, Tc can adopt a large number of coordination geometries, depending on the donor atoms and the type of the chelating agent. Several donor atoms, such as N, S, O and P, geometrically arranged in a chelating molecule, can form coordination complexes with technetium. A number of ligands, such as DTPA, Dimercaptosuccinic acid (DMSA), iminodiacetic acid (IDA) derivatives (such as HIDA, DISIDA, BrIDA), phosphates, and phophonates (such as PYP, MDP, EHDP) have been labeled with ^{99m}Tc, and routinely used for diagnostic imaging studies in nuclear medicine.

12.4.3.1 Tc(V) Complexes

The radiopharmaceutical chemistry of Tc(V) is dominated by the {TcO}$^{3+}$ core, which is stabilized by a wide range of donor atoms (N, S, O), but has a preference for thiolate, amido, and alkoxide ligands. Several tetraligand chelates designed to bind to Tc(V) are typically form complexes (such as N$_2$S$_2$, N$_3$S, N$_3$O, and N$_4$) having square pyramidal geometries (Fig. 12.8). In Ceretec™, the hexamethylpropyleneamineoxime (HMPAO) ligand forms a neutral square pyramidal complex with the {^{99m}TcO}$^{3+}$core, while Neurolite™ consists of a chelate (ECD) which is made up of two cysteine ethyl ester units that form a neutral complex with the same core. Following diffusion into the brain
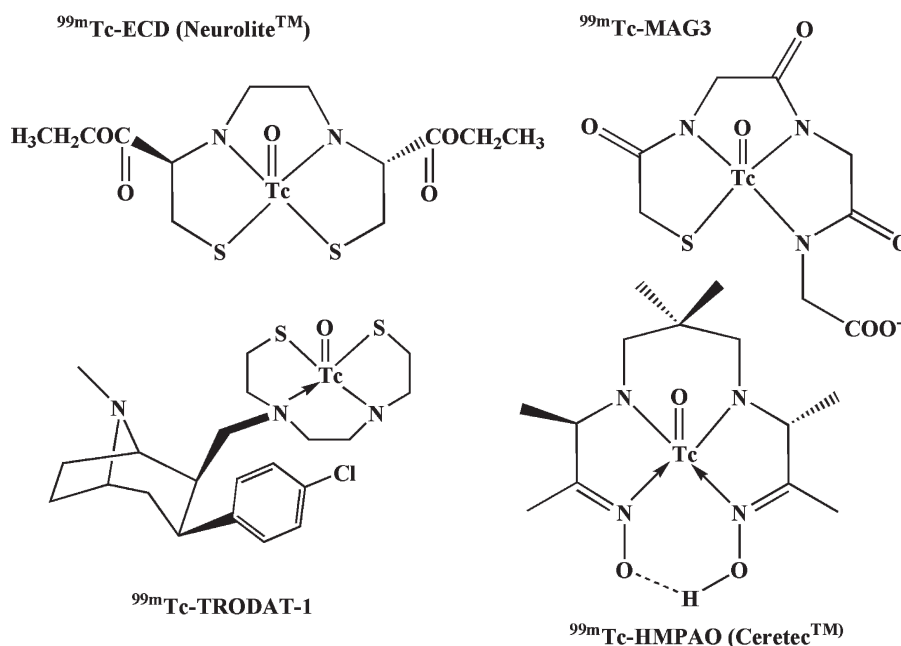
Fig. 12.8 Tc(V) complexes (such as N$_2$S$_2$, N$_3$S, N$_3$O, and N$_4$) having square pyramidal geometries that are routinely used for clinical imaging studies based on SPECT

cells, the ester group is hydrolyzed by an esterase, and the ^{99m}Tc-complex is trapped within the cell. The ^{99m}Tc complex of mercaptoacetyltriglycine (MAG3) also forms a square pyramidal complex with Tc(V) with the basal plane consisting of three nitrogen atoms and one sulfur donor atom. The carboxylic acid group does not coordinate to the metal center and is believed to help facilitate excretion via the kidneys.

^{99m}Tc-TRODAT-1 is a conjugate of a cocaine derivative with a ^{99m}Tc(V)oxo-diaminodithiol (N_2S_2) complex developed by Kung and coworkers for the diagnosis of Parkinson's disease based on SPECT (Meegalla et al. 1996; Kung et al. 1996). This is one of the most successful ^{99m}Tc labeled receptor imaging agents in clinical use, to date.

An important consideration when preparing complexes of Tc(V) is the formation of stereoisomers due to the fact that the substituents of the stereogenic center can be located *syn* (same side) or *anti* (opposite side) to the Tc-oxo bond. These compounds are also called diastereomers.

12.4.3.2 Tc(I) Organometallic Complexes

Complexes containing direct metal–carbon bonds are generally classified as organometallic compounds, which traditionally are prepared under strictly anhydrous conditions. Tc isonitrile complexes of the type [Tc(CNR)$_6$]$^+$ are widely used to assess cardiac function and, unlike most organometallic compounds, can be prepared in high yield in aqueous solutions.

The hexakis-((2-methoxy-2-methyl-1-propyl) isonitrile) complex of ^{99m}Tc(I) (Tc-Sestamibi, or Cardiolyte®) is the most prominent example of monoligand complexes, in which six methoxy isobutyl isonitrile (MIBI) groups bind to a single Tc (I) atom. A copper adduct is used as the precursor for ^{99m}Tc labeling and to prevent premature degradation of the reactive isonitrile ligands.

Tc-Tricarbonyl Core, [Tc(CO)$_3$]$^+$

A major advancement in Tc chemistry has been the discovery that a highly adaptable tricabonyl Tc core makes it possible to prepare organometallic complexes in aqueous solution (Alberto et al. 1999). In an effort to develop new organometallic precursors, for the preparation of ^{99m}Tc-complexes, investigators shown
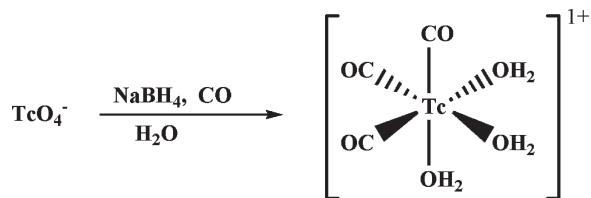
Fig. 12.9 The preparation of Tc-tricarbonyl core by treating ^{99m}Tc peertechnetate with sodium borohydride in the presence of carbon monoxide (CO) gas or potassium boranocarbonate (K$_2$H$_3$BCO$_2$)

that, by treating pertechnetate (TcO$_4^-$) with sodium borohydride (NaBH$_4$) in the presence of carbon monoxide (CO) gas, one can produce the reactive Tc(I) species, Tc(CO)$_3$(OH$_2$)$_3$]$^+$ (Fig. 12.9) (Waibei et al. 1999; Alberto et al. 1999). In this complex, the three facially oriented water molecules are sufficiently labile so that they can be readily displaced by a variety of mono-, bi- and tridentate ligands. Since it is difficult to work with CO gas, the technology is based on the use of a solid reagent, potassium boranocarbonate (K$_2$H$_3$BCO$_2$), which acts as both, a reducing agent and a source of CO gas (Alberto et al. 2001). The kit is available from Mallinckrodt (Tyco) Medical under the trade name Isolink. Further, it has been shown that both, bidentate and tridentate chelates bind rapidly to the [Tc(CO)$_3$]$^+$ core on a macroscopic scale and at the tracer level.

12.4.3.3 ^{99m}Tc-Labeled Biomolecules

The ability to incorporate ^{99m}Tc or the cyclotron produced ^{94m}Tc into tracer molecules, such as peptides and proteins, is of significant importance for the development of radiolabeled molecular imaging probes. In the 1990s several approaches have been developed to label peptides and proteins with ^{99m}Tc (Liu and Edwards 1999). New directions in developing chelators for developing ^{99m}Tc-chelate-biomolecule complex has been reviewed recently (Banergee et al. 2005). Three important labeling methods which have been developed are:

- The MAG$_3$-based bifunctional chelates
- The *N*-oxysuccinimidylhydrazino-nicotinamide system and
- The recently described single amino acid chelates for the [Tc(CO)$_3$]$^{1+}$core

The ^{99m}Tc(V)O complex of mercaptoacetyltriglycine (MAG$_3$H$_5$), was developed by Fritzberg et al., in 1986

as an anionic kidney-imaging agent. The parent ligand is readily derivatized as the *S*-acetyl MAG$_3$-ethyl ester, containing a *p*-isothiocyanatobenzyl substituent, or as the *S*-acetyl MAG3-hydroxysuccinimidyl ester for conjugation to biomolecules (Ram and Buchsbaum 1994). An alternative pendant approach to radiolabeling is provided by the *N*-oxysuccinimidylhydrazino-nicotinamide (HYNIC) as a bifunctional chelator (Babich and Fischman 1995).

The $[Tc(CO)_3]^{1+}$ carbonyl core offers the possibility of radiolabeling by appending a labeling group to the biomolecule (peptide or protein) by means of tridentate chelators or a combination of bidentatate and monodentate ligands. The carbonyl chelators, diaminoproprionic acid (DAP), retroNα-carboxymethyl histidine, and L-propargyl glycine are water-soluble, and the aqua groups readily undergo ligand exchange. These chelators are readily attached to the N-terminus of a peptide or to an orthogonally deprotected amino group side chain during chemical synthesis and bind ^{99m}Tc(I) carbonyl aquaions. Further improvements in the radiolabeling of proteins with the ^{99m}Tc using the tricarbonyl core can be accomplished by introducing thiol groups to protein structure by preparing derivatives with mercaptobutyrimidyl groups (MBG), which can be generated following reaction with 2-iminothiolane. It has been shown that the addition of three MBG groups could double the radiolabeling yields to more than 90% in a short time, at room temperature (Biechlin et al. 2005).

References

Alberto R, Schlibi R, Schubiger AP (1999) First application of fac-[^{99m}Tc(OH$_2$)$_3$(CO)$_3$]$^+$ in bioorganometallic chemistry: design, structure, and in vitro affinity of a 5-HT1A receptor ligand labeled with ^{99m}Tc. J Am Chem Soc 121:6076–6077

AL-Nahhas A, Win Z, Szyszko T, et al (2007) What can gallium-68 PET add to receptor and molecular imaging? Eur J Nucl Med Mol Imaging 34:1897–1901

Anderson CJ, Dehdashti F, Cutler, et al (2001) Copper-64-TETA-octreotide as a PET imaging agent for patients with neuroendocrine tumors. J Nucl Med 42:213–221

Anderson CJ, Green MA, Fujibayashi Y (2003) Chemistry of copper radionuclides and radiopharmaceutical products. In: Welch MJ, Redvanly CS (eds) Handbook of radiopharmaceuticals. Wiley, West Sussex, England

Anderson CJ, Wadas TJ, Wong EH, et al (2008) Cross-bridged macrocyclic chelators for stable complexation of copper radionuclides for PET imaging. Q J Nucl Med Mol Imaging 52:185–192

Antunes P, Ginj M, Zhang H, et al (2007) Are radiogallium-labelled DOTA-conjugated somatostatin analogues superior to those labelled with other radiometals? Eur J Nucl Med Mol Imaging 34:982–993

Azhdarinia A, Yang DJ, Chao C, et al (2007) Infrared-based module for the synthesis of 68Ga-labeled radiotracers. Nucl Med Biol 34(1):121–127

Babich JW, Fischman AJ (1995) Effect of "co-ligand" on the biodistribution of ^{99m}Tc-labeled hydrazino nicotinic acid derivatized chemotactic peptides. Nucl Med Biol 22:25–30

Banerjee SR, Maresca KP, Francesconi L, et al (2005) New directions in the coordination chemistry of ^{99m}Tc: a reflection on technetium core structures and a strategy for new chelate design. Nucl Med Biol 32:1–20

Bartolo ND, Sargeson AM, Smith SV (2006) New ^{64}Cu PET imaging agents for personalised medicine and drug development using the hexa-aza cage, SarAr. Org Biomol Chem 4:3350–3357

Bases R, Brodie SS, Rubenfeld S (1963) Attempts at tumor localization using Cu-64-labeled porphyrins. Cancer 11:259–263

Basken NA, Mathias CJ, Lipka AE, et al (2008) Species dependence of the [^{64}Cu]Cu-Bis(thiosemicarbazone) radiopharmaceutical binding to serum albumins. Nucl Med Biol 35:281–286

Bass LA, Wang M, Welch MJ, Anderson CJ (2000) In vivo transchelation of Copper-64 from TETA-octreotide to superoxide dismutase in rat liver. Bioconjugate Chem 11:527–532

Baum R, Niesen A, Leonhardi J, et al (2005) Receptor PET/CT imaging of neuroendocrine tumors using the Ga-68 labelled, high affinity somatostatin analogue DOTA-1-Nal^3 octreotide (DOTA-NOC): clinical results in 327 patients. Eur J Nucl Med Mol Imaging 32:S54–S55

Baum RP, Prasad V, Hommann M, et al (2008) Receptor PET/CT imaging of neuroendocrine tumors. Recent Res Cancer Res 170:225–242

Blower PJ, Lewis JS, Zweit J (1996) Copper radionuclides and radiopharmaceuticals in nuclear medicine. Nucl Med Biol 23(8):957–980

Börjesson PKE, Jauw YWS, Boellaard R, et al (2006) Performance of immuno-positron emission tomography with zirconium-89-labeled chimeric monoclonal antibody U36 in the detection of lymph node metastases in head and neck cancer patients. Clin Cancer Res 12:2133–2140

Boswell CA, Sun X, Niu W, et al (2004) Comparative in vivo stability of copper-64 labeled cross-bridged and conventional tetraazamacrocyclic complexes. J Med Chem 47:1465–1474

Breeman WAP, Verbruggen AM (2007) The ^{68}Ge/^{68}Ga generator has high potential, but when can we use ^{68}Ga-labelled tracers in clinical routine? Eur J Nucl Med Mol Imaging 34:978–981

Breeman WA, de Jong M, de Blais E, et al (2005) Radiolabelling DOTA-peptides with ^{68}Ga. Eur J Nucl Med Mol Imaging 32:478–485

Brunner UK, Renn O, Ki M, et al (1995) Radiometals and their chelates. In: Wagner HN Jr, Szabo Z, Buchanan JW (eds) Principles of nuclear medicine. WB Saunders, Philadelphia

Cai W, Ebrahimnejad A, Chen K, et al (2007a) Quantitative radioimmunoPET imaging of EphA2 in tumorbearing mice. Eur J Nucl Med Mol Imaging 34:850–858

Cai W, Chen K, He L, et al (2007b) Quantitative PET of EGFR expression in xenografts bearing mice using ^{64}Cu-labeled cetuximab, a chimeric anti-EGFR monoclonal antibody. Eur J Nucl Med Mol Imaging 34:850–858

Chakrabarti A, Zhang K, Aruva MR, et al (2007) KRAS mRNA expression in human pancreatic cancer xenografts imaged externally with [^{64}Cu]DO3A-peptide nucleic acid-peptide chimeras. Cancer Biol Ther 6:948–956

Chen X, Park R, Tohme M, et al (2004a) MicroPET and autoradiographic imaging of breast cancer $\alpha_v\beta_3$-integrin expression using ^{18}F- and ^{64}Cu-labeled RGD peptide. Bioconjugate Chem 15(1):41–49

Chen X, Hou Y, Tohme M, et al (2004b) Pegylated Arg-Gly-Asp peptide: ^{64}Cu labeling and PET imaging of brain tumor $\alpha V\beta_3$-integrin expression. J Nucl Med 45:1776–1783

Chong HS, Mhaske S, Lin M, et al (2007) Novel synthetic ligands for targeted PET imaging and radiotherapy of copper. Bioorg Med Chem Lett 17:6107–6110

Cowley AR, Dilworth JR, Donnelly PS, et al (2007) Bifunctional chelators for copper radiopharmaceuticals: the synthesis of [Cu(ATSM)-amino acid] and [Cu(ATSM)-octreotide] conjugates. Dalton Trans:209–217

Decristoforo C, Knopp R, von Guggenberg E, et al (2007) A fully automated synthesis for the preparation of ^{68}Ga-labelled peptides. Nucl Med Commun 28:870–875

Dejesus et al (1990) Production and purification of ^{89}Zr, a potential PET antibody label. Appl Radiat Isot 41(8):789–790

DeNardo GL, DeNardo SJ, Meares CF, et al (1991) Pharmacokinetics of Cu-67 conjugated Lym-1, a potential therapeutic radioimmnoconjugate, in mice and in patients with lymphoma. Antibod Immunoconjugate Radiopharm 4:777–785

Deutsch E, Libson K, Jurisson S, et al (1983) Technetium chemistry and technetium radiopharmaceuticals. Prog Inorg Chem 30:75–139

Di Bartolo NM, Sargeson AM, Donlevy TM, Smith SV (2001) Synthesis of a new cage ligand, SarAr, and its complexation with selected transition metal ions for potential use in radioimaging. J Chem Soc Dalton Trans 15:2303–2309

Dijkgraaf I, Boerman OC, Oyen WJ, et al (2007) Development and application of peptide-based radiopharmaceuticals. Anticancer Agents Med Chem 7:543–551

Fichna J, Janecka A (2003) Synthesis of target-specific radiolabeled peptides for diagnostic imaging. Bioconjugate Chem 14:3–17

Forster GJ, Englebach M, Brockmann J, et al (2001) Preliminary data on biodistribution and dosimetry for therapy planning of somatostatin receptor positive tumors: comparison of ^{86}Y-DOTATOC and ^{111}In-DTPA-octreotide. Eur J Nucl Med 28:1743–1750

Fritzberg AR, Kasina S, Eshima D, et al (1986) Synthesis and biological evaluation of technetium-99m MAG$_3$ as a hippuran replacement. J Nucl Med 27:111–116

Froidevaux S, Calame-Christe M, Schuhmacher J, et al (2004) A gallium-labeled DOTA-alphamelanocyte-stimulating hormone analog for PET imaging of melanoma metastases. J Nucl Med 45:116–123

Fukumura T, Okada K, Suzuki H, et al (2006) An improved ^{62}Zn/^{62}Cu generator based on a cation exchanger and its fully remote-controlled preparation for clinical use. Nucl Med Biol 33:821–827

Gabriel M, Decristoforo C, Kendler D, et al (2007) ^{68}Ga-DOTA-Tyr^3-Octreotide PET in neuroendocrine tumors: comparison with somatostatin receptor scintigraphy and CT. J Nucl Med 48:508–518

Garrison JC, Rold TL, Sieckman GL, et al (2007) In vivo evaluation and small-animal PET/CT of a prostate cancer mouse model using 64Cu bombesin analogs: side-by-side comparison of the CB-TE2A and DOTA chelation systems. J Nucl Med 48(8):1327–1337

Green MS, Welch MJ (1989) Gallium radiopharmaceutical chemistry. Int J Rad Appl Instrum B 16:435–448

Haddad F, Ferrer L, Guertin A, et al (2008) ARRONAX, a high-energy and high-intensity cyclotron for nuclear medicine. Eur J Nucl Med Mol Imaging 35:1377–1387

Haynes NG, Lacy GL, Nayak N, et al (2000) Performance of a ^{62}Zn/^{62}Cu generator in clinical trials of PET perfusion agent ^{62}Cu-PTSM. J Nucl Med 41:309–314

Hofmann M, Maecke H, Borner A, et al (2001) Biokinetics and imaging with the somatostatin receptor PET radioligand ^{68}Ga-DOTATOC: preliminary data. Eur J Nucl Med 28:1751–1757

Koukouraki S, Strauss LG, Georgoulias V, et al (2006) Evaluation of the pharmacokinetics of ^{68}Ga-DOTATOC in patients with metastatic neuroendocrine tumors scheduled for ^{90}Y-DOTATOC therapy. Eur J Nucl Med Mol Imaging 33:460–466

Kowalski J, Henze M, Schuhmacher J, et al (2003) Evaluation of positron emission tomography imaging using [^{68}Ga]-DOTA-DPhe1-Tyr^3-Octreotide in comparison to [^{111}In]-DTPAOC SPECT. First results in patients with neuroendocrine tumors. Mol Imaging Biol 5:42–48

Kukis DL, DeNardo SJ, DeNardo GL, et al (1998) Optimized conditions for chelation of yttrium-90-DOTA immunoconjugates. J Nucl Med 39:2105–2110

Kung HF, Kim H-J, Kung MP, et al (1996) Imaging of dopamine transporters in humans with technetium-99m-TRODAT-1. Eur J Nucl Med 23:1527–1530

Lankinen P, Mäkinen TJ, Pöyhönen TA, et al (2008) ^{68}Ga-DOTAVAP-P1 PET imaging capable of demonstrating the phase of inflammation in healing bones and the progress of infection in osteomyelitic bones. Eur J Nucl Med Mol Imaging 35:352–364

Lewis JS, Welch MJ (2001) PET imaging of hypoxia. Q J Nucl Med 45:183–188

Lewis JS, Lewis MR, Srinivasan A, et al (1999) Comparison of four ^{64}Cu labeled somatostatin analogs in vitro and in a tumor bearing rat model: evaluation of new derivatives for PET and targeted therapy. J Med Chem 42:1341–1347

Lewis JS, Welch MJ, Tang L (2008) Workshop on the production, application and clinical translation of "nonstandard" PET nuclides: a meeting report. Q J Nucl Med Mol Imaging 52(2):101–106

Li Z-B, Chen K, Chen X (2008) ^{68}Ga-labeled multimeric RGD peptides for MicroPET imaging of integrin $\alpha v\beta 3$ expression Eur J Nucl Med Mol Imaging 35:1100–1108

Liu S, Edwards DS (1999) ^{99m}Tc-labeled small peptides as diagnostics radiopharmaceuticals. Chem Rev 99:2235–2268

Loc'h C, Maziere B, Comar D (1980) A new generator for ionic gallium-68. J Nucl Med 21:171–173

Lövqvist A, Humm JL, Sheikh A, et al (2001) PET imaging of ^{86}Y-labeled anti-Lewis Y monoclonal antibodies in a nude mouse model: comparison between ^{86}Y and ^{111}In radiolabels. J Nucl Med 42:1281–1287

Lucignani G (2008) Labeling peptides with PET radiometals: vulcan's forge. Eur J Nucl Med Mol Imaging 35:209–215

Maecke HR, Andre JP (2007) ^{68}Ga-PET radiopharmacy: a generator-based alternative to ^{18}Fradiopharmacy. Ernst Schering Res Found Workshop 62:215–242

Maecke HR, Hofmann M, Haberkorn U (2005) ^{68}Ga-labeled peptides in tumor imaging. J Nucl Med 46:172S–178S

Mäkinen TJ, Lankinen P, Pöyhönen T, et al (2005) Comparison of ^{18}F-FDG and ^{68}Ga PET imaging in the assessment of experimental osteomyelitis due to Staphylococcus aureus. Eur J Nucl Med Mol Imaging 32:1259–1268

Mathias CJ, Welch MJ, Raichle ME, et al (1990) Evaluation of a potential generator-produced PET tracer for cerebral extraction measurements and imaging with copper-labeled-PTSM. J Nucl Med 31:351–359

McCarthy DW, Shefer RE, Klinkowstein RE, et al (1997) Efficient production of high specific activity ^{64}Cu using a biomedical cyclotron. Nucl Med Biol 24:35–43

McCarthy DW, Bass LA, Cutler PD, et al (1999) High purity production and potential applications of copper-60 and copper-61. Nucl Med Biol 26:351–358

Meegalla S, Plössl K, Kung M-P, et al (1996) Tc-99m-labeled tropanes as dopamine transporter imaging agents. Bioconj Chem 7:421–429

Meijs WE et al (1992) Evaluation of desferal as a bifunctional chelating agent for labeling antibodies with Zr-89. Int J Rad Appl Instrum 43(12):1443–1447

Mindt TL, Struthers H, Brans L, et al (2006) "Click to Chelate": synthesis and installation of metal chelates into biomolecules in a single step. J Am Chem Soc 128:15096–15097

Orlova A, Tolmachev V, Pehrson R, et al (2007) Synthetic affibody molecules: a novel class of affinity ligands for molecular imaging of HER2-expressing malignant tumors. Cancer Res 67:2178–2186

Parry JJ, Kelly TS, Andrews R, et al (2007) In vitro and in vivo evaluation of ^{64}Cu-labeled DOTA-linker-bombesin analogues containing different amino acid linker moieties. Bioconjugate Chem 18:1110–1117

Perik PJ, Lub-De Hooge MN, et al (2006) Indium-111-labeled trastuzumab scintigraphy in patients with human epidermal growth factor receptor 2-positive metastatic breast cancer. J Clin Oncol 24:2276–2282

Pettinato C, Sarnelli A, Di Donna M, et al (2008) ^{68}Ga-DOTANOC: biodistribution and dosimetry in patients affected by neuroendocrine tumors. Eur J Nucl Med Mol Imaging 51:72–79

Prasanphanich AF, Nanda PK, Rold TL, et al (2007) [^{64}Cu-NOTA-8-Aoc-BBN(7–14)NH$_2$] targeting vector for positron-emission tomography imaging of gastrin-releasing peptide receptorexpressing tissues. Proc Natl Acad Sci U S A 104:12462–12467

Pressly ED, Rossin R, Hagooly A, et al (2007) Structural effects on the biodistribution and positron emission tomography (PET) imaging of well-defined ^{64}Cu-labeled nanoparticles comprised of amphiphilic lock graft copolymers. Biomacromolecules 8:3126–3134

Ram S, Buchsbaum DJ (1994) A peptide-based bifunctional chelating agent for ^{99m}Tc and ^{186}Re labeling of monoclonal antibodies. Cancer 73(s3):769–773

Raynaud C, Comar D, Dutheil M, et al (1973) Lung cancer diagnosis with Cu-67: preliminary results. J Nucl Med 14:947–950

Robinson GD Jr, Zielinski FW, Lee AW (1980) The ^{62}Zn/^{62}Cu generator: a convenient source of ^{62}Cu for radiopharmaceuticals. Int J Appl Radiat Isot 31:111–116

Robinson S, Julyan PJ, Hastings DL, et al (2004) Performance of a block detector PET scanner in imaging non-pure positron emitters–modeling and experimental validation with 124I. Phys Med Biol 49:5505

Roivainen A, Tolvanen T, Salomäki S, et al (2004) ^{68}Ga-labeled oligonucleotides for in vivo imaging with PET. J Nucl Med 45:347–355

Rossin R, Pan D, Kai Q, et al (2005) ^{64}Cu labeled folate conjugated shell cross-linked nanoparticles for tumor imaging and radiotherapy: synthesis, radiolabeling and biologic evaluation. J Nucl Med 46:1210–1218

Rufini V, Calcagni ML, Baum RP (2006) Imaging of neuroendocrine tumors. Semin Nucl Med 36:228–247

Sampath L, Kwon S, Ke S, et al (2007) Dual-labeled trastuzumab-based imaging agent for the detection of human epidermal growth factor receptor 2 Overexpression in breast cancer. J Nucl Med 48:1501–1510

Schuhmacher J, Maier-Borst W (1981) A new ^{68}Ge/^{68}Ga radioisotope generator system for production of 68Ga in dilute HCl. Int J Appl Radiat Isot 32:31–36

Sharma V, Prior JL, Belinsky MG, et al (2005) Characterization of a ^{67}Ga/^{68}Ga radiopharmaceutical for SPECT and PET of MDR1 P-glycoprotein transport activity in vivo: validation in multidrug-resistant tumors and at the blood-brain barrier. J Nucl Med 46:354–364

Smith SV (2004) Molecular imaging with copper-64. J Inorg Biochem 98:1874–1901

Smith SV (2007) Sarar technology for the application of copper-64 in biology and materials science. Q J Nucl Med Mol Imaging 51:1–10

Smith-Jones PM, Solit D, Afroze F, et al (2006) Early tumor response to Hsp90 therapy using HER2 PET: comparison with ^{18}F-FDG PET. J Nucl Med 47:793–796

Sprague JE, Kitaura H, Anderson CJ, et al (2007) Noninvasive imaging of osteoclasts in parathyroid hormone-induced osteolysis using a ^{64}Cu-labeled RGD peptide. J Nucl Med 48:311–318

Tang L (2008) Radionuclide production and yields at Washington University School of Medicine. Q J Nucl Med Mol Imaging 52(2):121–133

Thakur ML, Aruva MR, Gariepy J, et al (2004) PET imaging of oncogene overexpression using ^{64}Cu-vasoactive intestinal peptide (VIP) analog: comparison with ^{99m}Tc-VIP analog. J Nucl Med 45:1381–1389

Vallabhajosula S, Harwig JF, Siemsen JK, et al (1980) Radiogallium localization in tumors: blood binding and transport and the role of transferrin. J Nucl Med 21:650–656

Velikyan I, Maecke H, Langstrom B (2008) Convenient preparation of ^{68}Ga-based PETradiopharmaceuticals at room temperature. Bioconjugate Chem 19(2):569–573

Verel I, Visser GWM, Boellaard R, et al (2003) ^{89}Zr immuno-PET: comprehensive procedures for the production of ^{89}Zr labeled monoclonal antibodies. J Nucl Med 44(8):1271–1281

Verel I, Visser GWM, Boellaard R, et al (2003) Quantitative ^{89}Zr-immuno-PET for in vivo scouting of ^{90}Y-labeled monoclonalantibodies. J Nucl Med 44:1663–1670

Verel I, Visser GWM, Van Dongen GAMS (2005) The promise of immuno-PET in radioimmunotherapy. J Nucl Med 46:164S–171S

Voss SD, Smith SV, Sargeson AM, et al (2007) Positron emission tomography (PET) imaging of neuroblastoma and mela-

noma with ^{64}Cu-SarAr immunoconjugates. PNAS 104: 17489–17493

Wadas TJ, Wong EH, Weisman GR, et al (2007) Copper chelation chemistry and its role in copper radiopharmaceuticals. Curr Pharm Design 13:3–16

Waibei R, Alberto R, Willude J, et al (1999) Stable one-step technetium-99m labeling of His-tagged recombinant proteins with a novel Tc(I)-carbonyl complex. Nat Biotechnol 17:897–901

Weiner RE, Thakur ML (2003) Chemistry of gallium and indium radiopharmaceuticals. In: Welch MJ, Redvanly CS (eds) Handbook of radiopharmaceuticals. Wiley, West Sussex, England

Wild D, Schmitt JS, Ginj M, et al (2003) DOTA-NOC, a high-affinity ligand of somatostatin receptor subtypes 2, 3 and 5 for labelling with various radiometals. Eur J Nucl Med Mol Imaging 30:1338–1347

Wild D, Macke HR, Waser B, et al (2005) ^{68}Ga-DOTANOC: a first compound for PET imaging with high affinity for somatostatin receptor subtypes 2 and 5. Eur J Nucl Med Mol Imaging 724

Williams HA, Robinson S, Julyan P, et al (2005) A comparison of PET imaging characteristics of various copper radioisotopes. Eur J Nucl Med Mol Imaging 32: 1473–1480

Win Z, Al-Nahhas A, Rubello D, (2007) Somatostatin receptor PET imaging with Gallium-68 labeled peptides. Q J Nucl Med Mol Imaging 51:244–250

Yano J, Anger OH (1964) A gallium-68 positron cow for medical use. J Nucl Med 5:484–487

Yoo J, Tang L, Perkins TA, et al (2005) Preparation of high specific activity [86]Y using a small biomedical cyclotron. Nucl Med Biol 32:891–897

Zalutsky MR, Lewis JS (2003) Radiolabeled antibodies for tumor imaging and therapy. In: Wagner HN Jr, Szabo Z, Buchanan JW (eds) Principles of nuclear medicine. WB Saunders, Philadelphia

Zhang H, Schuhmacher J, Waser B, et al (2007) DOTA-PESIN, a DOTA-conjugated bombesin derivative designed for the imaging and targeted radionuclide treatment of bombesin receptor-positive tumours. Eur J Nucl Med Mol Imaging 34(8):1198–1208

Zhernosekov KP, Filosofov DV, Baum RP, et al (2007) Processing of generator-produced ^{68}Ga for medical application. J Nucl Med 48:1741–1748

Quality Control of PET Radiopharmaceuticals

<div style="text-align:right">**13**</div>

There are two possible outcomes: If the result confirms the hypothesis, then you have made a discovery. If the result is contrary to the hypothesis, then you have made a discovery.

<div style="text-align:right">Enrico Fermi</div>

13.1 Quality Assurance

The requirements of quality assurance (QA) for any drug product include quality control test procedures, acceptance criteria, and testing schedule. In the United States, the U.S. Pharmacopoeia (USP) is recognized as an official compendium and the QA standards described in USP-published monographs for each drug product have served to standardize QA procedures. Other countries, similarly, also have their own Pharmacopoeias, such as the European Pharmacopoeia (EP) and the British Pharmacopoeia (BP). In the United States, the Food and Drug Administration (FDA) formally regulates the drug manufacturing process and develops the necessary requirements for good manufacturing practices (GMP) involved in manufacturing drugs.

The FDA Modernization Act of 1997 (the Modernization Act or FDAMA) directs the FDA to establish current good manufacturing practice (cGMP) requirements for PET drugs. Until the FDA develops and formalizes the GMP requirements for PET drugs, the FDAMA requires that the manufacturers of PET drugs must use the standards in USP General Chapter <823> *Radiopharmaceuticals for Positron Emission Tomography-Compounding*. The FDA has also issued a draft Chemistry, Manufacturing, and Controls (CMC) section concerning three PET drug products; Fludeoxyglucose F18 injection, Ammonia N13 Injection, and Sodium Fluoride F18 Injection.

All radiopharmaceuticals (for both, PET and SPECT) must be tested to assure acceptable quality prior to administration to human subjects. The USP describes the general guidelines for the safety, quality assurance, and quality control of radiopharmaceuticals.

Quality control tests are also performed at various steps in the manufacturing process of every single batch (or lot) of a drug. Because of the relatively short half-lives of positron-emitting radonuclides, each batch of the PET radiopharmaceutical may be released for administration into human subjects, based on quality control tests performed only on the final batch preparation. This special requirement for PET radiopharmaceuticals is based on the following facts:

- PET drugs are produced within strict time limits
- The mass of PET drug (especially, molecular imaging probe) produced in each batch is very small (0.01–0.1 mg)
- Each batch of a PET drug is typically prepared in a small volume (10–50 mL)
- There is insufficient time between production (manufacturing) of a PET drug and administration into patients to comply with all the official QC requirement guidelines for drugs

It is important, however, to emphasize that the safety of a patient should never be compromised under any circumstances; therefore, the quality of the final drug product must meet all the criteria required to assure safety and efficacy.

13.1.1 What are CGMPs?

Manufacturing practices are the methods, facilities, and controls used in the preparation, processing, packaging, or storing of a drug. A current good manufacturing practice (cGMP) is a minimum standard which ensures that the drug meets the requirements of safety and has the identity strength, quality, and purity characteristics it is represented to possess. cGMPs are demonstrated through written documentation of procedures and practices by the manufacturer. The documents and practices may be similar or identical to those requested by other oversight bodies (e.g., NRC, and state and local agencies). Documents produced for other oversight bodies, where appropriate, can be used to provide the documentation of compliance with CGMPs. However, because of institutional, local, or state differences, some of these documents may not have sufficient overlap to address the issues in the guidance provided by FDA. Therefore, to ensure uniformity, supplemental documentation should be developed.

A more detailed description of cGMPs and regulatory controls of radiopharmaceuticals will be discussed in greater detail in Chap. 20.

13.2 Quality Control

There are two types of quality control tests; *physicochemical tests* and *biological tests*. Physicochemical tests define the quality of the PET drug as a radiochemical, while biological tests are performed to assure the *pharmaceutical quality* of the PET radiopharmaceutical.

The *criteria for quality* of the final drug product must be carefully defined for every radiopharmaceutical and appropriate tests must be designed and validated prior to implementation. As specified in the cGMPs and USP, and as required by the FDA, various quality control tests must be performed on every single batch of PET drug, manufactured for human use.

13.2.1 Physicochemical Tests

13.2.1.1 Appearance

The radiopharmaceutical drug product is inspected visually to check for the color and presence of any particulate matter. The following procedure may be used:

- Standing behind a nontinted leaded glass shield, hold the final drug product vial against the light source and gently shake it to check for the presence of any particulate matter.
- Hold the product vial against the colorless background of taped white paper and quickly look at the color of the product solution.
- Record the results.

13.2.1.2 Radionuclidic Identity and Purity

Radionuclidic purity may be defined as the fraction of total radioactivity that is present as the specified radionuclide in the final drug product formulation. Radionuclidic impurities may also be other radioisotopes of the same element as the radiolabel or some other radionuclides of different elements. The nature and levels of radionuclidic impurities depend on the type of nuclear reaction, in which the radionuclidic impurities may arise because of other undesirable nuclear reactions in the target. For example, with ^{123}I radiopharmaceuticals, the presence of ^{125}I and ^{124}I are considered as radionuclidic impurities.

With PET radionuclides, the radionuclidic identity is determined by measuring the half-life of the radioactivity (using a dose calibrator) in a sample of final drug preparation. Positron-emitting radionuclides show a major peak at 511 KeV due to annihilation photons. The levels of contaminants can be easily detected and measured by γ-ray spectrometry based on NaI(Tl) detector or Ge(Li) detector coupled to a multichannel analyzer. Radionuclidic contaminants that decay β⁻ emission can be measured by β spectrometry using a liquid scintillation counter.

13.2.1.3 Radioassay or Concentration

The concentration of radioactivity in every batch of the final drug preparation must be determined and expressed as mCi/mL or GBq/mL at the end of synthesis (EOS). Higher concentration of a radiopharmaceutical may generate undesirable radiochemical impurities because of radiolysis.

The total amount of radioactivity in the vial containing the final drug preparation is usually measured using a *radionuclide dose calibrator*. In order to determine the concentration, a known volume (0.5 or 1.0 mL) of the final drug preparation is withdrawn into a syringe

and then the activity in the syringe is measured. To ensure that the dose calibrator performs properly, daily quality control tests must be performed using ^{137}Cs (γ energy 611 KeV) and/or other radionuclide standards according to the NRC guidelines.

13.2.1.4 Radiochemical Purity and Identity

Radiochemical purity (RCP) of a radiopharmaceutical may be defined as the fraction of total radioactivity that is present in the desired radiochemical form of the final drug formulation. The RCP should not be confused with the labeling efficiency or radiolabeling yield, which is a measure of percent incorporation of the radionuclide during the synthesis procedure. Also, it is important that the radiolabel is in the specified molecular position. If the radiolabel is in any other position in the molecule or in any other chemical form it is regarded as radiochemical impurity. Several radiochemical impurities may originate from the radionuclide production during the manufacturing process (because of incomplete reactions, side reactions, or incomplete removal of protective groups in the precursor molecule) or even because of radiolysis.

Since the radiochemical impurities may contain the desired radionuclide, the amount of the total radiochemical impurities in the final drug formulation must be minimal, compared to the RCP of the final drug product. The presence of unacceptable levels of radiochemical impurities in the final drug formulation will produce poor quality images because of the undesirable distribution of the radiochemical impurities, in vivo.

During the synthesis of 2-[^{18}F]fluoro-2-deoxy-D-glucose (FDG), the ^{18}F atom is incorporated into the desired molecular position, 50–80%, which implies that the labeling efficiency is 50–80%. The remaining ^{18}F radiolabel may be present in the form of undesirable radiochemical species, such as [^{18}F]fluoride ion, 2-[^{18}F]fluoro-2-deoxy-mannose (FDM), and partially acetylated [^{18}F]fluoro-deoxy-glucose derivatives. One of the important steps in the manufacturing process is to separate (purify) the desired radiochemical form (FDG) from all other radiochemical impurities. The final drug formulation must have >90% RCP (^{18}F activity in the desired radiochemical form) and a minimal amount (<10%) of radiochemical impurities (such as ^{18}F as fluoride or in any other radiochemical form).

The radiopharmaceutical identity (that is, the desired radiochemical form) must be established by demonstrat-ing that the chromatographic behavior of the radiolabeled drug product is similar to that of a nonradiolabeled drug product (or the "Standard"). For example, in the case of [^{18}F]FDG, the standard is an ultrapure [^{19}F]FDG chemical. The comparison of the radiolabeled drug product with a known standard may be performed using either a thin-layer chromatography (TLC) or a high-performance (or pressure) liquid chromatography (HPLC) method. The relative front or the retention factor (R_f) value of the radiopharmaceutical must correspond to or be within the acceptable range of the R_f value of the USP standard for that radiopharmaceutical.

In order to determine both the RCP and identity, it is very important to develop testing procedures that are practical and sensitive for the estimation of relatively small amounts of radiochemical impurities. A number of analytical methods are available depending on the chemical nature of the radiopharmaceutical and undesirable radiochemical impurities. Because of time limitations with PET radiopharmaceuticals, the routine quality control tests to determine RCP must be relatively fast, but must also be extremely reliable and reproducible.

The most applicable analytical method for radiopharmaceuticals is HPLC with an appropriate column, eluting buffer (or solvent), and detectors to identify both the chemical (such as UV detector, refractive index detector) and the radiation signals (high-sensitivity γ or β+ radiation detectors). TLC also provides a rapid and reliable method to determine the RCP and the radiochemical impurities. However, the HPLC method provides separation of different chemical species with much greater resolution than does TLC. Figures 13.1 and 13.2 show the typical RCP testing of [^{18}F]FDG and [^{11}C]PIB.

13.2.1.5 Chemical Purity

The chemical purity of a radiopharmaceutical may be defined as the absence of any undesirable chemical species in the final drug product formulation. Chemical purity testing involves an estimation of the amounts (masses) of all the undesirable chemical compounds in the final drug formulation. The chemical impurities may arise from the breakdown of a precursor or other chemicals in the reaction mixture before, after or during the reaction. The mass of chemical impurities may be significantly more than the mass of the desired chemical form and may interfere with the specific interaction of the radiopharmaceutical or may cause undesirable pharmacological side effects.
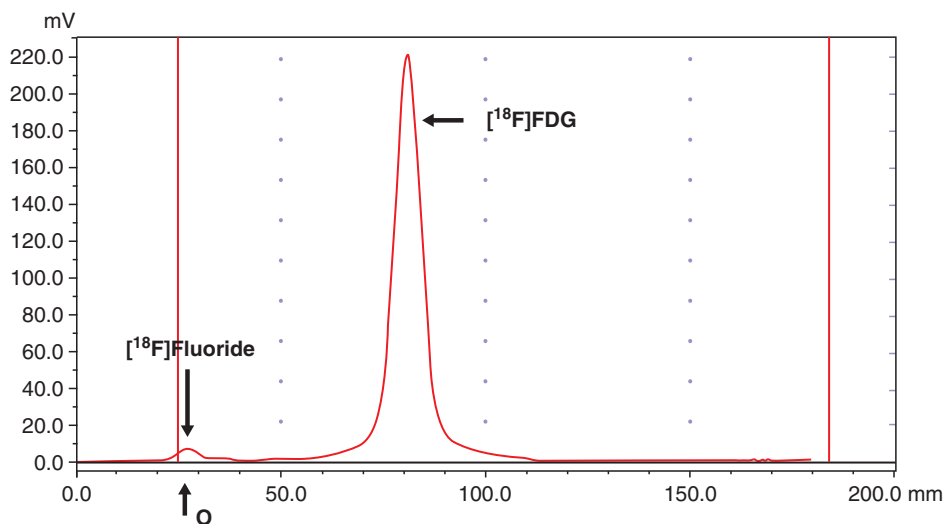
Fig. 13.1 Radiochemical purity testing of [^{18}F]FDG based on TLC using SG, and acetonitrile and water (95:5). The free [^{18}F] fluoride stays at the origin (O), while the migration of [^{18}F]FDG is compared to that of cold FDG standard (R_f = 0.3–0.4)
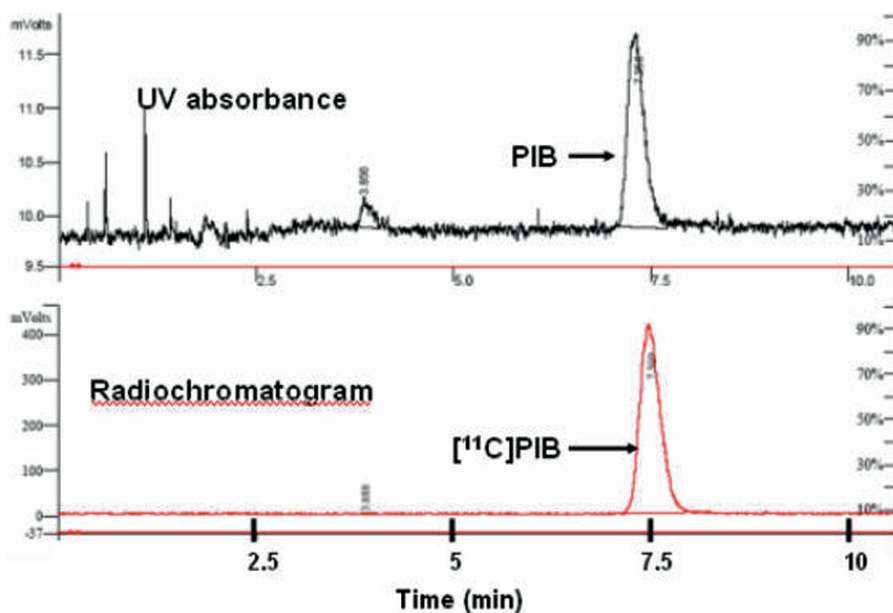
Fig. 13.2 Radiochemical purity testing of [^{11}C]PIB based on HPLC using Phenomenex Prodigy 5μ ODS$_3$ column, and 50 mM of phosphate and acetonitrile (60:40) as an eluant. [^{11}C]PIB is mixed with a standard PIB in order to identify PIB by UV absorbance

In the final [^{18}F]FDG drug formulation, the only desirable chemical is 2-fluorodeoxy-D-glucose or FDG. However, some of the FDG will be labeled with ^{18}F while a fraction of the FDG molecules could be labeled with stable ^{19}F. Nonradioactive FDG is not a chemical impurity, but will decrease the SA of [^{18}F] FDG.

Some of the important chemical impurities in [^{18}F] FDG drug formulation include [^{19}F]FDM, chloro-

deoxy-glucose (CDG), D-glucose, and aminopolyether (kryptofix 222).

To determine the chemical impurities quantitatively, HPLC is the best analytical technique. TLC with special staining techniques may also be used for the semiquantitative estimation of the levels of impurities. Kryptofix is usually determined based on a color reaction on a SG-TLC plate using an acidic iodoplatinic acid reagent. The intensity of the color depends on the kryptofix

level. The color in the test sample is compared to a known concentration of standard kryptofix.

13.2.1.6 Residual Solvents

Since most of the molecular imaging probes are organic molecules, it is necessary to use organic solvents (absolute alcohol, ether, acetonitrile, etc.) during the chemical synthesis. After the synthesis and final purification, the final drug formulation may contain small amounts of organic solvents, known as *residual solvents*, which can also be regarded as chemical impurities. Gas chromatography using a DS–PS wax column and a flash ionization (FI) detector is the most common technique for the estimation of the residual solvent concentration, as shown in Fig. 13.3.

The USP recommends acceptable levels for organic solvents in the final drug formulations, based on LD_{50} values. The USP specified limit is no more than 0.5% dehydrated alcohol, 0.5% ether, and 0.04% acetonitrile.

13.2.1.7 Specific Activity

SA is one of the most important quality control criteria for RMIPs. It is a measure of the amount of radioactivity

Fig. 13.3 Estimation of residual solvents using gas chromatography (GC): (**a**). standards; acetonitrile 0.01% and ethanol 0.04%. (**b**). Chromatogram of FDG solution

per unit mass of the radiopharmaceutical and is usually expressed as mCi/μmole, GBq or TBq/μmole. For certain radiopharmaceuticals, such as [^{18}F]FDG, radiolabeled amino acids and fatty acids, SA determination is not crucial because these radiotracers do have natural physiologically abundant levels of nonradioactive counterparts in vivo, especially in circulation. However, for receptor-binding radiotracers, radiolabeled mAbs, and peptide hormone analogs, relatively high SA is absolutely necessary. Chemical contaminants which have similar biological activity and compete with the radiotracer for binding to the specific receptors or antigen, will reduce the *apparent or effective SA*, in vivo.

The concentration of radioactivity of the radiopharmaceutical can be easily determined, as described above. The concentration of the radiopharmaceutical in terms of mass/mL (μmoles/mL) should also be determined. For most organic radiopharmaceuticals, the mass (mg or μg) can be determined based on analytical HPLC and a known concentration of an ultra pure standard. Knowing the activity/mL and mass/mL, SA can then be calculated, and expressed as mCi or MBq/μmole. When appropriate, the term, "No Carrier Added" (NCA) should be specified.

13.2.1.8 pH

All radiopharmaceutical formulations, intended for intravenous administration, should maintain relatively stable pH (a measure of hydrogen ion concentration) over an optimal range, preferably very close to the pH of blood. In general, the pH values in the range of 4.5–7.5 are quite acceptable since blood has very good buffering capacity.

Since the pH of the final drug formulation may likely vary from batch to batch, it is important that the actual pH of the final drug formulation is tested using pH paper or, if necessary, a suitably calibrated pH measuring device. The color change, following exposure to the test solution, is compared to that of known standards of the buffer solution of appropriate pH values.

13.2.1.9 Osmolality or Isotonicity

The final drug formulation of a radiopharmaceutical must be *isotonic*, meaning that the ionic strength of the drug formulation is the same or similar to that of blood. Most radiopharmaceutical preparations are generally formulated using physiological saline or a phosphate
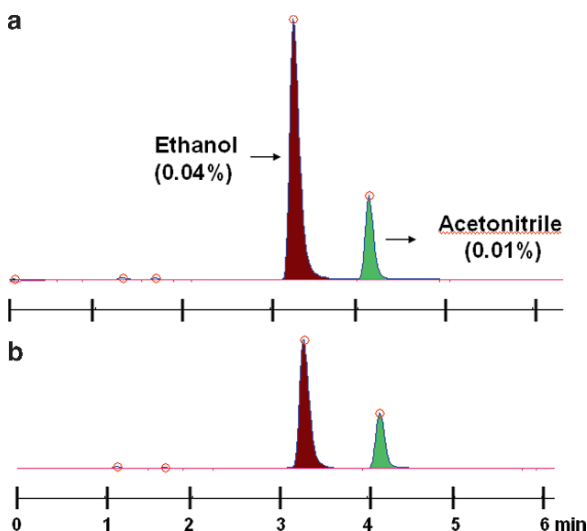
buffered saline (PBS) solution. If the drug formulation is prepared using some other physiologically acceptable buffer solution, such as sodium citrate and sodium acetate buffer, the ionic strength should be adjusted to maintain isotonicity of the final drug product formulation.

Routine testing of isotonicity for every batch preparation of the drug formulation may not be necessary. However, periodic testing on the decayed (nonradioactive) drug formulation may be appropriate and necessary. Osmolality (ionic strength) can be measured by the freezing point technique using an Osmometer. For any given batch, the osmolality can be in the range 285–356 mOsm Kg^{-1}.

13.2.1.10   Stability

The PET drug product should remain stable while it is being stored. Appropriate parameters should be evaluated to establish and document the stability of a PET drug product under proposed storage conditions. Examples of stability parameters include radiochemical identity and purity, appearance, pH, and SA. Appropriate stability-indicating methods that can distinguish degradation products and impurities should be used. Stability testing of the PET drug product should be performed at the highest radioactive concentration, and the whole batch volume in the intended container/closure should be stored. On the basis of the stability data, the expiration of the radiopharmaceutical can be determined.

13.2.2   Biological Tests

The USP requires that radiopharmaceuticals intended for intravenous administration must be tested to ensure that the final drug product is a sterile solution and that the *bacterial endotoxin* (*pyrogen*) concentration is within acceptable limits. The quality control tests on the finished drug product (Fludeoxyglucose F 18 injection) will be performed as described in the USP General chapter <823>, "Radiopharmaceuticals for positron-emission tomography – Compounding."

13.2.2.1   Bacterial Endotoxin Test

The USP *Bacterial Endotoxins Test* (BET) or *pyrogenicity testing* should be performed for a sterile PET drug intended for injection. USP specifies that no more

than 175/*V* endotoxin units (EU)/mL of the final drug product solution, in which V is the maximum administered dose in mL, at the expiration time.

Pyrogens are fever-producing materials – that most often originate from gram-negative bacterial cell walls – referred to as bacterial endotoxin and that are readily detected by a *gel-clot technique* based on *Limulus amebocyte lysate* (*LAL*). The LAL gel-clot testing is a semiquantitative method that is well suited for batch release testing of PET radiopharmaceuticals.

The BET specified in the USP<85> uses a gel-clot technique for the determination of levels of EU and requires a 60-min incubation time. The USP<283> indicates that an in-process 20-min endotoxin limit test can be used for PET drugs with a half-life >20 min; however, the standard 60-min BET must be performed and completed. If necessary, the PET drug product can be distributed, provided BET is initiated. The BET results should meet the acceptance criteria before administering the product to humans.

13.2.2.2   Membrane Filter Integrity

In order to ensure the sterility of the final drug product, most PET radiopharmaceuticals are filtered using a 0.22 μ membrane filter (such as Millipore) in the final step of the synthesis procedure. The sterility test of the final drug product must be performed using microbiological media as specified in USP. Since the sterility test is completed retrospectively, the sterility of the final drug product is indirectly assessed based on the membrane filter integrity (bubble point test) of the filter used to sterilize a single batch of radiopharmaceutical drug product.

The most widely used nondestructive integrity test is the bubble point test. The principle of this test is based on the fact that liquid is held in the pores of the filter by surface tension and capillary forces. The minimum pressure required to the force liquid out of the pores is a measure of the pore diameter. The bubble point test detects minor filter defects and out-of-size pores and correlates with the bacteria passage test. Prior to using each lot of filters and performing the bubble test, it may be necessary to validate the manufacturer's specifications of filter integrity by using similar conditions and aqueous media specified by the manufacturer. These values may differ depending on the nature of the aqueous media, buffer strength and pH. For each lot of membranes, the minimum acceptable bubble point pressure (P_m) is determined first. With the membrane filter used in the synthesis

of radiopharmaceutical, the pressure at which bubbles appeared in water (P_t) is determined. The membrane filter integrity test results must show that $P_t \geq P_m$.

13.2.2.3 Sterility

A sterility test must be started within 24 h of the final manufacture of the drug product and after an appropriate decay period. The USP<71> provides information about the incubation media and incubation conditions. Sterility tests are designed to determine the presence of mesophilic bacteria and fungi in solutions. The standard USP sterility test specifies using both *soybean–casein digest broth* (SCD) and *fluid thioglycollate media* (FTM). SCD is incubated at 20–25°C and FTM at 30–35°C. SCDB normally grows aerobic bacteria and fungi, while FTM normally grows aerobic and anaerobic bacteria. Both media are normally incubated for 14 days.

The sterility testing must be conducted in a controlled area, such as a laminar airflow workbench (LAFW) with clean-room apparel. Aseptic techniques should be used for the sterility testing. The greatest risk of false-positive results arises in the sampling and transfer of the test aliquot from the vial to the media. It may be convenient to apply direct inoculation into the commercial media. The media must be observed periodically on days 3, 7, and 14 after inoculation, but it is prudent to observe the media more often during the first week of incubation.

13.3 Quality Assurance

On the basis of the USP and FDA CMC guidelines, the regulatory specifications, procedures, and testing schedules for [18F]Fluorodeoxyglucose (FDG) final drug formulation is summarized in Table 13.1.

Similar QA and regulatory specifications have been developed for every PET and SPECT radiopharmaceutical intended for human use.

Table 13.1 FDG: Quality assurance

Test	Acceptance criteria	Procedures	Testing schedule
Appearance	Colorless and free from particles	Visual inspection	Completed prior to the release of drug
Radionuclidic identity	$T_{1/2}$ = 105–115.0 m	Measure $T_{1/2}$	Same as above
Radionuclidic purity	511 ± 5% KeV 99.5% of photons	Gamma spectrocopy	Same as above
Radioassay	10 – 200 mCi/mL at EOS	Measure using dose calibrator	Same as above
Radiochemical identity	The R_f of [18F]FDG = R_f of Std FDG (±10%)	TLC-SG using acetonitrile/ water (95:5)	Same as above
Radiochemical purity	NLT[a] 90.0% [18F]FDG	TLC-SG and solvent (95:5, Acetonitrile: water)	Same as above
Radiochemical impurities	NMT[b] 5.0% [18F]fluoride	Same as above	Same as above
pH	Range: 4.5–7.5	pH paper	Same as above
Kryptofix 222	Color intensity of drug product < the color of kryptofix 222 (50 μg/ml)	TLC-SG	Same as above
Residual solvents[d]		Gas chromatography, with flame-ionization detector	Same as above
Acetonitrile	1. NMT[b] 0.04% (w/v)		
Diethyl ether	2. NMT[b] 0.5% (w/v)		
Ethanol	3. NMT[b] 0.5% (w/v)		
Bacterial endotoxins	NMT 175/V EU/V^c	USP<>	Same as above
Membrane Filter Integrity	$P_t \geq P_m$	Bubble point test	Same as above
Sterility testing	Sterile	USP<>	Start test within 24 h
Osmolality	Isotonic (specify range) Range: 250–350 mOsm	USP	Calculate/Validate
CIDG	NMT[b] 1.0 mg/V^c	HPLC method	Initial validation/ annual testing

[a]*NLT* No less than; [b]*NMT* No more than; [c]V = Total volume of the batch of fludeoxyglucose F 18 injection produced; [d]Acceptance criteria should assure that the amount of each residual solvent impurity administered to a human subject is within the limits provided in the ICH Guidance on Impurities: residual solvents (Federal Register 1997)

References

Current Good Manufacturing Practice (CGMP) for PET drug products, Guidance (draft), prepared by the PET Steering Committee, of at U.S. Department of Health and Human Services, Food and Drug Administration, Center for Drug Evaluation and Research (CDER), March 2002

Federal Register (1997) December 24, 62(247):67377–67388

FDA (2000) Fludeoxy F 18 injection, CMC section. In: Sample Formats. FDA 2000:24–26

Guidance for Industry PET Drug Applications-Content and Format for NDAs and ANDAs http://www.fda.gov/cder/guidance/index.htm or http://www.fda.gov/cder/regulatory/pet/default.htm

Huang JC (2002) Comparison of various requirements of the quality assurance procedures for ^{18}F-FDG injection. J Nucl Med 43:1495–1506

Nakao R, Ito TT, Yamaguchi M (2005) Improved quality control of [^{18}F]FDG by HPLC with UV detection. Nucl Med Biol 32:907–912

Positron emission tomography (1997) Food and Drug Administration Modernization Act of 1997, Pub L No 105–115 §121

Saha GB (2004) Fundamentals of nuclear pharmacy. Springer, New York

Stocklin G, Pike VW (1993) Radiopharmaceuticals for positron emission tomography. Kluwer, The Netherlands

USP<71> (2003) Sterility Tests. USP 26 NF 21, 2003, 2011–2016

USP<85> (2003) Bacterial Endotoxins Test. USP 26 NF 21, 2023–2026

USP<823> (2000) Radiopharmaceuticals for Positron Emission Tomography – Compounding. USP 24 NF 19. or USP 26 NF 21, 2003, 2213–2216

USP<1015> (2000) Automated Radiochemical Synthesis Apparatus. USP 24 NF 19. 1412, or USP 26 NF 21, 2003, 2235–2236

U.S. Pharmacopeia.<621> (2000) Chromatography. USP 24 NF 19. 1414 or USP 26 N21, 2003, 2126–2138

USP<821> (2003) Radioactivity. USP 24 NF 19, 2000. 1416, or USP 26 NF 21, 2205–2212

USP<1225> (2000) Validation of Compendial Methods. USP 24 NF 19 or USP 26 NF 21, 2003, 2439–2442

Pharmacokinetics and Modeling

14

Everything that can be counted does not necessarily count; everything that counts cannot necessarily be counted

Albert Einstein

14.1 Quantitation

Molecular imaging of radiotracer distribution by PET or SPECT following intravenous injection shows the pattern of relative uptake of radioactivity in different organs and also in different regions within any particular organ of interest. These imaging studies permit measurement of the time course of uptake and clearance of specific tracers. Quantitative measurement of the local radiotracer activity is essential to assess the local physiological function quantitatively. Semi quantitative methods have been developed for the interpretation of routine clinical diagnostic studies. However, absolute measurement of physiologic parameters generally requires accurate measurement of radioactivity concentrations in the arterial blood and in a specific region of interest (ROI) or volume of interest (VOI) in a tissue, in order to extract quantitative information based on tracer kinetic or compartmental modeling techniques.

In PET, the count rate per voxel in the reconstructed tomographic image, in principle, is proportional to the activity concentration in a given ROI. Since the attenuation and scatter corrections are not reliable in SPECT, the count rate per voxel in a SPECT image does not necessarily reflect the true activity concentration. As a result, true quantitation with SPECT technique, is not practically feasible at this time. Some of the basic principles and concepts involved in quantitative methods will be described briefly here with specific examples.

14.1.1 Standardized Uptake Value

To make the PET images quantitative, the PET camera is first calibrated using a cylindrical phantom with known radioactivity concentration (Bq mL^{-1}). The count rate per voxel (cps or cpm) is then divided by the measured system calibration factor, CF [(Bq cc^{-1})/(cps voxel^{-1})], to convert cps in a given ROI to the corresponding activity concentration units, C_t (Bq cc^{-1}).

It is common practice in animal studies to express the biodistribution of radiotracers using the parameter, the percent injected dose per gram of tissue (%ID/g of tissue), which is calculated using the following equation.

$$\%ID/g = \frac{\text{Activity in a gram of tissue } (C_t)}{\text{Injected dose}} \times 100 \quad (14.1)$$

The %ID/g parameter, however, does not take into consideration the total body mass (weight) of a patient. The standardized uptake value (SUV) is a semi quantitative unit developed in order to include the total body weight of a patient (Zasadny and Wahl 1993; Huang 2000; Acton et al. 2004).

$$SUV = \frac{C_t \text{ in a ROI } (MBq/cc)}{\text{Injected dose } (MBq)} \times \text{Body wt } (g) \times 100 \quad (14.2)$$

The SUV value, therefore, is a unit-less number that normalizes the lesion uptake to the injected dose per unit of body weight. It has also been proposed that normalization of SUV based on body surface area (BSA) may

improve the accuracy of SUV, but method of normalization has not been routinely employed by most PET users. It is important to recognize that many factors (dose infiltration, serum glucose levels, total body fat, and the lesion volume) other than the metabolic status of the lesion can significantly affect the reliability of the SUV measurement in routine clinical practice. In addition, a number of factors, including regional blood flow, enzyme activity, active transport mechanisms, and binding site concentrations, may also contribute to the amount of radioactivity present in a given ROI at any given time. The SUV determination is regarded as semiquantitative since it does not take into account many of these biochemical processes and all the possible contributions to overall tissue activity levels.

14.2 Physiological Modeling

PET and SPECT permit sequential measurements of the radioactivity distribution in vivo following intravenous administration of a radiopharmaceutical at tracer levels. The measured time–activity distribution, however, is influenced by various factors, such as blood flow and clearance from plasma, and the number of specific and nonspecific binding sites, and their affinity. For a tracer to have any value in clinical practice, the uptake and distribution of the tracer must quantitatively and accurately reflect the concentration of available binding sites or the rate of some biochemical processes.

The extraction of quantitative values from dynamic PET imaging data requires the fitting of the data to a mathematical model that describes the uptake and retention of the tracer in tissue. Tracer kinetic physiologic modeling provides the link between activity levels measured in a specific ROI in the functional scan and the physiologic parameters associated with the particular function being studied. The kinetic models can be classified as noncompartmental, compartmental or distributive. With most molecular imaging radiopharmaceuticals, compartmental models have become the model of choice. These models describe the transfer and behavior of the radiotracer between compartments, each of which represents distinct anatomic, physiologic, or biochemical space (capillaries, extracellular, intracellular and receptor bound) mathematically using a set of differential equations. It is important to realize that the segmentation of the physiologic processes into these compartments is only a simple approximation to derive quantitative parameters and may not necessarily reflect real in vivo biological processes.

14.2.1 Radiotracer Binding

The radiotracers or the radioligands used in molecular imaging studies are generally assumed to bind selectively to the target site receptor (R) or an enzyme (E). The simplest model is the bimolecular reaction (Michaelis and Menten 1913), describing the kinetics

$$[L] \;+\; [R] \quad \underset{k_{off}}{\overset{k_{on}}{\rightleftharpoons}} \quad [RL] \qquad (14.3)$$

At equilibrium,
$$k_{on}\,[L]\,[R] \quad \rightleftharpoons \quad K_{off}\,[RL] \qquad (14.4)$$
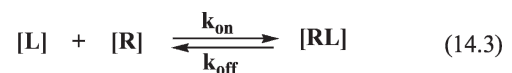
The equilibrium constant,
$$K_D \;=\; K_{off}/K_{on} \qquad (14.5)$$

The total number of receptors,
$$B_{max} = [R] + [RL] \qquad (14.6)$$

The concentration of bound receptors
$$[RL] \;=\; \frac{B_{max}\,[L]}{[L] \;+\; K_D} \qquad (14.7)$$

The Binding Potential (BP)
$$BP \;=\; \frac{B_{max}}{K_D} \;=\; \frac{[RL]}{[L]} \;=\; \frac{B}{F} \qquad (14.8)$$

Fig. 14.1 Basic equations of ligand (L) and receptor (R) binding or interaction

of the radioligand (L) binding with a specific receptor (R) or an enzyme (E) to form a complex, LR or LE. According to the law of mass action (14.3), the rate of the reaction will proceed in proportion to the product of concentration of the reactants. Several equations pertinent to ligand–receptor interactions and their relationships are summarized in Fig. 14.1.

14.2.1.1 Binding Potential

In PET and SPECT studies with high SA radiotracers (L^*), the concentration of the bound receptors, $[RL^*]$ is very small (<5%) and the receptor concentration, $[R]$ is approximately equal to B_{max}. Under these conditions, the binding potential (BP) is defined as B_{max}/K_d and is equal to the ratio of the bound radioligand concentration to the free radioligand concentration (B/F) at equilibrium (14.8). BP is proportional to B_{max} if K_d can be regarded as a constant (Ichise et al. 2001; Laruelle et al. 2003).

14.2.1.2 Affinity

The affinity of a ligand for a receptor refers to the binding strength and can be expressed as a K_D or K_i value, which can be calculated from the measured IC_{50} value as shown in Fig. 14.2.
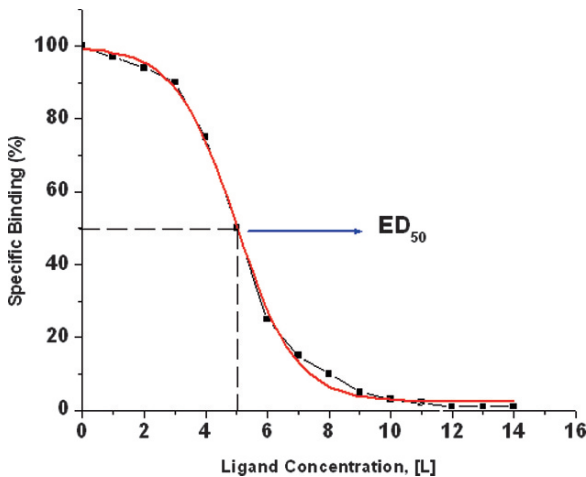
In a typical "saturation" radioligand binding assay experiment in vitro, increasing amounts of a radioligand are added to a fixed concentration of receptors, and the amount of radiotracer bound, B or $[RL]$ is measured as a function of $[L]$. Nonlinear regression analysis can be used to fit the data to the equation 15.7 in order to estimate both, B_{max} and K_D (Fig. 14.3).

The IC_{50} value is also determined in vitro by measuring the competitive effect of different concentrations of the ligand of interest (10^{-12}–10^{-4} M) on the binding of a reference radioligand with known affinity and concentration to a preparation of cells or cell membranes known to express specific receptors for the ligand under investigation.

In order to obtain high contrast images, the radiotracer must have high affinity (low K_D) for its receptor. The required affinity, however, depends on the receptor concentration, B_{max}, in a given ROI. Typically, for radio labeled antagonists, high affinity in the nanomolar range is needed to obtain high contrast images.

In order to image the distribution of one specific receptor subtype, the radioligand should preferably bind only to that specific receptor with high affinity. Most ligands, i.e., certain radioligands, may have affinity for many receptor subtypes or even different receptors. Therefore, in addition to high affinity, radioligands should also have *selectivity*, which is defined as the ratio of affinity of a ligand for the receptor of interest to the affinity for each of the other receptor types.

Fig. 14.2 Saturation of specific binding sites by carrier-added ligand concentration, $[L]$. ED_{50} can be defined as the $[L]$, which reduces the specific binding signal by 50%. The specific binding can be determined ex vivo studies, or in vivo using MicroPET or MicroSPECT imaging
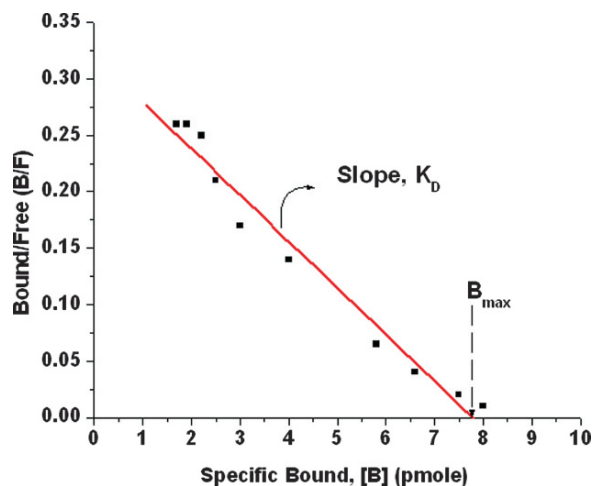
Fig. 14.3 A Scatchard plot of the ligand (L)-receptor (R) binding data in order to estimate receptor concentration (B_{max}) and affinity (K_D)

14.2.2 Tracer Kinetics

Following intravenous administration, the radiotracer is cleared from circulation rapidly and enters a tissue compartment in which the tracer may bind to an enzyme, a specific receptor, or even undergo metabolism and subsequent intracellular trapping. For most of the radiotracers, the kinetics can be described using a maximum of three different compartments (Fig. 14.4). The first compartment is the arterial blood, in which the radiotracer may be present either as "free" species or exhibit plasma protein binding (PPB). From the arterial blood, the radiotracer passes through a second compartment (extracellular or intracellular fluid), also known as a free compartment. The third compartment is the region where the tracer is bound to either an enzyme or a specific receptor, or metabolically trapped.

In tracer kinetic modeling, certain fundamental or physiologically reasonable assumptions are usually made to minimize the number of kinetic parameters needed to improve the fit to the measured data (from imaging studies) to the physiological model or to simplify the imaging and analysis protocols. These simplifications, however, must be physically meaningful and must be validated against the complete model (Ichise et al. 2001; Laruelle et al. 2003).

Although most physiological and biological processes are nonlinear, the behavior (transport and or chemical reactions) of radiotracers in vivo is assumed to be linear or approximately linear due to the fact that the mass of the tracer is very small. First-order kinetics can describe the exchange of a radioligand between compartments.
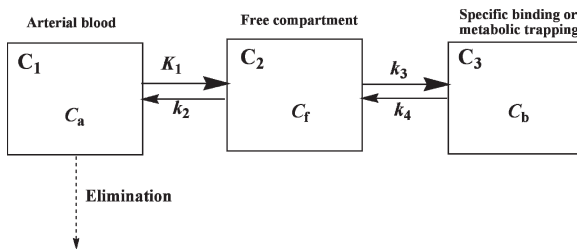
Fig. 14.4 Two and three compartment models used to describe radiotracer kinetics in vivo. Different terms used to describe the movement of radiotracer in different compartments are listed in Table 14.1

- In general, the system under study is effective in a *steady state* and the administration of the radioligand does not perturb the steady state.
- Since arterial blood delivers radioligand to all tissues, the input function is always the blood time–activity concentration (TAC). Also, the radioligand can pass back and forth freely from the arterial plasma to the free compartment.
- For most radioligands, the nonspecific-binding (NSB) compartment is assumed to be in rapid equilibrium with the free compartment and the two compartments are treated as a single compartment.

A number of parameters used in the modeling equations below and the terms used in the description of 3-compartmental model are defined in Table 14.1

14.2.2.1 Two-Compartment Model

This model generally represents the movement of the radiotracer between the blood pool (C_1) into the tissue pool (C_2), as shown in Fig. 14.4. The change of tissue concentration of the radiotracer (C_t) over time is described by the following differential equation.

$$\frac{dC_t}{dt} = K_1 C_a - k_2 C_t \qquad (14.9)$$

In the above equation, K_1 describes the speed of transfer of the ligand from the blood to the tissue and depends on the concentration of the tracer in the plasma $C_a(t)$, and on the properties of the transport process (e.g., the activity of carrier enzyme). Because the tracer dose does not saturate the transport process, the transfer from the blood to the tissue is simply given by the product of $K_1 C_a(t)$. Similarly, the transport from the tissue to the blood is given by the product of $k_2 C_t(t)$.

This two-compartment (or one tissue compartment) model is generally utilized with some minor modifications in the measurement of radiotracer transport across the BBB.

The measurement rCBF is one of the major clinical applications of PET using freely diffusible radiotracers, such as [^{15}O]water. With diffusible radiotracers, the initial tracer activity in the brain is directly related to the blood flow (F) (Lassen et al. 1978; Raichle et al. 1983). Free diffusion of the tracer also leads to

Table 14.1 Important parameters used in physiological modeling

Parameter	Description	Units
C_a	Tracer concentration in arterial blood or plasma	Bq mL^{-1}
C_f	Free tracer concentration in tissue	Bq mL^{-1}
C_t	Concentration of free tracer in tissue	Bq mL^{-1}
C_b	Concentration of tracer specifically bound to receptors, enzyme, or metabolically trapped	Bq mL^{-1}
K_1	Kinetic constant for transfer of tracer from blood to tissue ($C_a \rightarrow C_f$)	mL min^{-1} g^{-1}
k_2	Kinetic constant for transfer of tracer from tissue to blood ($C_f \rightarrow C_a$)	L min^{-1}
k_3	Kinetic constant for conversion of free tracer in tissue to specific binding or metabolic trapping ($C_f \rightarrow C_b$)	L min^{-1}
k_4	Kinetic constant for the dissociation of specifically bound or metabolically trapped tracer to free tracer in tissue ($C_b \rightarrow C_f$)	L min^{-1}
DV	Distribution volume	mL g^{-1} of tissue
B_{max}	Maximum receptor binding capacity	Mol g^{-1}
K_D	Equilibrium dissociation constant	
BP	Binding potential	mL g^{-1}
K_M	Michaelis–Menten constant (substrate concentration at half-maximum velocity)	
λ	Tissue/blood partition coefficient	
E	Tracer extraction fraction from blood (capillaries) into tissue	Unit less parameter
P	Capillary permeability for the tracer	cm min^{-1}
S	Capillary surface area	cm^2 g^{-1}

equilibration of C_t with that of C_v (concentration in out flowing venous blood). Thus, C_t is the same as $C_v \lambda$, where λ is the tissue/blood partition coefficient (synonymous with distribution volume) of the radiotracer. As a result, the equation 14.9 is modified to replace K_1 with F and k_2 with F/λ, as shown below.

$$\frac{dC_t}{dt} = FC_a - \frac{F}{\lambda}C_t \qquad (14.10)$$

For radiotracers that are not entirely freely diffusible, the first pass extraction from the blood to the tissue is important. The transfer from the blood to the brain (K_1) is determined by the product of the blood flow (F) and tracer extraction fraction (E). The relationship between E, S, P, and F is given by the Renkin–Crone equation (Crone 1964).

$$E = 1 - e^{-\frac{PS}{F}} \qquad (14.11)$$

When the tracer arrives in the capillaries, some fraction of it is extracted into the tissue across the capillary walls. This unidirectional extraction fraction (E) is a unitless parameter and depends on the capillary permeability (P) for the tracer, total available capillary surface area (S), and the blood flow (F). The extraction

fraction, E will increase if S or P increases, but E will decrease if blood flow, F increases.

14.2.2.2 Three-Compartment Model

Many radiotracers undergo metabolism (FDG, FDOPA, FLT) or are bound to specific receptors in the brain or some other tissues (Raclopride, Flumazenil, FET, Ga-DOTATOC). For most of the molecular imaging radiotracers, metabolism and specific intracellular binding are the physiological processes of interest. The dynamic behavior of many of these radiotracers in vivo is assumed to follow a standard three-compartment kinetic model (Fig. 14.4) with a single arterial input function and two tissue compartments.

Compartment C_1 represents the arterial concentration of the free, unmetabolized tracer. The passage into the tissue is considered to appear either through passive diffusion in the presence of a concentration gradient or through an active transport mechanism. Compartment C_2 is the first tissue compartment and represents an extra vascular pool of the tracer in the tissue; this tracer is available for binding or further reaction. Compartment C_3 is the concentration of the

tracer that is specifically bound to the target molecule (C_b) or has undergone some chemical reaction or metabolism (C_m). The transfer of the radiotracer in these three compartments is described by the following two differential equations.

$$\frac{dC_2}{dt} = K_1 C_a - (k_2 + k_3)C_2 + k_4 C_3 \quad (14.12)$$

$$\frac{dC_3}{dt} = k_3 C_2 - k_4 C_3 \quad (14.13)$$

For radiotracers with irreversible metabolism or metabolic trapping (such as FDG and FLT), k_4 is negligibly small, and the total tissue tracer activity, $C_f(t)$ can be split into two components, the reversible free tracer, $C_f(t)$ and the trapped metabolized tracer, $C_m(t)$.

FDG Metabolism: Measurement of MRglc

The technique of measuring MRglc using FDG metabolic intracellular trapping is based on the autoradiographic DG technique (Sokoloff et al. 1977; Phelps et al. 1979). It is important to understand that the transport of FDG and the enzyme mediated reactions are distinct from those for glucose. In order to estimate MRglc, however, the competitive kinetics between FDG and glucose must be taken into account.

In a 3-compartmental model (Fig. 14.4), C_1 represents FDG in plasma, C_2 represents free FDG in tissue, and C_3 represents FDG-6-phosphate. The basis for using FDG as a tracer to measure FDGglc is because FDG-6-phosphate is not a substrate for further metabolism, unlike glucose-6-phosphate. As a result, with FDG, only the transport and phosphorylation steps are incorporated into this model, and not the remaining steps as in glycolysis. To calculate MRglc, however, measurement of the plasma glucose concentration (C_a^o) is needed to estimate intracellular glucose levels. A *lumped constant* (LC) was introduced to correct the differences in the in vivo behavior of FDG and glucose. The actual value of LC may vary (0.4–0.8) depending on the tissue (brain, myocardium, tumor) or plasma glucose levels. Based on the measured rate constants for FDG, LC, and (C_a^o) the MRglc can be calculated, at steady state, using the following equations.

$$\text{MRglc} = \left(\frac{K_1\, k_3}{k_2 + k_3} \right) \frac{C_a^0}{\text{LC}} \quad (14.14)$$

$$\text{MRglc} = K^* \frac{C_a^0}{\text{LC}} \quad (14.15)$$

Since arterial blood sampling is not practical in routine clinical applications, several different approaches have been developed to measure MRglc (Ichise et al. 2001; Mankoff et al. 2003; Acton et al. 2004). The Patlak plot is one approach that is based on a graphical method, which estimates the influx rate constant, K_1^* using only the time–activity data of dynamic FDG-PET images (Patlak et al. 1983).

Receptor Binding

The dynamics of receptor binding studied by PET and SPECT imaging techniques can be analyzed using the 3-compartmental model (Fig. 14.4). In this model, C_a represents the unmetabolized free radioligand in the blood, C_f (or C_2) represents both the free, and the nonspecifically bound radioligand, and finally C_b represents only the receptor bound radioligand. The transfer of receptor binding radioligand in a 3-compartment model can be described using the differential equations, shown above (14.13 and 14.14), in which C_2 represents the free (nonspecifically bound) radioligand, while C_3 represents C_b, the receptor bound radioligand. The rate constant K_1, k_2, k_3 and k_4 are defined as delivery, washout, forward receptor–ligand reaction, and reverse receptor–ligand reaction, respectively. Many of the neuroreceptor ligands are lipophilic and may have nonspecific protein binding in blood or in tissue. Therefore, the fraction of the free ligand in the plasma (f_1) and the fraction of the free ligand in the tissue (f_2) that is available for specific receptor binding are important in the calculations.

Unlike the radiotracers that undergo metabolism, with the receptor binding radioligands, SA of the radioligand is very important. Since an unlabeled ("cold") ligand is present in the preparations of many radioligands, the cold ligand competes for the specific receptor binding sites with the labeled radioligand. Therefore, k_3 is very much dependent on the SA of the radioligand, as shown below.

$$k_3(t) = k_{on}\, f_2 \left(B_{max} - \frac{C_b}{\text{SA}} \right) \quad (14.16)$$

In the above equation, if the SA is high, then C_b/SA (occupancy of receptors by the labeled compound) is negligibly small, and $k_3 \approx k_{on} f_2 . B_{max}$. If the receptor

occupancy by the radioligand cannot be disregarded, k_3 is not constant and the individual variables and constants must be determined separately by compartmental analysis, complicated curve-fitting, and analytic procedures. The clinical imaging studies would then require multiple radioligand injections with different SAs in order to determine the receptor density, B_{max} or affinity, K_D (Heiss and Herholz 2006).

In routine clinical PET or SPECT neuroreceptor imaging studies, with a single radioligand, one can only determine the BP, which is B_{max} relative to K_D. (BP = B_{max}/K_D). Also, to prevent saturation effects, the intravenously administered radioligand should preferably bind to only a small fraction (<5%) of all the available receptor sites. Therefore, it is essential that the radioligand must be prepared in high SA (>1.0 Ci μmole^{-1}) so that the total mass of the ligand administered (labeled + cold ligand) is minimal. Very high SA is especially desirable when the receptor concentration is low, or when the radio labeled agonists are used to image high affinity receptor states. Under these conditions, the BP is related to the kinetic constants, and can be estimated based on the following equation.

$$\text{BP} = \left(\frac{k_1 \, k_3}{k_2 \, k_4 \, f_1} \right) \quad (14.17)$$

Under equilibrium conditions,

$$\left(\frac{k_1 \, k_3}{k_2 \, k_4 \, f_1} \right) = \frac{C_b}{f_1 \, C_p} \quad (14.18)$$

The equilibrium *distribution volume* (DV or V) of compartment C_i is defined as the ratio of the tracer concentration in this compartment to the free arterial concentration ($f_1 C_f$) at equilibrium. With neuroreceptor imaging studies, we have

$$V_2 = \frac{C_t}{f_1 \, C_p}; V_3 = \frac{C_b}{f_1 \, C_p}; V_T = V_2 + V_3 \quad (14.19)$$

V_3 in the above equation, is the closest PET and SPECT equivalent of BP (BP = B/F), discussed under classical in vitro conditions, as shown in the equation 14.8. While C_3 represents the receptor bound activity (B), and the product $f_1 C_p$ represents the free ligand activity in plasma (L) (Ichise et al. 2001; Laruelle et al. 2003). BP was originally defined as a ratio of B_{max}/K_D (based on in vitro receptor binding studies) or k_3/k_4 (based on kinetic parameters) (Mintun et al. 1984).

The determination of BP based on the equation for V_3, described above, does require an arterial input func-

tion based on blood samples to determine (a) the free concentration of the radioligand (C_p) in plasma, and (b) the free fraction in plasma (f_1). At equilibrium, the free radioligand concentration in plasma ($f_1 C_p$) can be assumed to be equal to the free radioligand concentration in the tissue ($f_2 C_t$). Since a reliable f_1 measurement is difficult to obtain for many tracers, the term f_1 is often neglected and assumed to be a constant across subjects. This leads to a more practical definition of BP and V_3 denoted here BP and V'$_3$ (Laruelle et al. 2003)

$$\text{BP} = V_3 = \frac{C_b}{f_1 \, C_p} = \text{BP}' = V_3^{'} = \frac{C_b}{C_p} \quad (14.20)$$

In order to avoid blood samples, one can also assume that a reference tissue compartment ($C_{t, \, ref}$) represents both free radioligand and nonspecifically bound radioligand. Now, at equilibrium, the BP can be expressed relative to the free and nonspecific binding in a reference tissue region such as the cerebellum ($C_3/C_{t, \, ref}$) (Ichise et al. 2001; Laruelle et al. 2003), as shown below.

$$\text{BP}' = V_3^{'} = \frac{C_b}{C_p} = \text{BP}^* = V_3^{''} = \frac{V_3}{V_2} = \frac{C_b}{C_{t,ref}} \quad (14.21)$$

14.2.2.3 Graphical Analysis Methods

Graphical analysis (GA) techniques are simple methods for the analysis of data from radiotracer PET and SPECT imaging studies. In the initial evaluation of new radiotracers, they provide a visual way to distinguish between reversible and irreversible types of binding. They also provide considerable ease of computation compared to the optimization of individual model parameters in the solution of the differential equations generally used to describe the binding of radiotracers. GA methods are based on reformulating the model equations so that a linear relationship exists between the data and some quantitative parameter describing the nature of radio tracer binding or metabolism. These methods, however, do require an arterial input function although in some instances a reference region devoid of specific binding sites can be used in place of the plasma input function.

Patlak Plot

The theoretical foundation of GA for irreversible tracers was first developed and applied initially for the

estimation of MRglc from dynamic FDG-PET data (Patlak et al. 1983). The method is based on performing linear regression on the total tissue concentration (C_p^*) divided by the plasma concentration at time (C_T^*), as a function of the integral of the plasma concentration divided by the plasma concentration at time t (Table 14.1). The Patlak equation predicts that if one plots:

$$\frac{C_T^*(t)}{C_P^*(t)}(y-\text{axis}) \text{ vs. } \frac{\int_0^t C_P^*(t)dt}{C_P^*(t)}(x-\text{axis}) \quad (4.22)$$

The plot (Fig. 14.5), becomes linear over time with a slope of K^* (the influx constant) describing the transfer of the tracer from the plasma compartment to the irreversible compartment. It is important to note that K^* is dependent both on the binding or trapping rate and on the transport rate constants, K_1 and k_2. The Patlak plot is applicable for radiotracers that are metabolically trapped (FDG, FLT, FDOPA), but not for receptor binding radioligands.

Logan Plot

Based on the original work of Patlak, the GA for reversible receptor binding radiotracers was initially developed by Logan and further refinements were proposed

by Ichise (Logan et al. 1990; Ichise et al. 1999). In the Logan plot, the integral of the ROI activity over the current ROI activity in the receptor binding tissue is plotted versus the integral of the plasma activity over the current ROI in the receptor binding tissue.

$$\frac{\int_0^t C_t(\tau)d\tau}{C_t(t)}(y-\text{axis}) \text{ vs. } \frac{\int_0^t C_p(\tau)d\tau}{C_t(t)}(x-\text{axis}) \quad (14.23)$$

The plot (Fig. 14.6) eventually becomes linear with a slope equal to the total radioligand volume of the distribution (V_T). The time to reach linearity (equilibrium), however, depends on the number of compartments and the nature of the radioligand.

The GA can be extended to obtain a distribution volume ratio (DVR) directly without blood sampling by using a tissue reference region (T_{ref}) instead of the plasma integral. This can be done by rearranging the GA equation for the T_{ref} to solve for the plasma integral in terms of the T_{ref} radioactivity. Based on the Logan plots, DV_{rec} and DV_{ref} tissue regions can also be determined separately in order to calculate the distribution volume ratio (DVR). Then the BP is given by

$$BP^*\left(\frac{VD_{rec}}{VD_{ref}}\right) - 1 = DVR - 1 \quad (14.24)$$
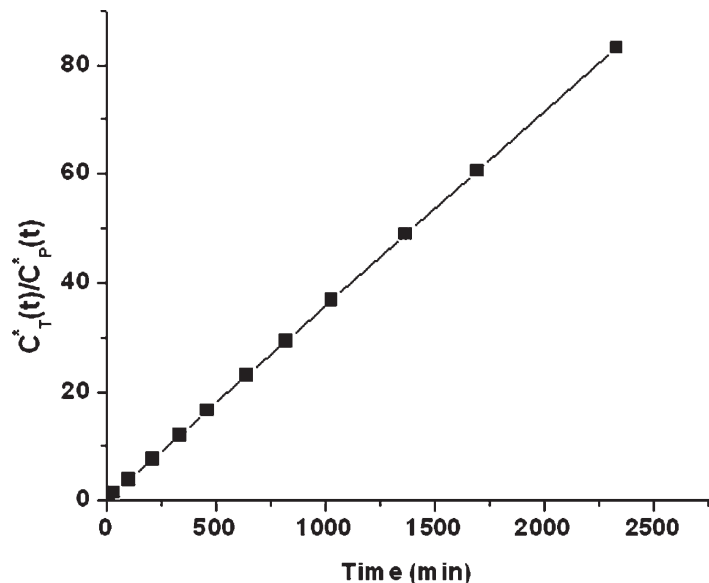
Fig. 14.5 The Patlak equation predicts that after some time $t > t^*$, a plot of total tissue concentration (C_p^*) divided by the plasma concentration at time (C_T^*) as a function of the integral of the plasma concentration divided by the plasma concentration at time t becomes linear. The plot based on data from Table 14.2 shows that the slope K^* is 0.036 (Gambhir 2004)

Table 14.2 Plasma and brain tissue time-activity data* following administration of [^{18}F]FDG

Time min	Plasma nCi/mL	Time min	Tissue nCi/mL	$\dfrac{C_T^*(t)}{C_P^*(t)}$	$\dfrac{\int_0^t C_P^*(t)dt}{C_P^*(t)}$
0.28	0.02	0.23	0.0	0	0
0.73	201	1.23	33	0.5	0.03
0.98	1150	2.23	96	2.3	0.13
1.48	1454	3.48	125	6.3	0.33
1.95	832	5.48	145	13	0.64
2.97	478	8.98	155	34	1.47
3.47	379	17.48	158	103	3.9
4.97	249	27.48	163	210	7.64
7.97	120	37.48	168	336	12.15
11.95	62	47.48	172	462	16.64
19.95	31	57.48	175	641	23.03
29.95	18	67.48	177	819	29.36
39.95	12	77.48	179	1028	36.82
59.97	7	87.48	180	1368	48.92
89.95	3.4	97.48	181	1694	60.55
119.95	1.8	112.48	182	2329	83.13

* The above simulated data is reproduced from Gambhir 2004

Fig. 14.6 Logan plots of graphical analysis: Time constant for start of the linear analysis for the basal ganglia is 25 min (**a**) and for the cerebellum is 15 min (**b**). The shorter time for the cerebellum is due to its more rapid kinetics
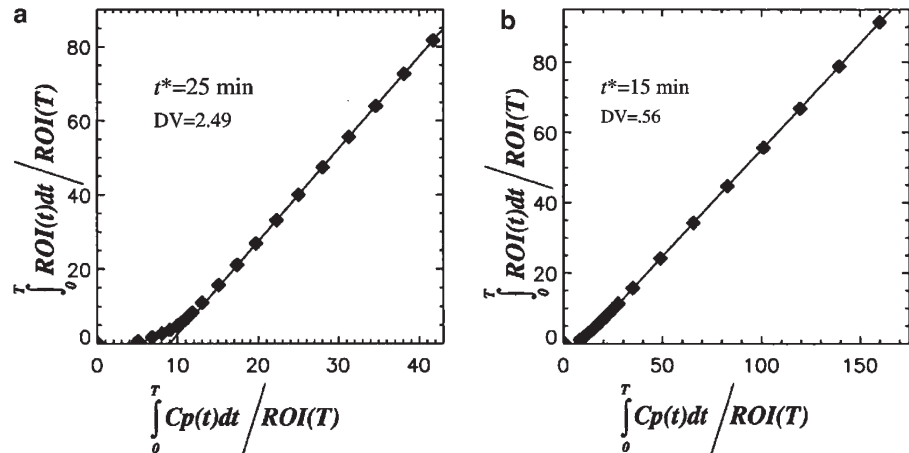
References

Acton PD, Zhuang H, Alavi A (2004) Quantification in PET. Radiol Clin N Am 42:1055–1062

Crone C (1964) Permeability of capillaries in various organs as determined by the indicator diffusion method. Acta Physiol Scand 58:292–305

Farde L, Eriksson L, Blomquist G, et al (1989) Kinetic analysis of central [^{11}C]raclopride binding to D2-dopamine receptors studied by PET: a comparison to the equilibrium analysis. J Cereb Blood Flow Metab 9:696–708

Gambhir SS (2004) Quantitative assay development for PET. In: Phelps ME (ed) PET molecular imaging and its biological applications. Springer, New York

Heiss W-D, Herholz K (2006) Brain receptor imaging. J Nucl Med 47:302–312

Herholz K, Herscovitch P, Heiss W-D (2004) NeuroPET: positron emission tomography in neuroscience and clinical neurology. Springer, Berlin, Germany

Huang S (2000) Anatomy of SUV: standardized uptake value. Nucl Med Biol 27:643–646

Huang SC, Barrio JR, Phelps ME (1986) Neuroreceptor assay with positron emission tomography: equilibrium versus

dynamic approaches. J Cereb Blood Flow Metab 6(5): 515–521

Ichise M, Fujita M, Seibyl J, et al (1999) Graphical analysis and simplified quantification of striatal and extrastriatal dopamine D2 receptor binding with [^{123}I]epidepride SPECT. J Nucl Med 40:1902

Ichise M, Meyer JH, Yonekura Y (2001) An introduction to PET and SPECT neuroreceptor quantification models. J Nucl Med 42(5):755–763

Krohn KA, Link JM (2003) Interpreting enzyme and receptor kinetics: keeping it simple, but not too simple. Nucl Med Biol 30:819–826

Lammertsma AA, Hume SP (1996) Simplified reference tissue model for PET receptor studies. Neuroimage 4(3 Pt 1): 153–158

Laruelle M, Slifstein M, Huang Y (2003) Relationships between radiotracer properties and image quality in molecular imaging of the brain with positron emission tomography. Mol Imaging Biol 5:363–375

Lassen NA, Ingvar DH, Skinhoj G (1978) Brain function and blood flow. Sci Am 239:62–71

Logan J (2000) Graphical analysis of PET data applied to reversible and irreversible tracers. Nucl Med Biol 27(7):661–670

Logan J (2003) A review of graphical methods for tracer studies and strategies to reduce bias. Nucl Med Biol 30:833–844

Logan J, Fowler J, Volkow N, et al (1990) Graphical analysis of reversible radioligand binding from time-activity measurements applied to [N-^{11}C-methyl]-(-)-cocaine PET studies in human subjects. J Cereb Blood Flow Metab 10:740–747

Logan J, Fowler JS, Volkow ND, et al (1996) Distribution volume ratios without blood sampling from graphical analysis of PET data. J Cereb Blood Flow Metab 16(5):834–840

Mankoff DA, Muzi M, Krohn KA (2003) Quantitative positron emission tomography imaging to measure tumor response to therapy: what is the best method? Molecular Imaging and Biology 5:281–285

Michaelis L, Menten ML (1913) Die Kinetik der Invertinwirkung. Biochem Z 49:1333

Mintun MA, Raichle ME, Kilbourn MR, et al (1984) A quantitative model for the in vivo assessment of drug binding sites with positron emission tomography. Ann Neurol 15:217–227

Patlak CS, Blasberg RG (1985) Graphical evaluation of blood-to-brain transfer constants from multiple-time uptake data. Generalizations. J Cereb Blood Flow Metab 5(4):584–590

Patlak CS, Blasberg RG, Fenstermacher JD (1983) Graphical evaluation of blood-to-brain transfer constants from multiple-time uptake data. J Cereb Blood Flow Metab 3(1):1–7

Phelps ME, Huang SC, Hoffman EJ, et al (1979) Tomographic measurement of local cerebral glucose metabolic rate in human with [^{18}F]2-fluoro-2-deoxyglucose. Validation of method. Ann Neurol 6:371–388

Raichle ME, Martin WR, et al (1983) Brain blood flow measured with intravenous [^{15}O]H$_2$O. II. Implementation and validation. J Nucl Med 24:790–798

Sokoloff L, Reivich M, Kennedy C, et al (1977) The [^{14}C]deoxyglucose method for the measurement of local cerebral glucose utilization: Theory, procedure, and normal values in the conscious and anesthetized albino rat. J Neurochem 28:897–916

Wong DF, Gjedde A, Wagner HN Jr (1986a) Quantification of neuroreceptors in the living human brain. I. Irreversible binding of ligands. J Cereb Blood Flow Metab 6:137–146

Wong DF, Gjedde A, Wagner HN Jr, et al (1986b) Quantification of neuroreceptors in the living human brain. II. Inhibition studies of receptor density and affinity. J Cereb Blood Flow Metab 6:147–153

Zasadny KR, Wahl RL (1993) Standardized uptake values of normal tissues at PET with 2-[fluorine-18]-fluoro-2-deoxy-D-glucose: variations with body weight and a method for correction. Radiology 189:847–850

Molecular Imaging in Oncology

<div style="text-align:right">

15

</div>

I believe there is no philosophical high-road in science, with epistemological signposts. No, we are in a jungle and find our way by trial and error, building our road behind us as we proceed.

Max Born

15.1 Cancer

Cancer is a collection of more than 100 different diseases and, for most cancers, the molecular characteristics have not been fully classified and there are no known or validated markers for early detection, treatment planning, or targeted therapy (Nass and Moses 2007). A long-standing goal of cancer research has been to identify the molecular mechanisms by which cancers develop, and then to design the diagnostic techniques (both imaging and nonimaging), to detect those molecular markers of cancers early, and finally to develop targeted specific therapeutic strategies for the treatment of cancer.

Traditional noninvasive imaging techniques, such as CT and MRI, are used primarily for imaging anatomical and morphological changes associated with an underlying pathology. These techniques, however, often lack the necessary sensitivity and specificity for early diagnoses of many cancers and for the detection of subcentimeter neoplasms and preneoplastic disease. In order to develop effective treatment modalities, especially, patient specific treatments, a more sensitive and specific detection of early malignancies is essential.

Radioisotope based molecular imaging techniques such as PET and SPECT have the potential to capture functional or phenotypic changes associated with abnormal molecular mechanisms by which cancers develop. It is an emerging field that aims to integrate patient specific and disease-specific molecular information with traditional anatomical or structural imaging readouts. Also, the hybrid or fusion-imaging of PET/CT improves the sensitivity and specificity of clinical FDG-PET imaging technique.

Highly "tumor-specific" and "tumor cell signal-specific" radiopharmaceuticals are essential to meet the growing demand of radioisotope based molecular imaging technology for various applications to manage the highly complex patient-specific tumor biology. Molecular imaging has made rapid strides that go beyond the clinical applications of FDG-PET, to probe multiple aspects of tumor biology. The real power of molecular imaging, however, goes beyond diagnosis by identifying different biologic processes in a tumor using tracers that characterize both genotypic and phenotypic signatures. Future clinical trials, with appropriate study design and regulatory guidance, will need to examine prospectively the use of imaging to help select cancer treatment. This is an important paradigm shift for PET, moving beyond detection in the direction of treatment selection (Rajendran and Mankoff 2007).

Numerous molecular imaging radiopharmaceuticals are in various stages of preclinical and clinical development and, hopefully, some of them will be approved in the near future for routine clinical use. In this chapter, the basic aspects of tumor biology and the design and development strategies of the most promising new radiopharmaceuticals is presented.

15.1.1 Tumor Pathology and Biology

15.1.1.1 Histopathology

Social control genes regulate cell division, proliferation, and differentiation under normal conditions. An uncontrolled growth of an abnormal cell will give raise to a

tumor or neoplasm that can either be *benign* or *malignant*. A tumor is regarded as cancer only if it is malignant. In the past, the general concept was that tumors of certain phenotypes arise from their normal cell counterpart. Recent evidence, however, indicates that most tumors arise from immature cells that can transform and acquire pheonotypic features similar to those of one or more normal cell types (Kumar 2003). *Transformation* is the process by which a normal cell becomes a cancer cell. Cancer cells are characterized by *anaplasia* or loss of *differentiation* and become more like embryonic undifferentiated cells.

The classification and typing of tumors is based on histopathological diagnosis (Ibrahim and Al-Maghrabi 2006). In general, a benign tumor is composed of well-differentiated cells that resemble their normal counterpart, remain localized and can not spread to other sites. Malignant tumors are neoplasms that extend into surrounding tissue, are capable of invading lymphatics and blood vessels, and can be transported into distant sites. Certain tumors may exhibit intermediate behavior, and are designated as "borderline or undermined," which represents low-grade malignant tumors. Currently, the malignant category is restricted to tumors that have metastatic properties. *Metastases* are tumor implants discontinuous with primary tumor. All tumors have two components; proliferating *neoplastic cells*, and supportive *stroma*, which is host derived and made up of connective tissue and blood vessels. While the neoplastic cells determine the nature of the tumors, tumor growth and evolution depend on the stroma (Kumar 2003).

Cancer cells differ according to the cell type from which they derive. The common characteristics of cancerous tissue include local increase in cell population, loss of normal arrangement of cells, variation of cell shape and size, increase in nuclear size and density of staining, increase in mitotic activity, and abnormal mitoses and chromosomes. Progressive infiltration, invasion, and the destruction of the surrounding tissue accompany the growth of cancer. A number of cell surface changes occur in cancer cells resulting in a decreased communication or signaling between cells and an altered membrane transport or permeability. Cells become anchorage independent and are allowed to metastasize.

Grading and Staging

Tumor grade is a qualitative assessment of the differentiation of the tumor compared to normal tissue at a specific site; the grading scheme provides a measure of the degree of malignancy. In general, a three-grade system as defined based on the subjective judgment of the pathologist is as follows:

Grade I: well differentiated
Grade II: Moderately differentiated
Grade III: Poorly differentiated

The rate of tumor growth depends on the tumor type and grade. In general, most benign tumors grow slowly while most malignant neoplasms grow much faster. Also, rapidly growing malignant tumors are generally well differentiated (grade 1) and contain central areas of necrosis due to poor blood (oxygen) supply.

Staging of cancer depends on the size of the primary neoplasm, its extent to regional lymph nodes, and the presence or absence of metastasis. The TNM system is an expression of the anatomical extent of disease and is based on the assessment of three components:

T: The extent of primary tumor
N: Absence or presence, and the extent of regional lymph node metastasis
M: Absence or presence of distant metastasis

The above TNM classification is based on the assumption that cancers of similar histological type or site of origin share similar patterns of growth and extension. The tumor staging will help plan the treatment strategy, indicate prognosis, and assist in the evaluation of therapy.

15.2 Molecular Basis of Cancer

15.2.1 Genetic Changes

Carcinogenesis is a multistep process at both, the phenotypic and genetic levels (Hanahan and Weinberg 2000). The genetic hypothesis of cancer implies that cancer results from the clonal expansion of a single progenitor cell. In the first step (initiation), the cell has incurred a genetic damage in the DNA caused by a point mutation, gene deletion, or gene rearrangement. In the second step (promotion), the initiated cells become cancerous. In the third step (progression), the cancerous cell becomes biologically defective or undifferentiated. Because of this multistep process, most human tumors, however, do show genetic heterogeneity even if they originate from a single cell.

A wide variety of chromosomal alterations are found in cancers, such as change in number, translocations, rearrangements, amplifications and deletions. Many of these changes are associated with genes that are directly responsible for causing cancer. The principle targets of genetic damage are three classes of normal regulatory genes; *oncogenes*, *antioncogenes*, and genes that regulate apoptosis (Kumar 2003). Damage to DNA repair genes may also be involved in carcinogenesis. A number of biochemical features associated with the genetic changes that clearly distinguish malignant proliferation from normal growth pattern are as follows:

- Tumor cells usually have an unlimited potential for tumor growth and are, thus, immortalized.
- Tumor cells exhibit a variety of metabolic differences when compared to their normal untransformed counterparts.
- Malignant cells have the ability to escape the human immune surveillance pathways.

15.2.1.1 Oncogenes

Genes that promote autonomous cell growth are called oncogenes or cancer causing genes. These are derived from proto-oncogenes, which are normally present in the human genome and are essential for normal cell growth. The mutant *alleles* of proto-oncogenes are called oncogenes. Many oncogene products and oncoproteins are part of the cell's signal transduction pathway (Table 15.1). Some oncogenes code for proteins that are either growth factors or growth factor receptors. Some oncoproteins are transmembrane signal molecules, such as *tyrosine kinases*. The activation of a mutated oncogene could greatly affect a cell's growth potential by increasing the production of growth factors, increasing the growth factor receptor expression on the cell surface, or by encoding a protein that binds to DNA and stimulates cell division. The proteins molecules involved in the signaling pathways are called *signal-transducing proteins*, and are responsible for the communication between growth factor receptors and their nuclear targets.

15.2.1.2 Antioncogenes

In a normal cell, the physiological function of *antioncogenes* or cancer suppressor genes is to regulate cell growth and to prevent tumor formation. The loss of these genes, however, is a key event in many human tumors. Tumor suppressor genes encode for proteins that act as negative transducers of growth factor stimulation. The loss of tumor suppressor genes, such as *Rb* and *p53*, is associated with a wide variety of human malignancies. The *p53* gene encodes a 53 kd protein that binds in the nucleus, and at high levels causes the cell to undergo apoptosis (Kirsch and Kastan 1998). A mutated *p53* allele in a cancer cell may encode a mutant form of p53 protein without the ability to induce apoptosis. Mutations of the *p53* gene is the common DNA abnormality in more than 50% of cancers. Some cancers in

Table 15.1 Oncogenes and antioncogenes

Gene	Gene product	Biologic function	Cancer
Oncogenes: cancer causing genes			
Sis	PDGF-β chain	Heparing binding GF	Astrocytoma, Osteosarcoma
int-2	Fibroblst GF	Platelet-derived GF	Breast cancer, Melanoma
Erb-B2	EGF receptor	GF receptor	Breast, ovarian, and lung cancer
Fms	CSF-1 receptor	GF receptor	Leukemia
Abl	Tyrosine kinase	Intracellular signaling	Chronic myeloid leukemia
Ras	GTP binding protein	Intracellular signaling	Many cancers
c-myc	Transcriptional factor	Binds DNA	Burkitt's lymphoma
L-myc	Transcriptional factor	Binds DNA	Small cell carcinoma of lung
Antioncogenes: Tumor-suppressor genes			
Rb	Transcription factor	Regulation of cell cycle	Retinoblastoma, Osteosarcoma
p53	Transcription factor	Regulation of cell cycle and apoptosis	Most human cancers
NF-1	GTPase activating protein	Inhibition of ras signal transduction	Schwannomas, Neurofibroma
WT-1	Nuclear transcription factor	Binds DNA	Wilm's tumor

which the loss of function of the tumor suppressor genes may be involved are summarized in Table 15.1.

15.2.1.3 Tumor Antigens

Most tumor cells synthesize many proteins or *glycoproteins* that are antigenic in nature. These antigens may be intracellular, expressed on the cell surface, or shed or secreted from the cell into the extracellular fluid or circulation. These tumor associated antigens (TAA) may also be expressed in small amounts in normal cells, but typically tumor cells produce them in large amounts. Based on the source and origin of antigen, TAAs can be categorized into 5 different groups (Kumar 2003).

(a) Oncofetal antigens: These antigens are derived from *epitopes* that were expressed in fetal life and appear on tumor cells as a result of undifferentiated growth process associated with malignant process. These antigens are not expressed in completely differentiated cells. Some of these antigens, such as *Carcinoembryonic antigen* (CEA) and *Alpha-fetoprotein* (AFP), are expressed on the cell surface and are also present in the circulation.

(b) Epithelial surface antigens: The antigens are derived from cell surface structural components that are exposed due to an architectural disruption of malignant tissue. Antigens, such as *epithelial membrane antigen* (EMA) and *human milk fat globule* (HMFG), are excluded from the blood by biological barriers and are present in the tumor tissue only.

(c) Tumor derived antigens: These epitopes are expressed mainly by tumor tissues and in some tumors there may even be an increase in the expression of these epitopes. The antigen, *tumor associated glycoprotein-72* (TAG-72), is expressed on the tumor cell surface in a variety of adenocarcinomas, such as colon, breast and ovarian. *Prostate specific antigen* (PSA) and *prostatic acid phosphatase* (PAP) are secreted by prostate carcinoma cells and are present in the tumor tissue and in circulation. *Prostate specific membrane antigen* (PSMA) is an integral transmembrane glycoprotein with intra and extracellular epitopes.

(d) Receptor antigens: Tumor cells express regulator receptors that promote interaction with a number of growth factors. The increased expression of receptor proteins on tumor tissues may be regarded as receptor antigens. The human *epidermal growth factor receptor* (EGF-r) is a transmembrane glycoprotein that contains extracellular and cytoplasmic epitopes for EGF binding. EGF-r overexpression has been found in a variety of malignant epithelial tumors arising in the breast, colon, lungs and bladder.

(e) Viral antigens: These epitopes are present in certain tumor cell membranes where the induction of malignancy is associated with the presence of transforming genes carried by the DNA viruses. Congenital or acquired immunodeficiency developed Epstein–Barr virus (EBV)-positive malignancies (such as Burkitt's lymphoma) are examples of receptor antigens.

15.2.1.4 Tumor Angiogenesis

Blood supply is the most important factor that could modify the rate of tumor growth. Perfusion supplies nutrients, oxygen, as well as growth factors. Beyond 1–2 mm in diameter, the tumor fails to proliferate because hypoxia induces apoptosis. Angiogenesis or *neovascularization* is a necessary biologic correlate of malignancy (Kumar 2003). Tumor-associated angiogenic factors, such as *vascular endothelial growth factor* (VEGF) and *basic fibroblast growth factor* (bFGF), may be produced by tumor cells or derived from inflammatory cells (e.g., macrophages). Hypoxia promotes angiogenesis by the release of *hypoxia-inducible factor-1* (HIF-1), which controls the transcription of VEGF.

A number of antiangiogenesis molecules may be produced by tumor cells themselves (such as *thrombospondin-1*) or may induce the production of these factors (*angiostatin*, *endostatin*, and *vasculostatin*) by other cells. The balance between the angiogenic and antiangiogenic factors controls tumor growth.

Apoptosis

Apoptosis is executed by a family of intracellular proteases called, *caspases* and occurs as an end result of signaling through the death receptor CD95 (Fas) and by DNA damage (Kumar 2003). Defects in the processes that control normal apoptosis extend the life of the cell and also promote cancer growth. Several genes that regulate apoptosis have been identified. Apoptosis may be inhibited by *cytochrome c* from mitochondria, which forms a complex with APAF-1,

ATP and procaspase 9. The release of cytochrome is very important in apoptosis and is regulated by the genes of the *BCL2* family, which inhibit apoptosis by inhibiting the release of cytochrome *c* (Adams and Cory 2001).

15.3 Tumor Imaging

15.3.1 Objectives

A variety of both genetic and tumor microenvironmental factors determine the behavior of cancer. As a result of alterations in genotype, phenotypic functional changes (Table 15.2), such as altered metabolism, proliferation protein synthesis and angiogenesis occur in cancer tissue, which ultimately lead to the development of discrete mass lesions. The challenge of an imaging technique is to demonstrate the morphology (structure and tissue characterization) and functional status of tumor tissue. Tumors are classified on the basis of the tissue of origin, cell type, whether benign or malignant, degree of differentiation, anatomic site and function. Because of this diversity, no single imaging technique is capable of detecting all tumors. While the radiological techniques (X-ray, CT, MRI, Ultrasound) can provide information, regarding location and size of the tumor with better resolution than nuclear imaging techniques, these lack the specificity and sometimes can not even distinguish residual, viable disease from fibrosis. PET and SPECT techniques, on the other hand, have the potential to provide functional status of the tumor tissue (metabolism, receptor expression) and offer higher specificity with limited resolution. A number of radiopharmaceuticals (Table 15.3) were designed and developed over the last three decades to image and identify a unique biochemical characteristic of tumor tissue. The application of molecular imaging procedures in oncology can best be classified based on the various objectives of the imaging, as described below:

1. Diagnosis of malignancy: Differentiating malignant from benign disease
2. Identifying the site(s) of disease: In order to plan biopsy or surgery especially when cancer is suspected based on clinical biomarkers
3. Detecting the primary tumor: In patients with metastatic disease with an unknown or small primary tumor
4. Grading malignancy: Based on quantifying the amount of radiotracer uptake
5. Staging disease: Whole body scans would provide the relative uptake of tracer through out the body
6. Residual disease: Identification of residual viable cell mass following treatment
7. Detection of recurrences: Confirming the sites of recurrent (new) disease
8. Measuring the response to therapy: Objective assessment of the efficacy of specific treatment modalities
9. Guide radiation therapy: Identify regions of tumor tissue with differences in radiosensitivity for effective radiation treatment

Several new radiotracers have been proposed and were evaluated in preclinical and clinical studies in order to characterize the tumor biology more appropriately. Several publications have extensively reviewed the potential advantages and limitations of many PET radiopharmaceuticals (Stocklin 1998; Varagnolo 2000; Shiue and Welch 2004; Couturier et al. 2004; Vallabhajosula 2007). [18]F labeled radiotracers appear to be the most attractive option, mainly due to the wide availability of ^{18}F and the possibility of automated routine synthesis of these agents. Some of these tracers have been evaluated extensively in the clinic. In addition to ^{18}F labeled tracers, many other radiotracers have a significant potential for routine clinical imaging studies. The advantages of many of these tracers is described below based on their

Table 15.2 Molecular and functional alterations in cancer[a]

Function	Increased	Decreased
Glucose metabolism	X	
Amino acid transport	X	
Protein synthesis	X	
DNA synthesis	X	
Membrane or lipid synthesis	X	
Receptor expression	X	
Angiogenesis, vascular density	X	
Vascular permeability	X	
Oncogene products	X	
Signal transduction	X	
Hypoxia	X	
Oxygen tension		X
Blood Flow	X	X
Apoptosis	X	X
Many other genetic markers	X	X

[a]Modified from Wahl (2002)

Table 15.3 PET radiopharmaceuticals: mechanisms of uptake and localization

Biochemical process	Radiotracer	Mechanism of uptake or localization
Blood flow/perfusion	[^{15}O]Water	Freely diffusible across membranes
Glucose metabolism	[^{18}F]FDG	Facilitated diffusion via glucose transporters. Substrate for *hexokinase* in glucose metabolism
Bone metabolism	^{18}F-fluoride	Incorporation in the hydroxyapatite crystals in bone
Membrane synthesis	[^{11}C]Choline, [^{18}F]Fluorocholine	Substrates for *choline kinase* in choline mtabolism
Lipid synthesis	[^{18}F]Fluoroacetate	Acetate is activated to acetyl-CoA in both the cytosol and mitochondria by *acetyl-CoA synthetase*.
DNA synthesis	[^{11}C]Thymidine, [^{18}F] Fluoro-thymidine	Substrates for *thymidine kinase (TK-1)* in DNA synthesis and reflects tumor cell proliferation rate
Hypoxia	[^{18}F]FMISO	Intracellular reduction and binding
Receptor Binding	[^{18}F]FES	Specific binding to estrogen receptors in breast cancer
	^{68}Ga-DOTATOC	Specific binding to somatostatin receptor (SSTR-II)
	^{68}Ga-DOTANOC	Specific binding to somatostatin receptor (SSTR-II, III, V)
Amino acid transport and protein synthesis	[^{18}F]FDOPA	Precursor for the synthesis of dopamine
	[^{11}C]L-methionine, [^{18}F] FMT, [^{18}F]FCCA	Transport into the cells involves amino acid carrier protein. Intracellular trapping involves protein synthesis or transmethylation
Binding to tumor antigens	^{124}I, ^{64}Cu, ^{86}Y labeled mAbs	Specific binding to tumor associated antigenic binding sites (such as CEA, PSMA, CD20 and CD22)
Apoptosis	^{124}I-Annexin V, ^{64}Cu-Annexin V	Specific binding to Phosphatidylserine (PS) on cell membrane
Angiogenesis	RGD peptide, ^{18}F-FB-E[c(RGDyK)]2	Integrin receptors ($\alpha_v\beta_3$) on endothelial cells of neovasculature
Gene expression	[^{18}F]Oligonucleotide	In vivo hybridization with mRNA
	[^{18}F]FHBG	Substrate to herpes virus *thymidine kinase*

ability to image a specific biochemical process or based on their unique mechanism of localization in a specific organ/tissue of interest (Table 15.3).

15.3.2 Radiolabeled Molecular Imaging Probes: Biochemical Basis

15.3.2.1 Glycolysis

The most important molecule to provide energy for various biochemical reactions in the body is adenosine triphosphate (ATP), which is generated in the mitochondria following the metabolism of glucose in the mitochondria. Accelerated glucose metabolism is one of the phenotypic or functional changes observed in cancer tissue, first observed by Warburg, more than 80 years ago (Warburg 1924, 1956). The transport of glucose into cells is mainly through *facilitated diffusion*, also called *carrier-mediated diffusion* since the carrier facilitates the transport of glucose into the cell. This mechanism, however, also allows the glucose molecule to diffuse out of the cell. Insulin can increase the rate of facilitated diffu-

sion 10- to 20-fold. Six isoforms of glucose transporters (GLUT) have been identified, which differ in kinetic properties, tissue location, etc. It has been shown that the overexpression of GLUT-1, GLUT-3 and GLUT-5 play a major role in the increased transport of glucose by tumor cells (Wahl 2002). Glucose may also be transported into the cell by active transport, which mostly occurs in renal tubules and gastrointestinal membrane.

The phosphorylation of glucose (Fig. 15.1), an initial and important step in cellular metabolism, is catalyzed by the enzyme *glucokinase* in the liver and *hexokinase (HK)* in most other cells. Four different types of hexokinses are known; Type 1 is predominant in the brain, Type-2 in insulin sensitive tissue, Type-3 is present in any other tissue and Type-4 is known as glucokinase in the liver. In the cytosol, glucose is phosphorylated by the enzyme *hexokinase* to glucose 6-phosphate, which subsequently is metabolized to carbon dioxide and water. This phosphorylation step is almost completely irreversible except in the liver, kidney and GI epithelium. The enzyme *glucose-6-phosphatase*, responsible for the breakdown of phosphorylated glucose is absent in most cancer cells (Jana and Abdel-Dayem 2006). As a result, once glucose enters the cells, it goes through the glycolysis pathway.

Fig. 15.1 Intracellular metabolism of glucose and [^{18}F] FDG. Unlike glucose, FDG-6-phosphate does not undergo further metabolism, and is trapped in the cell
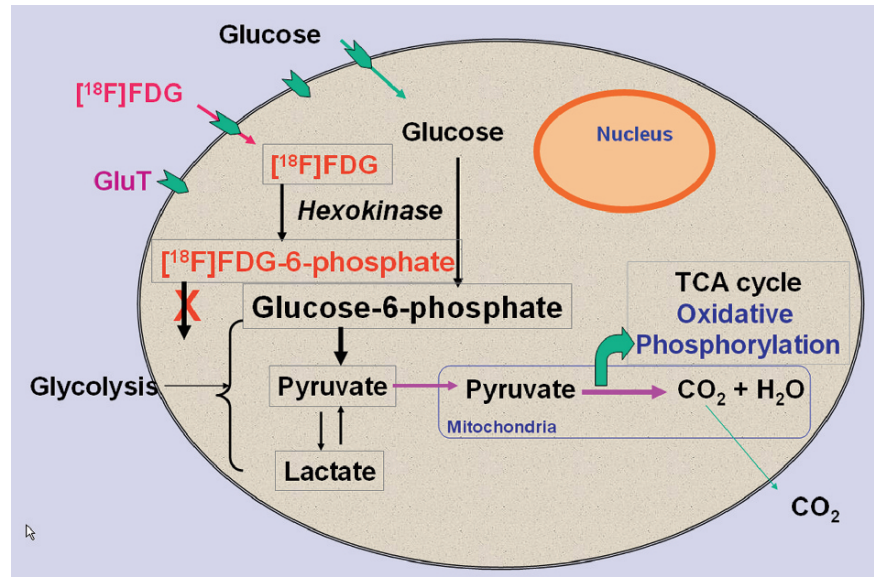
Tumor pH: In glucose metabolism, the initial reaction sequence known as "glycolysis" takes place in the cytoplasm where glucose is converted to two molecules of pyruvate. Under anaerobic conditions (hypoxia), this mechanism is unavailable; pyruvate is converted to lactic acid by lactate dehydrogenase (LDH) and accumulates. Consequently, the pH of the tumor tissue is lightly acidic compared to that of normal tissue pH of 7.4 (Warburg 1956). The acidic pH of the tumor tissue possibly may play a significant role in the localization of several radiotracers in tumors.

2-[^{18}F]Fluoro-2-Deoxy-D-Glucose

In the 1950s it was shown that the hydroxyl group on carbon-2 of the glucose molecule (Fig. 9.1) is not necessary for phosphorylation by *hexokinase*. The deoxyglucose (DG) enters the cell similar to glucose and is converted to deoxyglucose 6-phosphate, which however, does not undergo further metabolism and is trapped in the cell (Sols and Crane 1954). Therefore, the design of the 2-deoxy-2-fluoro-deoxyglucose (FDG) molecule is based on labeling a carbon-2 atom in DG with ^{18}F (Ido et al. 1978). Incidentally the C–F bond, which is more stable than the C–H bond, is chemically unrecognizable by *hexokinase*. As a glucose analogue, FDG enters the cell membrane using the same transporters as glucose. It is then phosphorylated into [^{18}F]FDG-6-phosphate. This metabolite is not a substrate for further enzymes and, thus, is trapped and accumulates inside the cell (Fig. 15.1) in proportion to the metabolism of glucose. Experimental studies in vitro and in vivo have clearly documented that the magnitude of the FDG uptake in tumors, in general, relates quite directly to the number of viable cells (Wahl 2002). FDG is a model PET radiopharmaceutical and is regarded as the "molecule of the century" in nuclear medicine. The simplified mechanism of uptake of FDG by tumor cells is now well understood. FDG-PET can therefore be considered as the imaging of the rate-limiting step of glucose metabolism, namely the hexokinase activity. The imaging signal detected with PET tomography is achieved based on the trapped phosphorylated metabolite.

The glycolytic activity of a given tumor is generally assumed to be characteristic of its state of differentiation. The extent of FDG uptake in tumors, especially untreated tumors, appears to relate directly to the number of viable cells. However, it has also been shown that inflammatory cells (macrophages) in tumors also accumulate FDG. It has also been well documented that FDG-PET is clinically useful for the staging and restaging of malignancy, metabolic characterization of malignancy, and monitoring of response to therapy (Fig. 15.2) (Gambhir et al. 2001; Wahl 2002; Margolis et al. 2007).

Limitations of FDG-PET: Although FDG-PET/CT imaging provides high specificity and sensitivity in several types of cancer, with many applications in the clinical management of an oncologic patient, it is important to

[¹⁸F]FDG-PET
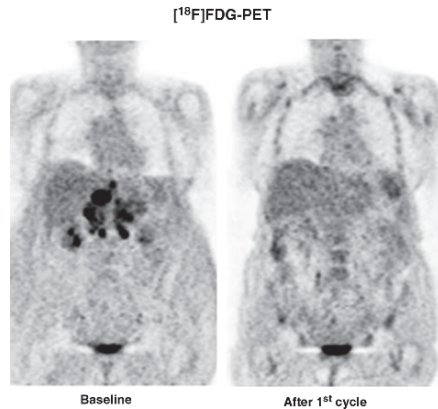
Fig. 15.2 FDG-PET to assess treatment response. In a patient with diffuse large cell lymphoma, FDG-PET scan shows significant reduction in FDG uptake after only one cycle of chemotherapy, compared to pretherapy scan

Table 15.4 Factors affecting FDG uptake in tumors[a]

Factor	Increased	Decreased
Viable cancer cell number	X	
Tumor perfusion	X	
Hypoxia	X	
Glucose transporter expression	X	
Hexokinase activity	X	
Inflammation or infection	X	
Receptor agonists	X	
Chemotherapy acute	X	
Radiation therapy acute	X	
Receptor blockade		X
Chemotherapy effective		X
Radiation therapy chronic		X
Hyperglycemia		X
Insulin		X
Necrosis		X

[a]Modified from Wahl (2002)

recognize that FDG is not a "specific" radiotracer for imaging malignant disease. A number of factors (Table 15.4) can affect the FDG uptake in tumors and may explain the causes of false-positive and false-negative imaging data (Wahl 2002). Various tissues and processes in the body use glucose to generate ATP to meet the increased energy demands. For example, the normal brain depends exclusively on glucose metabolism. Further, inflammatory cells and macrophages have higher glucose metabolic rates and accumulate higher amounts of FDG than tumor cells. Since FDG competes with glucose, the net uptake of FDG by tumor tissue depends on the plasma glucose levels. In any given patient the absolute tumor uptake of FDG depends on many factors and may not necessarily reflect tumor aggressiveness, or the rate of tumor proliferation (Wahl 2002).

15.3.2.2 Bone Metabolism

Bone is a rigid connective tissue and is made up of two types of tissues; compact or cortical and cancellous, trabecular or spongy bone. While the cortical bone forms the outer layer (cortex), the spongy bone in the medulla contains the bone marrow. Three types of cells are seen in the bone: (a) osteoblasts that produce the organic bone matrix, (b) osteocytes that produce the inorganic matrix, and (c) osteoclasts, which are active in bone resorption. At the molecular level, the bone matrix is composed of approximately 35% organic (such as collagen, proteoglycans, albumin,) and 65% inorganic matrix, which includes cations (Na^+, K^+, Ca^{2+}, Mg^{2+}, Sr^{2+}), anions (F^-, OH^-, $PO4^-$, and Cl^-) and the hydroxyapatitie crystals, $Ca_{10}(PO_4)_6(OH)_2$ (Elgazzar and Shehab 2006).

The normal bone undergoes constant remodeling, maintaining a balance between osteogenesis (osteoblastic) and bone resorption (osteoclastic) activity. Various primary tumors originate from the bone. In addition, in metastatic bone disease, bone involvement by cancer occurs most commonly when the tumor cells from other cancers (such as prostate and breast cancer) are transported into the marrow. Most of the bone metastases are found in the red active marrow present mainly in the axial skeleton. As the lesion grows, in the marrow, the surrounding bone undergoes osteoclastic and osteoblastic reactive changes (Hamaoka et al. 2004; Even-Sapir et al. 2004). The osteoblastic component of the metastasis represents the reaction of normal bone to the metastatic process and most sites of malignant bone involvement show increased reactive osteoblastic activity. In general, the radiographic appearance of a bone metastasis may be lytic, sclerotic (blastic), or mixed. Rapidly growing aggressive metastases tend to be lytic, whereas sclerosis is considered to indicate a slower tumor growth rate. Sclerosis may also be a sign of repair after treatment (Hamaoka et al. 2004). The incidence of lytic, blastic, and mixed types of bone metastases is different in various tumor types. In general, the purpose of bone imaging is to identify early bone involvement and to determine the full extent

of the skeletal disease, to assess the presence of accompanying complications such as fractures and cord compression, and to monitor response to therapy (Even-Sapir 2004). Detection of bone involvement by various imaging modalities is based on either direct visualization of the tumor infiltration or detection of the reaction of bone to the malignant process.

[^{18}F]Fluoride

In 1940, the absorption of fluorides by enamel, dentin, bone, and hydroxyapatite was first reported (Volker et al. 1940). [^{18}F]-Fluoride was first introduced as a bone-imaging agent in 1962 (Blau et al. 1962). FDA approved the NDA for bone imaging to define areas of altered osteogenic activity in 1972. In plasma, [^{18}F]fluoride ions do not bind to plasma proteins and clear from circulation faster than ^{99m}Tc-phosphonates. Fluoride ions diffuse through capillaries into the bone's extracellular fluid, and chemisorbed onto the bone surface by exchanging with hydroxyl (OH) groups in hydroxyapatite crystal of bone to form fluoroapatite (Blake et al. 2001). The fluoride bone uptake mechanism is similar to that of ^{99m}Tc-MDP. The uptake of both tracers in malignant bone lesions reflects the increased regional blood flow and bone turnover. However, due to faster blood clearance and higher capillary permeability, fluoride uptake in bone metastases is significantly higher than that in normal bone (Blake et al. 2001). While increased fluoride uptake has been reported in both

sclerotic and lytic metastases (Schiepers et al. 1997; Even-Sapir et al. 2007), the uptake of ^{99m}Tc-MDP in lytic lesions is relatively nonsignificant. Since both these tracers may also be seen in benign bone pathologies and non malignant orthopedic problems, bone agents are not considered as tumor specific tracers. Although, the ^{18}F-fluoride uptake mechanism corresponds to the osteoblastic activity, it is also sensitive for detection of lytic and early marrow-based metastases, by identifying their accompanying reactive osteoblastic changes, even when minimal. Also, the instant fusion of increased fluoride uptake with morphological data of CT using hybrid PET/CT systems improves the specificity of ^{18}F-fluoride-PET in cancer patients by accurately differentiating between benign and malignant sites of uptake (Even-Sapir et al. 2007). It must also be noted that FDG-PET is useful to detect bone metastases. Unlike fluoride and phosphonates, the uptake of FDG, however, is directly into tumor cells and not into the reactive bone. A comparison of ^{99m}Tc-MDP planar and SPECT images with [^{18}F]fluoride-PET images is shown in Fig. 15.3.

15.3.2.3 Membrane Lipid Synthesis

All cells utilize choline (CH), a quaternary ammonium base, as a precursor for the biosynthesis of phospholipids, which are essential components of all membranes (Zeisel 1981). In 1998, choline received the status of vitamin (group B) from the US Food and Nutrition
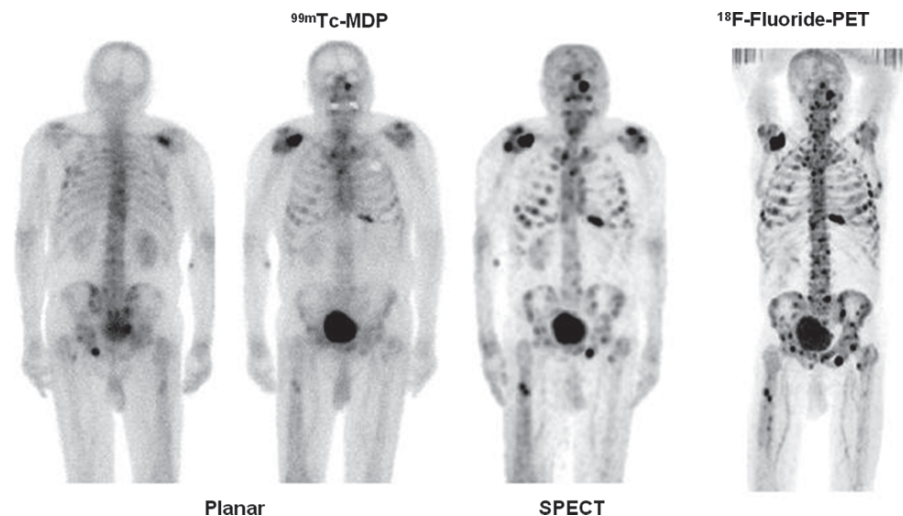
Fig. 15.3 Comparison of [^{18}F]Fluoride-PET with ^{99m}Tc-MDP planar and SPECT scintigraphy in a patient with numerous bone metastases. [^{18}F]Fluoride-PET detects more lesions compared to conventional bone scan. (Grant et al. 2008)

^{99m}Tc-MDP

^{18}F-Fluoride-PET

Planar

SPECT

Fig. 15.4 Metabolism of choline. Following phosphorylation by the enzyme *choline kinase*, phosphoryl-choline is converted to lecithin and gets incorporated in the membrane synthesis
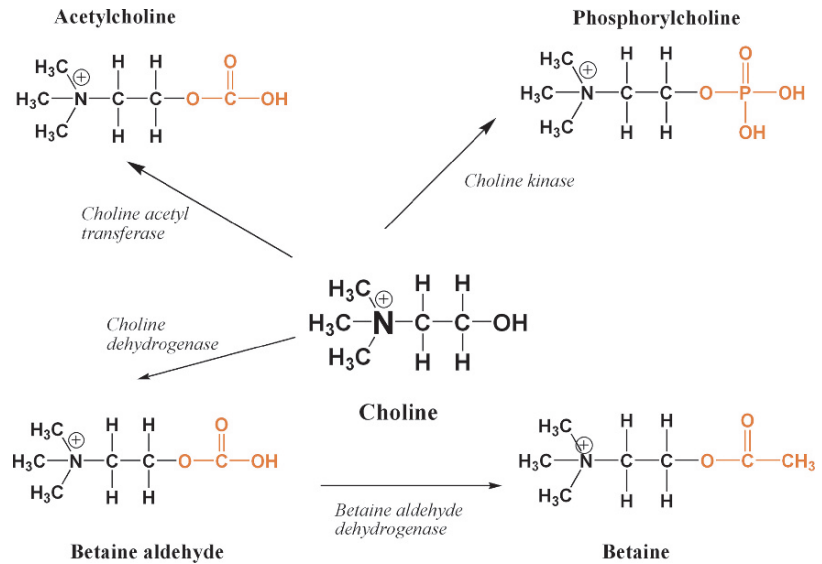
Board of the Institute of Medicine. Choline enters most cells using specific low affinity, sodium-independent transporters. Within the cell, choline can be phosphorylated, acetylated or oxidized (Fig. 15.4). The phosphorylation of choline is catalysed by the enzyme *choline kinase* (Clary et al. 1987). Phosphorylcholine is an intracellular storage pool of choline and is further incorporated into phosphatidylcholine (lecithin), a major phospholipid of all membranes (Zeisel 1981). Choline is also a precursor for the synthesis of the neurotransmitter, acetylcholine. In addition, the metabolic pathway of choline also involves oxidation to betaine aldehyde and then to betaine in the blood, liver and kidneys, the major sites for choline oxidation (Wettstein et al. 1998; Roivainen et al. 2000).

It has been suggested that the malignant transformation of cells is associated with the induction of *choline kinase* activity resulting in increased levels of phosphorylcholine. Furthermore, it is also known that rapidly proliferating tumors contain large amounts of phospholipids, particularly lecithin (Jackowski 1994). The formation and accumulation of membrane phospholipids is coordinated with the cell cycle and occurs during the *S* phase (Cornell 1997; Tedeschi et al. 1997). The cells depleted with choline can not synthesize lecithin, resulting in the arrest in the *G*1 phase. Thus, it is assumed that the uptake of radiolabeled choline reflects the proliferative activity by estimating membrane lipid synthesis. Tumor cells with high proliferation rate will have high uptake of choline in order to keep up with the increased demands for the synthesis of phospholipids.

[¹¹C]Choline and [¹⁸F]Fluorocholine

[¹¹C]Choline was introduced in 1997 as a potential PET tracer to image brain and prostate cancer (Hara et al. 1997). Since [¹¹C]choline is rapidly oxidized in vivo, ¹⁸F labeled choline analogs (Fig. 15.5), [¹⁸F] Fluoromethylcholine or fluorocholine (FCH), and [¹⁸F] fluoroethylcholine (FECH) were developed (DeGrado et al. 2001; Hara 2002). In vitro studies have clearly documented that these fluorinated choline analogs are good substrates for the enzyme *choline kinase*, but not for the enzymes involved in the oxidation of choline. As a result, no fluorinated derivatives of betaine have been observed (DeGrado et al. 2001). The biodistribution of both, FCH and FECH is very similar to that of choline, except for their very rapid urinary excretion. A nonmetabolizable fluorinated choline analog, known as deshydroxy-[¹⁸F]fluorocholine, (FDOC), was developed as a tracer to image the transport of choline into the tumor tissue (Henriksen et al. 2004). FDOC, however, is not a substrate for the enzyme choline kinase and as a result, the tracer is not retained in the tumor. Further studies have to clarify whether quantification of the transport capacity or the *choline kinase* activity may result in a better pathophysiological correlate and, thus, is the more useful process for tumor characterization (Henriksen et al. 2004).

In a recent review (Kwee et al. 2007), it has been summarized that the majority of clinical studies have focused on the use of the FCH PET in prostate cancer, for detecting primary and metastatic cancer.

[methyl-11C]Choline

Deshydroxy [18F]Fluorocholine

[18F]Fluoroethylcholine

[18F]Fluorocholine
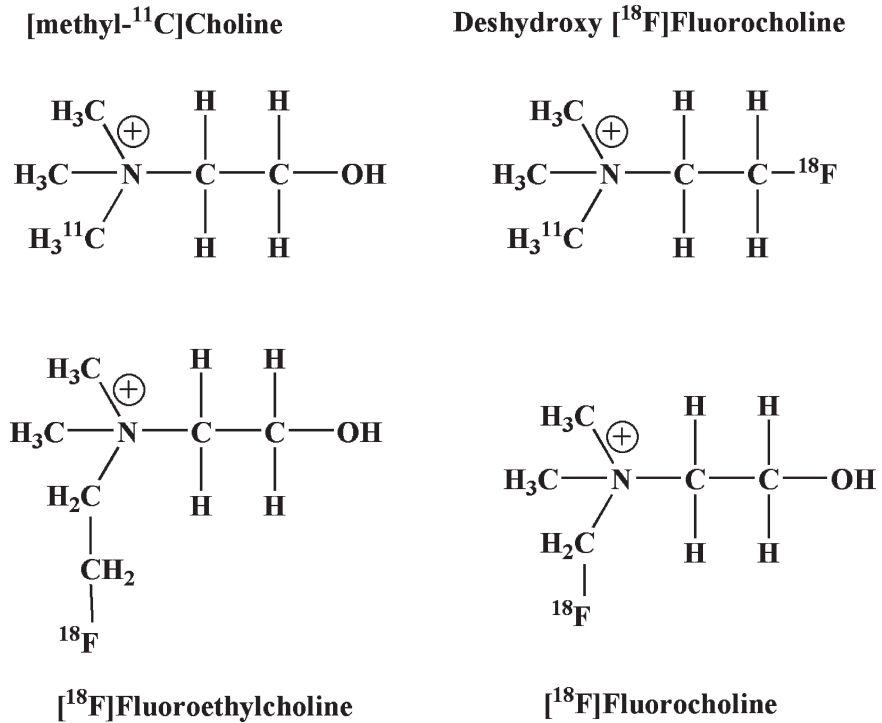
a FCH-PET

b FCH-PET/CT
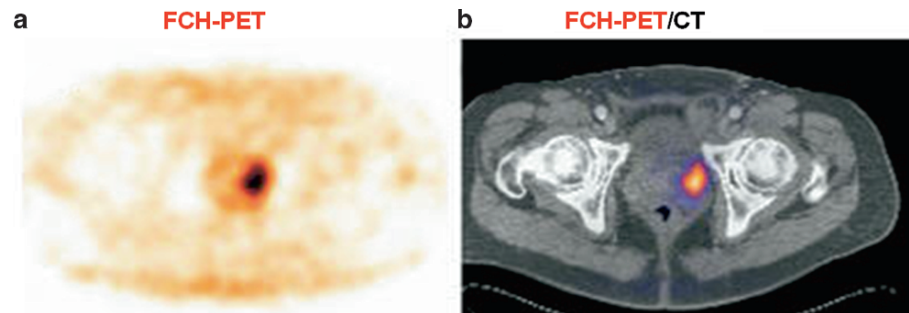
Experience with other tumor types, such as brain and liver tumors is growing. In most organs, high tumor-to-background contrast is achieved with FCH within minutes of injection due to very rapid blood clearance. Excellent discrimination can be achieved in the brain, where there is very little physiological uptake of FCH. In other organs, such as the liver, malignant discrimination is still possible despite a moderate degree of physiological uptake. Although the renal excretion of FCH is not ideal for evaluations of the urinary tract, it has not proven intractable in actual practice. Choline-PET can accurately detect and locate major areas with PCa and differentiate segments with

PCa from those with benign hyperplasia, chronic prostatitis, or normal prostate tissue. Also, the maximal tumoral choline uptake is related to the pT stage. FCH-PET may have a potential role for guiding the augmentation of a radiation dose based on intensity-modulated radiation therapy protocols for prostate tumors (Fig. 15.6) (Kwee et al. 2007). In patients with brain tumors, low-grade and high-grade tumors are characterized by low and high uptake of choline, respectively (Fig. 15.7). Further, following surgery or radiotherapy, accurate information on the residual tumor, tissue necrosis and recurrence of tumor can be provided with choline-PET.
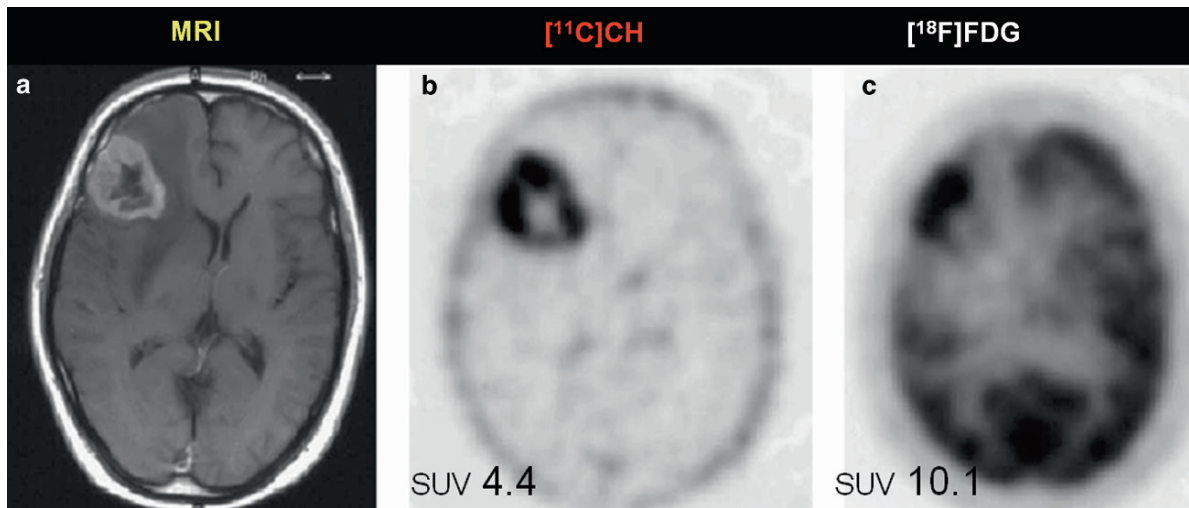
Fig. 15.7 [^{11}C]Choline-PET in a patient with glioblastoma in the right frontal lobe

[^{11}C]Acetate and [^{18}F]Acetate

Acetate is readily taken up by cells and is activated to acetyl-CoA in both, the cytosol and mitochondria by *acetyl-CoA synthetase*. Acetyl-CoA is a common metabolic intermediate for synthesis of cholesterol and fatty acids, which are then incorporated into the membrane (Howard and Howard 1975). In normal cells and in the myocardium, Acetyl-CoA is oxidized in the mitochondria by the tricarboxylic acid (TCA) cycle to carbon dioxide and water. However, in tumor cells, most of the acetate is converted into fatty acids by a key enzyme *fatty acid synthetase*, which is overexpressed in cancer cells (Swinnen et al. 2003). Acetyl-CoA is predominantly incorporated into intracellular phosphatidylcholine membrane microdomains that are important for tumor growth and metastasis. Therefore, [^{11}C]Acetate and [^{18}F] Acetate have also been proposed as tumor imaging agents (Oyama et al. 2003; Ponde et al. 2003, 2007). In vitro studies have demonstrated that [^{14}C]Acetate is much better as a proliferation marker than [^{14}C]Choline (Yoshimoto et al. 2004). The differences in sensitivity for tumor detection of these two tracers may be due to the different enzymes and mechanisms involved in the tumor uptake and retention of these two substrates.

15.3.2.4 DNA Synthesis

Increased cellular proliferation is a hallmark of the cancer phenotype (Hanahan and Weinberg 2000).

Increased mitotic rate, cell proliferation, and lack of differentiation are regarded as the main factors responsible for the accelerated growth of malignant tissue. Most benign tumors grow slowly over a period of years, while most malignant tumors grow rapidly, sometimes at an erratic pace. Cellular proliferation is specific to tumors, whereas increased glucose metabolism is not only a feature of tumors, but is also associated with a variety of other processes, including inflammation. Certain anticancer drugs were designed to stop the cell division but may not necessarily lead to cell death. As a result, tumor cellular proliferation drops without any significant change in the tumor energy metabolism. Therefore, molecular imaging probes, designed specifically to measure proliferation, are tumor-specific and may provide an impetus for PET imaging to be indicated as an appropriate technique, especially for measuring early response to treatment.

The DNA synthesis is a measure of proliferation. Since the number of cells in the *S*-phase of cell cycle is higher in tumor tissue than in normal cells, there is also an increased requirement of substrates (nucleotides) for DNA synthesis in the tumor (Cleaver 1967). The four nucleotides required for DNA synthesis are cytosine, guanine, adenine, and thymidine. Thymidine is the only one incorporated exclusively into the DNA, but not into RNA. Intracellularly, thymidine is first phosphorylated in the cytoplasm by the enzyme *thymidine kinase-1* (*TK-1*) to thymidine monophosphate (TMP), prior to incorporation into the DNA. The level

Fig. 15.8 Intracellular metabolism of thymidine and [18F]FLT: In an exogenous solvage pathway, FLT is transported into the cell and phosphorylated by *thymidine kinase* similar to thymidine
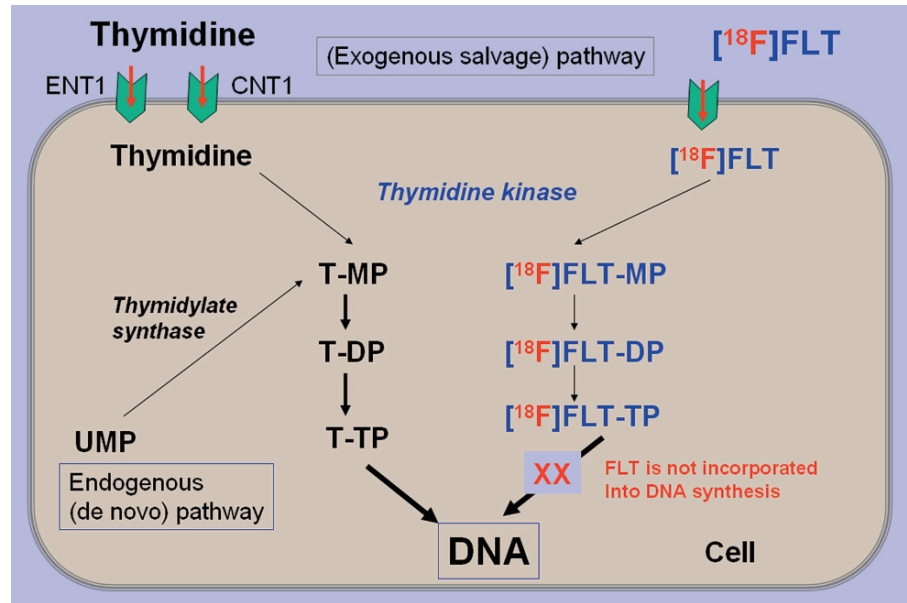
of *TK-1* in a cell increases several-fold as it goes from a resting state to the proliferative phase and is destroyed at the end of the *S*-phase (Cleaver 1967). TMP is then further phosphorylated to thymidine diphosphate (TDP) and then to thymidine triphosphate, (TTP) prior to incorporation into the DNA (Fig. 15.8). Therefore, several radiolabeled thymidine analogs (Fig. 15.9) have been developed that have the potential to provide a measure of DNA synthesis and tumor cell proliferation. In contrast, TK-2 is a mitochondial enzyme and is not regulated by the cell cycle.

[11C]Thymidine and [18F]Fluorothymidine

In the 1950s, [3H]Thymidine was introduced to measure thymidine incorporation into the DNA (thymidine labeling index) in tumor tissues (Cleaver 1967; Livingston 1974). Subsequently in 1972, [11C]thymidine was developed as a PET tracer and to measure the proliferation rate (Christman 1972). However, due to the rapid in vivo metabolism of this tracer, [11C]thymidine is not optimal for routine PET imaging studies. In 1996, metabolically stable thymidine analogs, which are also substrates for the enzyme *TK-1* were developed (Shields et al. 1996, 1998).

3′-deoxy-3′-[18F]fluorothymidine (FLT) is the most extensively investigated tracer to image cell proliferation. FLT is transported into the cell similar to thymidine and then phosphorylated to [18F]FLT-5′-monophosphate by the enzyme, *TK-1*. In vitro studies with tumor cell lines have demonstrated that FLT-MP is further phosphorylated to FLT-TP by the enzyme *thymydilate kinase* (Seitz et al. 2002; Grierson et al. 2004). FLT phosphates, however, are impermeable to the cell membrane, resistant to degradation, and are metabolically trapped inside the cells. The incorporation of FLT into DNA, however, is relatively insignificant (<1%).

FLT uptake and PET quantitative measures (SUV and FLT flux) have been shown to correlate with pathology-based proliferation measurements, including the Ki-67 score (Fig. 15.10), in a variety of human cancers (Salskov et al. 2007). FLT-PET may, therefore, be a useful tool for assessing tumor aggressiveness, predicting outcome, planning therapy, or monitoring response to treatment (Figs. 15.11 and 15.12). Also, FLT-PET has shown greater specificity for cancer than FDG-PET, which can show false-positive uptake in areas of infection or inflammation. FLT-PET should be considered a powerful addition to FDG-PET, providing additional diagnostic specificity and important biological information that could be useful in predicting the prognosis, planning the treatment, and monitoring the response.

Among other nucleoside analogs, [18F]Florouridine shows accumulation by proliferating cells, but the tracer is also incorporated into the DNA and RNA.

Fig. 15.9 Radiolabeled thymidine and uridine analogs to assess tumor cell proliferation

[^{11}C]Thymidine

3'-deoxy-3'-[18F]fluorothymidine (FLT)

[^{18}F]Fluorouridine

2-[^{18}F]Fluoro-methyl-1-b-arabino furanosyluracil (FMAU)

[^{18}F]FLT
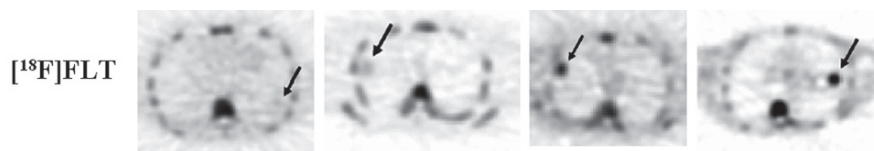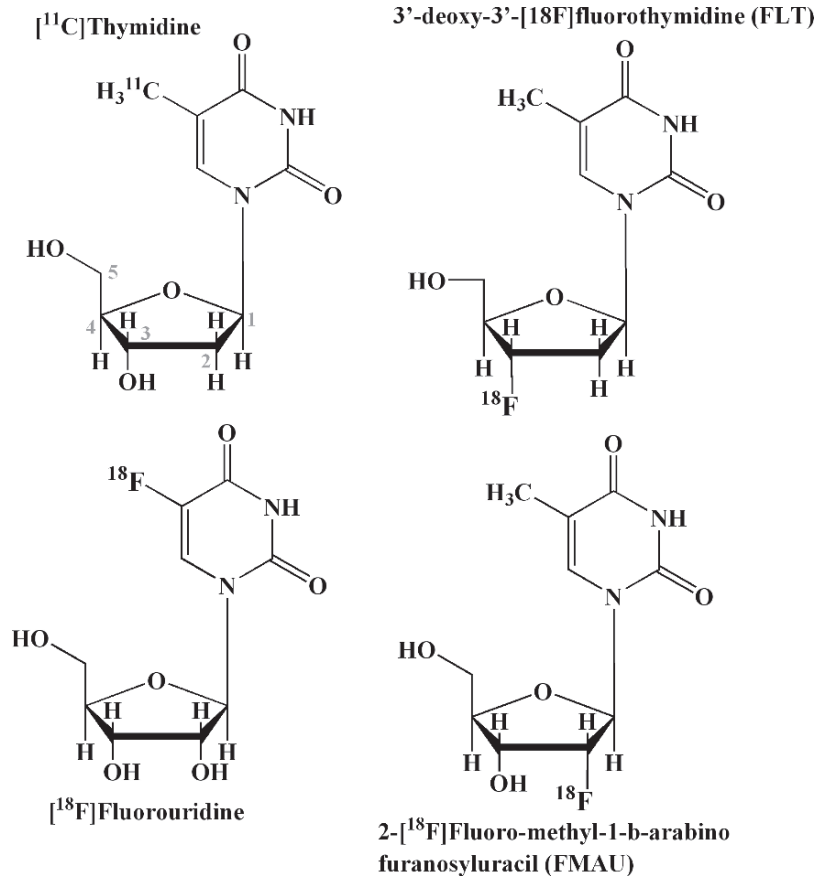
Histology	Benign infla- mmatory Lesion	Squammous cell carcinoma	Non-small cell Lung cancer	Undifferentiated Large cell carcinoma
Lesion (cm)	3.9	2.1	1.6	1.6
Ki-67 score (%)	<5	20	70	90
SUVmax	0.9	2.6	3.0	4.0
FLT flux	0.8	2.0	2.6	5.4

Fig. 15.10 FLT-PET images and corresponding Ki-67 scores in nonsmall cell lung cancer lesions: FLT uptake appears to correlate with proliferation assessed by Ki-67 immunohistochemical scoring. A benign lesion with minimal Ki-67 expression shows no FLT uptake (Salskov et al. 2007)

Fig. 15.11 FLT-PET to assess response to treatment in a patient with nonsmall cell lung cancer with extensive hilar and mediastinal lymph node metastases. The pretherapy FDG and thymidine PET images show increased uptake at the tumor sites. Following chemotherapy, FLT shows an early decline in uptake, but not FDG. At 10 weeks both FDG and FLT images show the response to treatment (Mankoff et al. 2005)
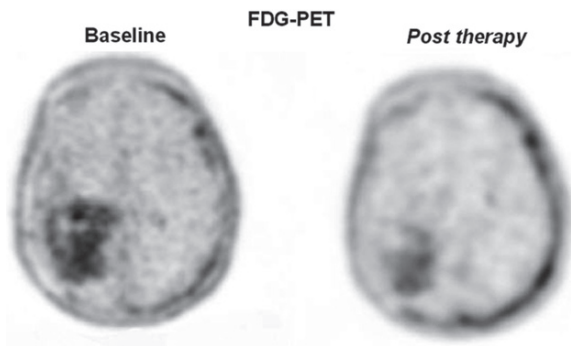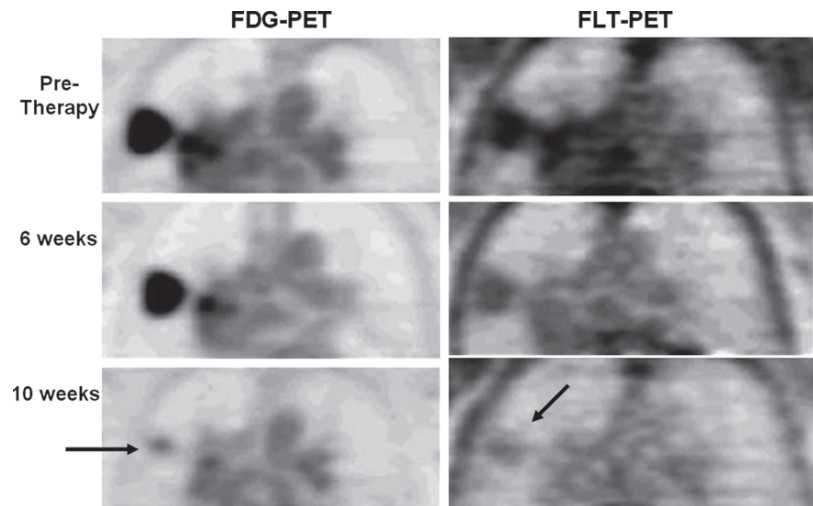
Fig. 15.12 FLT-PET to assess response to treatment in a patient with recurrent glioblastoma: FLT uptake 1 week after starting treatment shows significant reduction compared to baseline FLT uptake (Chen et al. 2007)

The pyrimidine analog, 2′-fluoro-5-methyl-1-β-D-arabino-furanosyluracil (FMAU) labeled with ^{11}C or ^{18}F has been shown to be useful for imaging tumor cell proliferation (Conti et al. 1995, 2008; Shields 2003). FMAU can be taken up by cells and phosphorylated by TK-1 and TK-2 followed by DNA incorporation through *DNA polymerase* (Sun et al. 2005). FMAU employs the same DNA synthetic pathway as thymidine and, therefore, has the potential to image DNA synthesis in tumors and normal proliferating tissues. Comparison of FMAU and FLT PET images in a patient with right parietal bone metastasis is shown in Fig. 15.13.

15.3.2.5 Amino Acid Transport and Protein Synthesis

The tumor growth and development is characterized by an increase in the rate of protein synthesis. Since amino acids (AA) are the building blocks for protein synthesis, carrier-mediated transport of AAs into cells is one of the most important and essential steps in protein synthesis. Subsequently, AAs are converted to the aminoacyl-t-RNA, which forms the polypeptide chain in the ribosome. AAs also undergo metabolism, such as transamination and decarboxylation. They also are precursors for many other biomolecules, such as hormones or neurotransmitters, and enter several metabolic cycles as, for example, methyl group donors.

Although AAs may simply diffuse into the cells, their transport principally depends on more than 20 ubiquitous membrane transport systems. Most of the AAs are taken up by tumor cells not only through a Na^{+} or an energy-independent L-type AA transporter system but also by the Na^{+}-dependent transporter systems A and B° (Jager et al. 2001; Langen et al. 2003). These transporters deal with aromatic AAs and ramified side-chain AAs, including leucine, valine, tyrosine and phenylalanine (Couturier et al. 2004).These amino acids are retained in the tumor cells because of their higher metabolic activities than most normal cells. Malignant transformation increases the use of amino acids for energy, protein synthesis, and cell division. Since tumor cells often overexpress transporter systems,
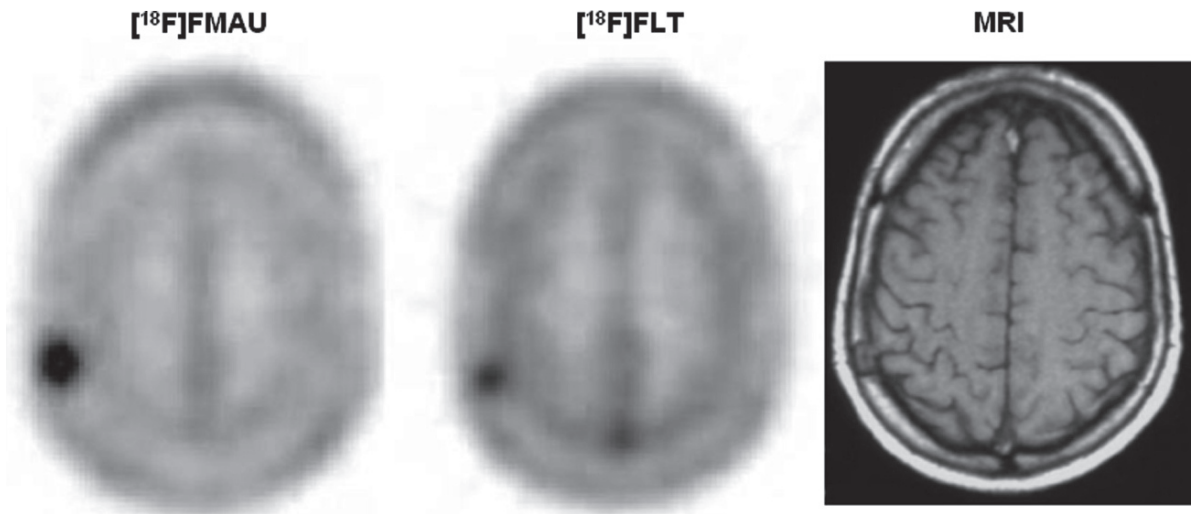
Fig. 15.13 Comparison of [^{18}F]FMAU and [^{18}F]FLT-PET in a patient with lung cancer and right parietal bone metastasis (Sun et al. 2005)
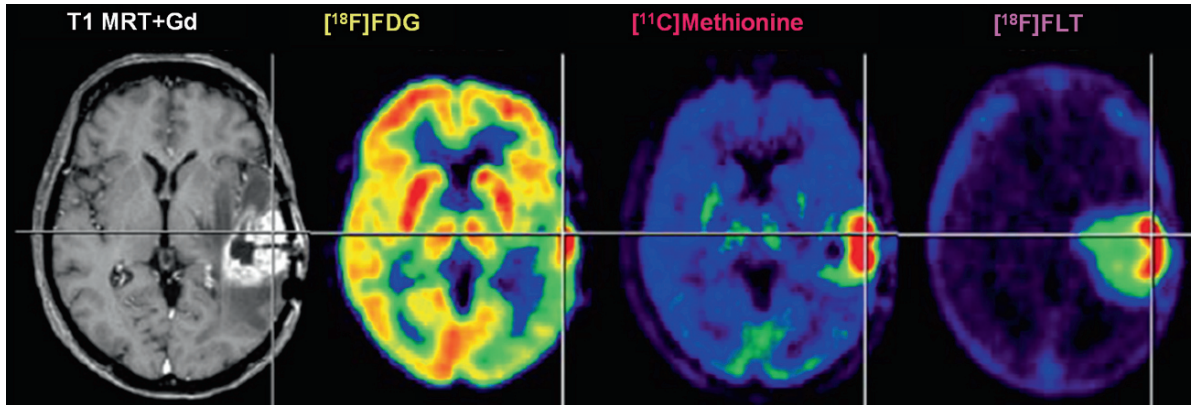
Fig. 15.14 [^{11}C]Methionine-PET and [^{18}F]FLT-PET to assess increased cell proliferation in a patient with brain tumor. Comparison with FDG-PET. Gd-MRI shows alteration of BBB and the extent of peritumoral oedema

Fig. 15.15 Radiolabeled amino acid (AA) analogs with potential clinical utility to assess cell proliferation based on increased AA membrane transport
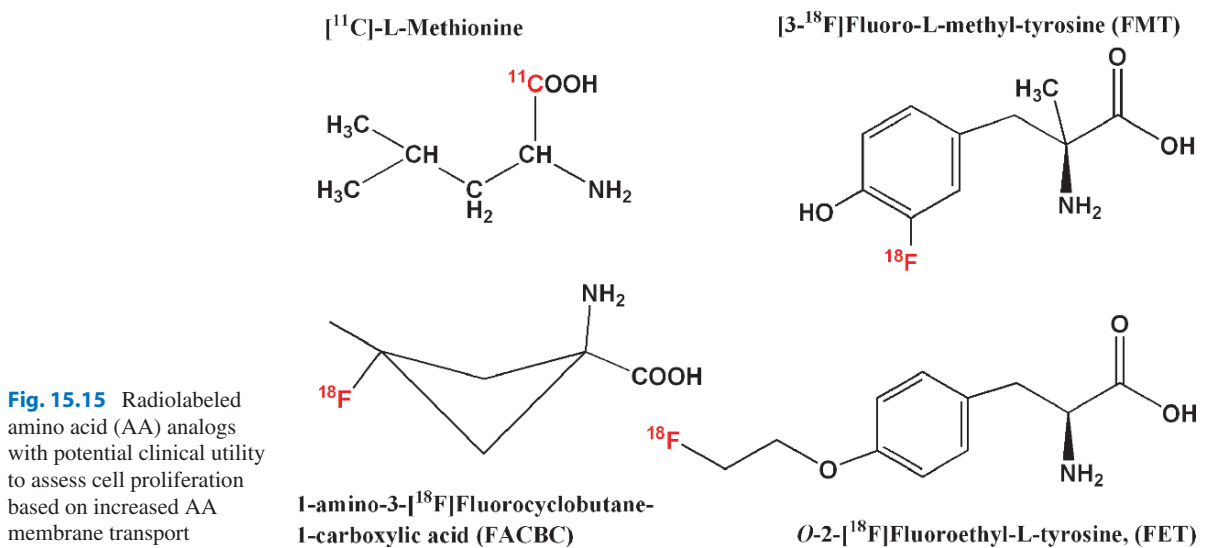
an overall increase in the AA transport and/or an increase in the protein synthesis rate by tumor cells may reflect proliferation.

[11C]Methionine

[carboxyl-11C]-L-leucine, [11C]-L-methionine and [11C]-L-tyrosine are involved in the synthesis of proteins. These radiotracers were introduced almost 30 years ago as tumor imaging agents. Since they undergo metabolism in vivo, the exact position where 11C is incorporated in the molecule is crucial for the measurement of protein synthesis.

The 11C labeled amino acid with significant clinical potential for tumor imaging is [11C]methionine, which is accumulated to a higher extent in malignant tumors compared with most normal tissues (Herholz et al. 1998; Ribom et al. 2001; Becerer et al. 2003). For imaging of brain tumors, in particular, this tracer has been shown to be superior to FDG (Chen 2007; Chen et al. 2007). A comparison of [11C]-L-methionine-PET with FDG and FLT in a patient with brain tumor is shown in Fig. 15.14.

18F Labeled Amino Acids

A number of 18F labeled tracers have been developed based on tyrosine and phenylalanine (Fig. 15.15). The tumor uptake of 18F labeled AAs is mainly related to the carrier mediated active transport, and not to the protein synthesis. Several important 18F labeled amino acids are under extensive clinical investigation. Among them, O-(2-[18F]fluoroehtyl)-L-tyrosine (FET) (Langen et al. 2006) and L-3-[18F]fluoro-α-methyl-tyrosine (FMT) have shown significant diagnostic potential to image brain tumors (Inoue et al. 1998). Also, a radioiodinated tracer, 3-[123I]iodo-α-methyl-L-tyrosine (IMT) is frequently used for SPECT. A comparison of FET-PET and IMT-SPECT is shown in Fig. 15.16.

The potential clinical utility of a synthetic, nonmetabolizable amino acid analog, known as anti1-amino-3-[18F]fluorocyclo-butane-1-carboxylic acid (FACBC) was first demonstrated in preclinical studies (Shoup et al. 1999). With FACBC, the cellular uptake is through both the L-type transporter and the energy-dependent A-type transporters. As a result, it can be
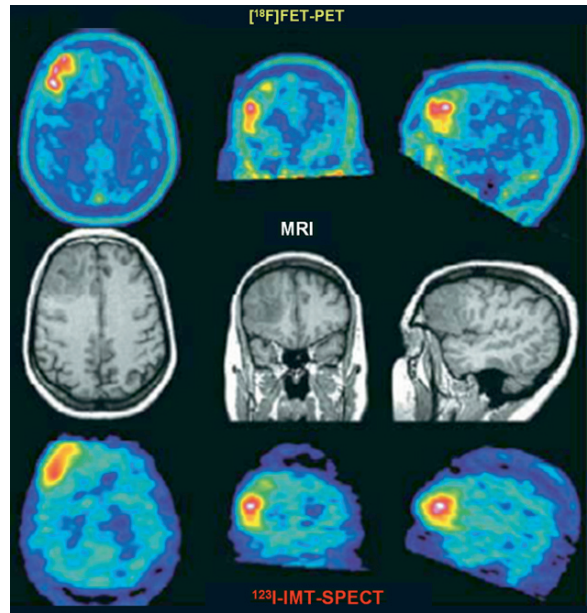
Fig. 15.16 Comparison of [18F]FET-PET and 123I-IMT-SPECT to image tumor cell proliferation in a patient with brain tumor (Langen et al. 2006)

accumulated intracellularly and retained in high concentrations. Recent clinical studies have also demonstrated its potential clinical utility in the detection of both, primary and metastatic prostate carcinoma (Fig. 15.17) and also primary brain tumors (Schuster et al. 2007; Chen 2007).

Amino Acid Precursors

Neuroendocrine tumors (NETs) are a heterogeneous group of neoplasms characterized by their endocrine metabolism and histological pattern. The endocrine cells from which neuroendocrine tumors (NETs) derive are capable of producing biogenic amines and polypeptide hormones. Carcinoids, together with the endocrine pancreatic tumors (EPTs), for example, gastrinomas, insulinomas, and glucagonomas, belong to the so-called NETs and therefore, have been regarded as APUD-omas characterized by their capacity for amine precursor uptake and decarboxylation (Pearse 1980). NETs are often highly differentiated and slow growing and tend to express hormonal activity corresponding to that of the normal cell type.

FACBC-PET   FACBC-PET/CT   MIP at 20 min
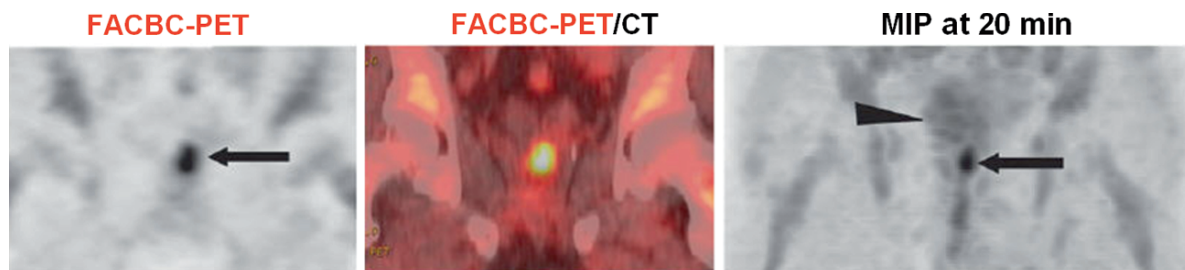
Fig. 15.17 [18F]FACBC-PET to identify prostate bed recurrence extending toward left seminal vesicle in a patient for restaging with biopsy proven lesion. MIP image even at 20 min demonstrates uptake in prostate bed (*arrow*) but little bladder uptake (Schuster et al. 2007)
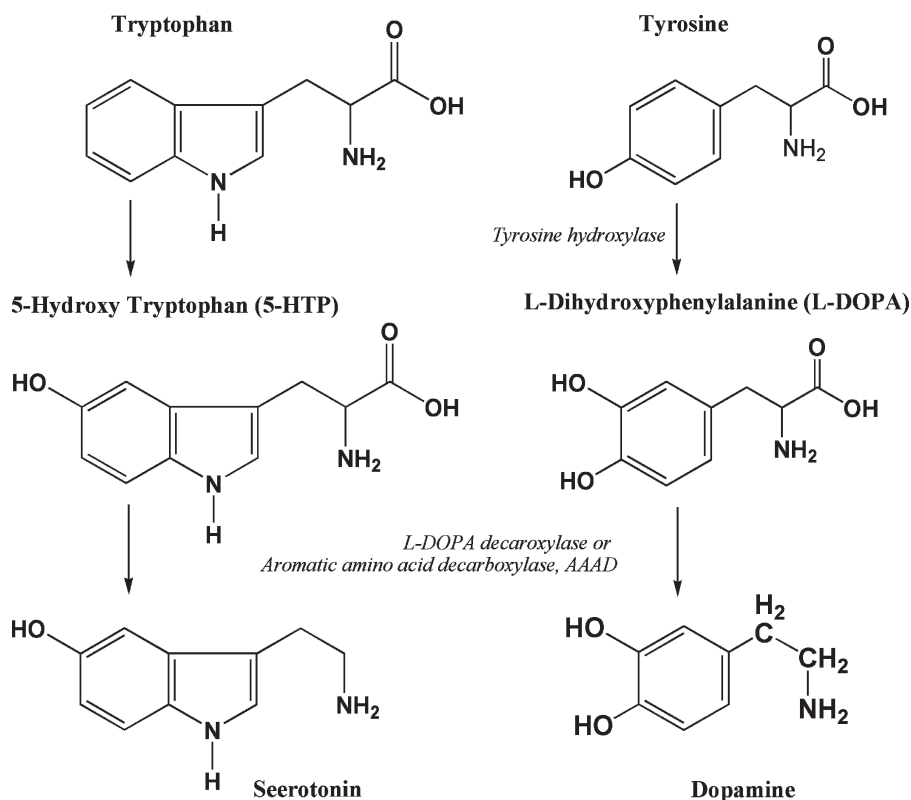
Fig. 15.18 Synthesis of serotonin and dopamine from amino acid precursors in vivo. Radiolabeled analogs of 5-HTP and L-DOPA are useful tracers for imaging neuroendocrine tumors

Amine precursors such as 5-hydroxy-L-tryptophan (5-HTP) and L-dihydroxy-phenylalanine (L-dopa), thus, may also be taken up by the tumor cells. Subsequently, through the action of *aromatic amino acid decarboxylase* (AADC), these precursors become decarboxylated and converted to the corresponding amines, serotonin and dopamine (Fig. 15.18). The resulting amines are then stored within the cell, and in response to stimuli, are released into the circulation through exocytosis.

Based on the biochemical mechanism described above, ^{11}C-labeled amine precursors L-DOPA and 5-HTP were developed for PET imaging of NETs. (Bjurling et al. 1990; Ahlstrom et al. 1995; Sundin et al. 2000). [18]F labeled L-DOPA (FDOPA), developed initially for imaging the dopamine metabolism in the

brain is also being evaluated for imaging NETs (Hoegerle et al. 2001).

Following intravenous administration, both [¹¹C]5-HTP and [¹⁸F]FDOPA undergo extensive metabolism (Bergstrom 1996; Luxen 1992). [¹¹C]5-HTP is rapidly decarboxylated to [¹¹C]5-Hydroxytryptamine (serotonin) by the enzyme *aromatic amino acid decarboxylase* (AADC). Subsequently, [¹¹C]serotonin is further metabolized to [¹¹C]5-hydroxy indole acetic acid (HIAA) by the enzyme *monoamine oxidase* (MAO). Finally both of these C-11 metabolites are excreted into the urine.

[¹⁸F]FDOPA is converted to [¹⁸F]Fluorodopamine (FDA), which can be oxidized by the enzyme MAO to L-3,4-dihydroxy-6-[¹⁸F]fluorophenyl-acetic acid ([¹⁸F]FDOPAC), which subsequently is O-methylated by catechol O-methyl transferase (COMT) to 6-[¹⁸F]fluoro-homovanillic acid ([¹⁸F]FHVA). Both, *AAAD* and *COMT* are present in peripheral tissues such as liver, kidneys, and lung. Further, both the decarboxylation of the radiolabeled amino acid precursors, and the release of radiometabolites into the blood can be reduced with carbidopa, a *decarboxylase* inhibitor. Carbidopa pretreatment improves overall image quality, image interpretation and may help detection of more lesions (Orlefors et al. 2006).

Based on a number of clinical studies, it has been documented that [¹¹C]5-HTP-PET is clinically useful for the detection of NETs (Oberg 2003; Orlefors 2003). The imaging technique is sensitive in imaging small NET-lesions (Fig. 15.19), such as primary tumors, and can, in a majority of cases, image significantly more tumor lesions than somatostatin receptor imaging using OctreoScan or CT scans (Orlefors et al. 2005). 5-HTP-PET can also be helpful for evaluating the metabolic effects of treatment, which are not obtained with other imaging modalities. This functional approach to imaging, however, may yield false-negative results in detecting undifferentiated carcinoids.

FDOPA was proposed initially as a biomarker for melanomas. The ability of NETs to accumulate and decarboxylate L-DOPA is well known and increased activity of *L-DOPA decarboxylase* was found to be a hallmark of NETs (Gazdar et al. 1988). Recently, very encouraging results have been reported in infrequent tumors such as neuroendocrine tumors (NETs), medullary thyroid carcinomas, and phaeochromocytomas (Hoegerle et al. 2001; 2002a, b; Becherer et al. 2004). In order to assess lung and liver involvement in patients
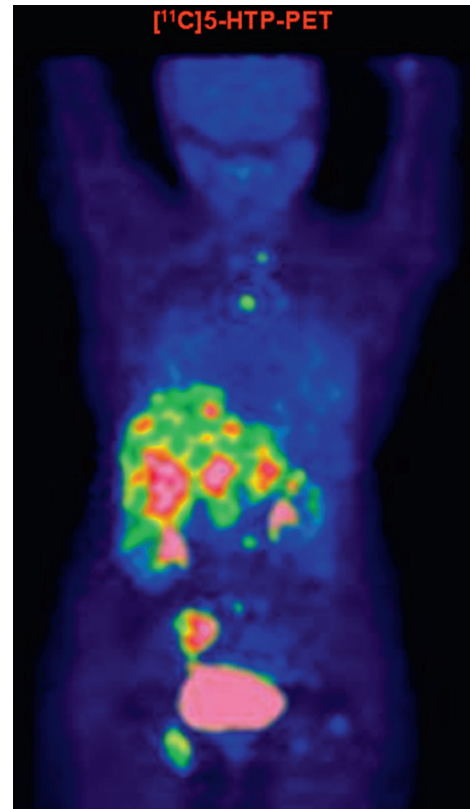
[¹¹C]5-HTP-PET

Fig. 15.19 [¹¹C]5-HTP-PET in a patient carcinoid with multiple metastatic liver lesions

with NETs, FDOPA-PET is regarded as being more accurate than conventional somatostatin receptor-SPECT based on OctreoScan (Becherer et al. 2004; Rufini et al. 2006). A recent review has also concluded that FDOPA-PET has excellent sensitivity and detects significantly more disease than all other currently applied modalities, and has a significant effect on patient management. Also in other conditions, such as medullary thyroid cancer, paraganglioma, and pheochromocytoma, FDOPA may have potential clinical utility (Jager et al. 2008).

As an amino acid analog, FDOPA is taken up at the BBB in the normal brain. In patients with brain tumors, the diagnostic accuracy of FDOPA has been compared with FDG (Chen et al. 2006, 2007; Chen 2007; Seibyl et al. 2007) and F-DOPA demonstrated excellent visualization of high- and low-grade tumors, and was able to detect low-grade, and recurrent tumors with greater sensitivity than FDG (Fig. 15.20).

15.3.2.6 Receptor Binding Ligands

A number of hormones and neurotransmitters bind to specific binding sites or receptors on the cell membrane (such as somatostatin receptors and dopamine receptors) or within the cell (such as estrogen receptors) in order to initiate specific actions. To measure the receptor expression as a function of disease status, radiolabeled receptor ligands (such as peptides and drug molecules) have been developed as molecular imaging probes. The binding of these probes to a target site, the receptor, is highly specific and depends on the *affinity*

(K_D) of the probe to the receptor and the number of total receptors (B_{max}) available for binding. Since the number of receptor sites is very limited and low in concentration (typically, nanomoles), high specific activity $(1–10\,Ci/\mu mole)$ radiotracers are essential for measuring the receptor expression. In addition, these radiotracers may have either low or high affinity to the receptors and are generally trapped in the target tissue following specific binding (reversible or irreversible) to the receptors. Further, since agonists are quickly metabolized (or inactivated) following binding to receptors, imaging probes are generally developed using receptor binding antagonists (or receptor blockers).

Somatostatin Receptors

A number of peptide receptors have been demonstrated to be overexpressed with higher incidence and/or density in various NETs (Table 15.5) (Reubi 2003). Because the majority of NETs express somatostatin (SS) receptors, they have been successfully targeted with radiolabeled SS analogs in vivo. SS receptor scintigraphy with ^{111}In-DTPAoctreotide (OctreoScan®) has become the main imaging technique for NETs and is used routinely.

SS, a 14-amino acid cyclic peptide is secreted throughout the body and has multiple physiological functions, including inhibition of secretion of growth hormone, glucagon, insulin, gastrin, and other hormones secreted by the pituitary and gastrointestinal tract. The diverse biological effects of SST are mediated through a family of G protein coupled receptors of which 5 subtypes have been identified. Human SST receptors (SSTR1-SSTR5) have been identified on most of the neuroendocrine tumors, small cell lung cancers, and medullary thyroid carcinoma, which express high densities of SSTRs (Reubi et al. 1992). The expression of

Fig. 15.20 [^{18}F]FDOPA-PET and ^{111}In-DTPA-Octreotide-planar scintigraphy in a patient with ileocecal carcinoid: FDOPA identifies multiple rib lesions and one sternal lesion in addition to carcinosis in the liver capsule and multiple abdominal nodes. In contrast, somatostatin receptor imaging shows rib lesions less clearly and misses sternal lesion and some of the abdominal nodes

Table 15.5 Potential peptide receptor systems for developing RMIPs for clinical use

Peptide	Receptor/subtype	Tumor expression	Peptide labeled with ^{99m}Tc, ^{111}In, or [123]I
Somatostatin	SSTR I–V	Neuroendocrine	Octreotide analogs
Bombesin	GRP-R	Prostate, Breast, GISTs, SCLC	Bombesin
CCK/gastrin	CCK2	MTC, insulinoma, SCLC, GISTs	Minigastrin
GLP-1	GLP-1-R	Insulinoma, gastrinoma	GLP-1
Neuropeptide-Y	NPY-R	Breast, Ovarian	Neuropeptide-Y
Neurotensin	NT-R1	Pancreatic, Meningioma	Neurotensin
Substance P	NK1	Glial tumors	Substance-P
VIP	VPAC1	GI and other epithelial tumors	VIP, TP3654

SSTR subtypes in human tumor tissues, however, seems to vary among different tumor types (Virgolini et al. 1997). Although various SS receptor subtypes are expressed in tumors, SSTR2 is the predominant one in NETs and clinically used SS analogs bind predominantly to SSTR2. Therefore, it is the presence of SSTR2 as well as its density that provides the molecular basis for a number of clinical applications of SS analogs.

The cyclic octapeptide octreotide was the first SS analog to be used in clinical practice as ^{111}In-DTPA-Octreotide. Subsequently, a number of octreotide analogs (Fig. 15.21) were conjugated with DOTA, which enables stable labeling with various metal ions (In, Ga, Y, Lu, Cu) resulting in tracers that are suitable for a variety of clinical applications (Henze et al. 2001; Maecke et al. 2005, Rufini et al. 2006). The affinity profiles for human somatostatin receptor subtypes of several SS radiotracers (Reubi et al. 2000; Rufini et al. 2006) useful for imaging studies is summarized in Table 15.6.

The peptides DOTA-TOC and DOTA-NOC have been developed recently and are becoming the gold standard for peptide based ^{68}Ga-PET (Henze et al. 2001; Eriksson et al. 2002; Gabriel et al. 2007). Preclinical data suggests that these radiotracers are superior to existing radiolabeled SS analogs, because they have a higher affinity for SSTR2 and, most importantly, for SSTR5 (Reubi et al. 2005; Wild et al. 2005). Preliminary clinical evaluation with ^{68}Ga-DOTA-TOC have demonstrated a rapid renal clearance and are rapidly accumulated in the tumors (80% within 30 minutes), thus, providing higher contrast imaging (Hofmann et al. 2001; Kowalski et al. 2003). The semiquantitative measurements such as SUV are useful to assess the response to treatment following radiopeptide therapy. Based on a recent clinical evaluation, in patients with known or suspected neuroendocrine tumors, it was concluded that SSTR imaging with ^{68}Ga-DOTA-TOC-PET is superior for the detection of NET compared to conventional planar imaging, SPECT with Octreo-Scan®, and diagnostic CT, in various clinical situations, such as initial diagnosis, staging, and follow-up (Gabriel et al. 2007). A comparison of ^{68}Ga-DOTA-TOC-PET

Ala – Gly – Cys – Lys – Asn – Phe – **Phe – Trp – Lys – Thr** – Phe – Thr – Ser – Cys   **Somatostatin**

DTPA - D-Phe – Cys – **Phe – D-Trp – Lys – Thr** – Cys – Thr(ol)   **DTPA-Octreotide**

DOTA- D-Phe – Cys – **Tyr – D-Trp – Lys – Thr** – Cys – Thr(ol)   **DOTATOC**

DOTA- D-Phe – Cys – **Tyr – D-Trp – Lys – Thr** – Cys – Thr(OH)   **DOTATATE**

DOTA- D-Phe – Cys – **Nal – D-Trp – Lys – Thr** – Cys – Thr(ol)   **DOTANOC**

(Nal = 3- (1-naphtalenyl)-L-alanyl)
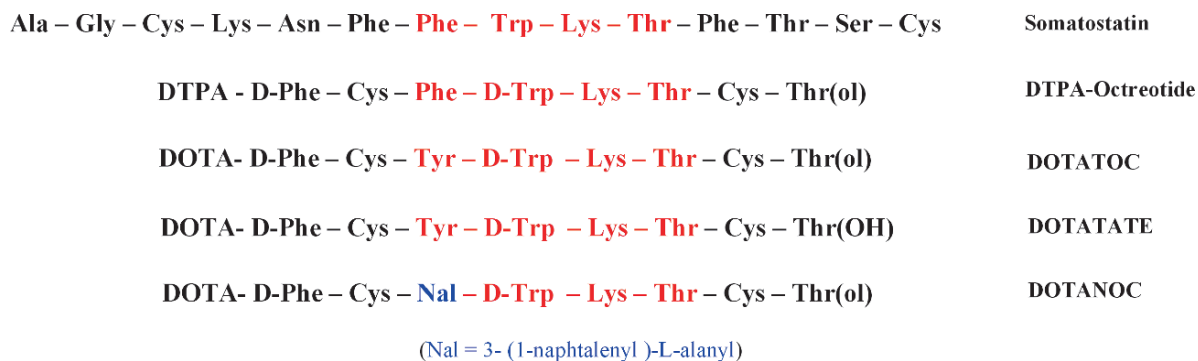
Fig. 15.21 The amino acid (AA) sequences of somatostatin and octreotide analogs: The four AA in *red* and *blue* color are essential for receptor binding. [68]Ga labeled DOTATOC and DOTANOC are under evaluation for imaging somatostatin receptors in patients with neuroendocrine tumors

Table 15.6 Somatostatin analogs: Affinity Profiles IC_{50}^a for the somatostatin receptor (SSTR) subtypes

Peptide	SSTR1	SSTR2	SSTR3	SSTR4	SSTR5
Somatostatin	5.2	2.7	7.7	5.6	4.0
DTPA-Octreotide	>10,000	22	182	>1,000	237
In-DOTA-TOC	>10,000	4.6	120	230	130
Ga-DOTA-TOC	>10,000	2.5	613	>1,000	73
DOTA-TATE	>10,000	1.5	>1,000	453	547
In-DOTA-NOC	>10,000	2.9	8.0	227	11.2
Ga-DOTANOC	>1,000	1.9	40	–	7.2
In-DOTA-BOC-ATE	>1,000	1.4	5.5	135	3.9

[a]IC_{50} values expressed in nanomoles (Rufini et al. 2007)
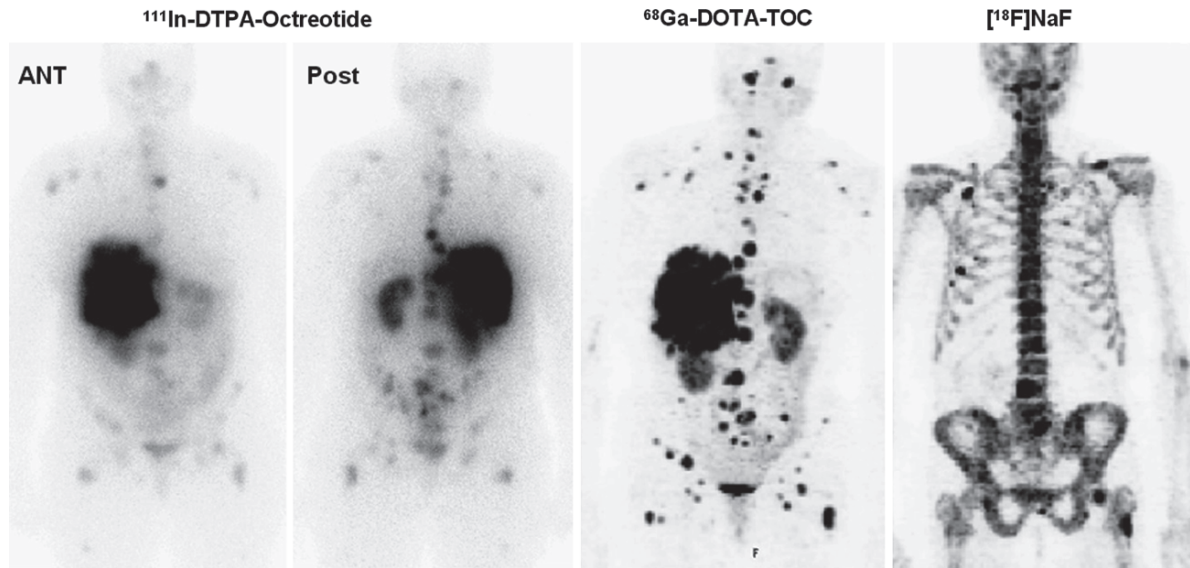
Fig. 15.22 ⁶⁸Ga-DOTATOC-PET in a patient with multiple liver and lymph node metastases: Comparison with ¹¹¹In-DTPA-Octreotide planar scintigraphy and [¹⁸F]Fluoride-PET. Beside the visceral metastases, some additional osteoblastic and osteolytic bone metastases were clearly depicted with ⁶⁸Ga-PET. Osteoblastic bone lesions were confirmed by [¹⁸F]Fluoride-PET. In contrast, only some of these bone metastases were delineated by conventional ¹¹¹In scintigraphy. (D). Retrospective CT analysis after image fusion revealed some of these bone metastases (Gabriel et al. 2007)

images with ¹¹¹In-Octreotide and ¹⁸F-fluoride-PET in a patient with multiple liver and lymph node metastases is shown in Fig. 15.22.

Neuroblastoma (NB), which arises from precursors of the sympathetic nervous system, is the most common extracranial, highly malignant, solid tumor of childhood. In NB, SSTRs are associated with favorable clinical and biological prognostic factors. A comparison between FDG PET and ⁶⁸Ga-DOTA-NOC (Fig. 15.23), performed in a patient with NB, demonstrated high glucose metabolism and intense SSTR expression in the same sites, ie, the primary tumor arising from the right adrenal and multiple bone lesions.

Due to the favorable half-life, dosimetry and pharmacokinetics, ⁶⁴Cu labeled SS analogs provide a good alternative to ⁶⁸Ga labeled peptides. It has been reported that ⁶⁴Cu-TETA-octreotide has potential clinical utility to image NETs. (Anderson et al. 2001). Since TETA is not an ideal macrocyclic chelate for Cu, a new generation of ⁶⁴Cu labeled peptides based on cross-bridged TETA analogs may provide radiolabeled peptides with higher in vivo stability in the near future. A novel carbohydrated analog of octreotide, ¹⁸F- fluoropropionyl-Lys⁰–Tyr³-octreotate (¹⁸F-FP-Gluc-TOCA), is also under investigation (Wester et al.
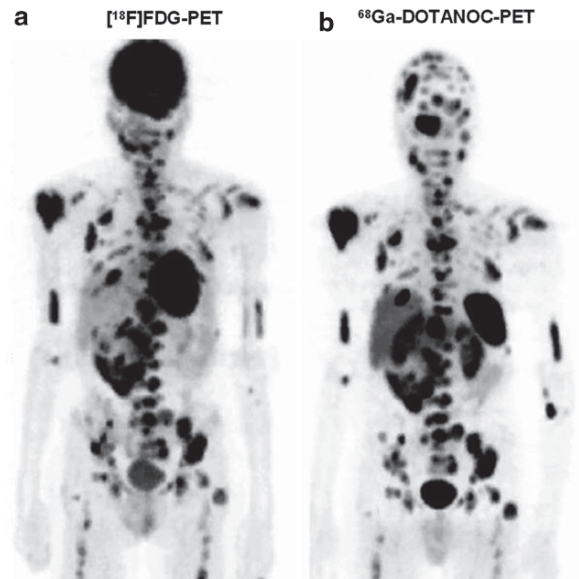
Fig. 15.23 Comparison of ⁶⁸Ga-DOTA-NOC-PET with [¹⁸F] FDG-PET in a patient with neuroblastoma (Rufini et al. 2006)

2003; Meisetschlager et al. 2006). Preliminary data indicate that the biodistribution of this ¹⁸F peptide resembles that of other SS analogs, suggesting its potential clinical utility (Fig. 1.6).

The ^{99m}Tc-labeled SS analog ^{99m}Tc-P829 or depreotide (NeoTec®) has shown high sensitivity and specificity in the evaluation of solitary pulmonary nodules, including small cell lung carcinoma (Lebtahi et al. 2002). Further, a new ^{99m}Tc labeled SS analog, ^{99m}Tc-EDDA-hydrazinonicotinyl-Tyr^3-octreotide (^{99m}Tc-EDDA-HYNIC-TOC) appears to be the most promising agent with clear advantages over the conventional SSTR imaging agent OctreoScan®.

Adrenergic Presynaptic Transporters: ^{131}I-MIBG

Tumors arising from the neural crest share the characteristic of amine precursor uptake and decraboxylation (APUD) and contain large amounts of adrenaline, dopamine and serotonin within the secretary granules in the cytoplasm. Tumors of the adrenergic system include pheochromocytoma (arise in adrenal medulla) or paragangliomas (extraadrenal tissue). Meta iodobenzylguanidine (MIBG) is an analog of noradrenaline (Fig. 15.24) originally developed by linking the benzyl portion of bretylium with the guanidine group of guanethidine (Wieland et al. 1980). Among the three isomers of iodobenzylguanidines, the meta isomer (MIBG) has less in vivo deiodination and liver uptake than the other two isomers. ^{131}I-MIBG and ^{123}I-MIBG are both available for routine clinical studies, but clinical experience indicates that ^{123}I-MIBG is the agent of choice. ^{123}I-MIBG, however, has not yet been approved by the FDA, although it is commercially available in Europe. The SA for diagnostic studies are typically 107–148 MBq/mg (2.9–4.0 mCi/mg) for ^{131}I-MIBG and 111–259 MBq/mg (3.0–7.0 mCi/mg) for ^{123}I-MIBG. For therapeutic studies with ^{131}I-MIBG, higher SAs of 15–40 mCi/mg are typically used. After an intravenous administration, the tracer is cleared mainly by excretion into the urine (Wafelman et al. 1994). It has also been observed that ^{131}I-MIBG accumulates in the chromaffin cells of the adrenal medulla. Since MIBG is structurally similar to noradrenaline, MIBG is believed to be transported into the cell by the reuptake pathways of the adrenergic presynaptic neurons. Within the cells, MIBG is transported into the catecholamine-storing granules by means of the ATPase-dependent proton pump. The major difference between MIBG and noradrenaline is that MIBG does not bind to post synaptic adrenergic receptors.

^{131}I-MIBG was initially used to image pheochromocytoma (McEwan et al. 1985). Reduced ^{131}I-MIBG uptake by the tumor has also been seen in patients using drugs like labetolol, calcium channel blockers, antipsychotic and sympathomimetic agents. The main indication for MIBG scintigraphy in oncology is the imaging of NETs and in particular catecholamine-secreting tumors, which are visualized with high sensitivity. MIBG is especially suitable for imaging tumors with functional activity, such as pheochromocytomas, functioning paragangliomas, neuroblastomas, medullary thyroid carcinomas, and carcinoids (Rufini et al. 2006).

Estrogen Receptors

In breast cancer, the stimulatory effect of estrogen and progesterone are mediated through nuclear estrogen receptors and progesterone receptors. Estrogen, a steroidal hormone, produces many physiological effects primarily by regulating gene expression by binding to specific estrogen receptors (ERs). Therefore, ER expression is an important determinant of breast cancer behavior and is critical for response to endocrine therapies, such as tamoxifen and aromatase inhibitors (Sundararajan et al. 2007). In current practice, ER expression is determined by an assay of biopsy material.

Estradiol (Fig. 15.25), the most potent form of estrogen in the body binds to ERs found in the cell nucleus of the female reproductive tract, breast, pituitary, hypothalamus, bone, liver, and other tissues, as well as in various tissues in men (Van de Wiele et al. 2000). For decades, it was assumed there was only one type of ER known as αER. However, a second ER form, βER, found to bind estradiol with a comparable
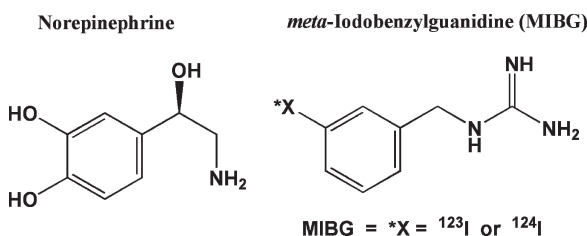
Fig. 15.24 ^{123}I or ^{124}I labeled MIBG for imaging patients with neuroendocrine tumors. MIBG is an analog of adrenergic neurotransmitter, norepinephrine

Estradiol

16β-[^{18}F]Fluoro-17β-estradiol (FES)

17β-[^{18}F]Fluoroestradiol (FES)

11β-methoxy-4,16α-[16α-^{18}F]difluoro-estradiol (4F-MFES)
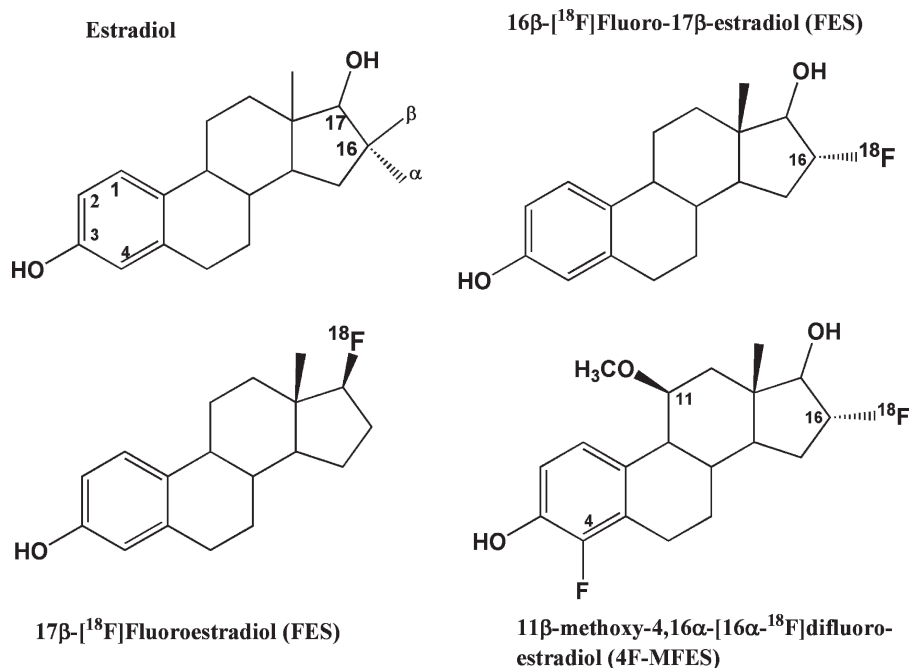
Fig. 15.25 ^{18}F labeled estradiol analogs for imaging estrogen receptor positive breast cancer metastases. Among these analogs, FES has been investigated extensively

K_d to αER, was recently described (Mosselman et al. 1996). Like αER, βER is a nuclear receptor that looks nearly identical to alpha in its so-called DNA-binding domain, the segment of the receptor that acts as a genetic switch, flicking some genes on and some genes off. While the αER predominates in the uterus and mammary gland, the βER is mostly in the ovaries, the testes and also in osteoblasts.

The growth of breast epithelial cells is an estrogen-mediated process that depends on estrogen acting through an ER and results in the induction of a progester one receptor. The ER status is an important prognostic factor in breast cancer because ER+ tumors have a slower rate of growth and are likely to respond to hormonal therapy (Van de Wiele et al. 2000). The main mechanism of action of antiestrogen tamoxifen is believed to be a block of division of estrogen-dependent tumor cells with arrest in the G_0 or G_1 phase of the cycle. However, 30–40% of all breast cancers do not express estrogen receptors (EŘ), and of the tumors with estrogen receptors (ER+), up to 50% will not respond to endocrine treatment (Vollenweider-Zerargui et al. 1986). Therefore, a noninvasive method which would accurately evaluate and quantify the presence of ER on the tumor and its metas-tases could help in the selection of patients for treatment and in predicting the therapeutic response.

In the last 25 years, a number of steroidal and non-steroidal estrogens have been labeled with positron emitting halogens. Retention of radiolabeled estradiol in estrogen target tissues through specific binding on the αER target was first reported in 1967 (Jensen et al. 1967). Estradiol and its derivatives are lipophilic and transported in the bloodstream bound either to a sex hormone binding protein (SBP) or to albumin. SBP binding protects steroids against liver metabolism and ensures their transport to the target tissues. Moreover, their affinity for SBP also contributes to their cell uptake, through membrane receptors for SBP (Van de Wiele et al. 2000). SBP receptors are present in a higher percentage of ER+ tumors (75%) than in ER-tumors (37%). Thus, membrane sequestration of estra-diol is likely to occur preferentially in hormone responsive tumors.

The most promising radiolabeled estrogen analog, identified to date is 16α-[^{18}F]fluoro-17β-estradiol (FES), which has good ER binding affinity and can be prepared effectively with a higher SA (Kiesewetter 1984; Mankoff et al. 1997). A number of clinical trials have docu-

mented the potential utility of FES-PET to identify ER+ breast tumors. FES-PET, however, is not necessarily an optimal tracer due to its rapid conversion to circulating radiometabolites, which prevent optimal localization of the tracer at ER binding sites (Mankoff et al. 1997). Several estradiol analogs with substitutions at various positions have been prepared to improve target selectivity. Among these analogs, two important agents may have significant potential for clinical evaluation (Fig. 15.25). Replacing the hydroxyl group with ^{18}F at the C17 position would result in [^{18}F] Fluoro-17β-estradiol, which has high affinity for the ER, and an excellent correlation between the tumor uptake in vivo and the tumor ER concentration measured in vitro (Kiesewetter et al. 1984). Addition of both a 4-fluoro and 11β-methoxy group to FES yields 11β-methoxy-4,16α-[16α-^{18}F]difluoroestradiol (4F-MFES) with potentially improved properties for estrogen receptor imaging studies (Ahmed et al. 2007). This tracer has shown increased in vivo stability and the highest target-to-nontarget ratios in an animal model (Seimbille et al. 2002).

The most studied and successful agent, so far, has been FES. Initially studies have demonstrated an excellent correlation between FES uptake in the primary tumor measured by PET images and the tumor ER concentration measured in vitro by radioligand binding

after excision of tissue from patients with primary breast masses (Mintum et al. 1988). Post-menopausal patients, patients with lower serum estradiol levels, patients with lower SHBG levels, and patients with prior hormonal therapy have greater average SUVs. FES-PET studies suggest that the initial FES uptake measurements in patients with ER-positive tumors is correlated with subsequent tumor response to 6 months of hormonal therapy (Linden et al. 2006). The clinical utility of FES-PET, to assess hormonal therapy, can be assessed based on FES-PET and FDG-PET as shown in Fig. 15.26.

15.3.2.7 Tumor Hypoxia

Hypoxia generally refers to a deficiency in the amount of oxygen that reaches body tissues. Hypoxia occurs in tumors as a consequence of the tumor cell proliferation exceeding the rate of angiogenesis, i.e., tumor cells are growing beyond the maximum range of oxygen diffusion in the tissue. In malignant tumors, hypoxia is an indicator of poor prognosis, regardless of the treatment modality used (Schöder and Ong 2008).

With increasing tumor size, there is a reduced ability of the local vasculature to supply sufficient oxygen to the rapidly dividing tumor cells (Vaupel et al. 1992).
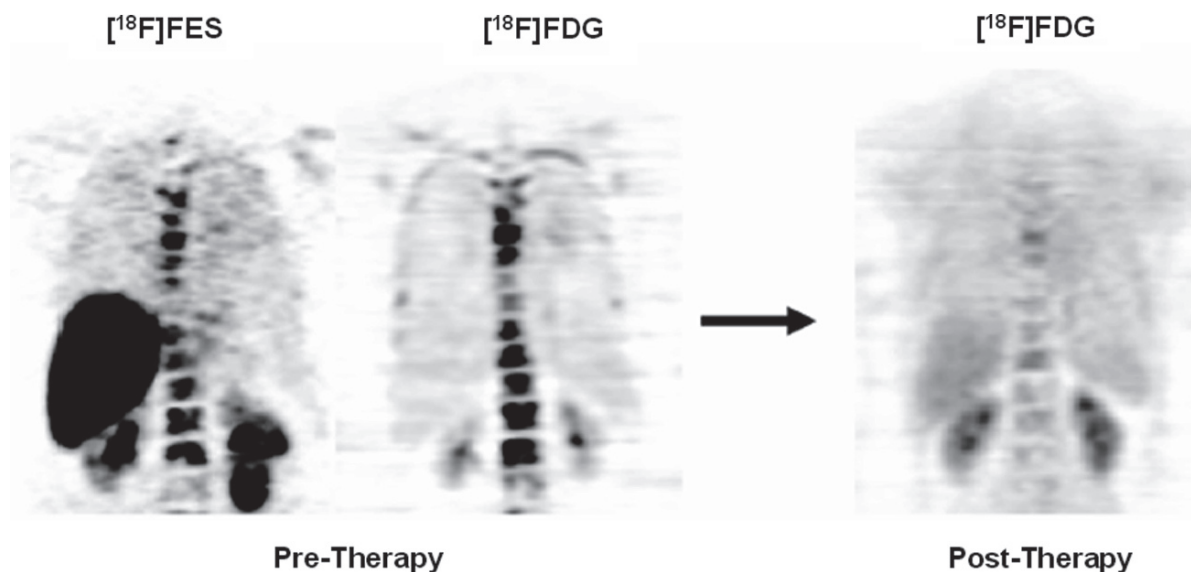
Fig. 15.26 [^{18}F] FES-PET in a patient with documented bone metastases from an ER+ primary breast cancer showed high FES uptake (indicating preserved ER expression), at all sites imaged, prehormonal therapy with FES and FDG. Following hormonal therapy, FDG-PET shows response to treatment

The resulting hypoxia may inhibit new cell division or even lead to cell death, but it may also lead to adaptive responses that will help cells to survive and progress. The presence of hypoxia in tumors has long been established as a key factor in the tumor progression and in the resistance of tumors to therapy (Foo et al. 2004). Well-oxygenated cells are more sensitive to the cytotoxic effects of ionizing radiation compared to poorly oxygenated cells. Therefore, hypoxia in tumor tissue seems to be an important prognostic indicator of response to either chemotherapy or radiation therapy.

2-Nitroimidazole (azomycin) was developed in the 1950s as an antibiotic targeted against anaerobic germs. In 1979, nitroimidazoles were first introduced as bioreducible markers of hypoxia and as sensitizing factors for radiation therapy of hypoxic tumors (Chapman et al. 1981). It has been observed that nitroimidazoles enter the cells by passive diffusion and undergo a single electron reduction to form a potentially reactive species (Whitmore and Varghese 1986). When oxygen is abundant, the molecule is immediately reoxidized. However, under hypoxic conditions, further reduction of the nitroimidazole molecule that forms covalent bonds to intracellular macromolecules, in a process of metabolic trapping within the hypoxic cell, occurs (Fig. 15.27).

[18F]Fluoromisonidazole (FMISO) was first introduced as a tracer for determining tumor hypoxia (Rasey et al. 1987). It binds selectively to hypoxic cells both *in vitro* and *in vivo*. FMISO-PET has been used to quantitatively assess tumor hypoxia in the lung, brain, and head-and-neck cancer patients and in patients with myocardial ischemia. FMISO is relatively hydrophilic

and diffuses across cell membranes, showing a passive distribution in normal tissues. Because of high lipophilicity, slow clearance kinetics, reaction mechanisms, low uptake in hypoxic cells, and the absence of active transport of this radiotracer, the identification and quantification of hypoxic tumor areas necessitates imaging for longer periods of time post injection. FMISO is the most extensively studied hypoxic PET radiopharmaceutical (Rajendran et al. 2006). Several other analogs (Fig. 15.28), such as [18F]fluoroerythronitroimidazole (FETNIM), [18F]Fluoro-etanidazole (FETA), and 1-(5-[18F]Fluoro-5-deoxy-α-D-arabinofuranosyl)-2-nitroimidazole (FAZA), have been developed with more favorable pharmacokinetics (Gronroos et al. 2001; Rasey et al. 1999; Piert et al. 2005; Beck et al. 2007). FETNIM is more hydrophilic than FMISO and shows promise for hypoxia imaging in humans. FETA demonstrates oxygen-dependent binding and retention in tumors that are very similar to that for FMISO, but metabolizes less rapidly. Recently, it has also been reported that FAZA displays a hypoxia-specific uptake mechanism and provides tumor-to-background ratios (T/B ratios) superior to that of the standard hypoxia tracer FMISO (Piert et al. 2005).

Several other radiolabeled PET markers of hypoxia have been developed. Cu(II)-diacetyl-*bis*(N4-methylthiosemicarbazone) (Cu-ATSM) has efficient uptake and washout kinetics due to its high membrane permeability and fast tumor uptake (Lewis and Welch 2001). Preliminary clinical studies with 60Cu-ATSM and 62Cu-ATSM have shown it to be a selective marker for hypoxia in human cancers and predicted response to therapy.

Based on initial preclinical studies with 123I-iodoazomycin arabinoside (Urtasun et al. 1996), 124I-labeled iodoazomycin galactoside (IAZGP), another nitroimidazole derivative, but with the long lived iodine radionuclide, was also developed to permit imaging studies at later points in time to achieve potentially superior target-to-background ratios (Zanzonico et al. 2004).

The importance of hypoxia in disease pathogenesis and prognosis is gathering increasing clinical significance and, thus, may have a great impact on patient management and outcome. The most extensively investigated and validated PET radiotracer of hypoxia, to date, is [18F]FMISO (Lee and Scott 2007). In patients with head and neck and nonsmall cell lung cancer
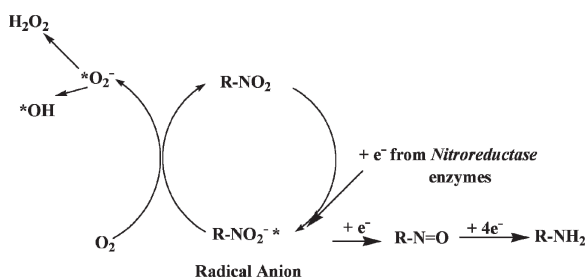
Fig. 15.27 The mechanism of intracellular trapping of nitroimidazoles. Under hypoxic conditions, the nitro group undergoes electron reduction to form reactive radicals which after further reduction form covalent bonds with intracellular macromolecules

[¹⁸F]Fluoromisonidazole (FMISO)

[¹⁸F]Fluoroerythronitroimidazole (FETNIM)

[¹⁸F]FAZA

[¹⁸F]Fluoroetanidazole (FETA)
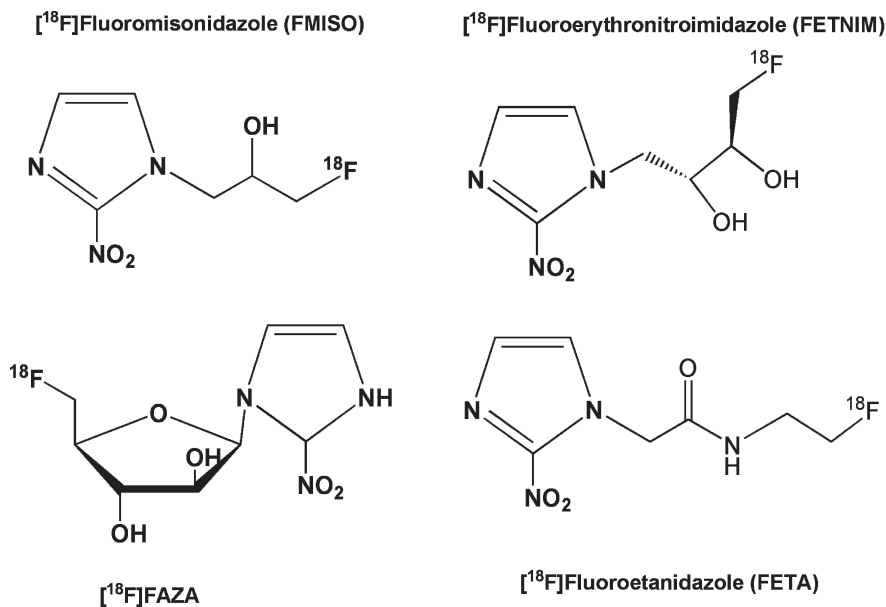
Fig. 15.28 ¹⁸F labeled nitroimidazole analogs to image hypoxia
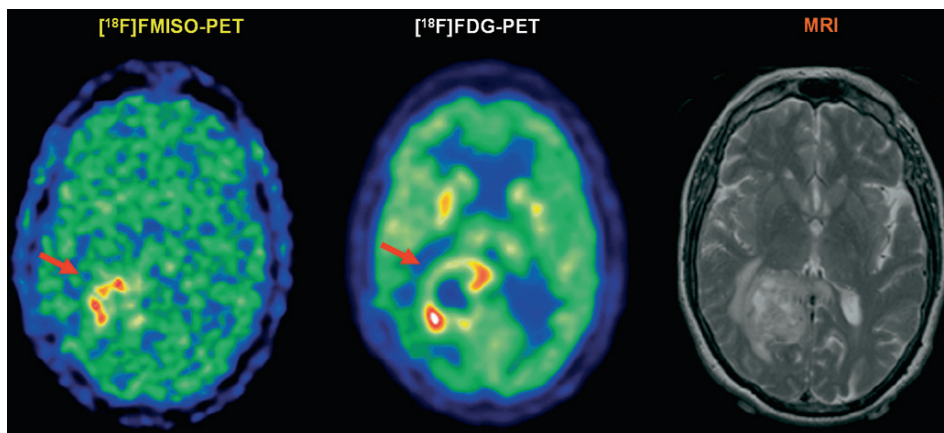
Fig. 15.29 ¹⁸F labeled analogs of nitroimidazole for imaging hypoxia

FMISO-PET has been used to document the extent of hypoxic tissue and/or as a prognostic indicator of treatment response. Overall decrease in tumor uptake of both FMISO and FDG may predict treatment response and overall survival (Lee and Scott 2007). In a patient with high-grade glioma, FMISO-PET can be used to identify hypoxic areas of postsurgical residual tumor (Fig. 15.29).

15.3.2.8 Angiogenesis

Angiogenesis, the formation of new blood vessels, is an important aspect of the tumor phenotype. It is essential to deliver nutrients for tumor growth, invasion, and metastatic spread. Tumors switch to angiogenesis under a variety of stress signals, which results in tumor growth and metastases. As a general rule, tumors do not grow

beyond 1 to 2 mm without producing new blood vessels (Folkman 1971). Many solid tumors develop areas of hypoxia during their evolution. This is primarily caused by the unregulated cellular growth, which results in a greater demand for oxygen for energy metabolism. Hypoxia in tumor cells leads to amplification and over-expression of various signaling factors, such as HIF-1α or HIF-2α, which promote tumor growth, invasion, metastasis, and resistance to apoptosis. Tumor hypoxia and angiogenesis are intimately related and HIF-1α is probably the single most important factor promoting the expression of proangiogenic proteins (Pugh and Ratcliffe 2003). Although, angiogenesis is a frequent consequence of hypoxia, some tumors develop extensive angiogenesis without the presence of hypoxia and, vice versa. The emergence of angiogenesis, as an important target for cancer therapy, has prompted a great deal of new research in an attempt to understand this molecular process and to develop molecular imaging probes to image accelerated angiogenesis or monitor the response to antiangiogenic therapies.

Cell adhesion receptors of the integrin family are responsible for a wide range of cell–extracellular matrix and cell–cell interactions, and have been well studied in many tumor types. One of the most prominent members of this receptor class is $\alpha_V\beta_3$ integrin, which is highly expressed on activated endothelial cells, which undergo angiogenesis and vascular remodeling, and solid tumor cells, particularly in pathways stimulated by vascular endothelial growth factor (Friedlander 1995). It is not expressed on mature vessels or on non neoplastic epithelium. The expression of integrin $\alpha_V\beta_3$ on sprouting capillary cells and its interaction with specific matrix ligands has been shown to play a key role in angiogenesis and metastasis (Kumar 2003). The data from preclinical tumor models and from phase I/II clinical trials suggest that antibody, peptide and peptidomimetic antagonists of $\alpha_V\beta_3$ integrin inhibit tumor angiogenesis and metastasis (Jin and Warner 2004).

Several radiolabeled ligands of the $\alpha_V\beta_3$ receptor have been developed based on the integrin's recognition of the RGD sequence of adhesive proteins first reported using ^{125}I labeled RGD (Haubner et al. 1999). A dimeric RGD peptide, E-[c(RGDfK)]$_2$, was conjugated with DOTA and HYNIC chelators, which enabled efficient labeling with ^{111}In, ^{64}Cu and ^{99m}Tc, respectively (Haubner and Wester 2004). It was, subsequently, observed that the receptor-binding characteristics of dimeric and multimeric RGD peptides are better than that of monomeric

RGD peptide based on polyvalency. The cyclic RGD peptide, E[c(RGDyK)]$_2$ has been labeled with ^{18}F by conjugation coupling with *N*-succinimidyl-4-^{18}F-fluorobenzoate (^{18}F-SFB) and product, ^{18}F-FB–E[c(RGDyK)]$_2$ or ^{18}F-FRGD2 has shown high intergrin specificity and in vivo targeting in tumor bearing mice (Zhang et al. 2006). A RGD peptide tetramer was also developed with repeating c(RGDfK) units connected through glutamate linkers and, subsequently, conjugated with DOTA. The ^{64}Cu-DOTAE{E[c(RGDfK)]$_2$}$_2$ has shown favorable biokinetics (Wu et al. 2005).

[18]F-galacto-RGD (FG-RGD) peptide was developed for specific imaging of $\alpha_V\beta_3$ receptor expression and a significant correlation has been demonstrated in tumor xenografts between FG-RGD uptake and $\alpha_V\beta_3$ receptor expression (Haubner et al. 2001). In cancer patients, FG-RGD has shown accumulation in some of the tumor lesions, however, in a comparative study, no correlation between FDG and FG-RGD RGD tracer uptake in the tumors was found, indicating that the sensitivity of FG-RGD for tumor detection is clearly inferior to that of FDG (Fig. 15.30) (Beer et al. 2008).

15.3.2.9 Apoptosis

It is now widely acknowledged that apoptosis, also known as programmed cell death, is central to homoeostasis and the normal development and physiology in all multicellular organisms, including humans. The formation of cancer, as a result of dysregulation of apoptosis, and the successful treatment of cancer (iatrogenic modification, cell removal) both represent opposite sides of the apoptosis coin (Blankenberg 2008).

Apoptosis is an active, highly conserved, and genetically controlled process. The basic biochemical and morphological changes of apoptosis have been reviewed extensively (Böhm and Schild 2003; Blankenberg 2008). The histological changes of apoptosis are preceded by an initiation stage called the "lag or trigger phase." Multiple triggers of apoptosis are known, such as withdrawal of growth factors, DNA damage, immune reactions, ionizing radiation, chemotherapy, and ischemic injury. Most apoptotic pathways, however, converge on a common cascade of cysteine aspartate– specific proteases, collectively known as the *caspases*, which upon activation cross-link and cleave specific intracellular proteins involved with apoptosis. A milestone in apoptosis research is the discovery
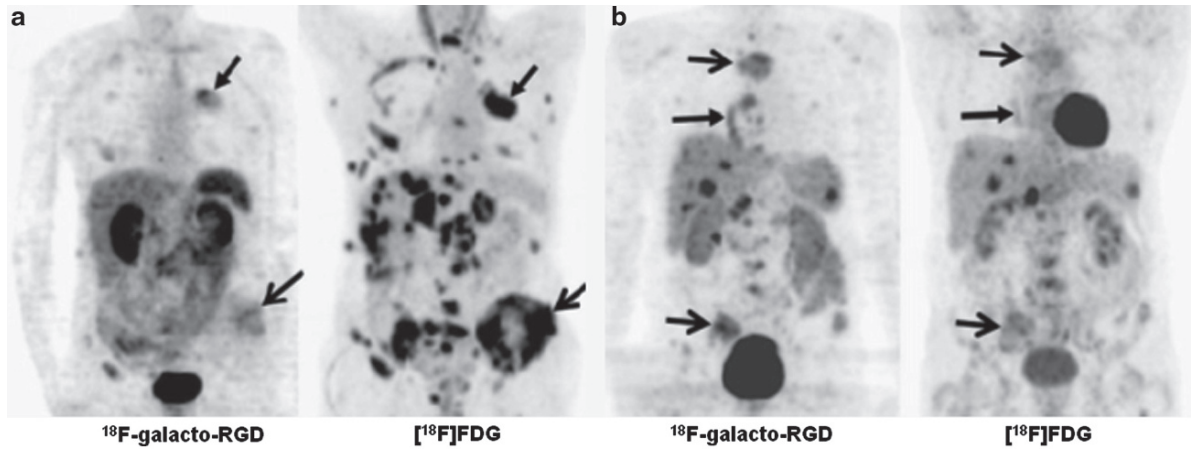
Fig. 15.30 Comparison of ^{18}F-galacto-RGD (FG-RGD-PET) with [^{18}F]FDG-PET in patients with cancer. (**a**) Patient with NSCLC of left upper lobe (*arrow, closed tip*) and multiple metastases to bone (*arrow, open tip*), liver, lymph nodes, and adrenal glands. (**b**). Patient with neuroendocrine tumor of bronchus in right lower lobe (*arrow, closed tip*) and multiple metastases to bone (*arrows, open tip*), liver, spleen, and lymph nodes (Beer et al. 2008)
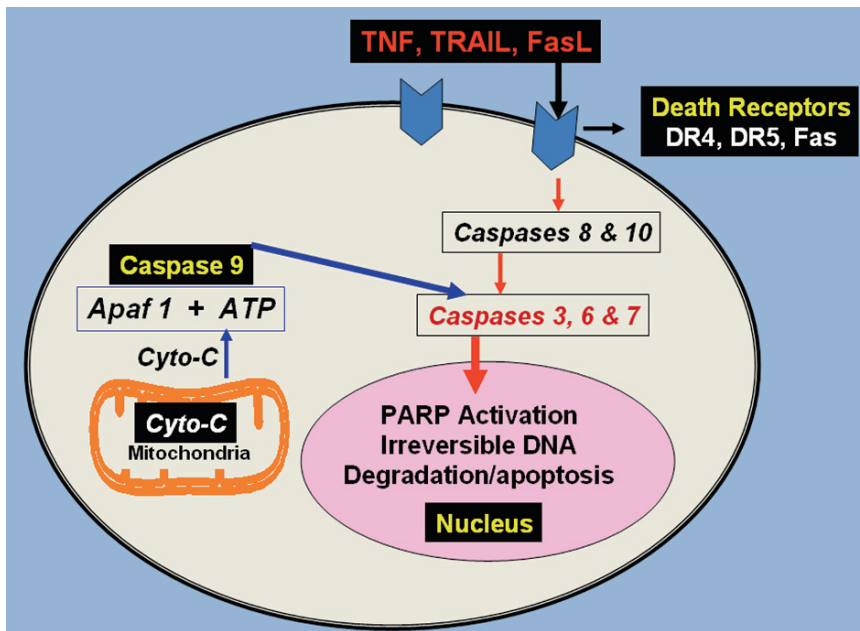
Fig. 15.31 Biochemical events in apoptosis. Extrinsic pathway of apoptosis is initiated by the binding of specific ligands to the death receptors. These ligands include tumor necrosis factor (TNF), a TNF-related, apoptosis-inducing ligand (TRAIL), and Fas ligand (FasL). The intrinsic pathway is initiated by cytochrome c from the mitochondria into the cytosol. The final enzyme activated within the cascade is caspase-3, following which the morphologic events of apoptosis quickly follow, resulting in the orderly breakdown of cellular proteins, including the cytoskeleton and nuclear matrix

of the apoptosis receptor APO-1 (CD95, Fas) (Krammer 2000). The biochemical events associated with the interaction of death receptors and caspases leading to apoptosis are shown in the Fig. 15.31.

Even at the early stages of apoptosis the cell membrane displays functional alterations. The hallmark of the start of the execution phase is the redistribution and exposure of phosphatidylserine (PS) on the cell

surface. PS is normally restricted to the inner surface (inner leaflet) of the lipid bilayer by an ATP dependent enzyme called *translocase* (Zwaal et al. 2005). Translocase in concert with a second ATP-dependent enzyme, *floppase*, which pumps cationic phospholipids, such as phosphatidylcholine (PC) and sphingomyelin to the cell surface, maintains an asymmetric distribution of different phospholipids between the inner and outer leaflets of the plasma membrane. The rapid redistribution of PS and PC, across the cell membrane (measured in minutes), at the beginning of the execution phase of apoptosis is facilitated by a calcium ion–dependent deactivation of translocase and floppase, and activation of a third enzyme, called *scramblase* (Blankenberg 2008). PS can also be expressed at low levels in a reversible fashion under conditions of cell stress by the presence of physiological stressors, such as nitricoxide, p53 activation, allergic mediators, and growth factor deprivation. Therefore, PS expression can be used to define tissues at risk for cell death that may recover or be amenable to prompt therapeutic intervention.

Annexin V ($\approx$36,000kD) is an endogenous human protein that is widely distributed intracellularly, in the placenta, endothelial cells, kidneys, myocardium, skeletal muscle, skin, red cells, platelets, and monocytes (Boersma et al. 2005). Annexin V binds to the externalized PS with extremely high affinity (Kd = 7nmol/l), as well as specificity. Consequently, annexin V has been used in vitro to identify apoptotic cells. The annexin V binding to PS, however, needs all 4 calcium binding sites and the affinity declines greatly over a calcium range of 2.5–1.25mmol/L. Although, the precise physiological function of annexin is uncertain, it has a specific function in the inhibition of coagulation, *phospholipase A2* (an enzyme responsible for the release of arachidonic acid from the cell membrane), and *protein kinase C*, a system responsible for intracellular signaling. It may also play a significant role in the immunomodulatory effects of dying and dead cells. Following binding to rafts of PS exposed on the cell surface, annexin V forms a protein crystal with subsequent and rapid internalization via pinocytosis (Kenis et al. 2004).

Imaging Apoptosis

^{99m}Tc-labeled recombinant human (rh)–annexin V (based on N_2S_2 labeling method) was introduced in

1990s as a tracer for imaging apoptotic tissue (Tait et al. 1994). In the first clinical study with cancer patients (SCLC and NDCLC, lymphoma, and metastatic breast cancer), ^{99m}Tc-Annexin V-SPECT was performed prior to therapy and immediately after the first course of treatment (Belhocine et al. 2002). In the majority of patients (13/15), the relative change in ^{99m}Tc-annexin uptake corresponded to the treatment response, compared to the baseline.

An improved labeling method using the bifunctional agent hydrazinonicotinamide (HYNIC) was subsequently developed to prepare ^{99m}Tc-HYNIC-annexin V (Kemerink et al. 2003). Multiple clinical trials have confirmed the clinical utility of ^{99m}Tc-HYNIC-annexin V imaging in determining the efficacy of chemotherapy in oncology patients for the detection of apoptosis in areas of acute myocardial infarction, for monitoring the effects of ischemic preconditioning), and for imaging acute stroke (Blan-kenberg 2008). The potential clinical utility of apoptosis imaging, to monitor treatment response in oncology patients, is shown in Fig. 15.32.

A number of radiolabeled derivatives of annexin V have also been developed for SPECT and PET imaging studies. These include ^{18}F-annexin V, ^{123}I or ^{124}I-annexin V, ^{111}In or ^{64}Cu labeled DOTA-annexin V and self-chelating ^{99m}Tc- annexin V analogs (V117, V128 and annexin B1). Some of these preparations, however, rely on the random modification of annexin V with BFCs. Several studies have demonstrated that the chemical modification of annexin V is damaging to the bioactivity of annexin V and a loss of in vivo PS binding affinity, compared to unmodified wildtype annexin V.

Because the field of apoptosis imaging is changing quite rapidly, it is difficult to make predictions about which set of tracers or imaging modalities will prove successful for clinical applications. For the time being, it appears that agents that bind to the surface of stressed or apoptotic cells, including annexin V and its derivatives, have an advantage, with respect to sensitivity and specificity, over metabolically directed tracers, such as caspase-related radiopharmaceuticals (Blankenberg 2008).

15.3.2.10 Antigen–Antibody Binding

With Immuno-SPECT and Immuno-PET, the tracking and quantification of mAbs in vivo, is an exciting novel

Fig. 15.32 Apoptosis imaging with
^{99m}Tc-HYNIC-Annexin V in a patient
with new right humeral metastasis and
stage IV NSCLC. The images revealed a
faint uptake at level of the bony metasta-
sis 2 h before the first course of chemo-
therapy (*yellow arrow*), which
significantly increased 1 day after start of
therapy. In addition, increased tracer
uptake was detected in primary lung
tumor as early as 1 day after initiation of
cis-platinum-based chemotherapy (*black
arrow*). *White arrow* shows intravenous
injection site in left arm (Blankenberg
2008)
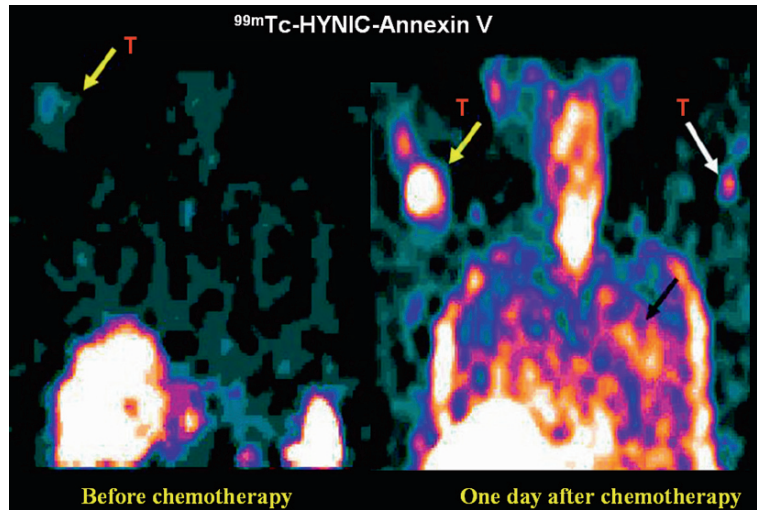
Table 15.7 FDA approved monoclonal antibodies for diagnosis and therapy in oncology

Year	Generic(Trade) name	Target	Type	Indication
	^{111}In-satumomab pendetide (OncoScint™)	Tumor associated glycoprotein-72	Murine IgG	Ovarian and colorectal cancer
	^{99m}Tc-acritumomab (CEA-Scan™)	Carcinoembryonic antigen (CEA)	Murine F(ab')	Colorectal cancer
	^{99m}Tc-Nofetumomab Merpentan (Verluma™)	Epithelialccell adhesioncmolecule	Murine Fab	Small cell lung cancer
	^{111}In-capromab pendetide (ProstaScint™)	Prostate specific membrane antigen (PSMA)	Murine IgG$_1$	Prostate cancer
1997	Rituximab (Rituxan®)	CD20	Chimeric IgG$_1$	Lymphoma
1998	Trastuzumab (Herceptin®)	Human epidermal growthcfactor receptor (HER-2 neu)	Humanized IgG$_1$	Breast cancer
2000	Gemtuzumab ozogamicin (Myelotarg®)	CD33	Humanized IgG$_4$ conjugated to calicheamicin	Acute myeloid leukemia
2001	Alemtuzumab (Campath®)	CD52	Humanized IgG$_1$	Chronic lymphatic leukemia
2002	^{90}Y-ibritumomab tiuxetan (Zevalin®)	CD20	Murine IgG$_1$	Non Hodgkin's lymphoma
2003	^{131}I-Tositumomab (Bexxar®)	CD20	Murine IgG$_{2A}$	Non Hodgkin's lymphoma
2004 2006	Bevacizumab (Avastin®)	VEGF	Humanized IgG$_1$	Colorectal cancer Nonsmall cell lung cancer
2004 2006	Cetuximab (Erbitux®)	Epidermal growth factor receptor (EGFR)	Chimeric IgG$_1$	Colorectal cancer Head and neck cancer
2006	Panitumumab (Vectibix®)	EGFR	Human IgG$_1$	Colorectal cancer

option to improve diagnostic imaging, and, this option
may, in the future, play an important role in cancer
staging, in the improvement and tailoring of therapy
with existing mAbs, and in the development of effi-
cient and novel mAbs. To date, the U.S. FDA has
approved five mAbs for diagnosis (four for the detec-
tion of cancer) and 21 mAbs for therapy, most of them
for the systemic treatment of cancer (Table 15.7). Also,

hundreds of new mAbs are under development world-
wide (Van Dongen et al. 2007). Also, a variety of
promising antigens/targets are currently being evaluated
in clinical trials, at various stages. Tumor-associated
antigens and receptors present on the tumor cell surface
include CD20, CD22, PSMA, mucin 1 (MUC1), CEA,
pancarcinoma antigens (TAG-72), sialyl Lewis anti-
gens, HER2/neu receptors, tumor-necrosis-factor-related
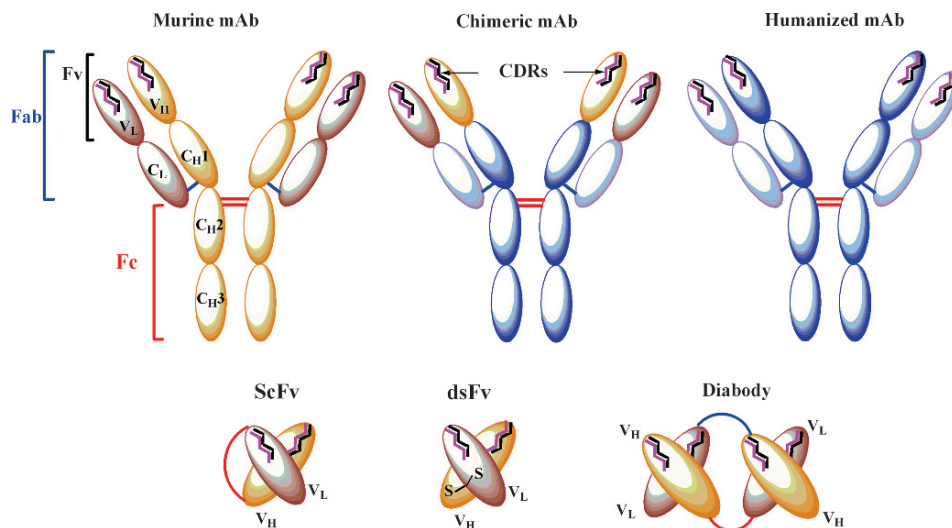
Fig. 15.33 The classification of monoclonal antibodies (mAbs): The fundamental structure of an intact, single immunoglobulin G (IgG) molecule has a pair of light chains and a pair of heavy chains. Light chains are composed of two separate regions (one variable region (V_L) and one constant region (C_L)), whereas heavy chains are composed of four regions (V_H, C_H1, C_H2 and C_H3). The complementarity-determining regions (CDRs) are found in the variable fragment (Fv) portion of the antigen-binding fragment (Fab). In a chimeric antibody, the mouse heavy- and light-chain variable region sequences are joined onto human heavy-chain and light-chain constant regions. In a humanized antibody, the mouse CDRs are grafted onto the human V-region FRs and expressed with human C-regions. Monovalent and multivalent antibody fragments are shown at the bottom of the figure; Single chain Fv fragments (scFv); Disulfide-stabilized Fv fragments (dsFv); Noncovalent scFv dimer (diabody)

apoptosis-inducing ligand receptors and, epidermal growth factor receptors (EGFR). In contrast, VEGF and integrins are more abundant on the vascular endothelial cells within newly sprouting blood vessels, which nourish the nearby tumor during angiogenesis.

A century ago, Paul Ehrlich postulated the notion that a *magic bullet* could be developed to selectively target disease and he envisioned that antibodies could act as such (Himmelweit 1957). The introduction of hybridoma technology for the mAb development turned this magic bullet concept into a reality (Köhler and Milstein in 1975). The first generations of mAbs were of murine origin and had limited clinical use; however, developments in recombinant DNA technology have resulted in the production of chimeric (c-mAb), humanized (h-mAb), and complete human mAbs (Fig. 15.33).

Chimeric mAbs are constructed with variable regions (V_L and V_H) derived from a murine source and constant regions derived from a human source. Humanized therapeutic mAbs are predominantly derived from a human source except for the CDRs, which are murine. There is a significant difference between the IgG subclasses in terms of their half-lives

in the blood (IgG_1, IgG_2 and IgG_4 approximately 21 days; IgG_3 approximately 7 days) and in terms of their capability to activate the classical complement pathway and to bind Fc-receptors. The choice of an IgG subclass is a key factor in determining the efficacy of therapeutic mAbs. Most of the FDA approved mAbs belong to the IgG_1 subclass, which has a long half-life and triggers potent immune-effector functions, such as complement-dependent cytotoxicity (CDC), complement-dependent cell-mediated cytotoxicity (CDCC), and antibody-dependent cellular cytotoxicity (ADCC).

In addition to intact mAb molecules, mAb fragments, like F(ab')$_2$, F(ab'), Fab, and engineered variants, such as single chain Fv (scFv), the covalent dimers scFv$_2$ diabodies, and the minibodies (molecular weights ranging from 25 to 100 kDa) have all been developed to improve pharmacokinetics, tumor localization, and antigen binding (Holliger and Hudson 2005; Sharkey and Goldenberg 2005). More recently it has also become possible to produce totally human recombinant antibodies derived either from antibody libraries or single immune B cells, or from transgenic mice, bearing human immunoglobulin loci. Single chains are formed by linking the variable light (V_L)

and variable heavy (V_H) chains with an amino acid (AA) linker. Diabodies, triabodies, and even tetrabodies are formed spontaneously when smaller length AA chains are used to hold the V_H and V_L units together. Recombinant bispecific diabodies and other bispecific constructs can be prepared by pairing V_H and V_L of two antibodies with different specificities (Sharkey and Goldenberg 2005).

Size, Penetration and Clearance Rate of Antibodies and Fragments

Intact mAbs have a long residence time in humans, ranging from a few days to weeks, which results in optimal tumor-to-nontumor ratios at 2–4 days postinjection. In contrast, mAb fragments have a much faster blood clearance and as a result optimal tumor-to-nontumor ratios can be obtained at earlier time points; however, the absolute tumor uptake may be much lower compared to intact mAbs. The targeting properties of various antibody molecules of different sizes is compared in Table 15.8. In general, intact mAbs are preferable for therapy, while the optimal format for diagnosis is still under discussion.

Size is one factor that impacts the circulation time of Abs (Boswell and Brechbiel 2007). A full IgG mAb is a large 150-kDa protein that can remain in circulation for 3–4 weeks while being metabolized slowly by the reticuloendothelial system. In contrast, a 25-kDa monovalent fragment (scFv) has a blood clearance time of <10 h with primarily renal excretion in 2–4 h. The Fv fragment, consisting only of the V_H and V_L domains, is the smallest immunoglobulin fragment available that carries the whole antigen-binding site.

However, scFvs have never fared well in the clinic, despite their small size (25 kDa), because of their poor tumor retention. Molecules with molecular weights above >70 kDa (the glomerular filtration threshold) remain in circulation much longer than smaller more rapidly eliminated molecules. Recent protein engineering has been used to produce designer bispecific antibodies that are based on antibody Fv or scFv fragments as building blocks, rather than whole antibodies. One such fragment is the diabody, a dimer, each chain comprising two domains. Each chain consists of a V_H domain connected to a V_L domain using a linker to short to allow pairing between domains on the same chain (Holliger and Winter 1997). Diabodies (55 kDa) are the smallest engineered fragments that are bivalent, retaining the chief advantage of whole antibodies, namely, avidity. Increased tumor uptake has been observed for intermediate-sized bivalent Ab formats, such as 75-kDa triabodies and 80-kDa minibodies (scFv-CH_3); however, slower blood clearance was evident. Larger bivalent antibody fragments, such as F(ab')$_2$ fragments, have slower blood clearance than diabodies, resulting in optimal tumor-to-normal tissue ratios only at prolonged times (18–24 h) relative to those of diabodies (3–5 h).

Choice of Radionuclide for Labeling Antibodies

For imaging studies, a successful diagnostic mAb or a low molecular weight fragment must be radiolabeled with a radionuclide that has an appropriate half-life adequate for target accumulation and nonspecific clearance. For example, labeling an intact IgG with ^{18}F ($T_{1/2}$ = 110 min) or ^{68}Ga ($T_{1/2}$ = 68 min) is an impractical

Table 15.8 Comparison of targeting properties of representative forms of antibody and chemically prepared or engineered fragments

Antibody/fragment	Size (kDa)	Relative $T_{1/2}$ rank[a]	Target organ	Tumor binding properties		
				Relative uptake[b]	Relative duration[c]	Time to optimum accretion time
IgG	150	1 day	Liver	1	1	Day(s)
F(ab')$_2$	100	2 days	Liver	2	2	Day
Fab'	50	3 h	Kidneys	3	3	Hours
Daibody	40	3 h	Kidneys	3	3	Hours
ScFv	20	4 h	Kidneys	4	4	Hour

[a]Relative biologic half-life from blood (grading: slowest (1) and fastest (4))
[b]Based on intravenous infusion. Numbers represent grading from highest (1) to lowest (4)
[c]Numbers represent grading from longest (1) to shortest (4)
The above table is from Sharky and Goldenberg (2005)

endeavor. Perhaps the best radionuclides are those that possess half-lives compatible with mAb biological half-lives, such as ^{111}In ($(T_{1/2} = 67.3\,h)$, ^{89}Zr ($T_{1/2} = 78.4\,h$)) or ^{124}I($T_{1/2} = 100.2\,h$). Labeling intact IgGs with radionuclides with relatively longer half-life, such as ^{64}Cu ($T_{1/2} = 12.7\,h$), ^{86}Y ($(T_{1/2} = 14.7\,h$) or ^{123}I ($T_{1/2} = 13\,h$), however, would be a more reasonable choice.

The radionuclide decay, particle charge and associated γ emissions are all equally important. ^{111}In has always been a popular choice for SPECT imaging studies. For immuno-PET, high-energy β^+ emission (e.g., ^{66}Ga) may produce PET images of relatively poor quality and resolution; lower-energy β^+-emitters with no or minimal γ photons (e.g., ^{64}Cu) are more desirable.

Radiolabeling procedures must be simple, efficient, reproducible, and affordable. In addition, labeling an antibody with a radionuclide must fulfill a single critical requirement which is to maintain the affinity/avidity of the antibody for its target antigen. Direct radioiodination using ^{123}I or ^{124}I is a well established technique, but due to in vivo dehalogenation, direct iodination of internalizing antibodies is not an appropriate method. Metallic radionuclides such as ^{64}Cu, $^{66/68}$Ga, ^{86}Y and ^{89}Zr require chelation chemistry for radiolabeling to an antibody molecule. BFCs have been coupled directly to the protein or to the carbohydrates that reside on the Fc portion of the mAb. Choosing a BFC that forms an adequately, kinetically and thermodynamically stable complex within the context of radionuclide choice and application is also critical (Chap. 12). Acyclic DTPA-based and macro-cyclic DOTA-based chelators represent the most commonly utilized classes of agents used for radiolabeling protein molecules with radiometals such as ^{111}In and $^{66/68}$Ga. Further, cross-bridged macrocyclic TETA analogs (such as Sar and SarAr) have shown to provide greater in vivo stability with ^{64}Cu (II) protein complexes.

Antibody Imaging

Before PET technology became broadly available, the potential utility of immunoimaging was demonstrated extensively with mAbs labeled with radionuclides (^{111}In, ^{131}I, ^{186}Re and ^{99m}Tc) useful for SPECT imaging studies. Although these SPECT camera images were very informative, the need for more accurate quantification i.e. to the exploration of the potential of PET for mAb imaging. In 1995, the potential utility of immuno-PET was demonstrated using anticolorectal carcinoma, ^{64}Cu-DOTA-mAb 1A3 in patients with suspected advanced primary or metastatic colorectal cancer (Philpott et al. 1995). The long-lived positron emitters $_{124}$I and ^{89}Zr are particularly suitable for immuno-PET when used in combination with intact mAbs. Several clinical studies have demonstrated the potential clinical value of immuno-PET based on ^{64}Cu, ^{89}Zr, and ^{124}I labeled mAbs (Table 15.9). In addition, a number of new mAbs, engineered mAb fragments, and nontraditional antibody-like scaffolds directed against either validated or novel tumor targets are under develop-

Table 15.9 Radiolabeled antibody imaging studies: clinical and preclinical applications

Radiolabeled antibody	Target	Imaging study	Reference
^{64}Cu-DOTA-mAb 1A3	Colorectal carcinoma	Clinical study	Philpott et al. (1995)
^{64}Cu-DOTA-minibody T84.66/GS18	CEA	MicroPET	Wu et al. (2000)
^{64}Cu-DOTA-cetuximab	EGFR	MicroPET	Cai et al. (2007b)
^{64}Cu-DOTA-MEDI-522,	Integrin $\alpha_v\beta_3$	MicroPET	Cai et al. (2006)
^{124}I-HuMV833	VEGF121 and VEGF165,	Patients with solid tumors	Jayson et al. (2002)
^{124}I-labeled c-mAb G250	Carbonic anhydrase-IX expression	Patients with clear cell renal carcinoma	Divgi et al. (2007)
^{89}Zr-bevacizumab	VEGF	MicroPET	Nagengast et al. (2007)
^{89}Zr-labeled c-mAb U36	CD44v6	Patients with head and neck squamous cell carcinoma	Borjesson et al. (2006)
^{89}Zr-trastuzumab	HER-2 expression	Patients with metastatic breast cancer	Dijkers et al. (2007)
^{111}In-trastuzumab	HER-2 expression	Patients with metastatic breast cancer	Perik et al. (2006)
^{68}Ga-trastuzumab F(ab')$_2$	HER2 expression	MicroPET	Smith-Jones et al. (2004)
^{18}F-T84.66 Anti CEA diabodies	Colorectal cancer	MicroPET	Cai et al. (2007a)

Fig. 15.34 Immuno-PET images with ^{89}Zr-cmAb U36 in a patient with head and neck cancer: (**a**) sagittal image; (**b**) axial image, and (**c**) coronal image. The tumor in the left tonsil (*red arrow*) and the lymph node metastases (*black arrows*) at the left (level II and III) and right (level II) side of the neck. Images were obtained 72 h postinjection (Börjesson et al. 2006)

^{89}Zr-cmAB U36 mAb-PET
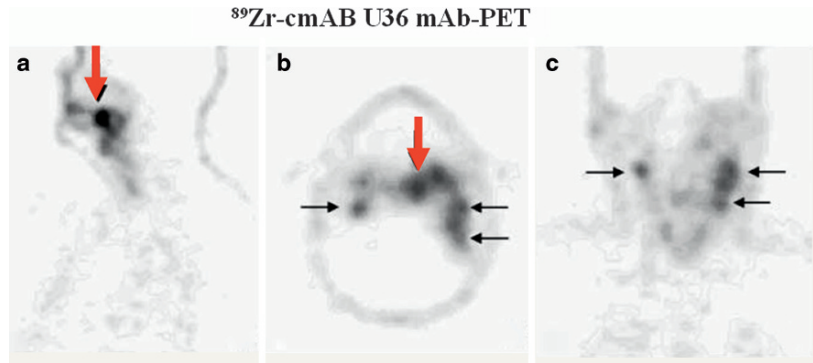
ment. Immuno-PET, the tracking and quantification of mAbs with PET in vivo, is an exciting novel option to improve diagnostic imaging and to guide mAb-based therapy (van Dongen et al. 2007) (Fig. 15.34).

References

Adams JM, Cory S (2001) Life-or-death decisions by the Bcl-2 protein family. Trends Biochem Sci 26:61–66

Ahlstrom H, Eriksson B, Bergstrom M, et al (1995) Pancreatic neuroendocrine tumors: diagnosis with PET. Radiology 195:333–337

Ahmed N, Langlois R, Rodrigue S, et al (2007) Automated synthesis of 11β-methoxy-4-16α-[16α-^{18}F]difluoroestradiol (4F-M[^{18}F]FES) for estrogen receptor imaging by positron emission tomography. Nucl Med Biol 34:459–464

Anderson CJ, Dehdashti F, Cutler PD, et al (2001) ^{64}Cu-TETA-octreotide as a PET imaging agent for patients with neuroendocrine tumors. J Nucl Med 42:213–221

Becherer A, Karanikas G, Szabo M, et al (2003) Brain tumour imaging with PET: a comparison between [^{18}F]fluorodopa and [^{11}C]methionine. Eur J Nucl Med Mol Imaging 30:1561–1567

Becherer A, Szabo M, Karanikas G, et al (2004) Imaging of advanced neuroendocrine tumors with [^{18}F]-FDOPA PET. J Nucl Med 45:1161–1167

Beck R, Roper B, Carlsen JM, et al (2007) Pretreatment ^{18}F-FAZA PET predicts success of hypoxia-directed radiochemotherapy using tirapazamine. J Nucl Med 48:973–980

Beer A, Lorenzen S, Metz S, et al (2008) Comparison of integrin avb3 expression and glucose metabolism in primary and metastatic lesions in cancer patients: a PET study using ^{18}F-Galacto-RGD and ^{18}F-FDG. J Nucl Med 49:22–29

Belhocine T, Steinmetz N, Hustinx R, et al (2002) Increased uptake of the apoptosis imaging agent ^{99m}Tc recombinant human Annexin V in human tumors after one course of chemotherapy as a predictor of tumor response and patient prognosis. Clin Cancer Res 8:2766–2774

Belhocine T, Steinmetz N, Li C, Green A, et al (2004) The imaging of apoptosis with the radiolabeled annexin V: optimal timing for clinical feasibility. Technol Cancer Res Treat 3:23–32

Bergstrom M, Lu L, Eriksson B, et al (1996) Modulation of organ uptake of ^{11}C-labelled 5-hydroxytryptophan. Biogenic Amines 12:477–485

Bjurling P, Antoni G, Watanabe Y, et al (1990) Enzymatic synthesis of carboxy-11C-labelled l-tyrosine, l-DOPA, l-tryptophan and 5-hydroxy-l-tryptophan. Acta Chem Scand 44:178–182

Blake GM, Park-Holohan SJ, Cook GJ, et al (2001) Quantitative studies of bone with the use of ^{18}F-fluoride and ^{99m}Tc-methylene diphosphonate. Semin Nucl Med 31:28–49

Blankenberg FG (2008) In vivo detection of apoptosis. J Nucl Med 49:81S–95S

Blau M, Nagler W, Bender MA (1962) A new isotope for bone scanning. J Nucl Med 3:332–334

Boersma HH, Kietselaer BL, Stolk LM, et al (2005) Past, present, and future of annexin A5: from protein discovery to clinical applications. J Nucl Med 46:2035–2050

Böhm I, Schild H (2003) Apoptosis: the complex scenario for a silent cell death. Mol Imaging Biol 5:2–14

Borjesson PKE, Jauw YWS, Boellaard R, et al (2006) Performance of immuno positron emission tomography with zirconium-89-labeled chimeric monoclonal antibody U36 in the detection of lymph node metastases in head and neck cancer patients. Clin Cancer Res 12:2133–2140

Cai W, Wu Y, Chen K, et al (2006) In vitro and in vivo characterization of ^{64}Cu labeled Abegrin, a humanized monoclonal antibody against $\alpha_v\beta_3$. Cancer Res 66:9673–9681

Cai W, Olafsen T, Zhang X, et al (2007a) PET imaging of colorectal cancer in xenografts-bearing mice by use of an ^{18}F-labeled T84.66 anti-carcinoembryonic antigen diabody. J Nucl Med 48:304–310

Cai W, Chen K, He L, et al (2007b) Quantitative PET of EGFR expression in xenograft-bearing mice using ^{64}Cu-labeled cetuximab, a chimeric anti-EGFR monoclonal antibody. Eur J Nucl Med Mol Imaging 34:850–858

Chapman JD, Franko AJ, Sharplin J (1981) A marker for hypoxic cells in tumours with potential clinical applicability. Br J Cancer 43:546–550

Chen W (2007) Clinical applications of PET in brain tumors. J Nucl Med 48:1468–1481

Chen W, Silverman DHS (2007) Advances in evaluation of primary brain tumors. Semin Nucl Med 38:240–250

Chen W, Silverman DHS, Delaloye S, et al (2006) ^{18}F-FDOPA PET imaging of brain tumors: comparison study with ^{18}F-FDG PET and evaluation of diagnostic accuracy. J Nucl Med 47:904–911

Chen W, Delaloye S, Silverman DHS, et al (2007) Predicting treatment response of malignant gliomas to bevacizumab and irinotecan by imaging proliferation with [18F] fluorothymidine positron emission tomography: a pilot study. J Clin Oncol 25:4714–4721

Christman D, Crawford EJ, Friedkin M, et al (1972) Detection of DNA synthesis in intact organisms with positron-emitting methyl-[C-11]-thymidine. Proc Natl Acad Sci U S A 69:988–992

Clary GL, Tsai C-F, Guynn RW, et al (1987) Substrate specificity of choline kinase. Arch Biochem Biophys 254:214–221

Cleaver JE (1967) Thymidine metabolism and cell kinetics. Front Biol 6:43–100

Conti P, Alauddin M, Fissekis J, et al (1995) Synthesis of 2′-fluoro-5-[11C]-methyl-1-beta-D-arabinofuranosyluracil ([11C]-FMAU): a potential nucleoside analog for in vivo study of cellular proliferation with PET. Nucl Med Biol 22(6):783–789

Conti PS, Bading JR, Mouton P, et al (2008) In vivo measurement of cell proliferation in canine brain tumor using C-11 labeled FMAU and PET. Nucl Med Biol 35:131–141

Cornell R, Grove GL, Rothblat GH, et al (1997) Lipid requirement for cell cycling: the effect of selective inhibition of lipid synthesis. Exp Cell Res 109:299–307

Couturier O, Luxen A, Chatal JF, et al (2004) Fluorinated tracers for imaging cancer with positron emission tomography. Eur J Nucl Med Mol Imaging 31:1182–1206

DeGrado TR, Coleman RE, Wang S, et al (2001) Synthesis and evaluation of ^{18}F labeled choline as an oncologic tracer for positron emission tomography: initial findings in prostate cancer. Cancer Res 61:110–117

Dijkers E, Lub-de Hooge MN, Kosterink JG, et al (2007) Characterization of [89]Zrtrastuzumab for clinical HER2 immunoPET imaging. J Clin Oncol 25(suppl. 18):3508

Divgi CR, Pandit-Taskar N, Jungbluth AA, et al (2007) Preoperative characterization of clear-cell renal carcinoma using iodine-124-labelled antibody chimeric G250 ([124]I-cG250) and PET in patients with renal masses: a phase I trial. Lancet Oncol 8:304–310

Elgazzar AH, Shehab D (2006) Musculoskeletal system. In: Elgazzar A (ed) The pathologic basis of nuclear medicine, 2nd edn. Spriger, Berlin

Eriksson B, Bergstrom M, Sundin A, et al (2002) The role of PET in localization of neuroendocrine and adrenocortical tumors. Ann N Y Acad Sci 970:159–169

Even-Sapir E, Metser U, Flusser G, et al (2004) Assessment of malignant skeletal disease with ^{18}F-fluoride PET/CT. J Nucl Med 45:272–278

Even-Sapir E, Mishani E, Flusser G, et al (2007) ^{18}F-fluoride positron emission tomography and positron emission tomography/computed tomography. Semin Nucl Med 37:462–469

Folkman J (1971) Tumor angiogenesis: therapeutic implications. N Engl J Med 285:1182–1186

Foo SS, Abbott DF, Lawrentschuk N, et al (2004) Functional imaging of intra-tumoral hypoxia. Mol Imaging Biol 6:291–305

Friedlander M, Brooks PC, Shaffer RW, et al (1995) Definition of two angiogenic pathways by distinct α_v integrins. Science 270:1500–1502

Gabriel M, Muehllechner P, Decristoforo C, et al (2005) ^{99m}Tc-EDDA/HYNIC-Tyr(3)-octreotide for staging and follow-up of patients with neuroendocrine gastro-entero-pancreatic tumors. Q J Nucl Med 49:237–244

Gabriel M, Decristoforo C, Kendler D, et al (2007) ^{68}Ga-DOTA-Tyr[3]-Octreotide PET in neuroendocrine tumors: comparison with somatostatin receptor scintigraphy and CT. J Nucl Med 48:508–518

Gambhir SS, Czernin J, Schwimmer J, et al (2001) A tabulated summary of the FDG PET literature. J Nucl Med 42(suppl 5):1S–93S

Gazdar AF, Helman LJ, Israel MA, et al (1988) Expression of neuroendocrine cell markers L-dopa decarboxylase, chromogranin A, and dense core granules in human tumors of endocrine and nonendocrine origin. Cancer Res 48: 4078–4082

Goldenberg DM, Rossi EA, Sharkey RM (2008) Multifunctional antibodies by the dock-and-lock method for improved cancer imaging and therapy by pretargeting. J Nucl Med 49:158–163

Grant FD, Fahey FH, Packard AB, et al (2008) Skeletal PET with ^{18}F-fluoride: applying new technology to an old tracer. J Nucl Med 49:68–78

Grierson JR, Schwartz JL, Muzi M, et al (2004) Metabolism of 3′-deoxy-3′-[F-18]fluorothymidine in proliferating A549 cells: validations for positron emission tomography. Nucl Med Biol 31:829–837

Gronroos T, Eskola O, Lehtio K, et al (2001) Pharmacokinetics of [18F]FETNIM: a potential marker for PET. J Nucl Med 42:1397–1404

Hamaoka T, Madewell JE, Podoloff DA, et al (2004) Bone imaging in metastatic breast cancer. J Clin Oncol 22:2942–2953

Hanahan D, Weinberg RA (2000) The hallmarks of cancer. Cell 100:57–70

Hara T, Kosaka N, Shinoura N, et al (1997) PET imaging of brain tumor with [methyl-^{11}C] choline. J Nucl Med 38:842–847

Hara T, Kosaka N, Kishi H (2002) Development of [18F]-fluoroethylcholine for cancer imaging with PET: synthesis, biochemistry, and prostate cancer imaging. J Nucl Med 43:187–199

Haubner R, Wester HJ (2004) Radiolabeled tracers for imaging of tumor angiogenesis and evaluation of anti-angiogenic therapies. Curr Pharm Des 10:1439–1455

Haubner R, Wester H-J, Reuning U, et al (1999) Radiolabeled $\alpha_v\beta_3$ integrin antagonists: a new class of tracers for tumor targeting. J Nucl Med 40:1061–1071

Haubner R, Wester HJ, Weber WA, et al (2001) Noninvasive imaging of alpha$_v$ beta$_3$ integrin expression using ^{18}F-labeled RGD-containing glycopeptide and positron emission tomography. Cancer Res 61:1781–1785

Henriksen G, Herz M, Hauser A, et al (2004) Synthesis and preclinical evaluation of the choline transport tracer deshydroxy-[18F]fluorocholine ([18F]dOC). Nucl Med Biol 31:851–858

Henze M, Schuhmacher J, Hipp P, et al (2001) PET imaging of somatostatin receptors using [68Ga]DOTA-D-Phe1-Tyr[3]-Octreotide: first results in patients with meningiomas. Eur J Nucl Med 42:1053–1056

Herholz K, Holzer T, Bauer B, et al (1998) ^{11}C-methionine PET for differential diagnosis of low-grade gliomas. Neurology 50:1316–1322

Himmelweit B (ed) (1957) The Collected Papers of Paul Ehrlich. Pergamon, Elmsford, NY

Hoegerle S, Altehoefer C, Ghanem N, et al (2001) Whole-body ^{18}F-DOPA PET for detection of gastrointestinal carcinoid tumors. Radiology 220:373–380

Hoegerle S, Altehoefer C, Ghanem N, et al (2002a) ^{18}F-DOPA positron emission tomography for tumor detection in patients with medullary thyroid carcinoma and elevated calcitonin levels. Eur J Nucl Med 28:64–71

Hoegerle S, Nitzsche E, Altehoefer C, et al (2002b) Pheochromocytomas: detection with ^{18}F DOPA whole body PET–initial results. Radiology 222:507–512

Hofmann M, Maecke H, Börner AR, et al (2001) Biokinetics and imaging with the somatostatin receptor PET radioligand Ga-68 DOTATOC preliminary data. Eur J Nucl Med 28:1751–1757

Holliger P, Winter G (1997) Diabodies: small bispecific antibody fragments. Cancer Immunol Immunother 45:128–130

Holliger P, Hudson PJ (2005) Engineered antibody fragments and the rise of single domains. Nat Biotechnol 23:1126–1136

Howard BV, Howard WJ (1975) Lipids in normal and tumor cells in culture. Prog Biochem Pharmacol 10:135–166

Ibrahim EM, Al-Maghrabi JA (2006) Basis of tumor imaging 1: principles of tumor pathology and biology. In: Elgazzar A (ed) The pathologic basis of nuclear medicine, 2nd edn. Springer, Berlin

Ido T, Wan CN, Casella JS, et al (1978) Labeled 2-deoxy-D-glucose analogs: [18]F labeled 2-deoxy-2-fluoro-D-glucose, 2-deoxy-2-fluoro-D-mannose and ^{14}C-2-deoxy-2-fluoro-D-glucose. J Label Compd Radiopharmacol 14:175–183

Inoue TJ, Tomiyoshi K, Higuchi T, et al (1998) Biodistribution studies on L-3-[^{18}F]fluoro-α-methyl tyrosine: a potential tumor-detecting agent. J Nucl Med 39:663–667

Institute of Medicine: Food and Nutrition Board (1998) Dietary reference intakes for thiamin, riboflavin, niacin, vitamin b6, folate, vitamin b12, pantotheni acid, biotin and choline. National Academy Press, Washington, DC

Jackowski S (1994) Coordination of membrane phospholipid synthesis with the cell cycle. J Biol Chem 269:3858–3867

Jager PL, Vaalburg W, Pruim J, et al (2001) Radiolabeled amino acids: basic aspects and clinical applications in oncology. J Nucl Med 42:432–445

Jager PL, Chirakal R, Marriott CJ, et al (2008) 6-L-18F-fluorodihydroxyphenyl-alanine PET in neuroendocrine tumors: basic aspects and emerging clinical applications. J Nucl Med 49:573–586

Jana S, Abdel Dayem HM (2006) Basis of tumor imaging 2: principles of tumor pathology and biology. In: Elgazzar A (ed) The pathologic basis of nuclear medicine, 2nd edn. Spriger, Berlin

Jayson GC, Zweit J, Jackson A, et al (2002) Molecular imaging and biological evaluation of HuMV833 anti-VEGF antibody: implications for trial design of antiangiogenic antibodies. J Natl Cancer Inst 94:1484–1493

Jensen EV, DeSombre ER, Jungblut PW (1967) Estrogen receptors in hormone-responsive tissue and tumors. In: Wissler RW, Dao TL, Wood S Jr (eds) Endogenous factors influencing host tumor balance. University of Chicago Press, Chicago

Jin H, Varner J (2004) Integrins: roles in cancer development and as treatment targets. Br J Cancer 90:561–565

Kelloff GJ, Krohn KA, Larson SM, et al (2005) The progress and promise of molecular imaging probes in oncologic drug development. Clin Cancer Res 11:7967–7985

Kemerink GJ, Liu X, Kieffer D, et al (2003) Safety, biodistribution, and dosimetry of ^{99m}Tc-HYNIC-annexin V, a novel human recombinant annexin V for human application. J Nucl Med 44:947–952

Kenis H, van Genderen H, Bennaghmouch A, et al (2004) Cell surface-expressed phosphatidylserine and annexin A5 open a novel portal of cell entry. J Biol Chem 279: 52623–52629

Kiesewetter DO, Kilbourn MR, Landvatter SW, et al (1984) Preparation of four fluorine-18-labeled estrogens and their selective uptakes in target tissues of immature rats. J Nucl Med 25:1212–1221

Kirsch DG, Kastan MB (1998) Tumor suppressor p53: implications for tumor development and prognosis. J Clin Oncol 16:3158–3168

Köhler G, Milstein C (1975) Continuous cultures of fused cells secreting antibody of predefined specificity. Nature 256:495–497

Kowalski J, Henze M, Schuhmacher J, et al (2003) Evaluation of positron emission tomography imaging using [^{68}Ga]-DOTA-DPhe1-Tyr[3]-octreotide in comparison to [^{111}In]-DTPAOC SPECT: first results in patients with neuroendocrine tumors. Mol Imaging Biol 5:42–48

Krammer, PH (2000) CD95's deadly mission in the immune system. Nature 407:789–795

Kumar CC (2003) Integrin $\alpha_v\beta_3$ as a therapeutic target for blocking tumor-induced angiogenesis. Curr Drug Targets 4:123–131

Kumar V, Cotran RS, Robbins SL (2003) Basic pathology, 6th edn. Saunders, Philadelphia

Kwee SA, DeGrado TR, Talbot JN, et al (2007) Cancer imaging with fluorine-18–labeled choline derivatives. Semin Nucl Med 37:420–428

Langen KJ, Jarosch M, Muhlensiepen H, et al (2003) Comparison of fluorotyrosines and methionine uptake in F98 rat gliomas. Nucl Med Biol 30:501–508

Langen KJ, Hamacher K, Weckesser M, et al (2006) O-(2-[^{18}F]fluoroethyl)-L-tyrosine: uptake mechanisms and clinical applications. Nucl Med Biol 33:287–294

Lebtahi R, Le Cloirec J, Houzard C, et al (2002) Detection of neuroendocrine tumors: ^{99m}Tc-P829 scintigraphy compared with ^{111}In-pentetreotide scintigraphy. J Nucl Med 43:889–895

Lee ST, Scott AM (2007) Hypoxia positron emission tomography imaging with ^{18}F-fluoromisonidazole. Semin Nucl Med 37:451–461

Lewis JS, Welch MJ (2001) PET imaging of hypoxia. Q J Nucl Med 45:183–188

Linden HM, Stekhova SA, Link JM, et al (2006) Quantitative fluoroestradiol positron emission tomography imaging predicts response to endocrine treatment in breast cancer. J Clin Oncol 24:2793–2799

Link JM, Stekhova SA, Li X, et al (2007) Site-specific labeling of Annexin-V for in vivo imaging of cell death. J Label Compds Radiopharm 50(S1):S24

Livingston RB, Ambus U, George SL, et al (1974) In vitro determination of thymidine-[H-3] labeling index in human solid tumors. Cancer Res 34:1376–1380

Luxen A, Guillaume M, Melega WP, et al (1992) Production of 6-[^{18}F]fluoro-L-dopa and its metabolism in vivo– a critical review. Int J Rad Appl Instrum B 19:149–158

Maecke HR, Hofmann M, Haberkorn U (2005) ^{68}Ga-labeled peptides in tumor imaging. J Nucl Med 46(s1):172S–178S

Mankoff DA, Tewson TJ, Eary JF (1997) Analysis of blood clearance and labeled metabolites for the estrogen receptor tracer [F-18]-16 alpha-fluoroestradiol (FES). Nucl Med Biol 24:341–348

Mankoff DA, Shields AF, Krohn KA (2005) PET imaging of cellular proliferation. Radiol Clin N Am 43:153–167

Margolis DJA, Hoffman JM, Herfkens RJ, et al (2007) Molecular imaging techniques in body imaging. Radiology 245:333–356

McEwan AJ, Shapiro B, Sisson JC, et al (1985) Radioiodobenzylguanidine for the scintigraphic location and therapy of adrenergic tumors. Semin Nucl Med 5:132–153

Meisetschlager G, Stahl A, et al (2006) Gluc-Lys([^{18}F]FP)-TOCA PET in patients with SSTR-positive tumors: biodistribution and diagnostic evaluation compared with [^{111}In] DTPA-octreotide. J Nucl Med 47:566–573

Mintun MA, Welch MJ, Siegel BA, et al (1988) Breast cancer: PET imaging of estrogen receptors. Radiology 169:45–48

Mosselman S, Pohlman J, Dijkema R, et al (1996) Identification and characterisation of a novel human estrogen receptor. FEBS Lett 392:49–53

Nagengast WB, de Vries EG, Hospers GA, et al (2007) In vivo VEGF imaging with radiolabeled bevacizumab in a human ovarian tumor xenograft. J Nucl Med 48:1313–1319

Nass SJ, Moses HL (eds) (2007) Cancer biomarkers: the promises and challenges of improving detection and treatment. The National Academies Press, Washington DC

Oberg K (2003) Diagnosis and treatment of carcinoid tumors. Expert Rev Anticancer Ther 3:863–877

Orlefors H (2003) Positron emission tomography in the management of neuroendocrine tumors. PhD Thesis, Uppsala University, Sweden

Orlefors H, Sundin A, Ahlstrom H, et al (1998) Positron emission tomography with 5-hydroxytryprophan in neuroendocrine tumors. J Clin Oncol 16:2534–2541

Orlefors H, Sundin A, Garske U, et al (2005) Whole-body ^{11}C-5-hydroxytrypto-phan positron emission tomography as a universal imaging technique for neuroendocrine tumors – comparison with somatostatin receptor scintigraphy and computed tomography. J Clin Endocrinol Metab 90:3392–3400

Orlefors H, Sundin A, Lu L, et al (2006) Carbidopa pretreatment improves image interpretation and visualisation of carcinoid tumours with ^{11}C-5-hydroxytryptophan positron emission tomography. Eur J Nucl Med Mol Imaging 33:60–65

Oyama N, Miller TR, Dehdashti F, et al (2003) ^{11}C-acetate PET imaging of prostate cancer: detection of recurrent disease at PSA relapse. J Nucl Med 44:549–555

Pearse AG (1980) The APUD concept and hormone production. Clin Endocrinol Metab 9:211–222

Peñuelas I, Haberkorn U, Yaghoubi S, et al (2005) Gene therapy imaging in patients for oncological applications. Eur J Nucl Med Mol Imaging 32:S384–S403

Perik PJ, Lub-De Hooge MN, Gietema JA, et al (2006) Indium-111-labeled trastuzumab scintigraphy in patients with human epidermal growth factor receptor 2-positive metastatic breast cancer. J Clin Oncol 24:2276–2282

Philpott GW, Schwarz SW, Anderson CJ, et al (1995) RadioimmunoPET: detection of colorectal carcinoma with positron-emitting copper-64-labeled monoclonal antibody. J Nucl Med 36:1818–1824

Piert M, Machulla HJ, Picchio M, et al (2005) Hypoxia-specific tumor imaging with ^{18}F-fluoroazomycin arabinoside. J Nucl Med 46:106–113

Ponde DE, Oyama N, Dence CS, et al (2003) [^{18}F]-Fluoroacetate, an analogue of C-11 acetate for tumor imaging. J Nucl Med 44:296

Ponde DE, Dence CS, Oyama N, et al (2007) ^{18}F-Fluoroacetate: a potential acetate analog for prostate tumor imaging- in vivo evaluation of ^{18}F-fluoroacetate versus ^{11}C-acetate. J Nucl Med 48:420–428

Pugh CW, Ratcliffe PJ (2003) Regulation of angiogenesis by hypoxia: role of the HIF system. Nat Med 9:677–684

Rajendran JG, Mankoff DA (2007) Beyond detection: novel applications for PET imaging to guide cancer therapy. J Nucl Med 48:855–856

Rajendran JG, Schwartz DL, O'Sullivan J, et al (2006) Tumor hypoxia imaging with [F-18] fluoromisonidazole positron emission tomography in head and neck cancer. Clin Cancer Res 12:5435–5441

Rasey JS, Grunbaum Z, Magee S, et al (1987) Characterization of radiolabeled fluoromisonidazole as a probe for hypoxic cells. Radiat Res 111:292–304

Rasey JS, Hofstrand PD, Chin LK, et al (1999) Characterization of [^{18}F]fluoroetanidazole, a new radiopharmaceutical for detecting tumor hypoxia. J Nucl Med 40:1072–1079

Reske SN, Blumstein NM, Neumaier B, et al (2006) Imaging prostate cancer with ^{11}C-Choline PET/CT. J Nucl Med 47:1249–1254

Reubi JC (2003) Peptide receptors as molecular targets for cancer diagnosis and therapy. Endocr Rev 24:389–427

Reubi JC, Waser B (2003) Concomitant expression of several peptide receptors in neuroendocrine tumours: molecular basis for in vivo multireceptor tumour targeting. Eur J Nucl Med Mol Imaging 30:781–793

Reubi JC, Laissue J, Krenning EP, et al (1992) Somatostatin receptors in human cancer: incidence, characteristics, functional correlates and clinical implication. J Steroid Biochem Mol Biol 43:27–35

Reubi JC, Schar JC, Waser B, et al (2000) Affinity profiles for human somatostatin receptor subtypes SST1-SST5 of somatostatin radiotracers selected for scintigraphic and radiotherapeutic use. Eur J Nucl Med 27:273–282

Reubi JC, Mäcke HR, Krenning EP (2005) Candidates for peptide receptor radiotherapy today and in the future. J Nucl Med 46:67S–75S

Ribom D, Eriksson A, Hartman M, et al (2001) Positron emission tomography (^{11}C)-methionine and survival in patients with low-grade gliomas. Cancer 92:1541–1549

Roivainen A, Forsback S, Grönroos T, et al (2000) Blood metabolism of [methyl-^{11}C]choline; implications for in vivo imaging with positron emission tomography. Eur J Nucl Med 27:25–32

Rufini V, Calcagni ML, Baum RP (2007) Imaging of neuroendocrine tumors. Semin Nucl Med 36:228–247

Salskov A, Tammisetti VS, Grierson J, et al (2007) FLT: measuring tumor cell proliferation in vivo with positron emission tomography and 3′-Deoxy-3′-[^{18}F]fluorothymidine. Semin Nucl Med 37:429–439

Schiepers C, Nuytes J, Bormans G, et al (1997) Fluoride kinetics of the axial skeleton measured in vivo with fluorine-18-fluoride PET. J Nucl Med 38:1970–1976

Schoder H, Larson SM (2004) Positron emission tomography for prostate, bladder, and renal cancer. Semin Nucl Med 34:274–292

Schöder H, Ong SC (2008) Fundamentals of molecular imaging: rationale and applications with relevance for radiation oncology Semin Nucl Med 38:119–128

Schuster DM, John R, Votaw JR, Nieh PT, et al (2007) Initial experience with the radiotracer anti-1-amino-3-^{18}F-fluorocyclobutane-1-carboxylic acid with PET/CT in prostate carcinoma. J Nucl Med 48:56–63

Seibyl JP, Chen W, Silverman DHS (2007) 3,4-Dihydroxy-6-[^{18}F]-fluoro-L-phenylalanine positron emission tomography in patients with central motor disorders and in evaluation of brain and other tumors. Semin Nucl Med 37:440–450

Seimbille Y, Ali H, van Lier JE (2002) Synthesis of 2, 16α- and 4,16α difluoroestradiols and their 11β-methoxy derivatives as potential estrogen receptor-binding radiopharmaceuticals. J Chem Soc Perkin Trans 1:657–663

Seitz U, Wagner M, Neumaier B, et al (2002) Evaluation of pyrimidine metabolising enzymes and in vitro uptake of 3′-[^{18}F]fluoro-3′-deoxythymidine ([^{18}F]FLT) in pancreatic cancer cell lines. Eur J Nucl Med Mol Imaging 29:1174–1181

Sharkey RM, Goldenberg DM (2005) Perspectives on cancer therapy with radiolabeled monoclonal antibodies J Nucl Med 46:115S–127S

Shields AF (2003) PET imaging with ^{18}F-FLT and thymidine analogs: promise and pitfalls. J Nucl Med 44:1432–1434

Shields AF, Grierson JR, Kozawa SM, et al (1996) Development of labeled thymidine analogs for imaging tumor proliferation. Nucl Med Biol 23:17–22

Shields AF, Grierson JR, Dohmen BM, et al (1998) Imaging proliferation in vivo with [F-18]FLT and positron emission tomography. Nat Med 4:1334–1336

Shiue CY, Welch MJ (2004) Update on PET radiopharmaceuticals: life beyond fluorodeoxyglucose. Radiol Clin N Am 42:1033–1053

Shively JE (2007) ^{18}F Labeling for immuno-PET: where speed and contrast meet. J Nucl Med 48:171–172

Shoup TM, Olson JMH, Votaw J, et al (1999) Synthesis and evaluation of [^{18}F] 1-amino-3-fluorocyclobutane-l-carboxylic acid to image brain tumors. J Nucl Med 40:331–338

Smith-Jones PM, Solit DB, Akhurst T, et al (2004) Imaging the pharmacodynamics of HER2 degradation in response to Hsp90 inhibitors. Nat Biotechnol 22:701–706

Sols A, Crane RA (1954) Substrate specificity of brain hexokinase. J Biol Chem 210:581–595

Stocklin GL (1998) Is there a future for clinical fluorine-18 radiopharmaceuticals (excluding FDG)? Eur J Nucl Med 25:1612–1616

Sun H, Sloan A, Mangner T, et al (2005) Imaging DNA synthesis in vivo with [F-18]FMAU and positron emission tomography in patients with cancer. Eur J Nucl Med Mol Imaging 32:15–22

Sundararajan L, Linden HM, Link JM, et al (2007) ^{18}F-Fluoroestradiol. Semin Nucl Med 37:470–476

Sundin A, Eriksson B, Bergstrom M, et al (2000) Demonstration of (11C) 5-hydroxy-l-tryptophan uptake and decarboxylation in carcinoid tumors by specific positioning labeling in positron emission tomography. Nucl Med Biol 1:33–41

Sundin A, Eriksson B, Bergstrom M, et al (2004) PET in the diagnosis of neuroendocrine tumors. Ann N Y Acad Sci 1014:246–257

Swinnen JV, Van Veldhoven PP, Timmermans L, et al (2003) Fatty acid synthase drives the synthesis of phospholipids partitioning into detergent-resistant membrane microdomains. Biochem Biophys Res Commun 302:898–903

Tait JF, Cerqueira MD, Dewhurst TA (1994) Evaluation of annexin V as a platelet-directed thrombus targeting agent. Thromb Res 75:491–501

Tedeschi G, Lundbom N, Raman R, et al (1997) Increased choline signal coinciding with malignant degeneration of cerebral gliomas: a serial proton magnetic resonance spectroscopy imaging study. J Neurosurg 87:516–524

Urtasun RC, Parliament MB, McEwan AJ, et al (1996) Measurement of hypoxia in human tumours by non-invasive SPECT imaging of iodoazomycin arabinoside. Br J Cancer Suppl 27:S209–S212

Vallabhajosula S (2007) ^{18}F-Labeled PET radiopharmaceuticals in oncology: an overview of radiochemistry and mechanisms of tumor localization. Semin Nucl Med 37:400–419

Van de Wiele C, De Vos F, Slegers G, et al (2000) Radiolabeled estradiol derivatives to predict response to hormonal treatment in breast cancer: a review. Eur J Nucl Med 27:1421–1433

Van Dongen GAMS, Visser GWM, Lub-De Hoodge MN, et al (2007) Immuno-PET: a navigator in monoclonal antibody development and applications. The Oncologist 12:1379–1389

Varagnolo L, Stokkel MPM, Mazzi U, et al (2000) ^{18}F-labeled radiopharmaceuticals for PET in oncology, excluding FDG. Nucl Med Biol 27:103–112

Vaupel P, Schlenger K, Hoeckel M (1992) Blood flow and tissue oxygenation of human tumors: an update. Adv Exp Med Biol 317:139–151

Virgolini I, Pangerl T, Bischof C, et al (1997) Somatostatin receptor subtype expression in human tissues: a prediction for diagnosis and treatment of cancer? Eur J Clin Invest 27:645–647

Volker JF et al (1940) The absorption of fluorides by enamel, dentin, bone, and hydroxyapatite as shown by the radioactive isotope. J Biol Chem 134:543–548

Vollenweider-Zerargui L, Barrelet L, Wong Y, et al (1986) The predictive value of estrogen and progesterone receptors' concentrations on the clinical behavior of breast cancer in women: clinical correlation on 547 patients. Cancer 57:1171–1180

Wafelman AR, Hoefnagel CA, Maes RAA, et al (1994) Radioiodinated metaiodobenzylguanidine: a review of its biodistribution and pharmacokinetics, drug interaction, cytotoxicity and dosimetry. Eur J Nucl Med 21:545–559

Wahl RL (2002) Principles of cancer imaging with fluorodeoxyglucose, In: Wahl RL, Buchanan JW (eds) Principles and practice of positron emission tomography. Williams & Wilkins, Philadelphia

Warburg O (1956) On the origin of cancer cells. Science 123:309–314

Warburg O, Posener K, Negelein E (1924) The metabolism of cancer cells. Biochem Zeitschr 152:129–169

Wester HJ, Schottelius M, Scheidhauer K (2003) PET imaging of somatostatin receptors: design, synthesis and preclinical evaluation of a novel ^{18}F-labelled, carbohydrated analogue octreotide. Eur J Nucl Med Mol Imaging 30:117–122

Wettstein M, Weik C, Holneicher C, et al (1998) Betaine as an osmolyte in rat liver: metabolism and cell-to-cell interactions. Hepatology 27:787–793

Whitmore GF, Varghese AJ (1986) The biological properties of reduced nitroheterocyclics and possible underlying biochemical mechanisms. Biochem Pharmacol 35:97–103

Wieland DM, Wu JL, Brown LE, et al (1980) Radiolabeled adrenergic neuron blocking agents: adrenomedullary imaging with ^{131}I-iodobenzylguanidine. J Nucl Med 21:349–353

Wild D, Mäcke HR, Waser B, et al (2005) ^{68}Ga-DOTANOC: a first compound for PET imaging with high affinity for somatostatin receptor subtypes 2 and 5. Eur J Nucl Med Mol Imaging 32:724

Wu AM, Yazaki PJ, Tsai S, et al (2000) High-resolution micro-PET imaging of carcinoembryonic antigen-positive xenografts by using a copper-64-labeled engineered antibody fragment. Proc Natl Acad Sci U S A 97:8495–8500

Wu Y, Zhang X, Xiong Z, et al (2005) microPET imaging of glioma $\alpha_v\beta_3$ integrin expression using ^{64}Cu-labeled tetrameric RGD Peptide. J Nucl Med 46:1707–1718

Yoshimoto M, Waki A, Obata A, et al (2004) Radiolabeled choline as a proliferation marker: comparison with radiolabeled acetate. Nucl Med Biol 31:859–865

Zanzonico P, O'Donoghue J, Chapman JD, et al (2004) Iodine-124-labeled iodoazomycin-galactoside imaging of tumor hypoxia in mice with serial micro-PET scanning. Eur J Nucl Med Mol Imaging 31:117–128

Zeisel SH (1981) Dietary choline: biochemistry, physiology, and pharmacology. Annu Rev Nutr 1:95–121

Zhang X, Xiong Z, Wu Y, et al (2006) Quantitative PET imaging of tumor integrin $\alpha_v\beta_3$ expression with ^{18}F-FRGD2. J Nucl Med 47:113–121

Zuckier LS, DeNardo GL (1997) Trials and tribulations: oncological antibody imaging comes to the fore. Semin Nucl Med 27:10–29

Zwaal RFA, Comfurius P, Bevers EM (2005) Surface exposure of phosphatidylserine in pathological cells. Cell Mol Life Sci 62:971–988

Molecular Imaging in Neurology and Psychiatry

16

The brain is the last and grandest biological frontier, the most complex thing we have yet discovered in our universe. It contains hundreds of billions of cells interlinked through trillions of connections. The brain boggles the mind.

James D. Watson

16.1 Neuroscience

16.1.1 The Nervous System

The nervous system is traditionally divided into central and peripheral components. The *central nervous system* (CNS) comprises the brain (cerebrum, cerebellum and brain stem) and spinal cord. The *peripheral nervous system* (PNS) includes sensory neurons and motor neurons, which connect CNS to sensory receptors and muscles, and glands, respectively. In the PNS, the *somatic* division innervates the skeletal muscles, while the autonomic (sympathetic and parasympathetic) division innervates smooth muscles, cardiac muscle, and glands. In the PNS, *ganglia* are accumulations of nerve cell bodies and their supporting cells, while *nerves* are bundles of nerve cell axons and their supporting cells.

16.1.2 Nerve Cells

The cells of the nervous system can be divided into two broad categories: nerve cells or *neurons* and a variety of supporting cells, which consist mostly of *neuroglial cells–referred to simply as glial cells or glia (*from the Greek word meaning glue).

The structure of neurons (Fig. 16.1) in many respects resembles that of most other cells in the body. The neuron has a cell body (containing a nucleus, mitochondria, etc.) and specialized extensions (for intercellular communication and signaling), known as dendites and axon. Dendritic branches or processes are specialized for receiving information from other cells, while the axon is designed for signal conduction. Since the fundamental purpose of neurons is to integrate information from other neurons, the number of inputs received by each neuron in the human nervous system ranges from 1 to approximately 100,000. Some neurons transmit locally, while others may carry signals several feet away from the cell body.

The glial cells are quite different from neurons; they do not participate directly in electrical signaling. Also, there may be three times more glial cells than neurons and these cells are usually smaller, and lack dendrites and axons. The main role played by glia includes maintaining the ionic milieu of nerve cells, modulating the rate of nerve signal propagation/synaptic action, and aiding in the recovery from neural injury. The three types of glia are *astrocytes*, *oligodendrocytes*, and *microglia*. Astrocytes maintain the appropriate chemical environment for neuronal signaling. Oligodendrocytes provide a wrapping (*myelin*) around some axons to increase the speed of signal conduction. Microglia, derived from hematopoietic stem cells, are similar in some ways to macrophages and help repair neural damage.

Neurons are organized into ensembles called circuits that process specific kinds of information. Neurons that carry information towards the CNS are called *afferent neurons*, while the neurons that carry information away from the CNS, are called *efferent neurons*.
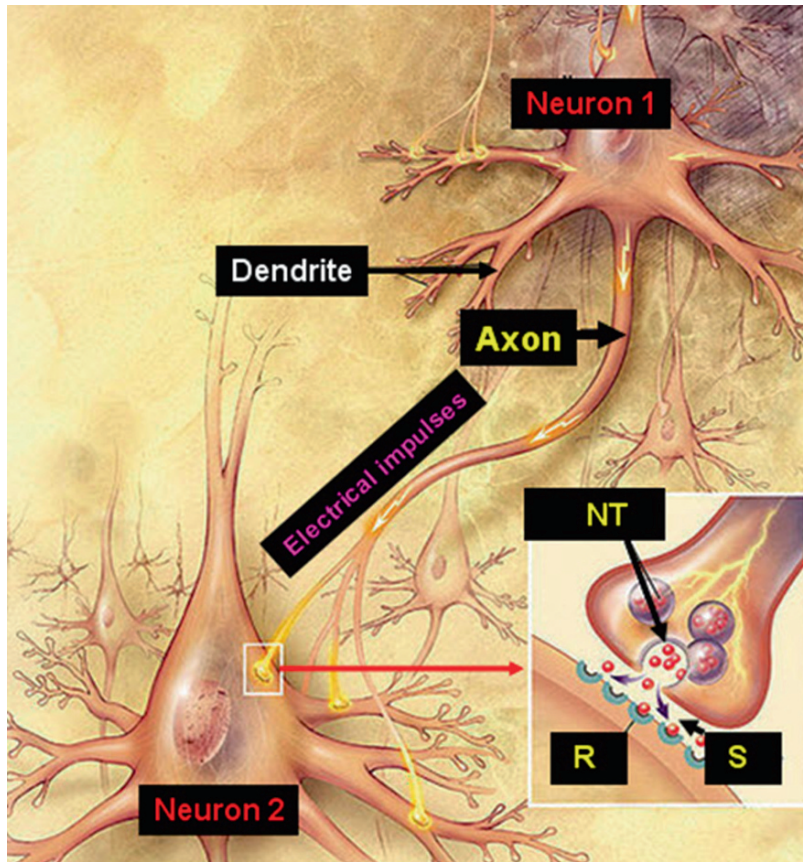
Fig. 16.1 The structure of a neuron with a cell body, dendrites, and the axon. The nerve signals transmitted along the axon trigger the release of neurotransmitter molecules into the synapse, the point of contact between two neurons or between a neuron and a target cell (modified from image at WordPress.com weblog)

Neurons that participate only in the local circuits are called interneurons. Sensory circuits provide information about the internal and external environment, while motor circuits respond to sensory inputs by generating movement.

16.1.3 The Human Brain

The CNS includes the brain and the spinal cord. The human brain (Fig. 16.2) consists of approximately 10,000 different types of neurons and a total of 100 billion neurons, and the adult brain weighs nearly 1,400 g. The brain is subdivided into three main regions: the *forebrain*, *midbrain* and *hind brain*. Collectively, the midbrain and hind brain are called the

1. Prefrontal cortex
2. Left cerebral artery
3. Let middle cerbral atery
4. Primary auditory cortex
5. Brain stem
6. Cerebellum
7. Optic radiation
8. Primary visual cortex
9. Wernicke's area
10. Gustatory area
11. Parietal lobe
12. Primary somatic sensory cortex
13. Motor cortex
14. Premotor cortex
15. Brocas area
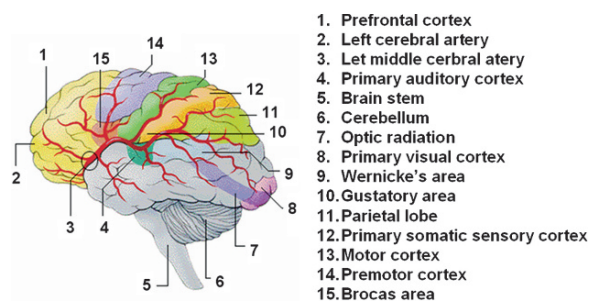
Fig. 16.2 The human brain showing the main lobes and major blood vessels

brain stem. The hindbrain has three principal subdivisions: the medulla oblongata, the cerebellum and the pons. The hindbrain tends to pass information to and receive controlling signals from the midbrain, which is itself controlled by the forebrain. The midbrain receives

and processes sensory information and distributes it to different parts of the forebrain for further processing. The forebrain integrates sensory information of various kinds and formulates motor commands that are executed by other parts of the CNS.

The forebrain is subdivided into the diencephalon (thalamus and hypothalamus) and telencephalon (the cerebrum and basal ganglia). The thalamus is a sensory relay station that distributes sensory information to appropriate regions in the cerebral cortex, while the hypothalamus maintains homeostasis. The cerebral cortex is the outer layer of the cerebrum (the two cerebral hemispheres) which contains most of the neurons and occupies a large convoluted surface area. The ridges are known as *gyri*, and the valleys are called *sulci* or *fissues*. The cerebral cortex is involved in the complex processing of sensory information to form perceptions, in the planning and initiation of movements, and in associative learning and higher cognition.

Each cerebral hemisphere is conventionally divided into four lobes (Fig. 16.3): the frontal, parietal, temporal, and occipital lobes. In addition to their role in primary and sensory processing, each lobe has characteristic cognitive functions. The frontal lobe is critical in planning behavior, the parietal lobe in attending to important stimuli, the temporal lobe in recognizing objects and faces, and the occipital lobe in a variety of visual analyses. The hippocampus, a highly specialized cortical structure that is folded into the medial temporal lobe plays a major role in memory.

When the brain is dissected, sectioned, or observed with noninvasive imaging techniques (CT, MRI, PET, SPECT), many deeper structures are apparent. Most of the cerebral cortex is made up of six layers and is referred to as neocortex. The *gray matter* refers to the cortex, whether cerebral, cerebellar, or hippocampal and is mainly made up of neuronal cell bodies, their dendrites, the axon terminals, and glia. The *white matter* makes up a large part of the subcortical tissue consisting mostly of axons entering or leaving the cortex. Among the internal structures, the *basal ganglia* play a major role in the organization and guidance of complex motor functions. The basal ganglia include the *striatum* (the *caudate* and the *putamen*) and the *globus pallidus*. Another important nucleus (collection of neurons) is the *amygdala*, which plays an important role in the emotional behavior.

The different parts of the cerebral hemispheres are interconnected by three large bundles of axons: the *corpus callosum*, *anterior commissure*, and *fornix*. The ventricular system in the CNS is a series of interconnected, fluid-filled spaces in the core of the forebrain and brain stem. The *cerebrospinal fluid* (CSF), produced by the choroid plexus, a network of specialized secretory tissue in the lateral, third, and fourth ventricles, percolates through the ventricular system into the *subarachnoid space*, which helps cushion the brain within the cranial cavity.

16.1.3.1 The Blood–Brain Barrier

The brain receives blood from two sources: the internal carotid arteries (ICA) and the vertebral arteries (VA). Many branches arising from ICA and VA supply blood to the brain and all the internal structures.

1. Higher intellect
2. Voluntary eye movement
3. Motor and speech production
4. Voluntary movement
5. Sensation
6. Language comprehension
7. Vision
8. Auditory
9. Memory
10. Equilibrium
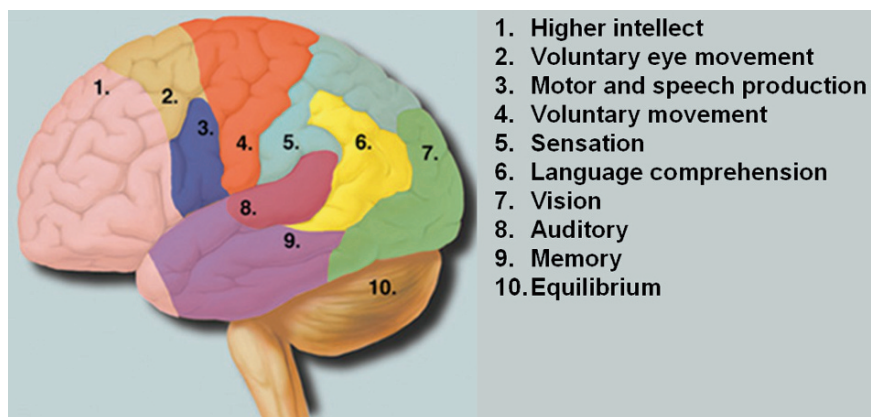
Fig. 16.3 The human brain showing the specific cortical areas associated with major functions

The blood supply of the brain is particularly significant because neurons are very sensitive to oxygen deprivation. The brain, more than any other organ, must be carefully shielded from toxic molecules and ionic species that would adversely affect the neuronal function. The interface between the walls of capillaries and the surrounding tissue is very important for the transport of various molecules and nutrients from the blood into the cells. In the brain, this interface has been given the special name, blood–brain barrier (BBB), since it protects and maintains homeostasis. Unlike in many other tissues, the adjacent capillary endothelial cells in the brain have very tight junctions, permitting the transport of molecules and ions, which can only move through the walls of the endothelial cell membranes. In addition to the tight junctions, the terminal regions of the astrocytic processes surround the outside of the capillary endothelial cells. As a result, only the neutral molecules that are lipid soluble (lipophilic) and molecules needed for cellular metabolism (such as glucose) that can be transported by facilitated diffusion are permitted to enter the brain tissue. Therefore, BBB presents a significant challenge in the development of molecular imaging probes to assess brain function (Chap. 9).

16.1.4 Neural Signaling

Neurons have evolved as a sophisticated means of generating electrical signals to convey information over long distances and transmit the signal to other cells. Ion pumps and ion channels on the cell membrane create substantial transmembrane gradients for most ions and are responsible for ionic movements across the cell membrane. In general, there are many more K^+ inside the neuron than outside, and many more Na^+ outside the neuron than inside. As a result, generally, neurons generate a negative potential, called the *resting membrane potential* (RMP), which typically is a fraction of a volt, -40 to $-90\,mV$. An increase in the external K^+ concentration makes the RMP more positive. *Action potentials* represent transient changes in the RMP of neurons. An action potential (AP) is generated when a transient rise in Na^+ permeability allows a net flow of Na^+ across the membrane. As a result, the Na^+ is much more inside the neuron than outside. This influx of Na^+ represents passing an electrical current

across membrane. *Depolarization* occurs when the membrane potential is more positive than the RMP. The brief period of depolarization is quickly followed by an increase in K^+ permeability that repolarizes the membrane and produces a brief undershoot of the AP. The membrane potential soon returns to the RMP. It is important to recognize that the membrane is depolarized in an all-or-none fashion. APs are propagated along the length of the axons and are the fundamental electrical signals of neurons.

16.1.5 Synaptic Transmission

The point at which a signal or activity is transmitted from one nerve cell to another, or from a motor neuron to a muscle cell is called a *synapse*. Synapses are classified into two general groups: electrical synapses and chemical synapses. In both types, the input cell, called the *presynaptic cell* comes into contact with the output cell, called the *postsynaptic cell*.

In an electrical synapse, the membranes of the two communicating neurons are usually close together, and are linked by a special kind of intercellular contact called a gap junction, which contains precisely aligned paired channels in the membrane of each neuron. The pores of the channels connect to one another allowing the exchange of ions and small molecules (such as ATP and second messengers). The gap junction permits the current to flow passively from the presynaptic neuron, and initiates or inhibits the generation of a postsynaptic membrane potential. Hormone-secreting neurons within the hypothalamus communicate through gap junctions.

16.1.5.1 Chemical Synapses

A generalized structure of a chemical synapse is shown in Fig. 16.6 The separation between the presynaptic and postsynaptic neurons is called the synaptic cleft. Transmission between the two neurons is on the basis of special molecules called neurotransmitters. The sequence of events involved in the chemical neurotransmission at a synapse is as follows:

- In the presynaptic neuron, the neurotransmitter molecules are synthesized and stored in the vesicles.

- An action potential reaching the presynaptic neuron terminal causes the opening of voltage gated Ca^{2+} channels.
- The influx of Ca^{2+} causes vesicles to fuse with presynaptic membrane.
- The neurotransmitter molecules are released into the synaptic cleft via exocytosis.
- The transmitter binds to specific receptors on the membrane of a postsynaptic neuron leading to (a) change in ionic permeability of postsynaptic neuron or (b) an intracellular release or production of a second messenger, which in turn interacts directly or indirectly with an ion channel, causing it to open or close.
- The postsynaptic current generated by the change in permeability of ions changes the membrane potential.
- The potential changes that increase the probability of firing an action potential are called excitatory, whereas those that decrease the probability of firing an action potential are called inhibitory.

16.1.6 Neurotransmitters and Receptors

Neurotransmitters are chemical signaling molecules released into the synaptic cleft from the presynaptic nerve terminal. The three major criteria that define a substance as a neurotransmitter are

1. The transmitter must be present within the presynaptic neuron.
2. The substance must be released in response to presynaptic depolarization, which must occur in a Ca^{2+}-dependent manner.
3. Specific receptors for the substance must be present on the postsynaptic cell.

In contrast to neurotransmitters, certain hormones typically influence target cells far removed from the hormone-secreting cells. This "action at a distance" is achieved by the release of hormones into the blood stream. Certain molecules such as vasopressin, oxytocin, and some other peptides may act as neurotransmitters in the brain, but as hormones in a different part of the body.

In general, neurotransmitters can be classified into two broad categories: small molecule neurotransmitters and neuropeptides. The small molecule neurotransmitters (Fig. 16.4) can be subdivided into acetylcholine, the amino acids (glutamate, aspartate, GABA, glycine), and the biogenic amines (dopamine, norepinephrine, epinephrine, serotonin, histamine). Neuropeptides are relatively large molecules composed of 3–36 amino acids. The peptide neurotransmitters may contain any different combinations of polar, hydrophobic, acidic, or basic amino acids.

The small molecule neurotransmitters are synthesized in the presynaptic nerve terminals. The precursor molecules are taken up by the nerve terminals by specific transporters. Following enzyme mediated synthesis (Fig. 16.5), the free neurotransmitter molecules are loaded into synaptic vesicles by specific vesicular membrane transport proteins. Following release of neurotransmitters into the synaptic cleft, they may bind to specific neuroreceptors on the membrane of the postsynaptic neuron. The transmitters may also be enzymatically degraded quickly or transported back (reuptake) into the presynaptic neuron by specific reuptake transporters.

Neuroreceptors are protein molecules embedded in the plasma membrane of the postsynaptic neuron. These receptors act as on and off switches for the receptor function. Each receptor has a distinctly shaped part that selectively recognizes a particular chemical messenger. A neurotransmitter fits into this region in much the same way as a key fits into a lock. When the transmitter is in place, this alters the neuron's outer membrane potential (excitability) by opening or closing the ion channels and triggers a change, such as the contraction of a muscle or increased activity of an enzyme in the cell.

Two broadly different families of receptors are involved in neurotransmitter–receptor interaction. (a) The ligand-gated ion channels combine the receptor site and ion channel in to one molecular entity and, therefore, give rise to rapid postsynaptic changes in the membrane potential. (b) Metabotropic receptors on the other hand, regulate the activity of ion channels indirectly, via G-proteins and induce slower, long lasting electrical response. These receptors may activate intracellular effector enzymes that modulate the phosphorylation of target proteins and/or gene transcription.

For each neurotransmitter, there may be more than one structurally and pharmacologically distinct receptor subtype (Table 16.1) that can be expressed on the membrane of a postsynaptic neuron depending on its exact location in the specific area of the brain. For example, dopamine has five receptor subtypes, while serotonin has fourteen 5-HT receptor subtypes (Barnes

Fig. 16.4 The neurotransmitters can be chemically classified into three groups: amino acids, acetylcholine, and biogenic amines
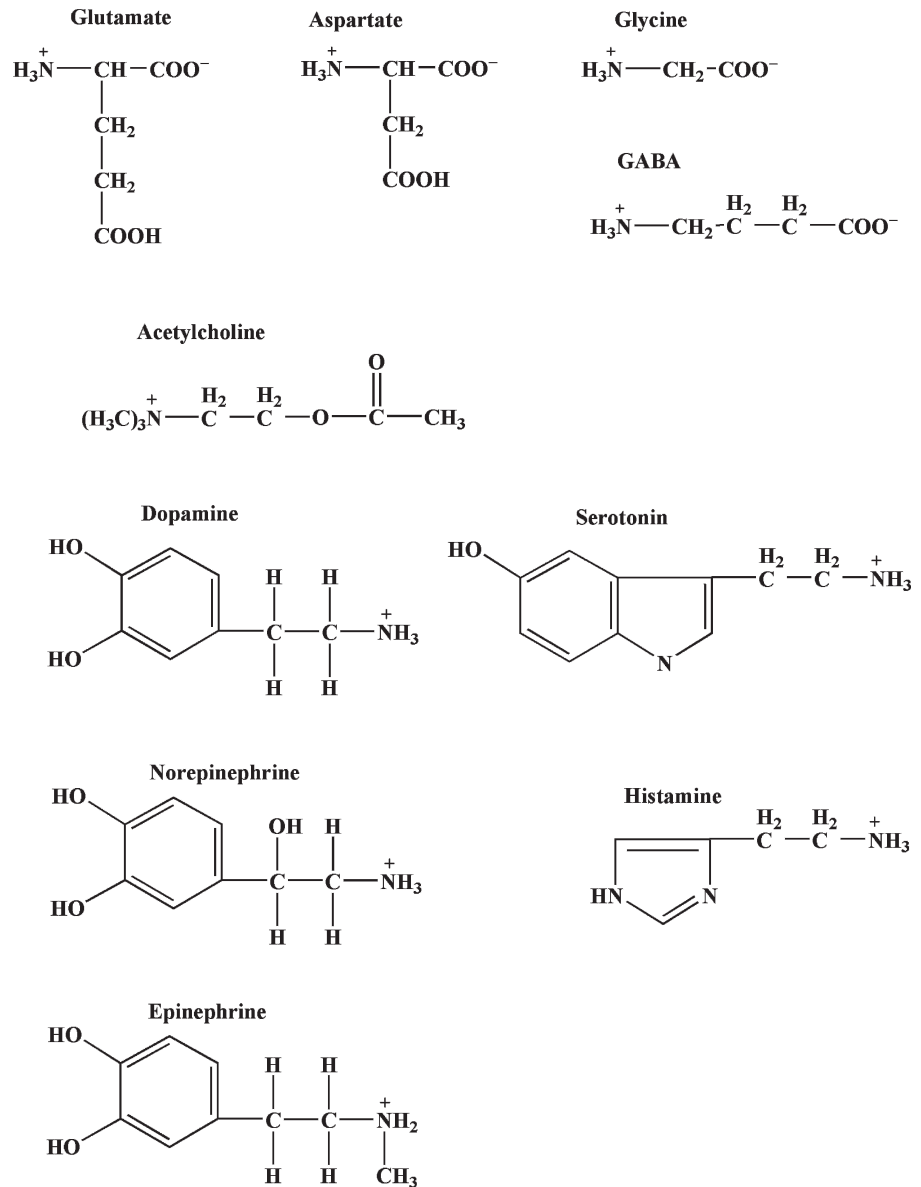
and Sharp 1999). Following binding of a neurotransmitter to a specific receptor or receptor subtype, the postsynaptic response, at a given synapse, is, therefore, dictated by the combination of receptor subtypes, G-protein subtypes, and ion channels that are expressed in a particular postsynaptic neuron. The second messengers are molecules that trigger the biochemical communication within cells, after the action of neurotransmitters at their and these intracellular effects may be responsible for long-term changes in the nervous system. These messengers convey the chemical message of a neurotransmitter (the first messenger) from the cell membrane to the cell's internal biochemical machinery. The effects of the second messenger may last for a few milliseconds to many minutes.

Knowledge of the role neurotransmitters play in the brain and the effect of drugs on receptor molecules are two of the most frequently studied areas, in neuroscience. Armed with this information, scientists hope to understand the circuits responsible for disorders, such

Acetyl CoA   +   Choline   —choline acetyltransferase→   Acetylcholine   —acetylcholinesterase→   Acetate   + Choline

Tyrosine   —tyrosine hydroxylase→   dihydroxyphenylalanine (DOPA)   —DOPA decarboxylase→   Dopamine

Dopamine   —dopamine b-decarboxylase→   Norepinephrine   —phenyethanolamine N-methyltransferase→   Epinephrine

Tryptophan   —tryptophan 5-hydroxylase→   5-Hydroxytryptophan   —Aromatic L-amino acid decarboxylase→   Serotonin

Glutamine   —glutaminase→   Glutamate   —glutamine synthetase→   Glutamine

Glutamate   —glutamic acid decarboxylase→   g-aminobutyric acid (GABA)

Glucose   →   Serine   —serine transhydroxymethylase→   Glycine

Fig. 16.5   The enzyme mediated synthesis of neurotransmitters in vivo

Table 16.1   Properties of some of the major neurotransmitters

Neurotransmitter	Receptors and subtypes	Postsynaptic effect	Specific role or functions
Acetylcholine (Ach)	Nicotinic, Muscuranic	Excitatory	Involved in muscle contraction, heart beat, memory, sleep, and normal attention
Glutamate	NMDA	Excitatory	Learning and memory
Aspartate	NMDA	Excitatory	
GABA	GABA	Inhibitory	Mood, Coordinate movement
Dopamine	D_1–D_5	Excitatory	Regulate movement, and endocrine function.
			Specific role in cognition and emotion.
Nor-epinephrine		Excitatory	Regulate heart rate and blood pressure, Learning and memory
Serotonin or 5-HT	5-HT_{1A}, 5-HT_{2A}	Excitatory	Sleep, mood, depression, anxiety
Enkephalin, Endorphin		Inhibitory	Minimize pain, induce sleep, enhance adaptive behavior

as Alzheimer's disease (AD), Parkinson's disease (PD), depression, and drug addiction. Sorting out the various chemical circuits involved in neuropsychiatric diseases is vital to understanding how the brain functions under normal physiological conditions and altered pathophysiological states. Radioisotope based molecular imaging probes provide the highest specificity and sensitivity needed to study and noninvasively image the neuroreceptor interaction within the human brain.

16.2   Radiopharmaceuticals for Functional Brain Imaging

The changes in electrical activity of neurons (excitation or inhibition) have been indirectly attributed to the alterations in the regional cerebral blood flow (rCBF) or local cerebral metabolic rate for glucose (LCMRglc). The functional coupling of rCBF and LCMRglc has

been well established in the normal human brain and certain neurological diseases. However, brain function is directly related to neural signaling and transmission of electrical activity via chemical and electrical synapses. In order to optimize the individualized patient treatment on the basis of targeted molecular therapies, and to select appropriate patients for specific drugs, need noninvasive molecular imaging techniques that can quantitatively assess the functional status and the underlying neurotransmitter and/or neuroreceptor abnormalities associated with a specific neuropsychiatric disease or disorder.

In general, there are four main classes of radiopharmaceuticals (Table 16.2) available for functional brain imaging studies to assess blood flow, metabolism, neurotransmission, and β-Amyloid plaques. A number of new, specific targeted molecular probes, designed spe-

cifically for both, diagnosis and assessment of treatment response, are under clinical evaluation. The potential clinical utility and limitations of the current, FDA approved radiopharmaceuticals and the new investigational drugs will be described briefly in this chapter.

16.2.1 Cerebral Blood Flow and Metabolism

CBF has been traditionally measured quantitatively either as a *flow rate*, expressed as volume of blood flowing per unit of time (mL min^{-1}) or as a *rate of tissue perfusion*, expressed as volume of blood flowing through a given quantity of tissue per unit of time (mL min^{-1} 100 g^{-1}). However, with respect to physiologic

Table 16.2 Radiopharmaceuticals for brain imaging studies

Biological process	Target	Radiopharmaceutical	
		PET	SPECT
Cerebral blood flow		[^{15}O]H$_2$O	^{99m}Tc-HMPAO (Ceretec™)
			^{99m}Tc-ECD (Neurolite™)
Glucose metabolism	*Hexokinase* and Glucose transporters	[^{18}F]FDG	
Neurotransmission	*AAAD*	[^{18}F]FDOPA	
	Dopamine	[^{11}C]SCH-23390	
	D$_1$ receptors	[^{11}C]NNC-112	
	Dopamine	[^{11}C]Raclopride	[^{123}I]IBZM
	D$_2$ receptors	[^{18}F]Fallypride	
	Dopamine transporters (DT)	[^{11}C]Cocaine	^{123}I-β-CIT
		[^{18}F]FP-CIT	^{123}I-Altropane
		[^{18}F]FE-CNT	^{99m}Tc-TRODAT1
	Vesicular amine transporter (VMAT)	[^{11}C]DTBZ	
		[^{18}F]DTBZ	
	5-HT$_{1A}$ receptor	[^{11}C]DWAY	
		[^{18}F]MPPF	
	5-HT$_{2A}$ receptor	[^{18}F]Altanserin	
		[^{18}F]Setoperone	
	5-HT transporter	[^{11}C](+)McN-5652	^{123}I-IDAM
		[^{11}C]DASP	
	mACh receptor	[^{18}F]FP-TZTP	
	nACh receptor	[^{18}F]NFEP	
		[^{11}C]PMP and AMP	
	μ-Opiate receptor	[^{11}C]Carfentanil	
	GABA receptor	[^{18}F]Flumazenil	^{123}I-Iomazenil
		[^{11}C]Flumazenil	
Amyloid plaques	β-Amyloid	[^{18}F]-FDDNP, [^{11}C]PIB	
		[^{18}F]-BAY94–9172	

function, perfusion directly relates to the supply of metabolic nutrient delivery to the tissue through the capillary beds. While there is a tight coupling between blood flow and metabolism in normal conditions, the coupling is disturbed in pathophysiologic conditions associated with several neuropsychiatric diseases.

A number of radiotracers have been used to assess CBF or perfusion. When the tracer reaches the capillaries, the process whereby a tracer leaves the blood pool and enters the tissue is critical for the quantitative measurement of perfusion. The fraction of the tracer which is extracted from the capillaries is referred to as the *extraction fraction* (E), a unitless parameter that can be estimated on the basis of the following Renkin-Crone equation:

$$E = 1 - e^{-PS/F} \qquad (16.1)$$

The magnitude of E depends on the total available capillary surface area (S), the capillary permeability (P) for the tracer, and the blood flow (F). E increases as S or P increases, but decreases with increased F, because the tracer spends less time in the capillaries of that region. In the above equation, P for a specific radiopharmaceutical depends on the physicochemical properties of the radiotracer.

An ideal flow radiotracer accumulates in a tissue or clears from it, in proportion linear to the blood flow. Such a linear relationship between blood flow and uptake or clearance of the tracer should be constant and independent of pathophysiological changes and metabolism of that tissue. [^{15}O]water most closely meets the criteria of an ideal tracer for measuring blood flow or tissue perfusion. It is freely diffusible and the first-pass extraction approaches unity, and is independent of tissue blood flow and metabolic state. This tracer is, therefore, the most common radiotracer used for the measurement of rCBF (Raichle et al. 1983; Herscovitch et al. 1983). Besides [^{15}O]water, several other tracers such as [^{18}F]fluoromethane, [^{11}C]butanol, and ^{77}Kr have been used to image brain blood flow.

Since CBF is related primarily to the synaptic activity at the level of the neuron's cell body, the gray matter requires 3–4 times more blood flow compared to that of white matter. In the normal brain, the rCBF is dependent on vascular integrity, cerebral anatomy, and cerebral function. Over the years, the rCBF measurements, in normal human subjects, have provided quantitative estimation, but have yielded values that showed wide variation. Most published studies have reported values in the range of 40–80 mL min^{-1} 100 g^{-1} for gray matter structure, while a recent study has estimated the cortical global flow to be 62 ± 10 mL min^{-1} 100 g^{-1} (Meltzer et al. 2000).

SPECT radiopharmaceuticals for measuring rCBF are lipophilic agents, known as chemical microspheres, which are transported into the brain tissue by diffusion and subsequently trapped intracellularly, in proportion to the blood flow. Two of the agents used clinically are ^{99m}Tc-HMPAO (Ceretec®) and ^{99m}Tc-ECD (Neurolite®). While assessment of rCBF using SPECT tracers has provided diagnostic clinical information, the SPECT technique does not provide high resolution images and the data are not optimal for the quantitative estimation of rCBF and perfusion. In the future, dedicated neuro-SPECT scanners capable of attenuation and scatter correction may provide rCBF measurements that may be acceptable for evaluating the therapeutic response of drugs, designed to improve the CBF.

16.2.1.1 Cerebral Oxygen Metabolism

In addition, to the measurement of rCBF, estimation of the cerebral blood volume (CBV) and cerebral metabolic rate of oxygen (CMRO$_2$) permit the discrimination of various compensatory mechanisms in occlusive vascular diseases. The ratio of CBF/CBV indicates a perfusion reserve, while the oxygen extraction fraction (OEF) is a marker of a metabolic reserve. The OEF reflects arteriovenous oxygen difference divided by the arterial oxygen content. Almost 30–40 years ago, the methods of quantitative measurement of rCBF, CMRO$_2$ and OEF were described in detail (Ter-Pogossian et al. 1969; Jones et al. 1976; Frackowiak et al. 1980).

The continuous inhalation of either molecular oxygen, [^{15}O]O$_2$ or carbon dioxide, [^{15}O]CO$_2$, will generate complementary images relating regional oxygen uptake and blood flow, while the assessment of CBV can be performed using carbon monoxide, [^{15}O]CO, a tracer that would label RBCs in vivo. The CMRO$_2$ can be estimated on the basis of the following relationship (Frackowiak et al. 1980):

$$CMRO_2 = CBF \times OEF \times \text{total blood oxygen count} \qquad (16.2)$$

CBF, CMRO$_2$ and OEF have been determined in normal human subjects (Table 16.3) on the basis of steady-state inhalation methods (Frackowiak et al. 1980).

Table 16.3 Normal Values

Brain Region	CBF mL/min/100 g	CMRO$_2$ mL O$_2$/min/100 g	μmoles/min/100 g	CMRglc mg/min/100 g	μmoles/min/100 g
Gray matter, temporal lobe	65.3 ± 7.0	5.88 ± 0.57	255 ± 25	7.9 ± 2.1	44 ± 12
Thalamus	–	–	–	6.5 ± 1.2	36 ± 7
White matter	21.4 ± 1.9	1.81 ± 0.22	78 ± 9	4.1 ± 1.4	23 ± 8

Data from Mazziotta et al. (1981)

Methods have also been developed to measure these quantitative parameters on the basis of the autoradiographic technique, using intravenous administration of [^{15}O]H$_2$O (Herscovitch et al. 1983).

16.2.1.2 Cerebral Glucose Metabolism

The energy metabolism in the adult human brain depends almost completely on the oxidation of glucose (Siesjo 1978). Since the brain does not store these nutrients (oxygen and glucose), it has been hypothesized that rCBF is continuously regulated to supply these nutrients locally depending on the demands of neural activity.

FDG was initially developed as a tracer to assess cerebral glucose metabolism with PET (Phelps et al. 1979; Reivich et al. 1979). On the basis of arterial sampling of ^{18}F, blood activity, and dynamic FDG-PET imaging studies, the global and regional cerebral metabolic rates of glucose utilization (CMRglc) were estimated to be $100\,g^{-1}$ or μmoles min^{-1} $100\,g^{-1}$, by several investigators. The results from the UCLA group (Mazziotta et al. 1981) are listed in Table 16.3. Since serial blood sampling in the clinic is not practical, the brain FDG-PET scans are typically interpreted qualitatively with visual analysis of the relative distribution of the FDG regional uptake in a specific patient, compared to that in age-matched normal control subjects. Also, in addition to age, other factors, such as blood glucose levels, sex, handedness, sensory environment, level of alertness, mood, and drugs, may also influence the uptake of FDG in different areas of brain.

16.2.2 Neuroreceptor Imaging

The design, synthesis, and development of molecular neuroimaging radiopharmaceuticals for the assessment of neurotransmission are some of the most active areas of molecular imaging research. The estimation

of the neuroreceptor occupancy is one of the most powerful examples of the utility of molecular imaging for developing CNS drugs for clinical trials and personalized patient therapy. The potential value of neuroreceptor imaging based on PET was first demonstrated in 1983, using the dopamine D$_2$ receptor ligand, [^{11}C]N-methylspiperone (Wagner et al. 1983). Since then, a number of PET and SPECT radiotracers have been developed to image neurotransmitter synthesis, neuroreceptor binding on the postsynaptic neuron, and specific transporters on the presynaptic neuron. Several review articles have discussed the development of receptor binding radiopharmaceuticals and their potential clinical applications (Fowler et al. 2003; Shiue and Welch 2004; Heiss and Herholz 2006; Hammoud et al. 2007). Some of the most promising agents shown to have potential clinical utility in several neuropsychiatric diseases are discussed below.

16.2.2.1 Dopamine System

Dopamine is synthesized in the dopaminergic neurons in the substantia nigra, the ventral tegmental area. and the retrorubral area of mesencephalon. Dopamine does not cross the BBB. It is synthesized in the neuron from the amino acid tyrosine and stored in the intracellular vesicles (Fig. 16.6). Specific vesicular amine transporters (VMAT$_2$) transport dopamine and other monoamines from the cytosol into the vesicles. The free dopamine in the cytosol is oxidized by the enzyme monoamine oxidase (MAO). Following release of the dopamine into the synapse, the dopamine interacts with the postsynaptic dopamine receptor sites. The five major subtypes of dopamine receptors can be classified into two major categories, depending on their ability to stimulate (D$_1$, D$_5$) or inhibit (D$_2$, D$_3$, D$_4$) adenylate cyclase, following binding to the receptor. The synaptic concentration of dopamine is regulated by the reuptake of dopamine into the presynaptic nerve terminal

Fig. 16.6 The dopaminergic system: Dopamine, synthesized in the presynaptic neuron is stored in the vesicles (V) and released into the synapse. Dopamine binds to specific receptors on the postsynaptic membrane or is transported back into the presynaptic neuron via dopamine transporters
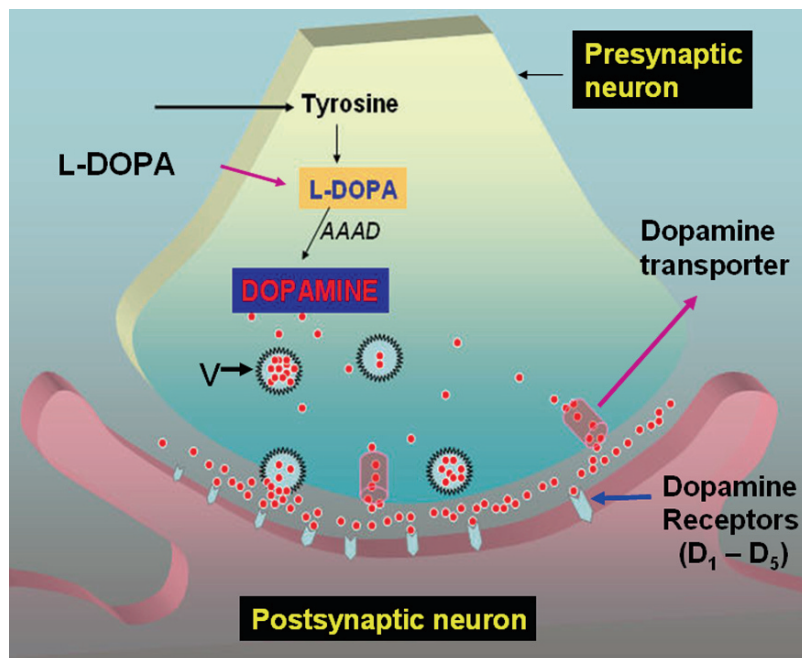
by specific dopamine transporters on the presynaptic plasma membrane. In the last three decades, the dopamine system has been a major focus in the development of PET and SPECT tracers.

Dopamine Metabolism

Since L-DOPA is the precursor for dopamine synthesis, $[^{18}F]$fluoro-L-DOPA (FDOPA) has been synthesized in order to image the dopamine synthesis and metabolism in the presynaptic nerve terminals (Garnett et al. 1983). FDOPA (Fig 16.7) is a substrate for the enzyme *AAAD, which* converts FDOPA to $[^{18}F]$fluorodopamine (FDA). Since tyrosine is the amino acid precursor for the synthesis of dopamine, both ^{18}F and ^{123}I- labeled *m*-tyrosine analogs have also been prepared (Fowler et al. 2003) and evaluated.

Dopamine Transporters

Following the synthesis of dopamine in the nerve terminal, the vesicular amine transporter (VMAT) transports the dopamine into the vesicles for storage. A more stable, stereoselective tracer, $\alpha(+)$- $[^{11}C]$dihydrotetrabenazine (DTBZ) has also been developed (Frey et al. 1996). Further, $[^{18}F]$9-fluoropropyl-DTBZ (AV-

133) was recently developed and evaluated in patients with PD.

Following the release of dopamine into the synapse, the dopamine is transported back into the presynaptic nerve terminal by a specific dopamine transporter (DAT) present on the presynaptic plasma membrane. The cocaine analog $[^{11}C]$cocaine (Fowler et al. 1987b) binds to this receptor, blocks the reuptake of dopamine, and increases the intrasynaptic dopamine levels. Therefore, a number of radiolabeled (^{11}C, ^{18}F, ^{123}I) analogs of cocaine have been prepared. Among them, $[^{18}F]$ FP-CIT (Chaly et al. 1996), $[^{18}F]$FECNT (Zoghbi et al. 2006), and ^{123}I-altropane (Fischman et al. 2001) have shown clinical utility. On the basis of a N_2S_2 chelating agent, known as bisaminoethanethiol (BAT), the tropane analog, ^{99m}Tc-TRODAT-1, was developed for SPECT imaging studies (Kung et al. 2003). Several PET and SPECT tropane analogs, useful for imaging DATs, are shown in Fig. 16.8.

Dopamine Receptors

Among the dopamine receptor subtypes, D_1 and D_2 are highly concentrated in the striatum and a number of radiotracers have been investigated on the basis of dopamine D_2 receptor blocking antagonists (Fowler et al 2003). Initial studies were performed with ^{11}C and ^{18}F

Fig. 16.7 Radiotracers used to image dopamine synthesis and metabolism in vivo

L-DOPA

6-[^{18}F]Fluoro-L-DOPA (FDOPA)

[^{11}C-carboxyl]L-DOPA

[b-^{11}C]L-DOPA

^{123}I- or ^{18}F-labeled m-tyrosine

[^{11}C]Cocaine

[^{18}F]FP-CIT
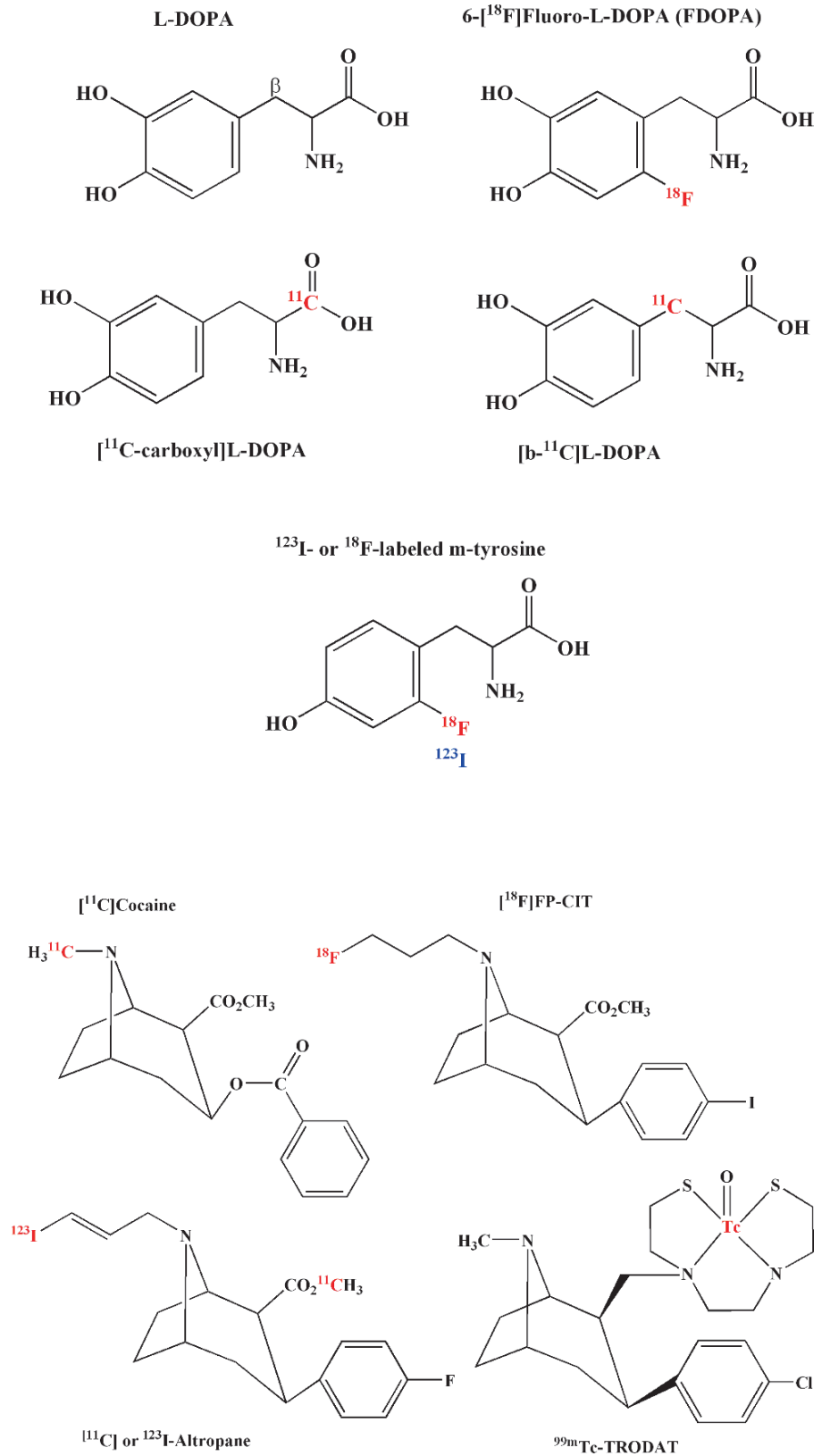
Fig. 16.8 PET and SPECT radioligands for dopamine transporter (DT)

[^{11}C] or ^{123}I-Altropane

^{99m}Tc-TRODAT

labeled *N*-methylspiperidol (MSP), an irreversible antag-onist that is not ideal for pharmacokinetic modeling and receptor quantitation studies. The benzamide analog, [¹¹C]raclopride, which has moderate affinity and reversible binding, is the most widely used PET tracer for imaging dopamine D₂ receptors, in vivo (Farde et al. 1985; Volkow et al. 1996). Radiotracer for SPECT,¹²³I-iodobenzamide (IBZM), has also shown to be very useful for assessing dopamine receptor density in human subjects (Kung et al. 2003a; Vallabhajosula et al. 1997). Among the high-affinity reversibly binding radiotracers, [¹⁸F]fallypride (Mukherjee et al. 1999) provides a longer scanning period, while [¹¹C]FLB-457 (Halldin et al. 1995) has shown clinical utility to assess extrastriatal dopamine receptors.

Several tracers designed to image both, striatal and extrastriatal dopamine D₁ receptors has been evaluated. While [¹¹C]SCH-23390 is a well studied D₁ anatagonist, the positive enantiomer of [¹¹C]NNC-112 binds selectively and reversibly, and shows favorable pharmacokinetics for in vivo quantitation (Abi-Dargham et al. 2000) of D₁ recep-tors. Several radiotracers, useful for imaging dopamine D₂ and D₁ receptors, are shown in Figs. 16.9 and 16.10.

MAO Expression

The enzyme MAO oxidizes dopamine in the presynaptic neuron. The suicide enzyme inhibitors, clorgyline and deprenyl (Fig. 16.11) block the oxidation of dopamine and increase the dopamine levels in the nerve terminal.

[¹¹C]clorgyline and [¹¹C]-L-deprenyl (deuterium-substi-tuted derivative) have been used to image the expression of MAO-A and MAO-B in human subjects (Fowler et al. 1987a, 2003).

16.2.2.2 Serotonin System

The cells that produce serotonin in the brain are located in the dorsal raphae nucleus, which extensively inner-vates neocortical regions. The amino acid tryptophan is the precursor for the synthesis of serotonin in vivo. Tryptophan is first hydroxylated to form 5-Hydro-xytryptophan (5-HTP). [¹¹C]5-HTP has been synthe-sized to assess serotonin metabolism, however, this tracer found its application in the imaging of neuroen-docrine tumors. Another tracer, [¹¹C]α-methyl-L-tryptophan has been synthesized to monitor the serotonin synthesis, indirectly (Diksic et al. 2000). The enzyme *tryptophan hydroxylase* converts this precur-sor to [¹¹C]α-methylhydroxy-tryptophan which is then decarboxylated by *AAAD* to a more stable analog of serotonin, [¹¹C]α-methylserotonin, which may reflect the rate of the serotonin synthesis, in vivo.

Serotonin Receptors

Although 14 serotonin receptor subtypes are known (Barnes and Sharp 1999), the major emphasis in the
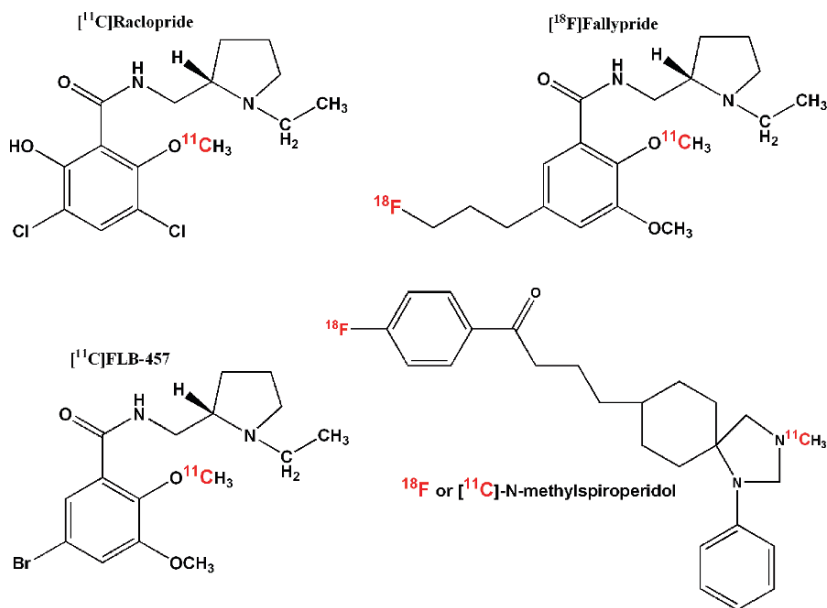
Fig. 16.9 PET radioligands for dopamine D₂ receptors
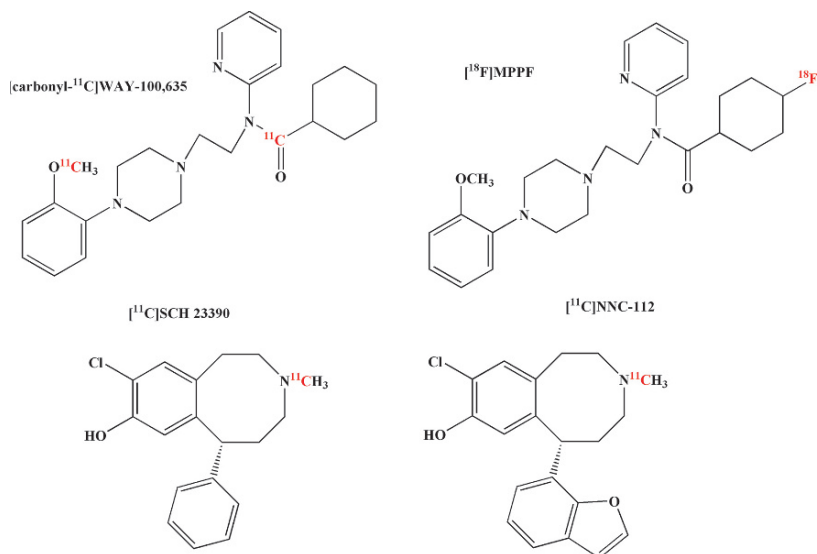
Fig. 16.10 PET radioligands for dopamine D_1 receptors

Fig. 16.11 Radioligands for the enzyme *monoamine oxidase (MAO)*
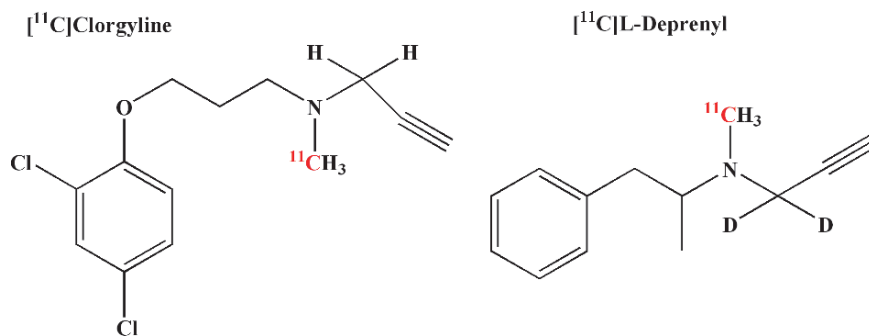
development of radiotracers has focused on the 5-HT$_{1A}$ and 5-HT$_{2A}$ receptor subtypes. The 5-HT$_{1A}$ receptors are present on the cell bodies of raphe nuclei and serve as autoreceptors mediating serotonin release. Also, they are present at the pre- and postsynaptic serotonergic terminals. The highest densities of these receptors are located in the limbic forebrain (hippocampus, entorhinal cortex, and septum), while the lowest densities are found in the extrapyramidal areas (basal ganglia, substantia nigra) and in the cerebellum. The presynaptic sites have been proposed to mediate drug treatment of anxiety and depression, while the postsynaptic sites have been found to be elevated in schizophrenic brains postmortems (Fowler et al. 2003). The 5-HT$_{2A}$ receptors are present in all neocartical regions, with a lower density in the hippocampus, basal ganglia, and thala-

mus, cerebellum and the structures of the brain stem are virtually devoid of these receptors (Herholz et al. 2004).

Some of the most important serotonin receptor binding radiotracers for PET imaging studies are shown in Figs. 16.12 and 16.13). Among the receptor antagonists, [O-methyl-^{11}C]WAY 100635 was the first radioligand used to image the 5-HT$_{1A}$ receptors in humans. However, because of the formation of a more lipophilic metabolite in vivo with greater brain uptake, the tracer was found not to be optimal for imaging studies. However, the [carbonyl-^{11}C]desmethyl-WAY-100635 (DWAY) analogue, in which ^{11}C is labeled in a different position to prevent in vivo metabolism, has shown superior binding to the 5-HT$_{1A}$ receptors (Passchier and van Waarde 2001). Because of their high affinities to this receptor subtype,
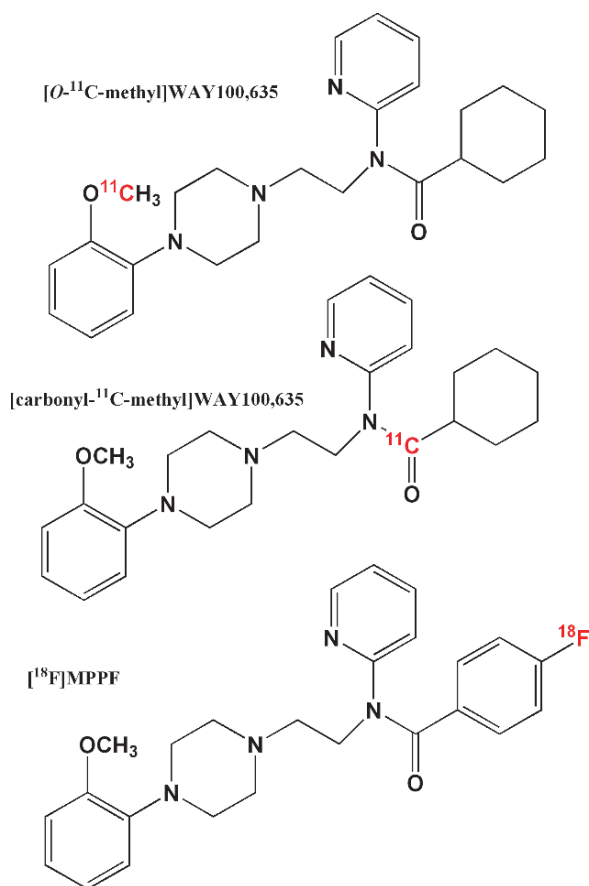
Fig. 16.12 PET radioligands for serotonin (5-HT$_{1A}$) receptors

Fig. 16.13 PET radioligands for serotonin (5-HT$_{2A}$) receptors

Serotonin Transporter

Serotonin transporters (SERTs) belong to the same family as the other monoamine transporters, for the presynaptic reuptake of dopamine and norepinephrine. A number of antidepressant drugs (citalopram, fluoxetine, fluvoxamine, paroxetine, and sertraline) belong to the pharmacologic class of serotonin transporter reuptake inhibitors (Belmaker and Agam 2008). Because of the need to understand the mechanism of this disease and to evaluate the relative clinical efficacy of therapeutic agents, a number of molecular imaging radiotracers for PET and SPECT have been developed (Shieu and Welch 2004; Kung et al. 2003a; Heiss and Herholz 2006). [^{11}C](+)McN-5652 was the first successful radiotracer (Fig. 16.14) to show the expected regional brain distribution and uptake in the areas of higher receptor density (striatum, thalamus and midbrain). However, because of the in vivo metabolism, nonspecific binding, and poor signal contrast, this radiotracer is not ideal. A new class of potent SERT reuptake inhibitors, based on the parent compound phenylthiophenyl derivative known as 403U76 (Fig. 16.14), have been reported to possess high selectivity and affinity for SERT over norepinephrine and dopamine

both WAY and DWAY, however, may not be appropriate for measuring changes in the endogenous serotonin levels. In contrast, ^{18}F analogs of WAY100,635 have been developed to increase clinical applicability. [^{18}F]MPPF is selective for 5-HT$_{1A}$ receptors and has been used to image 5-HT$_{1A}$ receptors in the human brain, and its binding has been shown to be sensitive to endogenous serotonin (Passchier et al. 2000).

^{11}C or ^{18}F labeled NMSP, an irreversible antagonist used for imaging dopamine D$_2$ receptors in the basal ganglia, also bind to the 5-HT$_{2A}$ receptors in the frontal cortex (Pike 1995). Among the more selective antagonists, [^{18}F]Altanserin provides slightly higher sensitivity for the detection of 5-HT$_{2A}$ receptors and is one of the most selective antagonists utilized for imaging studies. Further, [^{18}F]Setoperone and [^{11}C]MDL 100,907 have also shown utility in imaging 5-HT$_{2A}$ receptors in human studies.

Fig. 16.14 PET and SPECT radioligands for serotonin transporters (ST)
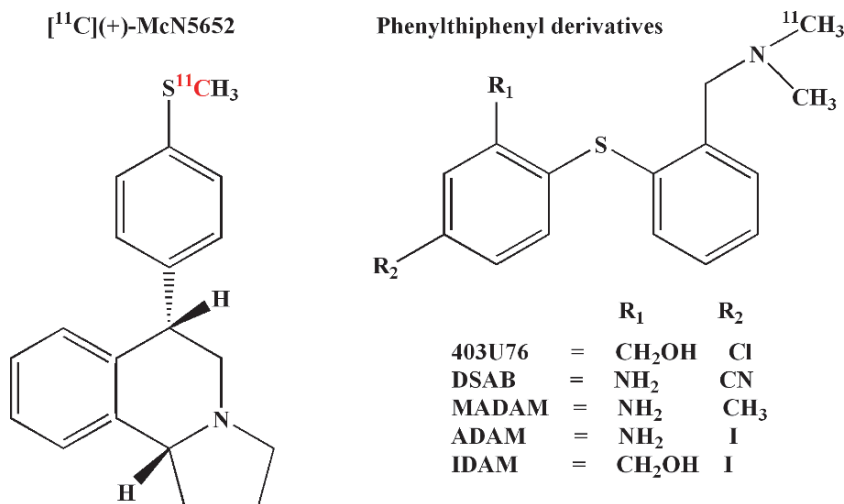
transporter binding sites. Among the many PET tracers, [^{11}C]DASB, [^{11}C]DASP and [^{11}C]MADAM exhibit high affinity and selectivity for SERT and have proven to be excellent PET tracers for imaging SERT in the human brain (Ginovart et al. 2003; Heiss and Herholz 2006). On the basis of the 403U76 compound, ^{123}I labeled IDAM and ADAM were also prepared for SPECT imaging studies. Initial human studies have shown that [^{123}I]ADAM localizes in the hypothalamus, a region known to have SERT concentration and was found to be superior to [^{123}I]IDAM as a SPECT imaging agent for SERT in the brain (Kauppinen et al. 2003). Also, the cocaine analogs, ^{123}I-β-CIT and ^{123}I-nor-β-CIT, useful to image dopamine transporters, have shown uptake in SERT sites in patients with depression and schizophrenia (Kung et al. 2003a).

16.2.2.3 Cholinergic System

The neurotransmitter Ach plays a major role in learning, memory, and AD. Consequently, the receptors that mediate cholinergic neurotransmission and the enzymes that mediate its synthesis, as well as termination of its action, are the targets for developing specific radiotracers for imaging studies. Two types of receptors for Ach are known: the muscarinic-cholinergic receptors (mAChR) and the nicotinic-cholinergic receptors (nAChR), however, multiple heterogeneous subtypes have been characterized. While nAChRs belong to the ligand-gated ion channels, mAChrs operate via several second messengers.

Muscarinic Receptor

In the brain, mAChRs are the dominant postsynaptic cholinergic receptors. The first ligand to map mAChRs in humans was ^{123}I-QNB, 3-R-quinuclidinyl-4-S-iodobenzilate (RSIQNB) (Eckelman et al. 1984). Subsequently, several PET and SPECT tracers have been developed on the basis of receptor antagonists (Fig. 16.15), since they may have higher affinity and provide more image contrast. Most of these tracers, however, have very low receptor subtype selectivity and unfavorable receptor binding kinetics. Since radiotracers, based on receptor agonists, are more sensitive to the affinity state of the receptor and provide more biologically relevant information, an mAChR M_2 selective agonist, [^{18}F]FP-TZTP was developed (Eckelman 2001; Podruchny et al. 2003). Prior to the administration of physostigmine, an acetylcholinesterase (AChE) inhibitor, which would increase the intrasynaptic Ach levels, was found to produce a 35% reduction, thus, demonstrating specific binding of the radiotracer to mAChRs.

Nicotinic Receptor

The primary action site of nicotine are the nAChRs and these receptors are widely distributed in the CNS, PNS, and the adrenal glands. These receptors exist as pentamers comprised of α and β subunits, leading to considerable diversity. The most abundant subtype in the mammalian brain is $\alpha_4\beta_2$, which has the highest

Fig. 16.15 PET radioligands for muscuranic cholinergic (mACh) receptors
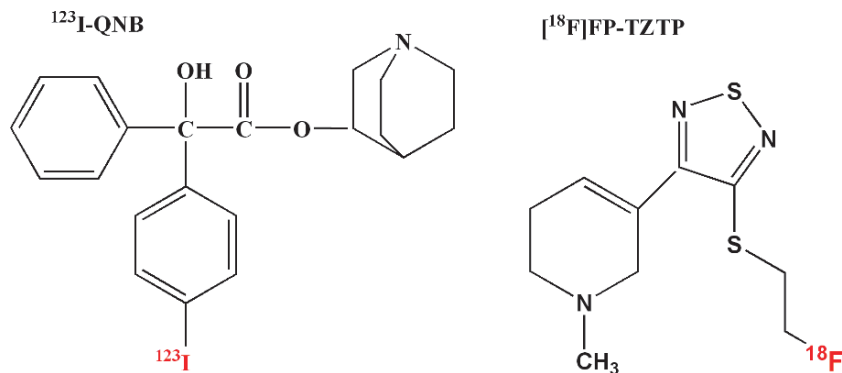
affinity for nicotine (Fowler et al. 2003). [^{11}C]nicotine (Fig. 16.16) has been used in human studies and high binding was reported in several cortical and subcortical regions, while low density was found in the pons, cerebellum, occipital cortex, and white matter. Higher uptake was observed in smokers compared to non-smokers, indicating an increased density of nicotinic binding with the chronic administration of nicotine. However, the highly nonspecific binding and its rapid washout have limited the clinical application of this tracer. Other radiolabeled nicotinic agonists have also demonstrated suboptimal imaging characterisitics.

Epibatidine, a potent analgesic, isolated from the Ecuadorian poisonous frog, has a high specificity for nicotinic receptors. [^{18}F]norchloro-fluoroepibatidine (NFEP) has been used to image the nicotine receptor occupancy in animal models, however, it is not suitable for human studies because of unacceptable high toxicity (Ding et al. 2000). The most promising tracer for imaging nAChRs in humans is based on the 3-pyridyl ether derivatives of the parent compound A-85380, an agonist which has higher selectivity for $\alpha_4\beta_2$ receptor subtypes, but significantly lower toxicity.

Acetylcholinesterase

Since the enzyme AChE hydrolyzes Ach, it regulates the amount of Ach available in the synapse. AChE enzyme inhibitors, such as physostimine, increase the synaptic levels of ACh. As a result, [^{11}C]physostigmine (PHY) uptake and retention, in principle, represents the enzyme activity (Pappata et al. 1996). Labeled analogs of acetylcholine, which are also substrates for AChE, can be used to measure and image its activity in vivo (Fig. 16.16). These analogs are ^{11}C labeled *N*-methyl-4-

piperidyl-acetate (MP4A, also known as AMP), which is 94% specific for AChE in the human brain, and *N*-methyl-4-piperidyl-propionate (MP4P or PMP). Hydrolysis of these tracers by AChE results in tissue trapping, while unhydrolysed tracers are washed out from the brain through blood flow (Koeppe et al. 1999; Herholz 2008).

16.2.2.4 Opiate System

Morphine and other opiate analgesic drugs, such as codeine, heroin and pethidine, affect the perception of pain by interacting with specific receptors expressed at a number of sites in the CNS and PNS. The endogenous opioids have been identified as a family of more than 20 peptides grouped into three classes: the endorphins, the enkephalins, and the dynorphins. Opiate receptors mediate the effects of opioid drugs and peptides in respiratory depression, analgesia, reward, and sedation. There are three opiate receptor subtypes; μ, δ, and κ. The μ subtype and its subclasses are the primary site for pleasurable reward feeling and the highest concentrations are found in the basal ganglia and thalamus. [^{11}C]Carfentanil (Fig. 16.17), a potent synthetic high affinity μ opiate receptor agonist was the first tracer investigated for opiate receptor imaging (Frost et al. 1985; Frost 2001). Its uptake in the basal ganglia and thalamus can be reduced by pretreatment with the opiate antagonist naloxone. Carfentanil binding is also sensitive to the release of endogenous opioids in response to pain. The high-affinity opiate antagonist [^{18}F]cyclofoxy binds to both μ and κ receptor sites and is distributed similarly to the distribution of naloxone in the caudate, amygdala, thalamus, and brain stem (Kling et al. 2000; Frost 2001).

Fig. 16.16 PET radio-ligands for nicotinic cholinergic (nACh) receptors

(-)-[^{11}C]Nicotine

[^{18}F]NFEP

Analogs of A-85380

	R$_1$	R$_2$	R$_3$
2-Fluoro-A-85380	H	^{18}F	H
6-Fluoro-A-85380	H	H	^{18}F
5-Iodo-A-85380	^{123}I	H	H

[^{11}C]PMP or MP4P

[^{11}C]AMP or MP4A

[^{11}C]Carfentanyl

(-)-[^{18}F]Cyclofoxy

[^{11}C]Diprenorphine

[^{11}C]GR89696
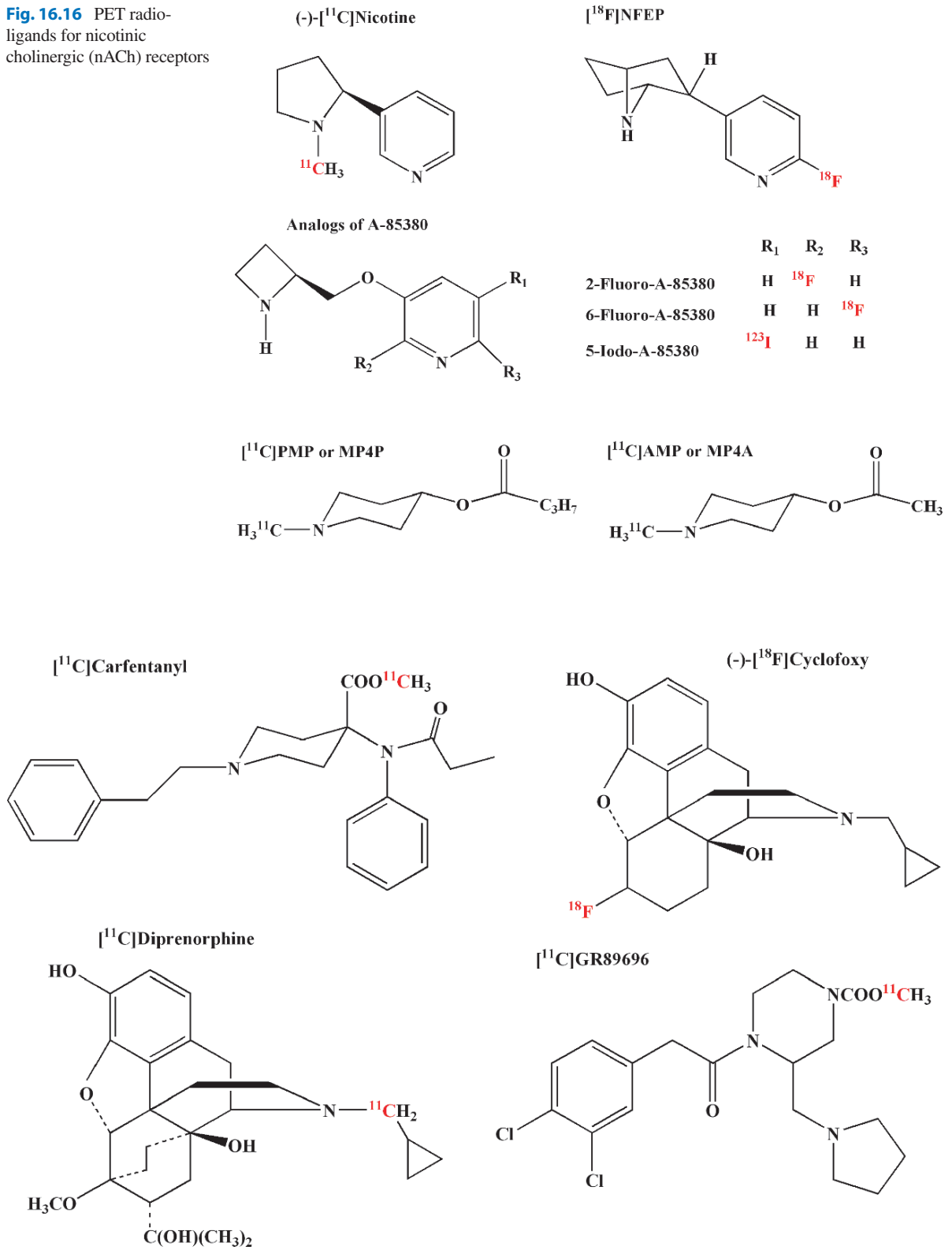
Fig. 16.17 PET radioligands for opiate receptors

[¹¹C]Diprenorphine, a nonselective opioid agonist, and [¹¹C]buprenorphine, a compound with both agonist and antagonist properties, have also been developed for opiate receptor imaging studies. Diprenorphine clears more rapidly from the cerebellum, making it more appropriate for imaging studies, however, buprenorphine has low toxicity and is an approved analgesic drug. Recent studies have shown that [¹¹C] GR103545, a stereotactic isomer of a potent κ-opioid receptor agonist, GR89696, displays excellent brain penetration and uptake kinetics (Talbot et al. 2005).

16.2.2.5 GABA System

γ-Aminobutyric acid (GABA), the most important inhibitory neurotransmitter in the brain, interacts with the GABA receptor system which is abundant in the cortex. Part of the GABA$_A$ receptor complex, which gates the Cl$_2$ channel, is the central benzodiazepine receptor, which specifically mediates all pharmacologic properties of drugs, which are known as the benzodiazepines (sedative, anxiolytic, anticonvulsant, myorelaxant) (Heiss and Herholz 2006). Binding sites for these benzodiazepines have been subdivided into *central* and *peripheral* types. Only the central sites are associated with neuronal GABA$_A$ receptors, while the peripheral binding sites in the brain are only expressed by non-neuronal microglia and ependymal cells. The peripheral sites also occur in the kidneys, liver, lungs, mast cells, and macrophages.

The radiotracers most widely used for imaging central benzodiazepine-binding sites (Fig. 16.18) are based on the antagonist, Ro-15-1788 (flumazenil). With [¹¹C] flumazenil, a clear dose-dependent binding has been demonstrated (Persson et al. 1985). The ¹²³I labeled analog, iomezenil, developed for SPECT studies, has also been labeled with ¹¹C for use in PET studies (Bremmer et al. 2000). Finally, a high specific activity ¹⁸F labeled flumazenil was also developed (Ryzhikov et al. 2005). These tracers bind mainly to a α$_1$ subtype of the GABA$_A$ receptors in the medial occipital cortex, followed by other cortical areas (the cerebellum, thalamus, striatum, and pons). [¹¹C]Ro-15-4513 (azidomazenil), a partial inverse agonist, which binds preferentially to the α$_5$ receptor subtype, has shown greater uptake in limbic areas, particularly in the anterior cingulate cortex, hippocampus, and insular cortex, but lower uptake in the occipital cortex and cerebellum compared to flumazenil (Suhara et al. 2003a).

The tracer most frequently used as the ligand for the peripheral benzodiazepine receptor (PBR) is the isoquinoline, [¹¹C]PK-11195 (Fig. 16.19), which binds to activated, but not resting, microglia (Banati et al. 2000).
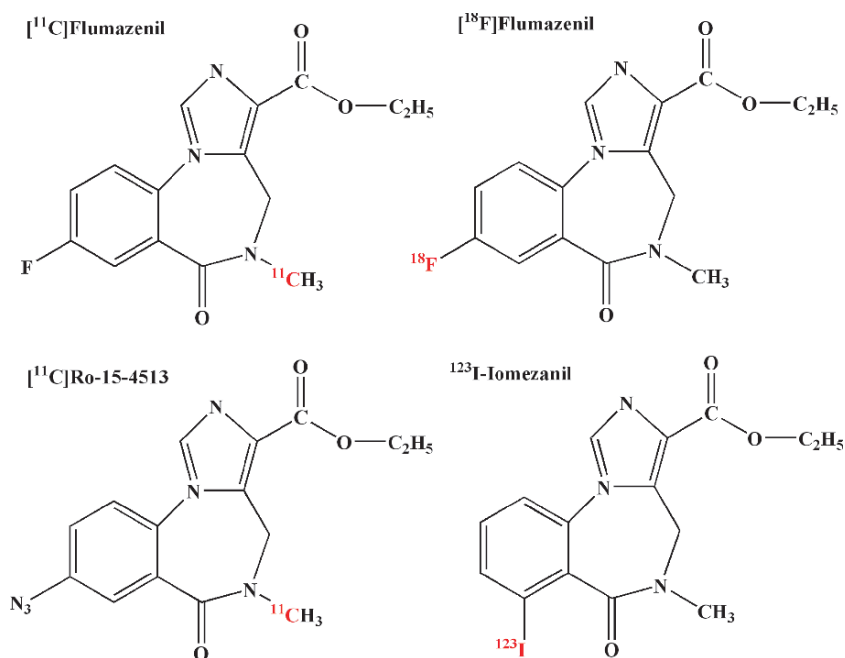
Fig. 16.18 PET and SPECT radioligands for GABA system (central benzodiazepine receptors)

Fig. 16.19 PET and SPECT radioligands for peripheral benzo-diazepine receptors
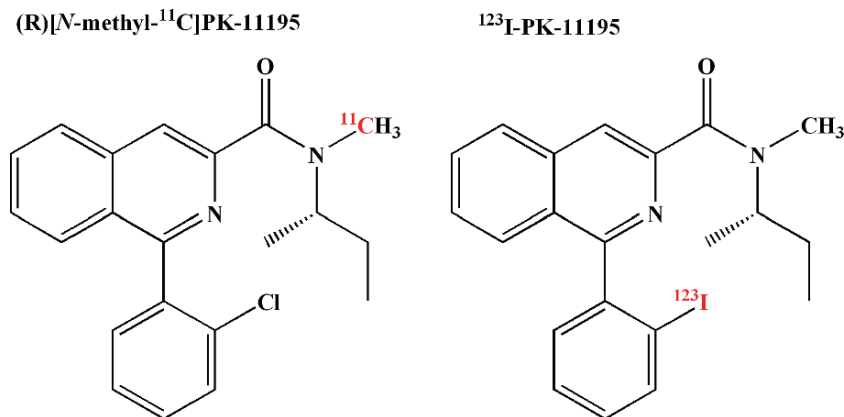
This tracer has been used to image active brain pathology associated with microglial activation and neurodegenerative conditions, including stroke, multiple sclerosis, encephalitis, PD, and AD. While PK11195 has provided the proof-of-principle that the estimation of PBR expression in vivo is possible, the high degree of nonspecific uptake of PK11195 complicates the quantification and modeling of the PET data. Other ligands displaying better brain kinetics have recently been described. Among them, [^{11}C]DPA-713, a compound from the family of pyrazolopyrimidines, has shown a higher affinity for PBR than PK11195. Also, [^{11}C]DPA-713 is substantially more selective for the PBR than for the CBR (Thominiaux et al. 2006, Boutin et al 2007).

16.2.3 β-Amyloid Imaging

Neuropathologic evidence suggests that the characteristic neuropathologic hallmark in AD is the deposition of senile plaques (SPs) which contain β-amyloid (Aβ) aggregates and neurofibrillary tangles (NFTs) consisting of highly phosphorylated tau protein (Morris and Naggy 2004). The main constituents of Aβ-deposits in the AD brain are peptides of 40 and 42 amino acids, Aβ$_{40}$ and Aβ$_{42}$, respectively, generated from the cleavage of the amyloid precursor protein (Fig. 16.20) (Price 1997). The subsequent arrangement of these peptide monomers into an amyloid fibril results in a characteristic β-plated sheet structure, which represents the target for tracers developed for noninvasive molecular imaging probes.

Compact plaques consist of a dense central core of amyloid fibrils, while noncompact plaques contain less fibrillar Aβ (Dickson 1997). A shift of the brain Aβ from the soluble to the fibrillar form is closely associated with the onset of AD (Wang et al. 1999). Previous neuropathologic studies have indicated that neuritic plaque densities are highest in the neocortex, especially in the temporoparieto– occipital region, and lowest in the cerebellum.

16.2.3.1 Radiotracers for Imaging Aβ Aggregates

The four promising chemical backbones for amyloid radioligands include aminonapthalenes, benzothiazoles, stilbenes, and imidazopyridines, from which several compounds have been developed as imaging probes to detect amyloid in the brain. The structures of three important tracers, [^{18}F]-FDDNP, [^{11}C]PIB, and [^{11}C] SB-13, are shown in Fig. 16.21.

The first radio tracer described was [^{18}F]-FDDNP which is based on aminonaphthalene (Bario et al. 1999). In vitro binding studies have shown that FDDNP is was bound to the synthetic Aβ1–40 with two binding sites, a high affinity site (0.12 nM) and a low-affinity site (1.9 nM). In contrast, [^{18}F]-FDDP binding studies with postmortem AD homogenates have shown a Bmax value of 144 nM with a K_D value of 0.75 nM (Agdeppa et al. 2001).

N-Methyl-[^{11}C]-2-(49-ethylaminophenyl)-6-hydroxy-benzothiazole or [^{11}C]-6-OH-BTA-1 (also known as Pittsburgh Compound-B or PIB) was developed on the basis of the thioflavin-T amyloid dye

Fig. 16.20 Amyloid precursor protein (APP) metabolism, elimination, and deposition in brain

[¹⁸F]FDDNP

[¹¹C]PIB

[¹¹C]SB-13
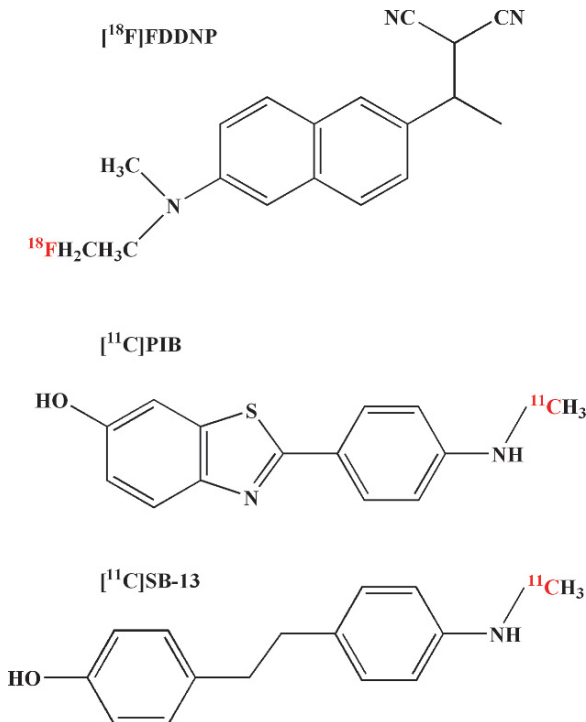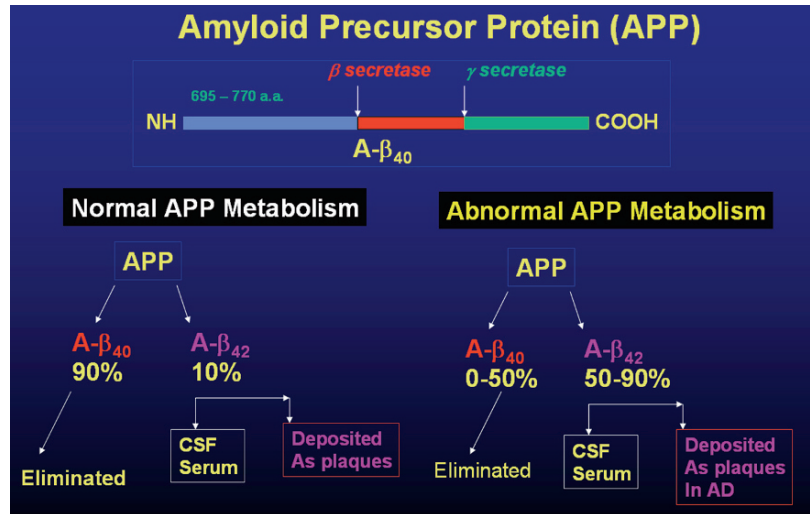
Fig. 16.21 PET radiotracers for imaging brain β-amyloid plaques and tangles in patients with Alzheimer's disease

(Mathis et al. 2002). PIB has shown two binding sites in human autopsy brain tissue, a high affinity binding site with a B_{max} of 1,407 pmol g⁻¹ and a K_D value of 2.5 nM, and a low-affinity binding site with a B_{max} of 13 nM and a K_D of 250 nM, respectively. Avid

Pharmaceuticals recently reported the development of an ¹⁸F labeled stilbene derivative, ¹⁸F-BAY94–9182 (also known as ¹⁸F-AV1/ZK), which shares common structural features with PIB (Zhang et al. 2005a, b). This tracer has been shown to bind avidly to neuritic and diffuse Aβ plaques, and to cerebral amyloid angiopathy in vitro (it does not show appreciable labeling of tangles, Pick bodies, Lewy bodies, or glial cytoplasmic inclusions). In brain homogenates from patients with AD, BAY94–9172 (Fig. 16.22) was found to bind with high affinity (67 nM), and in AD tissue sections, it selectively labeled Aβ plaques (Thominiaux et al. 2006). On the basis of the SB-13 ligand, the ¹²³I labeled tracer, 6-iodo-2-(4V-dimethylamino-)phenyl-imidazo[1,2-a] pyridine (the ¹²³I-IMPY) was developed for SPECT imaging of brain amyloid depositions (Kung et al. 2003b).

16.3   Applications in Clinical Neurology

Clinical examination is more powerful in neurology than in many other medical specialties with respect to its ability to precisely localize a lesion in various neuropathological conditions. As a result, neurologists, traditionally, are less inclined to pursue imaging techniques to guide medical management. While abnormal neuropathology can be easily documented with morphological imaging techniques, such as CT and MRI, many aspects of neurologic diseases, in particular the molecular mechanisms that underlie their clinical

Fig. 16.22 PET and SPECT radiotracers for imaging brain β-amyloid plaques in patients with Alzheimer's disease
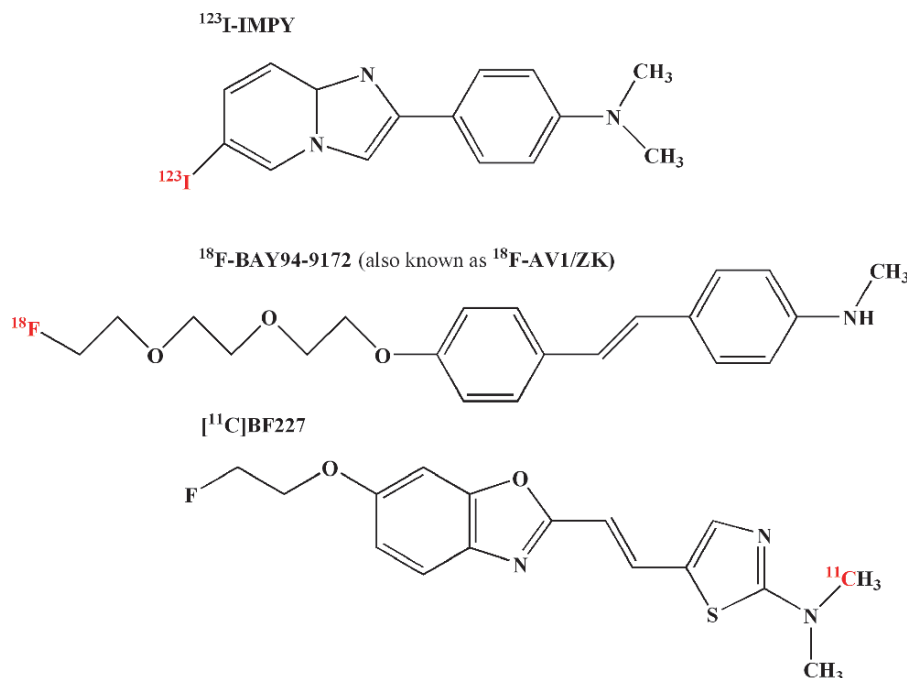
manifestation, cannot adequately be studied in vivo by clinical means and structural imaging (Herholz and Heiss 2004). In order to optimize individualized patient treatment, based on targeted molecular therapies, requires the selection of appropriate patients for specific drugs needs noninvasive molecular imaging techniques that can quantitatively assess the functional status, and the underlying neurotransmitter and/or neuroreceptor abnormalities associated with a specific neuropsychiatric disease or disorder. The changes in electrical activity of neurons (excitation or inhibition) have been indirectly attributed to the alterations in rCBF or LCMRglc. The functional coupling of rCBF and LCMRglc has been well established in the normal human brain and certain neurological diseases. With the availability of multimodality imaging technologies (such as PET/CT, SPECT/CT), radioisotope based molecular imaging radiopharmaceuticals will play a significant role in routine clinical management. The main areas in clinical neurology where molecular imaging techniques would play a major role are

- Diagnosis of AD and other dementias
- Differential diagnosis of movement disorders
- Localization of epileptic foci
- Diagnosis of primary and recurrent brain tumors
- Identification of viable tissue in ischemic stroke

In addition, molecular imaging will have great implications for the identification of potential molecular therapeutic targets, in the development of new treatment strategies, and in their successful implementation in clinical application. Various PET and SPECT radiopharmaceuticals with potential applications in clinical neurology are summarized in Table. 16.2. Some of the important clinical studies documenting the utility of these tracers are briefly described below.

16.3.1 Alzheimer's Disease

Dementia is a clinical syndrome characterized by impaired short- and long-term memory and is associated with deficits in abstract thinking, judgment, and other higher cortical functions. The degree of cognitive dysfunction, however, spans a wide spectrum. AD is a progressive, neurodegenerative disease characterized by loss of function and death of neurons in several brain areas, leading to the decline of prominent mental functions, including memory. AD is the most common cause of dementia in aging. AD was first characterized by Aloise Azheimer in 1907, who discovered that amyloid plaque (Aβ and NFTs) in the brain is a hallmark of this disease and the marker by which diagnosis is

confirmed, posthumously. One prominent hypothesis is that amyloid deposits and soluble forms of amyloid lead to neuronal dysfunction and cell death. The physiological role of Aβ is not exactly clear, but there is growing evidence which suggests that it is essential for the modulation of synaptic activity and neuronal survival under normal conditions (Drzezga 2008). Mild cognitive impairment (MCI) is considered a transitional stage between healthy aging (HA) and AD. Other causes of cognitive decline include dementia with Lewy bodies (DLB), vascular dementia (VD), frontotemporal dementia (FTD), Creutzfeldt–Jakob disease, HIV-associated dementia, neurosyphilis, Parkinson's dementia, normal pressure hydrocephalus, and dementias caused by exposure to toxic substances (heavy metals, alcohol, drugs), metabolic abnormalities, or psychiatric disorders (Herholz et al. 2004).

Although the exact causalities of most primary forms of dementias are not yet fully understood, growing evidence has been collected, supporting the assumptions that a common basis of many neurodegenerative dementias can be found in the increased production, misfolding, and pathological aggregation of proteins, such as β-amyloid, τ-protein, a-synuclein, or the recently described ubiquitinated TDP-43 (Drzezga 2008). In addition, amyloid pathology may occur in different stages of aggregation (oligomers, fibrils, plaques, etc.); it may show different configurations (diffuse, compact plaques, vascular amyloid, etc.) and different components ($A\beta_{40}$, $A\beta_{42}$, dystrophic neurites, etc.). The term Lewy bodies describes intracellular aggregations, mainly constituted of the a-synuclein protein, which is predominantly expressed in neurons.

Neuropathological studies indicate that two proteins, β-amyloid (in senile plaques) and τ-protein (in NFTs) accumulate abnormally in a predictable spatial pattern during aging and in AD (Mathis et al. 2007). Until recently, plaques and tangles could be assessed only during an autopsy or, rarely, during a biopsy.

The identification and differential diagnosis of AD is especially challenging in its early stages, such as MCI, partly because of the difficulty in distinguishing it from the mild decline in memory that can occur with normal aging and from mild cognitive manifestations of other neuropsychiatric conditions, such as depression, as well as other causes of dementia (Silverman et al. 2008). PET and SPECT have long been used to assess various forms of dementia, especially AD. The role of different

molecular imaging probes with specific clinical applications are briefly summarized below.

16.3.1.1 FDG-PET in AD

AD is progressive and is commonly unrecognized in its very early stages. Since functional changes usually precede the anatomic changes seen on CT and MR images, FDG-PET has been investigated extensively in the evaluation of AD. Classically, patients with AD have a pattern of bilateral parietotemporal hypometabolism that is not generally seen in patients with other forms of dementia or in age matched control subjects (Silverman 2004) (Fig. 16.23). Further, asymmetry of the metabolic deficits is not uncommon. The decline of the FDG uptake in the posterior cingulate, hippocampus, parietotemporal, and prefrontal association cortices (Fig. 16.24) allows for the identification of mild to moderate AD with high sensitivity and specificity. Also, there is typically sparing of the basal ganglia, thalamus, cerebellum, and primary sensory cortex. Even early in the disease process, before the appearance of volume loss, FDG-PET has been helpful in diagnosing AD. Histopathologically confirmed sensitivity and specificity of PET for detecting the presence of AD are in the range of 92–94% and 71–73%, respectively (Silverman et al. 2008). Since medications used to treat AD continue to emerge and since these medications have demonstrated the ability to improve memory, or at least delay the deterioration of cognitive functions, (Herholz et al. 2004), FDG-PET imaging could aid in determining patient prognosis, disease progression, and the efficacy of various medication regimens.

16.3.1.2 β-Amyloid

Initial studies with [¹⁸F]FDDNP have shown that PET scans show significantly higher values for FDDNP binding in the temporal, parietal, and frontal regions of the brain in patients with AD than in older control subjects without cognitive impairment (Shoghi-Jadid et al. 2002). More specifically, these studies have demonstrated a significantly greater "relative retention time" in AD subjects than control subjects, in the hippocampus, amygdala, and enthorinal cortex, areas with high concentrations of plaques and tangles

Fig. 16.23 FDG-PET showing hypometabolism in AD and differential diagnosis of AD from other forms of dementia (Jacobs et al. 2005)
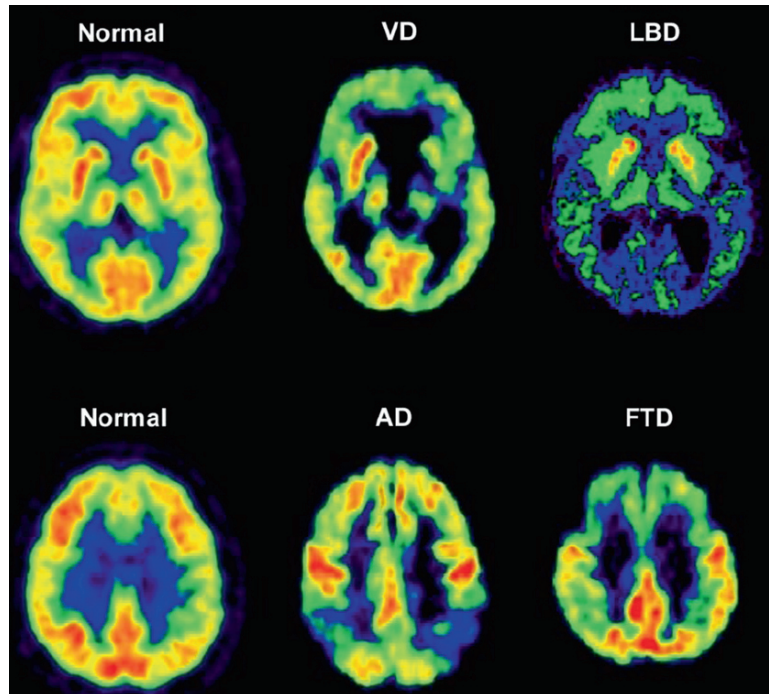
Fig. 16.24 FDG-PET in AD showing typical areas of hypometabolism in posterior cingulate, parietotemporal, and temporomesial cortices (Jacobs et al. 2005)
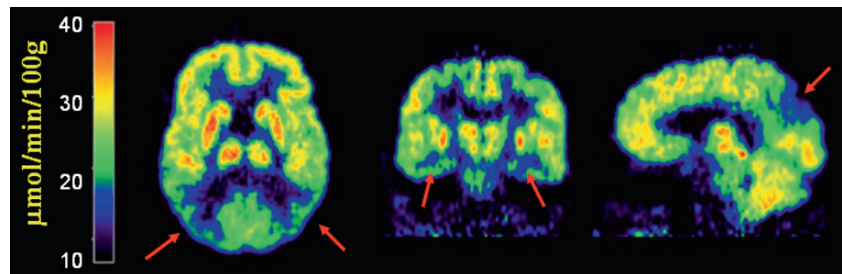
(Fig. 16.25). In a recent clinical study, FDDNP-PET scans appeared to differentiate persons with MCI from those with AD and those without cognitive impairment. Also, in vivo distributions of FDDNP in the brain followed patterns of pathological distribution seen during autopsy (Small et al. 2006). Limitations of this compound include high nonspecific binding (with a relatively low target-to-background ratio), low brain uptake (only about 9% higher cortical uptake), and lack of validated kinetic methods for quantitation (Shoghi-Jadid et al. 2002).

Studies with [^{11}C]PIB, the most specific and widely used radiotracer for Aβ, indicate that PIB-PET may allow earlier diagnosis of AD and accurate differential diagnosis of the dementias (Klunk et al. 2004; Mintun et al. 2006; Ng et al. 2007; Drzezga 2008). PIB-PET images (Fig. 16.26) show robust cortical binding in almost all AD patients (about 70% increase in cortical binding) and correlate well with a reduction in CSF Aβ$_{42}$. An inverse significant correlation has also been observed between brain PIB uptake in specific areas, and the corresponding glucose hypometabolism in the same areas imaged by FDG-PET (Klunk et al. 2004). In addition, PIB binding also correlates with the rate of cerebral atrophy as measured by MRI and with episodic memory impairment in apparently normal elderly individuals, and in patients with mild cognitive impairment (Archer et al. 2006). Increased PIB binding may also be predictive of the conversion of MCI to AD (Pike et al. 2007). Furthermore, the positive findings with PIB in AD subjects have been confirmed in more than 500 subjects by several research groups worldwide.

Fig. 16.25 Comparison of [¹⁸F]FDDNP-PET and FDG-PET images in a patient with AD and a normal control subject. Brain areas with decreased FDG uptake show high retention and localization of FDDNP in a patient with AD, but not in normal subjects (Shoghi-Jadid et al. 2002)
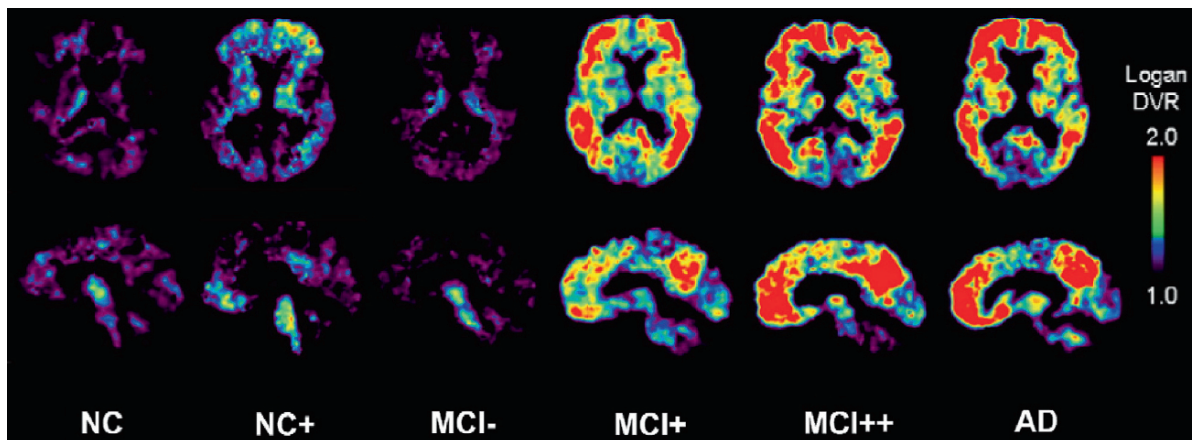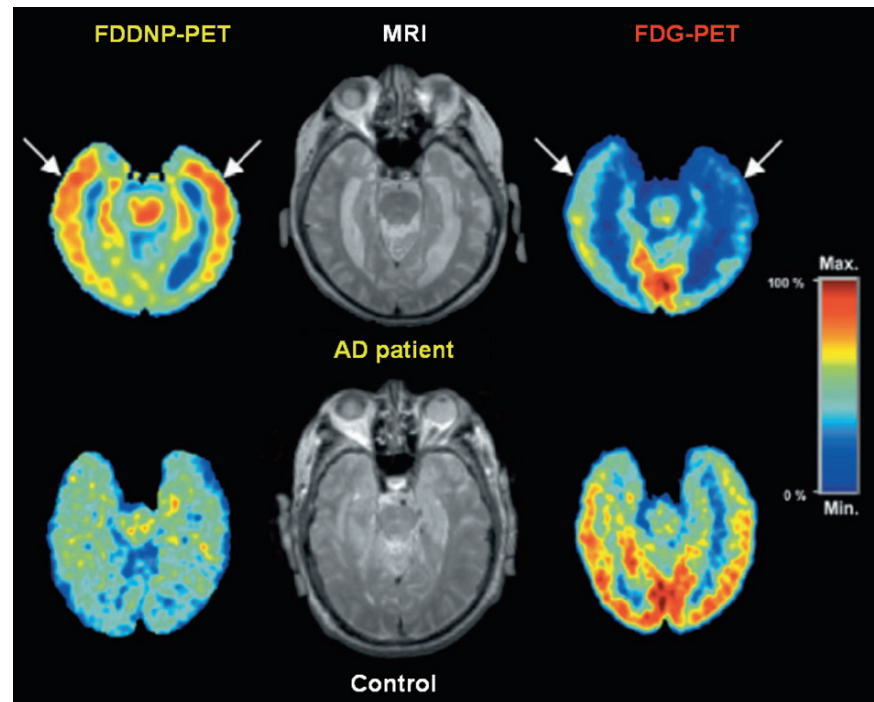
Fig. 16.26 [¹¹C]PIB-PET images (in the transaxial and sagittal planes) of parametric Logan distribution volume ratios (DVR) relative to the cerebellum in two normal controls (NC), three MCI subjects, and one AD subject. PIB uptake and retention may be either negative (−) or positive (+, ++) (Mathis et al. 2007)

In a recent clinical study, a stilbene derivative, ¹⁸F-AV1/ZK, has demonstrated (Fig. 16.27) the potential value of Aβ-PET imaging to discriminate between AD patients and individuals with frontotemporal lobar degeneration (FTLD) or healthy controls and might facilitate integration of Aβ imaging into clinical practice (Rowe et al. 2008). AD patients have also shown widespread neocortical binding, which was greater in the precuneus/posterior cingulate and frontal cortex than in the lateral temporal and parietal cortex, and with relative sparing of the sensorimotor, occipital, and medial temporal cortex. Healthy controls and FTLD patients have also shown only white-matter binding, although three controls and one FTLD patient had mild uptake in the

Fig. 16.27 ^{18}F-BAY94-9172 (Aβ ligand) PET images from three patients with AD and one patient with FTLD. There is cortical binding in the frontal, posterior cingulate/precuneus, and lateral temporal areas with relative sparing of the occipital and sensorimotor cortex in AD patients (**a**–**c**). By contrast, there is no cortical binding in the FTLD patient (**d**) (Rowe et al. 2008)
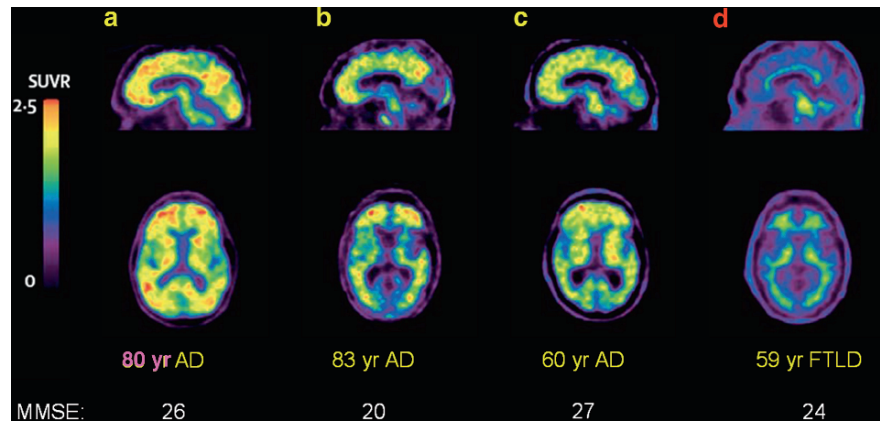
frontal and precuneus cortex. Another stilbene, [^{11}C]-SB13, has shown the same regional brain distribution pattern as PIB, when studied in the same population of AD patients and age-matched healthy controls (Verhoeff et al. 2004).

In summary, the potential applications of Aβ imaging agents include their use as diagnostic agents to detect cerebral β-amyloidosis, to help test the amyloid cascade hypothesis of AD, and to assist with the development of antiamyloid therapeutic drugs (Mathis et al. 2007 < Nordberg et al 2008). As diagnostic imaging markers in AD, PIB and other Aβ-PET molecular imaging probes depend on the ability to discriminate between AD and other forms of dementia. Some major issues and concerns need additional clinical studies to further validate the potential clinical utility of in vivo brain amyloid imaging.

16.3.1.3 Cholinergic System

The central role of the cholinergic system in the AD pathway is becoming increasingly significant. The cholinergic hypothesis implies that a degeneration of cholinergic neurons in the basal forebrain and the associated loss of cholinergic neurotransmission in the cerebral cortex and other brain areas contribute significantly to the deterioration in cognitive function seen in patients with AD (Bartus et al. 1982). These neurons express AChE, an enzyme responsible for the degradation of Ach. Also, in recent years, increasing evidence has emerged suggesting an interrelationship between the basal forebrain cholinergic neurotransmission and the metabolism of the amyloid precursor protein (APP). Significant improvement of cognitive function, relative to a placebo after therapy with acetylcholinesterase inhibitors (AChEIs) in AD provides support for the cholinergic hypothesis (Herholz et al. 2004). Abnormalities in the cholinergic system in AD include alterations in the Ach synthesis and receptor expression, and a decrease in nAChRs ($\alpha_4\beta_2$ subtype) are of particular interest.

With Ach analogs and substrates for AChE, [^{11}C] MP4A and [^{11}C]MP4P, reduced uptake has been observed in AD in all cortical areas, most severely in the occipital and temporal cortex, while uptake in basalis of Maynert is preserved, suggesting that cholinergic impairment begins in the cortical regions and affects the basal cell nuclei slowly, as a result of a "dying back" phenomenon (Fig. 16.28) (Kuhl et al. 1999; Heiss and Herholz 2006). The inhibition of acetylcholinesterase, which results from treatment with specific drugs, such as donepezil, can also be measured with these tracers (Kuhl et al. 2000). As discussed earlier, [^{11}C]epibatidine, is a highly specific ligand for AChE, but it is also very toxic and, therefore, not suitable for human studies.

Preliminary studies in humans with 6-[^{18}F]fluoro-A-85380 and 5-[^{123}I]iodo-A-85380 suggest that these tracers may have potential utility in assessing nAChRs (Fowler et al. 2003; Kulak et al. 2002). In a recent study (Sabri et al. 2008), 2-[^{18}F]fluoro-A-85380 was shown to be potentially useful in the diagnosis of patients at risk for AD (Fig. 16.29). Because of the extraordinary long acquisition time (>5 h) needed with this tracer, a new analog, (−)[^{18}F]norchloro-fluoro-homoepibatidine (NCFHEB) was investigated, which has shown twofold higher brain uptake and significantly shorter acquisition times. Therefore, NCFHEB should be a suitable radioligand for larger clinical investigations.

Fig. 16.28 Imaging acetylcholinesterase (AChE) activity in the brain using [^{11}C] MP4A-PET in mild-to-moderate AD. Reduction in cortex and amygdala with preserved activity in basal forebrain suggests a dying back of cholinergic neurons rather than initial loss of cell bodies (Heiss and Herholz 2006)
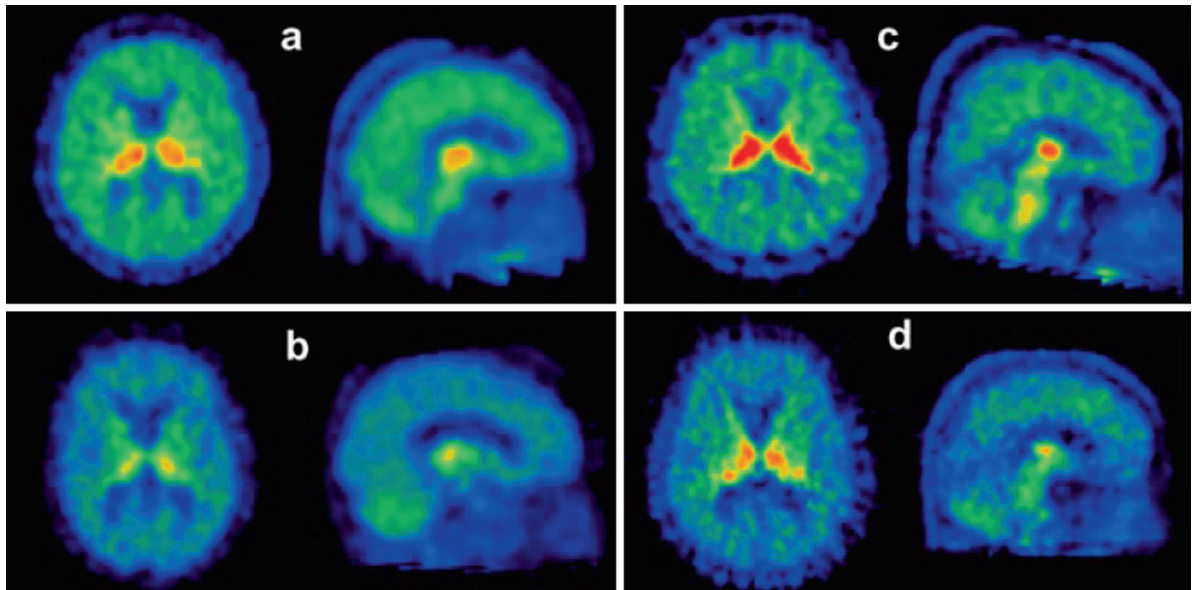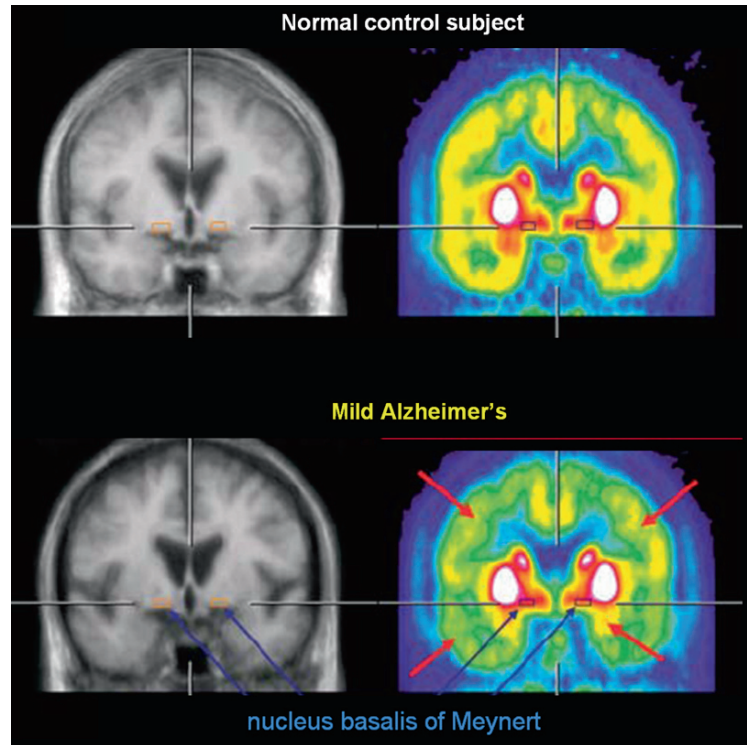
Fig. 16.29 Imaging nicotinic acetylcholine receptors (nAChR) using [^{18}F]fluoro-A-85380-PET in a normal aged healthy control (**a**), an AD patient (**b**), and two MCI patients (**c** and **d**). Patients **b** and **d** show significant reductions in binding potential compared to normal control (**a**), while MCI patient (**c**) is comparable to normal control (**a**) in all brain areas (Sabri et al. 2008)

A wide variety of other receptor binding radiotracers have also been used to study AD. An analog, [11C] R-PK11195 binds to the peripheral benzodiazepine receptors within the outer mitochondrial membrane of the activated microglia, which are mediators of CNS inflammation (90). One hypothesis for the pathophysiology of AD is that the activated microglia may produce cytokines that in turn produce neuronal damage, or, perhaps, mediates the neuronal damage caused by the β-amyloid protein. Consistent with this hypothesis are the salutary effects noted with anti-inflammatory drugs in patients with AD and the fact that [11C]R-PK11195 binding is significantly increased in the temporal cortex of patients with AD compared to that of age matched control subjects (Gilman et al. 1995).

16.3.2 Parkinson's Disease

PD is the prototypic movement disorder described almost 200 years ago by James Parkinson and is characterized by a constellation of motor (slowness of movement, muscular rigidity, tremor, and postural instability) and nonmotor symptoms (cognitive dysfunction and psychiatric features) that inexorably progress over time (Seibyl 2008). Idiopathic PD is the most common movement disorder among a spectrum of diseases with common features, but different causes, prognosis, and clinical course. Under normal circumstances, nerve cells in the substantia nigra communicate with other cells in the nearby striatum (the caudate nucleus and putamen) by releasing dopamine at nerve terminals in that region. Many neurons in the substantia nigra are destroyed in individuals with PD causing slowed movements, rigidity, and tremors. The discovery in the late 1950s that the level of dopamine was decreased in the brains of Parkinson's patients was followed in the 1960s by the successful treatment of this disorder by administration of the drug L-DOPA (levodopa), which is converted to dopamine in the brain. Levodopa is now combined with another drug, carbidopa that reduces the peripheral breakdown of levodopa, thus allowing greater levels to reach the brain and reducing side effects.

The discovery in the late 1970s that the neurotoxin, 1-methyl-4-phenyl-1,2,3,6-tetrahydropyridine (MPTP), can cause parkinsonism in drug addicts has stimulated intensive research on the causes of the disorder (Herholz et al. 2004). MPTP was found to be converted in the brain to a substance that destroys dopamine neurons, thus, the disturbance of dopamine synthesis is the hallmark of PD.

The diagnosis of PD is primarily made on the basis of clinical assessment and becomes difficult by the variability of the disease presentation, rate of progression, and response to medications. Morphological imaging techniques, such as CT and MRI, may help to exclude other diseases that may lead to Parkinsonism. The other important neurodegenerative diseases that present, clinically, as Parkinsonian syndromes, often in combination with dementia, include progressive supranuclear palsy (PSP), corticobasal degeneration (CBD), dementia with Lewy bodies (DLB), Alzheimer's and Huntington's dementia, and other hereditary neurodegenerative disorders. In most of the patients with PD, FDG-PET is generally normal and is, therefore, not necessarily useful clinically. However, in the last two decades, a number of PET and SPECT molecular imaging techniques to assess presynaptic dopaminergic function have demonstrated significant potential for providing a confirmative diagnosis of PD. These neuroimaging biomarkers in movement disorders may also serve as tools for the evaluation of novel therapeutics and as a powerful means for describing pathophysiology by revealing in vivo changes at different stages of disease and within the course of an individual patient's illness. A number of radiolabeled molecular imaging probes (Fig. 16.30) based on the dopaminergic system are available for imaging studies in PD and other movement disorders. The specific PET or SPECT radiotracer for use in movement disorders depends on the clinical or research question to be addressed by imaging. All presynaptic markers may have utility for the qualitative clinical evaluation of regional striatal signal loss to describe the presence or absence of a dopaminergic deficit in the context of making a diagnosis of PD or related disorder. If the goal is measurement of the progression of disease with serial imaging in a large clinical trial, then a tracer with a highly reproducible, semiquantitative, or quantitative imaging outcome is necessary (Seibyl 2008).

16.3.2.1 Dopamine Synthesis

In 1983, [18F]FDOPA-PET was introduced to image dopamine synthesis in vivo. In normal subjects, the images show higher tracer uptake in the striatum (caudate and putamen) and the midbrain, while uptake in the cerebral cortex and cerebellum is much lower

Fig. 16.30 PET and SPECT radiotracers for imaging dopaminergic system
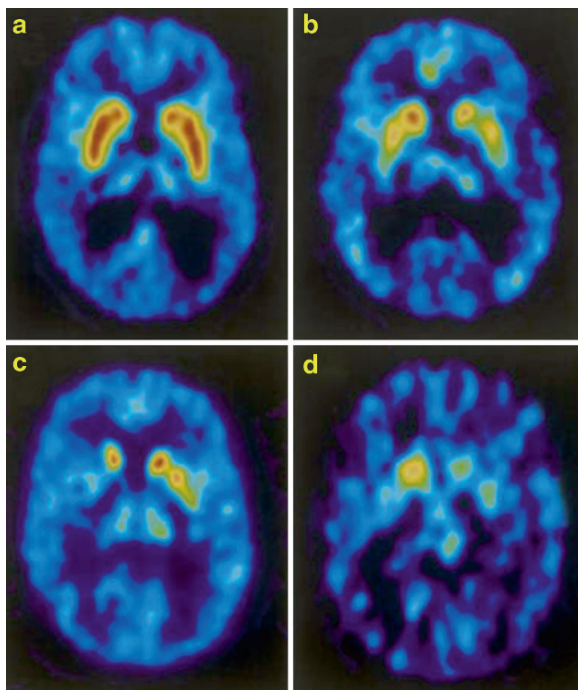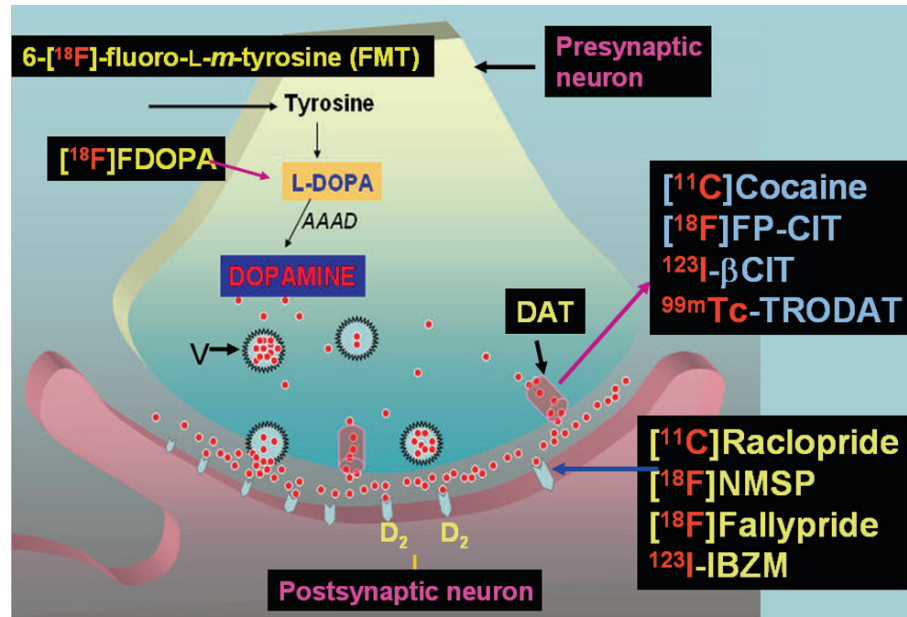
Fig. 16.31 [18F]FDOPA-PET to image presynaptic dopaminergic neurons in basal ganglia. Representative midstriatal transaxial images through the caudate and putamen of a healthy volunteer (**a**) and patients with unilateral PD (**b**), moderate severity PD (**c**), and severe PD (**d**) (Fischman 2005)

(Fig. 16.31). In patients with PD, the tracer uptake and retention in the striatum are reduced, most markedly on the opposite side of the major motor signs

(Garnett et al. 1984). The posterior parts of the putamen are most affected and the heads of caudate nuclei are the least affected, which is consistent with preferential degeneration of dopaminergic neurons in the caudal and mediolateral part of the substantia nigra pars compacta (Fischman 2005). This typical, differential intrastriatal distribution of reduced uptake is often referred to as the *rostrocaudal gradient*. While FDOPA images are useful to assess dopamine synthesis in presynaptic neurons of patients with PD, it is not possible to distinguish between PD and other disorders with Parkinsonian symptoms on the basis of FDOPA studies alone, because many of these disorders are associated with some degree of decreased striatal FDOPA uptake (Herholz et al. 2004). FDOPA is also not an ideal radiotracer to study dopamine synthesis, since the quantitative analysis with FDOPA-PET in humans is flawed by the presence of radioactive metabolites, which cross the BBB and contribute significantly to the radioactivity uptake in the brain (Firnau et al. 1988). 6-[18F]-fluoro-L-*m*-tyrosine (FMT) is regarded as an alternative tracer to FDOPA for the visualization of dopaminergic presynaptic integrity because of its lower in vivo metabolism. Following the synthesis of dopamine from L-DOPA, dopamine is transported and stored in the vesicles in the presynaptic neurons via specific $VMAT_2$ receptors. Because of degeneration of presynaptic neurons in PD, there is a significant reduction in these receptors. [11C]DTBZ has been shown to be useful to image the reduction of

$VMAT_2$ transporters in patients with PD and the reduction of these transporters is more severe than FDOPA striatal uptake (Frey et al. 2001; Kumar et al. 2003).

16.3.2.2 Dopamine Transporters

As discussed earlier, following release of dopamine into a synapse, dopamine is transported back into the presynaptic neuron via DATs. Therefore, DATs are important in the regulation of synaptic concentrations of dopamine. Several PET and SPECT radiopharmaceuticals based on tropane (cocaine) derivatives have been used to study and quantify brain DATs in patients with PD (Marshall and Grosse 2003; Ravina et al. 2005; Seibyl 2008). Among the ^{18}F labeled analogs, FP-CIT and FE-CNT have been evaluated in patients with PD (Ma et al. 2002). For example, FE-CNT-PET has shown to provide high striatum/cerebellum ratios and had the most favorable kinetics for quantitation of DATs (Davis et al. 2003). However, a recent preclinical investigation in a rat model suggests that a polar metabolite of FE-CNT may complicate quantitative assessment of DATs in human studies (Zoghbi et al. 2006). [18]F FP-CIT is a high affinity cocaine analog with fast kinetics and high signal-to-noise ratios and is suitable for PET neuroimaging (Ma et al. 2002; Robeson et al. 2003). The initial studies have indicated that DAT imaging might be more sensitive in detecting early stage of

PD than FDOPA imaging (Eshuis et al. 2006). A recent study in patients with PD at various clinical stages has indicated that FP-CIT-PET can serve as a suitable biomarker to represent the severity of PD in early and advanced stages (Fig. 16.32) (Wang et al. 2006).

A number of tropane analogs as radiotracers for SPECT, such as ^{123}I-βCIT, ^{123}I-FP-CIT, ^{123}I-Altropane, and ^{99m}Tc-TRODAT, have been investigated to assess the diagnostic potential for imaging the dopaminergic degeneration in patients with PD. ^{123}I-βCIT-SPECT images (Fig. 16.33) have been useful for the visual evaluation of the integrity of the dopaminergic projections to striatum in patient with PD (Jennigs et al. 2004). Similarly, ^{99m}Tc-TRODAT-1 also binds with high affinity to the DAT, allowing for SPECT imaging of the striatum in patients with PD (Kung et al. 2003a; Mozley et al. 2000; Chou et al. 2004).

In general the DAT ligands appear to provide a more sensitive indicator of dopaminergic degeneration than FDOPA. During the past decade, neuroimaging biomarkers have served in movement disorders as clinically available diagnostic agents (Europe), tools for evaluation of novel therapeutics, and powerful means for describing pathophysiology by revealing in vivo changes at different stages of disease and within the course of an individual patient's illness. However, challenges remain in the ideal application of neuroimaging in the clinical algorithms for patient assessment and management (Seibyl 2008).
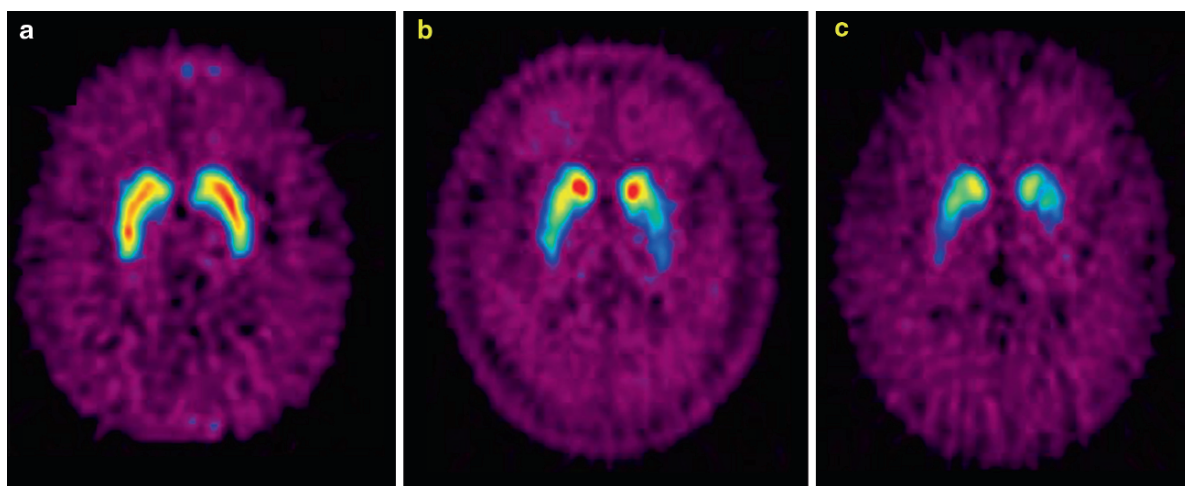
Fig. 16.32 [18F]FP-CIT-PET to image dopamine transporter (DAT) density in patients with PD. Compared to the healthy control (**a**), the two PD patients (patient (**b**) with early PD with HY stage I and patient (**c**) with advanced PD with HY stage IV) display progressive reduction in striatal DAT binding (Wang et al. 2006)
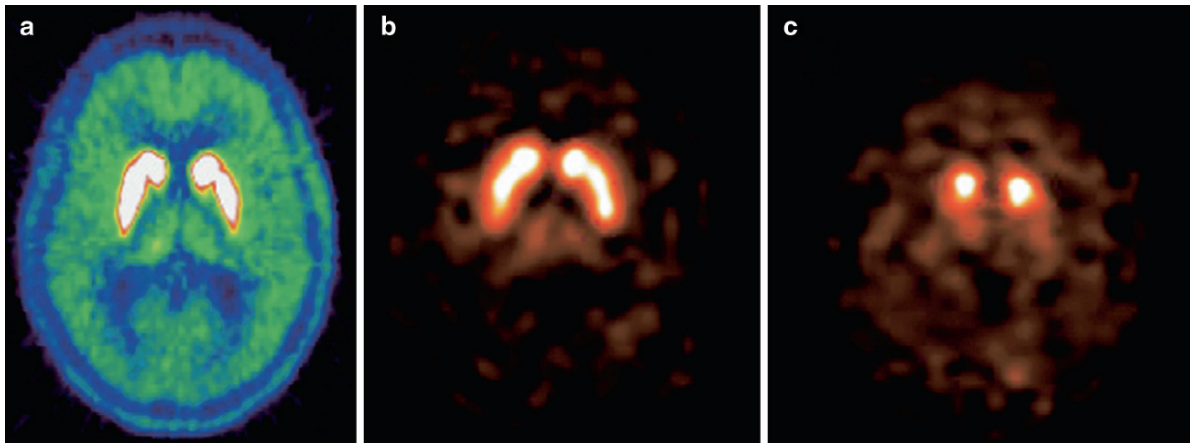
Fig. 16.33 ^{123}I-βCIT-SPECT for imaging dopamine transporters in patients with PD. ^{123}I-βCIT uptake in a patient with PD (**c**) shows significant reduction in striatal uptake compared to a healthy control (**b**). FDOPA-PET image of basal ganglia in a healthy control (**a**) is shown for comparison of SPECT image quality. (Seibyl 2008)

16.3.3 Epilepsy

Epilepsy is a common neurological disorder that is characterized by recurrent, unprovoked seizures. About 60–70% of patients experience focal or partial seizures and 30–40% generalized seizures (Newberg and Alavi 2005). Epilepsy is controlled with medication in approximately 70% of the cases. When seizures are medically intractable, resection of the epileptogenic cortex may be considered (Goffin et al. 2008). The seizure-onset zone is the region in which the seizures actually originate, while the epileptogenic zone is a theoretical construct, which is defined in terms of different cortical zones (Goffin et al. 2008).

16.3.3.1 Blood Flow and Metabolism

Patients with complex partial seizures (epilepsy that leads to temporary impairment, but not loss of consciousness) may be referred for functional brain imaging studies to assess the ictal perfusion or interictal glucose metabolism. During the epileptic activity, a hyperperfusion of the seizure onset zone occurs because of an autoregulatory response to the local neuronal hyperactivity. When a SPECT blood flow tracer ([99mTc]-HMPAO or [99mTc]-ECD) is injected intravenously immediately after the start of a seizure, the ictal SPECT images reflect the hyperperfusion changes in the early phase of the seizure. However, if
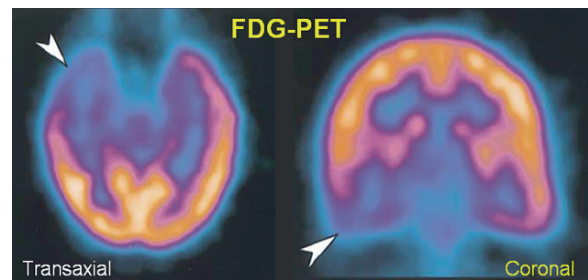
Fig. 16.34 FDG-PET in a patient with temporal lobe epilepsy. The images show markedly reduced glucose metabolism in the right temporal lobe (arrow) in transaxial and coronal views (Casse et al. 2002)

the tracer is injected after the seizure is terminated, hypoperfusion in the seizure onset zone can be observed. Ictal-SPECT is the only imaging modality that can define the ictal onset zone in a reliable and consistent manner. Brain glucose metabolism, as a measure of neural activity, can be studied with FDG-PET, which identifies cerebral hypometabolism characterizing epileptogenic sites (Fig. 16.34). FDG-PET is useful for presurgical planning in most temporal lobe epilepsy (TLE) patients. However, different antiepileptic drugs have shown to affect the cerebral glucose metabolism to varying degrees, with phenobarbital being a greater depressant (up to 37%) than valproate, carbamazepine, or phenytoin (Casse et al. 2002).

16.3.3.2 Neuroreceptors

Hyperexcitability, synapse reorganization, and imbalance between inhibitory and excitatory synapses are three dysfunctions characterizing the epileptogenic zone. GABA is the main inhibitory neurotransmitter in the brain and maintains the inhibitory tone that counterbalances neuronal excitation. Evidence from experimental and clinical studies indicates that GABA plays an important role in the mechanism and treatment of epilepsy (Treiman 2001). Several lines of evidence suggest that serotonin (5-HT) may also have an anticonvulsant effect through activation of the 5-HT$_{1A}$ receptor, because activation of this receptor affects the release and activity of other neurotransmitters such as glutamate, dopamine, and GABA (Theodore 2004; Goffin et al. 2008).

In the pathogenesis of epilepsy, the GABA$_A$ receptor, also known as the central benzodiazepine-receptor (BZR), is the most studied neuroreceptor with [11C] flumazenil (FMZ). In patients with TLE, arising from amygdala/hippocampal regions, a localized reduction of FMZ binding in the mesial temporal lobe is seen, in contrast to the more extensive hypometabolic changes seen with FDG-PET. The reduction in FMZ binding is proportional to the neuronal loss on histopathology and may be more sensitive than MRI in the detection of hippocampal sclerosis (Szelies et al. 2002). Also, in extratemporal epilepsies FMZ-PET shows a more localized reduction in receptor binding in the region of the cortical focus compared to the more extensive defects seen with FDG (Casse et al. 2002). Flumazenil is a biochemical marker of epileptogenicity and neuronal loss; BZR-density changes are more sensitive than FDG-PET in detecting hippocampal sclerosis or microdysgenesis. BZR studies have also been useful in the selection of patients for targeted surgery and for predicting outcome of these procedures (Heiss and Herholz 2006). The availability of [18F]flumagenil may provide greater opportunity to investigate the role of BZRs in epilepsy. [123I]iomazenil (IMZ) brain SPECT has also been used to detect epileptic foci, especially when surgical intervention is considered. In a recent study of patients with intractable epilepsy, IMZ-SPECT brain images, following MRI-based corrections for the partial volume effect (PVE), has shown improved sensitivity and specificity for the detection of cortical epileptogenic foci (Kato et al. 2008) (Fig. 16.35).

On the basis of 5-HT$_{1A}$ receptor antagonists, [18F] FCWAY and [11C]WAY-100635, several studies of patients with TLE have demonstrated a reduced serotonin receptor binding in the TLE foci (Toczec et al. 2003; Goffin et al. 2008). Compared to normal subjects, the epileptic patients have shown a decreased binding of another 5HT$_{1A}$ receptor antagonist, [18F] MPPF (Fig. 16.36), suggesting a decrease in the availability of 5-HT$_{1A}$ receptors (Merlet et al. 2004). This decrease is highly correlated to the degree of epileptogenicity of cortical areas explored by intracerebral recordings, and does not reflect only pathological changes or neuronal loss in the epileptic focus.

16.3.4 Cerebrovascular Disease

Acute cerebrovascular disease (CVD), the cause of clinical syndromes of stroke is the most common neurological
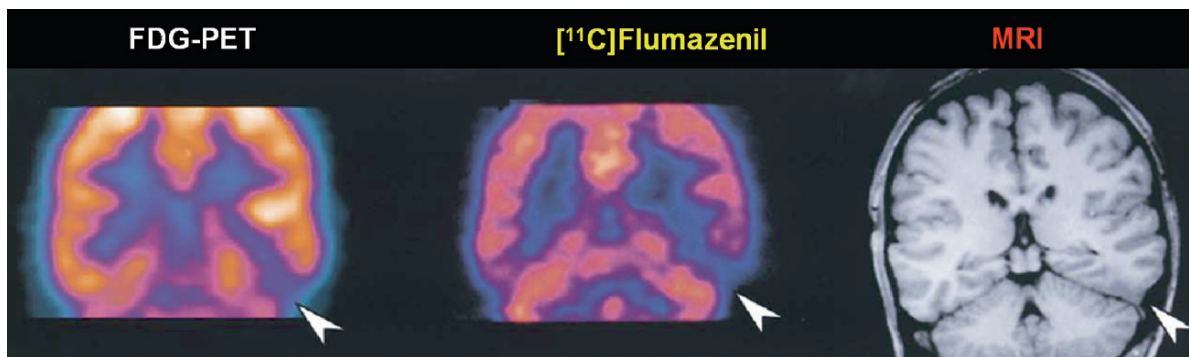
Fig. 16.35 [11C]Flumazenil-PET to image benzodiazepine-receptor (BZR) density in extratemporal epilepsy. Interictal FDG-PET shows reduced glucose metabolism in the left occipital lobe (*arrow*) and [11C]flumazenil PET also shows reduced BZD density in the same region, while MRI shows a poorly defined cortical margin consistent with dysplasia in this region (Casse et al. 2002)
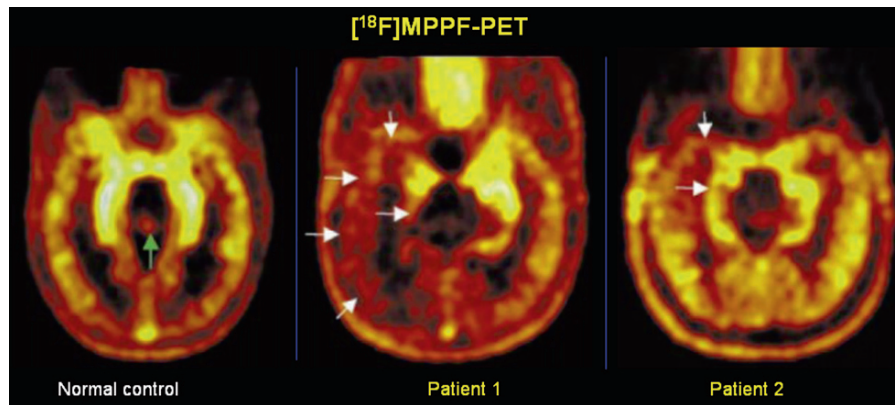
Fig. 16.36 [^{18}F]MPPF-PET to image 5-HT$_{1A}$ receptor binding and intracerebral activity in temporal lobe epilepsy. *White arrows* indicate asymmetries in FMPPF binding in patients 1 and 2. Patient 1 shows decreased binding in left mesiotemporal and lateral temporal structures, as well as in extratemporal regions (insula, operculum and frontal regions), while patient 2 shows a more focal asymmetry, with a binding decrease in the right hippocampus, part of the right inferior temporal gyrus, and in the right temporal pole (Merlet et al. 2004)

disorder. There are three main etiological categories: the ischemic stroke (70–80%), spontaneous intracerebral hematoma (10–20%), and subarachnoid hemorrhage (5–10%) (Herholz and Heiss 2004). The cause of ischemic stroke is a severe and usually sudden decrease of CBF (<15 mL 100 g^{-1} min^{-1}), mostly because of the atherothrombotic or embolic occlusion of a supplying artery. A central core of dense ischemia or necrosis (<12 mL 100 g^{-1} min^{-1}) surrounded by an area of reduced blood flow (12–22 mL 100 g^{-1} min^{-1}), where function is impaired but morphology is preserved, is known as *penumbra*. Metabolically an ischemic stroke is characterized by a condition known as *misery perfusion*, which is a mismatch of relatively well preserved oxygen metabolism due to increased oxygen extraction and severely reduced CBF. However, continued decline in CBF leads to a decline in oxygen delivery and metabolism (the onset of ischemia). Severe and prolonged compromise in blood flow results in infarction of brain tissue leading to a decline in oxygen extraction (onset of luxury perfusion). The role of imaging techniques is (a) to determine the regional CBF quantitatively and (b) to identify precisely the status and extent of penumbra.

16.3.4.1 Assessment of CBF

In 2007, the National Institute of Health, in conjunction with the American Society of Neuroradiology and the Neuroradiology Education and Research Foundation, sponsored a research symposium entitled *Advanced NeuroImaging for Acute Stroke Treatment* (Wintermark et al. 2008). The main goals of the meeting were to assess state-of-the-art practice in terms of acute stroke imaging research and to propose specific recommendations regarding (1) the standardization of perfusion and penumbral imaging techniques, (2) the validation of the accuracy and clinical utility of imaging markers of the ischemic penumbra, and (3) the validation of imaging biomarkers relevant to clinical outcomes.

A number of SPECT radiopharmaceuticals, such as ^{123}I-IMP, ^{99m}Tc-HMPAO, and ^{99m}Tc-ECD, have shown clinical utility for the qualitative assessment of rCBF. However, only PET based methods, using intravenous administration of [^{15}O]H$_2$O and inhalation of gases, such as [^{15}O]O$_2$ or [^{15}O]CO$_2$, can provide quantitative assessment of both rCBF and the extent of penumbra. Because of the potential for postischemic hyperperfusion (luxury perfusion), determination of the rCBF alone may not be sufficient to assess the area of penumbra, which is essential for optimal therapeutic management. However, PET images obtained with multiple radiotracers can demonstrate the value of PET in the assessment of rCBF, CMRO$_2$, and OEF in a patient with acute cerebral ischemia (Jacobs et al. 2005). The area with decreased rCBF, but increased OEF, represents the functionally viable tissue, the penumbra (Fig. 16.37).
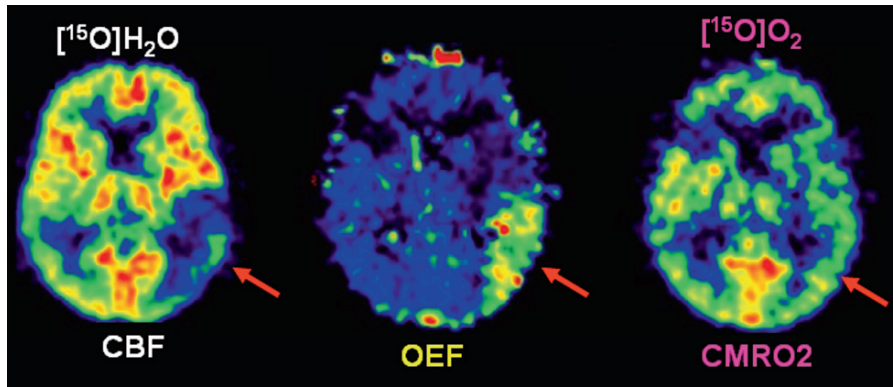
Fig. 16.37 Assessment of acute cerebral ischaemia. Cerebral blood flow (CBF) measured by [^{15}O]H$_2$O-PET demonstrates hypoperfusion in the posterior portion of the middle cerebral artery (MCA) territory. The cerebral metabolic rate of oxygen (CMRO2) as measured by [^{15}O]O$_2$-PET is still intact. On the basis of these two studies, the oxygen extraction fraction (OEF) shows relative increase indicating that the hypoperfused tissue is functionally disturbed but still viable, which is the classic definition of penumbra (Jacobs et al. 2005)
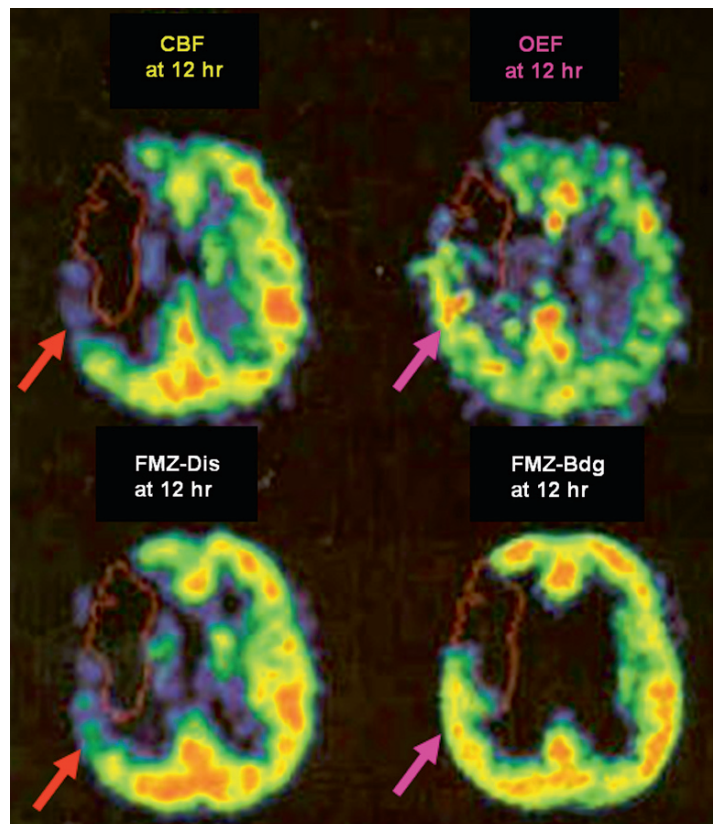
Fig. 16.38 [^{11}C]Flumazanil-PET for the precise identification of the status and extent of penumbra in patients with acute cerebral ischemia. FMZ-PET images showing early distribution (FMZ dis at 12 h) clearly identify the area of decreased cerebral perfusion. The delayed images (FMZ bdg at 13 h) reflect FMZ binding to the central benzodiazepine receptors and identify the area of penumbra as shown by OEF (Herholz et al 2004)

16.3.4.2 GABA Receptor Imaging

GABA receptors are very sensitive to ischemic damage because these receptors are expressed in high levels throughout the intact viable cortical neurons. Radiotracers, such as [^{11}C]Flumazenil, [^{18}F]Flumazenil, and [^{123}I]iomazenil, which bind to GABA receptors can be used as markers of neuronal integrity. The validity of this approach has been documented in patients with acute ischemic stroke (Herholz and Heiss 2004; Saur et al. 2006) by direct comparison with MRI or PET imaging studies of rCBF and OEF. The early images (10–20 min) reflect the distribution volume and provide a measure of rCBF, while the delayed images (at 1 h) represent the GABA receptor bound activity and provide a measure of the extent of the penumbra (Fig. 16.38).

16.3.4.3 Hypoxia Imaging

In ischemic stroke, the ischemic penumbra is likely to be hypoxic in nature. As a result, the hypoxic tissue can be identified using a nitroimidazole compound, such as [^{18}F]fluoromisonidazole (FMISO), which is trapped within the hypoxic cells after entering the cells by passive diffusion. Subsequently, FMISO is reduced by nitroreductase enzymes. Under normoxic conditions, the parent compound is regenerated by reoxidation. However, under hypoxic conditions reoxidation is prevented, additional reduction occurs, and the resulting metabolites are trapped by binding to intracellular molecules. Because trapping of the compound depends on active metabolism, no trapping occurs in the necrotic tissues (Read et al. 1998). FMISO-PET images performed within 4 h following acute ischemia clearly identify the hypoxic tissue as shown in Fig. 16.39 (Markus et al. 2002).

16.4 Psychiatric Disorders

The pathophysiological alterations in most of the neurological disorders have been well documented by morphological imaging studies (CT and MRI) and postmortem histopathological examination. In contrast, psychiatric diseases, such as depression, schizophrenia, anxiety, and addiction, can be due to functional abnormalities in the brain rather than significant structural abnormalities. In the last three decades, brain functional imaging studies of rCBF and rCMR$_{glu}$ based on PET have provided considerable insights into the understanding of psychiatric diseases. However, these functional imaging studies of blood flow and energy metabolism have not been useful for developing either well defined image based diagnostic criteria, or to assess therapeutic response of various psychopharmacological agents. Since neuronal firing and signal transmission are the basis for brain function, molecular imaging of neurotransmitter–neuroreceptor interaction based on PET and SPECT radiotracers may be the most appropriate noninvasive imaging modality to study psychiatric disorders. Neuroreceptor imaging can play an important role in quantifying the relationship between receptor occupancy, drug blood levels, and oral dose and may contribute to both therapeutics and drug development by rapid identification of the likely therapeutic dose range (compared with conventional parallel group dose comparisons or dose ranging studies) (Parsey and Mann 2003).

16.4.1 Schizophrenia

Schizophrenia is considered to reflect changes in the brain, possibly caused by disease or injury at the time of birth, and a genetic disposition that may be exacerbated by environmental stress. Marked by disturbances in thinking, emotional reactions, and social behavior, schizophrenia usually results in chronic illness and
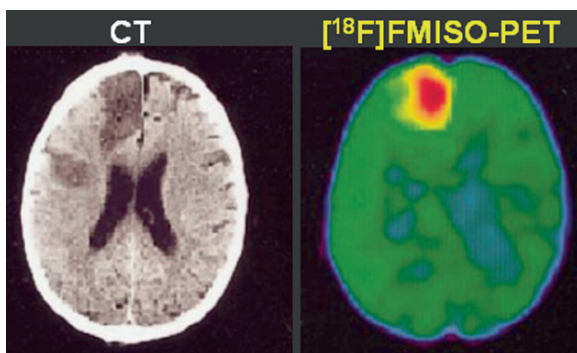
Fig. 16.39 [^{18}F]FMISO-PET to identify hypoxic tissue following acute cerebral ischemia. FMISO-PET performed 3.5 h after stroke onset, while the corresponding CT image performed on day 7 delineates the final infarct (Markus et al. 2002)

personality change. The positive symptoms include delusions and hallucinations, while the negative and cognitive deficits may involve attention and memory, and are associated with thought disorder.

16.4.1.1 Biology of Schizophrenia

The classical dopamine hypothesis formulated more than 35 years ago proposes that schizophrenia is associated with hyperactivity of dopaminergic neurotransmission. Until recently, the evidence supporting the dopamine hypothesis has been indirect: medications that share the ability to improve the psychotic symptoms of schizophrenia share the property of blocking dopamine D_2 receptors, and drugs that increase dopamine levels (such as amphetamine and cocaine) can both provoke psychotic symptoms in otherwise healthy individuals and worsen psychotic symptoms in patients with schizophrenia (Zipursky et al. 2007). The advent of neuroreceptor imaging with PET and SPECT has provided a new opportunity to systematically investigate the biology of schizophrenia.

Initial PET and SPECT ligand studies have focused on determining whether patients with schizophrenia have increased numbers of striatal dopamine (specifically D_2) receptors. Studies of never-medicated schizophrenia patients, using the PET D_2 ligands, [^{11}C]raclopride and N-[^{11}C]methylspiperone, and the SPECT ligand [^{123}I]IBZM, have not yielded consistent results (Frankle and Laruelle 2002). The discrepant results have been attributed to differences in the radiotracer binding to D_2 receptors (reversible vs irreversible or high vs. moderate affinity) or to the competition by the synaptic levels of endogenous dopamine.

Several drugs are known to alter the brain dopamine levels. For example, cocaine, cannabis, and stress can increase dopamine levels. Amphetamine causes the release of dopamine from the presynaptic terminals into the synapse. The tyrosine hydroxylase inhibitor AMPT depletes the dopamine levels in the synapse. Studies with ^{123}I-IBZM and [^{11}C]raclopride have made two important observations:

(a) Prior administration of amphetamine to unmedicated schizophrenic patients has shown a greater average decreases in D_2 receptor binding, compared control subjects (Laruelle et al. 1996; Breier et al. 1997).

(b) D_2 receptor availability increases after AMPT administration and is greater in patients, than in

control subjects, after dopamine is depleted, but not before (Abi-Dargham et al. 2000b). These findings suggest that the increased sensitivity of the dopamine system in schizophrenia patients is malleable and may reflect either the relapsed state or, perhaps, risk for relapse. The contemporary view of the role of dopamine is that subcortical mesolimbic DA projections may be hyperactive (resulting in positive symptoms) and the mesocortical DA projections to the PFC may be hypoactive (resulting in negative symptoms and cognitive impairement) (Laurelle et al. 2002)

16.4.1.2 Dopamine Receptor Occupancy and Antipsychotic drugs

PET and SPECT dopamine D_2 receptor imaging studies clearly demonstrated that clinical dosages of antipsychotic medications block striatal D_2 receptors (Fig. 16.40) (Farde et al. 1992; Kapur and Remington 2001). Treatment of schizophrenia patients with a range of antipsychotic medications resulted in the blockage of 65–90% of striatal D_2 receptors. Further, patients with acute extrapyramidal symptoms were shown to have higher levels of D_2 receptor occupancy. Although it is clear that clinical dosages of all first generation antipsychotics (FGAs), such as haloperidol, result in the blockage of a substantial percentage of D_2 receptors, it is not known whether a threshold level of blockage would be sufficient for antipsychotic action (Zipursky et al. 2007). These studies also clearly demonstrate that levels of D_2 receptor occupancy, associated with clinical response, can be achieved with dosages of FGAs that are, in some cases, only 5–10% of those used in common clinical practice. PET studies with the second generation of antipsychotics (SGAs), such as clozapine and risperidone have demonstrated that therapeutic dosages result in lower levels of D_2 occupancy, in the range of 38–63% (Farde et al. 1992), suggesting that continuous high levels of binding of the antipsychotic drug at the D_2 receptor are not required for ongoing antipsychotic efficacy.

Further, PET and SPECT radioligand research has provided evidence that patients with schizophrenia have a modest increase in D_2 receptor numbers, a substantial increase in endogenous dopamine, and that intermittent blockade of D_2 receptors is necessary to facilitate an antipsychotic response. Additional work is
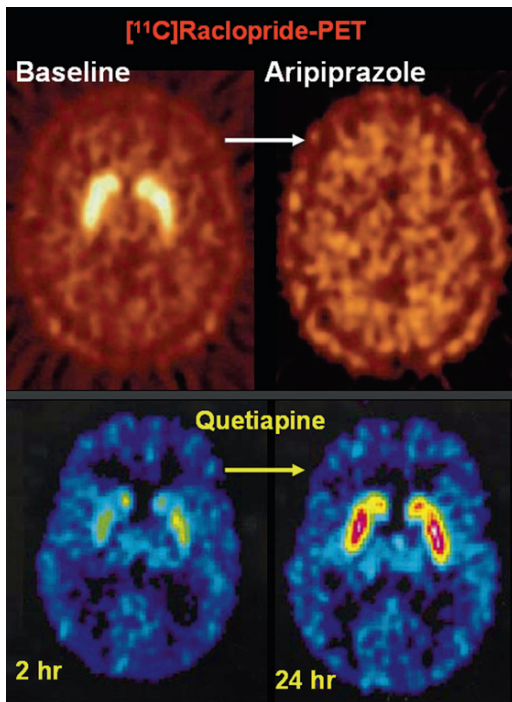
Fig. 16.40 Dopamine D_2 receptor imaging with [^{11}C] Raclopride-PET in patients with schizophrenia and the effect of antipsychotic drug treatment. The images (*top*) show 95% receptor occupancy (*compared to baseline*) after the administration of aripiprazole at a dose of 30 mg per day for 14 days (Hammoud et al. 2007). The images (*bottom*) show transient decrease in receptor occupancy (64%), only 2 h after a single dose of quetiapine (400 mg), but 24 h later, a repeat PET study shows 0% occupancy of dopamine D2 a receptors (Kapur et al. 2000)

required to determine what levels of occupancy are required and for what amount of time, why a minority of patients fail to respond well despite substantial D_2 occupancy, and how other domains of symptomatology may relate to medication binding at dopamine and nondopamine neuroreceptors (Zipursky et al. 2007).

16.4.2 Depression

The diagnosis of major depressive disorder (MDD) requires a distinct change of mood, characterized by sadness or irritability, accompanied by at least several psychophysiological changes, such as disturbances in sleep, appetite, or sexual desire, constipation, loss of the ability to experience pleasure in work or with friends, crying, suicidal thoughts, and slowing of speech and action.

These changes must last a minimum of two weeks and interfere considerably with work and family relations (Belmaker and Agam 2008; Meyer 2008).

Several SPECT and PET studies have documented significant regional differences in the CBF and glucose metabolism of patients with MDD. In acute major depression, imaging studies have primarily identified the prefrontal cortex, the temporal lobes, the cingulated cortex, and the related parts of the basal ganglia and thalamus, as an important neural correlate (Herholz et al. 2004). Also, both blood flow and glucose metabolic rate in the frontal cortex have been found to inversely correlate with disease severity. Patterns of [^{18}F]FDG and [^{15}O]H$_2$O uptake in MDD tend to demonstrate overactivity of regions that generate mood and underactivity of regions related to cognition (Meyer 2008).

The monoamine hypothesis of depression postulates a deficiency in serotonin or norepinephrine neurotransmission in both serotonergic and noradrenergic neurons in the brain. Cessation of the synaptic action of these neurotransmitters occurs by means of both reuptake through the specific serotonin and norepinephrine transporters and feedback control of release through the presynaptic regulatory autoreceptors for serotonin and norepinephrine. The hypothalamic–pituitary–cortisol hypothesis postulates that abnormalities in the cortisol response to stress may underlie depression. However, the clinical data do not support these hypotheses since monoamine-based antidepressants are most effective in patients with severe depression, when cortisol levels remain high after the administration of dexamethasone (Belmaker and Agam 2008).

16.4.2.1 Role of Serotonin Receptors and Transporters

If the original monoamine theory is true, one would expect increased 5-HT$_2$ receptor density in untreated subjects with depression, because extracellular-serotonin (5-HT) levels are low. PET studies of 5-HT$_{2A}$ receptors, using [^{18}F]setoperone in untreated subjects suffering from depression, have documented no difference in receptor status during the depressive episodes. However, higher 5-HT$_{2A}$ binding potential has been found in depressed patients with severe pessimism (Meyer et al. 2003). The regional 5-HT transporter binding potentials, based on [^{11}C]DASB-PET studies, are also higher during depressive episodes with more severe pessimism. These results may be interpreted to

mean that greater monoamine transporter density facilitates monoamine loss, which in turn contributes to greater severity of the depressive symptoms (Meyer et al. 2001a). Radioligand neuroimaging studies have also advanced the monoamine theory of MDD to explain the chronic loss of particular monoamines, such as serotonin, norepinephrine, and dopamine, which occurs to a greater extent when particular symptoms are more severe. In addition, neuroimaging has also identified mechanisms of monoamine loss, including greater monoamine metabolism, and excessive monoamine transporter density in the presence of monoamine depleting processes (Meyer 2008).

Antidepressants bind to the 5-HT transporter and raise extracellular serotonin levels of 5-HT.Serotonin transporter imaging with, [^{11}C](+)McN5652, [^{11}C]DASB, ^{123}I-β-CIT, and 123I-ADAM has made it possible to quantify more precisely the degree to which commonly prescribed antidepressant medications bind to the transporter at different dosages (Meyer et al. 2004). The first SSRI occupancy study with [^{11}C]DASB-PET reported an 80% occupancy in multiple regions after 4 weeks of paroxetine at 20 mg/day and citalopram at 20 mg/day (Meyer et al. 2001b). Similar occupancy levels have been reported with other antidepressants such as fluvoxamine, fluoxetine, sertraline, and venlafaxine (Suhara et al. 2003b; Meyer et al. 2004). These studies demonstrate that receptor ligand imaging can not only inform us about that mechanisms that may underlie major depression and its symptoms, but has also provides clinically relevant information about how antidepressants should be prescribed (Zipursky et al. 2007). Future ligand development will likely target other nonmonoaminergic pathophysiologies that are associated with MDD, such as excessive secretion of glucocorticoids, aberrant signal transduction, and markers of cell loss, to increase our understanding of how these pathologies may relate to clinical symptoms and course of illness, and the effects of novel treatments (Meyer 2008).

16.4.3 Drug Addiction

Drug addiction is a disease and is one of the medical consequences of drug abuse.

According to the Diagnostic and Statistical Manual of Mental Disorders (IV), addition is the condition that emerges from chronic drug use that leads to the compulsive administration of the drug despite the fact that the subject may no longer want to take it and even at the expense of seriously adverse consequences.

Abuse of drugs, such as cocaine, methamphetamine, MDMA, alcohol, opiates, tobacco, and marijuana affect genes, protein expression, and neuronal circuits, and engages the neurobiological mechanisms by which nature ensures that behaviors that are indispensable for survival motivate the procurement of more drugs, which can lead to repeated administration and addiction (Volkow 2004).

In the last two decades, PET and SPECT imaging technologies have provided the necessary tools to investigate how genes affect protein expression, how protein expression affects neurobiology, how neurobiology affects behavior, and how that, in turn, affects social interactions.

16.4.3.1 The Brain's Reward System

The brain dopamine system is central to the brain's reward system (BRS) (Fig. 16.41) and a major molecular target in the investigation of drug abuse (Koob and Bloom 1988). The cell bodies of neurons which produce dopamine are located in the substantia nigra and the ventral tegmental area in the midbrain and project to the striatal area that includes, what has come to be known as, the reward center (the nucleus accumbens). Dopamine cells from the midbrain also project to various cortical and limbic brain regions. Typically, drug induced elevations in dopamine occur rapidly after the administration of the drug and are associated with an intense euphoria or "*high.*" Although different drugs act by different
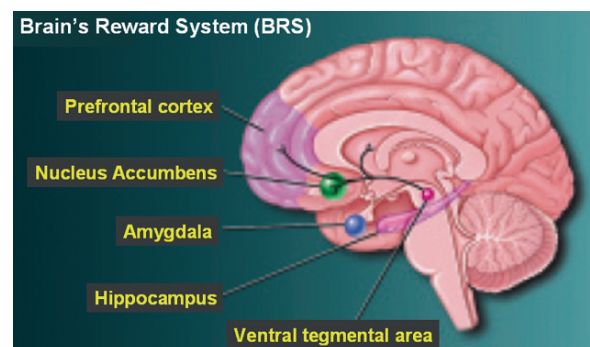
Fig. 16.41   The brain dopamine system is central to the brain's reward system (BRS) and a major molecular target in the investigation of drug abuse

mechanisms, increased levels of synaptic dopamine is common to all of them (Volkow et al. 2003).

Cocaine, a powerful addictive psychostimulant, binds to monoamine (dopamine, norepinephrine, and serotonin) transporters with micromolar to submicromolar affinity. Specifically, dopamine transporter (DAT) blockage results in the elevation of synaptic dopamine (DA) in the nucleus accumbens and the ensuing stimulation of dopamine receptors. However, on the basis of studies with [^{11}C]cocaine, it was observed that the highest density of DAT binding sites for cocaine is in the basal ganglia. Also, on the basis of imaging studies using [^{11}C]cocaine, it was determined that a DAT occupancy in excess of 60% is required to become high (Volkow et al. 2003).

[^{18}F]NMSP, as well as [^{11}C]raclopride (the dopamine D_2 receptor ligands), have been used to measure dopamine D_2 receptors (on the postsynaptic neurons in basal ganglia) in addicted individuals. Prior administration of cocaine (or methylphenidate) blocks DATs and increases the synaptic dopamine levels. The subsequent D_2 receptor imaging studies have clearly demonstrated that the binding of the radiotracer decreases, while the availability of D_2 receptors significantly decreases (Fig. 16.42). Also, PET studies have consistently shown long lasting decreases in dopamine D_2 receptors in cocaine abusers, compared to control subjects (Volkow et al. 2003). Several investigators have also documented dopamine D_2 reductions with alcohol and methamphitamine addictions.

Studies of brain glucose metabolism with FDG-PET in cocaine abusers, during short and long term withdrawal, have demonstrated decreased activity in the anterior cingulate gyrus (CG) and orbitofrontal cortex (OFC), which are both projection areas of the mesolimbic dopamine known to be involved in compulsive behavior (Volkow et al. 1992). The decrease in metabolic activity (CMRglc) in these areas could result in an inability to control the intake of the drug under emotionally stressful situations. During craving, one week after cocaine withdrawl, CMRglc is generally increased, and the intensity of cocaine craving is correlated with increased CMRglc in the prefrontal cortex (PFC) and OFC. Craving may also be associated with increased μ-opioid binding, as demonstrated with [^{11}C] carfenta-nil, in several brain regions of cocaine addicts for several weeks after their last use of cocaine (Zubieta et al. 1996).

Functional neuromaging can be expected to provide the means by which to objectively link behavioral and neurochemical changes and to objectively evaluate drug abuse and treatment. In addition, with the identification of new genes related to addictive behavior, neuro imaging promises to provide a tool for directly translating this knowledge to an evaluation in human subjects.

Fig. 16.42 Effect of cocaine abuse on dopamine D_2 receptors. Compared to normal control (NC) subject, [^{11}C] raclopride binding to dopamine receptors in the basal ganglia was significantly decreased in two cocaine abusers; 1 month after cessation of use (C1) and 4 months after cessation of use (C2) (Volkow 2004)
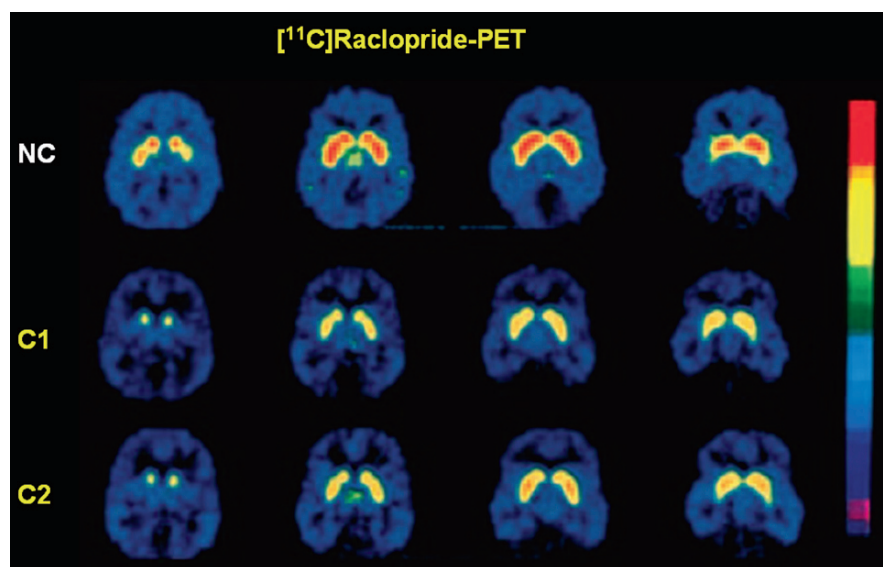
References

Abi-Dargham A, Martinez D, Mawlavi O, et al (2000a) Measurement of striatal and extrastriatal dopamine D1 receptor binding potential with [^{11}C]NNC-112 in humans: validation and reproducibility. J Cereb Blood Flow Metab 20:225–243

Abi-Dargham A, Rodenhiser J, Printz D, et al (2000b) Increased baseline occupancy of D2 receptors by dopamine in schizophrenia. Proc Natl Acad Sci U S A 97(14):8104–8109

Agdeppa ED, Kepe V, Liu J, et al (2001) Binding characteristics of radiofluorinated 6-dialkyl-amino-2-naphtylethylidene derivatives as positron emission tomography imaging probes for β-amyloid plaques in Alzheimer's disease. J Neurosci 21:1–5

Archer HA, Edison P, Brooks DJ, et al (2006) Amyloid load and cerebral atrophy in Alzheimer's disease: an ^{11}C-PIB positron emission tomography study. Ann Neurol 60:145–147

Banati RB, Newcombe J, Gunn RN, et al (2000) The peripheral benzodiazepine binding site in the brain in multiple sclerosis: quantitative in vivo imaging of microglia as a measure of disease activity. Brain 123:2321–2337

Barnes NM, Sharp T (1999) A review of central 5-HT receptors and their function. Neuropharmacology 38:1083–1152

Barrio JR, Huang S-C, Cole G, et al (1999) PET imaging of tangles and plaques in Alzheimer's disease with a highly hydrophobic probe. J Label Compd Radiopharm 42:S194

Bartus RT, Dean RL, Beer B, et al (1982) The cholinergic hypothesis of geriatric memory dysfunction. Science 217:408–17

Belmaker RH, Agam G (2008) Major depressive disorder. N Engl J Med 358:55–68

Bremmer JD, Horti A, Staib LH, et al (2000) Kinetic modeling of benzodiazepine receptor binding with PET and high specific activity [^{11}C]iomazenil in healthy human subjects. Synapse 35:68–77

Blasberg RG, Tjuvajev JG (2003) Molecular-genetic imaging: current and future perspectives. J Clin Invest 111:1620–1629

Bohnen NI, Frey KA (2003) The role of positron emission tomography imaging in movement disorders. Neuroimaging Clin N Am 13:791–803

Boutin H, Chauveau F, Thominiaux C (2007) ^{11}C-DPA-713: a novel peripheral benzodiazepine receptor PET ligand for in vivo imaging of neuroinflammation J Nucl Med 48:573–581

Breier A, Su TP, Saunders R, et al (1997) Schizophrenia is associated with elevated amphetamine-induced synaptic dopamine concentrations: evidence from a novel positron emission tomography method. Proc Natl Acad Sci U S A 94(6):2569–2574

Brooks DJ (2003) PET studies on the function of dopamine in health and Parkinson's disease. Ann N Y Acad Sci 991: 22–35

Brooks DJ (2005) Positron emission tomography and single-photon emission computed tomography in central nervous system drug development. NeuroRx 2:226–236

Buckner RL (2004) Memory and executive function in aging and AD: multiple factors that cause decline and reserve factors that compensate. Neuron 44: 195–208

Casse R, Rowe CC, Newton M, et al (2002) Positron Emission Tomography and Epilepsy Mol Imaging Biol 4:338–351

Chaly T, Dhawan V, Kazumata K, et al (1996) Radiosynthesis of [^{18}F]N-3-fluoropropyl-2-β-carbomethoxy-3-β-(4-iodophenyl)

nortropane and the first human study with positron emission tomography. Nucl Med Biol 23:999–1004

Chou KL, Hurtig HI, Stern MB, et al (2004) Diagnostic accuracy of [^{99m}Tc]TRODAT-1 SPECT imaging in early Parkinson's disease. Parkinsonism Relat Disord 10:375–379

Crone C (1964) Permeability of capillaries in various organs as determined by the use of indicator diffusion method. Acta Physiol Scand 58:292–305

Cunningham VJ, Gunn RN, Matthews JC (2004) Quantification in positron emission tomography for research in pharmacology and drug development. Nucl Med Commun 25: 643–646

Davis MR, Votaw JR, Bremner JD, et al (2003) Initial human PET imaging studies with the dopamine transporter ligand ^{18}F-FECNT. J Nucl Med 44:855– 861

Dickson DW (1997) The pathogenesis of senile plaques. J Neuropathol Exp Neurol 56:321–339

Diksic M, Tohyama Y, Takada A (2000) Brain net unidirectional uptake of α-methyltryptophan. Neurochem Res 25: 1537–1546

Ding YS, Fowler J (2005) New-generation radiotracers for nAChR and NET. Nucl Med Biol 32:707–718

Ding Y-S, Fowler JS, Volkow ND, et al (1994) Pharmacokinetics and in vivo specificity of [^{11}C]DL-threo-methylphenydate for the presynaptic dopaminergic neuron. Synapse 18: 152–160

Ding Y-S, Volkow ND, Logan J, et al (2000) Occupancy of brain nicotinic acetylcholine receptors by nicotine doses equivalent to those obtained when smoking a cigarette. Synapse 35:234–237

Drzezga A (2008) Basic pathologies of neurodegenerative dementias and their relevance for state-of-the-art molecular imaging studies. Eur J Nucl Med Mol Imaging 35:S4–S11

Eckelman WC (2001) Radiolabeled muscarinic radioligands for in vivo studies. Nucl Med Biol 28:485–491

Eckelman WC, Grissom M, Conklin J, et al (1984) In vivo competition studies with analogues of quinucidinylbenzilate. J Pharm Sci 73:529–533

Eckert T, Eidelberg D (2005) Neuroimaging and therapeutics in movement disorders. NeuroRx 2:361–371

Eshuis SA, Maguire RP, Leenders KL, et al (2006) Comparison of FP-CIT SPECT with FDOPA- PET in patients with de novo and advanced Parkinson's disease. Eur J Nucl Med Mol Imaging 33:200–209

Farde L, Ehrin E, Eriksson L, et al (1985) Substituted benzamides as ligands for visualization of dopamine receptor binding in the human brain by positron emission tomography. Proc Natl Acad Sci U S A 82:3863–3867

Farde L, Wiesel FA, Halldin C, et al (1988) Central D2-dopamine receptor occupancy in schizophrenic patients treated with antipsychotic drugs. Arch Gen Psychiatry 45(1):71–76

Farde L, Nordstrom AL, Wiesel FA, et al (1992) Positron emission tomographic analysis of central D1 and D2 dopamine receptor occupancy in patients treated with classical neuroleptics and clozapine: relation to extrapyramidal side effects. Arch Gen Psychiatry 49:538–544

Firnau G, Sood S, Chirakal R, et al (1988) Metabolites of 6-[^{18}F] fluoro-L-dopa in human blood. J Nucl Med 29:363–369

Fischman AJ, Bonab AA, Babich JW, et al (2001) [^{11}C, ^{127}I] Altropane: a highly selective ligand for PET imaging of dopamine transporter sites. Synapse 39:332–342

Fischman AJ (2005) Role of [^{18}F]-dopa–PET imaging in assessing movement disorders. Radiol Clin N Am 43:93–106

Fowler JS, MacGregor RR, Wolf AP, et al (1987a) Mapping human brain monoamine oxidase A and B with ^{11}C-suicide inactivators and positron emission tomography. Science 235:481–485

Fowler JS, Volkow ND, Wolf AP, et al (1987b) Mapping cocaine binding in human and baboon brain in vivo. Synapse 4:371–377

Fowler JS, Volkow ND, Wang G-J, et al (1996) Inhibition of monoamine oxidase B in the brains of smokers. Nature 379:733–736

Fowler JS, Ding Y-S, Volkow ND (2003) Radiotracers for Positron Emission Tomography Imaging. Semi Nucl Med 33:14–27

Frackowiak RS, Lenzi GL, Jones T, et al (1980) Quantitative measurement of regional cerebral blood flow and oxygen metabolism in man ^{15}O and positron emission tomography: theory, procedure and normal values. J Comput Assisted Tomogr 4:727–736

Frankle WG, Laruelle M (2002) Neuroreceptor imaging in psychiatric disorders. Ann Nucl Med 16(7):437–446

Frey KA, Koeppe RA, Kilbourn MR, et al (1996) Presynaptic monoaminergic vesicles in Parkinson's disease and normal aging. Ann Neurol 40:873–884

Frey KA, Koeppe RA, Kilbourn MR (2001) Imaging the vesicular monoamine transporter. Adv Neurol 86:237–247

Frost JJ (2001) PET imaging of the opioid receptor. The early years. Nucl Med Biol 28:509–513

Frost JJ, Wagner Henry JJ, Danals RF, et al (1985) Imaging opiate receptors in the human brain by positron emission tomography. J Comput Asstisted Tomogr 9:231–236

Garnett ES, Firnau G, Nahmias C (1983) Dopamine visualized in the basal ganglia in living human brain. Nature 305–137–138

Garnett ES, Nahmias C, Firnau G (1984) Central dopaminergic pathways in hemiparkinsonism examined by positron emission tomography. Can J Neurol Sci 11:174–179

Gibb AJ. Neurotransmitter receptors. In: Webster RA, ed. Neurotransmitters, drugs and brain function. Wiley, New York, NY, pp 57–79

Gilman S, Koeppe RA, Junck L, et al (1995) Benzodiazepine receptor binding in cerebellar degenerations studied with positron emission tomography. Ann Neurol 38:176–185

Ginovart N, Wilson AA, Meyer JH, et al (2003) [^{11}C]-DASB, a tool for in vivo measurement of SSRI-induced occupancy of the serotonin transporter: PET characterization and evaluation in cats. Synapse 47:123–133

Goffin K, Dedeurwaerdere S, Van Laere K, et al (2008) Neuronuclear assessment of patients with epilepsy. Semin Nucl Med 38:227–239

Gulyas B, Halldin C, Sandell J, et al (2002) PET studies on the brain uptake and regional distribution of [^{11}C]vinpocetine in human subjects. Acta Neurol Scand 106:325–332

Halldin C, Farde L, Hogberg T, et al (1995) Carbon-11-FLB 457: a radioligand for extra-striatal D$_2$ dopamine receptors. J Nucl Med 36:1275–1281

Hammoud DA, Endres CJ, Chander AR, et al (2005) Imaging glial cell activation with [^{11}C]-R-PK11195 in patients with AIDS. J Neurovirol 11:346–355

Hammoud DA, Hoffman JM, Pomper MG (2007) Molecular neuroimaging: from conventional to emerging techniques. Radiology 245:21–42

Harpstrite SE, Prior J, Piwnica-Worms D, et al (2005) Peptide conjugates for imaging-amyloid in the brain. J Label Compd Radiopharm 48(s1):S228

Henriksen G, Yousefi BH, Drzezga A, et al (2008) Development and evaluation of compounds for imaging of β-amyloid plaque by means of positron emission tomography. Eur J Nucl Med Mol Imaging 35(Suppl 1):S75–S81

Herscovitch P, Markham J, Raichle ME (1983) Brain blood flow measured with intravenous [^{15}O] water, I: theory and error analysis. J Nucl Med 24:782–789

Heiss WD, Herholz K (2006) Brain receptor imaging. J Nucl Med 47:302–312

Herholz K (2008) Acetylcholine esterase activity in mild cognitive impairment and Alzheimer's disease. Eur J Nucl Med Mol Imaging 35(Suppl 1):S25–S29

Herholz K, Heiss WD (2004) Positron emission tomography in clinical neurology. Mol Imaging Biol 6:239–269

Herholz K, Herscovitch P, Heiss W-D (2004). NeuroPET. Springer, Berlin

Holman BL, Gibson RE, Hill TC, et al (1985) Muscarinic acetylcholine receptors in Alzheimer's disease: in vivo imaging with iodine 123-labeled 3-quinuclidinyl-4-iodobenzilate and emission tomography. JAMA 254:3063–3066

Hume SP, Gunn RN, Jones T (1998) Pharmacological constraints associated with positron emission tomographic scanning of small laboratory animals. Eur J Nucl Med 25:173–176

Hustinx R, Pourdehnad M, Kaschten B, Alavi A (2005) PET imaging for differentiating recurrent brain tumor from radiation necrosis Radiol Clin North Am 43:35–47

Jack CR Jr, Lowe VJ, Senjem ML, et al (2008) ^{11}C PIB and structural MRI provide complementary information in imaging of Alzheimer's disease and amnestic mild cognitive impairment. Brain 131:665–680

Jacobs A, Voges J, Reszka R, et al (2001) Positron-emission tomography of vector mediated gene expression in gene therapy for gliomas. Lancet 358:727–729

Jacobs AH, Li H, Winkeler A, et al (2003) PET-based molecular imaging in neuroscience Eur J Nucl Med Mol Imaging 30:1051–1065

Jacobs AH, Winkler A, Castro MG, et al (2005) Human gene therapy and imaging in neurological diseases. Eur J Nucl Med Mol Imag 32:S358–S383

Jagust W (2004) Molecular neuroimaging in Alzheimer's disease. Neuro Rx 1:206–212

Jennings DL, Seibyl JP, Oakes D, et al (2004) (^{123}I) beta-CIT and single photon emission computed tomographic imaging vs clinical evaluation in Parkinsonian syndrome: unmasking an early diagnosis. Arch Neurol 61:1224–1229

Jones T, Chesler DA, Ter-Pogossian MM, et al (1976) The continuous inhalation of oxygen-15 for assessing regional oxygen extraction in the brain of man. Br J Radiol 49:339–343

Juhasz C, Chugani HT (2003) Imaging the epileptic brain with positron emission tomography. Neuroimaging Clin N Am 13:705–716

Kapur S, Remington G (2001) Dopamine D$_2$ receptors and their role in atypical antipsychotic action: still necessary and may even be sufficient. Biol Psychiatry 50(11):873–883

Kapur S, Zipursky R, Jones C, et al (2000) A positron emission tomography study of quetiapine in schizophrenia: a preliminary finding of an antipsychotic effect with only transiently

high dopamine D2 receptor occupancy. Arch Gen Psychiatry 57:553–559

Kato H, Shimosegawar E, Oku N, et al (2008) MRI-based correction for partial-volume effect improves detectability of intractable epileptogenic foci on 123I-Iomazenil brain SPECT images. J Nucl Med 49:383–389

Kauppinen T, Bergstrom K, Heikman P, et al (2003) Biodistribution and radiation dosimetry of [^{123}1]ADAM in healthy human subjects: preliminary results. Eur J Nucl Med 30:132–136

Kemppainen NM, Aalto S, Wilson IA, et al (2007) PET amyloid ligand [^{11}C]PIB uptake is increased in mild cognitive impairment. Neurology 68:1603–1606

Kirik D, Breysse N, Björklund T (2005) Imaging in cell-based therapy for neurodegenerative diseases. Eur J Nucl Med Mol Imaging 32:S417–S434

Kling MA, Carson RE, Borg L, et al (2000) Opioid receptor imaging with positron emission tomography and [^{18}F]cyclofoxy in long-term, methadone-treated former heroin addicts. J Pharm Exp Ther 295:1070–1076

Klunk WE, Wang Y, Huang G-F (2003) The binding of 2-(4′-ethylaminophenyl)benzothiazole to postmortem brain homogenates is dominated by the amyloid component. J Neurosci 23(6):2086–2092

Klunk WE, Engler H, Nordberg A, et al (2004) Imaging brain amyloid in Alzheimer's disease with Pittsburgh compound-B. Ann Neurol 55:306–319

Koeppe RA, Frey KA, Snyder SE, et al (1999) Kinetic modeling of N-[^{11}C]methylpiperidin-4-yl propionate: alternatives for analysis of an irreversible positron emission tomography tracer for measurement of acetylcholinesterase activity in human brain. J Cereb Blood Flow Metab19:1150–1163

Koob GF, Bloom FE (1988) Cellular and molecular mechanisms of drug dependence. Science 242:715–723

Kudo Y, Okamura N, Furumoto S, et al (2007) 2-(2-[2-Dimethylaminothiazol-5-yl]Ethenyl)-6-(2-[Fluoro]Ethoxy) Benzoxazole: a novel PET agent for in vivo detection of dense amyloid plaques in Alzheimer's disease patients. J Nucl Med 48:553–561

Kuhl DE, Koeppe RA, Minoshima S, et al (1999) In vivo mapping of cerebral acetylcholinesterase activity in aging and Alzheimer's disease. Neurology 52:691–699

Kuhl DE, Minoshima S, Frey KA, et al. (2000) Limited donepezil inhibition of acetylcholinesterase measured with positron emission tomography in living Alzheimer cerebral cortex. Ann Neurol. 48:391–395

Kulak JM, Sum J, Musachio JL, et al (2002): 5-Iodo-A-85380 binds to alpha-conotoxin MII-sensitive nicotinic acetylcholine receptors (nAChRs) as well as alpha4beta2* subtypes. J Neurochem 81:403–406

Kung HF, Kung M-P, Choi SR (2003a) Radiopharmaceuticals for single-photon emission computed tomography brain imaging. Semin Nucl Med 33:2–13

Kung HF, Kung M-P, Zhuang ZP, (2003b) Iodinated tracers for imaging amyloid plaques in the brain. Mol Imaging Biol 5:418–426

Kumar A, et al (2003) Brain 126:2648–2655

Laruelle M, Abi-Dargham A, van Dyck CH, et al (1996) Single photon emission computerized tomography imaging of amphetamine-induced dopamine release in drug-free schizophrenic subjects. Proc Natl Acad Sci U S A 93(17):9235–9240

Laruelle M, Talbot P, Martinez D, et al (2002) Psychiatric disorders. In: Wahl RL (ed) Principles and Practice of positron

emission tomography, Lippincott Williams & Wilkins, Philadelphia

Ma Y, Dhawan V, Mentis M, Chaly T, et al (2002) Parametric mapping of [18F]FPCIT binding in early stage Parkinson's disease: a PET study. Synapse 45:125–133

Ma B, Sherman PS, Moskwa JE, et al (2004) Sensitivity of [^{11}C] N-methylpyrroli-dinyl benzilate ([^{11}C]NMPYB) to endogenous acetylcholine: PET imaging vs tissue sampling methods. Nucl Med Biol 31:393–397

Machulla H-J, Heinz A (2005) Radioligands for brain imaging of the κ-opioid system. J Nucl Med 46:386–387

Maeda J, Suhara T, Zhang MR, et al (2004) Novel peripheral benzodiazepine receptor ligand [^{11}C]DAA1106 for PET: an imaging tool for glial cells in the brain. Synapse 52:283–291

Mahley RW, Weisgraber KH, Huang Y (2006) Apolipoprotein E4: a causative factor and therapeutic target in neuropathology, including Alzheimer's disease. Proc Natl Acad Sci U S A 103:5644–5651

Markus R, Donnan GA, Kazui S, et al (2002) Statistical parametric mapping of hypoxic tissue identified by [^{18}F] fluoromisonidazole and positron emission tomography following acute ischemic stroke. Neuroimage 16:425–433

Marshall V, Grosse D (2003) Role of dopamine transporter imaging in routine clinical practice. Mov Disord 18:1415–1423

Massoud TF, Gambhir SS (2003) Molecular imaging in living subjects: seeing fundamental biological processes in a new light. Genes Dev 17:545–580

Mathis CA, Bacskai BJ, Kajdasz ST, et al (2002) A lipophilic thioflavin-T derivative for positron emission tomography (PET) imaging of amyloid in brain. Bioorg Med Chem Lett 12:295–298

Mathis CA, Wang Y, Klunk WE (2004) Imaging beta-amyloid plaques and neurofibrillary tangles in the aging human brain. Curr Pharm Des 10:1469–1492

Mathis CA, Lopresti BJ, Klunk WE (2007) Impact of amyloid imaging on drug development in Alzheimer's disease. Nucl Med Biol 34:809–822

Mazziotta JC, Phelps ME, Miller J (1981) Tomographic mapping of human cerebral metabolism. Neurology 31:503–516

Meltzer CC, Cantwell MN, Greer PJ, et al (2000) Does cerebral blood flow decline in healthy aging? A PET study with partial volume correction. J Nucl Med 41:1842–1848

Merlet I, Ostrowsky K, Costes N, et al (2004) 5-HT$_{1A}$ receptor binding and intracerebral activity in temporal lobe epilepsy: an [^{18}F]MPPF-PET study. Brain 127:900–913

Meyer JH (2008) Applying neuroimaging ligands to study major depressive disorder. Semin Nucl Med 38:287–304

Meyer J, Kapur S, Houle S, et al (1999) Prefrontal cortex 5-HT2 receptors in depression: a [18F]setoperone PET imaging study. Am J Psychiatry 156(7):1029–1034

Meyer JH, Kruger S, Wilson AA, et al (2001a) Lower dopamine transporter binding potential in striatum during depression. Neuroreport 12(18):4121–4125

Meyer JH, Wilson AA, Ginovart N, et al (2001b) Occupancy of serotonin transporters by paroxetine and citalopram during treatment of depression: a [(11)C]DASB PET imaging study. Am J Psychiatry 158(11):1843–1849

Meyer JH, McMain S, Kennedy SH, et al (2003) Dysfunctional attitudes and 5-HT(2) receptors during depression and self-harm. Am J Psychiatry 160(1):90–99

Meyer JH, Wilson AA, Sagrati S, et al (2004) Serotonin transporter occupancy of five selective serotonin reuptake inhibitors at

different doses: an [¹¹C]DASB positron emission tomography study. Am J Psychiatry 161(5):826–835

Mintun MA, Larossa GN, Sheline YI, et al (2006) [¹¹C]PIB in a nondemented population: potential antecedent marker of Alzheimer disease. Neurology 67:446–452

Morris JH, Nagy Z (2004) Alzheimer's disease. In: Esiri MM, Lee VM, Trojanowski JQ (eds) The neuropathology of dementia, 2nd edn. Cambridge University Press, Cambridge, UK

Mozley PD, Schneider JS, Acton PD, et al (2000) Binding of ⁹⁹ᵐTc-TRODAT-1 to dopamine transporters in patients with Parkinson's disease and in healthy volunteers. J Nucl Med 41:584–589

Mukherjee J, Kang ZY, Brown T, et al (1999) Preliminary assessment of extrastriatal dopamine D2 receptor binding in the rodent and nonhuman primate brains using the high affinity radioligand, ¹⁸F-Fallypride. Nucl Med Biol 26:519–527

Newberg AB, Alavi A (2005) PET in seizure disorders. Radiol Clin North Am 43:79–92

Ng S, Villemagne VL, Berlangieri S, et al (2007) Visual assessment versus quantitative assessment of [¹¹C]PIB PET and [¹⁸F]FDG PET for detection of Alzheimer's disease. J Nucl Med 48:547–552

Nordberg A (2008) Amyloid plaque imaging in vivo: current achievement and future prospects. Eur J Nucl Med Mol Imaging 35:S46–S50

Parsey RV, Mann JJ (2003) Applications of positron emission tomography in psychiatry. Semin Nucl Med 33(2):129–135

Pappata S, Tavitian B, Traykov L, et al (1996) In vivo imaging of human cerebral acetylcholinesterase. J Neurochem 67:876–879

Passchier J, van Waarde A (2001) Visualization of serotonin-1A (5-HT1A) receptors in the central nervous system. Eur J Nucl Med 28:113–129

Passchier J, van Waarde A, Pieterman RM, et al (2000) In vivo delineation of 5-HT1A receptors in human brain with [18F] MPPF. J Nucl Med 41:1830–1835

Persson A, Ehrin E, Eriksson, et al (1985) [¹¹C]Ro-15–1788 binding to benzodiazepine receptors in the human brain by positron emission tomography. J Psychiatry Res 19: 609–622

Petrella JR, Mattay VS, Doraiswamy PM (2008) Imaging genetics of brain longevity and mental wellness: the next frontier? Radiology:246:20–32

Podruchny TA, Connolly C, Bokde A, et al (2003) In vivo muscarinic 2 receptor imaging in cognitively normal young and older volunteers. Synapse 48:39–44

Price JL (1997) Diagnostic criteria for Alzheimer's disease. Neurobiol Aging 18:S67–S70

Phelps ME, Huang SC, Hoffman EJ, et al (1979) Tomographic measurement of local cerebral glucose metabolic rate in human with [¹⁸F]2-fluoro-2-deoxyglucose. Validation of method. Ann Neurol 6:371–388

Pike VW (1995) Radioligands for PET studies of central 5-HT receptors and re-uptake sites- current status. Nucl Med Biol 22:1011–1018

Pike KE, Savage G, Villemagne VL, et al (2007) β-amyloid imaging and memory in non-demented individuals: evidence for preclinical Alzheimer's disease. Brain 130:2837–2844

Raichle ME, Martin WRW, Herscovitch P, et al (1983) Brain blood flow measured with intravenous H₂¹⁵O. II. Implementation and validation. J Nucl Med 24:790–798

Ravina B, Eidelberg D, Ahlskog JE, et al (2005) The role of radiotracer imaging in Parkinson disease. Neurology 64:208–215

Read SJ, Hirano T, Abbott DF, et al (1998) Identifying hypoxic tissue after acute ischemic stroke using PET and ¹⁸F-fluoromisonidazole. Neurology 51:1617–1621

Reiman EM, Chen K, Alexander GE, et al (2004) Functional brain abnormalities in young adults at genetic risk for late-onset Alzheimer's dementia. Proc Natl Acad Sci U S A 101:284–289

Reivich N, Kuhl D, Wolf A, et al (1979) The [¹⁸F] Fluorodeoxyglucose method for the measurement of local cerebral glucose utilization in man. Circ Res 44:127–137

Robeson W, Dhawan V, Belakhlef A, et al. (2003) Dosimetry of the dopamine transporter radioligand ¹⁸F-FPCIT in human subjects. J Nucl Med 44:961–966

Rosas HD, Feigin AS, Hersch SM (2004) Using advances in neuroimaging to detect, understand, and monitor disease progression in Huntington's disease. NeuroRx 1:263–272

Rowe CC, Ng S, Ackermann U, et al (2007) Imaging beta-amyloid burden in aging and dementia. Neurology 68:1718–1725

Rowe CC, Ackerman U, Browne W, et al (2008) Imaging of amyloid β in Alzheimer's disease with ¹⁸F-BAY94–9172, a novel PET tracer: proof of mechanism. Lancet Neurol 7:129–35

Ryzhikov NN, et al (2005) Preparation of highly specific radioactivity [¹⁸F]flumazenil and its evaluation in cynomolgus monkey by positron emission tomography. Nucl Med Biol 32:109–116

Sabri O, Kendziorra K, Wolf H, et al (2008) Acetylcholine receptors in dementia and mild cognitive impairment. Eur J Nucl Med Mol Imaging 35(s1):S30–S45

Saur D, Buchert R, Knab R, et al (2006) Iomazenil-single-photon emission computed tomography reveals selective neuronal loss in magnetic resonance-defined mismatch areas. Stroke 37:2713–2719

Seibyl JP (2008) Single-photon emission computed tomography and positron emission tomography evaluations of patients with central motor disorders. Semin Nucl Med 38:274–286

Selleri S, Bruni F, Costagli C, et al (2001) 2-Arylpyrazolo[1,5-a] pyrimidin-3-yl acetamides: new potent and selective peripheral benzodiazepine receptor ligands. Bioorg Med Chem 9:2661–2671

Shiue C-Y, Welch MJ (2004) Update on PET radiopharmaceuticals: life beyond fluorodeoxyglucose. Radiol Clin N Am 42:1033–1053

Shoghi-Jadid K, Small GW, Agdeppa ED, et al (2002) Localization of neurofibrillary tangles and beta-amyloid plaques in the brains of living patients with Alzheimer disease. Am J Geriatr Psychiatry 10:24–35

Siesjo BK (1978) Brain energy metabolism. Wiley, New York, pp 101–110

Silverman DHS (2004) Brain ¹⁸F-FDG PET in the diagnosis of neurodegenerative dementias: comparison with perfusion SPECT and with clinical evaluations lacking nuclear imaging. J Nucl Med 45:594–607

Silverman DHS, Mosconi L, Ercoli L, et al (2008) Positron emission tomography scans obtained for the evaluation of cognitive dysfunction. Semin Nucl Med 38:251–261

Small GW, Kepe V, Ercoli LM, et al (2006) PET of brain amyloid and tau in mild cognitive impairment. N Engl J Med 355:2652–2663

Smith GS, Koppel J, Goldberg S (2003) Applications of neuroreceptor imaging to psychiatry research. Psychopharmacol Bull 37:26–65

Suhara T, Maeda J, Kawabe K, et al (2003a) Visualization of alpha5 subunit of GABAA/benzodiazepine receptor by [^{11}C] Ro15–4513 using positron emission tomography. Synapse 47:200–208

Suhara T, Takano A, Sudo Y, et al (2003b) High levels of serotonin transporter occupancy with low-dose clomipramine in comparative occupancy study with fluvoxamine using positron emission tomography. Arch Gen Psychiatry 60(4):386–391

Sullivan JP, DonnellyRD, Briggs CA, et al (1996) A-85380 [3-(2(S)-azetidinylmethoxy)-pyridine]: in vitro pharmacological properties of a novel, high affinity α4β2 nicotinic acetylcholine receptor ligand. Neuropharmacology 35:725–734

Szelies B, Sobesky J, Pawlik G, et al (2002) Impaired benzodiazepine receptor binding in peri-lesional cortex of patients with symptomatic epilepsies studies by [C-11]-flumazenil PET. Eur J Neurol 9:137–142

Talbot PS, Narendran R, Butelman ER, et al (2005) [^{11}C] GR103545, a radiotracer for imaging κ-opioid receptors in vivo with PET: synthesis and evaluation in baboons J Nucl Med 46:484–494

Ter-Pogossian MM, Eichling JO, Davis DO, et al (1969) The determination of regional cerebral blood flow by means of water labeled with radioactive oxygen-15. J Clin Invest 93:31–40

Theodore WH (2004) Recent advances and trends in epilepsy imaging: pathogenesis and pathophysiology. Rev Neurol Dis 1(2):53–59

Thominiaux C, Dolle F, James ML, et al (2006) Improved synthesis of the peripheral benzodiazepine receptor ligand [^{11}C] DPA-713 using [^{11}C]methyl triflate. Appl Radiat Isot 64:570–573

Toczek MT, Carson RE, Lang L, et al (2003) PET imaging of 5-HT1A receptor binding in patients with temporal lobe epilepsy. Neurology 60:749–756

Toyama H, Ye D, Ichise M, et al (2005) PET imaging of brain with the beta-amyloid probe, [^{11}C]6-OH-BTA-1, in a transgenic mouse model of Alzheimer's disease. Eur J Nucl Med Mol Imaging 32:593–600

Treiman DM (2001) GABAergic mechanisms in epilepsy. Epilepsia 42(Suppl 3):8–12

Vallabhajosula S, Hirschowitz J, Machac J (1997) Effect of haloperidol dose on ^{123}I-IBZM brain SPECT imaging in schizophrenic patients. J Nucl Med 38:203–207

Verhoeff NP, Wilson AA, Takeshita S, et al (2004) In-vivo imaging of Alzheimer disease beta-amyloid with [^{11}C]SB-13 PET. Am J Geriatr Psychiatry 12:584–595

Volkow ND (2004) Imaging the addicted brain: from molecules to behavior. J Nucl Med 45:(11):13N–24N

Volkow ND, Hitzemann R, Wang GJ, et al (1992) Long-term frontal brain metabolic changes in cocaine dependence and withdrawal. Am J Psychiatry 148:621–626

Volkow ND, Fowler JS, Gatley SJ, et al (1996) PET evaluation of dopamine system of the human brain. J Nucl Med 37:1242–1256

Volkow ND, Fowler JS, Wang G-J (2003) Positron emission tomography and single-photon emission computed tomography in substance abuse research. Semin Nucl Med 34(2):114–128

Waarde A (2000) Measuring receptor occupancy with PET. Curr Pharm Des 6:1593–1610

Wagner HN Jr, Burns HD, Dannals RF, et al (1983) Imaging dopamine receptors in the human brain by positron tomography. Science 221:1264–1266

Wang J, Dickson DW, Trojanowski JQ, et al (1999) The levels of soluble versus insoluble brain Aβ distinguish Alzheimer's disease from normal and pathologic aging. Exp Neurol 158:328–337

Wang J, Zuo C-T, Jiang Y-P, et al (2006) ^{18}F-FP-CIT PET imaging and SPM analysis of dopamine transporters in Parkinson's disease in various Hoehn & Yahr stages. J Neurol 254:185–190

Webster R (2001) Neurotransmitter systems and function: overview. In: Webster RA, (ed) Neurotransmitters, drugs and brain function. Wiley, New York, NY, pp 1–32

Webster R (2001) Other transmitters and mediators. In: Webster RA, ed. Neurotransmitters, drugs and brain function. Wiley, New York, NY, pp 265–286

Whiteman M, Armstrong JS, Chu SH, et al (2004) The novel neuromodulator hydrogen sulfide: an endogenous peroxynitrite "scavenger"? J Neurochem 90:765–768

Wintermark M, Albers GW, Alexandrov AV (2008) Acute stroke imaging research roadmap. Am J Neuroradiol 29:E23–E30

Zhang MR, Maeda J, Ogawa M, et al (2004) Development of a new radioligand, N-(5-fluoro-2-phenoxyphenyl)-N-(2-[$_{18}$F]fluoroethyl-5-methoxybenzyl)acetamide, for PET imaging of peripheral benzodiazepine receptor in primate brain. J Med Chem 47:2228–2235

Zhang W, Oya S, Kung MP, et al (2005a) F-18 stilbenes as PET imaging agents for detecting beta-amyloid plaques in the brain. J Med Chem 48: 5980–88

Zhang W, Oya S, Kung MP, et al (2005b) F-18 polyethyleneglycol stilbenes as PET imaging agents targeting A beta aggregates in the brain. Nucl Med Biol 32: 799–809

Zipursky RB, Meyer JH, Verhoeff NP (2007) PET and SPECT imaging in psychiatric disorders. Can J Psychiatry 52: 146–157

Zoghbi SS, Shetty HU, Ichise M, et al (2006) ^{18}F-FECNT: a polar radiometabolite confounds brain radioligand measurements. J Nucl Med 47:520–527

Zubieta JK, Gorelick DA, Stauffer R, et al (1996) Increased μ-opioid receptor binding detected by PET in cocaine-dependent men is associated with cocaine craving. Nat Med 2:1225–1229

Almost all aspects of life are engineered at the molecular level, and without understanding molecules we can only have a very sketchy understanding of life itself.

Francis Harry Compton Crick

17.1 The Clinical Problem

Coronary artery disease (CAD), stroke, and congestive heart failure (CHF) are responsible for the majority of all cardiovascular deaths. The current major diagnostic imaging procedures in nuclear cardiology to address the issues of CAD and heart failure are based on the assessment of myocardial blood flow (MBF) and substrate metabolism using FDA approved SPECT and PET radiopharmaceuticals (Table 17.1). A number of review articles have extensively discussed various clinical issues and the relative significance of noninvasive imaging techniques in nuclear cardiology (Schwaiger and Bengel 2003; Machac 2005; Berman et al. 2007).

In the last 30 years, the application of qualitative perfusion imaging based on SPECT has been extended to allow for the combined evaluation of perfusion, perfusion reserve, and ventricular function. With PET, however, quantitative assessment of perfusion has become possible. In combination with pharmacological stress agents, the coronary flow reserve (CFR) can be quantitatively assessed as an early marker of endothelial dysfunction. Unfortunately, perfusion imaging often identifies the disease process after it is well established and has caused significant damage. Since many patients with CAD do not have angina, the majority of patients undergoing perfusion imaging may have advanced disease at the initial diagnosis. It is important to define the CAD process early, when therapeutic interventions to prevent clinical manifestations may be more appropriate. PET in combination with metabolic tracers has become an important clinical marker for the ischemically jeopar-dized myocardium. FDG-PET is widely considered as the gold standard for tissue viability in the management of patients with advanced CAD and impaired left ventricular function (LVF). Radiolabeled catecholamine analogues, such as MIBG and HED, provide visualization of sympathetic nerve terminals that are functionally altered in patients with diabetes mellitus and cardiomyopathy. These procedures, however, have not been approved by the FDA for routine clinical diagnostic use.

In cardiology, a paradigm shift is taking place with the emphasis from treatment to prevention of the disease. Current strategies involve the use of targeted markers of biological processes. With the recent advances in molecular biology, including genomics and proteomics, molecular imaging using biologically targeted radiopharmaceuticals (Table 17.2) will play a key role in this interdisciplinary approach to understanding the origins, pathogenesis, and progress of cardiac diseases, and in evaluating therapeutic interventions. These include novel imaging strategies for CAD, vulnerable

Table 17.1 FDA approved PET and SPECT radiopharmaceuticals in cardiology

Indication	SPECT	PET
Myocardial blood flow	^{201}Tl-chloride	$[^{13}N]NH_4^+$
	^{99m}Tc-Sestamibi (Cardiolite™)	^{82}Rb chloride
	^{99m}Tc-Teboroxime (Cardiotec™)	
	^{99m}Tc-Tetrofosmin (Myoview™)	
Blood pool	^{99m}Tc-RBC or HSA	
Infarction	^{99m}Tc-PYP	

Table 17.2 Molecular imaging in nuclear cardiology

Indication	Biological process	SPECT RP	PET RP
Blood flow	Myocardial perfusion		$[^{15}\text{O}]$Water
			$[^{13}\text{N}]\text{NH}_4^+$
			^{82}Rb chloride
			^{18}F-BMS-747158-02
			^{62}Cu-PTSM or ETS
Metabolism	Oxygen		$[^{15}\text{O}]\text{O}_2$
			$[^{11}\text{C}]$Acetate
	Glucose		$[^{18}\text{F}]$FDG
	Free fatty acids	^{123}I-BMIPP	$[^{18}\text{F}]$FTHA
Neurotransmission	Presynaptic –adrenergic	^{123}I-MIBG	$[^{11}\text{C}]$HED
			$[^{18}\text{F}]$Metaraminol
	Adrenoreceptors		$[^{11}\text{C}]$CGP-12177
Angiogenesis	$\alpha_v\beta_3$ integrin	^{111}In-VEGF$_{121}$	^{18}F or ^{64}Cu-RGD
Atherosclerosis	Macrophages		$[^{18}\text{F}]$-FDG
Apoptosis	PS expression	^{99m}Tc-HYNIC-Annexin V	^{18}F-Annexin V
			^{64}Cu-DOTA-Annexin V

plaque, atherothrombosis, angiogenesis, heart failure, apoptosis, stem cell transplantation, and gene therapy (Schwaiger and Bengel 2003; Strauss et al. 2004; Jaffer and Weissleder 2004; Dobrucki and Sinusas 2005; Wu et al. 2007; Sanz and Fayad 2008). The major goals of molecular imaging techniques in nuclear cardiology are (a) earlier detection of the disease, (b) objective monitoring of therapies, and (c) better prognostication of the disease progression.

17.2 Pathophysiology

The coronary arteries originate from the left and right coronary sinuses of the aorta (Fig. 17.1). The left main coronary artery divides into two major arteries: the left anterior descending artery (LAD) and the left circumflex artery (LCx). The right coronary artery (RCA) divides into a posterior descending artery (PDA) and a posterior left ventricular branch. The cardiac muscle has two essential properties: electrical excitability and contractility. The ability of myocardial muscle cells to contract and generate the force necessary to maintain blood circulation is achieved through the unique contractile function of two proteins of the sarcomere (actin and myosin) of the syncytially arranged myocardial fibers. Also, the heart muscle has a rich supply of the high-energy phosphates needed for the contraction.
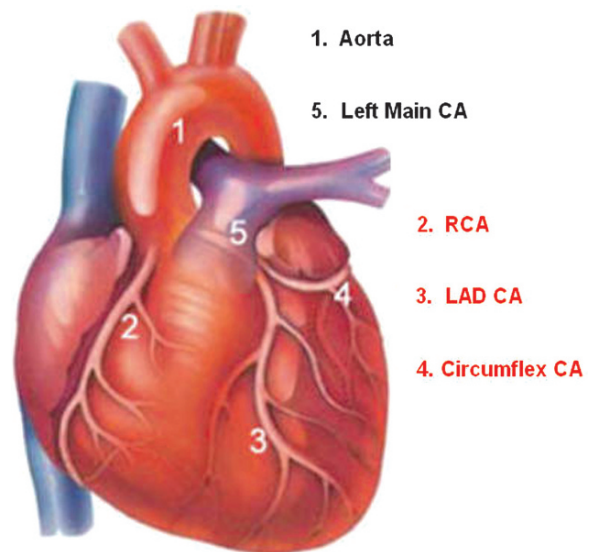
Fig. 17.1 Heart with coronary arteries

17.2.1 Coronary Artery Disease

The majority of patients with acute coronary syndromes (ACS) present with unstable angina, acute myocardial infarction, and sudden coronary death. The disease may be asymptomatic until advanced in severity or complications. CAD is an immune inflammatory process, which, over decades, results in arterial narrowing (Ross 1999; Libby 2002). Atherosclerosis is a
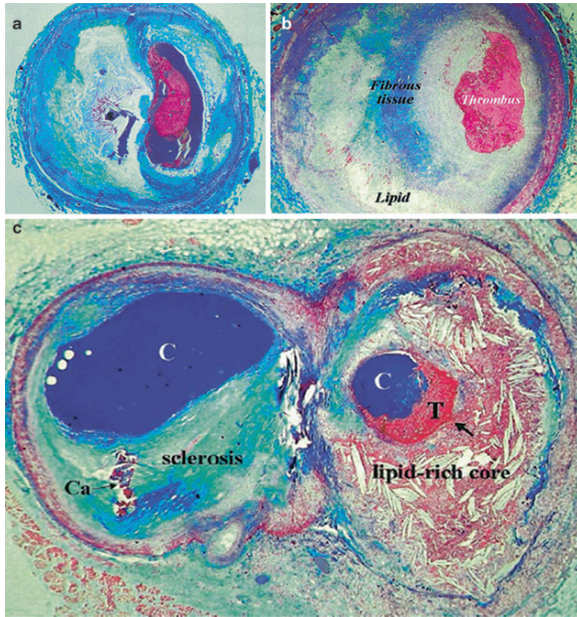
Fig. 17.2 Atherosclerosis and thrombosis in coronary arteries (CA): (**a**) Cross-sectioned CA containing a ruptured plaque with a nonocclusive platelet-rich thrombus superimposed; (**b**) Cross section of a CA containing a stenotic atherosclerotic plaque with an occlusive thrombosis superimposed (plaque erosion); (**c**) Atherothrombosis: a variable mix of chronic atherosclerosis and acute thrombosis. Cross-sectioned arterial bifurcation illustrating a collagen-rich (*blue-stained*) plaque in the circumflex branch (*left*) and a lipid-rich and ruptured plaque with a nonocclusive thrombosis superimposed in the obtuse branch (*right*). C = contrast in the lumen; Ca = calcification; T = thrombosis. (Fuster et al. 2005)

systemic disease with focal manifestations, and it is by far the most frequent underlying cause of CAD. It is also is a complex disease in which cholesterol deposition, inflammation, and thrombus formation play a major role. Atherosclerotic lesions (Fig. 17.2), according to the American Heart Association classification with recent modifications are divided into two groups: nonatherosclerotic intimal lesions and progressive atherosclerotic lesions (Spagnoli et al. 2007). A third group of lesions, healed atherosclerotic plaques, are the most prevalent lesions, particularly in the carotid arteries. A variety of factors contribute to the development and progression of atherosclerosis. Dysfunction of the endothelium, which maintains vascular homeostasis by regulating vascular tone, smooth muscle cell proliferation, and thrombogenicity, is thought to be the earliest step in the development of CAD. The endothelial dysfunction results in the imbalance of vascular

regulatory mechanisms to cause damage to the arterial wall. Inflammation, macrophage infiltration, lipid deposition, calcification, extracellular matrix digestion, oxidative stress, cell apoptosis, and thrombosis are among other molecular mechanisms that contribute to plaque development and progression (Libby 2002; Falk 2006; Virmani et al. 2006). Atherosclerosis, alone, is rarely fatal; it is thrombosis, superimposed on a ruptured or eroded atherosclerotic plaque, that precipitates the life-threatening clinical events, such as acute coronary syndromes (ACS) and stroke (Falk 2006). Therefore, the term atherothrombotic disease is more appropriate since the atherosclerotic and the thrombotic processes are interdependent (Fuster et al. 2005).

17.2.1.1 Vulnerable Plaque

Since the 1970s, scientists have sought to find the mechanisms responsible for converting chronic coronary atherosclerosis to acute coronary artery disease. Despite major advances in the treatment of coronary heart disease patients, a large number of victims of the disease, who are apparently healthy, die suddenly without prior symptoms. In the 1990s the term *vulnerable plaque* was introduced to describe the rupture prone plaques as being the underlying cause of most clinical coronary events (Muller et al. 1994). Based on histopathological observations, a nonthrombosed lesion, that most resembles the acute plaque rupture, has been identified as the thin cap fibroatheroma (TCFA), which is characterized by a necrotic core with an overlying fibrous cap measuring <65 µm, containing rare smooth muscle cells and numerous macrophages (Fig. 17.3) (Falk 2006; Virmani et al. 2006). An inflamed TCFA is suspected to be a high risk/vulnerable plaque (Muller et al. 2006).

Stable plaques are characterized by intimal thickening associated with lipid deposition, a chronic inflammatory infiltrate, but without evidence of necrosis, whereas vulnerable and ruptured plaques are characterized by an "active" inflammation involved in the thinning of the fibrous cap, predisposing the plaque to rupture (Spagnoli et al. 2007). Since rupture-prone plaques are not the only vulnerable plaques, it was proposed that all types of atherosclerotic plaques, with high likelihood of thrombotic complications and rapid progression, should be considered as vulnerable
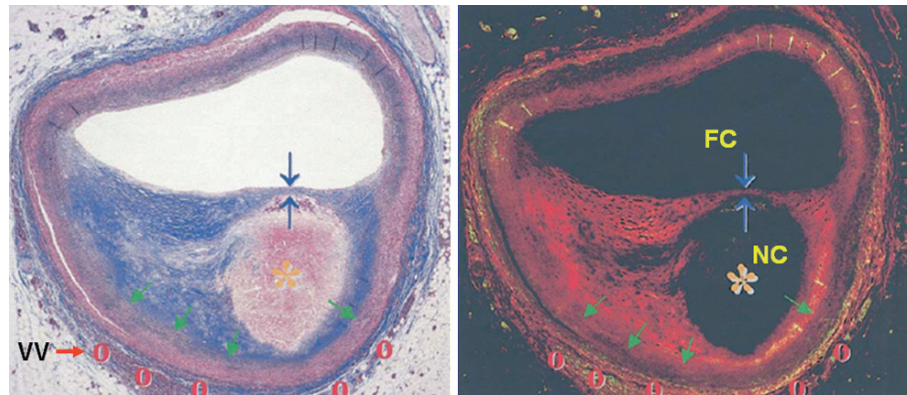
plaques. In addition, since the vulnerable blood
(prone to thrombosis) and vulnerable myocardium
(prone to fatal arrhythmia) play an important role in
the clinical outcome, the term "vulnerable patient"
has been regarded as being more appropriate (Naghavi
et al. 2003).

17.2.1.2 Myocardial Infarction

Myocardial infarction (MI) occurs in the setting of an
acute coronary vessel occlusion, with a variable
amount of spasm, and increased myocardial demand
as contributing factors. Most of the ACS are thought
to be the result of sudden luminal thrombosis which
occur from three different pathologies: plaque rup-
ture, erosion, and calcified nodules (Virmani et al.
2006). Histopathological studies reveal a large periph-
eral zone infiltrate by neutrophils that surround the
subendocardial central zone devoid of neutrophils.
The peri-infarct zone is a complex collection of
regions in different states of injury, depending on the
amount of blood flow reduction, myocardial meta-
bolic demand, and the rate of onset and duration of the
blood flow reduction. Myocardial necrosis and severe
acute ischemia lead to increased permeability, cell
membrane disruption, and leakage. Different myocar-
dial tissue states or zones, such as hibernating and
stunned myocardium, may be present depending on
the extent of damage, viability and function (Travin
and Bergmann 2005). The hibernating myocardium is
the term applied to a dysfunctional myocardium with
reduced perfusion (ischemia) at rest, but preserved
cell viability.

17.2.2 Congestive Heart Failure

CHF stems from inadequate cardiac output, due to sys-
tolic or diastolic left ventricular function. The primary
causes are ischemic heart disease and hypertension. Both,
idiopathic cardiomyopathy (ICM) and ischemic cardio-
myopathy (ISM) are widespread and are major underly-
ing cardiac diseases responsible for heart failure. Besides
the risk of sudden cardiac death, patients with CHF can
have intraventricular dyssynchrony (or left bundle branch
block), which causes the two ventricles to beat in an asyn-
chronous fashion, reduces systolic function, and increases
systolic volume. Autonomic dysfunction has been shown
to increase the risk of death in patients with heart disease
and may be applicable to all patients with cardiac disease,
regardless of etiology (Barron and Lesh 1996). The
impaired cardiac presynaptic function has pathophysio-
logical implications in the occurrence of lethal cardiac
events in patients with heart failure.

The autonomic innervation of the heart is the pri-
mary extrinsic control mechanism regulating cardiac
performance. The heart is innervated by the parasym-
pathetic and sympathetic nerve fibers. The left ventricle
of the heart is primarily supplied by sympathetic nerves
that modify cardiovascular performance in adapting to
the changing hemodynamic requirements. The para-
sympathetic nervous system primarily innervates the
atria and the conduction system. The major neurotrans-
mitters of the sympathetic and parasympathetic sys-
tems are norepinephrine and acetylcholine, which
define the stimulatory and inhibitory physiological
effects of each system. There is a highly regulated bal-
ance in the sympathetic and parasympathetic input to
optimize cardiac performance.

17.3 Radiopharmaceuticals in Nuclear Cardiology

The conventional imaging procedures in nuclear cardiology have focused on obtaining physiologic or metabolic information in the diagnostic and prognostic evaluation of cardiovascular diseases (Table 17.1). In the near future, several molecular imaging approaches will become important adjuncts to the clinical management of patients with CAD and heart failure. These techniques may offer the potential to directly track biochemical processes and signaling events that precede the pathophysiological changes. The basic principles involved in the development of targeted biological markers of molecular and physiological processes are briefly discussed.

17.3.1 Myocardial Blood Flow

MBF is regulated by anatomical, hydraulic, mechanical and metabolic factors. Autoregulation of MBF is driven by changes in regional myocardial metabolism and oxygen consumption. Under resting conditions, MBF is one fifth the maximum flow capacity, which occurs during reactive hyperemia and, or with maximum pharmacological vasodilation (Sinusas and Zaret 1995). Near-maximal MBF can be produced by intense metabolic stress associated with exercise. The differ-
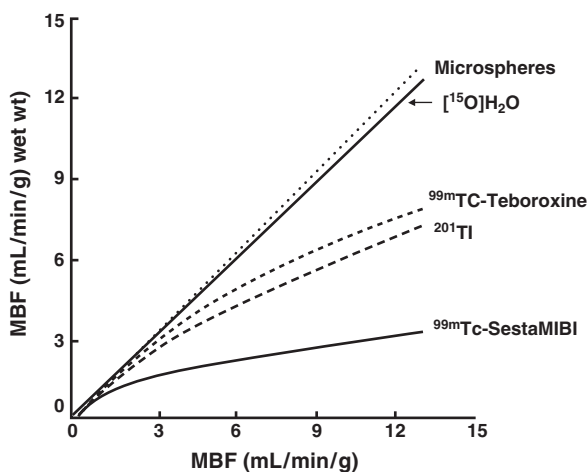
Fig. 17.4 Correlation between the measured MBF based on imaging studies and the expected MBF

ence between the peak and basal MBF represents the coronary flow reserve (CFR), which is reduced in the presence of severe CAD.

The resting MBF is not reduced until the stenosis exceeds 90% of the normal vessel diameter. The coronary flow reserve, however, is reduced with only a 50% diameter stenosis (Gould et al. 1974). Therefore, myocardial perfusion imaging (MPI) is performed in conjunction with exercise or pharmacological vasodilatation (using adenosine, dipyridamole, or dobutamine) in order to identify subcritical coronary stenosis. MPI maps the relative distribution of coronary flow, which is normally almost uniform in the absence of prior infarction or fibrosis.

17.3.1.1 PET Radiotracers for Perfusion

Several radiopharmaceuticals are available for evaluating the relative distribution of MBF based on SPECT or for measuring regional MBF in absolute quantitative units (mL/min/g) based on PET.

The ideal flow tracer accumulates in, or clears from, the myocardium linear in proportion to MBF. The relationship between uptake and clearance of the radiotracer and MBF should be constant and independent of MBF, physiological and pathological changes of the myocardial tissue state, and the myocardial metabolism. Most radiotracers used for imaging the myocardial perfusion/blood flow, however, do not fully meet these requirements (Schelbert 2004).

As described previously (Chap. 16), the first pass unidirectional extraction fraction E is the fraction of the tracer that changes across the capillary membrane during a single transit of tracer bolus through the coronary circulation. For most diffusible radiotracers, such as [^{15}O]water, $E < 1$ declines with increasing MBF. The relationship between E and the permeability-surface product and blood flow is described by Renkin and Crone. It is also important to note that the E for radiotracers administered as bolus is generally higher than the steady state extraction fraction, also called the extraction ratio (Schelbert 2004). Also, the first pass retention fraction R of the radiotracer may decrease at higher flow rates due to back diffusion of the radiotracer into the vascular space and blood. The plot of the myocardial net uptake ($E \times F$) for several radiotracers, as a function of MBF (Fig. 17.4), suggests that the net uptake would increase linearly with higher blood flows,

but correlates nonlinearly with blood flow, except for [^{15}O]water.

[^{15}O]water meets the criteria for an ideal radiotracer for MBF measurement most closely. Based on a single tissue compartment model, MBF (mL min^{-1} g^{-1}) estimates in normal human subjects are 0.90 ± 0.22 at rest and 3.55 ± 1.15 with stress, based on intravenous dipyridamole (Schelbert 2004).

[^{13}N]Ammonia (NH$_3$) in circulation exists predominantly as an ammonium ion NH$_4^+$ at normal pH. It may be actively transported into the myocardial cells via the Na$^+$/K$^+$ pump or by the passive diffusion of neutral lipid soluble ammonia. Inside the cell, ammonia is quickly converted to ammonium ion which is rapidly converted and trapped as glutamine by the enzyme *glutamine synthase* (Schelbert 2004). Because of the large intracellular levels of glutamine, the washout of N-13 activity from the cell is minimal. Since the rate of their back-diffusion depends on MBF, the retained fraction R declines with higher flow.

Intrasubject comparison studies have demonstrated a close linear correlation between MBF estimates determined by [^{15}O]water and [^{13}N]ammonia techniques, over a range of flows from 0.5–5.0 mL min^{-1} g^{-1} (Nitzsche et al. 1996). Also, global and regional MBF estimates with [^{13}N]ammonia have shown a close correlation to MBF estimates which were determined based on the inert argon gas washout technique (Kotzerke et al. 2001). In patients with CAD and previous myocardial infarctions, MBF estimates with [^{13}N] ammonia and [^{15}O]water may markedly differ in regions of previously infracted myocardium (Schelbert 2004). MBF imaging with [^{13}N]ammonia-PET, demonstrating anterior and lateral defects, is shown in Fig. 17.5.

^{82}Rb$^+$ as a K$^+$ analog, is actively transported into the myocardial cells via the Na$^+$/K$^+$ pump. The extraction fraction decreases at high flows and can be altered by drugs, severe acidosis, hypoxia and ischemia. ^{82}Rb$^+$ appears to leak from the irreversibly injured myocardium, but is retied or continues to accumulate in only reversibly injured myocardium (Schelbert 2004). In normal subjects, at base line, and with dipyridamole stress, there is a close correlation between MBF estimates with ^{82}Rb$^+$ and [^{15}O]water (Lin et al. 2001). An example of ^{82}Rb-PET images showing relatively normal perfusion (Machac 2005) is provided in Fig. 17.6.

^{62}Cu-PTSM is a lipophilic Cu(II) complex that can diffuse across the cell membrane. Following reduction by the sulfhydryl groups, copper binds to intracellular proteins and is trapped in the myocardium. While
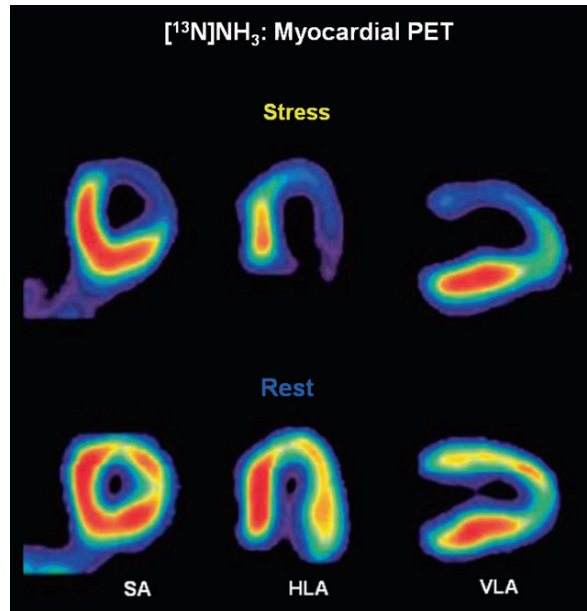
Fig. 17.5 Myocardial blood flow imaging with [^{13}N]ammonia-PET demonstrating anterior and lateral defects during pharmacological stress and significant improvement at rest, consistent with ischemia. SA, short axis; HLA, horizontal long axis; VLA, vertical long axis (Machac 2005)
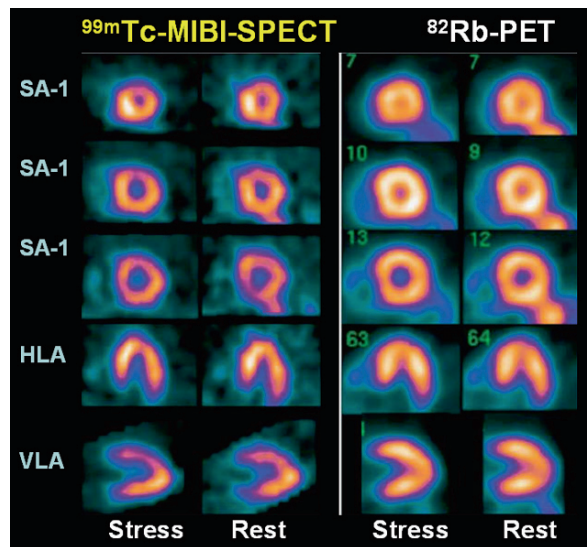
Fig. 17.6 Comparison of Myocardial SPECT and PET: ^{99m}Tc sestamibi dipyridamole stress and rest images show a mild-to-moderate anterior wall defect at stress with a suggestion of partial improvement at rest, while the ^{82}Rb-PET images shows normal perfusion (Machac 2005)

Cu-PTSM has demonstrated significant potential for imaging myocardial blood flow, very high binding to albumin in circulation impairs its ability for quantitative
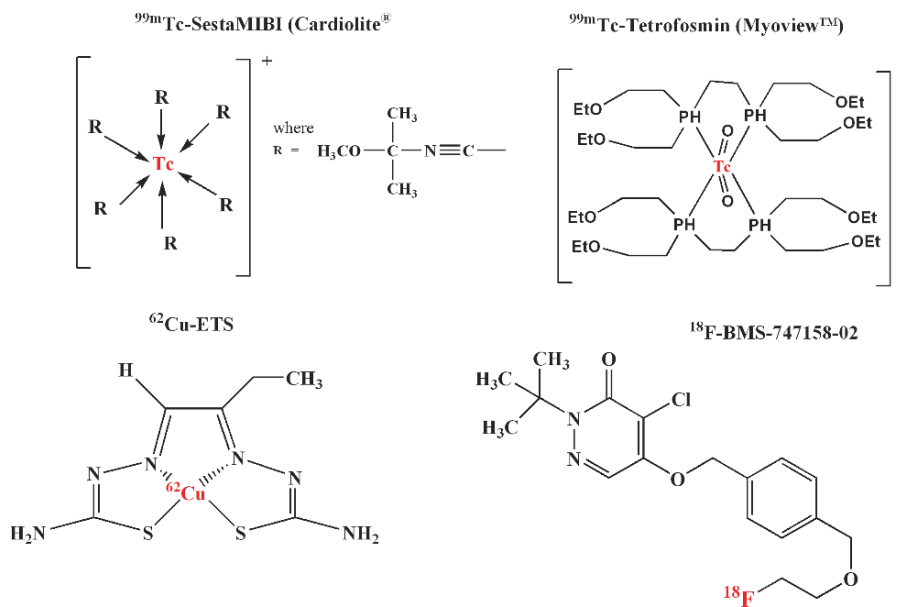
Fig. 17.7 SPECT and PET radiopharmaceuticals for imaging myocardial perfusion

determination of myocardial perfusion (Basken et al. 2008). A second generation of the Cu-BTS complex known as ^{62}Cu-ETS (Fig. 17.7), with minimal plasma protein binding, is under clinical evaluation.

Recently, the first ^{18}F-labeled radiopharmaceutical for the assessment of myocardial perfusion was proposed. More specifically, [^{18}F]fluorobenzyl triphenyl phosphonium (^{18}F-BMS-747158-02) (Fig. 17.7), a member of the class of potentiometric lipophilic phosphonium cations originally developed for the measurement of the mitochondrial membrane potential, was introduced for myocardial perfusion imaging (Madar et al. 2006). The accumulation of this tracer depends primarily on the mitochondrial membrane potential. Furthermore, the myocardium-to-liver uptake ratio is approximately one, hampering image contrast for myocardial structures (Huisman et al. 2008). Based on preclinical studies, it has been observed that a high and flow-independent first-pass extraction fraction promises linearity between tracer uptake and myocardial blood flow.

17.3.1.2 SPECT Radiotracers for Perfusion

^{201}Tl as thallous chloride behaves like a K$^+$ analogue and is highly extracted by the myocardial cell. It was first introduced in the 1970s as a radiopharmaceutical for myocardial perfusion imaging (Strauss et al. 1975). ^{201}Tl, with a physical half life of 73.1 h, decays by electron capture to ^{201}Hg, which emits useful x-ray photons (69–80 KeV; 94.4% abundance) for gamma camera imaging studies. It is produced in a cyclotron and is indirectly based on the following nuclear reaction.

$$^{203}_{81}\text{Tl}\,(p,3n)\,^{201}_{82}\text{Pb} \xrightarrow{EC,\,9.4\,\text{h}} {}^{201}\text{Tl} \xrightarrow{EC,\,73.1\,\text{h}} {}^{201}_{80}\text{Hg}. \quad (17.1)$$
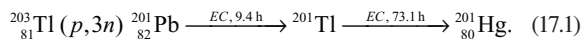
Following intravenous administration, it is rapidly cleared from the circulation and normal myocardial tissue extracts about 85% of the amount present in the coronary arteries. At pH 4–7, ^{201}Tl predominantly exists as a monocation, and like K$^+$ ion, it relies on cell-membrane integrity and active metabolic transport using Na$^+$/K$^+$ pump for its uptake into the myocardial cells. Approximately 3–5% of the injected dose localizes in the normal myocardial tissue and after initial localization, there is rapid redistribution of ^{201}Tl activity in the myocardium. Early stress-induced defects, which later normalize in redistribution images, imply myocardial ischemia, while persistent defects indicate scarring.

Three important ^{99m}Tc labeled radiopharmaceuticals (Fig. 17.7) were introduced for myocardial perfusion imaging studies (Jain 1999); sestamibi (cardiolite®), tetrofosmin (myoview™), and teboroxime (cardioTec). Six molecules of MIBI (2-methoxy isobutyl isonitrile) bind to the central ^{99m}Tc atom forming a coordination

complex with a single positive charge. As a cationic complex, it is transported into the myocardium by passive diffusion (extraction efficiency < 60%), and the myocardial retention is due to mitochondrial binding. Tetroformin (^{99m}Tc-1,2-bis[bis(2-ethoxyethyl)phosphino] ethane) is also a monocation complex and is transported into the myocardial tissue similar to sestamibi. Teboroxime is a boronic-acid (BATO) derivative and a neutral liophilic compound that passively diffuses into the myocardial cells (extraction efficiency ≈ 90%), but then rapidly washes out. As a result, imaging must be completed with in 10 min following intravenous administration. This compound, however, is not available commercially at this time.

17.3.2 Myocardial Metabolism

Understanding the myocardial metabolism of substrates is very important for understanding the pathophysiology of various cardiac diseases and for designing therapeutic interventions. The heart requires a constant supply of energy to sustain contractile function. The energy is supplied by hydrolysis of ATP, which is primarily derived from the aerobic metabolism. The myocardium chooses between various substrates, such as free fatty acids (FFA), glucose, lactate and ketone bodies (Fig. 17.8) (Bing 1954). The tricarboxylic acid (TCA) cycle is linked to the myocardial oxygen consumption via the electron transport chains, which supply most of the energy in the form of ATP. The amount of oxygen required for oxidation of carbohydrates, glucose or lactate, and fatty acids is summarized in Table 17.4. The selection of an appropriate substrate, however, depends on several conditions, such as plasma concentration of the substrate, hormonal control (insulin, glucagon, and catecholamines levels), stress and physical activity.

In the normal myocardium and also with moderate levels of exercise, FFAs are considered the preferred substrate for metabolism at rest. In the fasting state,
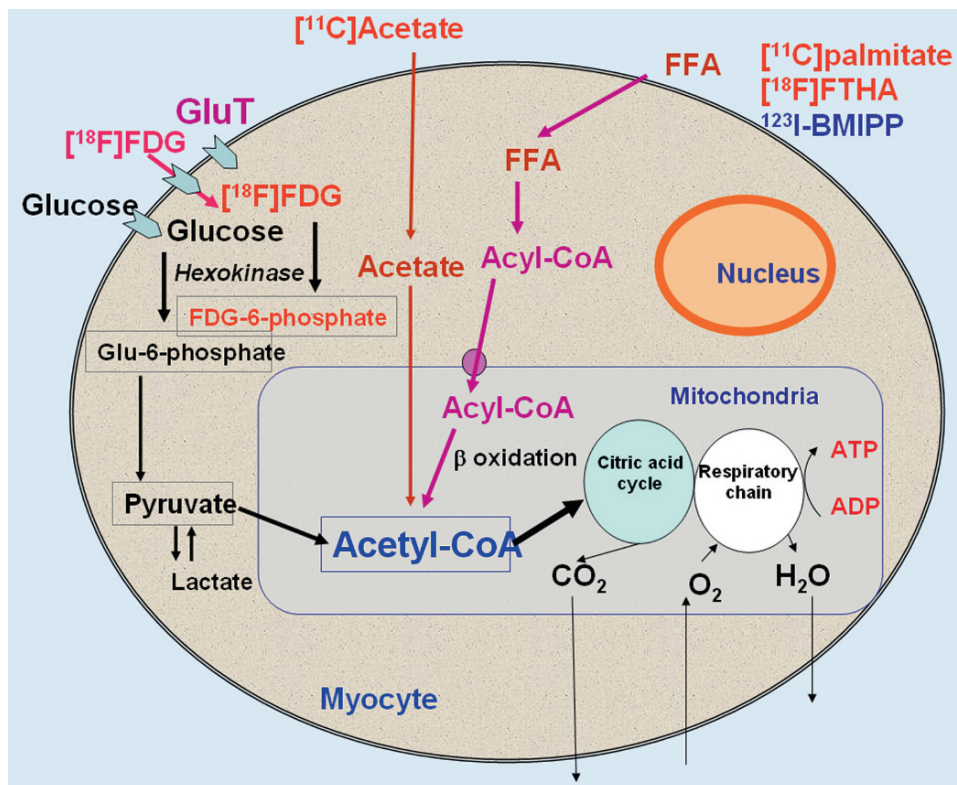
Fig. 17.8 PET and SPECT radiotracers to image myocardial substrate utilization and metabolism

FFA levels in circulation are high and insulin levels are low so that up to 80% of energy is derived from the FFA metabolism. A diet rich in carbohydrates increases the plasma glucose and insulin levels, and then glucose becomes the preferred substrate (Opie and Owen 1975; Heineman and Balaban 1993). With strenuous exercise, the release of lactate into the circulation from skeletal muscle increases and lactate will then become the major fuel for myocardial metabolism.

In various pathological conditions, the myocardial metabolism can be changed significantly. In ischemic myocardium, the oxidative metabolism is reduced and as a result, there is a shift from an aerobic to an anaerobic metabolism. With the lack of a sufficient oxygen supply, glucose is now metabolized to lactate (glycolysis). With ischemia, glucose is the preferred substrate regardless of the availability of other fuels (Opie and Owen 1975; Liedtke 1981). For ischemic heart disease, the major player in the disease pathophysiology is the reduction in regional or focal perfusion. Changes in regional metabolism are a consequence of reduced blood flow to these areas.

Changes in myocardial metabolism may also play a key role in various other cardiac conditions, such as heart failure, cardiomyopathy and diabetes, which involve the myocardium more globally, and involve the myocardium as a whole. However, due to difficulties in evaluating metabolism in human subjects, the alterations in the myocardial metabolism under such conditions are poorly understood Kudo 2007). The substrate utilization may vary depending on the extent of CAD and prior drug therapy to improve LV function. For example, long-term treatment with a β-adrenergic receptor antagonist was reported to be associated with a switch in myocardial metabolism away from FFA oxidation towards glucose metabolism (Wallhaus et al. 2001). Studies in animal models of diabetes mellitus have demonstrated an upregulation of myocardial fatty acid utilization and a reduction of the insulin-mediated glucose transport. However, little is known about the effect of diabetes mellitus on the human heart.

In the near future, the major focus of cardiovascular medicine will move from intervention for acute/chronic coronary disease to primary/secondary prevention. The non-invasive assessment of the metabolism in the ischemic and nonischemic myocardium, based on molecular imaging studies, may play a very important role in understanding the disease development, pathophysiology, and treatment (Kudo 2007; Taki and Matsunari 2007).

17.3.2.1 Glucose Metabolism

Glucose is transported into the myocardial cell by facilitated diffusion of insulin independent, GLUT 1 and insulin dependent, GLUT 4 glucose transporters (Lopaschul and Stanley 1997). Intracellularly, glucose is rapidly phosphorylated to glucose 6-phosphate, which is further metabolized (glycolysis) to pyruvate. Under aerobic conditions, pyruvate is converted to acetyl-CoA, which enters the TCA cycle in the mitochondria for oxidative metabolism (Fig. 17.8). Under anaerobic conditions, pyruvate is further metabolized to lactic acid.

[^{18}F]FDG that enters the myocardium is phosphorylated to FDG-6-phosphate, but then does not enter further metabolic pathways; instead it accumulates in the myocardium. Thus, the myocardial uptake of FDG reflects the uptake and metabolism of glucose (Sokoloff et al. 1977; Phelps et al. 1979). FDG-PET images reflect the relative distribution of FDG uptake in different regions of the myocardium. Also, the metabolic rate (MRglc) of glucose in absolute units can be measured with PET based on dynamic imaging studies, mathematical modeling, compartment model analysis, or graphical plot analysis. Since the rate of the glucose uptake and FDG uptake is not equal, a lumped constant (LC) was developed to convert the FDG uptake to glucose uptake. Usually, the value of LC is fixed, and is approximately 0.6–0.7 for the FDG-PET measurement of MRglc (Krivokapich et al. 1987). The LC, however can vary over a wide range, depending on blood insulin levels and cardiac disease (Botker et al. 1997).

Detection of viability in ischaemic heart disease is one of the most important aspects of the diagnostic and prognostic workup in patients with CAD. In some cases of hibernating myocardium, the resting flow based on PET or SPECT tracers cannot differentiate hibernating myocardium from irreversible myocardial scar formation. Relatively higher FDG uptake in an area of decreased myocardial blood flow in the dysfunctional myocardium, known as "flow metabolism mismatch," indicates viable myocardium (Tillisch et al. 1986). As a result, FDG-PET is considered as one of the gold standards for the determination of myocardial viability (Fig. 17.9).
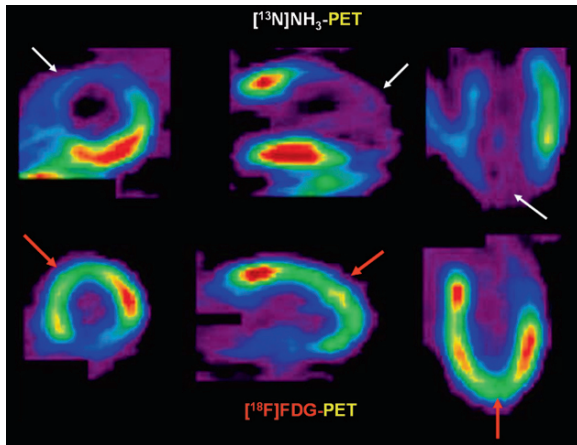
Fig. 17.9 FDG-PET to image myocardial viability. Classic mismatch showing FDG uptake in areas of decreased myocardial perfusion identified by [^{13}N]NH$_3$

17.3.2.2 Fatty Acid Metabolism

Since the FFAs are hydrophobic, they are delivered to the heart by binding to plasma proteins, albumin or lipoproteins. After dissociating from proteins, FFAs easily pass through the myocardial membrane by diffusion or a facilitated transport mechanism. Based on clinical and animal experiments, it has been shown that CD36 plays a crucial role in the fatty acid transport into the cells (Brinkmann et al. 2002; Taki and Matsunari 2007). Intracellularly, FFAs are activated as acylcoenzyme A, (Acyl CoA) and then carried into the mitochondria through an acyl carnitine carrier system and catabolised by β-oxidation into two-carbon fragments, acetyl-CoAs, which enter the TCA cycle for further oxidative metabolism (Fig. 17.8). A part of FFAs is not oxidized but is formed into triglycerides and myocardial structural lipids and stays in the myocardium for a long time. The straight-chain FFAs are generally metabolized through β-oxidation and released from the myocardium, while the development of modified FFAs is based on the concept of myocardial retention from metabolic trapping (Tamaki et al. 2000).

Radiolabeled Fatty Acids for PET

A physiological radiotracer 1-[^{11}C]palmitate (Fig. 17.10) was the first FFA introduced to image fatty acid metabolism of the heart (Schön et al. 1982).

Subsequently, 14(*RS*)-[^{18}F]fluoro-6-thia-heptadecanoic acid (FTHA) was developed as a metabolically trapped radiotracer (Stone et al. 1998).

[^{11}C]Palmitate is biologically identical to non-radioactive circulating palmitate. The first pass extraction fraction (0.67) is relatively high and the initial uptake and regional distribution in the myocardium are largely determined by MBF (Schelbert 2004). It clears from the myocardium in a biexponential fashion. Once the tracer is taken up into the myocardium, β-oxidation breaks it down to generate acetyl-CoA. This [^{11}C] acetyl-CoA is oxidised via the citric acid cycle and finally released from the myocardium in the form of [^{11}C]CO$_2$. The rapid clearance fraction corresponds to β-oxidation, whereas the slow-washout fraction reflects the turnover rate of the intracellular lipid pool and is an index of FFA metabolism (Tamaki et al. 2000). In severely ischemic myocardium, the regional uptake of [^{11}C]palmitate is reduced. The PET images provide qualitative and semiquantitative evaluation of fatty acid metabolism. The quantitative value of myocardial fatty acid use and oxidation is difficult to estimate in absolute units (milliequivalents of free fatty acid per minute per gram of myocardium). Since the C-1 label of 1-[^{11}C]palmitate is removed in the initial step of β-oxidation, ω-[^{11}C]palmitate was proposed as a potential tracer to prolong the myocardial retention of trapped metabolites (Buckman et al. 1994).

With FTHA, the rate of metabolic trapping is thought to be proportional to the rate of β-oxidation. In patients with CAD, estimates of myocardial FFA utilization (MFAU) in a normal myocardium was found to be approximately $5.8 \pm 1.7\,\mu$mol $100\,g^{-1}$ min^{-1}, while in patients with CHF, the MFAU was found to be elevated ($19.3 \pm 2.3\,\mu$mol $100\,g^{-1}$ min^{-1}) (Schelbert 2004; Taylor et al. 2001). Further, because FTHA does not trace the FFA uptake under hypoxic conditions accurately, several ^{18}F analogs have been developed. It is still not clear which tracer is the most reliable or the most clinically useful PET tracer to image fatty acid metabolism in different cardiac diseases (Kudo 2007).

Radiolabeled Fatty Acids for SPECT

Since the 1970s several iodinated fatty acid tracers for SPECT have been developed (Fig. 17.10) by introducing radioiodine to the terminal position of fatty acids without significant alteration of the extraction efficiency,

Palmitate $\qquad$ H_3C —— $(CH_2)_{14}$ —— $COOH$

$[^{11}C]$Palmitate $\qquad$ H_3C —— $(CH_2)_{14}$ —— $^{11}COOH$

$[^{11}C]$Palmitate $\qquad$ $H_3{}^{11}C$ —— $(CH_2)_{14}$ —— $COOH$

$[^{18}F]$FTHA $\qquad$ H_3C —— $(CH_2)_2$ —— $\underset{H}{\overset{^{18}F}{C}}$ —— $(CH_2)_7$ —— S —— $(CH_2)_4$ —— $COOH$

$[^{123}I]$p-IHA $\qquad$ ^{123}I —— $(CH_2)_{16}$ —— $COOH$

$[^{123}I]$p-IPPA $\qquad$ ^{123}I —— ⬡ —— $(CH_2)_{14}$ —— $COOH$

$[^{123}I]$-BMIPP $\qquad$ ^{123}I —— ⬡ —— $(CH_2)_{12}$ —— $\underset{H}{\overset{CH_3}{C}}$ —— $\overset{H_2}{C}$ —— $COOH$
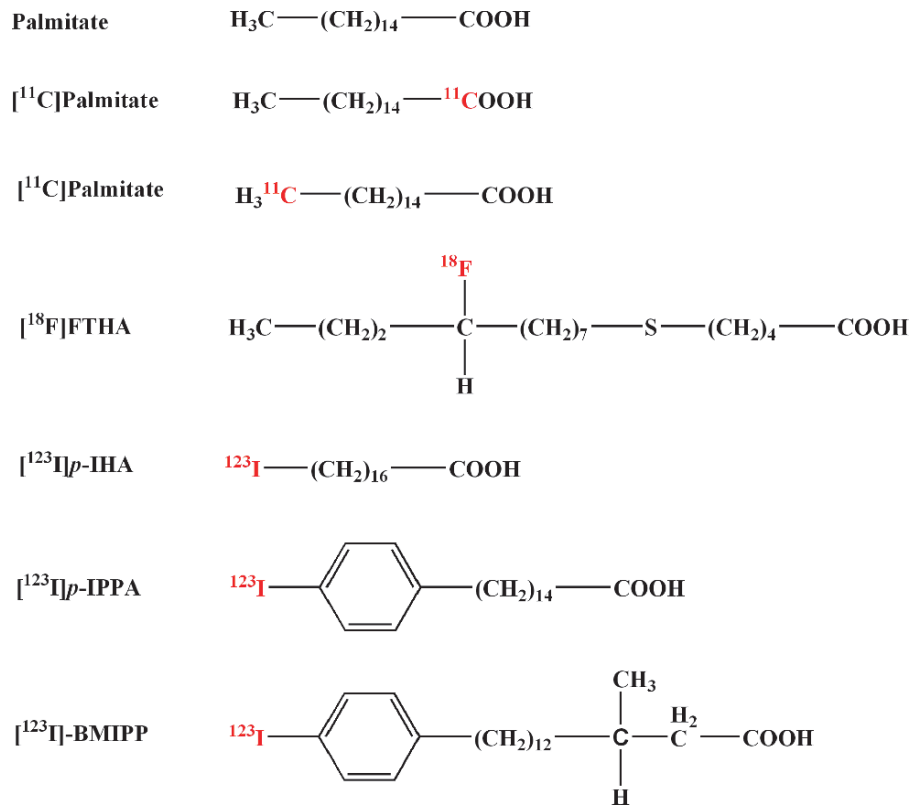
Fig. 17.10 PET and SPECT radiotracers of free fatty acid analogs to assess myocardial metabolism

compared with the natural FFAs (Poe et al. 1977; Tamaki et al. 2000; Taki and Matsunari 2007). The two groups of iodinated fatty acid compounds include straight-chain FFAs and modified branched FFAs. In a clinical study, ^{123}I-17-iodoheptadecanoic acid (IHA), an analog of stearic acid demonstrated a high-quality image early after injection, but the image quality deteriorated rapidly because of the rapid reduction of myocardial counts and increase in background counts due to deiodinated radioiodine (Freundlieb et al. 1980). To prevent in vivo deiodination, the phenyl fatty acids were developed by attaching iodide to the para or ortho position of the phenyl ring (IPPA). For routine clinical use, however, the rate of metabolism and clearance of IPPA is still relatively too fast for SPECT imaging studies.

In order to develop a tracer with more prolonged cardiac retention and with improved image quality, a methyl branching was introduced at the β-carbon position to slow the myocardial clearance by inhibiting β-oxidation. Two iodinated branched fatty acid analogs, 15-(p-iodophenyl)-3-R,S-methylpentadecanoic acid (BMIPP) and 15-p-iodophenyl)-3,3-methylpentadecanoic acid (DMIPP) were, therefore, developed (Knapp et al. 1986a, b; Tamaki et al. 2000; Taki and Matsunari 2007). FTHA has shown to be metabolically retained in the myocardium and has very good imaging properties in normal human subjects and in patients with CAD. The concept underlying BMIPP imaging is metabolic trapping of BMIPP-CoA, similar to FDG, but by inhibition of β-oxidation through the introduction of methyl branching, at the β-carbon position. Under the condition of ischemia, a reduction in BMIPP uptake is observed, reflecting the reduction in ATP production due to depressed oxidative fatty acid metabolism and substrate shift from fatty acids to glucose (Fig. 17.11). When compared with myocardial perfusion imaging, BMIPP imaging enables "ischemic memory imaging," with detection of previous myocardial ischemia (metabolically stunned myocardium) and viable but chronically dysfunctional myocardium (hibernating myocardium), (Taki and Matsunari 2007). Also, in cardiomyopathy, BMIPP
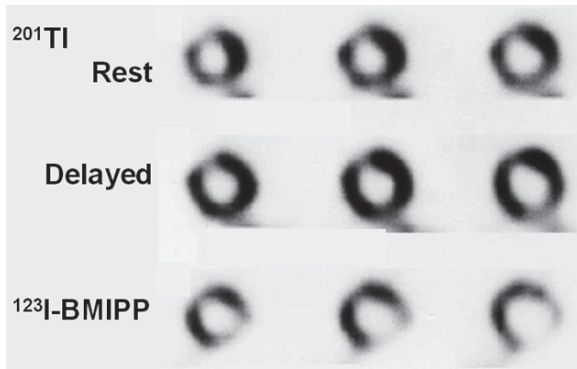
Fig. 17.11 Myocardial metabolic imaging using ^{123}I-BMIPP in patients with unstable angina: Although ^{201}Tl scans did not show definite perfusion abnormalities, decreased BMIPP uptake was noted in the lateral region, indicating decreased regional myocardial metabolism (Tamaki et al. 2000)

Fig. 17.12 Myocardial metabolic imaging using ^{123}I-BMIPP in patients with hypertrophic cardiomyopathy (HCM). There is increased ^{201}Tl uptake in the apex to the anteroseptal wall, but BMIPP uptake is reduced in that area. Discordant BMIPP uptake less than blood flow in the hypertrophic area is a rather early phenomenon of HCM (Taki and Matsunari 2007)

imaging may be useful for the early detection of HCM, the differentiation of ischaemic cardiomyopathy from idiopathic DCM, and also for the prediction of prognosis (Fig. 17.12). ^{123}I-BMIPP has been the most commonly used commercially available SPECT tracer to assess fatty acid metabolism in patients, especially in some of the European countries and in Japan.

17.3.2.3 Oxidative Metabolism

The assessment of myocardial oxidative metabolism involves the estimation of myocardial ventricular oxygen consumption (MVO_2) in absolute units, mL min^{-1}

g^{-1}. Under steady-state conditions, MVO_2 provides an accurate measure of overall myocardial metabolism regardless of which substrate or fuel is used. Based on the determination of myocardial blood flow, using [^{15}O] water, myocardial blood volume using [^{15}O]CO, and oxygen inhalation studies using [^{15}O]O$_2$, myocardial oxygen extraction can be determined. The MVO_2 is then estimated using the plasma oxygen content as the arterial input function. In normal subjects, an average MVO_2 is 0.097 ± 0.022 mL min^{-1} g^{-1} (Yamamoto et al. 1996). While this method provides an absolute quantitative estimation of regional MVO_2 in various cardiac diseases, the PET imaging studies involving ^{15}O ($T_{1/2} = 2$ min) are not practical got routine clinical use.

[^{11}C]Acetate

Acetate is avidly extracted from the coronary circulation and rapidly distributed in the myocardium. In cytosol, it is activated to acetyl-CoA and, subsequently, enters the TCA cycle in the mitochondria for oxidation and metabolism to [^{11}C]O$_2$ and water (Fig. 17.8). It is important to realize that the myocardial kinetics of [^{11}C] acetate is independent of the metabolic milieu, such as the blood glucose level or FFA concentration in the blood (Tamaki et al. 1992). Following intravenous bolus administration, the myocardial wash out of activity demonstrates a biexponential clearance. The myocardial oxidative metabolism, however, can be estimated based on the rapid washout rate determined, using monoexponential curve fitting of the time–activity data (Armbrecht et al. 1989). Because of its high myocardial first-pass extraction fraction, the early phase (1–3 min) is flow dependent and provides an estimation of regional myocardial perfusion (Gropler et al. 1991; Sciacca et al. 2001). With [^{11}C]acetate, simultaneous determination of myocardial blood flow and oxygen consumption can be performed with a single data acquisition (Kudo 2007).

17.3.3 Myocardial Neuronal Imaging

The mammalian heart is characterized by dense adrenergic innervation with a norepinephrine (NE) concentration gradient from the atria to the base of the heart and from the base to the apex of the ventricles. In contrast, parasympathetic innervation is distributed

throughout the atrial and ventricular walls, with a gradient from the former to the latter, with acetylcholine (ACh) being the main neurotransmitter. Both, the sympathetic and parasympathetic tone control the rate of the physiologic stimulation and conduction, while the contractile performance is primarily modulated by sympathetic neurotransmission. The major neurotransmitters of the sympathetic and parasympathetic systems, NE and ACh, define the stimulatory and inhibitory physiologic effects of each system.

The NE is produced from tyrosine within a neuron (Fig. 17.13). Tyrosine is converted to DOPA, which is converted to dopamine by *DOPA decarboxylase*. Dopamine is then transported by a vesicular monoamine transporter (VMAT2) into the vesicles, where it is converted to NE by dopamine β-hydroxylase. Adrenergic nerve stimulation leads to the release of NE into the synapse. The sympathetic neurotransmission in the heart is mediated by adrenoreceptors of type β_1 and β_2, which

are located on the myocardial cells. Only a small amount of NE, released into the synapse, binds to the adrenoreceptors while most of the NE in the synapse undergoes reuptake (uptake-1 mechanism) back into the presynaptic nerve terminal by a saturable and Na^+, temperature, and energy dependent mechanism (uptake-1) via a neuronal norepinephrine transporter (NET) or by nonsaturable, and not Na^+, temperature or energy dependent mechanism (uptake-2). The free cytosolic NE is degraded by MAO to dihydroxyphenylglycol (DHPG).

Choline, the precursor for the synthesis of ACh is transported into the parasympathetic presynaptic nerve terminal, where *choline acetyl transferase* (ChAT) catalyses the reaction between acetyl CoA and choline. ACh is then stored in the vesicles and upon nerve stimulation is released into the cholinergic synapse where it binds to specific receptors (mAChR). Within the synapse, ACh is also rapidly degraded by *acetylcholinesterase* (AChE) acetate and choline.
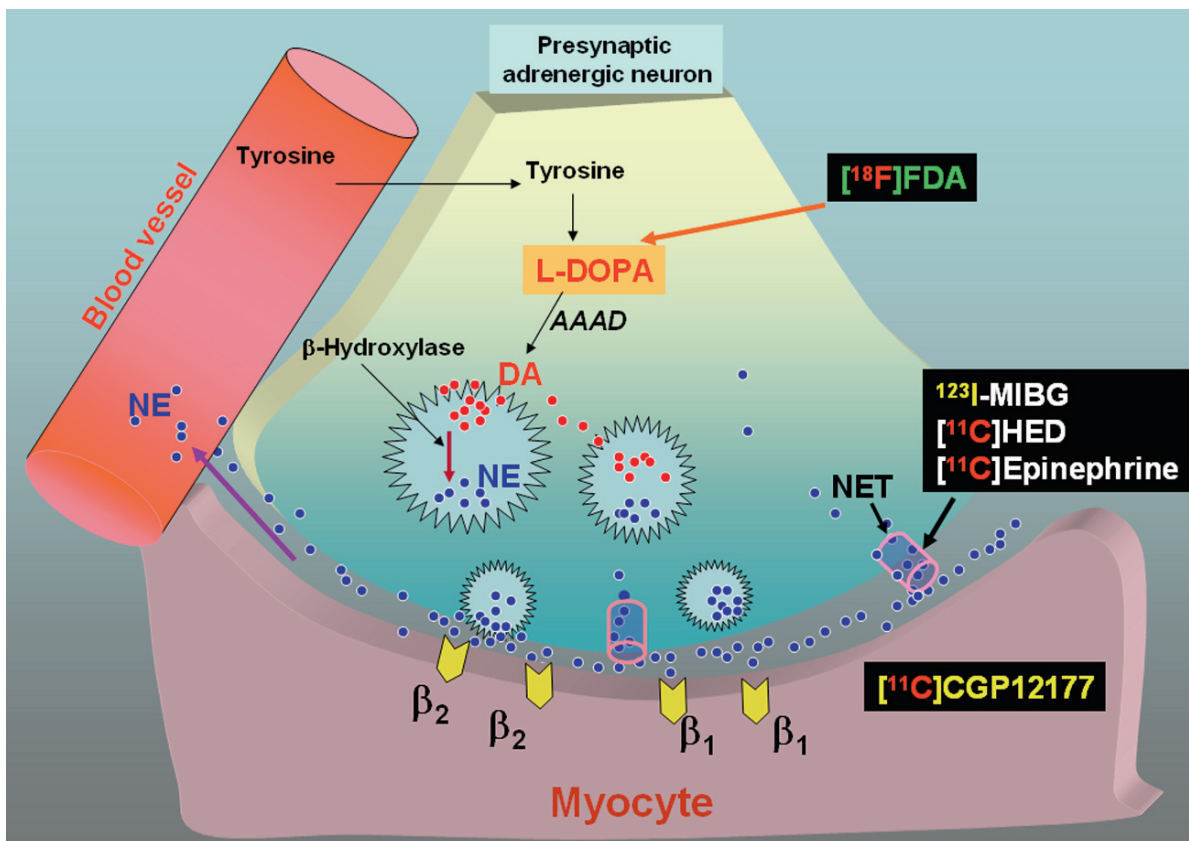
Fig. 17.13 Adrenergic neurotransmission in the heart. PET and SPECT tracers for imaging presynaptic adrenergic neurons and postsynaptic adrenoceptor density

With conventional anatomic imaging techniques, it is not possible to separate nerve fibers from myocardial or vascular cells. Using molecular imaging radiotracers, that are specifically retained in the neuronal structures, it is possible to image the cardiac neuronal innervation and regional distribution.

17.3.3.1 Radiotracers for Presynaptic Sympathetic Innervation

All of the radiotracers developed for imaging cardiac sympathetic innervation are analogs of NE (Fig. 17.14). As discussed earlier, NE within the synapse is transported back into the presynaptic neuron terminals via NETs, based on the uptake-1 mechanism. Structural analogs of NE such as epinephrine, guanethidine, and metaraminol are also transported into synaptic terminals by this uptake-1 mechanism (Raffel and Wieland 2001)

^{123}I-MIBG

Guanethidine is a potent neuron-blocking agent that acts selectively on sympathetic nerve endings. Based on this molecule, [131]I-*meta*-iodobenzylguanidine (MIBG) was initially developed as an agent for imaging
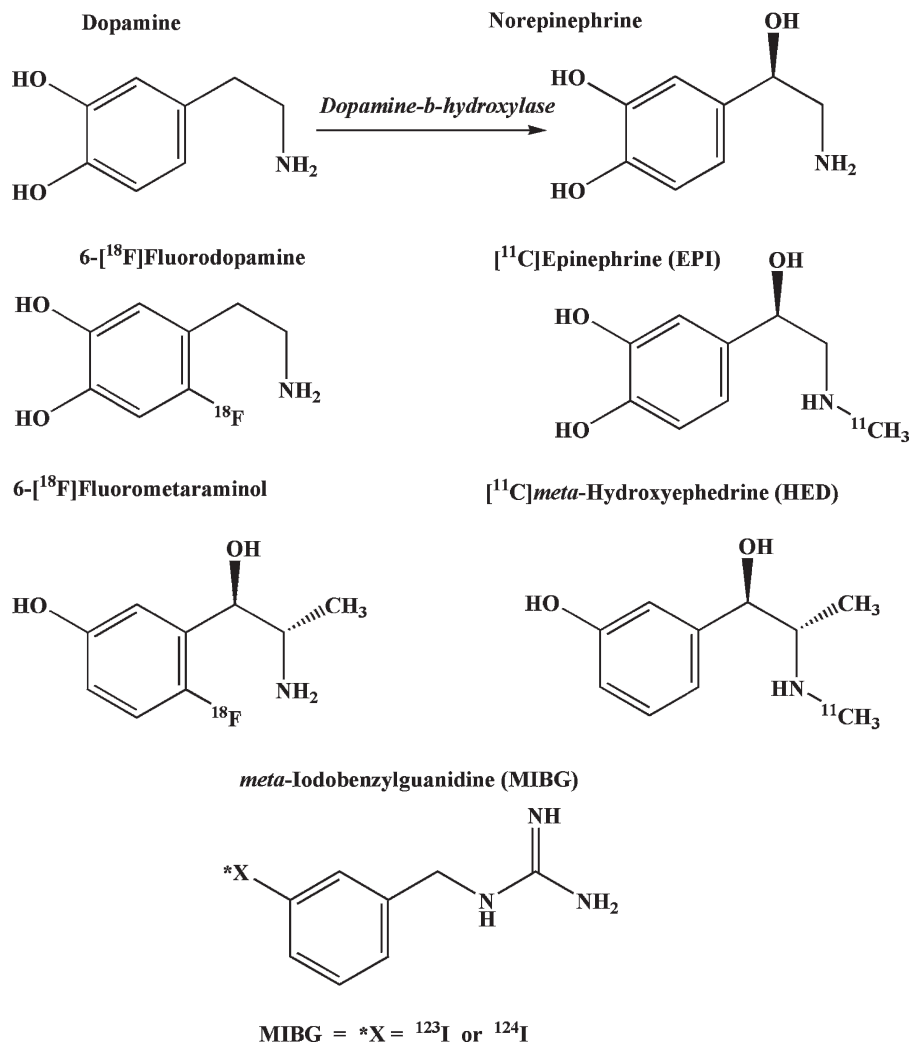
Fig. 17.14 Norepinephrine analogs labeled for PET and SPECT imaging studies to assess cardiac neurotransmission

tumors of adrenal medulla origin (Wieland et al. 1979). The avid heart uptake and retention of MIBG observed in animal biodistribution studies strongly suggested that MIBG might also be successfully used for imaging cardiac sympathetic neurons (Wieland et al. 1981). Consequently, ^{123}I-MIBG was developed for imaging the heart, in patient studies (Kline et al. 2001). MIBG is transported into presynaptic terminals by the uptake-1 mechanism and is stored mainly in the NE storage vesicles. In other words, MIBG and NE have the same mechanisms for uptake, storage and release. Unlike NE, MIBG does not bind to receptors on the myocardial cell membrane, and does not undergo any metabolism within the presynaptic terminals (Carrió 2001; Yamashina and Yamazaki 2007). As a result, MIBG is retained in sympathetic nerve endings, and provides clinically useful diagnostic information for different cardiac diseases.

For practical clinical application the SA and radiochemical purity of MIBG are critical factors. The unlabeled catecholamines (cold MIBG) may compete with the labeled tracer and may not only limit image quality but also cause pharmacologic action via adrenoceptor activation. Therefore, high SA ^{123}I-MIBG (1,665–2,035 MBq mg^{-1}) may be beneficial for clinical studies.

Radiotracers for PET

PET radiotracers (Fig. 17.14) resemble the endogenous NE more closely than MIBG. Two different groups of PET tracers are available for presynaptic sympathetic imaging of the heart; radiolabeled catecholamines and radiolabeled catecholamine analogs (Carrió 2001; Lautamäki et al. 2007).

[11C]Hydroxyephedrine (HED) is the most widely used tracer for cardiac neuronal imaging. HED has high affinity for the NETs and shows negligible nonspecific binding. Following transport into the presynaptic terminal, it is not metabolized by *MAO* or *COMT* enzymes (Rosenpire et al. 1990; Carrió 2001). Since HED is not metabolized, it diffuses out of the nerve terminal and is transported back into the nerve terminal. Therefore, HED myocardial retention is actually dependent on both the continuous release and reuptake by NETs (Lautamäki et al. 2007).

While HED is a false neurotransmitter, [11C]epinephrine (EPI) is a more physiological tracer since it is primarily a circulating hormone produced together with NE by the adrenal medulla and other chromaffin tissues. Unlike HED, EPI is degraded by MAO, but its storage in the vesicles is very efficient, preventing it from degradation and causing slow clearance of the tracer from the heart. Therefore, EPI reflects the whole cascade of uptake, metabolism, and storage of neurotransmission, while the primary target for HED and MIBG is the uptake-1 system. Both, HED and EPI can be synthesized with high chemical purity (> 95%) and SA (33–74 GBq µmol^{-1}). As a result, [11C] tracers may be better compared to the MIBG preparation for quantitative measurement of presynaptic NETs in cardiac disease.

6-[18F]fluorodopamine has been safely used in humans to assess cardiac and extracardiac sympathetic innervation. Based on the synthesis method used, one can obtain SA in the range of 7,400–29,600 MBq mmol^{-1} (Carrió 2001). Following intravenous administration, it is transported into the presynaptic sympathetic nerve terminals via the uptake-1 mechanism, after which it is rapidly internalized into the vesicles and β-hydroxylated, forming radiolabeled NE (Goldstein et al. 1993). The release of this tracer into the synapse and reuptake into the nerve terminal are similar to NE. However, [18F]fluorodopamine, can undergo extensive metabolism in vivo. While this tracer is potentially useful to assess NE synthesis, transport and storage in the vesicles of presynaptic adrenergic neurons, PET quantitation needs the incorporation of the fluorodopamine metabolism in the compartmental modeling techniques.

17.3.3.2   Radiotracers for Cardiac Neuroreceptors

The sympathetic adrenoreceptors β$_1$ and β$_2$, located on the myocardial cells, play a major role in the regulation of cardiac function. In the healthy myocardium, β$_1$-receptors are the most abundant, forming 80% of all β-receptors, while in heart failure the proportion of β$_2$-adrenoceptors may increase to 50% (Schaèfers et al. 2002; Lautamäki et al. 2007). Also, sympathetic activation results in the elevation of systemic catecholamine levels and subsequent down regulation of β-receptors. Many different pharmaceuticals, that act as cardiac receptor antagonists, such as β-blockers or β-receptor antagonists, are used in cardiological practice. The efficacy of these drugs depends on many different factors, especially the β-receptor density. Noninvasive imaging and quantitation of β-receptor

density (B_{max}) before initiation of therapy with β-blockers might predict the outcome of therapy.

[^{11}C]CGP-12177 (4-(3-t-butylamino-2-hydroxypropoxy)-benzimidazol-1), a hydrophilic, nonselective antagonist (Fig. 17.8), that binds to the β-receptors with high affinity (0.3 nmol L^{-1}), was one of the first ligands developed for cardiac PET adrenoreceptor imaging studies (Delforge et al. 1991). CGP-12177 can be labeled with ^{11}C using CGP-17704 and ^{11}C-phosgene as precursors. Subsequently, a number of β-blockers, such as pindolol, atenolol, propranolol, carazolol, metopronolol have all been labeled with ^{11}C, but none of these agents have optimal imaging characteristics. So far, [^{11}C]CGP-12177, is the only tracer, that has been used more extensively in patient populations, such as patients with dilated hypertrophic and arrhythmogenic right ventricular cardiomyopathy (Carrió 2001; Lautamäki et al. 2007). Because of the difficulties involved in the synthesis of this tracer, the N-isopropyl derivative, [^{11}C]CGP-12388 was developed as an alternative for clinical use (Elsinga et al. 2004).

Carazolol is a lipophilic, nonselective β-adrenoceptor antagonist and can be labeled with either ^{11}C or ^{18}F (Berridge et al. 1994). The in vivo binding is stereoselective because the R-isomer does not accumulate in the target organs.

17.3.3.3 Clinical Applications

Clinical PET findings in diseases associated with cardiac neuronal dysfunction of the adrenergic system are summarized in Table 17.3. MIBG myocardial scintigraphy is one of the few methods available for objectively evaluating cardiac sympathetic function at the clinical level, and provides an abundance of information useful for the evaluation of various heart diseases (Yamashina and Yamazaki 2007). Sympathetic nerve endings are easily damaged by ischemia, in comparison to myocardial cells, and sympathetic function disorders are known to persist for a certain period even after alleviation of the ischemia. In patients with unstable angina, MIBG-SPECT makes it possible to identify the culprit coronary artery with a high probability, and, thus is of diagnostic value (Fig. 17.15). In patients with heart failure, the increased washout rate and the decreased heart/myocardium (H/M ratio) on the delayed MIBG image become marked with an increase in hypofunction in the left ventricle, regardless of the underlying diseases (Imamura et al. 1995). Similar results have been reported from studies on dilated cardiomyopathy, hypertrophic cardiomyopathy (HCM), valvular heart disease, pulmonary hypertension, amyloidosis and diabetes (Yamashina and Yamazaki 2007).

Table 17.3 PET and SPECT studies to assess myocardial neuronal transmission

Disease	Radiotracer	Findings
Heart failure	[^{11}C]HED	Globally and regionally decreased uptake
	[^{11}C]CGP12177	Reduction in β-adrenoceptor density
	[^{11}C]CGP12388	
	^{123}I-MIBG	Increased washout rate and the decreased heart/myocardium ratio on the delayed MIBG image become marked with an increase in hypofunction in the left ventricle
Heart transplant	[^{11}C]HED	Denervated hearts show no tracer uptake.
Diabetes	[^{11}C]HED	Tracer uptake reduced in neuropathy. Sympathetic dysinnervation is related to impaired coronary reserve and diastolic dysfunction
CAD	[^{11}C]HED	Sympathetic dysinnervation in chronic CAD
	[^{18}F]Fluorodopamine	Association between coronary reserve and segmental tracer uptake
	^{123}I-MIBG	Decreased regional myocardial uptake in patients with unstable angina and vasospastic angina, and in nonQ-wave myocardial infarction
	[^{11}C]CGP12177	Reduced β-adrenoceptor density after myocardial infarction
Arrhythmias	HED	Normal, increased or reduced uptake
	[^{11}C]CGP12177	Decreased β-adrenoceptor density in patients with arrhythmogenic right ventricular cardiomyopathy and in RVOT tachycardia

$Note$: The above table was modified from Lautamäki et al. (2007)
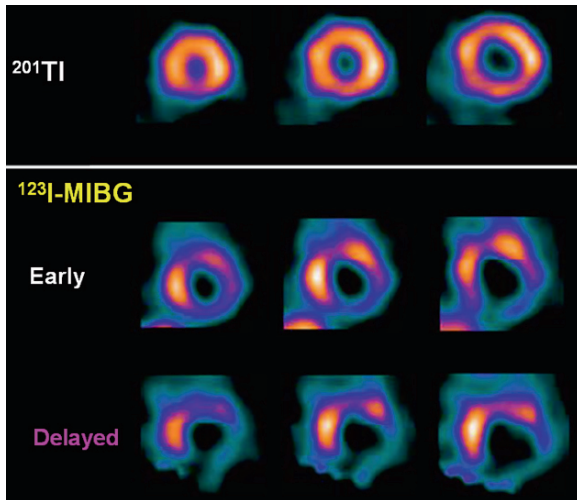
Fig. 17.15 ^{123}I-MIBG imaging in patient with ischaemic heart disease. In a patient with unstable angina, myocardial perfusion with ^{201}Tl-SPECT at rest was relatively normal with no significant findings. In contrast, MIBG SPECT (early and delayed) showed decreased accumulation in the infero-posterior wall. Coronary angiography performed later, advanced stenosis was recognized in the proximal part of the RCA (Yamashina and Yamazaki 2007)

PET imaging of the cardiac autonomic nervous system has advanced extensively in recent years, and multiple pre- and postsynaptic tracers have been used

to determine the involvement of the sympathetic dys-innervation at different stages of heart diseases, such as ischemia, heart failure, and arrhythmia. In general, [^{11}C]HED is the most widely used PET tracer for cardiac neuronal imaging. In a healthy heart, there is an even distribution of HED over the left ventricle, making it a valuable tracer for detecting specific regional defects of the presynaptic sympathetic system in disease (Lautamäki et al. 2007). In patients with dilated cardiomyopathy there is a loss of neurons or downregulation of uptake-1. In a patient with idiopathic dilated cardiomyopathy and severely reduced left ventricular ejection, the myocardial retention of HED was reduced significantly (Fig. 17.16). Similarly, a PET study with [^{11}C]-CGP12177 has shown that in patients with idiopathic dilated cardiomyopathy, there is a significant reduction in the amount of left ventricular β-adrenoceptors (Merlet et al. 1993).

17.3.4 Angiogenesis

Angiogenesis is a process fundamental to neovascularisation stimulated by inflammation and ischemia. Angiogenesis is generally defined as the growth and development of new capillary blood vessels from
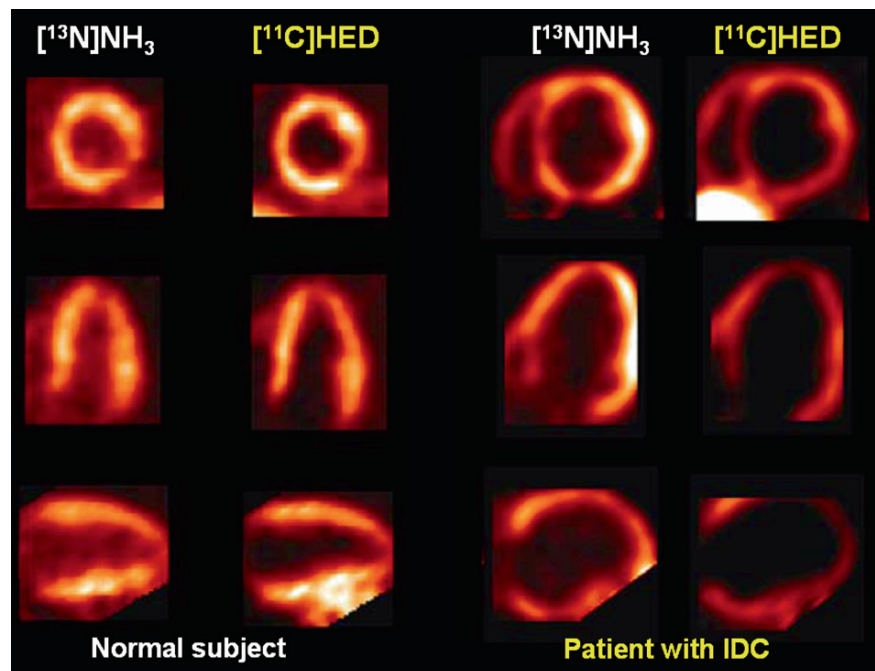
Fig. 17.16 [^{11}C]HED-PET for imaging presynaptic sympathetic innervation in the heart. In a normal subject, there is an even distribution of HED in the heart similar to the myocardial perfusion images of [^{13}N] ammonia-PET. In a patient with idiopathic dilated cardiomyopathy (IDC) and severely reduced left ventricular ejection fraction (22%), there is a significantly reduced retention of HED compared with the myocardial perfusion (Lautamaki et al 2007)

Fig. 17.17 ^{18}F-galacto-RGD, a specific radiotracer to image angiogenesis based on αvβ3 integrin expression in a rat model of coronary occlusion. In vivo short axis MicroPET images demon- strate a focal uptake of galacto-RGD in an area with a decrease in myocardial perfusion. The images were obtained 1 week after the ischaemic event (Higuchi et al 2007)

preexisting vasculature involving mature endothelial cells (Carmeliet 2000). Myocardial ischemia causes reversible or irreversible myocardial injury and trig- gers the formation of collateral vessels via angiogenesis, which occurs as part of the natural healing process after ischemic injury. The process of angiogenesis involves a complex interplay of many molecules and cells (vascular smooth muscle cells, endothelial cells, macrophages, and circulating stem cells), as well as the extracellular matrix (ECM) (Higuchi et al. 2007). Migration and proliferation of endothelial cells are promoted by angiogenic factors, such as vascular endothelial growth factor (VEGF) and basic fibroblast growth factor (bFGF), which are released from the endothelial and inflammatory cells via transcription factors, such as activation of hypoxia-inducible factors (HIFs). During angiogenesis endothelial cells must adhere to one another and to the ECM to construct and extend new microvessels. Integrins, a family of het- erodimeric cell surface receptors capable of mediating cell adhesion, migration, proliferation, differentiation, and survival play a major role in the angiogenic response. Among them, $\alpha_v\beta_3$ integrin has been identi- fied as a critical modulator of angiogenesis. Radiolabeled tracers targeting αvβ3 integrin expres- sion was evaluated in animal models of myocardial ischemia using ^{18}F-galacto-RGD, ^{111}In-RP747, and ^{99m}Tc-NC100692 (Higuchi et al. 2007). In preclinical studies, ^{18}F-galacto-RGD has shown focal tracer accu- mulation in the ischaemic heart in specific areas that have decreased perfusion on [1[3]N]ammonia-PET, one week after the ischaemic event (Fig. 17.17). Further,

the in vivo image data showed excellent correlation with autoradiographic data.

VEGF is one of the most important and potent angiogenic factor in the regulation of endothelial cell proliferation. Expression of the VEGF gene and VEGF receptors is strongly enhanced by hypoxia in the angio- genic process. Therefore, VEGF receptors are good candidates for imaging angiogenesis in ischaemic tis- sues. ^{111}In-labeled recombinant human VEGF[121] has shown specific tracer localization in a rabbit model of unilateral hindlimb ischemia (Lu et al. 2003).

Matrix metalloproteinases (MMP) are proteolytic enzymes that cause extracellular protein degradation and are involved in the endothelial cell migration and growth factor liberation. MMPs are also responsible for the left ventricular remodeling by degrading extracellular matrix in the heart after myocardial infarction. Recently, Su et al. demonstrated the feasibility of MMP activation imaging in a murine model of myocardial infarction. Further ^{111}In and ^{99m}Tc labeled RP782 were developed and evaluated in animal models (Su et al 2005).

17.3.5 Vulnerable Plaque and Atherothrombosis

The executive summary of the screening for heart attack prevention and education (SHAPE) task force report, published in 2006, suggests that a molecular imaging technique that could accurately identify the site of vulnerable plaques should be one of the four

Fig. 17.18 The biology of atherosclerosis initiation, progression, and complications. CCR2 = chemokine (CC motif) receptor 2; MCP = monocyte chemoattractant protein; M-CSF = monocyte colony-stimulating factor; MMP = matrix metalloproteinase; ROS = reactive oxygen species; VCAM = vascular cell adhesion molecule. (From Jaffer et al 2006)
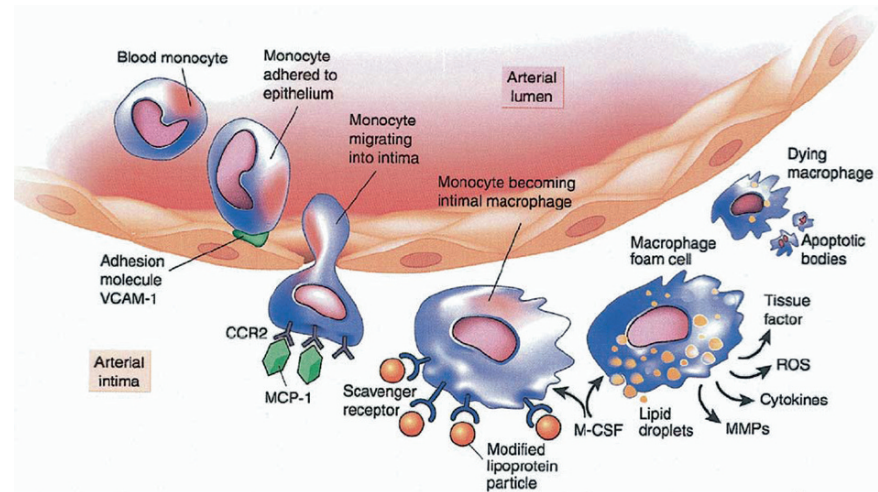
major areas of future research in CAD (Naghavi et al. 2006). A number of noninvasive and invasive diagnostic imaging techniques are being evaluated to accurately identify high-risk individuals, based on the presence of high-risk anatomical or structural features of atherosclerotic plaques in the coronary arteries. However, imaging coronary lesions is a challenge since they are contained within the wall of the vessel, and typically these lesions occupy a fraction of the vessel circumference and often extend from 1 to 2 cm. In addition, the residual activity of the radiotracer in blood, and the myocardial tissue uptake of the radiotracer make these lesions more difficult to detect. Molecular imaging technique based on specific β^+ emitting radiotracers, however, may provide the potential to detect coronary atherosclerotic lesions.

The biology of atherosclerosis (Fig. 17.18) provides a basis for the development of radiolabeled molecular imaging probes. Fundamentally, the process of inflammation regulates atherosclerosis. Specifically, the macrophage has emerged as the key cellular mediator of inflammation in atheroma, and participates in all phases of atherogenesis, including lesion initiation, progression, and complication (Falk 2006; Jaffer et al. 2006). Following the initial recruitment of monocytes into the arterial wall, the cells mature into macrophage, which ingest oxidized lipoproteins, become foam cells, and, thus, contribute to the atheroma expansion. A subset of macrophages can die within the atheroma, via oncosis and/or apoptosis (programmed cell death),

leading to the development of a paucicellular lipid core. Macrophages also produce and/or secrete a number of proteases, such as cathepsins and matrix metalloproteinases (MMP), that can degrade the extracellular matrix comprising the fibrous cap. Autopsy studies have demonstrated prominent macrophage accumulation in ruptured atherosclerotic lesions (Davies et al. 2006). These findings underscore the key role of macrophages in plaque complications (Naghavi et al. 2006). Under inflammatory conditions, endothelial cells express adhesion molecules, such as VCAM-1. In addition, the fragile endothelium in angiogenic vessels, typically associated with $\alpha_v\beta_3$ integrin, can promote lesion progression via intraplaque hemorrhage and may produce plaque complications. Apoptosis of both macrophages and vascular smooth muscle cells is seen in the wall of atherosclerotic vessels. Smooth muscle cells undergoing programmed death in the fibrous parts of plaque have been shown to express genes encoding for inflammatory cytokines and chemoattractant factors (Libby 2002), and colocalize with oxidized low-density lipoprotein. Apoptosis of macrophages is found in the vulnerable plaque. Thus, the biology of atherosclerotic lesion itself provides the basis for the development of atherosclerosis-targeted molecular imaging probes (Table 17.4). In order to identify the most specific radiotracers for imaging vulnerable plaques in patients who are at very high risk, several promising imaging agents need comparative evaluation in the same animal model, under similar pathophysiological conditions.

Table 17.4 Atherothrombosis: Imaging targets and radiotracers

Biological process	Class	Specific molecular target	Radiotracer
Cholestrol transport	Lipid core	Low density lipoprotein (LDL)	^{99m}Tc or ^{111}In-LDL Radiolabeled peptides (based on Apo B-100)
Macrophage activity	Surface receptors	Scavenger receptor A, Monocyte chemoattractant peptide (MCP)	^{99m}Tc-oxidized-LDL
		Peripheral Benzodiazepine receptor	^{123}I-MCP-1
			^{123}I- or [^{11}C]PK11195
	Metabolism	*Hexokinase Choline kinase*	[^{18}F]FDG, [^{18}F]Fluorocholine
	Proteases	Matrix metalloproteinase (MMP),Cathepsins	^{123}I-HO-CGS 27023A (MMP inhibitor)
	Peroxidases	Myeloperoxidase (MPO)	[methyl^{11}C]ABAH
	Modified lipoproteins	Oxidized LDL,	^{99m}Tc-oxidized-LDL
Angiogenesis	Increased vascularity	Perfusion markers	
	Endothelium	VCAM-1, E-selectin $\alpha_v\beta_3$ integrin	^{64}Cu-DOTA-RGD
			^{18}F-gluco-RGD
			^{111}In-RP748
			^{111}In-VEGF121
Apoptosis	Cell membrane	Phosphatidylserine	^{99m}Tc-Annexin V (A5)
			^{18}F-annexin V
			^{64}Cu-DOTA-Annexin V
	Enzymes	Caspases, scramblases	
Cell trafficking	Monocytes, lymphocytes, Stem cells	Specific molecular target	Radiolabeled cells
Thrombosis	Activated platelets	GP IIB/IIIA RGD peptides	^{111}In or ^{64}Cu-DOTA-P280, P748 peptides

Radiotracer	E	MBF (mL min^{-1} g^{-1})	
		Rest	Stress[a]
[^{15}O]Water	0.96 ± 0.05	0.90 ± 0.22	3.55 ± 1.15
[^{13}N]Ammonia	0.83–0.60	*Glutamine synthase*	
^{82}Rb chloride	0.68–0.60	0.80 ± 0.26	
^{62}Cu-PTSM			

[a]After intravenous dipyridamole

17.3.5.1 Radiotracers for Vulnerable Plaque

In the 1970s it was first demonstrated that ^{125}I-labeled LDL localizes in the carotid atherosclerotic lesions in human subjects (Lees et al. 1983). Since that time a number of radiolabeled LDL preparations, antibodies, and peptides have been extensively evaluated in animal models as potential radiotracers for imaging atherosclerotic lesions (Vallabhajosula et al. 1995).

Molecular imaging based on PET and SPECT radiotracers is a rapidly evolving discipline that aims to develop imaging agents and technologies to visualize the specific molecular processes associated with vulnerable plaque. In the 1990s, it was demonstrated that FDG-PET identifies macrophage rich atherosclerotic lesions in hypercholesterolemic rabbits (Fig. 17.18) (Vallabhajosula et al. 1995; Vallabhajosula and

Fuster 1997). It was also shown that FDG-PET is useful to detect the atherosclerotic lesions in the carotid arteries of patients undergoing surgery (Fig. 17.19) (Rudd et al. 2002). Based on the carotid specimens from these patients, it was also shown that FDG specifically localizes in the macrophages very close to the fibrous cap. Subsequently, localization of FDG in human atheromas has been documented for the carotid arteries, aorta and other major vessel (Weissberg 2004; Ben-Haim and Israel 2006). The potential of FDG-PET to identify vulnerable plaques characteristic of subclinical coronary disease, however, has not yet been validated. Several other radiotracers have also been proposed as specific markers for imaging vulnerable plaque and atherosclerosis (Table 17.4).

(*R*)-[11C]PK11195 (1-[2-chlorophenyl]-*N*-methyl-*N*-[1-methyl-propyl]-3-isoquinoline carboxamide) is a
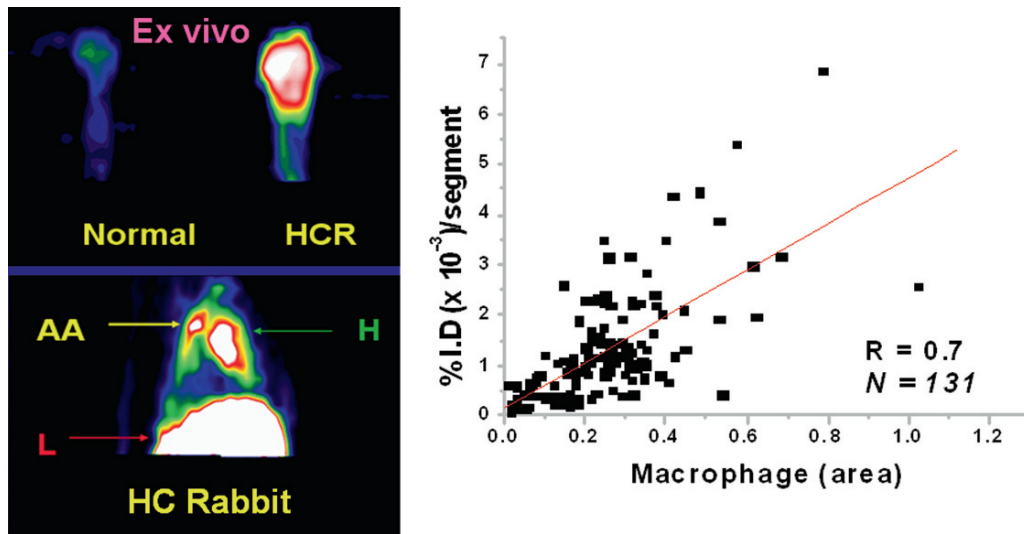
Fig. 17.19   [^{18}F]FDG-PET to image atherosclerosis in hypercholeterolemic rabbits (HCR). The bottom in vivo image shows FDG uptake in the ascending aorta (AA) of HCR while the top ex vivo image shows comparison of HCR and normal aortas. The FDG uptake in the atherosclerotic lesions appears to depend on the macrophage density

specific ligand for the peripheral benzodiazepine binding site, which is particularly abundant on cells of the mononuclear phagocyte lineage. Several investigators have previously used this tracer to image activated microglia/brain macrophages (Banati 2003). Choline is taken up into cells and phosphorylated by choline kinase, metabolized to phosphatidylcholine, and eventually incorporated into the cell membrane. [^{18}F]fluorocholine (FCH) has been introduced as a tracer for tumor, but it also is taken up by macrophages. Recently, FCH has been shown to be taken up by murine atherosclerotic lesions ex vivo and the uptake of FCH was even greater than that of FDG (Matter et al. 2006). As discussed above, apoptosis is a potential target for imaging atherosclerosis since annexin V specifically binds to apoptotic cells with nanomolar affinity. ^{99m}Tc-Annexin V has shown strong uptake in the balloon injured aortas of cholesterol-fed rabbits and identified coronary atherosclerotic lesions in a porcine model of atherosclerosis. In a clinical study, ^{99m}Tc-Annexin V has demonstrated in vivo uptake into carotid plaques, containing macrophages and intraplaque hemorrhage, but not in the carotid plaques with stable histological features (Kietselaer et al. 2004). Annexin V has been labeled with other SPECT radionuclides (^{123}I and ^{111}In) and can be also be labeled with PET radionuclides, such as ^{18}F, ^{124}I and ^{64}Cu. Matrix metalloproteases (MMP) can degrade extracellular matrix macromolecules, including elastin and collagen. Further, increased MMP activity in humans suggests a causative role for MMPs. Imaging of MMP activity in atherosclerosis, therefore, offers another method for detecting inflamed atherosclerotic lesions.^{123}I and ^{111}In labeled compounds that bind to MMP were recently shown to be taken up by carotid lesions in a mouse model (Schafers et al. 2004). Myeloperoxidase (MPO) is also present within human atherosclerotic plaques and its products may promote atherogenesis by modifying LDL to an atherogenic form, functionally inactivating HDL, activating MMPs, causing endothelial cell apoptosis, tissue factor release, and inactivation of nitric oxide. Recently benzoic acid hydrazides have also been identified as preferred inhibitors of MPO. Among these agents, 4-aminobenzoic acid hydrazide (ABAH) is the most potent inhibitor identified to date. Its binding leads to irreversible inactivation of the enzyme by a suicide substrate mechanism.

The "high risk," "thrombosis prone," and "vulnerable" plaques all describe a plaque that is at increased risk of thrombosis and rapid stenosis progression. Since these plaques are often not identified, before causing clinical events, there is great need to identify these plaques before the onset of symptoms. Based on noninvasive imaging techniques, patients identified as being at "high-risk" need further stratification to identify those with vulnerable plaques who are at "very high

risk." The development of novel imaging modalities capable of detecting vulnerable plaques is hindered by the lack of a suitable animal model with plaque characteristics that have clinical relevance. Also, the design of radiotracers capable of detecting and characterizing rupture-prone lesions in humans, may eventually lead to the development of (a) noninvasive, relatively safe, screening technique to identify patients with subclinical disease and (b) innovative therapeutic alternatives designed to "passivate" the plaque with the potential of preventing future major cardiovascular events.

17.3.5.2 Radiotracers for Intraarterial Thrombus

Blood clots or thrombi in veins are generally composed of layers of zones of polymerized fibrin with entrapped plasma proteins and red cells (red thrombus), interspersed with whitish layers primarily composed of aggregated platelets. In arteries and in areas where the thrombus is exposed to high blood flow rates, the thrombus may predominantly consist of activated platelet aggregates. In contrast, when the thrombus is completely occlusive, where the blood flow is sluggish, the thrombus may predominantly consist of fibrin deposits. In order to develop molecular imaging probes to image thrombus in vivo, radiotracers have been developed based on two different approaches; Radiotracers that bind specifically to fibrin or to activated platelets. Radioiodinated (^{125}I or ^{123}I) fibrinogen was introduced almost three decades ago for imaging deep vein thrombosis (DVT). Subsequently, platelets labeled with ^{111}In oxine were introduced for imaging active thrombi in vivo. Since radiolabeled fibrinogen and platelets have long circulation times a number of radiolabeled peptides and polypeptides have been developed for thrombus imaging. The development of radiopharmaceuticals for thrombus detection have been reviewed extensively (Knight 2001; Taillefer 2001)

Autologous platelets can be labeled efficiently with ^{111}In or ^{99m}Tc- lipophillic complexes, such as oxine and tropolone. A number of clinical studies have demonstrated ^{111}In-platelet uptake in atherosclerotic lesions of carotid and femoral arteries, and in the abdominal aorta (Knight 1990, 2001).The $\alpha_{IIb}\beta_3$ integrin (GP IIb/IIIa receptor) on platelets is the most commonly targeted receptor for imaging platelet deposits in thrombi. These receptors are present in high concentrations on activated platelets with fibrin-

ogen being main ligand for these receptors. The main binding region of fibrinogen contains a tripeptide motif RGD (Ag–Gly–Asp). Further, it has been shown that a number of small peptides containing RGD sequence also bind to these receptors. It has also been observed that in addition to the RGD sequence other tripeptide motifs, such as RYD (Arg–Tyr–Asp) present in PAC-1 antibody and KGD present in polypeptides known as disintegrans (such as bitistatin), bind to the glycoprotein IIb/IIIa receptor on activated platelets. A number of linear peptides (such as PAC-3 and PAC-8) and cyclic peptides (such as DMP-728, MK-0852 and integrilin) containing RGD or RYD motifs were developed. Among the cyclic peptides, integrilin is an FDA approved antithrombotic drug, while ^{99m}Tc-P280 or Apcitide (AcuTect) is approved for imaging DVT (Taillefer 2001; Knight 2003).

Radioiodinated fibrinogen was the first scintigraphic agent used successfully to detect thrombus. This tracer localizes only in actively growing thrombus, but requires delayed imaging for optimal diagnostic accuracy because the plasma clearance of the tracer is very slow. Fibrinogen is a bivalent plasma protein consisting of three polypeptide chains (a, b, and g). During clotting, the enzyme, thrombin cleaves the fibrinopeptides from the fibrinogen leading to the formation of a fibrin polymer. Within hours after acute thrombus formation, a number of fibrin degradation products are formed. Both, 1^{23}I and ^{99m}Tc labeled fibrin fragment E1 (60 kDa) have shown excellent thrombus uptake in vivo (Knight 1993). In addition it has been shown that a peptide with the sequence, Gly–Pro–Arg–Pro, is capable of inhibiting fibrin polymerization. It has also been shown that the pentapeptide, Gly–Pro–Arg–Pro–Pro (GPRPP), has the highest fibrinogen/thrombin clotinhibiting activity (Laudano and Doolittle 1978). An analog of GPRPP, ^{99m}Tc-TP850 with high affinity for a chain of fibrin polymer was also found to localize, in a swine model of experimental deep venous thrombosis and pulmonary emboli (Thakur et al. 2000; Aruva et al. 2006).

References

Arimoto T, Takeishi Y, Fukui A, et al (2004) Dynamic ^{123}I-MIBG SPECT reflects sympathetic nervous integrity and predicts clinical outcome in patients with chronic heart failure. Ann Nucl Med 18:145–150

Armbrecht JJ, Buxton DB, Brunken RC, et al (1989) Regional myocardial oxygen consumption determined noninvasively in human with [1–^{11}C]acetate and dynamic positron tomography. Circulation 80:863–872

Arora R, Ferrick KJ, Nakata T, et al (2003) I-123 MIBG imaging and heart rate variability analysis to predict the need for an implantable cardioverter defibrillator. J Nucl Cardiol 10:121–131

Aruva MR, Daviau J, Sharma SS, et al (2006) Imaging thromboembolism with fibrin-avid ^{99m}Tc-peptide: evaluation in swine. J Nucl Med 47:155–162

Banati RB (2003) Neuropathological imaging: in vivo detection of glial activation as a measure of disease and adaptive change in the brain. Br Med Bull 65:121–131

Barron HV, Lesh MD (1996) Autonomic nervous system and sudden cardiac death. J Am Coll Cardiol 27:1053–1060

Basken NA, Mathias CJ, Lipka AE, et al (2008) Species Dependence of the [^{64}Cu]Cu-Bis(thiosemicarbazone) radiopharmaceutical binding to serum albumins. Nucl Med Biol 35:281–286

Ben-Haim S, Israel O (2006) PET/CT for atherosclerotic imaging. QJ Nucl Med Mol Imaging 50:53–60

Bengel FM, Schachinger V, Dimmeler S (2005) Cell-based therapies and imaging in cardiology. Eur J Nucl Med Mol Imag 32:S404–S416

Berman DS, Shaw LJ, Hachamovitch R et al (2007) Comparative use of radionuclide stress testing, coronary artery calcium scanning, and noninvasive coronary angiography for diagnostic and prognostic cardiac assessment. Semin Nucl Med 37:2–16

Berridge MS, Nelson AD, Zheng L et al (1994) Specific beta-adrenergic receptor binding of carazolol measured with PET. J Nucl Med 35:1665–1676

Bing RJ (1954) The metabolism of the heart. In: Harvey Society of NY (ed) Harvey lecture series. Academic, New York

Botker HE, Bottcher M, Schmitz O et al (1997) Glucose uptake and lumped constant variability in normal human hearts determined with [^{18}F]fluorodeoxyglucose. J Nucl Cardiol 4:125–132

Brinkmann JF, Abumrad NA, Ibrahimi A et al (2002) New insights into long-chain fatty acid uptake by heart muscle: a crucial role for fatty acid translocase/CD36. Biochem J 367:561–570

Brooks P, Clark R, Cheresh D (1994) Requirement of vascular integrin alpha v beta 3 for angiogenesis. Science 264:569–571

Buckman BO, Van Brocklin HF, Dence CS et al (1994) Synthesis and tissue distribution of [omega-^{11}C]palmitic acid. A novel PET imaging agent for cardiac fatty acid metabolism. J Med Chem 27:2481–2485

Carmeliet P (2000) Mechanisms of angiogenesis and arteriogenesis. Nat Med 6:389–395

Carrio I (2001) Cardiac neurotransmission maging J Nucl Med 42:1062–1076

Davies JR, Rudd JHF, Weissberg PL, et al (2006) Radionuclide imaging for the detection of inflammation in vulnerable plaques. J Am Coll Cardiol 47:C57–68

Delforge J, Syrota A, Lancon JP et al (1991) Cardiac betaadrenergic receptor density measured in vivo using PET, CGP12177, and a new graphical method. J Nucl Med 32:739–748

Dilsizian V, Bateman TM, Bergmann SR, et al (2005) Metabolic imaging with beta-methyl-p-[(123)I]-iodophenyl-pentadecanoic

acid identifies ischemic memory after demand ischemia. Circulation 112:2169–2174

Dobrucki LW, Sinusas AJ (2005) Cardiovascular molecular imaging. Semin Nucl Med 35:73–81

Elsinga PH, van Waarde A, Vaalburg W (2004) Receptor imaging in the thorax with PET. Eur J Pharmacol 499:1–13

Falk E (2006) Pathogenesis of atherosclerosis J Am Coll Cardiol 47:C7–C12

Freundlieb C, Hock A, Vyska K (1980) Myocardial imaging and metabolic studies with [17–^{123}I]iodoheptadecanoic acid. J Nucl Med 21:1043–1050

Fuster V, Corti R, Fayad et al (2003) Integration of vascular biology and magnetic resonance imaging in the understanding of atherothrombosis and acute coronary syndromes J Thromb Haemost 1:1410–1421

Fuster V, Moreno PR, Fayad ZA et al (2005) Atherothrombosis and high-risk plaque part I: evolving concepts. J Am Coll Cardiol 46:937–954

Geng YJ, Libby P (1995) Evidence for apoptosis in advanced human atheroma. Am J Pathol 147:251–266

Goldstein DS, Eisenhofer G, Dunn BB et al (1993). Positron emission tomographic imaging of cardiac sympathetic innervation using 6-[^{18}F]fluorodopamine: initial findings in humans. J Am Coll Cardiol 22:1961–1971

Gould KL, Lipscomb K, Hamilton GW (1974) Physiologic basis for assessing critical coronary stenosis: instantaneous flow response and regional distribution during coronary hyperemia as measures of coronary flow reserve. Am J Cardiol 33: 87–94

Gropler RJ, Siegel BA, Geltman EM (1991) Myocardial uptake of carbon-11-acetate as an indirect estimate of regional myocardial blood flow. J Nucl Med 32:245–251

Heineman FW, Balaban RS (1993) Effects of after load and heart rate on NAD(P)H redox state in the isolated rabbit heart. Am J Physiol Heart Circ Physiol 264:H433–H440

Higuchi T, Wester HJ, Schwaiger M (2007) Imaging of angiogenesis in cardiology. Eur J Nucl Med Mol Imaging 34:S9–S19

Huisman MC, Higuchi T, Reder S et al (2008) Initial characterization of an ^{18}F-labeled myocardial perfusion tracer J Nucl Med 49:630–636

Imamura Y, Ando H, Mitsuoka W, et al (1995) Iodine-123 metaiodobenzylguanidine images reflect intense myocardial adrenergic nervous activity in congestive heart failure independent of underlying cause. J Am Coll Cardiol 26:1594–1599

Jain D (1999) Technetium-99 m labeled myocardial perfusion imaging agents. Semin Nucl Med 29:221–236

Jaffer FA, Weissleder R (2004) Seeing within: molecular imaging of the cardiovascular system. Circ Res 94:433–445

Jaffer FA, Libby P, Weissleder R (2006) Molecular and cellular imaging of atherosclerosis. Emerging applications. J Am Coll Cardiol 47:1328–1338

Kietselaer BL, Reutelingsperger CP, Heidendal GA, et al (2004) Noninvasive detection of plaque instability with use of radiolabeled annexin A5 in patients with carotid-artery atherosclerosis. N Engl J Med 350:1472–1473

Kline RC, Swanson DP, Wieland DM et al (2001) Myocardial imaging with I-123-metaiodobenzylguanidine. J Nucl Med 22:129–132

Knapp FF Jr, Ambrose KR, Goodman MM (1986a). New radioiodinated methyl-branched fatty acids for cardiac studies. Eur J Nucl Med 12:S39–S44

Knapp FF Jr, Goodman MM, CallahanAP, et al (1986b) Radioiodinated 15-(p-iodophenyl)-3,3-dimethylpentadecanoic acid: a useful new agent to evaluate myocardial fatty acid uptake. J Nucl Med 27:521–531

Knickmeier M, Matheja P, Wichter T, et al (2000) Clinical evaluation of no-carrieradded meta-(^{123}I)iodobenzylguanidine for myocardial scintigraphy. Eur J Nucl Med 3:302–307

Knight LC (1990) Radiopharmaceuticals for thrombus detection. Semin Nucl Med 20:526

Knight LC (1993) Scintigraphic methods for detecting vascular thrombus. J Nucl Med 34:554–561

Knight LC (2001) Radiolabeled peptide ligands for imaging thrombi and emboli. Nucl Med Biol 28:515–526

Knight LC (2003) Non-oncologic applications of radiolabeled peptides in nuclear medicine. Q J Nucl Med 47:279–91

Kotzerke J, Glatting G, van den Hoff J, et al (2001) Validation of myocardial blood flow estimation with nitrogen-13 ammonia PET by the argon inert gas technique in humans. Eur J Nucl Med 28:340–345

Krivokapich J, Huang SC, Selin CE et al (1987) Fluorodeoxyglucose rate constants, lumped constant, and glucose metabolic rate in rabbit heart. Am J Physiol 252:H777–H787

Kudo T (2007) Metabolic imaging using PET. Eur J Nucl Med Mol Imaging 34:S49–S61

Kyuma M, Nakata T, Hashimoto A, et al (2004) Incremental prognostic implications of brain natriuretic peptide, cardiac sympathetic nerve innervation, and noncardiac disorders in patients with heart failure. J Nucl Med 45:155–163

Landini L, Santarelli MF, Positano V, et al (2005) Molecular imaging: its application in cardiovascular diagnosis. Curr Pharm Des 11:2225–2234

Laudano AP, Doolittle RF (1978) Synthetic peptide derivatives that bind to fibrinogen and prevent polymerization of fibrin polymers. Proc Natl Acad Sci U S A 75:3085–3089

Lautamäki R, Tipre D, Bengel FM et al (2007) Cardiac sympathetic neuronal imaging using PET Eur J Nucl Med Mol Imaging 34:S74–S85

Lees RS, Lees AM, Strauss HW (1983) External imaging of human atherosclerosis. J Nucl Med 24:154–156

Libby P (2002) Inflammation in atherosclerosis. Nature 420:868–874

Liedtke AJ (1981) Alterations of carbohydrate and lipid metabolism in the acutely ischemic heart. Prog Cardiovasc Dis 23:321–336

Lin JW, Sciacca RR, Chou RL et al (2001) Quantification of myocardial perfusion in human subjects using ^{82}Rb and wavelet-based noise reduction. J Nucl Med 42:201–208

Lopaschul GD, Stanley W (1997) Glucose metabolism in the ischemic heart. Circulation 95:415–422

Lu E, Wagner WR, Schellenberger U, et al (2003) Targeted in vivo labeling of receptors for vascular endothelial growth factor: approach to identification of ischemic tissue. Circulation 108:97–103

Machac J (2005) Cardiac positron emission tomography imaging. Semin Nucl Med 35:17–36

Madar I, Ravert HT, Du Y, et al (2006) Characterization of uptake of the new PET imaging compound 18F-fluorobenzyl triphenyl phosphonium in dog myocardium. J Nucl Med 47:1359–1366

Matter CM, Wyss MT, Meier P, et al (2006) ^{18}F-Choline images murine atherosclerotic plaques ex vivo. Arterioscler Thromb Vasc Biol 26:584–589

Merlet P, Delforge J, Syrota A, et al (1993). Positron emission tomography with [^{11}C]CGP - 12177 to assess beta-adrenergic receptor concentration in idiopathic dilated cardiomyopathy. Circulation 87:1169–1178

Muller JE, Abela GS, Nesto RW, et al (1994). Triggers, acute risk factors and vulnerable plaques: the lexicon of a new frontier. J Am Coll Cardiol 23:809–813

Muller JE, Tawakol A, Kathiresan S et al (2006) New opportunities for identification and reduction of coronary risk: treatment of vulnerable patients, arteries, and Plaques. J Am Coll Cardiol 47:C2–C6

Münch G, Nguyen N, Nekolla S et al (2000). Evaluation of sympathetic nerve terminals with ^{11}C-epinephrine and ^{11}C-hydroxyephedrine and positron emission tomography. Circulation 101:516–523

Naghavi M, Libby P, Falk E et al (2003) From vulnerable plaque to vulnerable patient. A call for new definitions and risk assessment strategies: part I. Circulation 108:1664–1672

Naghavi M, Falk E, Hecht HS, et al (2006) From vulnerable plaque to vulnerable patient–Part III: Executive summary of the screening for heart attack prevention and education (SHAPE) task force report. Am J Cardiol 98(2A):2H–15H

Nitzsche EU, Choi Y, Czernin J, et al (1996) Noninvasive quantification of myocardial blood flow in humans. A direct comparison of the [^{13}N]ammonia and the [^{15}O]water techniques. Circulation 93:2000–2006

Opie LH, Owen P (1975) Assessment of myocardial free NAD + /NADH ratios and oxaloacetate concentrations during increased mechanical work in isolated perfused rat heart during production or uptake of ketone bodies. Biochem J 148:403–415

Phelps ME, Huang SC, Hoffman EJ et al (1979) Tomographic measurement of local cerebral glucose metabolic rate in humans with (F-18)2-fluoro-2-deoxy-D-glucose: validation of method. Ann Neurol 6:371–388

Poe ND, Robinson GD Jr, Zielinski FW (1977) Myocardial imaging with ^{123}I-hexadecenoic acid. Radiology 124:419–24

Raffel DM, Wieland DM (2001) Assessment of cardiac sympathetic nerve integrity with positron emission tomography. Nucl Med Biol 28:541–559

Rosenpire KC, Haka MS, Jewett DM et al (1990). Synthesis and preliminary evaluation of ^{11}C-meta-hydroxyephedrine: a false neurotransmitter agent for heart neuronal imaging. J Nucl Med 31:1328–1334

Ross R (1999) Atherosclerosis–an inflammatory disease. N Engl J Med 340:115–126

Rudd JH, Warburton EA, Fryer TD, et al (2002). Imaging atherosclerotic plaque inflammation with [^{18}F]-fluorodeoxyglucose positron emission tomography. Circulation 105:2708–2711

Sanz J, Fayad ZA (2008) Imaging of atherosclerotic cardiovascular disease. Nature 451:953–957

Schaèfers M, Riemann B, Levkau B et al (2002) Current status and future applications of cardiac receptor imaging with positron emission tomography Nucl Med Commun 23:113–115

Schafers M, Riemann B, Kopka K, et al (2004) Scintigraphic imaging of matrix metalloproteinase activity in the arterial wall in vivo. Circulation 109:2554–2559

Schelbert HR (2004) Positron emission tomography of the heart: methodology, findings in the normal and disease heart, and clinical applications. In: Phelps ME (ed) PET: molecular imaging and its clinical applications. Springer, New York

Schön HR, Schelbert HR, Robinson et al (1982) C-11 labeled palmitic acid for the noninvasive evaluation of regional myocardial fatty acid metabolism with positron-computed tomography. I. Kinetics of C-11 palmitic acid in normal myocardium. Am Heart J 103:532–547

Schwaiger M, Bengel FM (2003) From thallium scan to molecular imaging. Mol Imaging Biol 4:387–398

Sciacca RR, Akinboboye O, Chou RL et al (2001) Measurement of myocardial blood flow with PET using 1–^{11}Cacetate. J Nucl Med 42:63–70

Sinusas AJ, Zaret BL (1995) Coronary artery disease. In Wagner HN, Szabo Z, Buchanan JW (eds): Principles of Nuclear Medicine, ed 2, Saunders, Philadelphia, Saunders

Sokoloff L, Reivich M, Kennedy C et al (1977) The [^{14}C]deoxyglucose method for the measurement of local cerebral glucose utilization: theory, procedure, and normal values in the conscious and anesthetized albino rat. J Neurochem 28:897–916

Spagnoli LG, Bonanno E, Sangiorgi G et al (2007) Role of inflammation in atherosclerosis. J Nucl Med 48:1800–1815

Stone CK, Pooley RA, DeGrado TR et al (1998) Myocardial uptake of the fatty acid analog 14-fluorine-18-fluoro-6-thiaheptadecanoic acid in comparison to beta-oxidation rates by tritiated palmitate. J Nucl Med 39:1690–1696

Strauss HW, Harrison K, Langan J.K, et al (1975) Thallium-201 for myocardial imaging. Relation of thallium-201 to regional myocardial perfusion. Circulation 51:641–645

Strauss HW, Grewal RK, Pandit-Taskar N (2004) Molecular imaging in nuclear cardiology Semin Nucl Med 34:47–55

Su H, Spinale FG, Dobrucki LW, et al (2005) Noninvasive targeted imaging of matrix metalloproteinase activation in a murine model of postinfarction remodeling. Circulation 112:3157–3167

Taillefer L (2001) Radiolabeled peptides in the detection of deep venous thrombosis. Semin Nucl Med 31:102–123

Taki J, Matsunari I (2007) Metabolic imaging using SPECT Eur J Nucl Med Mol Imaging 34:S34–S48

Tamaki N, Magata Y, Takahashi N et al (1992) Myocardial oxidative metabolism in normal subjects in fasting, glucose loading and dobutamine infusion states. Ann Nucl Med 6:221–228

Tamaki N, Morita K, Kuge Y et al (2000) The Role of Fatty Acids in Cardiac Imaging. J Nucl Med 41:1525–1534

Taylor M, Wallhaus TR, Degrado TR et al (2001) An evaluation of myocardial fatty acid and glucose uptake using PET with [^{18}F]fluoro-6-thia-heptadecatnoic acid and [^{18}F]FDG in patients with congestive heart failure. J Nucl Med 42:55–62

Thakur ML, Pallela VR, Consigny PM, et al (2000) Imaging vascular thrombosis with ^{99m}Tc-labeled fibrin α-chain peptide. J Nucl Med 41:161–168

Tillisch J, Brunken R, Marshall R et al (1986) Reversibility of cardiac wall-motion abnormalities predicted by positron tomography. N Engl J Med 314:884–888

Travin MI and Bergmann SR (2005) Assessment of myocardial viability. Semin Nucl Med 35:2–16

Tseng H, Link JM, Stratton JR et al (2001) Cardiac receptor physiology and its application to clinical imaging: present and future. J Nucl Cardiol 8:390–409

Vaidyanathan G, Zhao XG, Strickland DK, et al (1997) No-carrier-added iodine-131-FIBG: evaluation of an MIBG analog. J Nucl Med 38:330–334

Vallabhajosula S, Fuster V (1997) Atherosclerosis: imaging techniques and the evolving role of nuclear medicine. J Nucl Med 38:1788–1796

Vallabhajosula S, Machac J, Knesaurek K et al (1995) Imaging atherosclerotic lesions by PET using [^{18}F]fluorodeoxyglucose (FDG): preclinical studies in hypercholesterolemic rabbits. Circulation 92: 313

Virmani R, Burke AP, Farb F et al (2006) Pathology of the vulnerable plaque J Am Coll Cardiol 47:C13–C18

Yamamoto Y, de Silva R, Rhodes CG (1996) Noninvasive quantification of regional myocardial metabolic rate of oxygen by ^{15}O$_2$ inhalation and positron emission tomography. Circulation 94:808–816

Yamashina S, Yamazaki J-I (2007) Neuronal imaging using SPECT. Eur J Nucl Med Mol Imaging 34:S62–S73

Wallhaus TR, Taylor M, DeGrado TR et al (2001) Myocardial free fatty acid and glucose use after carvedilol treatment in patients with congestive heart failure. Circulation 103: 2441–2446

Weissberg PL (2004) Noninvasive imaging of atherosclerosis: the biology behind the pictures. J Nucl Med 45:1974–1795

Wieland DM, Swanson DP, Brown LE et al (1979) Imaging the adrenal medulla with an I-131-labeled antiadrenergic agent. J Nucl Med. 20:155–158

Wieland DM, Brown LE, Rogers WL et al (1981) Myocardial imaging with a radioiodinated norepinephrine storage analog, J Nucl Med 22:22–31

Wolters SL, Corsten MF, Reutelingsperger PM et al (2007) Cardiovascular molecular imaging of apoptosis Eur J Nucl Med Mol Imaging 34:S86–S98

Wu JC, Yla-Herttuala S (2005) Human gene therapy and imaging: cardiology. Eur J Nucl Med Mol Imaging 32: S346–S357

Wu JC, Tseng JR, Gambhir SS (2004) Molecular imaging of cardiovascular gene products. J Nucl Cardiol 11:491–505

Wu JC, Bengel FM, Gambhir SS (2007) Cardiovascular molecular imaging. Radiology 244:337–355

Molecular Imaging of Gene Expression and Cell Trafficking

It is one of the more striking generalizations of biochemistry – which surprisingly is hardly ever mentioned in the biochemical text books – that the twenty amino acids and the four bases, are, with minor reservations, the same throughout Nature.

Francis Harry Compton Crick

18.1 Gene Therapy

The human genome consists of more than 3 billion base pairs and approximately 30,000 genes, most of which are conserved across the species (genetic universality). Natural interindividual variability (*singularity*), however, occurs in a substantial portion of the genome, giving rise to individual characteristics. Variability in the sequence of a particular gene locus (location) is known as a polymorphism and occurs when two or more forms (*alleles*) of the gene exist.

Gene therapy represents a new and promising therapeutic modality, which holds significant promise for the treatment of human diseases. Natural genes encode naturally occurring proteins and can be used to either complement an abnormal or deficient function, or to induce a new function in a target cell. In contrast, chimerical genes do not exist in nature but are encoded for engineered proteins designed to alter various biochemical functions of a cell. The main principle of gene therapy is based on achieving a controlled and effective target-specific expression of endogenous genes or *transgenes* (externally transferred genes into cells) in order to generate a beneficial biological effect, like a cure, or to slow down the progression of a disease, or even augment the growth of new cells (Miller 1992; Mulligan 1993). Several important genes involved in gene therapy protocols in oncology, cardiology, and neurology are listed in Table 18.1.

The goal of gene therapy sometimes is also to obtain genetically modified cells with a new or a restored function, and in other occasions genetic material is used to temporarily interfere with a cell function. The major goal, however, is to achieve a controlled and effective target-specific expression of genes. One of the important factors in the design of gene therapy strategies is the nature of the disease being treated. For certain diseases a specific organ may have abnormal pathology, while some other diseases may be systemic and involve several organs and tissues. Also, a disease may sometimes be caused by a single dominant gene, or a single recessive gene or multiple genes, as in the case of cancer.

Gene therapy protocols for cancer treatment are the most common approaches (Peñuelas et al. 2005a), however, this approach is also being used to treat other diseases in cardiology and neurology (Wu and la-Herttuala 2005; Inubushi and Tamaki 2007; Jacobs et al. 2005; Jeffrey et al. 2008).

One of the common approaches of gene therapy in cancer treatment is the suicide gene therapy, in which the genes (like non mammalian enzymatic genes) make the tumor cells more susceptible to a subsequently introduced *prodrug* that can be converted to a highly toxic active drug. The two most common suicide gene systems are Herpes Simplex Virus Type I *Thymidine Kinase* (HSV1-*tk*) (Moolten 1986) and *cytosine Deaminase* (CD) (Haberkorn et al. 1996). HSV1-tk is capable of phosphorylating pyrimidine and purine nucleoside derivatives which can be trapped intracellularly (Alrabiah and Sacks 1996). Following treatment, prodrugs, like acyclovir, gancyclovir, and pencyclovir, are phosphorylated and incorporated into the host DNA, in place of thymidine triphosphate. As a result, the cellular replication is blocked leading to a decrease in tumor growth. Similarly CD, a bacterial gene, converts 5-Fluorocytosine into the toxic chemical

Table 18.1 Role of genes in different diseases

Clinical	Target condition	Mechanism	Genes
Oncology	Replacement of tumor suppression effect	Cell cycle regulation	p53
	Antisense strategy	Inhibit oncogene expression	
	Drug sensitization, prodrug therapy	Suicide genes	HSV1 *tk-1*
	Proapoptotic	Promote cell death	Caspases Bax, FasL,
	Angiogenesis	Factors inhibiting angiogenesis	Antisense VEGF and EGF
Cardiac disease	Ischaemic heart disease	Promoting angiogenesis	VEGF, FGF, HGF, HIF-1α
	Heart failure	Correction of calcium handling	SERCA-2a
		Restoration of β-adrenergic receptor signaling	β-adrenergic receptor, β-ARK1 inhibitor
		Modulation of apoptosis	Bcl-2, IGF-1, PI 3-kinase, *Akt*, p38α
	Post PTCA	Limitation of restenosis by endothelial repair	VEGF
		Limitation of restenosis through cell cycle regulation	NO synthase, VEGF, PDGF-P receptor
	Atrial fibrillation	Modification of atrioventricular nodal conduction	Inhibitory G protein α subunit
		Increase in automaticity	Kir 2.1, HCN2
Neurology	Cerebral Ischaemia and stroke	Modulation of apoptosis	Bcl-2, NAIP, GDNF
	Alzheimer's disease	Extending the survival of cholinergic neurons	NGF
		Prevention and reduction of Aβ burden	ApoE2
	Parkinson's disease	Preventing the degeneration of dopaminergic neurons	Alpha-synuclein (PARK1) and parkin (PARK2) genes
		Improving the production and release of striatal dopamine	TH, GCHI, AADC and VMAT-2
		Neuroprotection	GDNF, BDNF

SERCA Sarcoendoplasmic reticulum $Ca^{2\pm}$ ATPase; *VEGF* Vascular endothelial growth factor; *FGF* Fibroblast growth factors; *HGF* hepatocyte growth factor; *HIF* Hypoxia-inducible factor; *IGF* Insulin-like growth factor; *PI* Phosphatidylinositol; *PDGF* Platelet-derived growth factor; *NO* Nitric oxide; *PTCA* Percutaneous transluminal coronary angioplasty; *NAIP* Neuronal apoptosis inhibitory protein; *GDNF* Glial-derived neurotrophic factor; *BDNF* Brain-cell derived neurotrophic factor; *NGF* Nerve growth factor; *GCHI* GTP cyclohydroxylase I; *VMAT-2* Vesicular monoamine transporter type 2; *AADC* Aromatic amino decarboxylase; *TH* Tyrosine hydroxylase; *HCN* Hyperpolarization-activated cyclic-nucleotide-gated

5-Fluorouracil (5-FU), which substitutes for uracil in the cellular RNA, and prevents translation or protein synthesis (Habelkorn et al. 1996).

Although gene therapy is still in its infancy, monitoring the targeting and expression of genes is very important to the successful clinical applications (Serganova et al. 2007). The most challenging issues for applying gene therapy to human diseases are as follows (Sangro et al. 2002)

- The choice of a relevant therapeutic gene
- The appropriate selection of promoter and regulatory sequences driving the expression of the transgene
- The characteristics of the vector used for the delivery of the transgene into cells

- The development of systems for clinical monitoring of gene expression in the target organs.

18.1.1 Gene Delivery

The genetic material used for gene therapy has to be introduced into the target cells to exert the intended therapeutic effect. The term *transduction* refers to the incorporation of the foreign gene by the target cells and the expression of the corresponding gene product (Fig. 18.1). Genes do not penetrate inside the cells easily; they and have to be driven by gene therapy vectors. Ideally, these vectors should be able to harbor large
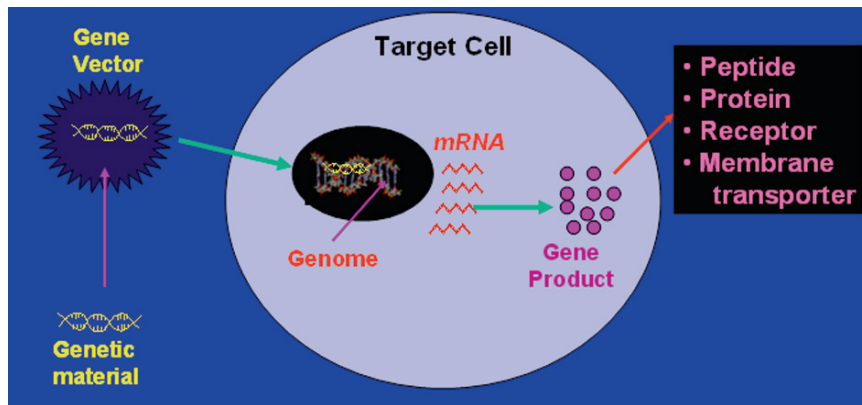
Fig. 18.1 The basic principle of gene therapy: Transduction of a therapeutic gene into a target cell and subsequent gene expression (gene product) leading to a therapeutic effect

DNA constructs with high transduction efficiency, allow for controlled and targeted gene expression, and be safe for both the patient and the environment. Many different vectors have been developed so far which can be divided into two broad categories: viral and nonviral vectors (De and Gambhir 2005).

Viruses are a natural delivery system for delivering their DNA or RNA. In viral vectors different portions of the wild-type viral genome have been replaced for the transgene of interest. Basically four different groups of viral vectors have been developed; Retrovirus (single stranded RNA), Adenovirus (double stranded DNA), Adeno associated virus (AAV), and Herpes Simplex Virus (HIV). The transgene capacity, however, varies from low (4.5 kb for AAV vectors) to medium (7–8 kb for retro- and lentiviral vectors) to high (36–150 kb for high-capacity adenovirus and HSV-1 amplicon vectors (Jacobs et al. 2005). Viral vectors are highly efficient for gene transfer, however, some are immunogenic while others have the inherent risk of inducing oncogenesis through integration in the host's genome. The nonviral vectors comprise a broad variety of vehicles for gene transfer including DNA–protein complexes, different formulation of liposomes (naked liposomes, immunoliposomes, virosomes), and naked DNA (direct injection or gene-gun mediated). The main advantages of these types of gene vectors are their larger DNA capacity, good toxic profile, and lack of immunogenicity (Peñuelas et al. 2004). In general, viral vectors, however, have substantial advantages over nonviral vectors, and therefore, are the most widely used vehicles for gene transfer in the clinical setting, to date.

Two general approaches have been used to deliver genes to the target cell: direct transfer of genetic material into cells in vivo and indirect methods involving the reimplantation of in vitro genetically modified cells (Peñuelas et al. 2004). The in vivo method of gene therapy is based on delivering the gene to a specific organ or tissue using a viral or nonviral *vector* that can be introduced into the patient by inhalation, intravenous, or even local administration. In the ex vivo method the cells from a tissue (to be treated) are removed from the patient, transfected with the therapeutic gene exvivo, and the transgenes are then reintroduced into the patient. Thus a diversity of natural (viruses) or artificial molecular constructs – named gene therapy vectors – are used to achieve efficient cell transduction.

18.1.2 Gene Expression

The process of gene expression of either endogenous or transfected genes involves the *transcription* of a gene into messenger RNA (*mRNA*), and subsequent *translation* of mRNA into a gene product or a protein (such as peptide, enzyme, receptor, membrane transporter) (Fig. 18.1). Transcription of a gene, however, is regulated by regulatory regions (such as promoters and enhancers), which are coded in the DNA. Universal promoters allow transgene expression in every transduced cell, while cell-type-specific regulatory proteins, known as *transcription factors,* interact with promoters and limit gene expression of specific cells.

18.2 Gene Imaging

In gene therapy imaging gene expression is important for monitoring the location(s), magnitude, and time-variation of gene expression from gene-therapy vectors, and also for measuring the efficacy of gene therapy. In vivo imaging techniques could, thus, play a pivotal role both, in preclinical and clinical research in gene therapy, since many crucial questions remain to be solved in this field. In an era of patient specific molecular medicine, the imaging technique should be able to provide quantitative information on many of the issues related to the gene therapy protocols (Peñuelas et al. 2004), such as:

- Has the vector used for gene transfer been efficiently delivered to the target organ/tissue?
- Is the distribution of vector in the target optimal?
- What is the biodistribution of intravenously administered vector?
- Did the gene transfer take place efficiently?
- Is the gene being expressed and the level of gene expression sufficient for the intended therapeutic effect?
- How long does gene expression persist both, in target and in nontarget tissues?
- What is the optimal moment for prodrug administration in "suicide" gene therapy protocols?
- Has the gene therapy protocol been efficient for the disease cure/remission?

The use of appropriate molecular imaging techniques, to trace the gene expression, is critical for determining the efficacy, or lack of efficacy of a given vector used for a specific gene therapy protocol. While optical imaging techniques are useful for evaluating the potential utility of gene therapy approaches in a wide variety of animal models, they are essentially not applicable in the clinic. Since the concentration of many of the gene products following transcription and translation are in the range of nano and picomolar levels, MRI techniques may not have the necessary sensitivity due to the mass limitations required for a useful MR signal. In contrast, because of their inherent high sensitivity of radiotracer imaging techniques, PET and SPECT may be more appropriate to identify the specific targeting of therapeutic genes, locate the magnitude of gene expression, and finally, monitor the response to gene therapy. Basically, two different strategies (Fig. 18.2) can be used to image gene expression (Gambhir et al. 1999a) as outlined below.

18.2.1 Direct and Indirect Gene Imaging

In direct gene imaging approach, the endogenous gene or transgene expression at the level of mRNA, or the subsequent gene products, (enzymes, receptors, etc) following translation, can be the specific target for developing radiolabeled probes (Fig. 18.2). Specific
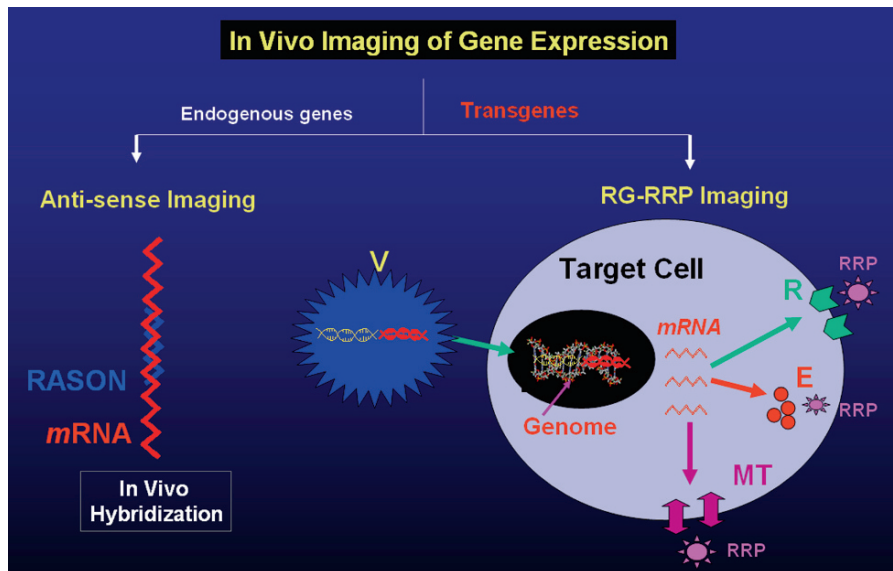
Fig. 18.2 In vivo imaging of gene expression of two types (**a**) in vivo hybridization of endogenous gene expression based on RASON, (**b**) imaging transgene expression based on a radiolabeled reporter gene probe. The gene product can be a receptor (R), an enzyme (E), or a membrane transporter (MT)

sequence of *m*RNA can be targeted for imaging using a radiolabeled antisense oligonucleotide (RASON), probe, such as ^{18}F labeled oligonucleotide, containing a complimentary sequence of mRNA to be imaged. Similarly, to the target a specific gene product or therapeutic protein, radiolabeled substrates for that protein can be used. While this approach has potential advantages, it may not necessarily be practical since each and every mRNA or gene product would require a specific radiolabeled molecule.

The indirect gene imaging approach involves coupling the therapeutic gene (TG) to a "reporter gene (RG)", such as HSV1-*tk*, and then targeting the reporter gene expression using a PET or SPECT "reporter probe (RP)" (Tjuvajev et al. 1996, Gambhir et al. 1999b). The TG and the RG are linked with a common promoter and administered into a patient using a virus (such as adenovirus) vector, which transfers both the therapy gene and RG to the target tumor cell. Subsequently, a radiolabeled RP (RRP) is used to image the expression of RG which indirectly will provide information about the expression of TG (Fig. 18.3). This RG-RRP approach may be used based on a gene for the production of a specific enzyme or an intracellular and/or cell-surface receptor in the target cell.

18.2.1.1 Antisense Imaging

mRNA molecules are typically several hundreds to thousands of base pairs long and the levels of mRNA in the cytoplasm are in the range of 1–1,000 pM. Antisense oligonucleotides (ASON) have a nucleotide base sequence complementary to a specific sequence of a small segment on the target mRNA molecule (Fig. 18.4). The interaction of *m*RNA and ASON is very specific and stoichiometric resulting in the *hybrid*ization through hydrogen bonds. In order to image intracellular levels of mRNA, small ASON molecules (12–35 bases) have been modified to develop radiolabeled antisense oligonucleotide (RASON) probes (Hnatowich 2000; Tavitian 2000). The validity of antisense imaging using RASON probe was first demonstrated based on an ^{111}In-DTPA-oligonucleotide targeted against *c-myc* oncogene (Dewanjee et al. 1994). Subsequently several RASON probes, based on ^{99m}Tc,
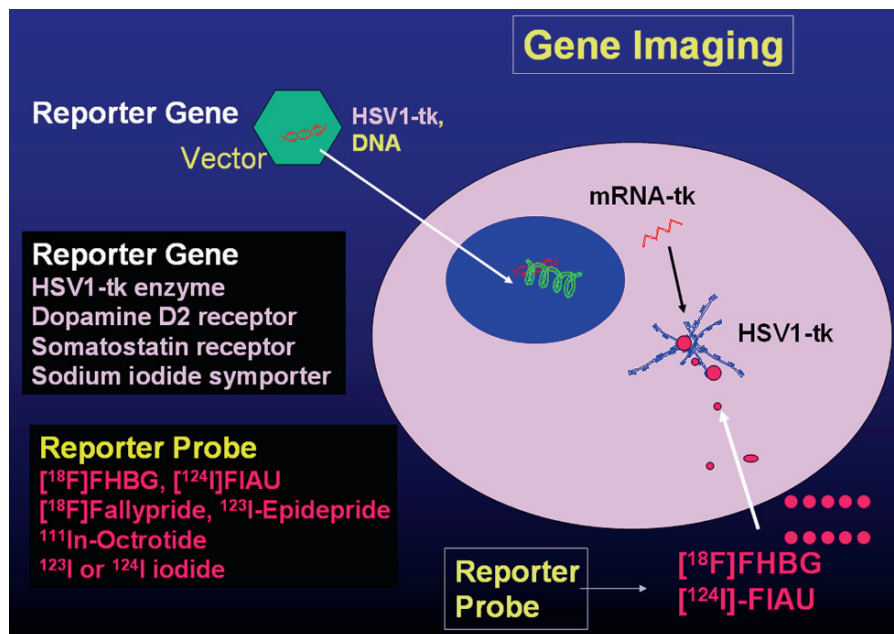
Fig. 18.3 Imaging transgene expression first involves transduction of a vector consisting of both the therapeutic gene and the reporter gene (such as HSV1-tk) into a target cell. Subsequent imaging of the gene product HSV1-*tk* enzyme, using reporter probe, such as [^{18}F]FHBG or ^{124}I–FIAU
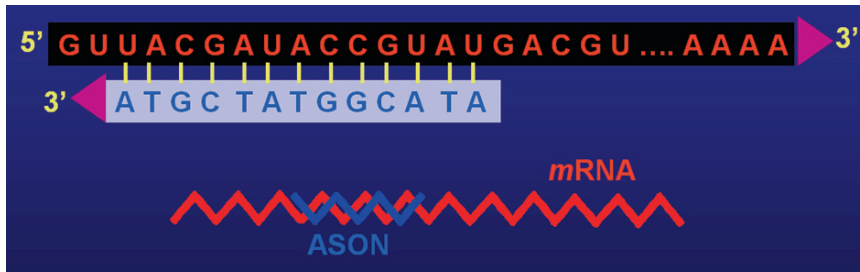
Fig. 18.4 Antisense oligonucleotides (ASON) have a nucleotide base sequence complementary to a specific sequence of a small segment on the target mRNA molecule. The interaction of *m*RNA and ASON is very specific and stoichiometric resulting in the *hybrid*ization through hydrogen bonds

[125]I and ^{18}F nuclides were evaluated in animal models to assess the utility of antisense imaging technique to monitor endogenous gene expression. The major requirements for a RASON probe are as follows (Barrio 2004):

- The complementary base pairing in the RASON probe must be very high and specific. Even a single mismatch can decrease the hybridization significantly.
- The SA of the RASON probe must be very high (1–10 Ci μmol^{-1}).
- Since oligonucleotides are charged molecules, membrane permeability may be a limiting factor. Membrane transport process must be optimal and favorable for the kinetics of cellular uptake and washout.
- Intracellular nonspecific binding must be relatively low or insignificant.
- Peripheral metabolism must be minimal.

18.2.1.2 Reporter Probe Imaging

Several human and non-human RGs have been proposed (Table 18.2) as potential candidates for developing gene imaging technique based on radiolabeled reporter probes (RRP). The RGs can be classified into three categories, based on whether a gene product is an enzyme, a receptor, or a membrane transporter. The HSV1-*tk* viral gene has been the most widely exploited RG in preclinical studies. Since this is a nonhuman gene, there is a small risk of generating an immune response against cells and tissues transduced with this gene. Therefore human genes may be more advantageous compared to the viral genes. Also several human

Table 18.2 Imaging transgene expression in vivo: Human and nonhuman reporter genes and the corresponding radiolabeled reporter probes

Class	Reporter gene	Reporter probe
Enzymes	*TK2, HSV1-tk*,	[124]I]FIAU, [^{18}F]FEAU, [^{18}F]FHBG, [^{18}F]FHPG
	HSV1-sr39tk	[^{18}F]FEAU
Receptor	Sodium iodide symporter (NIS)	[124]I]Iodide, [^{123}I]Iodide
	Norepinephrine transporter (NET)	[^{123}I]MIBG, [124]I]MIBG
Receptor	Somatostatin receptor (SSTR2)	^{68}Ga-DOTATOC, ^{111}In-DTPA_Octrotide
	Dopamine D2	[^{18}F]Fallypride, ^{123}I-epidepride

genes have been identified which can generate significant amounts of specific membrane receptors (such as SSTR, dopamine D2) and transporters (NIS, NET). A number of PET and SPECT radiotracers have already been developed for various receptors and transporters, and tested in humans as molecular imaging probes. Potential signaling and the cell biology effects of using receptors or transporters as RGs, however, may limit their potential clinical utility.

In order to develop the gene imaging technique, it is important to establish a method that would successfully generate expression of both the TG and the RG. Both of these genes can be given separately in separate vectors or can be linked together and administered in a single vector. It is also important to choose an appropriate promoter (P) driving the transcription. The following approaches have been developed to administer the TG and RG (De and Gambhir 2005) (Fig. 18.5).
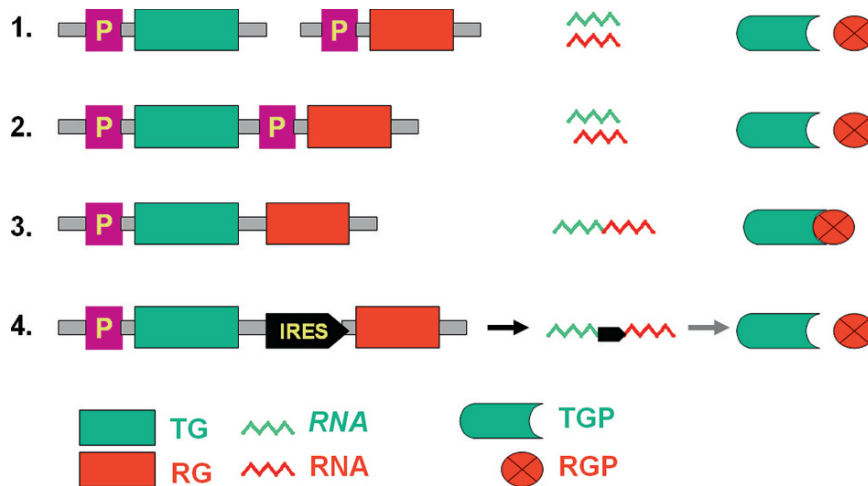
Fig. 18.5 Different approaches to administer therapeutic gene (TG) and reporter gene (RG). (1) Coadministration approach, (2) Fusion gene approach, (3) Dual promoter approach, and (4) Bicistronic approach. The gene expression involves both the therapeutic gene product (TGP) and the reporter gene product (RGP)

- Coadministration approach: the two genes are carried in two identical but distinct vectors. As a result two mRNAs and two distinct proteins are generated.
- Fusion gene approach: The two gene sequences are coupled together with a spacer sequence between them. As a result only one mRNA leading to one fusion protein is generated with both therapeutic and reporter functions.
- Dual promoter approach: The two genes are linked but two identical promoters are used, one for each gene. As a result two mRNAs with two distinct proteins are generated.
- Bicistronic approach: The two genes are linked together using an internal ribosomal entry site (IRES), a specific sequence to initiate translation. Transcription occurs under a single promoter to form a single mRNA molecule. However, translation under the direction of IRES generates two separate proteins.

Each of the approaches discussed above has its own advantages and disadvantages. Selection of an appropriate approach may depend on a particular combination of TG and RG. The ultimate goal is to image and quantitatively estimate the levels of TG expression.

The interaction of radiolabeled reporter probes (RRPs) with a specific gene product may lead to a significant trapping of RRPs within the cell or in a specific tissue or organ of interest. The ideal characteristics of any RG-RRP imaging approach should have the following minimum characteristics (Gambhir 2004).

- The RG should preferably be a human gene, and generally not be expressed in the target tissue of interest.
- The levels of RG expression (gene product) must be relatively high in the target tissue to allow significant trapping of RRP.
- The SA of RRP must be high (1–10 Ci μmol^{-1}) in order to detect even minimal levels of gene products (the specific targets).
- RRP should be stable in vivo, and rapidly cleared from blood and nonspecific binding sites.
- The radionuclide used for developing the RRP must be appropriate (a) to determine the kinetics of trapping of RRP in the target tissue and (b) to quantitatively estimate the levels of gene expression.

Enzyme-Based Reporter Genes

The expression of several RGs coding for different enzymes including β-galactosidase, luciferase, or green fluorescent protein (GFP) have been extensively studied in transgenic animals. However, measuring the expression of these genes requires a biopsy or the killing of the animals. The bioluminescence optical approaches with a firefly or luciferase provide rapid throughput in small animal models, but are not applicable for human studies. In contrast, HSV1-tk gene expression has been shown to be useful for developing noninvasive imaging strategies.

With HSV1-tk, the final gene product generated is an enzyme (protein), known as HSV1-tk. In contrast to the human intracellular thymidine kinase 1 (*hTK-1*), the HSV1-tk enzyme is less specific to thymidine, and has the ability to phosphorylate other nucleoside analogs (acyclovir, ganciclovir, and penciclovir) to their corresponding monophosphate metabolites (Keller et al. 1981). Since human *TK-1* can not phosphorylate these nucleoside analogs, the viral *TK* enzyme permits the development and use of radiolabeled probes that are selectively phosphorylated by the HSV1-*tk* enzyme. A mutant HSV1-*tk* RG was also developed which generates the HSV1-sr39*tk* enzyme that also has shown specificity for nucleoside analogs (Gambhir et al. 2000b).

Two main substrate groups have been used to develop RRPs for HSV1-*tk*. Among the pyrimidine analogs, the best radioiodinated (^{123}I, ^{124}I or ^{131}I) substrate with high affinity for the HSV1-*tk* enzyme is 5-iodo-2′-fluoro-2′-deoxy-1-β-ᴅ-arabinofuranosyl-5-iodouracil (FIAU) (Tjuvajev et al. 1998). FIAU however, is also a good substrate for *hTK-1*. The best substrate among the acycloguanosine derivatives is 9-(4-[^{18}F]-fluoro-3-hydroxy-methylbutyl) guanine (FHBG) (Alauddin and Conti 1998). Compared to FIAU, FHBG is a poor substrate for the endogenous *hTK-1*. FHBG has shown to be an even better substrate for the mutant HSV1-sr39tk enzyme (Gambhir 2004). The structures of several substrates for the human and viral TK enzyme are shown in Fig. 18.6.
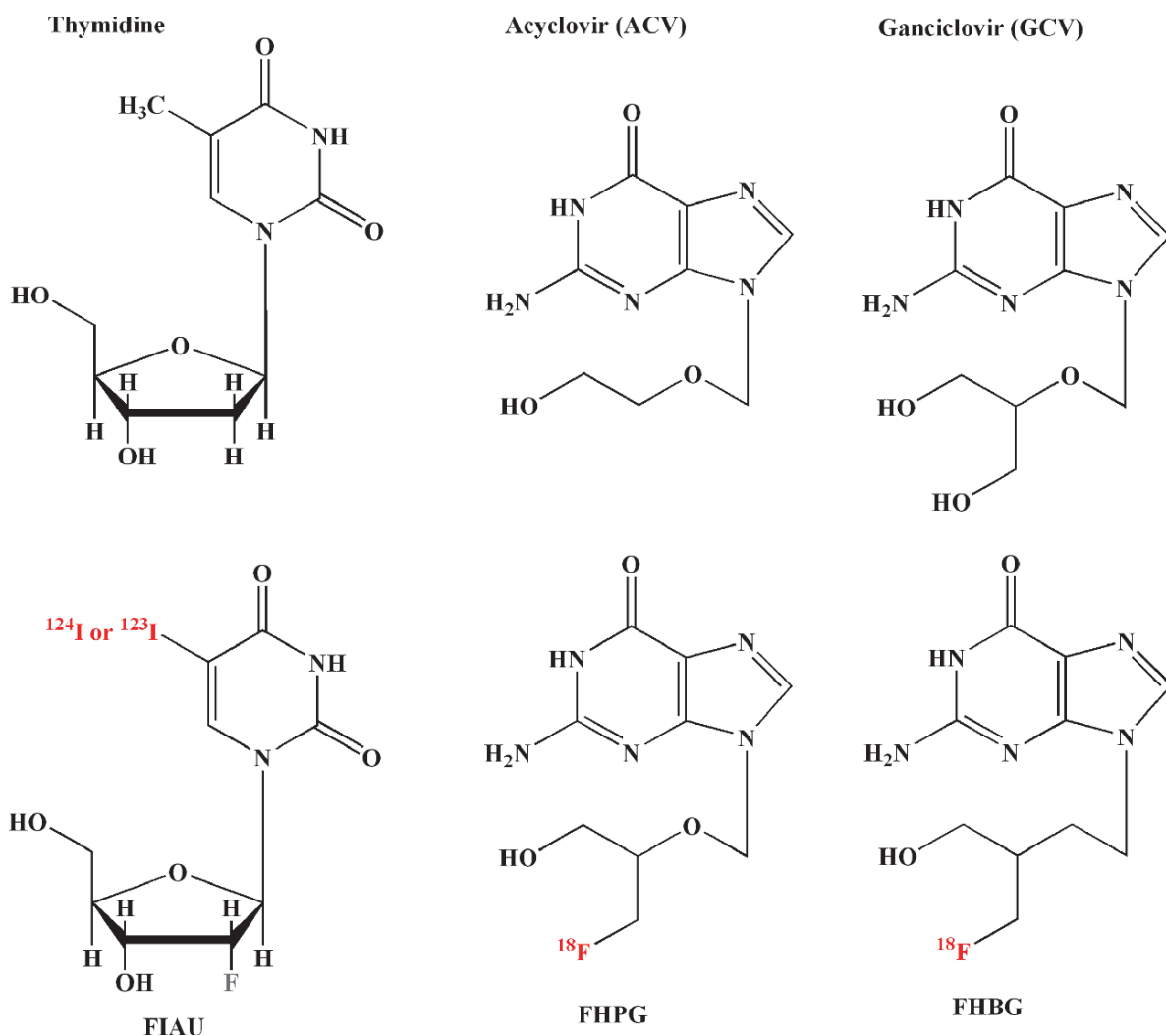
Fig. 18.6 Structure of several radiolabeled reporter probes for imaging the HSV1-tk enzyme

Since viral TK genes are not ideal for human studies, the human mitochondrial thymidine kinase 2 (*hTK2*) gene has been proposed as an appropriate RG (Ponomarev et al. 2007). There are several biochemical features of *hTK2* that make it an attractive RG. A truncated version of *hTK2* (Δ*hTK2*), which lacks the 18 N-terminal amino acids that are responsible for the mitochondrial localization of this protein, has been recently shown to function as a better reporter gene than the native *hTK2*.

Receptor-Based Reporter Genes

Specific membrane receptors have limited expression in the body and provide several advantages for gene imaging studies. Since the genes for the receptors are of human origin they are not immunogenic. Further, because the receptors are present on the cell membrane, the RRP does not require transport into the cell. Two receptor-based RG systems – somatostatin receptors and dopamine receptors – have been described and evaluated in preclinical studies (Zinn and Chaudhuri 2002; Serganoa et al. 2007).

The human somatostatin receptors subtype 2 (SSTR2) are mainly present in the pituitary gland and overexpressed in several neuroendocrine tumors. The human *SSTr2* gene has been incorporated into an adenoviral vector and has been used as a RG for noninvasive imaging of xenografts (Rogers et al. 1999, 2005). A number of SPECT and PET radiotracers for the SSTR2 system have already been developed and tested in clinical studies. Among these, ^{111}In-DTPA-octreotide (OctreoScan®), ^{99m}Tc-P829 peptide, and ^{68}Ga-DOTATOC can be used as RRPs since they are known to have very high SSTR2 subtype specificity (Serganoa et al. 2007).

The human dopamine D_2 receptors (D_2R) are predominantly present in the nigrostriatal system of the brain. The D_2R gene has been used as RG both, in the adenoviral delivery vector and in stably transfected tumor cell xenografts. The receptor expression has been imaged using 3-(2′-[^{18}F]fluoroethyl)-spiperone (FESP), a D_2R antagonist (MacLaren et al. 1999). In addition, using a rat dopamine D_2R and its mutant variant as an RG, the gene expression has been imaged using FESP. The nonhuman origin of mutant D2R does not favor their use in human studies. Therefore, there is a need for further work in developing mutant genes for human receptors in order to use receptor-based RGs.

Membrane Transporter-Based Reporter Genes

In contrast to receptors that usually have a 1:1 binding relationship with an RRP, membrane transporters provide signal amplification (similar to enzymes) through the transport-mediated concentrative intracellular accumulation of RRPs. Two human transporter genes, that are potentially good candidates for RG applications, have been reported: the human sodium iodide symporter (*hNIS*) gene and the human norepinephrine transporter (*hNET*) gene (Barton et al. 2003; Anton et al. 2004; Serganoa et al. 2007).

The *NIS* is an intrinsic transmembrane glycoprotein that is mainly expressed in the thyroid, however, lower levels of expression are also present in the salivary glands, stomach, thymus, breast, and other tissues (Dai et al. 1996; Dadachova and Carrasco 2004). NIS will transport a number of different anions, including iodide (I^-) and pertechnetate (TcO_4^-). The potential for using hNIS as a RG in human studies is well recognized (Mandell et al. 1999; Boland et al. 2000; Niu et al. 2004). Further, the hNIS gene has been successfully transferred into cultured cells and small animal tumors, and the symporter gene products have successfully accumulated both [^{131}I]iodide and ^{99m}Tc pertechnetate (Haberkorn et al. 2001; Che et al. 2005).

hNET is a transmembrane protein that mediates the transport of norepinephrine, dopamine, and epinephrine across the cell membrane (Pacholczyk et al. 1991). It functions as a rapid reuptake membrane transporter located at or near presynaptic terminals and facilitates the rapid reuptake of norepinephrine that was released into the synapse by the presynaptic terminals. hNET is a homo/oligomer complex, where Na^+ and Cl^- ions provide an inward electrochemical gradient and ATP/ATPase are critical elements for neurotransmitter accumulation. Successful imaging of hNET expression in neuroendocrine tumors and altered sympathetic enervation of the heart based on norepinephrine analogs (^{131}I–MIBG, [^{11}C]HED) have led to the suggested application of hNET as a human RG (Altman et al. 2003; Anton et al. 2004; Buursma et al. 2005; Moroz et al. 2007). Consequently, new and better norepinephrine analogs for imaging studies are under development (Ding and Fowler 2005).

18.2.2 Gene Imaging: Clinical Studies

Gene therapy has emerged as a new and promising therapy for many diseases (Haberkorn 2002; Isner 2002; Brewster et al. 2006; Lowenstein et al. 2004), and hundreds of clinical trials have been designed for the treatment of inherited disorders and a wide variety of acquired diseases. The majority of these clinical trials are, in fact, devoted to the treatment of cancer (Edelstein et al. 2004). Molecular imaging techniques for monitoring gene expression have been developed and successfully used in many animal models (Jacobs

et al. 2005; Peñuelas et al. 2005a, b; Wu and la-Herttuala 2005). While the initial pilot studies in human subjects have demonstrated the safety and potential use of gene imaging technique based on RRPs, the sensitivity, reproducibility, and potential clinical utility, however, need to be tested and validated by carefully designed multicenter studies (Peñuelas et al. 2005a, b; Serganova et al. 2007). The pilot clinical studies of gene imaging technique based on RRPs for several different diseases are briefly discussed here.

The first clinical use of [124I]FIAU–PET in a gene therapy procedure in humans may be considered as a
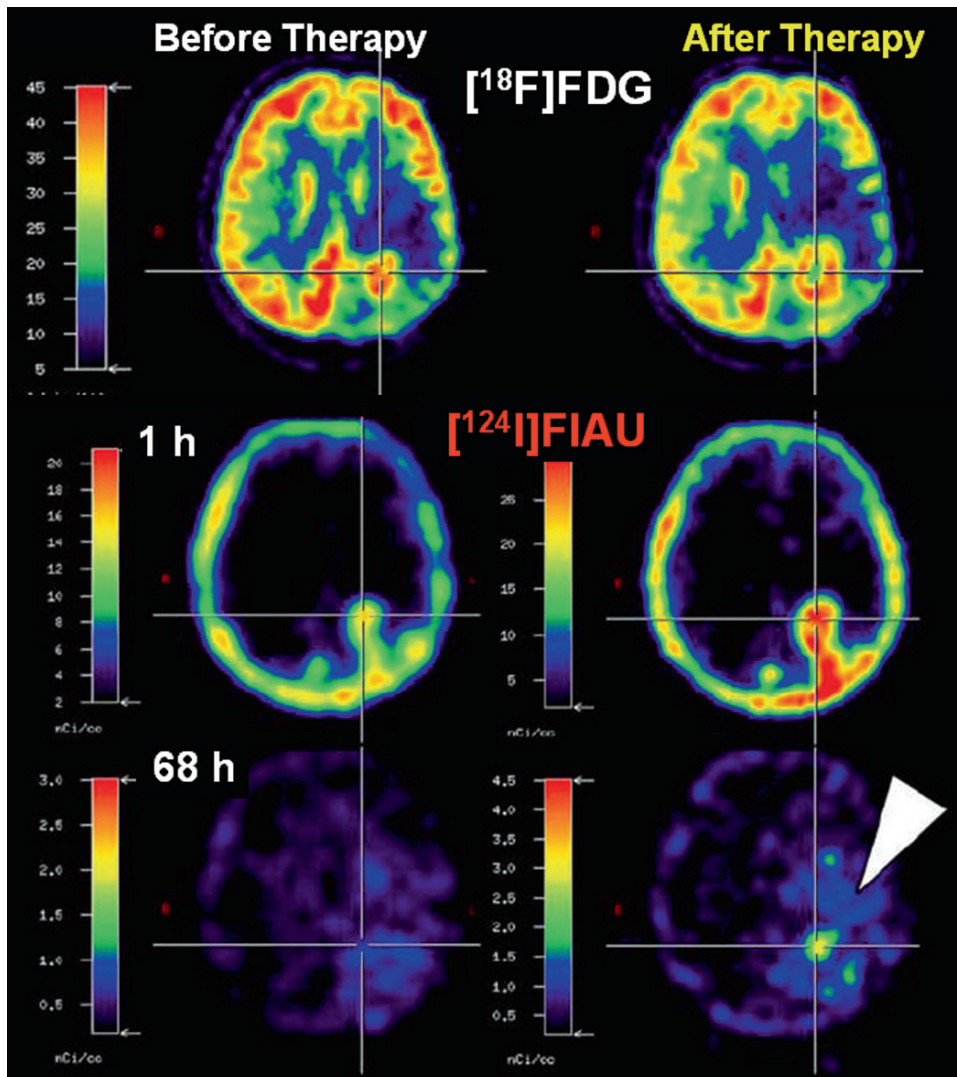
Fig. 18.7 PET imaging studies with FDG and [124]I–FIAU to monitor gene therapy (intratumorally infused liposome-plasmid gene therapy vector followed by ganciclovir administration) in a patient with a brain tumor. FDG–PET scan post therapy shows a central area of decreased uptake (due to necrosis) compared to the scan before therapy. Following administration of the [124]I–FIAU, the delayed image (at 68 h) shows a tumor retention of [124]I activity, indicating successful gene expression (Jacobs et al 2005)
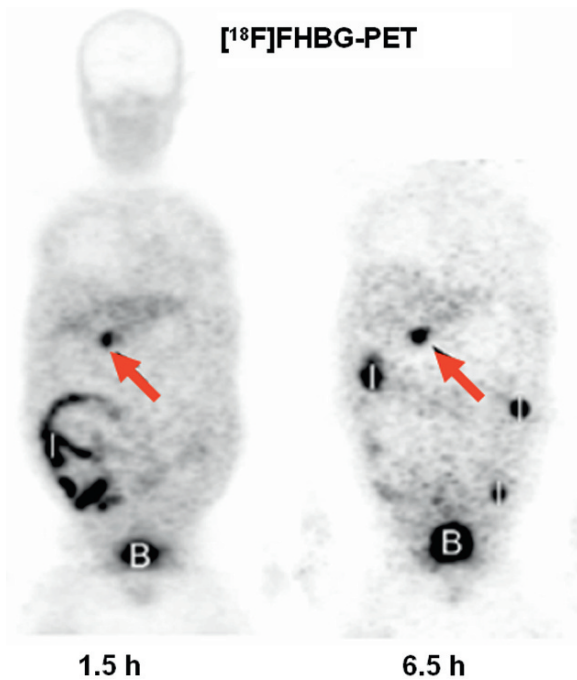
Fig. 18.8 [^{18}F]FHBG PET whole-body images show that specific accumulation of the tracer (and hence HSV1-tk expression) is restricted to the vector (10^{12} viral particles) injection site in the liver tumoral nodule (arrows). Later (6.5 h) the tracer accumulates in the bladder (B) and the intestines (I) owing to physiological elimination (Peñuelas et al 2005b)

Fig. 18.9 Viral dose-dependent imaging of HSV1-tk transgene expression with [^{18}F]FHBG–PET in five patients receiving five different doses of viral particles (2×10^{10}–2×10^{12}). Detectable tumor transduction can only be observed when the dose of vector administered reaches a certain threshold of 10^{12} particles (Peñuelas et al 2005b)

typical example of the use of molecular imaging in gene therapy (Jacobs et al. 2001, 2005). More specifically, in patients with glioma, a phase I study was designed to evaluate the safety and potential therapeutic action of intratumorally infused liposome–plasmid DNA complex followed by the administration of ganciclovir (GCV) using intratumoral catheters. The initial identification of biologically active target tumor lesion was based on MRI and PET. A dynamic ^{124}I–FIAU–PET series acquired over three days was performed before the gene transduction and after the gene therapy to monitor the success of the gene delivery. The images in Fig. 18.7 show an increase in the accumulation rate of ^{124}I–FIAU in a single patient after intratumoral infusion of a vector encoding HSV1-tk. In addition, a FDG–PET study after gene therapy showed a significant decrease in FDG tumor uptake and central necrosis in the same area where ^{124}I–FIAU–PET confirmed gene delivery and expression.

In a larger series of patients, HSV-1-tk expression in tumoral hepatocarcinoma nodules treated by suicide gene therapy, was demonstrated using [^{18}F]FHBG, a tracer specific for HSV-1-tk (Peñuelas et al. 2005b).

Patients received the vector (1.0×10^{10}–2.0×10^{12} particles) by direct injection into the tumor nodule two days prior to the FHBG–PET; some patients had several FHBG–PET scans following multiple doses of therapy gene vector. Based on these preliminary studies, the following three findings were reported: (a) the signal to background ratio between the lesion and the nontreated liver increases with time after injection of the FHBG tracer (Fig. 18.8), (b) the magnitude of radiotracer accumulation in the treated lesion varies from patient to patient and cannot be directly correlated with the adenoviral dose used in each particular case (Fig. 18.9), and (c) the second dose of gene vector did not result in FHBG tumor localization, probably

[^{18}F]FHBG-PET

After 1st dose   After 2nd dose
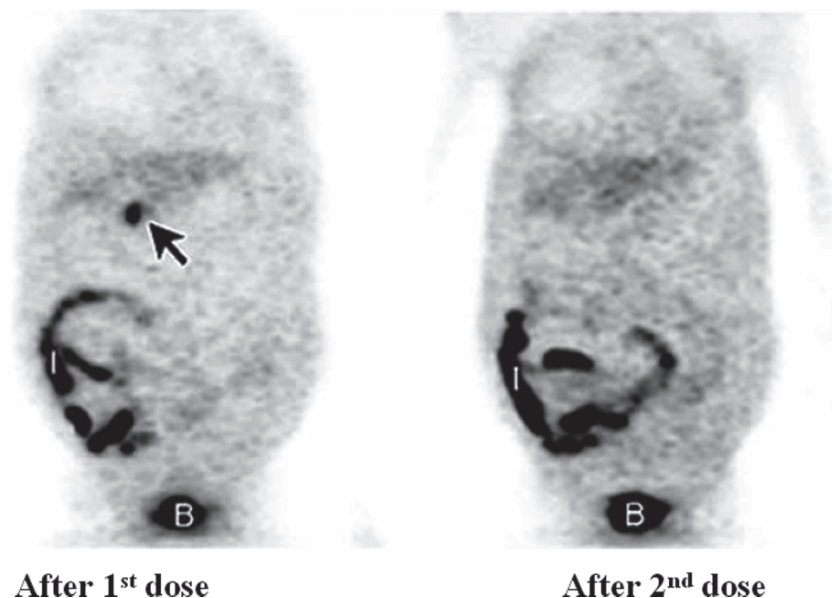
Fig. 18.10 [^{18}F]FHBG–PET whole-body images of the same patient two days after the first dose of the vector and two days after a second dose given 30 days after the first one are shown. No transgene expression can be observed after the retreatment in the tumor nodule, although it is evident in the first treatment (*arrow*). Accumulation in the intestines (I) and bladder (B) can be seen in both cases due to the physiological elimination of the tracer (Peñuelas et al 2005b)

due to increase in the titer of neutralizing antiadenovirus antibodies (Fig. 18.10).

In summary the preliminary clinical studies discussed above demonstrate that transgene expression, in cancer patients, can be monitored by PET. This noninvasive methodology represents a valuable tool for the assessment of gene expression in gene therapy in the clinical setting, and could be useful to (a) define the transduction efficiency of a given vector (in a specific tissue or lesion), (b) study transgene expression distribution, to determine its duration, and (c) help in the evaluation of new vectors and the design of novel therapeutic strategies.

References

Alauddin MM, Conti PS (1998) Synthesis and preliminary evaluation of 9-(4-[^{18}F]-fluoro-3-hydroxymethylbutyl)guanine ([^{18}F]FHBG): a new potential imaging agent for viral infection and gene therapy using PET. Nucl Med Biol 25:175–180

Al-Madhoun A, Tjarks W, Eriksson S (2004) The role of thymidine kinases in the activation of pyrimidine nucleoside analogues. Mini Rev Med Chem 4:341–350

Alrabiah FA, Sacks SL (1996) New anti-herpes virus agents: their targets and therapeutic potential. Drugs 52:17–32

Altmann A, Kissel M, Zitzmann S, et al (2003) Increased MIBG uptake after transfer of the human norepinephrine transporter gene in rat hepatoma. J Nucl Med 44:973–980

Anton M, Wagner B, Haubner R, et al (2004) Use of the norepinephrine transporter as a reporter gene for noninvasive imaging of genetically modified cells. J Gene Med 6:119–126

Barrio JR (2004) The molecular basis of disease. In: Phelps ME (ed) PET: Molecular Imaging and Its Biological Applications. Springer, New York

Barton KN, Tyson D, Stricker H, et al (2003) GENIS:gene expression of sodium iodide symporter for noninvasive imaging of gene therapy vectors and quantification of gene expression in vivo. Mol Ther 8:508–518

Blasberg R (2002) Imaging gene expression and endogenous molecular processes: molecular imaging. J Cereb Blood Flow Metab 22:1157–1164

Boland A, Ricard M, Opolon P, et al (2000) Adenovirus-mediated transfer of the thyroid soium/iodide symporter gene into tumors for a targeted radiotherapy. Cancer Res 60:3484–3492

Brewster LP, Brey EM, Greisler HP (2006) Cardiovascular gene delivery: The good road is awaiting. Adv Drug Deliv Rev 58:604–629

Buursma AR, Beerens AM, de Vries EF, et al (2005) The human norepinephrine transporter in combination with ^{11}C-m-hydroxyephedrine as a reporter gene/reporter probe for PET of gene therapy. J Nucl Med 46:2068–2075

Che J, Doubrovin M, Serganova I, et al (2005) hNIS-IRES-eGFP dual reporter gene imaging. Mol Imaging 4:128–136

Chun HJ, Wilson KO, Huang M, et al (2007) Integration of genomics, proteomics, and imaging for cardiac stem cell therapy. Eur J Nucl Med Mol Imaging 34:S20–S26

Dadachova E, Carrasco N (2004) The Na/I symporter (NIS): imaging and therapeutic applications. Semin Nucl Med 34:23–31

Dai G, Levy O, Carrasco N (1996) Cloning and characterization of the thyroid iodide transporter. Nature 379:458–460

De A, Gambhir SS (2005) PET as a tool in multimodality imaging of gene expression and therapy. In: Bailey DL et al (eds) Positron Emission Tomography: Basic Sciences. Springer, London

Dewanjee MK, Ghafouripour AK, Kapadvanjwala M, et al (1994) Noninvasive imaging of c-myc oncogene messenger RNA with indium-111-antisense probes in a mammary tumor-bearing mouse model. J Nucl Med 35:1054–1063

Ding YS, Fowler J (2005) New-generation radiotracers for nAChR and NET. Nucl Med Biol 32:707–718

Edelstein ML, Abedi MR, Wixon J, et al (2004) Gene therapy clinical trials worldwide 1989–2004 – an overview. Gene Med 6:597–602

Gambhir SS (2004) Quantitative assay development for PET. In: Phelps ME (ed) PET: Molecular Imaging and Its Biological Applications. Springer, New York

Gambhir SS, Barrio JR, Herschman HR, et al (1999a) Imaging gene expression: principles and assays. J Nucl Cardiol 6:219–233

Gambhir SS, Barrio JR, Phelps ME, et al (1999b) Imaging adenoviral-directed reporter gene expression in living animals with positron emission tomography. Proc Natl Acad Sci U S A 96:2333–2338

Gambhir SS, Herschman HR, Cherry SR, et al (2000a) Imaging transgene expression with radionuclide imaging technologies. Neoplasia 2:118–138

Gambhir SS, Bauer E, Black ME, et al (2000b) A mutant herpes simplex virus type 1 thymidine kinase reporter gene shows improved sensitivity for imaging reporter gene expression with PET. Proc Natl Acad Sci U S A 97:2785–2790

Green LA, Yap CS, Nguyen K, et al (2002) Indirect monitoring of endogenous gene expression by positron emission tomography (PET) imaging of reporter gene expression in transgenic mice. Mol Imaging Biol 4:71–81

Haberkorn UA (2002) Imaging gene expression. In: Wahl RL, Buchanan JW (eds) Principles and Practice of Positron Emission Tomography. Williams & Wilkins, Philadelphia

Haberkorn U, Oberdorfer F, Gebert J, et al (1996) Monitoring of gene therapy with cytosine deaminase: in vitro studies using ^{3}H-5-fluorocytosine. J Nucl Med 37:87–94

Haberkorn U, Henze M, Altmann A, et al (2001) Transfer of the human NaI symporter gene enhances iodide uptake in hepatoma cells. J Nucl Med 42:317–325

Hnatowich DI (2000) Antisense imaging: where are we now? Cancer Biother Radiopharm 15:447–457

Inubushi M, Tamaki N (2007) Radionuclide reporter gene imaging for cardiac gene therapy. Eur J Nucl Med Mol Imaging 34:S27–S33

Isner JM (2002) Myocardial gene therapy. Nature 415:234–239

Jacobs A, Voges J, Reszka R, et al (2001) Positron-emission tomography of vector-mediated gene expression in gene therapy for gliomas. Lancet 358:727–729

Jacobs AH, Winkler A, Castro MG, et al (2005) Human gene therapy and imaging in neurological diseases. Eur J Nucl Med Mol Imaging 32:S358–S383

Jeffrey R. Petrella JR, Mattay VS, Doraiswamy PM (2008) Imaging genetics of brain longevity and mental wellness: the next frontier? Radiology 246:20–32

Keller PM, Fyfe JA, Beauchamp L, et al (1981) Enzymatic phosphorylation of acyclic nucleoside analogs and correlations with antiherpetic activities. Biochem Pharmacol 30:3071–3077

Liang Q, Satyamurthy N, Barrio JR, et al (2001) Noninvasive, quantitative imaging in living animals of a mutant dopamine D2 receptor reporter gene in which ligand binding is uncoupled from signal transduction. Gene Ther 8:1490–1498

Lowenstein PR, Castro MG (2004) Recent advances in the pharmacology of neurological gene therapy. Curr Opin Pharmacol 4(1):91–97

MacLaren DC, Gambhir SS, Satyamurthy N, et al (1999) Repetitive, noninvasive imaging of the dopamine D2 receptor as a reporter gene in living animals. Gene Ther 6:785–791

Mandell RB, Mandell LZ, Link Jr CJ (1999) Radioisotope concentrator gene therapy using the sodium/iodide symporter gene. Cancer Res 59:661–668

Miller AD (1992) Human gene therapy comes of age. Nature 357:455–460

Miyagawa M, Beyer M, Wagner B, et al (2005) Cardiac reporter gene imaging using the human sodium/iodide symporter gene. Cardiovasc Res 65:195–202

Moolten FL (1986) Tumor chemosensitivity conferred by inserted herpes thymidine kinase genes: paradigm for prospective cancer control strategy. Cancer Res 46:5276–5281

Moroz M, Serganova I, Zanzonico P, et al (2007) Imaging hNET reporter gene expression with [^{124}I]MIBG. J Nucl Med 48:827–836

Mulligan RC (1993) The basic science of gene therapy. Science 260:926–932

Niu G, Gaut AW, Ponto LL, et al (2004) Multimodality noninvasive imaging of gene transfer using the human sodium iodide symporter. J Nucl Med 45:445–449

Pacholczyk T, Blakely RD, Amara SG (1991) Expression cloning of a cocaine- and antidepressant-sensitive human noradrenaline transporter. Nature 350:350–354

Peñuelas I, Boán JF, Martí-Climent JM (2004) Positron emission tomography and gene therapy: basic concepts and experimental approaches for in vivo gene expression imaging. Mol Imaging Biol 6:225–238

Peñuelas I, Haberkorn U, Yaghoubi S, et al (2005a) Gene therapy imaging in patients for oncological applications. Eur J Nucl Med Mol Imaging 32:S384–S403

Penuelas I, Mazzolini G, Boan JF, et al (2005b) Positron emission tomography imaging of adenoviral-mediated transgene expression in liver cancer patients. Gastroenterology 128:1787–1795

Ponomarev V, Doubrovin M, Shavrin A, et al (2007) A novel human derived reporter gene for noninvasive imaging in humans: mitochondrial thymidine kinase type 2. J Nuc Med 48:819–826

Rogers BE, McLean SF, Kirkman RL, et al (1999) In vivo localization of ^{111}In-DTPA-D-Phe^1-octreotide to human ovarian

tumor xenografts induced to express the somatostatin receptor subtype 2 using an adenoviral vector. Clin Cancer Res 5:383–393

Rogers BE, Parry JJ, Andrews R, et al (2005) MicroPET imaging of gene transfer with a somatostatin receptor-based reporter gene and [94m]Tc-Demotate 1. J Nucl Med 46:1889–1897

Sangro B, Qian C, Ruiz J, et al (2002) Tracing transgene expression in cancer gene therapy: a requirement for rational progress in the field. Mol Imaging Biol 4:27–33

Serganova I, Blasberg R (2005) Reporter gene imaging: potential impact on therapy. Nucl Med Biol 32:763–780

Serganova I, Ponomarev V, Blasberg R (2007) Human reporter genes: potential use in clinical studies. Nucl Med Biol 34:791–807

Tavitian B (2000) In vivo antisense imaging. Q J Nucl Med 44:236–255

Tjuvajev JG, Stockhammer G, Desai R, et al (1995) Imaging the expression of transfected genes in vivo. Cancer Res 55:6126–6132

Tjuvajev JG, Finn R, Watanabe K, et al (1996) Noninvasive imaging of herpes virus thymidine kinase gene transfer and expression: a potential method for monitoring clinical gene therapy. Cancer Res 56:4087–4095

Tjuvajev JG, Avril N, Oku T, et al (1998) Imaging herpes virus thymidine kinase gene transfer and expression by positron emission tomography. Cancer Res 58:4333–4341

Tjuvajev J, Doubrovin M, Akhurst T, et al (2002) Comparison of radiolabeled nucleoside probes (FIAU, FHBG, and FHPG) for PET imaging of HSV1-tk gene expression. J Nucl Med 43:1072–1083

Wu JC, la-Herttuala S (2005) Human gene therapy and imaging: cardiology. Eur J Nucl Med Mol Imaging 32:S346–S357

Wu JC, Tseng JR, Gambhir SS (2004) Molecular imaging of cardiovascular gene products. J Nucl Cardiol 11:491–505

Yaghoubi, S.S.; Wu, L.; Liang, Q, et al (2001) Direct correlation between positron emission tomographic images of two reporter genes delivered by two distinct adenoviral vectors. Gene Ther 8:1072–1080

Yaghoubi SS, Barrio JR, Namavari M, et al (2005) Imaging progress of herpes simplex virus type 1 thymidine kinase suicide gene therapy in living subjects with positron emission tomography. Cancer Gene Ther 12(3):329–339

Zinn KR, Chaudhuri TR (2002) The type 2 human somatostatin receptor as a platform for reporter gene imaging. Eur J Nucl Med Mol Imaging 29:388–399

Radiation Dosimetry and Protection

A theory, is the more impressive the greater the simplicity of its premises is, the more different kind of things it relates, and the more extended is its area of applicability.

Albert Einstein

19.1 Introduction

The continued development of molecular imaging probes based on radionuclides depends to a large extent on the understanding of fundamental issues involved in radiation exposure and radiation dosimetry. Because of the very high energy of annihilation photons (511 keV) and the abundance (100–200%) of PET radionuclides, radiation levels in the PET imaging rooms and the research laboratories dealing with PET radiotracers are high compared to the radiation levels with conventional SPECT radionuclides used in nuclear medicine. As a result, there is an increased concern that the personnel or the occupational workers (technologists, scientists, and physicians) may receive substantially higher radiation exposure. Also, with the continued use of dual-modality imaging systems, whole body PET/CT and SPECT/CT examinations there is an increased radiation exposure compared to an individual PET, SPECT or CT procedures.

The use of radioactivity is highly regulated, and over the years extensive regulatory and institutional policies and procedures have been promulgated to ensure its safe and compliant use. The International Committee on Radiological Protection (ICRP) and the National Council on Radiation Protection and Measurement (NCRP) have developed guidelines for the safe handling of radiopharmaceuticals. The Nuclear Regulatory Commission (NRC) adopts these recommendations and formally provides the regulations for implementing radiation protection programs in the Unites States, pursuant to Title 10, Part 35 of the Code of Federal Regulations, 10CFR35 (NRC 2002). The

NRC regulates all the reactor-produced byproduct of radioactive materials with regard to their use and disposal. In addition, the NRC regulates the radiation safety for all occupational workers and the general public. The use of cyclotron or accelerator produced radionuclides is regulated by the individual state agencies, in the United States. In well over half of the states, the so-called "Agreement States," the NRC has agreed to delegate its regulatory authority to the state. Therefore, in Agreement States, the use of radioactivity is directly regulated by a state agency (or even by a specific City in a state) rather than the NRC. In addition, the FDA, the United States Department of Transportation (US DOT), and other federal agencies maintain regulatory authority over certain aspects of the medical use of radioactivity.

In every country the general public is exposed to various natural sources of radiation (such as ^{40}K, uranium, and thorium decay products) and to medical procedures and every year receives a certain radiation dose, conveniently called *natural background radiation*. Therefore, it is important to understand the relative increase of radiation exposure received by occupational workers compared to that received by the general public.

Because the imaging procedures (PET, SPECT, PET/CT, and SPECT/CT) require the administration of radiopharmaceuticals, the human subjects involved in these procedures may receive high radiation doses to different organs and tissues in the body, depending on the radionuclide and the corresponding radiopharmaceutical. Therefore, it is also important to understand the technical and biological issues involved in

organ and tissue dosimetry, when using PET and SPECT radiopharmaceuticals.

The main purpose of this chapter is not to discuss extensive technical and regulatory issues related to radiation protection, but to focus on specific practical issues involved in radiation protection, dosimetry, and safety precautions to minimize the radiation exposure.

19.2 Dosimetry

19.2.1 Quantities and Units

Radiation dosimetry is the branch of science that attempts to quantitatively relate specific measurements made in a radiation field to chemical and/or biological changes that the radiation would produce in a target. The three basic SI units related to radiation are *roentgen* (R) for *exposure*, *gray* (Gy) for radiation *absorbed dose*, and *Sievert* (Sv) for radiation *dose equivalent* to man.

19.2.1.1 Exposure

For electromagnetic radiation (x and γ rays) exposure is defined in terms of the ionization they produce in the air. The unit of exposure is called *roentgen* (R) and was originally defined in 1928 as the amount of radiation that produces 1 esu of charge of either sign (includes both primary and secondary ions) per 0.001293 g (the mass of air that occupies 1 cm^3 at STP), in the air.

The unit roentgen is now defined as

$$1\ R = 2.58 \times 10^{-4}\ C\ kg^{-1} \qquad (19.1)$$

19.2.1.2 Absorbed Dose

The concept of exposure and the definition of the *R* provide a practical, measurable standard for the radiation in the air. The primary physical quantity used in radiation dosimetry is the absorbed dose, *D*, which is the mean energy ($d\bar{E}$) deposited per unit mass of an absorbing material (d*m*), including biological tissue.

$$D = \frac{d\bar{E}}{dm} \qquad (19.2)$$

In SI units, the unit of an absorbed dose, J kg^{-1}, is called the *gray* (Gy). The older unit, the rad, is defined as 100 ergs g^{-1}. These units are related as follows:

$$1\ Gy = \frac{1\ J}{kg} = \frac{10^7\ erg}{10^3\ g} = 10^4\ \frac{erg}{g} = 100\ rads \quad (19.3)$$

Since the average energy needed to produce an ion pair is 34 eV, an exposure of 1 R gives a dose of 8.8×10^{-3} Gy (=0.88 rad), in the air.

A radiation dose of 1 cGy(rad) is always 1 cGy in 1, 2, or 100 g of the material. However, the integral absorbed dose is given in units of gram-rads (g.rad or g.Gy). For example, if the radiation dose to a 20 g tumor mass is 1 Gy, the integral dose to the entire tumor mass is 20 Gy.

19.2.1.3 Equivalent Dose and Effective Dose

It has long been recognized that the absorbed dose needed to achieve a given level of biological damage (e.g., LD$_{50}$) is often different for different types of radiation (penetrating and non-penetrating). Radiation with a high LET (such as protons and neutrons) is generally more damaging to a biological system per unit dose than radiation with a low LET (such as X rays, γ-rays and electrons). Radiation quality is characterized by LET.

$$LET = \frac{dE}{dl} \qquad (19.4)$$

where, d*E* is the energy lost by a charged particle in traversing a distance d*l* in matter. The SI unit is the J/m and the conventional unit the keV μ^{-1}; 1 J m^{-1} = 6.25 × 10^9 keV μ^{-1} and 1 keV μ^{-1} = 1.60 × 10^{-10} J m^{-1}. LET is in the order of 1 keV μ^{-1} for x-, γ-, and β-rays, 10 keV μ^{-1} for *n* and *p*, and 100 keV μ^{-1} for α-rays (Zanzanico and Heller 2007).

Due to the difference in the biological effectiveness of different types of radiation, two derived dose quantities have been invoked to regulate the exposure of persons at work and the public at large: the *equivalent dose* (*H*) and the *effective dose* (*E*), both of which are expressed in sieverts (Sv). With the dose in rad, the older unit of the dose equivalent is the *rem* (roentgen-equivalent-man). As 1 Gy = 100 rads, 1 Sv = 100 rem and 1 rem = 1 cSv (10 mSv)

The dose equivalent is the product of the dose (D) and a quality factor (Q), which depends on LET. Since the value of Q is the unity ($=1$) for any radiation with LET $< 10\,\text{keV}\,\mu\text{m}^{-1}$,

$$H = Q\,D \qquad (19.5)$$

The influence of LET on the frequency and/or severity of biological effects are quantified by the relative biological effectiveness (RBE). In order to simplify RBE, a *radiation weighting factor* (W_R), was devised for purposes of radiation protection. (H) is absorbed dose weighted for the type of radiation and averaged over the whole organ or tissue. Equivalent dose, H_T, in tissue or organ T, is related to the radiation weighting factors, W_R, and the mean absorbed doses, $D_{T,R}$, to the tissue or organ T due to radiations R:

$$H_T = \sum_R W_R \times \sum_R W_{T,R} \qquad (19.6)$$

For X-rays, γ-rays, and electrons, the W_R is 1. Therefore, the equivalent dose in Sv is numerically equal to the absorbed dose in Gy. Also, the radiation weighting factor (W_R), and the equivalent dose (H_T) are similar to the older quantities of quality factor (Q), and dose equivalent (H), respectively.

Effective dose (E) is a weighted sum of the equivalent doses to the individual organs and tissues of the body. The tissue weighting factors (W_T) take account of the relative susceptibility of different tissues to radiation damage (Table 19.1).

Table 19.1 Tissue weighing factors recommended by the ICRP[a]

Tissue (T)	Weighing factors recommended in		
	1979	1991	2007
Gonads	0.25	0.20	0.08
Red marrow	0.12	0.12	0.12
Colon		0.12	0.12
Lung	0.12	0.12	0.12
Stomach		0.12	0.12
Bladder		0.05	0.04
Breast	0.15	0.05	0.12
Liver		0.05	0.04
Esophagus		0.05	0.04
Thyroid	0.03	0.05	0.04
Skin		0.01	0.01
Bone Surface	0.03	0.01	0.01
Salivary glands, brain			0.01
Remainder	0.30	0.05	0.12

[a]The above table was modified from Stabin (2008); ICRP 1971 factors were used in estimating EDE (HE); ICRP 1991 factors were used in estimating ED (E)

$$E = \sum_T W_T\,H_T \qquad (19.7)$$

where, W_T is the weighting factor for tissue or organ T, a dimensionless quantity representing the fraction contributed by tissue or organ T to the *total* stochastic risk. The effective dose (ED or E) is intended to provide a single-value estimate of the overall stochastic risk (i.e., the total risk of cancer and genetic defects) of a given irradiation, whether received by the whole body, part of the body, or only one or several individual organs (Zanzanico and Heller 2007).

The effective dose is similar in concept to the effective dose equivalent, EDE (H_E) representing a single-value estimate of the net "harm" from any *lowdose* exposure. While E includes all fatal and nonfatal cancer risks, and serious hereditary effects on all generations, H_E includes all fatal cancer risks and significant first generation hereditary effects. As a result, the tissue weighing factors are different for these two parameters.

19.2.2 Equilibrium Absorbed Dose Constant (Δ)

The dose rate (R) is the defined as the amount of radiation energy absorbed per unit time per gram of material

$$R\,(\text{rad}/h) = \frac{A\,(\mu\text{Ci})}{m\,(\text{g})} \times \sum \Delta_i \qquad (19.8)$$

The amount of energy deposited, locally or at a distance from the disintegrating atoms in an infinite medium, is indicated by the equilibrium absorbed dose constant (Δ_i), as shown in the above equation. The contribution of Δ from the non-penetrating (particles) and penetrating radiation for a selection of radionuclides is shown in Table 19.2. Electrons (β⁻ and β⁺), being a non-penetrating radiation, deposit their energy locally and account for most of the dose to the organs and tissues. All PET isotopes give rise to two 511 keV photons per emitted positron. In addition, there can be additional γ-rays from the nuclear decay and bremsstrahlung radiation emitted, as the positron slows down. Several PET radionuclides ([86]Y, [124]I, [94m]Tc) also have significant γ-rays in very high abundance. All these penetrating electromagnetic radiations account for the exposure to persons standing close to the radioactive sources. The high dose rates

(μJ MBq^{-1} min^{-1}) from PET radionuclides, relative to other radionuclides used for diagnostic imaging, are because of their high photon energy (511 keV) and abundance (197–200%) (Table 19.2).

19.2.3 Air Kerma Rate Constant (Γ_δ)

It is often necessary to estimate the exposure rate at a distance from the radionuclides emitting electromagnetic radiations. Traditionally, the exposure from the X-ray and γ-ray emitting radionuclides is estimated on the basis of the exposure rate constant Γ, which is defined as the exposure in R/h from 1 mCi at a distance of 1 cm.

The factor relating activity and exposure rate has been given various names: the k factor, the specific gamma ray constant, exposure rate constant, and gamma ray constant (Ninkovic et al. 2005). Conversion to SI units required that this factor be replaced by the air kerma rate constant, which is now defined as,

$$\Gamma_\delta = \frac{l^2}{A}\left(\frac{dK_{air}}{dt}\right)_\delta \qquad (19.9)$$

where, $(dK_{air}/dt)_d$ is the air kerma rate due to photons of energy $> \delta$, at a distance l from a point source of activity A. The SI unit for Γ_δ is J m^2 kg^{-1} or Gy m^2 kg^{-1}, which becomes Gy m^2 s^{-1} kg^{-1}, when the terms Gy and Bq are used (Ninkovic et al. 2005). Because photons <20 keV are generally absorbed by the container and do not significantly contribute to the radiation exposure, photons >20 keV are often included in the calculation of the Γ values. The exposure rate constants for several radionuclides are shown in Table 19.3. The values reported here were calculated using the latest appropriate decay data and numerical data for mass energy transfer coefficient. As a result, the values in Table 19.3 for air kerma rate constants are the most accurate data that can be found in the literature, to date (Ninkovic et al. 2005).

Table 19.2 Equilibrium absorbed dose constant (Δ)

Radionuclide	$T_{\frac{1}{2}}$ min	Equilibrium dose constant (Δ) g Gy MBq^{-1} h^{-1}			Energy from total decay of 1 MBq (μJ)	Energy μJ MBq^{-1} min^{-1}
		Δ for n–p	Δ for p	Total		
^{15}O	2.07	0.415	0.589	1.004	50	24.15
^{13}N	10.0	0.281	0.589	0.870	209	20.9
^{11}C	20.4	0.277	0.588	0.815	397	19.46
^{18}F	110	0.139	0.570	0.709	1868	16.98
^{131}I	11578	0.109	0.219	0.328	91250	7.88
^{99m}Tc	360	0.010	0.072	0.082	708	1.967

Table 19.3 Exposure rate constants for PET and SPECT radionuclides

Radionuclide	$T_{\frac{1}{2}}$ Hour (h)	Photon Energy KeV	Abundance %	Air kerma rate constant[a] μGy m^{-2} GBq^{-1} h^{-1}	Gamma ray constant[b] R cm^2 mCi^{-1} h^{-1} at 1 cm
^{18}F	1.828	511	200	135.1	4.998
^{11}C	0.3396	511	200	139.3	5.154
^{13}N	0.1662	511	200	139.4	5.158
^{15}O	0.0333	511	194	139.5	5.162
^{68}Ga	1.1333	1–1,883	180	129.0	4.773
^{111}In	67.31	3.1–245.5		83.13	3.076
^{131}I	192.5	4.1–722.9		52.2	1.931
^{123}I	13.27	3.8–783.6		36.1	1.336
^{67}Ga	78.26	1–888		19.45	0.720
^{99m}Tc	6.01	2.4–142.6		14.1	0.522

[a]The values from Ninkovic et al. (2005)
[b]R cm^2 mCi^{-1}. H is equal to 27.027 μGy m^{-2} GBq^{-1} h^{-1}

Table 19.4 Occupational radiation dose limits[a]

| Dose | Organ | Radiation dose (mSv) per year | | |
		Worker	Pregnant worker[b]	General Public
Effective dose (ED)		50	5	1.0
Equivalent dose	Lens of the eye	150		
	Any other organ	500		
	Skin and other extremities	500		

[a]Code of Federal Regulations, Title 10, Part 20
[b]It is recommended that no more than 0.5 mSv be received by the embryo or fetus in any 1 month

19.2.4 Dose Limits

The NRC sets the radiation dose limits (Table 19.4) for both, individuals working with radiation workers and members of the general public in the restricted areas. However, when a female worker becomes pregnant, a difficult regulatory problem is created. Should the dose limits for the mother (a radiation worker) or the dose limits for the fetus (a member of the public) be used? The short answer is that the woman has the right to choose, but not the fetus. The reason for lower dose limits is that the cells of a fetus replicate at a very high rate and, therefore, the possibility of doing damage to the cells is increased dramatically. Thus it is recommended that the embryo or fetus receive no more than 0.5 mSv be in any 1 month. Members of the public have very low dose limits in comparison with those assigned to radiation workers.

19.3 Internal Dosimetry

Radiation absorbed doses to various internal organs and tissues, following administration of diagnostic radiopharmaceuticals are estimated on the basis of the methodology developed by the Medical Internal Radiation Dose (MIRD) Committee of the Society of Nuclear Medicine (Loevinger et al. 1988). Personal computer software programs ((The MIRDOSE program or OLINDA program) are available to determine the dose (Stabin 1996).

The MIRD method requires an estimate of the kinetics and biodistribution (spatial and temporal dis-

tribution) of a radiopharmaceutical in the body. Any organ or a volume of interest containing significant amount of radioactivity is regarded as a *source organ* (s), while a region or a volume of interest for which the absorbed dose is to be estimated, is regarded as the *target organ* (t). The source and target volumes become the same when the source organ has non-penetrating radiation. Radiation doses also need to be estimated for various target volumes, which receive radiation energy from a source organ containing the radioactivity. The MIRD formula for estimating the radiation dose to a target volume, from a source organ, is as, follows:

$$\bar{D}_{(rt \leftarrow rs)} = \frac{\tilde{A}_s}{m} \sum_i \varphi_i(rt \leftarrow rs)\Delta_i \qquad (19.10)$$

$$\bar{D}_{(rt \leftarrow rs)} = \bar{A}_s \sum_i \Phi_i(rt \leftarrow rs)\Delta_i \qquad (19.11)$$

$$\bar{D}_{(rt \leftarrow rs)} = \bar{A}_s S_{st} \qquad (19.12)$$

In the above equations, $\tilde{A}_s$ is the *cumulated activity* in a source organ, ϕ represents the *absorbed fraction*, while Φ represents the *specific absorbed fraction* (ϕ/m). $\tilde{A}_s$ is the cumulated activity in a source organ and S_{st} is the *S factor*, the absorbed dose in a target organ per unit cumulated activity in the source organ (mGy MBq^{-1} h^{-1}). The S factor is determined by the physical properties of the radionuclide and includes both, a specific absorbed fraction and an equilibrium dose constant. Tabulated S factors for pairs of standardized source and target organs are available for many radionuclides (Snyder et al. 1975).

19.3.1 Cumulative Activity (Ã)

The $\tilde{A}$ (MBq h^{-1}) in a given *source organ* can be calculated on the basis of the percentage of the injected dose (% ID/organ) or fraction of the administered activity (F_s) in an organ and the rates of the biological uptake ($T_{1/2u}$) and/or clearance ($T_{1/2b}$) from that organ. It represents the total number of disintegrations, which occur in the source organ, and is the area under the activity–time curve for the organ. The $\tilde{A}_s$ per unit-administered activity, A_0 ($\tilde{A}_s/A_0$), is called the *residence time* (τ) for

the radioactivity in that organ. $\tilde{A}_s$ in any source organ can be calculated as follows:

$$\tilde{A}_s = F_s \times A_0 \times 1.44 \times T_{eff} \qquad (19.13)$$

Effective half-life, $T_{eff} = \dfrac{T_{1/2p} \times T_{1/2b}}{T_{1/2p} + T_{1/2b}}$ (19.14)

19.3.2 Dosimetry of Radiopharmaceuticals

PET research involves the development and use of a variety of new tracers for imaging and quantifying an ever increasing range of molecular targets. Radiation dose estimates for radiopharmaceuticals are widely reported by different groups and individuals, using various modeling assumptions and computational techniques. The reported estimates are mean or median values for large populations of individuals and are sometimes reported with uncertainty estimates, but usually with observed standard deviations (SD) and coefficients of variation for the group of subjects studied. The estimation the equation of effective dose and the dose critical to an organ or organs (organs receiving highest dose) are biodistribution studies of appropriate animal models (usually rodents). Further, the estimates and are calculated using residence times and reference man geometry developed by MIRD) on standardized individuals, that is, reference man, reference woman, and reference pediatric individual (Loevinger et al. 1988). The anthropomorphic models, or phantoms that have been derived to represent these standard individuals, when used in these calculations, provide doses to the supposedly median individual in a reference group. It is important to recognize that patients, however, vary substantially in body size and shape, and the dose estimates for the standard individuals are accurate for only a small percentage of the individuals encountered in actual practice (Stabin 2008). Some of the recent phase I biodistribution protocols have incorporated more accurate individual organ masses which were estimated based on CT or MR volumetrics. Also, the OLINDA/EXM computer code does allow for a first-order scaling of standard phantom organ doses for individual-subject organ mass (Stabin et al. 2005).

The first step in fitting the biokinetic data of both PET and SPECT radiopharmaceuticals to various models, is simply the data acquisition. The strengths and limitations of the various data-gathering methods must be carefully assessed prior to the design of a specific imaging protocol, in order to obtain the data needed for estimating the radiation dosimetry of molecular imaging radiopharmaceuticals (Siegel 1999). Influences on the quality of the data include inherent system limitations on energy resolution, degradation of spatial resolution because of collimator septal penetration by high-energy photons (if present in the decay scheme), data loss due to scatter and attenuation, and, of course, the inherent statistical variability in any measurement of a radioactive source. Also, the ICRP has noted the difficulties of applying conventional dosimetry methods to very short-lived PET tracers (ICRP 1987). Further, generally better results, with perhaps 10–30% uncertainty for objects of various sizes, have been reported with high-quality SPECT quantitative imaging (Stabin 2008).

Radiation dose estimates for different diagnostic radiopharmaceuticals should be appreciated and considered, however, small differences in dose estimates between radiopharmaceuticals don't need to be given too much importance when choosing radiopharmaceuticals for general clinical use. Diagnostic accuracy, ease of use, image quality, patient comfort, and other similar factors should dominate the evaluation, while at the same time radiation dose being another issue considered, in balancing the risks and benefits appropriately (Stabin 2008).

19.3.2.1 Importance of Effective Dose (ED)

The concept of ED was introduced by the ICRP in 1977. In principle, ED is the dose that, if uniformly received by all tissues in the body, gives the same risk of somatic and genetic effects as that given by the actual non-uniform dose pattern received. Although the MIRD Committee of the Society of Nuclear Medicine does not accept the use of this quantity, the ICRP has promoted its use in nuclear medicine for diagnostic agents and the user community has generally accepted its use (Stabin 2008). The ICRP has also endorsed the use of the ED in nuclear medicine, noting that "Despite the wide range of organ doses in diagnostic nuclear medicine and the differences in age structure, effective dose [can be] used to provide a relative index of harm for various procedures in diagnostic radiology and nuclear medicine." (Streffer 2007).

An interesting, and perhaps unexpected, variability is introduced when EDs are calculated using different

tissue-weighting factors (Table 19.1) recommended by the ICRP for the calculation of ED. The recommended numeric values have changed as new information about cancer induction in various populations has been reported. Thus, given the exact same biokinetic model and reference phantom, the calculated ED, using two different sets of weighting factors, will be different.

When a new PET or SPECT radiopharmaceutical for a specific molecular target has been developed, studies in normal volunteers are required to define normal uptake and distribution. More specifically, data obtained from patients can only be interpreted if the normal pattern is known. One area for which the ED may be considered is the recruitment of volunteers for research studies. Commonly, the dose limits defined by the ICRP are used, however, these guidelines (Table 19.5) are somewhat unclear since the actual limits depend on the importance of the information obtained from the projected study.

For most diagnostic PET radiopharmaceuticals, the ED values are generally in the range of 2–10 mSv, which is comparable to the dose from many nuclear medicine procedures, including the dose from CT examinations. PET procedures often include a CT based transmission scan for attenuation correction of the image data. The additional radiation dose from the CT scan would be similar to that from the equivalent CT scan obtained separately from the PET scan, assuming that the scan parameters are the same. Therefore, with multi-slice hybrid scanners, the average ED may be higher compared to that of a single-slice CT scanner.

19.3.2.2 Radiation Dosimetry of [¹⁸F]FDG

Early dosimetry of FDG by the Radiation Internal Dose Information Center (RIDIC) group is based on a com-

Table 19.5 ICRP guidelines for using effective dose in clinical imaging studies

ED (mSv)	Outcome of clinical imaging study
< 0.1	Study expected only to increase knowledge
0.1–1.0	Study to increase knowledge leading to health benefit
1.0–10.0	Study aimed at the cure or prevention of disease
> 10	Study with direct benefit for subject
	Study related to saving of live
	Study to prevent or mitigate serious disease

ICRP 62, 1991

bination of organ distribution data gathered in dogs and data for the brain and urinary bladder gathered in human subjects (Gallagher et al. 1977; Jones et al. 1982) The MIRD group published a dose estimate report for ¹⁸F-FDG in which biokinetic data from several human studies were combined as input data for dose estimates (Hays et al. 2002). The ICRP, however, found discrepancies between the findings of the MIRD group and other published datasets and developed an independent assessment of dosimetry. The dose estimates did not differ markedly (Table 19.6), except for the estimates related to brain, urinary bladder wall, and pancreas (Stabin 2008). For the urinary bladder, the MIRD estimates

Table 19.6 Radiation dosimetry for [¹⁸F]FDG

Organ	Dose (μSv MBq⁻¹) estimated by			mSv/10 mCi (0.37 GBq)$
	RIDIC	MIRD	ICRP	ICRP
Adrenal glands	13.0		12.0	4.44
Brain	19.0	46.0	28.0	10.36
Breasts	9.2		8.6	3.182
Gallbladder wall	14.0		12.0	4.44
Lower large intestine wall	17.0		15.0	5.55
Small intestine	14.0		13.0	4.81
Stomach wall	13.0		11.0	4.07
Upper large intestine wall	13.0		12.0	4.44
Heart wall	60.0	68.0	62.0	22.94
Kidneys	20.0	21.0	21.0	7.77
Liver	16.0	24.0	11.0	4.07
Lungs	17.0	15.0	10.0	3.70
Muscle	11.0		11.0	4.07
Ovaries	17.0	11.0	15.0	5.55
Pancreas	26.0	14.0	12.0	4.44
Red marrow	13.0	11.0	11.0	4.07
Bone surfaces	12.0		11.0	4.07
Skin	8.4		8.0	2.96
Spleen	37.0	15.0	11.0	4.07
Testes	13.0	11.0	12.0	4.44
Thymus	12.0		11.0	4.07
Thyroid	10.0		10.0	3.70
Urinary bladder wall (UBW)	190.0	73.0[a]	160.0	59.20
Uterus	23.0		21.0	7.77
Effective dose (E)	30.0	16.0[b]	19.0	7.03

[a]Dose to UBW is based on 2-h void intervals, starting 2 h after administration
[b]Not provided by authors; estimated from input data
RIDIC data (Radiation Internal Dose Information Center) (Stabin et al. 1996); MIRD data (Hays et al. 2002); ICRP data (International Commission on Radiological Protection 1988); Dosimetry: (μSv/MBq)*(0.37) = mSv/for 10 mCi FDG dose; The above table was modified from Stabin (2008)

Table 19.7 Radiation dosimetry estimates for PET radiopharmaceuticals based on human studies

Radiopharmaceutical	Dose[a] MBq	Radiation dose (mSv 370MBq^{-1}) to the critical organ				ED mSv/370MBq	Reference
		Liver	Kidneys	GBW	UBW		
[^{11}C]Raclopride	370			11.7		2.31	Slifstein et al. (2006)
[^{11}C]Methionine	370				10.0	2.00	Deloar et al. (1998)
[^{11}C]PIB	370			15.4		1.753	Scheinim et al. (2007)
[^{13}N]Ammonia	370		1.702		3.0	0.74	Stabin (2008)
[^{15}O]Water	370		0.629			0.344	Stabin (2008)
[^{18}F]FDG	370				59.2	7.03	Stabin (2008)
[^{18}F]Fluoride	370				81.4	10.0	Grant et al. (2008)
[^{18}F]Fluorothymidne	370				65.4	11.4	Vesselle et al. (2003)
[^{18}F]FDOPA	370				55.6	7.4	Harvey et al. (1985)
[^{18}F]Fluorocholine	370		64.2			13.7	DeGrado et al. (2002)
[^{18}F]FMISO	370				10.73	5.18	Graham et al (1997)
[^{18}F]Fluoroestradiol	370				19.0	8.14	Mankoff et al. (2001)
^{64}Cu-DOTA-hLM609-II mAb	370	122.0				12.7	Cai et al. (2006)
^{64}Cu-TETA-Ctreotide	370				112	21.0	Anderson, et al. (2001)

GBW Galla bladder wall; *UBW* Urinary bladder wall
[a]Dose estimates based on animal studies

were base on an irregular bladder voiding interval; therefore, the MIRD dose estimates cannot be directly compared with the other two sets of dose estimates. However, the ICRP and MIRD estimates (Hays et al. 2002) are more reliable than the RIDIC data. The ICRP estimates include all the datasets used by RIDIC and MIRD as well as other recent data sources and are therefore preferred (Stabin 2008).

The radiation dosimetry estimates for several ^{18}F radiopharmaceuticals, based on biodistribution studies in human subjects have been reported (Vallabhajosula 2007). A summary of the published estimates for several ^{18}F agents compared to the currently accepted FDG radiation dosimetry estimates is shown in Table 19.7. With FDG, the whole body ED is approximately 7 mSv (700 millirem) for 370 MBq (10 mCi) of dose administered and the urinary bladder (critical organ) receives approximately 59.2 mSv. The dose for the urinary bladder wall is based on a 2 h void interval. For all other ^{18}F radiopharmaceuticals, listed in Table 19.7, the ED is between 5 and 15 mSv for a total administered dose of 370 MBq. In contrast, with radiotracers labeled with ^{11}C, the ED is approximately 2 mSv for an administered dose of 370 MBq.

19.3.2.3 Radiation Dose from Radiological Exams

Radiation dose estimates from other non-PET radiological procedures are shown in Table 19.8. The radiation

Table 19.8 Typical effective dose (ED) values for several common radiological exams (CT and non-CT)

Non-CT		CT	
Exam	ED (mSv)	Exam	ED (mSV)
Hand radiograph	<0.1	Head CT	1–2
Dental bitewing	<0.1	Chest CT	5–7
Chest radiograph	0.1–0.2	Abdomen CT	5 –7
Mammogram	0.3–0.6	Pelvis CT	3 – 4
Lumbar spine radiograph	0.5–1.5	Abdomen and pelvis CT	8 – 14
Barium enema exam	3–6	Coronary artery calcium CT	1 – 3
Coronary angiogram (diagnostic)	5–10	Coronary CT angiography	5 – 15
^{99m}Tc-sestamibi myocardial perfusion	13–16		
^{201}Tl myocardial perfusion	35–40		

Note: Average U.S.background radiation from naturally occurring sources ≈ 3.0 mSv (range 1–10 mSv) (NCRP 1987)

The ED values for radiological procedures are from reference, AAPM 2008

doses from typical CT exams of the chest and pelvis are comparable to those from ^{18}F radiopharmaceuticals. It is important to appreciate that the standard nuclear medicine SPECT scans with ^{201}Tl and ^{99m}Tc-sestamibi deliver even more radiation dose to the patient compared to PET and CT imaging scans.

Since the 1990s, the technology and capabilities of CT scanners have changed tremendously with the introduction of the helical and spiral CT. More specifically, with the dual-slice and multi-slice systems (four detector arrays along the z-axis), the number of slices or data channels that can be acquired per axial rotation has increased to 16- and 64, respectively. The radiation dose levels imparted in CT exams with the multi-slice CT systems exceed those of conventional radiography and fluoroscopy. However, it is important to remember that the ED describes the *relative whole bodydose* for a particular exam and scanner, but is *not* the dose for any one individual (AAPM 2008).

19.4 Radiation Protection

19.4.1 ALARA Program

The radiation dose limits, shown in Table 19.3, indicate the maximum occupational dose (OD) allowed for radiation workers in a year. However, the NRC instituted a policy, which states that one should make considerable efforts to adopt strict protective measures for working with radiations in order to reduce the radiation exposure to *as low as reasonably achievable* (ALARA). Under this concept, techniques, equipment, and procedures must be critically evaluated and adopted to minimize the radiation exposure. The NRC has set two action levels for taking some corrective measures. *Action level 1* is when a radiation worker receives >5 mSv per quarter (10% of OD per year) and *Action level 2* is when a radiation worker receives >15 mSv (30% of OD per year). If these limits are exceeded, corrective actions must be taken by the RSO, or higher limits must be justified for a particular situation.

19.4.2 Principles of Radiation Protection

The cardinal principles of radiation protection from external radiation sources are governed by four factors: *time, distance, shielding, and activity*.

It is almost intuitive that the longer the exposure time, the higher the radiation dose. Therefore, it is very important to spend the minimum amount of time necessary near radiation sources.

19.4.2.1 Distance and Dose Rate

For all electromagnetic radiations, the intensity of the radiation (or the radiation exposure) varies inversely with the square of the distance from the source. Therefore, working at a maximum possible distance from the radiation source is prudent in reducing radiation exposure. The radiation levels from a source emitting high energy photons can be estimated on the basis of the exposure rate constant, Γ, which is given in units of R-cm^2/mCi-h at 1 cm, or mGy-m^2/GBq-hr at 1 m. The exposure rate, X, from an unshielded radionuclide source (n-mCi) at a distance, d, cm is given by

$$X = \frac{n\Gamma}{d^2} \qquad (19.15)$$

What is the radiation exposure at 50 cm from a vial containing 100 mCi of ^{18}F or 100 mCi of ^{99m}Tc radioactivity?

The Γ (R cm^2/mCi h at 1 cm) from Table 19.3: ^{18}F = 4.998; ^{99m}Tc = 0.522.

The exposure rate (X) for ^{18}F:

$$X = \frac{100 \text{ mCi} \times 4.998}{(50 \text{ cm})^2} = 0.1999 \text{ R/h} \ \ or \ \ 200 \text{ mR/h}.$$

The exposure rate (X) for ^{99m}Tc:

$$X = \frac{100 \text{ mCi} \times 0.522}{(50 \text{ cm})^2} = 0.0209 \text{ R/h} \ \ or \ \ 20.9 \text{ mR/h}.$$

The above example shows that the exposure rate from ^{18}F is almost ten times that from ^{99m}Tc suggesting that shielding is very important when working with positron emitting radionuclides.

19.4.2.2 Shielding

The aim of a shielding design is to achieve a desired transmission, K, the ratio of dose rates – or doses integrated over a specified interval – with and without the shield in place (Towson 2005). The containers with high atomic number (Z) materials, such as lead, tungsten, and depleted uranium, absorb radiation and provide radiation protection. These containers should be designed to attenuate the maximum expected intensity (I_0) to an acceptable value (I), for example, $10\,\mu Sv\ h^{-1}$, at a specified close distance. Similarly, barriers, such as walls or floors between a source (patient with radioactivity) and an occupied area (control room) should attenuate the dose (D_0) for the maximum anticipated workload during a specified interval, for example, 1 week, to an acceptable value (D, the design limit) (Towson 2005).

$$K = \frac{I}{I_0}\ or\ \frac{D}{D_0} \qquad (19.16)$$

Under narrow-beam conditions, the attenuation of a beam of radiation through an absorbing medium is described by

$$I = I_0\ e^{-\mu x}, \qquad (19.17)$$

where, μ is the linear attenuation coefficient of the shielding material. The radiation shielding capacity of a material is measured in *Half-Value Layer* (HVL) and *Tenth-Value Layer* (TVL). Thus, if HVL of a shielding material is known, it is possible to determine how much material is needed to reduce the radiation intensity to less than 1%. Similarly, the TVL for a particular shielding material is the thickness required to reduce radiation intensity by a factor of 10. However, the effect of broad-beam geometry should be considered when shielding radiation sources (having energies, more than a few hundred keV) with material of low atomic number, in which Compton scattering is the predominant interaction. Under broad-beam conditions, the above equation is modified to

$$I = I_0\ B\ e^{-\mu x}, \qquad (19.18)$$

Where, B is the build-up factor that accounts for the transmitted radiation, which has been scattered within the barrier. In practice, tabulated HVL and TVL values under broad-beam conditions are generally used for simple shielding assessments. The HVL and TVL values in lead for several radionuclides are shown in Table 19.9.

Table 19.9 Lead Shielding required for PET and SPECT radionuclides[a]

Radionuclide	HVL (mm)	TVL (mm)
^{124}I	8.0	31.0
^{18}F	6.0	17.0
^{64}Cu	6.0	17.0
^{131}I	3.0	11.0
^{67}Ga	1.0	6.0
^{111}In	0.72	3.0
^{99m}Tc	0.25	1.0
^{201}Tl	0.051	1.0
^{125}I	0.02	0.07

[a]Nuclide Safety Data Sheet: www.nchps.org

Working with PET Radionuclides

As previously discussed, the external exposure is the most significant pathway for occupational exposure while working with PET radionuclides, mainly because of the high dose rates from the 511 KeV annihilation photons. Following administration of β^+ emitting radiotracers to patients and animals, these photons represent a source of radiation exposure to the professional staff involved in the imaging studies. An important contribution to the dose to personnel is handling of the injection syringe. Therefore, the syringes must be shielded using lead or preferably tungsten. Further sampling of arterial or venous blood throughout the time course of a dynamic scan is required for many research studies. The rapid manual sampling can lead to a substantial (finger) dose.

The radiation exposure increases with the intensity of the radioactive source. Shielding is an important means of protection from radiation, however, it is also important to minimize the time spent near the unshielded radiation source (patients or animals) in the scanner room.

References

American Association of Physicists in Medicine, AAPM (2008) The measurement, reporting, and management of radiation dose in CT, AAPM Report No. 96. Report of AAPM Task Group 23, Published by AAPM, College Park, MD

Anderson CJ, Dehdashti F, Cutler PD, et al (2001) ^{64}Cu-TETA-octreotide as a PET imaging agent for patients with neuroendocrine tumors. J Nucl Med 42(2):213–221

Brix G, Lechel U, Glatting G (2005) Radiation exposure of patients undergoing whole-body dual-modality ^{18}F-FDG PET/CT examinations. J Nucl Med 46:608–613

Cai W, Wu Y, Chen K, et al (2006) In vitro and in vivo characterization of 64Cu-abeled AbegrinTM, a humanized mono-

clonal antibody against integrin {alpha}v{beta}₃. Cancer Res 66(19):9673–9681

DeGrado TR, Reiman RE, Price DT, et al (1985) Pharmacokinetics and radiation dosimetry of ^{18}F-fluorocholine. J Nucl Med 43:92–96

DeGrado TR, Reiman RE, Price DT, et al (2002) Pharmacokinetics and radiation dosimetry of [^{18}F]fluorocholine. J Nucl Med 43:92–96

Deloar HM, Fujiwara T, Nakamura T, et al (1998) Estimation of internal absorbed dose of L-[methyl-^{11}C]methionine using whole-body positron emission tomography. Eur J Nucl Med 25:629–633

Gallagher BM, Ansari A, Atkins H (1977) Radiopharmaceuticals XXVII. ^{18}F-labeled 2-deoxy-2-fluoro-D-glucose as a radiopharmaceutical for measuring regional myocardial glucose metabolism in vivo: tissue distribution and imaging studies in animals. J Nucl Med 18:990–996

Graham MM, Peterson LM, Link JM, et al (1997) Fluorine-18-fluoromisonidazole radiation dosimetry in imaging studies. J Nucl Med 38:1631–1636

Harvey J, Firnau G, Garnett ES (1985) Estimation of the radiation dose in man due to 6-[^{18}F]fluoro-L-dopa. J Nucl Med 26:931–935

Hays MT, Watson EE, Thomas SR, et al (2002) MIRD dose estimate report no. 19: Radiation absorbed dose estimates from ^{18}F-FDG. J Nucl Med 43:210–214

International Commission on Radiological Protection (1977) ICRP Publication 26. Recommendations of the international commission on radiological protection. Pergamon, New York

International Commission on Radiological Protection (1987) ICRP publication 52. Radiation dose to patients from radiopharmaceuticals. Pergamon, Oxford

International Commission on Radiological Protection (1987) ICRP Publication 53. [^{18}F]Fluoride radiation dosimetry, vol 18(l–4). ICRP, Canada, pp 73–74

International Commission on Radiological Protection (1988) ICRP Publication 53. Radiation dose to patients from radiopharmaceuticals. Pergamon, New York, NY

International Commission on Radiological Protection (1991) ICRP Publication 62. Radiologica protection in biomedical research. ICRP, Canada

International Commission on Radiological Protection, Addendum to ICRP 53 (1998) Radiation dose from radiopharmaceuticals. ICRP publication 80. Elsevier, Philadelphia, PA

International Commission on Radiological Protection (1998) ICRP Publication 80. Radiation dose to patients from radiopharmaceuticals. Pergamon, New York, NY

Jones SC, Alavi A, Christman D, et al (1982) The radiation dosimetry of 2-[F-18]fluoro-2-deoxy-D-glucose in man. J Nucl Med 23:613–617

Lockwood AH (1980) Absorbed doses of radiation after an intravenous injection of N-13 ammonia in man: concise communication. J Nucl Med 21:276–278

Loevinger R, Budinger TF, Watson EE (1988). MIRD primer for absorbed dose calculations. Society of Nuclear Medicine, New York

Mankoff DA, Peterson LM, Tewson TJ, et al (2001) [^{18}F]fluoroestradiol radiation dosimetry in human PET studies. J Nucl Med 42:679–684

National Council on Radiation Protection and Measurements (1987) Ionizing radiation exposure of the population of the United States. Report No. 93. Bethesda

Ninkovic MM, Raicevic JJ, Adrovic F (2005) Air kerma rate constants for gamma emitters used most often in practice. Radiation Protection Dosimetry 115:247–250

Nuclear Regulatory Commission, NRC (2002) Medical use of byproduct material. 10CFR Part 35, Washington, DC

Robeson W, Dhawan V, Belakhlef A, et al (2003) Dosimetry of the dopamine transporter radioligand ^{18}F-FPCIT in human subjects. J Nucl Med 44:961–966

Saha GB (2004) Fundamentals of nuclear pharmacy. Springer, New York

Scheinim NM, Tolvanen TK, Wilson IA, et al (2007) Biodistribution and radiation dosimetry of the amyloid imaging agent ^{11}C-PIB in humans. J Nucl Med 48:128–133

Seltzer MA, Jahan SA, Sparks R, et al (2004) Radiation dose estimates in humans for [^{11}C]-acetate whole-body PET. J Nucl Med 45(7):1233–1236

Siegel JA, Thomas SR, Stubbs JB, et al (1999) MIRD pamphlet no. 16: techniques for quantitative radiopharmaceutical biodistribution data acquisition and analysis for use in human radiation dose estimates. J Nucl Med 40(suppl):37S–61S

Slifstein M, Hwang D-R, Martinez D, et al (2006) Biodistribution and radiation dosimetry of the dopamine D2 ligand ^{11}C-Raclopride determined from human whole-body PET. J Nucl Med 47:313–319

Snyder WS, Ford MR, Warner GG et al (1975) Absorbed dose per unit cumulated activity for selected nuclides and organs. MIRD Pamphlet No.11, Society of Nuclear Medicine, New York

Stabin MG (1996) MIRDOSE: Personal computer software for internal dose assessment in nuclear medicine. J Nucl Med 37:538–546

Stabin MG, Stubbs JB, Toohey RE (1996) Radiation dose estimates for radiopharmaceuticals. U.S. Nuclear Regulatory Commission NUREG/CR-6345, U.S. Department of Energy, U.S. Department of Health and Human Services, Washington, DC

Stabin MG, Sparks RB, Crowe E (2005) OLINDA/EXM: The second-generation personal computer software for internal dose assessment in nuclear medicine. J Nucl Med 46: 1023–1027

Stabin MG (2008) Uncertainties in internal dose calculations for radiopharmaceuticals. J Nucl Med 49:853–860

Stabin MG (2008) Radiopharmaceuticals for nuclear cardiology: radiation dosimetry, uncertainties, and risk. J Nucl Med 49:1555–1563

Streffer C (2007) The ICRP 2007 recommendations. Radiation Protection Dosimetry; doi:10.1093/rpd/ncm246, Published by Oxford University Press

Towson JEC (2005) Radiation dosimetry and protection in PET. In: Bailey DL et al (eds) Positron emission tomography: basic sciences, Springer, London

Vallabhajosula S (2007) ^{18}F-labeled positron emission tomographic radiopharmaceuticals in oncology: an overview of radiochemistry and mechanisms of tumor localization. Semin Nucl Med 37:400–419

Vesselle H, Grierson J, Peterson LM, et al (2003) ^{18}F-Fluorothymidine radiation dosimetry in human PET imaging studies. J Nucl Med 44:1482–1488

Zanzonico P and Heller S (2007) Physics, instrumentation, and radiation protection. In: Biersack H-J, Freeman LM (eds). Clicial Nuclear Medicine, Springer-Verlag, Berlin

Radiopharmaceuticals: Drug Development and Regulatory Issues

The FDA is under attack for paying too little attention to drug safety, while the pharmaceutical industry is being criticized both for unsafe drugs and too little innovation. Fortunately, incentives for maintaining safety are very strong. But obsolete regulation stands in the way of efficient utilization of recent advances in technology and basic science. With the fates of the FDA and the industry more intertwined than ever, our health depends on regulatory innovation as much as on scientific progress.

John E. Calfee
American Enterprise Institute.

20.1 Drug Development

The discovery of drugs and their development rely on the scientific understanding of pathology and biology at the molecular, cellular, system, and organism level. The widespread availability of radio labeled PET and SPECT molecular imaging probes increase our understanding of the in vivo biology associated with the new targeted imaging (or diagnostic) agents and therapeutic drugs (Klimas 2002; Maclean et al. 2003). Specifically, molecular imaging will provide the necessary techniques and specific tools:

- To assay and identify important and key alterations in molecular pathways, signal transduction and receptor levels due to disease.
- To elucidate the behavior of many diseases and their response to certain drugs and therapies.
- To individualize and personalize treatments on the basis of a "molecular phenotype" of the disease.
- To characterize and monitor therapy noninvasively and over time.

Linking imaging-based diagnosis with targeted molecular therapy will become an important tool in ushering in the age of personalized medicine. The personalized approach to therapy could improve patient care, since individuals would receive the most appropriate and targeted therapy that would improve outcomes, minimize unnecessary morbidity associated with ineffective therapies, and provide substantial cost savings (Hofman et al. 2007).

Drugs lead to probes, and probes lead to drugs, therefore, the development of clinical diagnostics will greatly benefit from the availability of chemical insights gathered that may most widely be obtained from the efforts of from pharmaceutical discoveries. In turn, the availability of radiolabeled PET tracers will allow a much greater understanding of the in vivo biology associated with new drugs and the targets they affect, and will increase the likelihood of success in the clinic (Maclean et al. 2003). Since radiotracer based molecular imaging has the potential to provide a much-needed holistic approach to drug research, it will have a particularly important niche in the therapeutic discovery of drugs and their development process (Bergstrom et al. 2003; Eckelman et al. 2005).

The discovery of drugs and their development process from the test tube to the clinic (Fig. 20.1) involves basically three steps; (1) the initial in vitro studies linking biology and chemistry to identify suitable biologic targets and appropriate lead compounds, (2) the preclinical in vivo studies in animal models to assess drug in vivo specificity, biodistribution, pharmacokinetics and toxicology, and (3) the clinical studies designed to study safety, biodistribution, pharmacokinetics, target (receptor, enzyme, antigen, etc) specificity, metabolism, and, finally, efficacy. The drug development process, including that for the development of diagnostic imaging agents, is a very costly process that requires many years (5–15 years) from the time of discovery to the final approval of the drug for use in humans (Nunn 2006). It is envisioned that molecular imaging will have the potential to shorten the timeline and reduce the costs for all three stages of the drug development

process described above, by enabling expedient and more direct measurements of the drug effects in the body, using target specific radio labeled probes (Fig 20.2).
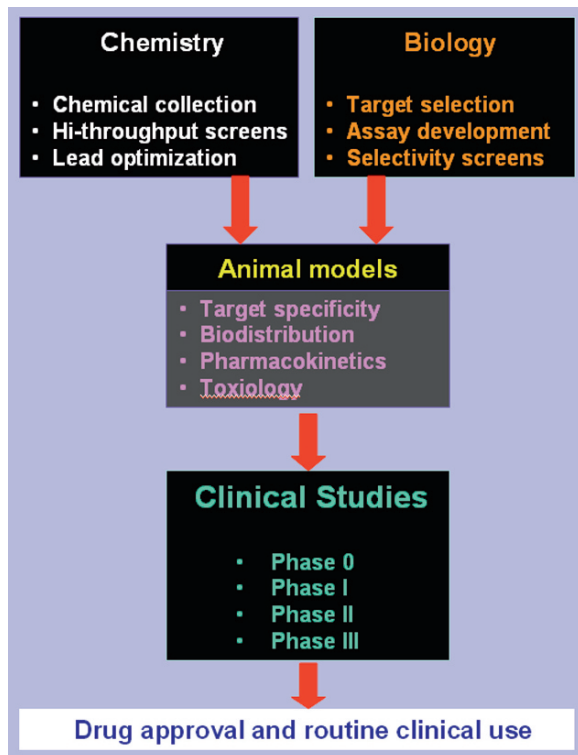
Fig. 20.1 The drug discovery and development process

20.1.1 The Critical Path to New Medical Products

The *Critical Path Initiative* is the FDA's effort to stimulate and facilitate a national effort to modernize the scientific process through which a potential human drug, biological product, or a medical device is transformed from a discovery or *proof of concept* into a medical product (FDA 2004a). Imaging technologies provide powerful insights into the distribution, binding and other biological effects of pharmaceuticals. As part of its Critical Path initiative, the FDA has joined the National Cancer Institute (NCI), the pharmaceutical industry, and academia, in a number of activities that will facilitate the development of new imaging agents and increase the use of medical imaging during product development. The FDA believes that imaging agents and technologies can contribute important biomarkers and surrogate endpoints during disease progression and contribute to the development of new therapies to treat diseases. The future of molecular imaging drug discovery is substantial, and the functional and anatomical information it provides will be central to solving many challenges related to treatment. In summary, molecular imaging studies conducted at various stages of the drug development process will provide significant information for the following:
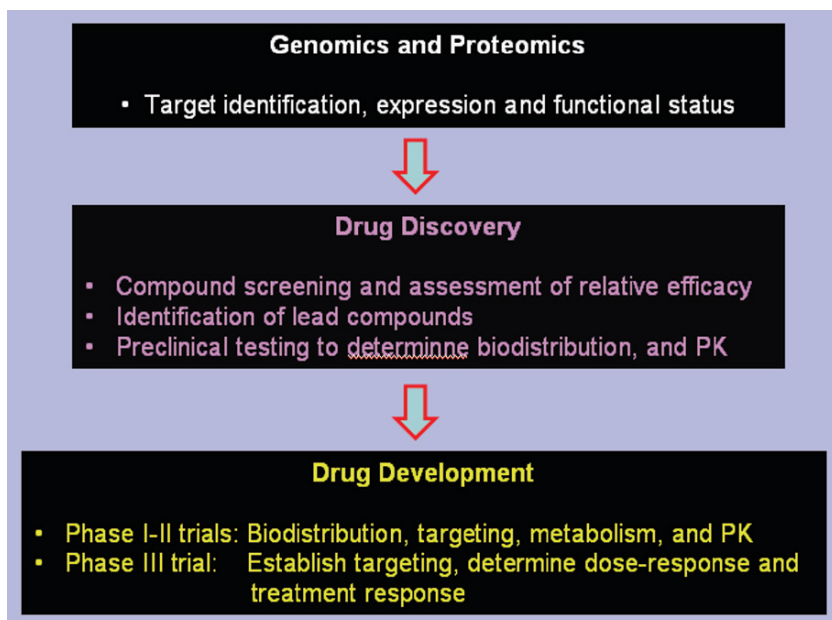
Fig. 20.2 The role of molecular imaging in the drug discovery and development process

- The imaging probes may enable visualization of the phenotypic expression of key molecular targets associated with the disease process by using probes that image specific molecular targets and pathways in vivo.

- To display biochemical and physiologic abnormalities that occur early in the disease process, as opposed to the structural changes that eventually occur and are visualized with more standard anatomic imaging techniques.

- The imaging biomarkers may be potentially useful to track the physiologic events taking place in vivo, to discover new biological targets, and for the pivotal clinical trials needed for therapeutic drug approval.

- The imaging disease biomarkers have great potential to help define, stratify and enrich various groups of promising molecularly targeted therapeutic drugs that are undergoing clinical trial testing and to noninvasively assist in the identification, characterization, and quantitation of the therapeutic drug target in various patient study populations.

- Studies with the radiolabeled drug may also be invaluable for assessing the target interaction and modulation that might occur with the administration of a therapeutic drug in the diseased tissue and the body as a whole.

- Molecular imaging techniques could be invaluable when they are used in early-phase clinical studies comparing several leading candidate drugs designed to interact with the same target.

- The noninvasive molecular imaging-type biomarkers may have tremendous promise in accelerating the drug evaluation process by replacing or supplementing time- and labor-intensive dissection, histologic and pathologic analyses in both, preclinical and clinical testing.

- Noninvasive molecular imaging techniques also have the potential to enable longitudinal preclinical studies in various animal models with greater relevance to the future clinical trials that will be relied upon for therapeutic drug approval.

Since the FDA treats molecular imaging probes like drugs, except in certain circumstances, these probes must be subjected to the same development and regulatory approval process as drugs. This critical path may prove to be beneficial for decreasing the cost and improving the time to market molecular imaging probes as well as therapeutic drugs. The typical development and the subsequent regulatory approval process for new imaging agents, including the new molecular imaging probes, depends on the type of the probe and whether or not it is a radioactive agent. The radioactively labeled molecular imaging probes are typically administered in tracer quantities (nanomolar or picomolar concentrations). These tracer levels have a much lower propensity to cause pharmacologic effects and, thus, may have minimal or no toxicities. MR imaging agents, on the other hand, may require administration at the milligram level to achieve concentrations that enable adequate imaging.

The medical imaging agents generally are governed by the same regulations as other drug and biological products. However, because medical imaging agents are used solely to diagnose and monitor diseases or conditions as opposed to treat these conditions, developmental programs for medical imaging agents can be tailored to reflect these particular uses. The FDA has developed three separate guidance documents (FDA 2004b) that explicitly describe the developmental process of the imaging agent. These documents are entitled (a) *Conducting Safety Assessments*; (b) *Clinical Indications*; (c) *Design, Analysis, and Interpretation of Clinical Studies*. These documents describe and elaborate on the important differences between various types of imaging agents. Medical imaging agents can be classified into at least two general categories: contrast agents and diagnostic radiopharmaceutical agents. The FDA also makes a distinction, as defined in guidance document 1, between what is referred to as group 1 (nonbiologic) and group 2 (biologic potential for eliciting an immunologic response) medical imaging agents.

20.2 FDA and Clinical Research

Initially, the Atomic Energy Commission (AEC), and the Nuclear Regulatory Commission (NRC) were responsible for the regulation of the use of reactor produced imaging probes. From 1963 until 1975, the Commissioner of Food and Drugs exempted the new radioactive drug and biologic products used for investigational purposes in humans from compliance with the new drug requirements, as long as these products were safe. In 1975, the FDA and the newly formed

NRC agreed that all radioactive drugs and biologic products should become subject to the same FDA requirements for investigational use, as other new drugs. Also in 1975, the FDA decided to assume jurisdiction over accelerator-produced imaging probes and adopted essentially the same regulations for nuclear medicine imaging probes as those in existence for the traditional therapeutic drug industry. Subsequently, the FDA began requiring IND applications and New Drug Approvals (NDA) to demonstrate the safety and efficacy of these imaging probes

To help ensure the safety of human subjects, research studies involving the administration of radioactive drugs or biologic products must be conducted under the direct oversight of a radioactive drug research committee (RDRC), an FDA-approved body charged with the review of such studies, or under a FDA investigational new drug (IND) application, unless specifi-

cally exempt from IND requirements. The clinical trials of a new drug product are generally conducted in different phases as outlined in Fig. 20.3.

20.2.1 RDRC

The current RDRC regulations, promulgated on July 25, 1975, clarified under what circumstances certain radioactive drugs would be generally recognized as safe and effective (GRASE) and thus, eligible for use in basic research studies involving humans without requiring an IND (FDA 2005).

Research overseen by RDRC is considered as basic science research when its purpose is to advance scientific knowledge rather than the determination of a radioactive drug's safety and effectiveness as a
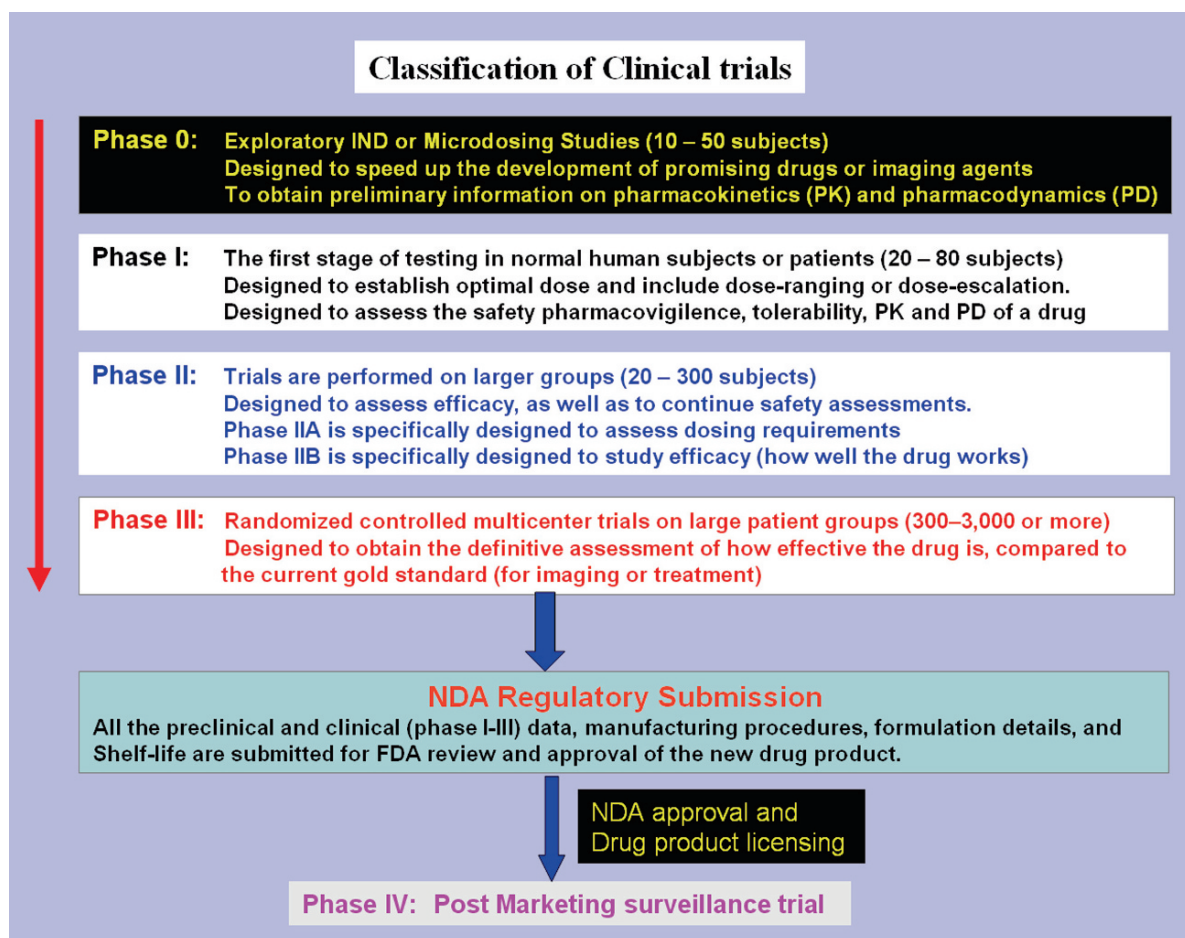
Fig. 20.3 Classification of clinical trials and the drug approval process

therapeutic, diagnostic or preventive medical product in humans. To use a radioactive drug in human research subjects, in an RDRC-supervised study, the drug must be GRASE and the research conducted must be basic in nature. The intent of basic science research is to obtain basic information, such as metabolism and excretion data. Such research may also investigate the biodistribution or pharmacokinetic properties of a radiolabeled drug or its physiologic, pathophysiologic, or biochemical characteristics. Other types of basic science research may investigate receptor binding or occupancy, transport processes, enzyme activity, or multistep biochemical processes (Suleiman et al. 2006). To be GRASE, the radio labeled drugs must meet two specific criteria:

a. Pharmacologic dose: The mass dose of the radio labeled drug to be administered must not be known to cause any clinically detectable pharmacologic effect in human beings. This criterion rules out first-in-humans (FIH) testing under RDRC authority.

b. Radiation dose: The human subjects must receive the smallest radiation doses possible to perform the study and the radiation doses received from a single study or from several studies conducted within a 1-year period should not exceed the regulatory dose limits (Table 20.1). For an adult, the limit is 30 mSV (3 rem) for whole-body exposure from a single dose and 50 mSv (5 rem) for whole-body exposure from the total number of RDRC studies conducted annually.

To ensure that RDRC research complies with these requirements, the FDA vests each RDRC with the

responsibility for direct oversight of the basic science research conducted at the designated medical institution, by directly approving research protocols. In addition to the requirement of an approval by the RDRC, prospective human research study subjects must also be approved by an institutional review board (IRB). Since the inception of the RDRC program in 1975, the FDA has approved a total of 201 committees, primarily at major medical institutions (Suleiman et al. 2006). The local RDRC is approved by the FDA through an application process. Another important aspect of the RDRC process is the composition of the RDRC, which is defined by the FDA. To establish an RDRC at an institution, certain requirements for committee membership must be met, as outlined in regulations (FDA 2005a).

RDRCs, a tool used primarily by large medical research institutions, have for more than three decades enabled these institutions to conduct basic science research in a relatively safe manner. Nevertheless, these 30-year-old regulations need to be revised to render them consistent with current scientific knowledge and health policy, especially with regard to drug quality standards and radiation dose limits (Suleiman et al. 2006).

20.2.2 IND Process

The FDA's role in the development of a new drug begins when the drug's sponsor (the investigator or more typically the manufacturer or potential marketer), seeks to test the diagnostic or therapeutic potential of a new molecule in humans. At that point, the molecule changes its legal status, under the Federal Food, Drug and Cosmetic Act, and becomes an investigational new drug (IND).

There are two IND categories; *Commercial* and *Research* (noncommercial); Commercial INDs are applications that are submitted primarily by companies whose ultimate goal is to obtain marketing approval of a new drug application (NDA) for a new drug product. However, there is another class of filings broadly known as "noncommercial" INDs and the vast majority of INDs are, in fact, filed for noncommercial research. These types of INDs include "Investigator INDs," "Emergency Use INDs," and "Treatment INDs."

An investigator-initiated IND is the most relevant IND process to assess the potential clinical utility of

Table 20.1 Radiation dose limits for RDRC subjects[a]

| Organ or system | Radiation dose (mSv) limits[b] for | |
	Single dose	Annual and total dose
Whole body	30	50
Active blood-forming organs	30	50
Lens of the eye	30	50
Gonads	30	50
Other organs	50	150

[a]RDRC: Radiation Dose Limits- CFR, Title 21, Part 361.1 (b) (3)
[b]For subjects <18 y of age, the dose should not exceed 10% of the adult dose
Radiation doses from all X-ray procedures that are part of the research study shall be included in the calculation of dose estimations

any investigational new drug intended either for diagnostic or therapeutic purpose. An Investigator IND is submitted by a physician who both, initiates and conducts an investigation, and under whose immediate direction the investigational drug is administered or dispensed. A physician might submit a research IND to propose studying (a) an unapproved drug, (b) an approved product for a new indication or, (c) studying the drug in a new patient population.

Clinical trials are conducted in a series of steps, called phases; each phase is designed to answer a separate research question. Clinical trials involving new drugs are commonly classified into four phases (Fig. 20.2). The IND application (FDA form 1571) must contain information in three broad areas (FDA 2007): (a) animal pharmacology and toxicology studies, (b) manufacturing information, and (c) clinical protocol and investigator information (Table 20.2). Once the IND application is submitted, the sponsor must wait 30 calendar days before initiating any clinical trial. During this time, the FDA has an opportunity to evaluate the IND for safety to ensure that research subjects will not be exposed to unreasonable risks. If there is no response from the FDA in the form of requests for clarification or additional information, then the trial can commence after the 30-day waiting period.

20.2.2.1 Exploratory IND

In January 2006, the FDA published its final guidelines for what it called an exploratory IND (FDA 2006). A typical exploratory IND (or Phase 0) study would involve a clinical trial conducted early in phase I with very limited human exposure and no therapeutic or diagnostic intent. This type of exploratory IND study should be less complicated and expensive to perform, because less animal toxicity data will, typically, be required. The exploratory IND provides an opportunity to assess early in the process which candidate products hold promise and which do not. This new clinical investigative mechanism will also allow the sponsor:

- To study the mechanism of localization or action of a drug
- To obtain important information on pharmacokinetics
- To improve the selection of the most promising lead product from a group of candidate products designed to interact with a particular diagnostic or therapeutic biological target in vivo
- To explore a product's biodistribution characteristics by using various imaging technologies

20.2.3 Drug Manufacturing and GMP

As shown in Table 20.2, manufacturing of a radiopharmaceutical for SPECT or PET is one of the important aspects of developing a new drug product. Radiopharmaceuticals must be manufactured in accordance with the basic principles of good manufacturing practices (GMP).

The US first promulgated *GMP* regulations for drug products in 1963. The GMP were, subsequently, updated and revised in 1978 and, not with standing several clarifying revisions, remains in effect today. The GMP

Table 20.2 IND requirements

IND requirement	Description
Drug manufacturing	Chemistry, manufacturing, and controls (CMC) section: Information pertaining to the composition, manufacturer, and stability of the drug substance and the drug product (formulation) and the controls used to manufacture and supply consistent batches of the drug
	A Drug Master File (DMF) is a submission to the FDA that may be used to provide confidential detailed information about facilities, processes, or articles used in the manufacturing, processing, packaging, and storing of one or more human drugs
Preclinical pharmacology and toxicology	Preclinical data to permit assessment of whether the product is reasonably safe for initial testing in humans
Clinical protocol	Detailed protocols for proposed clinical studies (Phase I–III)
Investigator information	Information on the qualifications of the clinical investigators (FDA Form 1572)
Commitments	Commitments to obtain informed consent from the research subjects, obtain documentation on the review of the study by an institutional review board (IRB), and adhere to the IND regulations

requirements for human drugs are contained in regulations 21 Code of Federal Regulations (CFR), Parts 210 and 211 (FDA 1997b). These laws are binding regulations and are to be considered the minimum standards below which products are deemed adulterated. The FDA enforces the current GMP (cGMP) based on the cGMP provision in the FDA Drug and Cosmetic (FD & C) Act. This provision states that a drug is deemed adulterated if the methods used in, or the facilities used for drug product manufacture, processing, packing, or holding, do not conform to or are not operated or administered in conformity with cGMP.

The routine FDA approved radiopharmaceuticals used in nuclear medicine for planar or SPECT imaging are manufactured by commercial pharmaceutical industries. As a result, the routine manufacture of these radiopharmaceuticals is regulated by 21 CFR Parts 210 and 211.

For almost two decades, the framework for the regulation of PET radiopharmaceuticals has been marked by controversy, and remains unfinished to this day. In 1997, President Clinton signed into law the FDA Modernization Act (FDAMA) to regulate PET drugs (FDA 1997a), mandating that the FDA provide guidelines for developing procedures for obtaining NDA (or ANDAs) for PET radiopharmaceuticals. Subsequently, the FDAMA suspended the requirement that PET drugs not be marketed under approved applications until two years after FDA established approval procedures and cGMP requirements for the manufacture of PET drugs.

Following almost a decade of evaluation and feedback, the FDA recently proposed regulations intended to ensure that PET drug products meet the safety, identity, strength, quality and purity requirements, as put forth by the FDAMA (FDA 2005b). The proposed rule, which would create Part 212 of 21 CFR, would apply only to the production, quality control, holding, and distribution of PET drugs. The proposed rule incorporates several principles from the 28th Edition of the U.S. Pharmacopeia 2005 (USP 2005) set forth in Chapter <823>, entitled *Radiopharmaceuticals for Positron Emission Tomography – Compounding*, which has served as the Agency "safety net" for PET drug standards, during the development of the proposed PET cGMPs. The USP contains standards that remain significant for PET drugs. Indeed, under the FDAMA, a compounded PET drug is adulterated unless it is produced in compliance with the USP's PET drug compounding standards and the official monograph for the particular PET drug. While Part 212 would be gener-

ally applicable to all PET drug products for human use, the FDA has proposed that PET drugs would meet cGMP by adhering to USP 28 Chapter <823>, even though these provisions are generally less specific and explicit than the proposed requirements.

20.2.3.1 CGMPs for PET Drugs

In September 2005, the FDA formally proposed a rule and a guidance document on the cGMP regulations for the production of PET drugs (FDA 2005b). This guidance document clearly describes acceptable approaches that would enable PET drug producers to meet the requirements in the proposed regulation. In addition, the guidance addresses resources, procedures, and documentation for all PET drug production facilities – academic and commercial. It is important to recognize that the proposed regulations regarding the cGMP requirements contain the minimum standards for quality production of PET drugs at all types of PET production facilities; not-for-profit, academically oriented institutions, as well as commercial producers. This document represents the outcome of many years of interaction between the FDA and the PET community. As proposed, the rule mimics-categorically the general cGMPs, covering:

- Personnel and resources
- Quality assurance
- Facilities and equipment
- Control of components, containers, and closures
- Production and process controls
- Laboratory controls (including stability)
- Finished product controls and acceptance criteria (as well as actions to be taken if the product does not conform to specifications)
- Labeling and packaging; distribution; and complaint
- Handling

The proposed cGMP requirements for the PET drug products differ from the general drug CGMPs of Part 211 in several ways. The key differences in the proposed PET cGMP requirements are as follows (Messplay and Heisey 2005):

- There are fewer organizational restrictions and required personnel
- Multiple operations or storage in the same area are permitted as long as the manufacturer employs adequate organization and other controls

- Aseptic processing requirements are streamlined to be consistent with the nature of the production process
- There are streamlined quality control requirements for components
- Self-verification of significant steps in PET drug production is permitted
- Oversight of production, review of batch records, and authorization of product release, by the same person is allowed
- Specialized quality control requirements for PET drugs produced in multiple subbatches
- Simplified labeling requirements, and
- Conditional final release of PET drug products under certain conditions

Neither the proposed rule nor the draft guidance is final at this time, meaning that the proposed rule is not binding or effective. After the FDA evaluates the comments received regarding the rule and guidance, the agency expects to publish the final version of both documents in the near future. Two years after the final rule takes effect, PET producers will be required to submit NDAs before marketing a PET drug. In the meantime, various PET radiopharmaceuticals can be evaluated clinically under the radioisotope drug research committee (RDRC) approval or using the formal "Investigational New Drug" (IND) research protocols. Also, for the next 2–3 years, the manufacture and distribution of PET drugs, in the United States, can operate under the Practice of Medicine and Pharmacy laws.

20.2.3.2　European GMPs for Radiopharmaceuticals

The role of the European regulatory agency (EMEA) on radiopharmaceuticals, drug development, and regulations was recently discussed in detail (Salvadori 2008). In Europe, radiopharmaceuticals have been exempted from adopting the pharmaceutical regulations, for quite a long time. The only applicable rules were related to the radiation protection and compliance with Pharmacopoeial monographs. As of 1992, the European Pharmacopoeia had more than 30 monographs covering the majority of routinely used radiopharmaceuticals. Directive 89/343/EC extended the existing rules of medicinal products to radiopharmaceuticals compounds used as diagnostic or therapeutic

agents. This Directive is due for implementation by EU Member States in two years. European directives, however, need to be adopted (implemented) by single Member States, as it usually happens with the possibility of introducing changes and with different timeframes. Over the years, several directives (2001/20/EC; 2001/83/EC; 2003/94/EC; 2005/28/EC), relating to pharmaceuticals, have been issued. Since the 1989 Directive, however, nothing has been really done to clarify the regulations concerning radiopharmaceuticals. From a certain point of view, things appear to have worsened. Because pharmaceutical regulations have been always kept as a unique code, mostly focused on conventional medicinal products, regulators have been reluctant to adopt separate regulations for special situations, such as that of radiopharmaceuticals.

Revised GMP requirements for the production of radiopharmaceuticals have been finalized and were published by the European Commission (EC) (EANM 2007). The updates to the annex are intended to make it in compliance with GMP Part II, which lays out additional requirements for active substances used as starting materials. In addition, the EC has sought to bring the regulations up-to-date with advances in the manufacture of radiopharmaceuticals. An initial draft was published for public consultation in December 2006. This process has now been completed and companies now must become compliant with the new requirements. The regulations are broken down into subcategories including quality assurance, personnel, production and documentation and are intended to provide the necessary regulation to prevent cross-contamination, the spread of radioactive material and ensure the quality of the product. This guideline is applicable to manufacturing procedures employed by industrial manufacturers, Nuclear Centers/Institutes and PET Centers for the production and quality control of the following types of products:

- Radiopharmaceuticals
- Positron Emitting (PET) Radiopharmaceuticals
- Radioactive Precursors for radiopharmaceutical production
- Radionuclide Generators

In March 2007, the radio pharmacy committee of the European Association of Nuclear Medicine (EANM) has also released guidelines specifically related to the small-scale preparation of radiopharmaceuticals, also known as guidelines on current good radio pharmacy

practice (CGRP) (EANM 2007). The major aim of EANM was to achieve a consensus document that specifies the needs for radiopharmaceutical preparations in hospitals and academic institutions, not only for research and clinical trial applications, but also for every day nuclear medicine. To cover these specific needs, two distinct parts were included: Part A dealing with radiopharmaceuticals prepared from generators and kits and Part B dealing with other radiopharmaceuticals mainly, but not exclusively, for PET applications.

20.3 FDA Approved PET Drugs

As discussed earlier, FDA approval of a drug or any radiopharmaceutical typically involves submission of an NDA by a manufacturer or a company clearly documenting two major aspects of the drug; (a) Manufacturing of a PET drug and (b) Safety and Effectiveness of a drug with specific indications. Following an extensive review of the NDA application, the FDA may approve the NDA for routine clinical use. The first PET radiopharmaceutical (Table 20.3) to get FDA approval was the $^{82}Sr \rightarrow ^{82}Rb$ generator (Cardiogen-82®, Bracco Diagnostics, Inc) used for myocardial perfusion imaging studies, in 1989. Since that time, approval of NDAs for PET radiopharmaceuticals has been complicated because most of the ^{18}F and ^{11}C radiotracers are prepared by cyclotron facilities in academic research facilities. In 1994, however,

the FDA approved the first NDA for the manufacture of FDG by The Methodist Medical Center (and CTI, Inc) in Peoria, IL, for two clinical indications; (a) to assess myocardial glucose metabolism and (b) to identify epileptic foci with altered glucose metabolism. The NDA (20–306), however, was not valid for FDG manufactured at other centers. In the last two decades, FDG has been used by many investigators as an Investigational New Drug (IND). Today, all the clinical FDG-PET imaging in oncology, in the United States, operates under the Practice of Medicine and Pharmacy laws, that is, through prescription by a physician and dispensing by a registered pharmacist (Callahan et al. 2007).

Since certain PET drugs have been used clinically for 10–20 years, under INDs, the FDA decided to conduct its own review of the published literature. More specifically, the FDA's goal was to evaluate the safety and effectiveness of certain PET drugs, in order to facilitate the process of submitting NDAs for these products by the PET drug industry. Based on its literature review and findings and the recommendations of the Advisory Committee, the FDA has developed the basis for the approval of NDAs and ANDAs for three PET radiopharmaceuticals; [^{18}F]FDG, [^{13}N]Ammonia and [^{18}F]Fluoride. In a notice in the *Federal Register,* in March 2000 (the PET Safety and Effectiveness Notice), FDA presented its findings for three PET drugs for certain indications. It is important to appreciate that the success of FDG-PET in oncology was primarily due to the FDA's approval, by documenting the

Table 20.3 FDA approved PET radiopharmaceuticals

Radiopharmaceutical	A. FDA approval of clinical utility			B. FDA approval of NDA		
	Year	Indication		Year	Number	Applicant/ Company
[^{18}F]Fluoride	1972	Bone Imaging		1972	17–042	New England Nuclear
^{82}Rb- generator	1992	Myocardial Perfusion		1989	19–414	Squibb Diagnostics
[^{18}F]FDG	1994	Epileptic foci		1994	20–306	Methodist Medical and CTI, Peoria, IL
[^{18}F]Fluoride[a]	2000	Bone imaging				
[13N]NH$_4^+$	2000	Myocardial perfusion				NSMC, New York
[^{18}F]FDG	2000	Epileptic foci in brain		2004	70–638	WMCCU, New York
		Myocardial glucose metabolism		2005	21–870	NSMC, New York
		Tumor glucose metabolism				
[^{18}F]FDG	2005	Alzheimer's Disease (AD) and Fronto-temporal dementia (FTD)				

[a]The NDA holder ceased marketing this drug product in 1975. The FDA currently lists sodium Fluoride F 18 injection in the Orange Book's "Discontinued Drug Product List"
WMCCU Weill Medical College of Cornell University, New York, NY; *NSMC* North Shore Medical Center, Manhasset, Long Island, NY

safety and effectiveness based on the published litera-
ture (over a period of 20 years) and not based on data
generated in multicenter Phase I, II, and III clinical
studies sponsored by a manufacturer of FDG. Since
the FDA approved the indications in oncology and car-
diology, the Center for Medicare and Medicaid
Services (CMS) and the insurance companies were
willing to reimburse for FDG-PET studies, in these
areas. In 2005 the FDA also approved the use of
FDG-PET brain scans in the differential diagnosis of
AD and Fronto-temporal dementia (FTD). It must be
noted that, at this time, more than 150 sites in this
country manufacture FDG without a formal NDA
approval.

20.4 PET Drugs and USP

The United States Pharmacopeia (USP), Inc. is a pri-
vate, nonprofit, scientific organization incorporated in
the District of Columbia. USP standards are widely
recognized as authoritative and are enforced by the
FDA and state agencies. The USP establishes stan-
dards through an open participatory process with
established integrity. Volunteers from all areas of
industry, education, medicine, and pharmacy carry out
these activities.

Drug standards are established by the Council of
Experts and by Expert Committees, which are the
USP's scientific decision making bodies. Of the 62
Expert Committees, two deal directly with radiophar-
maceuticals (Hung and Callahan 2004). The commit-
tee charged with setting standards for radio-
pharmaceuticals is the Expert Committee on
Radiopharmaceutical and Medical Imaging Agents,
in the Noncomplex Actives and Excipients Division.
Drug information related to radiopharmaceuticals is
the responsibility of the Expert Committee on
Radiopharmaceuticals in the Information Division.
The USP standards are under continuous revision and
these revisions may include either the creation of a
new standard (i.e., monograph or general chapter) or
revision of an existing standard.

The USP first provided standards for PET radiop-
harmaceuticals in 1988 and currently includes several
general chapters and official monographs related to
PET radiopharmaceuticals (Tables 20.4 and 20.5).

Table 20.4 USP (2004)-NF general chapters related to PET
radiopharmaceuticals

USP General Chapter	
No.	Title
<75>	Sterility tests
<81>	Bacterial endotoxins test
<621>	Chromatography
<821>	Radioactivity
<823>	Radiopharmaceuticals for PET-compounding
<1015>	Automated radiochemical synthesis apparatus
<1225>	Validation of compendial methods

Table 20.5 PET radiopharmaceuticals listed in 2004 USP-NF

[^{11}C]Carbon monoxide (CO)
[^{11}C]Flumazenil
[^{11}C]Mespiperone
[^{11}C]Methionine
[^{11}C]raclopride
[^{11}C]Sodium Acetate
[^{18}F]Fluorodeoxyglucose
[^{18}F]Fluorodopa (FDOPA)
[^{18}F]Sodium Fluoride
[^{13}N]Ammonia
[^{15}O]Water
^{82}Rb-chloride

The 2004 USP-NF contains 73 monographs for
radiopharmaceuticals of which 12 are PET radiophar-
maceuticals. While this regulatory process evolves at
the Federal level, the United States Pharmacopeia
(USP) has continued its role in the development of
drug standards and informational activities relating to
PET radiopharmaceuticals. These activities are aimed
at providing guidance to the profession, thereby help-
ing to ensure the maintenance of high standards for
public health (Hung and Callahan 2004).

References

Aboagye EO, Price PM, Jones T (2001) In vivo pharmacokinet-
ics and pharmacodynamics in drug development using posi-
tron emission tomography. Drug Disc Today 6:293–302
Barrio JR, Marcus CS, Hung JC, et al (2004) A rational regula-
tory approach for positron emission tomography imaging
probes: from "first in man" to NDA approval and reimburse-
ment. Mol Imag Biol 6:361–367

Bergstrom M, Grahnen A, Langstrom B (2003) Positron emission tomography micro dosing: a new concept with application in tracer and early clinical drug development. Eur J Clin Pharmacol 59(5–6):357–366

Callahan RJ, Chilton HM, Ponto JA, et al (2007) Procedure guideline for the use of radiopharmaceuticals 4.0. J Nucl Med Tech 35(4):272–275

Eckelman WC, Rohatagi S, Krohn KA, et al (2005) Are there lessons to be learned from drug development that will accelerate the use of molecular imaging probes in the clinic? Nucl Med Biol 32(7):657–662

European Association of Nuclear medicine, EANM (2007) Guidelines on current good Radiopharmacy Practice (cGRPP) in the Preparation of Radiopharmaceuticals. http://www.eanm.org/scientific_info/guidelines/gl_radioph_cgrpp.php

European Commission (2008) EU Guidelines to GMP. Manufacture of Radiopharmaceuticals, Annex 3, http://ec.europa.eu/enterprise/pharmaceuticals/eudralex/vol-4/2008_09_annex3.pdf

FDA Modernization act (1997a) Positron emission tomography, USC, Pub L, No. 105–115 §121

FDA, Department of Health and Human Services (1997b) 21CFR 210, 211. Washington: Office of the Federal Register National Archives and Records Administration

FDA (2004a) FDA's Critical Path Initiative to new medical products. U.S. Food and Drug Administration Website: http://www.fda.gov/oc/initiatives/criticalpath/

FDA (2004b) FDA's Guidance documents. U.S. Food and Drug Administration Web site: http://www.fda.gov/cder/guidance/index.htm. Created June 16, 2004. Updated August 28, 2007.

FDA (2005a) FDA's Code of Federal Regulations, title 21, volume 5, 21 CFR §361.1. FDA's RDRC program Web site: http://www.fda.gov/CDER/regulatory/RDRC/default.htm

FDA (2005b) FDA's Guidance PET Drug Products. Current Good Manufacturing Practice (CGMP). U.S. Department of Health and Human Services, FDA, Center for Drug Evaluation and Research (CDER) Web site http://www.fda.gov/cder/guidance/index.htm

FDA (2006) FDA's Guidance for industry, investigators, and reviewers, exploratory IND studies. U.S. Food and Drug Administration Web site. http://www.fda.gov/cder/guidance/7086fnl.htm., Created January 12, 2006

FDA (2007) Investigational new drug (IND) application process. U.S. Food and Drug Administration Web site. http://www.fda.gov/cder/regulatory/applications/ind_page_1.htm. Updated May 3, 2007

Hoffman JM, Gambhir SS, Kelloff GJ (2007) Regulatory and reimbursement challenges for molecular imaging. Radiology 245:645–660

Hung JC (2001) Regulation of the compounding of positron emission tomography drugs. Am J Health Syst Pharm 58:134–139

Hung JC, Callahan RJ (2004) USP and PET radiopharmaceuticals: 1997 FDAMA puts standard-setting body at center of regulatory process. J Nucl Med 45:13N–14N

Klimas MT (2002) Positron emission tomography and drug discovery: contributions to the understanding of pharmacokinetics, mechanism of action and disease state characterization. Mol Imaging Biol 4:311–337

Maclean D, Northrop JP, Padgett HC, et al (2003) Drugs and probes: the symbiotic relationship between pharmaceutical discovery and imaging science. Mol Imaging Biol 5:304–311

Messplay GC, Heisey C (2005) PET drugs and cGMPs. Contract Pharma, November/December, www.contractpharma.com

Nunn AD (2006) The cost of developing imaging agents for routine clinical use. Invest Radiol 41(3):206–212

Reichert JM (2003) Trends in the development and approval times for new therapeutics in the United States. Nat Rev Drug Discov 2(9):695–702

Rudin M, Rausch M, Stoeckli M, et al (2005) Molecular imaging in drug discovery and development: potential and limitations of nonnuclear methods. Mol Imaging Biol 7(1):5–13

Salvadori PA (2008) Radiopharmaceuticals, drug development and pharmaceutical regulations in Europe. Curr Radiopharm 1:7–11

Suleiman OH, Fejka R, Houn F, et al (2006) The radioactive drug research committee: background and retrospective study of reported research data (1975–2004). J Nucl Med 47:1220–1226

United States Pharmacopeia, USP (2005) United States Pharmacopeia, 28th edn. Rockville, MD

Wang J, Maurer L (2005) Positron emission tomography: applications in drug discovery and drug development. Curr Top Med Chem 5(11):1053–1075

Index